Fracture Potential of Evaporite Seals during CO_2 Injection Operations
A numerical modelling & field study approach

A thesis submitted in fulfilment of the requirements for the degree of
Doctor of Philosophy

By
Sérgio Carreiras Esperancinha

IMPERIAL COLLEGE LONDON
Department of Earth Science and Engineering

May 2017

Copyright

The copyright of this thesis rests with the author and is made available under a Creative Commons Attribution Non-Commercial No Derivatives license. Researchers are free to copy, distribute or transmit the thesis on the condition that they attribute it, that they do not use it for commercial purposes and that they do not alter, transform or build upon it. For any reuse or redistribution, researchers must make clear to others the license terms of this work.

Declaration of Originality

I, Sérgio Carreiras Esperancinha declare that the work presented in this thesis is my own and all else is appropriately referenced.

Acknowledgements

I thank Professor John Cosgrove, without whom this thesis would not exist in this form. I lack of words to describe my gratitude for having taught me, guided and corrected the various manuscripts of this thesis. Also, a special word of appreciation for all the support and encouragement during some difficult times. Thank you very much.

I would like to thank QCCSRC for the funding, jointly provided by Qatar Petroleum, Shell, and the Qatar Science & Technology Park which allowed me to carry this research. In particular I would like to thank the support given by Iain Macdonald and Bhavna Patel.

To Dr. J.P. Latham, Dr. Jiansheng Xiang and the colleagues Qinghua Lei, Liwei Guo and Ado Farsi for the many hours of patient discussion, the teachings and ideas which enriched this work.

To my colleagues at Imperial, Chris Dean, Chandra Taposeea, Martin Hönig, Marijn van Cappelle and Manuela Stehle who have always been around for a laugh. Also to Mohammed for the great discussions about our passion: football!

A special thank you to the friends for life I have made while in London: Renato, Miriam, Armando, Letícia, Andrew, Francesco, Paulo Sousa and Pedro Barreto. I'm proud to call myself your friend and you certainly gave me strength to keep going even in the toughest times.

To those who are gone but I'm sure would be proud of my achievements: Chico, Artur, Emília and Carlos.

To my dear parents, who instigated in me the love for geology and the pursue of knowledge. They have taught me to question the world, to think, to live and have unconditionally supported me even when my choices took me to distant places. You are my greatest pride.

Finally to Carolina, "a minha Branquinha", that endured four and a half years of what has been very long journey with many ups and downs. It seems we kept the boat afloat in the end and I believe it was all thanks to you.

Abstract

This project, focuses on the potential for evaporite cap-rocks to undergo fluid induced failure as a result of CO_2 injection in underlying carbonate reservoirs. The specific rock properties that control fracture propagation through layered evaporites and the features that might influence fluid flow in these low permeability units were studied using a multidisciplinary approach. Field work was carried out on a local scale studying a gypsum mine, drill cores and several outcrops in order to determine the internal structures within seals that might influence fracture formation. On a regional scale studies were carried out to determine the stress history of the seal in Qatar and the likely fractures it might contain as a result of burial, diagenesis and tectonism. A detailed study of the theory of brittle failure (in particular of fluid induced failure) was also conducted in order to lay down the principles that control stress distribution in the crust. This information allowed to define the boundary conditions for the Finite Discrete Element Method models used to look at fracture propagation in layered materials. It was concluded that evaporite sequences are vertically and horizontally heterogeneous with both primary and secondary layers and interfaces, some of which are linked to internal hydraulic fracturing of the rock. The field studies together with the numerical models show that low friction along an interface contributes to fracture arrest; that the thickness of an incompetent layer is not a decisive factor in determining whether or not a fracture propagates through that weak layer and that a weak layer (low Young's Modulus) is able to impede a fracture that formed in a strong layer from propagating into it. It is also suggested that trough-going fractures are not always formed by the propagation of a fracture through successive adjacent layers but that they occur by the linking of individual extensional fractures to form a through-going fracture.

Table of Contents

PAGE

1. Introduction

1.1 $C0_2$ and sustainability 16

1.2 Enhanced Oil Recovery using CO_2 (CO_2EOR) 19

1.3 Geological Storage of CO_2 24

1.3.1 General Principles 24

1.3.2 Risk assessment – potential for cap-rock failure 27

1.4 Cap-Rock failure: hydraulic fracturing of the cap-rock and fracture impact on permeability – an introduction 29

1.5 Project objectives 33

1.6 Rationale and Methodology 33

2. Cap- Rock Seals and Evaporites

2.1 Cap-Rock Seals 36

2.1.1 General Considerations 36

2.1.2 Evaporites as cap-rocks 39

2.1.3 Evaporite Textures 45

2.2 Evaporites as high fluid pressure indicators 49

3. Field Work

3.1 Introduction 56

3.2 An analysis of the regional geology of Qatar 56

3.2.1 The Arabian Platform 58

3.2.2 The Qatar–South Fars Arch 63

3.2.3 Stratigraphy of Qatar: The Geological Setting of the Hydrocarbon Play in the Arab Basin. 65

3.3 Gypsum Mines Study – Brightling Mine 70

3.3.1 Introduction 70

3.3.2 The Wessex/Weald Basin 70

3.3.3 Brightling Mine and the Purbeck Formation 73

3.3.4 Pillar Face Analysis 78

3.3.4.1 Lithological and stratigraphic description. 79

3.3.4.2 Structural description 86

3.4 Core Analysis 91

3.5 Outcrop studies in Gloucestershire & Somerset 119

3.5.1 Introduction 119

3.5.2 Rationale 121

3.5.3 Tytherrington Quarry Field Work 122

3.5.4 Field work in Lilstock Beach 136

3.5.5 Field work in Watchet – Mercia Mudstone 146

3.6 Summary and learnings obtained from the field observations 151

4. Theoretical Analysis

4.1 Introduction 154
4.2 Stresses in the Earth's Crust 157
4.2.1 Relation between stress and strain 162
4.2.2 Elastic vs Plastic Materials 163
4.3 Brittle Deformation 167
4.3.1 Failure and failure criteria 169
4.3.2 The link between extensional and shear failure 177
4.4 Fluid pressure, effective stresses and hydraulic fractures. 180
4.4.1 Internal hydraulic fractures, vs hydraulic intrusion fractures 184
4.5 Fracture spacing and saturation 188
4.6 Fracture propagation within and through layered media – the state of the art 196
4.6.1 Literature Review - chronological order 196
4.6.2 Learnings from the literature review – a summary 201

5. Numerical Modelling

5.1 Introduction - Numerical Methods for the study of fractures 206
5.1.1 Continuum Problems – Finite Element Modelling 207
5.1.2 Discontinuum Problems – Discrete Element Modelling 208
5.1.3 Transition from Continuum to Discontinuum –The FEMDEM methodology 209
5.2 Verification and calibration of the numerical method 219
5.2.1 Stress distribution in an elastic material, and fracturing of multilayered systems. 220
5.2.2 Fracture propagation 228
5.2.3 Validation of frictional sliding along interfaces 236
5.3 Numerical Simulations for Fracture propagation through layered rocks 238
5.3.1 Effect of interfacial friction along the interface and of overburden stress 239
5.3.1.1 The study of the effect of increasing the interfacial coefficient of sliding friction between two layers on fracture propagation across the interface – Fracture Patterns 241
5.3.1.2 A Study of the impact of vertical (layer-normal) load on fracture propagation – Fracture patterns 248
5.3.1.3 Relation between the coefficient of sliding friction along the layer interfaces, normal load and fracture formation on the development of horizontal stresses. 252
5.3.2 The effect of the elastic modulus (Young's Modulus – E) of adjacent layers on the propagation of fractures across the interface between them 290
5.3.3 The effect of the thickness of an incompetent layer on fracture propagation across it 299

6. Results Discussion and Conclusions

6.1 Introduction 324
6.2 Field Work 327
6.2.1 Brightling Mine and Drill Cores 327
6.2.2 Thyterington 327

6.2.3 Somerset - Lilstock 330
6.2.4 Somerset – Watchet 333
6.3 Numerical Modelling 335
6.3.1 The effect of interfacial friction along an interface and of an overburden stress 335
6.3.2 The effect of the elastic modulus (Young's Modulus – E) of adjacent layers on the propagation of fractures across the interface between them 338
6.3.3 The effect of the thickness of an incompetent layer on fracture propagation across it 346
6.4 Regional Considerations 349
6.5 Conclusions and Recommendations 354
6.5.1 Conclusions 354
6.5.2 Future Considerations 358
Bibliography 360

List Of Figures

FIGURE	PAGE
Figure 1.1: Observed global mean combined land and ocean surface temperature anomalies, from 1850 to 2012	17
Figure 1.2: oil and gas reserves to production ratio (r/p) at the end of 2012	19
Figure 1.3: active world-wide and USA CO2EOR projects from 1986 to 2010.	20
Figure 1.4: Enhanced Oil Recovery process overview.	21
Figure 1.5: Distribution of CO_2 sources, injection sites and transport paths via pipeline across USA	22
Figure 1.6: Main CO_2 projects using anthropogenic CO_2 in North America, April 2003.	22
Figure 1.7: CO2 storage capacity of the Weyburn field during and after EOR operations	24
Figure 1.8: Carbon dioxide pressure-temperature phase diagram	26
Figure 1. 9: workflow for CO2 storage site evaluation.	27
Figure 1.10: potential escape mechanisms of CO2 injected on a sandstone reservoir	28
Figure 1.11: network of satin-spar veins in the Mercia Mudstone, England, UK	31
Figure 1.12: Seismic expression of pipes crossing sealing sequences.	31
Figure 2.1: classification of hydrocarbon seals based upon the mechanism by which seal failure occurs	38
Figure 2.2: graphical representation of the two types of cap-rock seals.	40
Figure 2.3: the production of ten largest oil fields in the world	40
Figure 2.4: ranking of sedimentary rocks according to their ability to form a seal.	42
Figure 2.5: relative permeabilities of different lithologies.	43
Figure 2. 6: Classification of evaporite formation in the depositional-diagenetic setting	43
Figure 2.7: postdepositional evolution through time of evaporitic textures	44
Figure 2.8: sabkha classification	44
Figure 2. 9: summary of the evaporitic carbonate textures and its depositional significance	46
Figure 2.10: summary of the CaSO4 and NaCl syndepositional textures and their typical position in a depositional basin	47
Figure 2.11: types of secondary anhydrite textures	47
Figure 2.12: evolution of gypsum/anhydrite sediments when subjected to secondary alterations as a result of burial and exhumation	48
Figure 2.13: Pore pressure increase graph	52
Figure 2.14: schematic rehydration of nodular anhydrite to porphyroblastic and alabastrine gypsum	55
Figure 3.1: A satellite image of the Persian Gulf area, with the Qatar Peninsula in the centre.	57
Figure 3.2: A simplified map of the Arabian Plate	57
Figure 3.3: Selected structural and tectonic features of the Arabian Plate	59
Figure 3.4: Simplified geologic cross section across Saudi Arabia and Qatar	61
Figure 3.5: Arabian Platform stratigraphic chart	62
Figure 3.6: Simplified plate tectonic evolution of the Persian Gulf and Arabian Peninsula.	63
Figure 3.7: Tectonic map of the central Persian Gulf	65
Figure 3.8: Stratigraphic column of the Late Jurassic and Early Cretaceous of the Arab Basin	67
Figure 3.9: Depositional model for the Arab Formation and the corresponding idealized cycles	68
Figure 3.10: drill-cores showing the typical aspect of the Hith Formation.	69
Figure 3.11: Geographical location of the Wessex and Weald Basins	71
Figure 3.12: Depth contour map of the Variscan basement and simplified north-south geological cross section through the central Weald Basin	72
Figure 3.13: Generalized stratigraphical column for the Wessex Basin	75
Figure 3.14: Gross isopach map for the Portland Sandstone in the Weald and Wessex basins	76

Figure 3.15: Geographical location and aerial photography of the British Gypsum, Brightling Mine. 77
Figure 3.16: traditional room and pillar mining technique 77
Figure 3.17: Sketch of an aerial view of the study location at Brighling Mine 79
Figure 3. 18: general view of a pillar at Brightling Mine 81
Figure 3. 19: detail of the base of two different pillars at Brightling mine 82
Figure 3.20: Close up view of a pillar of Brightling mine and detail of a secondary satin spar vein 83
Figure 3. 21: detail of the top section of a pillar at Brightling mine where the different facies can be observed 84
Figure 3.22: detailed view of a pillar at Brightling Mine with the various identified facies. 85
Figure 3. 23: General view of the studied pillars in Brightling Mine 86
Figure 3. 24: image of a mudstone rich section at the base of one of the pillars in Brightling Mine. 88
Figure 3. 25: pillar showing large joints (VFc) highlighted in yellow with no infill. 88
Figure 3. 26: Detail of the rock face showing horizontal and vertical fractures filled with satin spar 90
Figure 3. 27: Location of the cored wells within the Weald Basin showing their location relative to Brightling Mine. 92
Figure 3.28: Winchester-1 side wall cores showing the sequence of evaporites 94
Figure 3.29: section of core from the Goodley Bridge Well 95-97
Figure 3.30: section of core of from Normandy-1 well 99-110
Figure 3.31: section of core of from Warlingham well 113-117
Figure 3. 32: Location and structural map showing the Bristol Channel Basin in relation to surrounding basins in southwest England 118
Figure 3. 33: N-S cross section through the Bristol Channel area 119
Figure 3. 34: geographical location and aerial photo of the studied section at Tytherington Quarry. 121
Figure 3. 35: Exposure of the 30° dipping limestone occurring ath Tytherington Quarry. 122
Figure 3. 36: stages of evolution of a thrust. 123
Figure 3. 37: limestone bed bounded by two different types of bedding planes, an upper irregular stylolite plane and a lower, smooth plane defined by a thin layer of clay. 123
Figure 3. 38: two different views of stylolite surfaces that have formed by pressure solution along a bedding plane in limestones of Thyterrington 124
Figure 3. 39: The three stress configurations linked to the three major types of shear fractures 125
Figure 3. 40: Overall view of the quarry cliff face towards the NE (top) and SE (bottom). 126
Figure 3. 41: example of a thrust plane being cut by a through-going strike-slip (wrench) fault in the limestones of Thyterrington Quarry. 127
Figure 3.42: photograph of the cliff face where a conjugate pair of strike slip faults planes showing the vertical tensile fractures that intersect them can be seen. 128
Figure 3. 43: structural map of the Bristol channel area 129
Figure 3. 44: The strain distribution in a buckled homogeneous isotropic layer. 129
Figure 3.45: vertical section of Tytherington quarry showing 7 limestone layers where the interfaces between them are stylolitized. 131
Figure 3. 46: general view of the cliff face at Tytheringtonquarry showing two thick limestone sections separated by a thin clay layer 132
Figure 3. 47: photograph and sketch of a small section of the cliff face at Tytheringtonquarry showing how bedding-normal are able to cut through the stylolitized interfaces between limestone layers but are arrested at a very thin clay layer. 133
Figure 3.48: photograph and sketch of a small section of the cliff face at Tytheringtonquarry showing how bedding-normal are able to cut through the stylolitized interfaces between limestone layers but are arrested at a very thin clay layer. 134
Figure 3. 49: Geographical location, aerial photo and general view of the outcrops in Lilstock Beach, Somerset. 135
Figure 3. 50: structural framework of Lilstock, Somerset 137
Figure 3. 51: Vertical tensile fractures being arrested at the interface between a limestone and a shale. 138
Figure 3. 52: Vertical trensile fractures propagating through a shale layer vs vertical tensile fractures being arrested at that interface 139

Figure 3. 53: view of the cliff face at Lilstock Beach, which shows from different angles two independent tensile fractures that have formed in the competent limestone layers being linked by an oblique fracture in the shale. 140
Figure 3. 54: Vertical tensile fractures being arrested at the interface between a limestone and a shale. 141
Figure 3. 55: A limestone-shale interface at Lilstock Beach showing how fractures do not propagate across the interface. 142
Figure 3.56: Fracture mismatch between two adjacent limestone layers 143
Figure 3.57: Different families of fractures in adjacent limestone layers 144
Figure 3. 58: Outcrops of the Mercia Mudstone Group in England and Wales. 146
Figure 3. 59: Triassic lithofacies in England and the Southern North Sea. 146
Figure 3. 60: geographical location, aerial view and genral view of the studied section at Watchet, Somerset. 147
Figure 3. 61: base of the Mercia Mudstone outcrop analysed in Watchet showing the layers of primary anhydrite nodules 148
Figure 3. 62: Close up of the cliff face at Watchet showing the pervasive network of satin spar veins of the Mercia Mudstone. 149
Figure 3. 63: comparison of the cross-cut relationship between the of the satin-spar veins observed in Mercia Mudstone outcrops in Watchet and those observed in Brightling Mine. 150

Figure 4. 1: A graph of frequency against vertical extent for natural hydraulic fractures (pipes) identified on 3D seismic data from offshore Mauritania 155
Figure 4.2: a) Sketch of a normal fault and associated damage zones in Jurassic (Liasic) rocks at Kilve, Somerset 155
Figure 4.3: The resolution of a force into its normal and shear force components 158
Figure 4.4: The resolution of stress in a uniaxial stress field 158
Figure 4.5: stress ellipsoid showing the principal stresses acting on a point in the centre of the ellipsoid 159
Figure 4.6: stress components acting on the faces of a small cube that represents a point 161
Figure 4.7: The Mohr circle: Graphical representation of Equations (11) and (12). 161
Figure 4.8: Homogeneous strain. a) Undeformed state. b) Simple shear. c) Pure shear. 163
Figure 4.9: stress-strain curve for elastic-plastic deformation. 166
Figure 4. 10: three types of deformation (elastic, viscous and plastic) 167
Figure 4.11: a) Natural examples of extensional and shear fractures in Utah, USA b) the two modes of brittle failure: i) Shear failure and ii) Tensile Failure 167
Figure 4. 12: a) potential shear failure plane; b) and c) triaxial deformation rig set up in which a confining pressure ($\sigma 3$) is applied via a fluid pressure, Pf. 170
Figure 4.13: graphical expression of the results rock failure experiments 170
Figure 4.14: same data as Figure 4.12, plotted as a series of Mohr circles. 172
Figure 4.15: Mohr circle representing a stress state that causes rock failure. 172
Figure 4. 16: schematic representation of stress concentration around a microscopic flaw inside a body subjected to tensile stress 173
Figure 4.17: graphical expression of the Griffith criterion for tensile failure. 174
Figure 4.18: the graphical expression of the combined Mohr-Coulomb-Griffith criteria 175
Figure 4.19: Mohr circle representing a tensile fracture. 176
Figure 4.20: Mohr circle representing an hybrid fracture. 177
Figure 4.21: Range of magnitudes of differential stress and 2Θ angles for the several types of failure. 177
Figure 4.22: Conjugate sets of en echelon tension fractures defining zones of shear failure in the rock. 178
Figure 4. 23: field example of an embryonic shear fracture through a shale layer linking tensile fractures that formed in the limestone layers. 179
Figure 4.24: Idealised model showing the formation of through-going shear fractures by the linking of individual, isolate extensional fractures 179
Figure 4. 25: Six stages in the deformation (left to right) of an axially loaded elastic slab in which an inclined crack is initially present 180
Figure 4.26: effect of increasing fluid pressure pf in a rock, illustrated by a Mohr Diagram. 182

Figure 4. 27: Biot's poroelastic effect as illustrated by a porous rock within a container. 183
Figure 4. 28: a flaw in a permeable porous rock will "feels" the effect of the poroleastic effect when the stress across the grain-flaw part of the flaw is less than the pore fluid pressure. 184
Figure 4. 29: internal hydraulic fracturing VS hydraulic intrusion fractures 186
Figure 4. 30: a) Mohr circle representing a stable stress configuration; b) the effect of fluid pressure increase Δp on an horizontally unconfined layer; c) the effect of fluid pressure increase Δp on horizontally confined layer 186
Figure 4. 31: An anisotropic (bedded) rock subjected to a biaxial stress field 187
Figure 4. 32: Uniform tensile stress σT acting in a single, competent unit caused by the lateral flow of the adjacent, less competent beds in response to a layer-normal load caused by the overburden. 190
Figure 4. 33: Relationship between fracture separation and bed thickness for different rock types. 191
Figure 4. 34: Mechanism for the control of the spacing of hydraulic fractures by the permeability of the rock. 193
Figure 4. 35: Three types of spacing distribution found in natural fractures 194
Figure 4. 36: fracture propagation at a strong interface vs arrest at a weak interface. 201
Figure 4. 37: influence of the elastic modulus on the propagation of a fracture across an interface. 202
Figure 4. 38: influence of the coefficient of sliding friction along a layer interface on fracture propagation across it. 203
Figure 4. 39: influence of the thickness of the incompetent layer on the propagation of a fracture across it. 203

Figure 5.1: numerical methods for rock mass analysis 206
Figure 5.2: numerical integration using the Finite Element Analysis method. 207
Figure 5.3: Through-thickness crack in an infinite plate subjected to a remote tensile stress. 210
Figure 5.4: stresses near the tip of a crack in an elastic material 210
Figure 5.5: Mode I fracture propagation in a discrete crack model 211
Figure 5.6: strain softening stress-strain curve. 213
Figure 5.7: Schematic illustration of the transition from the elastic zone to the fracture (broken) zone via the plastic zone around the tip of a mode I fracture: single-crack model. 213
Figure 5.8: Representation of a fracture-matrix solid system 214
Figure 5.9: representation of a pre-existing fracture in a) the initial closed state, and b) a deformed state after opening and sliding 214
Figure 5.10: Three-layer elastic model and its boundary conditions 216
Figure 5.11: FEMDEM numerical simulation stages of fracture patterns forming in a shale-limestone composite subject to steady shortening normal to the layering 217
Figure 5.12: seven-layer elastic model and its boundary conditions 218
Figure 5.13: effect of an increasing normal stress on fracture propagation through a multi-layered model. 217
Figure 5.14: Three-layer elastic model and its boundary conditions: 220
Figure 5.15: horizontal stress distribution within the three-layer model shown in Figure 5.14 221
Figure 5.16: 1MPa (confining pressure) model showing shear fractures developing in the bounding shale layers and tensile fractures forming in the limestone middle layer 221
Figure 5. 17: Boundary conditions used for evaluation of the differential stresses development within a single layer during layer-parallel extension 222
Figure 5. 18: Fracture models showing the change in orientation and fracture type resulting from the increasing differential stresses generated by an increasing vertical load 224
Figure 5. 19: Geological examples showing the effect of the differential stress magnitude on the geometry of extensional fractures. 225
Figure 5.20: differential stress magnitudes vs spatial organization of fractrures 225
Figure 5. 21: Differential stress build up for different values of vertical pressure 226
Figure 5. 22: Sampling points (black dots) where horizontal stress data were collected during the course of the experiment. 226
Figure 5. 23: Horizontal stress plots for a one layer model similar to the one presented on Figure 5.22 versus accumulated strain. 227

Figure 5. 24: FEMDEM Model setup for a) the uniaxial compressive strength (UCS) test and b) the Brazilian disc (BD) test 230
Figure 5.25: results obtained for BD and UCS tests for a value of GI =20 J/m2and GII = 600 J/m2 231
Figure 5.26: Calibration of energy release rates for simulating intact rock failure of a limestone 232
Figure 5.27: Calibration of energy release rates for simulating intact rock failure of a shale 233
Figure 5. 28: Calibration of energy release rates for simulating intact rock failure of gypsum: 234
Figure 5.29: Model set-up for the sliding friction testing 236
Figure 5.30: Results of the modelling of a sliding block on a horizontal surface. 239
Figure 5.31: boundary conditions used for modelling the impact of the coefficient of sliding friction and the layer-normal stress on fracture propagation through multilayered sequences. 242
Figure 5.32: Numerical models testing the influence of the coefficient of sliding friction of layer boundaries on the propagation of fractures through a multilayered sequence when the layer normal load is 1MPa. 243
Figure 5.33: Numerical models testing the influence of the coefficient of sliding friction of layer boundaries on the propagation of fractures through a multilayered sequence when the layer normal load is 10MPa 244
Figure 5.34: Numerical models testing the influence of the coefficient of sliding friction of layer boundaries on the propagation of fractures through a multilayered sequence when the layer normal load is 25MPa 245
Figure 5.35: Numerical models testing the influence of the coefficient of sliding friction of layer boundaries on the propagation of fractures through a multilayered sequence when the layer normal load is 50 Mpa 246
Figure 5.36: Numerical models testing the influence of the coefficient of sliding friction of layer boundaries on the propagation of fractures through a multilayered sequence when the layer normal load is 75 Mpa 247
Figure 5. 37: sequence of models that compares the effect of increasing the layer-normal load on fracture development 248
Figure 5. 38: Stress distribution in the 5 experiments represented in Figure 5.37 at the moment where the first fracture appears 249
Figure 5. 39: horizontal stress plots for experiments where the coefficient of friction is 0.6 to the point where the first fracture is formed. 250
Figure 5. 40: location of the sampling points at which the horizontal stress was monitored in the three-layer models 251
Figure 5. 41: Horizontal stress profiles for 3 models with a coefficient of friction along the layer interfaces of zero (μ=0). Point A. 1, 10 and 25 Mpa 253
Figure 5. 42: Horizontal stress profiles for a model in which the coefficient of friction (μ) along the layer interfaces is zero . Point A. 1, 10 and 50 Mpa 254
Figure 5. 43: Horizontal stress profiles for a model in which the coefficient of friction (μ) along the layer interfaces is zero . Point A. 75 Mpa 254
Figure 5. 44: 3-layer fracture model with μ=0 and a σv = 50MPa. 255
Figure 5.45: Horizontal stress profiles for models in which the coefficient of friction (μ) along the layer interfaces is zero. Point B. 1, 10, 25 and 50 Mpa 256
Figure 5. 46: The horizontal stress profile for a model with the coefficient of friction (μ) along the layer interfaces of zero and subjected to a layer-normal stress of 75Mpa. Point B 257
Figure 5. 47: The horizontal stress profile for a model with the coefficient of friction (μ) along the layer interfaces of zero and subjected to a layer-normal stress of 1, 10, 25, 50 and 75Mpa. Point C 258
Figure 5. 48: horizontal stress profiles for an experiments where the layer-normal stress, σv, was 1Mpa (blue line) and a coefficient of friction along the layer interfaces of zero (μ=0). Point C 258
Figure 5.49: 3-layer fracture model with μ=0 and a $\sigma_{v=}$1MPa. 259
Figure 5. 50: Horizontal stress profiles for models with the coefficient of friction (μ) along the layer interfaces equal to zero subjected to a 10 and 25 MPa of layer-normal stress. Point C. 260
Figure 5. 51: Horizontal stress profiles for models with the coefficient of friction (μ) along the layer interfaces equal to zero subjected to a 50 MPa (yellow lineo) of layer-normal stress. Point C 260
Figure 5. 52: 3-layer fracture model with μ=0 and a σv=50MPa. 261
Figure 5. 53: Horizontal stress profile for model with the coefficient of friction (μ) along the layer interfaces equal to zero subjected to a 75 Mpa of layer normal stress. Point C. 262

Figure 5. 54: Horizontal stress profiles for models with the coefficient of friction (μ) along the layer interfaces equal to 0.6 (blue line) and 0 (blue doted line), subjected to a 1MPa layer-normal stress 263
Figure 5. 55: comparison between models with a coefficient of sliding friction of 0.6 and 0 at different accumulated strains. 264
Figure 5. 56: Horizontal stress profiles for models with the coefficient of friction (μ) along the layer interfaces equal to "0.6" (red line) and "0" (red doted line), subjected to a 10MPa layer-normal stress. Point A 265
Figure 5. 57: Horizontal stress profiles for models with the coefficient of friction (μ) along the layer interfaces equal to "0.6" (grey line) and "0" (grey doted line), subjected to a 25MPa layer-normal stress. Point A 265
Figure 5. 58: Horizontal stress profile for models with the coefficient of friction (μ) along the layer interfaces equal to "0.6" (yellow line) and "0" (yellow dotted line), subjected to a 50MPa layer-normal stress. Point A. 266
Figure 5. 59: snapshot of two 3-layer models with a layer normal stress of 50MPa and a coefficient of sliding friction along the layer interfaces equal to 0 (top) and 0.6 (bottom) 267
Figure 5. 60: a) Horizontal stress profile for models with the coefficient of friction (μ) along the layer interfaces equal to "0.6" (blue line) and "0" (blue doted line), subjected to a 1MPa layer-normal stress. Point B 268
Figure 5. 61: a) Horizontal stress profile for models with the coefficient of friction (μ) along the layer interfaces equal to "0.6" (red line) and "0" (red doted line), subjected to a 10MPa layer-normal stress. Point B 269
Figure 5. 62: a) Horizontal stress profile for models with the coefficient of friction (μ) along the layer interfaces equal to "0.6" (grey line) and "0" (grey doted line), subjected to a 25MPa layer-normal stress . Point B 270
Figure 5. 63: a) Horizontal stress profile for models with the coefficient of friction (μ) along the layer interfaces equal to "0.6" (yellow line) and "0" (yellow doted line), subjected to a 50MPa layer-normal stress. Point B 271
Figure 5. 64: a) Horizontal stress profile for models with the coefficient of friction (μ) along the layer interfaces equal to "0.6" (green line) and "0" (green doted line), subjected to a 75MPa layer-normal stress. Point B 272
Figure 5. 65: a) Horizontal stress profile for models with the coefficient of friction (μ) along the layer interfaces equal to "0.6" (blue line) and "0" (blue doted line), subjected to a 1MPa layer-normal stress. Point C 273/274
Figure 5. 66: a) Horizontal stress profile for models with the coefficient of friction (μ) along the layer interfaces equal to "0.6" (red line) and "0" (red doted line), subjected to a 10MPa layer-normal stress . Point C 275
Figure 5. 67: a) Horizontal stress profile for models with the coefficient of friction (μ) along the layer interfaces equal to "0.6" (grey line) and "0" (grey doted line), subjected to a 25MPa layer-normal stress. Point C 276
Figure 5. 68: a) Horizontal stress profile for models with the coefficient of friction (μ) along the layer interfaces equal to "0.6" (yellow line) and "0" (yellow doted line), subjected to a 50MPa layer-normal stress. Point C 277
Figure 5. 69: Horizontal stress profile for models with the coefficient of friction (μ) along the layer interfaces equal to "0.6" (green line) and "0" (green doted line), subjected to a 75MPa layer-normal stress. Point C. 278
Figure 5. 70: Horizontal stress profile obtained from four points (G - red dotted line/G'- red line and H- green dotted line/H'- green line) on opposite sides of the bonded interface between the top and middle layers and the bottom and middle layers. 280
Figure 5. 71: Sampling points to measure stress propagation across layer boundaries. 280
Figure 5. 72: Horizontal stress profiles obtained for points A and A' (see Figure 5.71). 283
Figure 5. 73: Fracture patterns for a 3-layer model at ε=1% (end of deformation). 284
Figure 5. 74: Horizontal stress profiles obtained for points B and B' (see Figure 5.71). 285
Figure 5. 75: Fracture patterns for a 3-layer model at ε=1% (end of deformation) 286

Figure 5. 76: Fracture patterns and stress distribution for a 3-layer model at ε=1% (end of deformation). The coefficient of sliding friction at the layer interface is μ=0.6 and layer-normal load is 25 MPa. E2 = 15 GPa 291/293
Figure 5. 77: Fracture patterns and stress distribution for a 3-layer model at ε=1% (end of deformation). The coefficient of sliding friction at the layer interface is μ=0.6 and layer-normal load is 25 Mpa. E2 = 3 GPa. 294
Figure 5. 78: Fracture patterns and stress distribution for a 3-layer model at ε=1% (end of deformation). The coefficient of sliding friction at the layer interface is μ=0.6 and layer-normal load is 25 Mpa. E2 = 1.5GPa. 295
Figure 5. 79: Fracture patterns and stress distribution for a 3-layer model at ε=1% (end of deformation). The coefficient of sliding friction at the layer interface is μ=0.6 and layer-normal load is 25 Mpa. E2 = 0.6GPa. 296
Figure 5. 80: seven stages in the layer-parallel deformation of a multilayer model containing a thin weak layer (2mm thick) 304/305
Figure 5. 81: eight stages in the layer-parallel deformation of a multilayer model containing a thin weak layer (6mm thick) 306-308
Figure 5. 82: six stages in the layer-parallel deformation of a multilayer model containing a thin weak layer (2.5cm thick) 309/310
Figure 5. 83: six stages in the layer-parallel deformation of a multilayer model containing a thin weak layer (5 cm thick) 311/312
Figure 5. 84: eight stages in the layer-parallel deformation of a multilayer model containing a thin weak layer (7.5 cm thick) 313/314
Figure 5. 85: six stages in the layer-parallel deformation of a multilayer model containing a thin weak layer (10 cm thick) 315/316
Figure 5. 86: eight stages in the layer-parallel deformation of a multilayer model containing a thin weak layer (10 cm thick) 317-320

Figure 6.1: Flowchart showing the several information sources used in this project and how they relate to each other. 326
Figure 6.2: Uniform tensile stress acting in a single, competent unit caused by the lateral flow of the adjacent, less competent beds in response to a layer-normal load caused by the overburden. 332
Figure 6.3: link between tensile and shear fractures 333
Figure 6.4: graph of strain versus extensional stress for materials with different values of Young's Modulus. 340
Figure 6. 5: horizontal stress versus accumulated strain within the central layer for the four experiments. 340
Figure 6.6: classical versus proposed model for fracture propagation into a low modulus layer 341
Figure 6.7: Fracture patterns and stress distribution for a 3-layer model after an extension of ε=1% (end of deformation). The coefficient of sliding friction at the layer interface is μ=0.6 and layer-normal load is 10 MPa. 342
Figure 6. 8: Fracture patterns and stress distribution for a 3-layer model after an extension of ε=1% (end of deformation). The layers are bonded and the layer-normal load is 10 MPa. 343-345
Figure 6. 9: The linking of extensional fractures in adjacent strong layers by fractures forming in the intervening weak rock. 347
Figure 6. 10: A simplified map of the Arabian Plate, with plate boundaries, showing the approximate plate convergence vectors, and principal geologic features 349
Figure 6.11: Cross section of a lithospheric plate and corresponding stress regimes associated with the formation of a) normal faults b) wrench faults and c) thrust faults 350
Figure 6.12: Failure criteria for the formation of new wrench/thrust faults or the reactivation of pre-existing wrench/thrust faults. 353
Figure 6. 13: Part of the stratigraphic column for Qatar showing the Hith Formation (the main seal) and the underlying carbonate rich reservoir. 353

Chapter 1

Introduction

1.1 $C0_2$ and sustainability

One of the biggest sustainability challenges facing the world today is to provide the necessary energy for a growing economy while changing the paradigm by which that energy is utilized. For the necessary economic prosperity – one that enables the rich countries to maintain their average quality of living while also sustaining part of the cost to allow poorer countries to improve theirs - this energy will have to be abundant, accessible and affordable. On the other hand it is essential that anthropogenic carbon emissions are lowered so that the effects of climate change are mitigated. In other words, the world needs to find a solution to two seemingly conflicting issues: lowering CO_2 emissions and provide energy to an increasingly populated world and in economic development. In this context CO_2EOR and Carbon Capture and Storage (CCS) might represent essential tools in helping to solve these two important problems.

According to Sachs, J. (2014), director of the UN Sustainable Development Solutions Network, the world's current energy consumption is at an equivalent of 170 kg of oil in primary energy per $ 1,000 of output. This value is obtained by adding the annual consumption of oil, gas, coal, renewable and nuclear energies and converting it in units of oil equivalent. Also according to the same source, in terms of CO_2 emissions, each unit of primary energy (measured in tonnes of oil equivalent) contributes with 2.4 tonnes of this gas to the atmosphere, which at the present day world economy (estimated value of $90 trillion) represents around 36 billion tonnes of CO_2 emitted into the atmosphere annually.

These large amounts of carbon dioxide being emitted to the atmosphere have had an in impact on the global climate patterns, and the 2013 IPCC report, clearly states that since the mid-20th century the dominant cause of observed climate change is human activity. The report also asserts that warming in the climate system is unequivocal; stating that global surface temperature change for the end of the 21st century is likely to exceed 1.5°C relative to 1850 to 1900 (IPCC, 2013)(Figure 1.1).

In a report for the World Bank made by the Potsdam Institute for Climate Impact Research and Climate Analytics (World Bank - PIK, 2012), the likely impacts and risks that would be associated with a 4°C warming (a real possibility according to the latest estimates) within this century are presented. Events such as heat waves, severe drought and major floods are thought to become recurrent as a result of increasing temperatures, and to have worldwide effects, reducing agricultural production, industrial output, and political stability. Real action to tackle this problem was then needed, and since the 2009 Climate Convention Conference in Copenhagen, the international community has agreed to

establish that global mean warming should not overcome a 2°C increase above the preindustrial climate. In order for this to be accomplished it will be necessary that today's annual emissions decline to around 15 billion tons by mid-century (Sachs, 2014). For this reduction to occur without jeopardizing the much needed economic development, it is essential to operate deep changes in the way the world uses energy. Cities and industrial processes have to become more efficient and means of transportation have to shift towards electrical power, at the same time that primary production of energy becomes low on carbon which can be achieved by replacing the use of coal by lower carbon natural gas, nuclear power or renewable energies such as solar and wind.

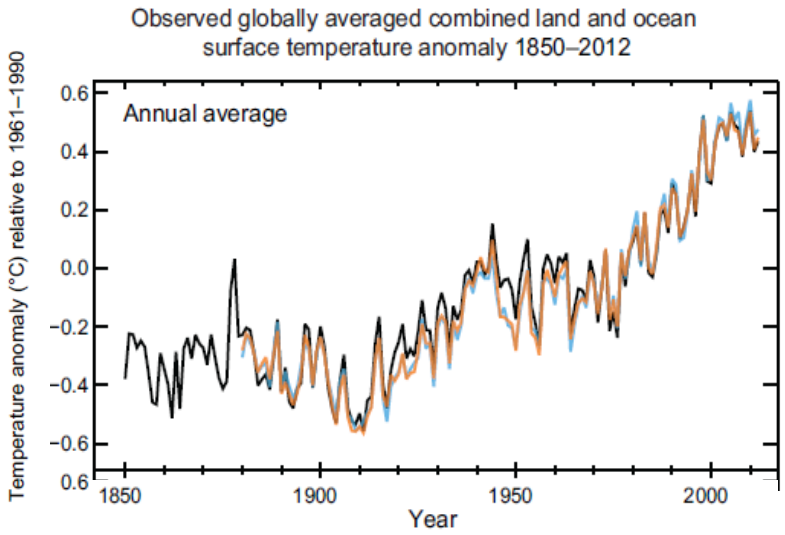


Figure 1.1: Observed global mean combined land and ocean surface temperature anomalies, from 1850 to 2012 from three data sets compared to the mean temperatures of 1961-1990. Adapted from IPCC, 2013.

Even though, and despite the fact that the world will most likely evolve into energy systems fed by alternative energy sources, it is widely accepted within the scientific community that the use of fossil fuels will still be a reality for many years, as most present day human activities and used materials depend on this source. In that sense one of the most valuable and effective options might be the carbon capture and storage technology (CCS), which allows large amounts of CO_2 to be stopped from being sent to the atmosphere and stored in deep underground geological formations as several experts agree:

Fossil fuels such as oil, gas and coal will be dominant energy sources for decades to come, and carbon capture and storage, CCS, is therefore one of the most important measures in the long term for reducing carbon emissions globally. - Arne Fredheim, Specialist Downstream Processing Statoil, Norway.

All future energy demand scenarios agree that fossil fuels will continue to be the major energy source for most, if not all, of this century. Implementation of CCS technology, sooner rather than later, is therefore essential as one of the many carbon mitigation mechanisms needed to avoid catastrophic climate change. - Prof. Geoff Maitland, Professor of Energy Engineering, Director of the Qatar Carbonates and Carbon Storage Research Centre, Imperial College, London

In a 2009 interview, Marvin Odum president of Shell Oil Corporation stated that oil demand would double by 2050, in order to sustain the needs of a growing world economy (Odum, 2009). Whether this prediction is fulfilled or not (global energy consumption has slowed down in 2012, mainly due to an worldwide economic crisis), it is a fact that global oil consumption has increased by 890 000 barrels per day (b/d) and oil producing countries have increased their total production by 1.9 million b/d (BP, 2013) which clearly means that there is a rising demand for this energy source.

According to the 2013 BP Statistical Review, the world proved oil reserves at the end 2012 reached 1668.9 billion barrels, sufficient to meet 52.9 years of global consumption, and the proved natural gas reserves at end- 2012 stood at 187.3 trillion cubic metres, sufficient to meet 55.7 years of global production, at current production rates (Figure 1.2). These numbers clearly demonstrate that there is still a large amount of reserves remaining in the several known reservoirs around the world to which we have to add the prospective resources which can be discovered in frontier areas (deserts, ice-covered lands, deep waters, and remote continental interiors). A good example are the giant discoveries made in the pre-salt carbonate reservoirs in the offshore Santos Basin, Brazil which were considered to be a frontier area until the first well was successfully drilled. These reserves have largely boosted the reserves to production ratio (r/p) of South America – and consequently the world's average r/p – around 2007. Having said this, the existence of unexplored areas of the globe which may contain large amounts of hydrocarbons is a reality: it was estimated by a 2008 USGS survey (USGS, 2008) that the area north of the Artic Circle has a total of 412 billion barrels of oil equivalent undiscovered and technically recoverable, distributed along 25 geologically defined areas thought to have potential for petroleum. The problem lies in the accessibility of these reservoirs, which is extremely difficult, making their exploitation a costly task. It is also important to refer that to date, it is estimated the world has consumed less than 8% of the total volume of oil discovered so far in the several reservoirs around the world (Sandrea & Sandrea, 2007), and that the average recovery factor for this hydrocarbon - calculated using data from mature fields around the world - is between 20% and 40% (Muggeridge, et al., 2013). In other words, there is an average of 65% of oil resources that are left behind (BP Global). In contrast, gas reservoirs experience much higher recovery factors (between 80 to 90%).

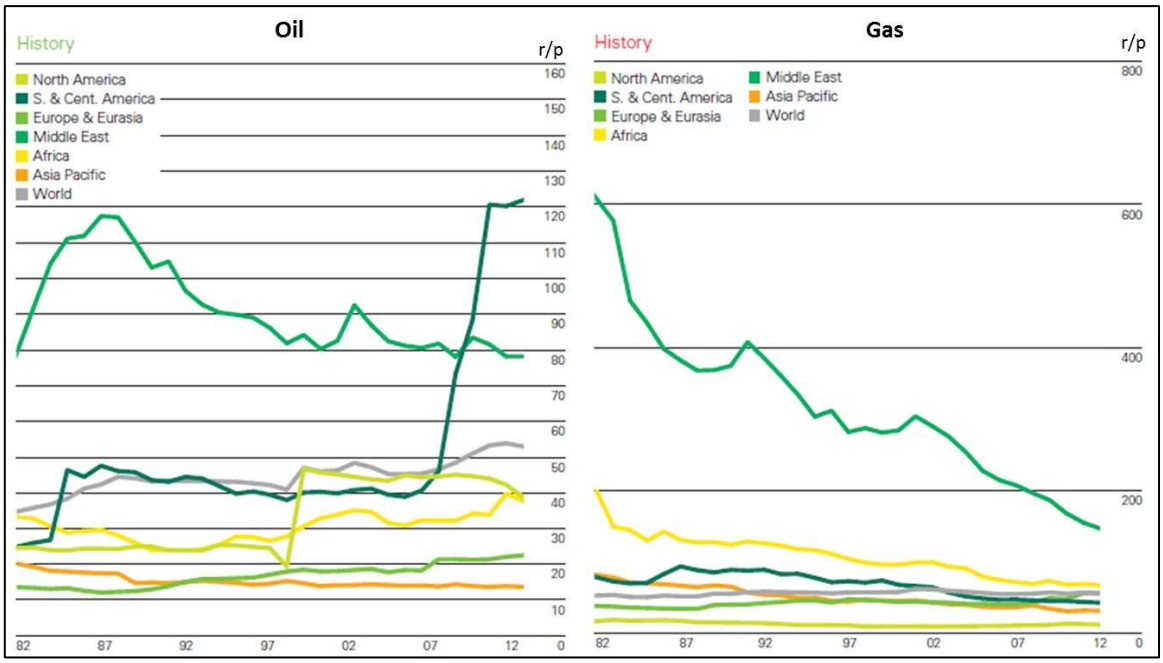


Figure 1.2: oil and gas reserves to production ratio (r/p) at the end of 2012. This ratio is obtained by dividing the remaining reserves the end of any year by the production in that year, the result is the length of time that those remaining reserves would last if production were to continue at that rate. Adapted from BP, 2013.

If recovery is improved to a point where it meets that of typical gas fields, it could double the current reserves to production ratio and consequently provide more time for the world to develop alternative energy sources and technologies (Muggeridge, et al., 2013). In this context, CO_2 injection could play a very important role in EOR as gases captured as bypasses from industrial processes can be injected into the reservoir as a supercritical fluid at high pressure, causing the oil to swell, to become less viscous and also forcing it out of the pores. CO_2EOR was firstly employed in the early 70's in Texas and since then it has been a case of success in several projects, being currently the method which is gaining most popularity.

1.2 Enhanced Oil Recovery using CO_2 (CO_2EOR)

Enhanced oil recovery techniques, also called tertiary recovery come into play when primary – production using natural pressure of the reservoir and that allows about 5 to 10% of the oil in the reservoir to be extracted - and secondary- injection of high pressure fluids, usually water, to drive the residual crude oil and gas remaining after the primary phase and allows additional 25-30% of the oil in the reservoir to be extracted - techniques are not able to deliver enough production. Three major categories of EOR have been found to be commercially successful: thermal recovery, chemical injection and gas injection. The first involves the introduction of heat such as steam to lower the viscosity of the oil;

chemical injection uses polymers to increase the effectiveness of water-flooding operations, and gas injection uses gases (natural gas, nitrogen or CO_2) to maximise recovery.

CO_2EOR is included in the third group and it was firstly tested at large scale in the 1970s in the Permian Basin of West Texas and south-eastern New Mexico. Since then, this technique has been increasingly used in order to increase the recovery factors of several oil reservoirs (Figure 1.3) (Melzer, 2012). The overall objective of flooding a reservoir with CO_2 is to displace additional oil trapped in the formation. Immiscible or miscible processes between reservoir fluids and the injected CO_2 may occur depending on the properties of the gas and the reservoir fluids at reservoir conditions (Gozalpour, Ren, & Tohidi, 2005). The difference between both processes lies mainly on the pressure at which the reservoir is. For reservoirs which are below the minimum miscibility pressure (the lowest pressure at which contact miscibility can be achieved) or heavy oils, the CO_2 will only partially mix with the oil, and its main function will be to raise and maintain reservoir pressure (low displacement). In reservoirs at higher pressures, or lighter oils, CO_2 will form a single phase liquid with the hydrocarbons causing them to swell, reducing viscosity and surface tension with the reservoir rock (Global CCS Institute; Parsons Brickerhoff, 2011). Figure 1.4 shows an overview on how the CO_2EOR process works.

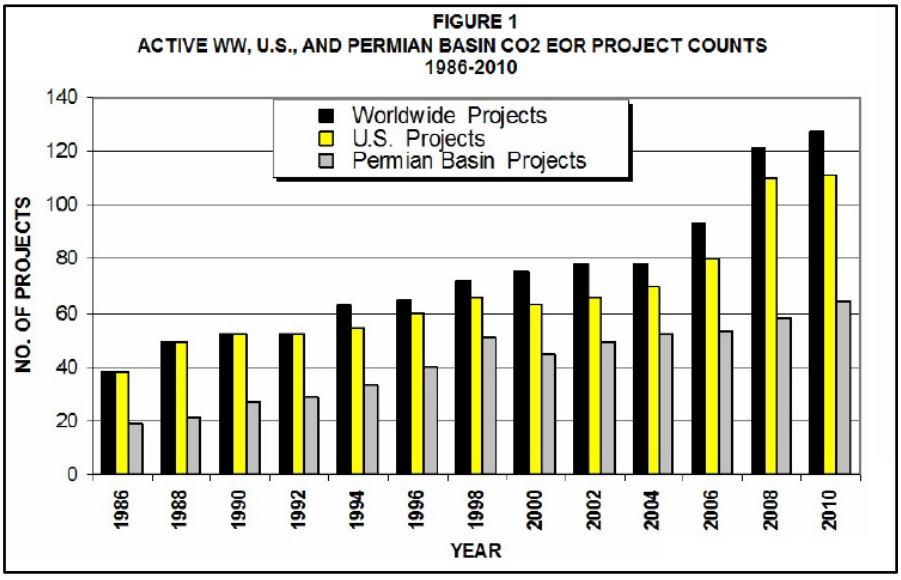


Figure 1.3: active world-wide and USA CO2EOR projects from 1986 to 2010. If in the 1980's CO2EOR projects were restricted to USA, the 90's have seen a great expansion of this technique in other regions of the globe (Melzer, 2012).

Most of the CO_2EOR projects to date have used either naturally occurring CO_2 or CO_2 extracted from produced natural gas. In the Permian Basin, Texas, companies started with projects that injected CO_2 extracted from natural gas (SACROC and North Cross) but later developed source fields such as Sheep Mountain and McElmo Dome in Colorado and Bravo Dome in New Mexico and then built pipelines to transport the gas from the source to the injection sites (Gozalpour, Ren, & Tohidi, 2005) (Figure 1.5).

In these projects the motivation was purely to improve the performance of the reservoirs rather than avoiding the emission of CO_2, as the injected CO_2 would not have been emitted to the atmosphere.

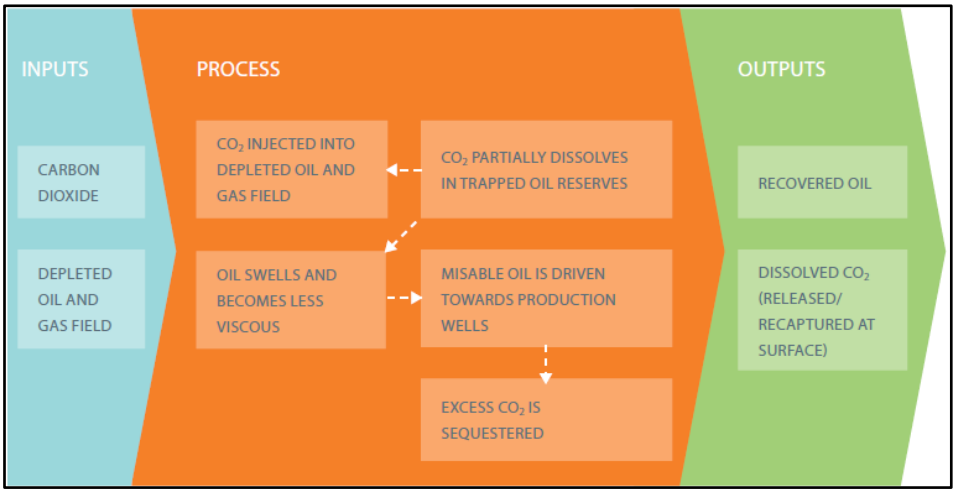


Figure 1.4: Enhanced Oil Recovery process overview. (Global CCS Institute; Parsons Brickerhoff, 2011).

More recently a new series of CO_2EOR projects have started to use anthropogenic CO_2 in tertiary recovery operations. In these operations, the CO_2 is produced as a by-product of industrial processes and is then conducted through pipelines to the injection sites (Figure 1.6). According to the Global CCS Institute there are currently fourteen carbon dioxide injection projects in operation around the world, of which ten are CO_2EOR projects and only three of those are dedicated geological storage projects, having a total CO_2 capture capacity of around 26 million tonnes per annum (Mtpa). Examples where anthropogenic CO_2 is successfully being used to enhance production are presented below.

Rangely Weber Field (Colorado, Chevron Texaco): This field located on the Northeastern flank of the Uinta Basin, Colorado has been in production since the early 1940s and has produced to date over 800 million barrels of oil and over 8.7 million barrels of natural gas liquids. After a serious drop in reservoir pressure in the late 1950's, Chevron initiated a full scale water-flooding program which lasted until 196 when tertiary recovery using carbon dioxide injection was put into place. The company estimates that this change in methodology will allow an increase in recovery of around 15% relative to the water flooding method (Energy and Minerals Field Institute - Colorado School of Mines, 2005). The ExxonMobil LaBarge natural gas processing unit in Wyoming supplies the CO2 which transported along 248 km via pipeline to the field. It is estimated that a total of 25 Mt of CO2 will have been stored in the oil reservoir by the time the project is completed (Gozalpour, Ren, & Tohidi, 2005).

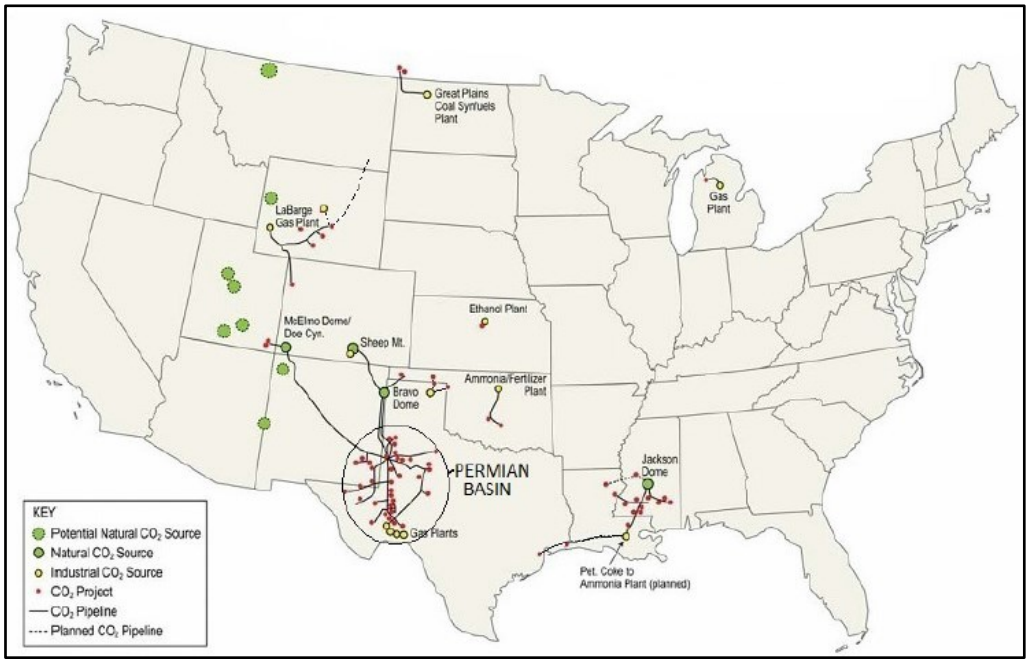


Figure 1.5: Distribution of CO_2 sources, injection sites and transport paths via pipeline across USA (Melzer, 2012).

Main CO_2EOR Projects using anthropogenic CO_2 in North America				
Location	**Plant Type**	**CO_2 Supply Mt/y**	**EOR Field**	**Operator**
Oklahoma	Fertiliser	0.7	NE Purdy, Sho-Vel-Tum	Anadarko, Chaparrel Energy
Colorado	Gas Processing	1.2	Rangeley	Chevron Texaco
Wyoming	Gas Processing	0.6	Lost Soldier, Wertz	Merit Energy
Texas	Gas Processing	1.3	Sharon Ridge	ExxonMobil
Saskatchewan	Coal Gasification	1.8	Weyburn	EnCana Energy
Alberta	Ethylene Plant	0.1	JoffreViking	PanWest Petroleum

Figure 1.6: Main CO_2 projects using anthropogenic CO_2 in North America, April 2003. Source: Advanced Resources International

Weyburn Field (Canada, EnCana): This field is located 130 km southeast of the city of Regina in Saskatchewan province, Canada. It was discovered in 1954 with an estimated 1.4 billion barrels of original oil in place. The peak of production for this field occurred in 1966 at about 47,200 barrels per day and over the next 20 years, production declined steadily to just 9,400 barrels per day by 1986. Several techniques of enhanced oil recovery were applied in order to extend the production time of this field (additional vertical drilling, the introduction of horizontal drilling, and the use of waterflooding) and by 1998 around 23% of the OIIP had been produced, and it was estimated that this would amount to 25% if no other solution was found (SEED - Schlumberger, 2014). In 2000 the operator started to inject CO_2 into the reservoir which is bought from the Dakota Gasification Company as a by-product of the extraction of methane from coal. The gas is being transported via a 330 km pipeline, and current

injection rates are around 6500 tonnes per day, which anticipate a total of 20 Mt of CO_2 being permanently stored underground over the lifespan of the project and additional 130 MMbo of oil to be produced, extending the life of the Weyburn Field by 25 years (SEED - Schlumberger, 2014).

This field has become a world class example of the use of CO_2 in EOR operations and a case study for the transition from a purely EOR project to a CCS project sponsored by the International Energy Agency (IEA) - Greenhouse Gas Weyburn-Midale CO2 Monitoring and Storage Project. The IEA estimates that Weyburn has a total CO_2 storage capacity of around 55Mt which is 25Mt more than the estimates for CO_2EOR operations (Figure 1.7). A geophysical and geochemical monitoring program is in place to evaluate the reservoir conditions along the storage process, and information on brine-rock interaction, pore scale mineral alteration, fracture flow and pressure conditions at reservoir depth are being gathered to ensure the environmental safety of the project (Steve Whittaker, PTRC, 2010).

From the above it is clear that CO_2EOR is a widely accepted and utilized technology to increase hydrocarbon recovery factors, and because utilizes carbon dioxide to achieve this objective it is seen as a promising method to contribute for the reduction of this gas in the atmosphere – Carbon Capture and Storage. Despite the fact that CCS is now considered to be technically feasible at commercial scale[1] (Gibbins & HannahChalmers, 2008), it is still facing the barrier of high cost (a pure storage scheme generates no revenue and it actually represents a cost because no significant value has yet been attributed on CO_2 storage) and absence of legislation so that it can become widely implemented. In that context CO_2EOR is seen as one of the ways of narrowing down the economic gap for CCS as the infrastructures created to enhance hydrocarbons production are already in place, the increment in hydrocarbon recovery rates and the potential economic incentives will help offset the cost of CO_2 capture, transportation and storage (Jafari & Faltinson, 2013).

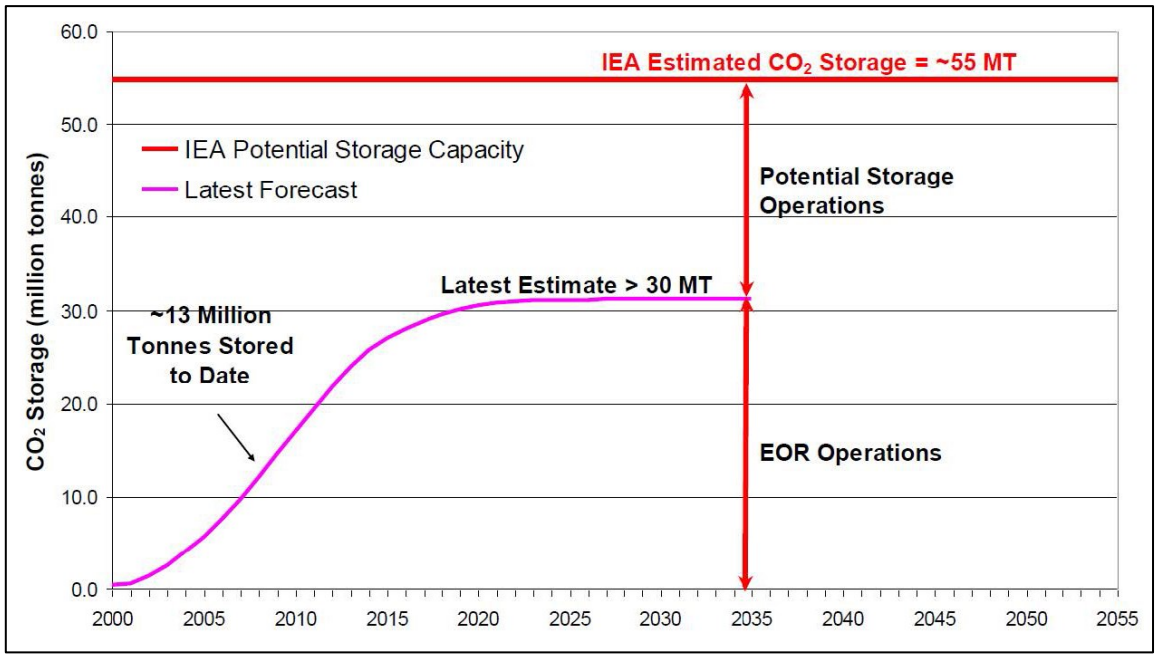


Figure 1.7: CO2 storage capacity of the Weyburn field during and after EOR operations (Steve Whittaker, PTRC, 2010).

1.3 Geological Storage of CO2

1.3.1 General Principles

Three types of geological formations are considered to be the most suitable for CO_2 storage: oil and gas reservoirs, deep saline formations and unminable coal beds (Busch, Amann, Bertier, Waschbusch, & Kroos, 2010). Storage in hydrocarbon reservoirs and deep saline formations is likely to occur at depths above 1000m and temperature and pressure equal or exceeding the critical point of 31°C and 73 atm. At these conditions carbon dioxide is in its supercritical fluid state (Figure 1.8) having both gas-like and liquid-like qualities. Several processes such as flow in response to pressure gradients (caused by the injection process or natural hydraulic gradients), buoyancy caused by density differences between CO_2 and formation fluids or diffusion and dispersion control the primary migration of the CO_2 inside the reservoir. Primary retention of the CO_2 is dependent on the existence of a cap-rock with good sealing properties to ensure this gas remains underground. On a later phase additional trapping is provided by the capillary forces that retain the CO_2 in the pore space and by the reaction of the CO_2 with the in situ fluids and host rock: chemical reactions of the CO2 with the formation fluids make them denser and sink in the formation and later in the process chemical reactions between the CO_2 and the rock minerals creates solid carbonate minerals (IPCC, 2005). For deep saline aquifers convective currents will control and induce the dissolution of the CO_2 in the formation brine (Lindeberg & Bergmo, 2002) improving retention.

In the case of storage in coal beds, the storage is processed at shallower depths and adsorption is replaced by absorption when temperatures and pressures rise above a critical value which is dependent on the maturity of the coal, maceral and ash content, and on the confining stress (Larsen, 2004). The process leads to swelling of the coal and a reduction of the permeability affection injectivity.

Regarding the selection of storage sites, these need to fulfil several conditions in order to ensure that the CO_2 does not leak to the adjacent geological formations and/or ultimately to the surface. The 2005, IPCC stresses that *potential leakage pathways must be identified and procedures must be established, to set appropriate design and operational standards as well as monitoring, measurement and verification requirements*. It is considered that geological storage sites for CO_2 should obey the following characteristics (IPCC, 2005):

1) Regional stable geological environment: to avoid compromising the integrity of the storage site (Bachu S. , 2002) this evaluation is intended to narrow down the regions adequate to CO_2 storage. Basin geology and hydrostratigraphy should be addressed to identify specific areas and strata suitable for CO_2 storage. Parameters such as regional tectonic context, oil and gas reservoirs location or temperature and pressure distribution should be evaluated.
2) Adequate capacity and injectivity: this parameter relates to the porosity, thickness and permeability of the potential storage units. Porosity and thickness are essential in conveying storage capacity while permeability plays a role in the injectivity capacity of the geological formation.
3) Satisfactory sealing caprock or confining unit: to ensure that CO_2 does not leak, storage formations should be overlain by other formations that by their low permeability, thickness and extension, are able to retain the fluids in the reservoir.

In a general approach, evaluation of a potential CO_2 storage site should follow a methodology of evaluation similar to the one depicted in Figure 1.9. Having the above requirements in mind, hydrocarbon reservoirs have been considered the best candidates for storing CO_2 for a number of reasons (IPCC, 2005) :

- Their capacity for retaining fluids is proven by the existence of an HC accumulation: Fluids only accumulate if a series of requisites are fulfilled such as the existence of a reservoir rock, a seal rock and a trap (structural or stratigraphic). For hydrocarbons a matured source rock, the right timing, and a migration path are also imperatives to the generation of an effective accumulation, but in order to retain CO_2 the first three parameters are sufficient.
- Commercial hydrocarbon accumulations have been extensively studied and characterized. Models of fluid displacement and reservoir behaviour are usually available and this allows decisions to be taken with a high level of confidence.

- The infrastructure used to exploit these accumulations is already in place and it may be used in CO_2 injection operations.

Other options include deep saline formations (sedimentary rocks which are at high depths and are saturated with water containing high concentrations of dissolved salts), like in the case of the Sleipner Field[1] in Norway and unminable coal beds where the CO_2 can be stored through adsorption processes.

[1]A good example of a successful commercial project of CO_2 is the Sleipner West field in Norway, operated by Statoil. The Sleipner project was the first commercial example of CO_2 storage in a deep saline aquifer and from 1996 to 2011; Statoil has captured almost 12 million tons of C02 in this North Sea field. The Sleipner field produces natural gas and condensate (light oil) from the Heimdal Fm. sandstones, which are about 2,500 m below sea level. The CO_2 which is extracted from the gas is injected into the Utsira formation a 200-m-thick sandstone layer at about 800 m depth which contains no commercial oil or gas. It is estimated that the Utsira sandstone has enough pore space to allow the storage of about 600 billion tons of CO2, which is equivalent to all the anthropogenic CO_2 produced along 15 years at current rates (SEED - Schlumberger, 2014).

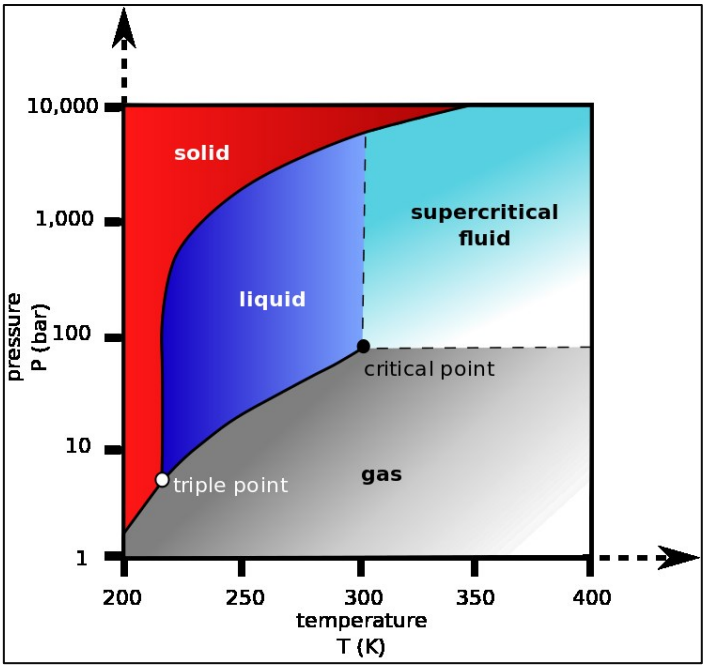


Figure 1.8: Carbon dioxide pressure-temperature phase diagram (Wikipedia, 2005).

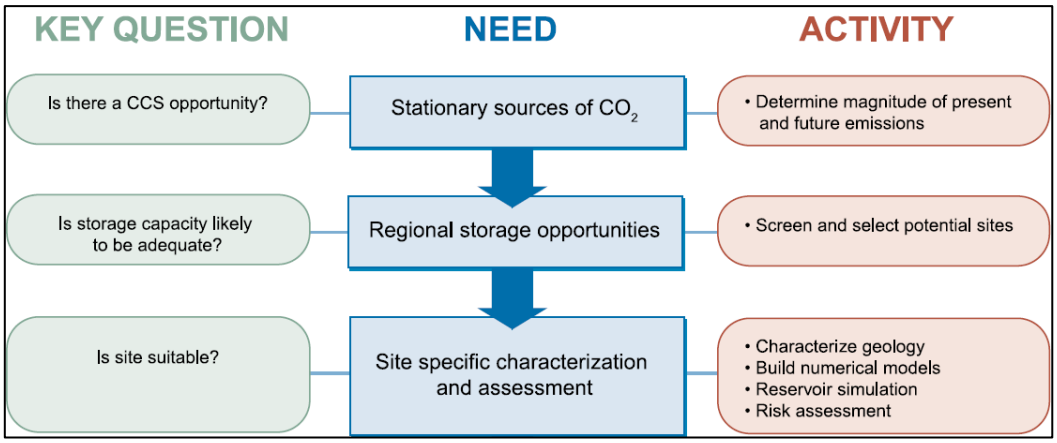


Figure 1. 9: workflow for CO2 storage site evaluation. Adapted from (IPCC, 2005).

Depending on the geological context on which the CO_2 is injected, its retention can occur through different trapping mechanisms which acting together allow this gas to be trapped underground (IPCC, 2005):

- Trapping below an impermeable layer (caprock), the focus of this work.
- Retention as an immobile phase trapped in the pore spaces of the storage formation
- Dissolution in the in situ formation fluids
- Adsorption onto organic matter
- Reacting with the minerals in the reservoir and seal to produce carbonate minerals

1.3.2 Risk assessment – potential for cap-rock failure

When considering depleted hydrocarbon reservoirs or deep saline formations as potential CO_2 storage sites, one major concern is the sealing efficiency of the seal rock overlying the reservoir – the cap-rock - where the gas is to be injected. For this reason a risk assessment of these types of reservoirs needs to address the potential for leakage. CO_2 can escape from the reservoir formations through several different pathways (Busch, A. et al., 2010; IPCC, 2005) (Figure 1.10) but the most common are:

- Seal breaching through mechanical failure as a consequence of excess pressure resulting from buoyancy forces and injection related overpressure
- Seepage along existing fault systems and fracture networks
- Seepage through damaged wells

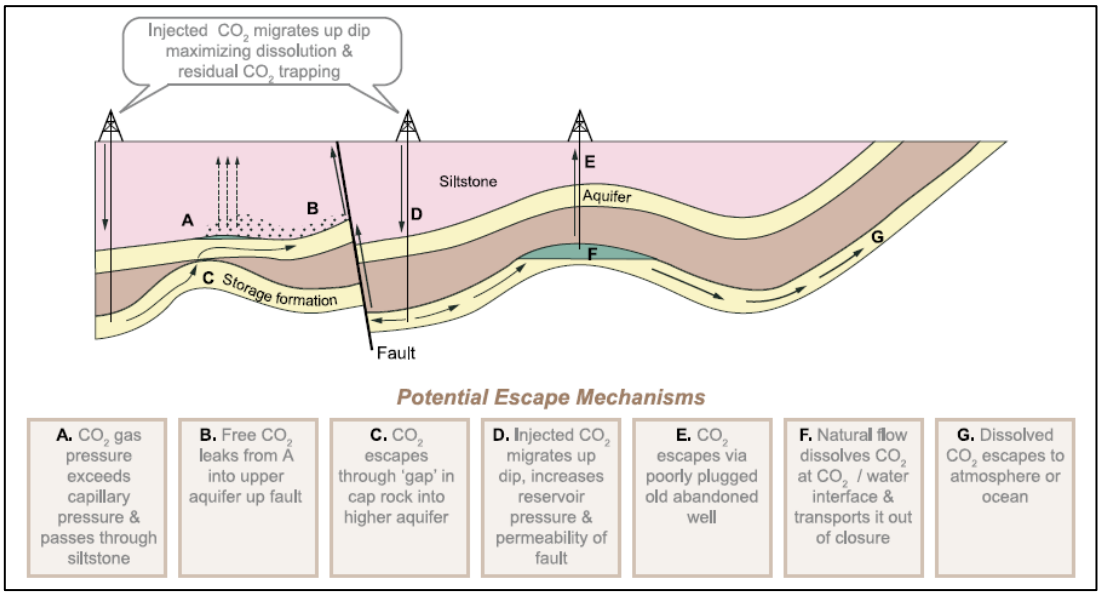


Figure 1.10: potential escape mechanisms of CO2 injected on a sandstone reservoir (IPCC, 2005).

A study by Vidal-Gilbert, Nauroy, & Brosse, (2008) used a 3D geomechanical model to evaluate the impact of the induced deformations and in situ stress changes caused by the injection of CO2 on surrounding faults. They have found that these do not affect the mechanical stability of the reservoir-cap rock system. Hangx et. al (2010) used conventional triaxial deformation experiments performed on anhydrite rock from the base of the Permian Zechstein sequence to determine the mechanical behaviour of this material and to assess if there are any mechanical or chemically coupled effects that might threaten seal integrity as stresses evolve during CO2 injection posing a risk in the longer term. The study found no short - term chemical effects of CO_2 and pore fluid on the strength of anhydrite and that cap-rock integrity will not be compromised by mechanical damage. It has also concluded that long - term chemical reactions of anhydrite with CO_2 will most likely not lead to significant CO_2 penetration, but recognized that more research is needed. However, another study by Orlic, Heege, & Wassing (2011) analysed the poro-mechanical, thermal and chemical effects of CO_2 injection on the integrity of fault- and top seals and concluded that fracturing in the near-well area may be induced by the combined poro-elastic and thermal effects of CO_2 injection and that long term chemical reactions of anhydrite caprock with CO_2-rich fluids can lead to significant reduction in failure strength at timescales of ~50000 years. These studies analysed different combinations of mechanical changes that can occur on the reservoir-cap rock system due to CO_2 injection operations and obtain different conclusions, demonstrating the importance for further investigating this subject and the extent of the mechanical changes that can occur. Risks associated with operational and maintenance activities are considered to be similar to those of CO_2EOR operations and for that reason fall into a different category which won't be approached in this work.

1.4 Cap-Rock failure: hydraulic fracturing of the cap-rock and fracture impact on permeability – an introduction

Fractures are discontinuities caused by the rupturing of the rock material which may be restricted to individual grains or may cut continuously through rock bodies over distances varying from millimetres to kilometres (Mandl, 2005). These discontinuities are the result of brittle failure which in its turn is the result of different mechanisms. Geological fracture models, which are postulated from the combination of geological and rock mechanics approaches, classify fracture as being the result of:

- Tectonic forces: forming large kilometric scale fractures, normally faults (a fracture with relative movement of its walls).
- Thermal loading: a thermal gradient can cause the rock to expand by different amounts and produce an applied stress which may exceed the strength of the material forming a fracture) ,
- Overburden: when buried, the vertical load caused by the sediments can lead to fracture formation when the strength of the rock is exceeded.
- High fluid pressure: high fluid pressures may reduce the applied differential stress to effective stresses which are lower that the latter causing them to become tensile and enabling rock failure.

Other authors classify fractures as being: tectonic (fold and/or fault related), regional, contractional (diagenetic) or surface related (Aguilera, 1998; Stearns and Friedman 1972; Nelson 1979). Both models assume that natural fracture patterns depict the local state of stress at the time of fracturing, and that subsurface rocks fracture in a manner qualitatively similar to equivalent rocks in laboratory tests performed at analogous environmental conditions. This way, natural fracture patterns are interpreted in light of the laboratory-derived fracture patterns (Handin and Hager, 1957) and in terms of postulated paleo-stress fields and strain distributions at the time of fracturing.

Fractures are of paramount importance for most industries that deal with mechanical problems such as aeronautics, naval, civil and geotechnical engineering or hydrocarbon industry. These features can affect the stability and mechanical strength of a solid and consequently the integrity of structures such as aircrafts, vessels, tunnels or wellbores. In rocks of which hydrocarbon reservoirs are a particular case, fractures may also act as pathways or barriers to fluid flow therefore affecting the effective permeability of the reservoir and its productivity. For the present study, the most important question to consider is the impact of fractures in the integrity of a rock mass, namely the cap-rock. This impact is of such importance that Downey (1984) calculated that a single fracture 25 μm wide atop a 150m oil column would leak oil at a rate of more than 150 million barrels per million years.

As mentioned in section 1.3.1, in order for fluids to be retained in a porous rock (the reservoir) one of the key parameters is the existence of a seal: a low permeability rock which prevents natural upward migration of the fluids.

When fluids are trapped beneath a seal, they exert an upward pressure called buoyancy pressure which is related to the contrast in density between the water trapped in the pores (connate water) and the fluids (hydrocarbons for example), and the height of the hydrocarbon column above the free water level (FWL – depth at which the water saturation first reaches 100%) at which both are in equilibrium (Gluyas & Swarbrick, 2004). The capacity of a seal rock to retain fluids is determined by the minimum pressure required to displace connate water (fluid that was trapped in the pores of sedimentary rocks as they were deposited) from pores in the seal, thereby allowing leakage. Therefore, the pressure that the fluids exert in a rock – pore fluid pressure - is an essential parameter when evaluating the potential for cap rock failure. This pressure can be such that can lead to mechanical failure by fracturing of the rock mass. Fluid induced failure or hydrofracturing is proven to be a common natural occurrence despite the fact that its record is not very obvious. The importance of pore pressure is such that it has been a focus of studies since the early 20th century when Karl Terzaghi introduced the concept of *effective stresses* for soil mechanics in 1923: the difference between the actual or confining stress and the pore fluid pressure.

An excellent example of the role of fluid pressure in the formation of fractures can be seen in the Bristol Channel area in the Mercia Mudstone Group rocks (Figure 1.11). Record of the presence of high fluid pressures during both the opening and inversion of the basin can be found here. During the opening of the basin (Permian-Triassic), bodies of sand were injected along some of the hydraulic fractures created, preserving them as sedimentary dikes and sills; and during its inversion in the Tertiary, hydraulic fracturing provided a transient permeability that relived the excess of fluid pressure which was preserved as a network of satin-spar veins in some evaporite-rich horizons (Cosgrove, 2001) .

At another scale, other authors such as Zuhlsdorff & Spieß (2004) and Cartwright et al (2007) have used three-dimensional (3D) seismic data to show that natural hydraulic fractures are able to breach several hundreds of meters sealing sequences allowing fluids to flow vertically or subvertically across them and in some cases reaching the surface forming vents (Figure 1.12). Davies et al. (2012) have analysed thousands of hydraulic fracture structures from hydraulic fracturing operations in the Marcellus, Barnett, Woodford, Eagle Ford and Niobrara shale (USA) and three-dimensional seismic data from offshore of West Africa and mid-Norway and found that the probability of a stimulated and/or natural hydraulic fracture extending vertically >350 m is approximately 1% and 33% respectively.



Figure 1.11: network of satin-spar veins in the Mercia Mudstone, England, UK.

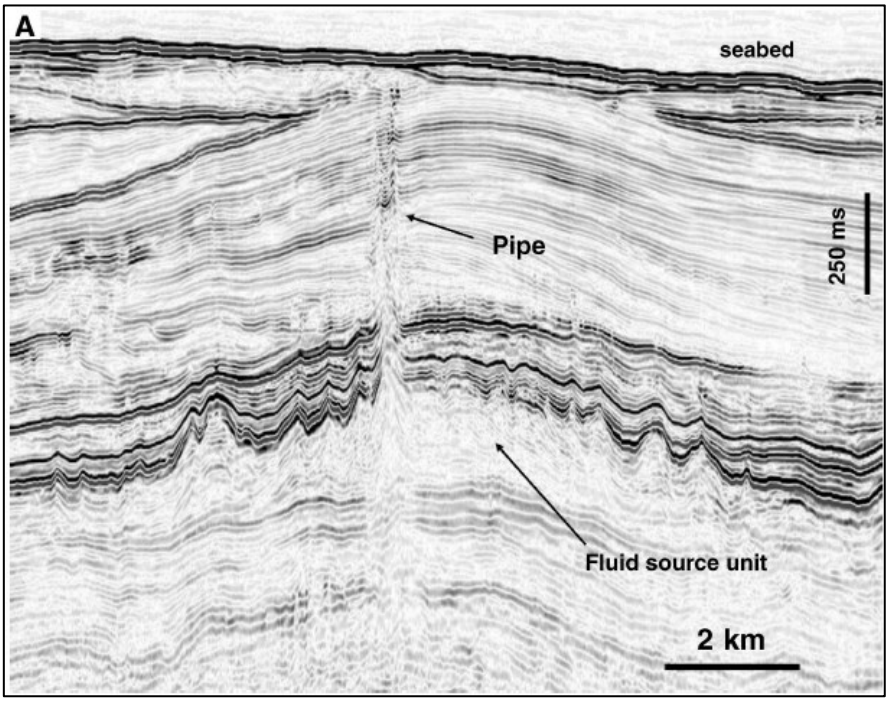


Figure 1.12: Seismic expression of pipes crossing sealing sequences. A large pipe from the Faeroe-Shetland Basin, offshore United Kingdom, characterized by a vertical zone of disrupted reflections, with small offsets. (Cartwright et al, 2007).

From the above it is fair to say that high fluid pressures in sediments and its consequence – the formation of fractures – has a very strong impact on the permeability of rock sequences and on the integrity of low permeability cap rocks overlying reservoirs containing fluids at such high pressures. Their importance is such that when they are dominant in a rock mass the fluid transport in that mass is fully controlled by them. Some of the main effects of fractures on permeability may be summarised as follows (Gudmundsson, 2011):

- A major active (water-conducting) fracture can increase the average permeability of a test area by several orders of magnitude over adjacent sections.
- Permeability is not a direct function of the total fracture frequency as active fractures may be only between and on fourth of the total number .
- Conducting fractures may easily increase in-situ permeability by three orders of magnitude or more over laboratory values.

Fractures can also impact permeability in a different way if they are not formed in-plane (Hegelson & Aydin, 1991):

- Out of plane joints (fractures that terminate at sedimentary contacts being strata-bound) in layered rocks will result in geometries that decrease the degree of connectivity among joint segments
- Side stepping joint segments across shale lenses or thin layers are clearly disconnected and any fluid going from one segment to the other has to go through the markedly less permeable shale.
- The angle between fractures in adjacent layers also has an important implication for vertical and horizontal fracture permeability:
    - Horizontal permeability: If the angle between joints is large, then horizontal permeability can change drastically from one unit to the next not only in magnitude but also in direction.
    - Vertical Permeability: Because the fractures in the two adjacent units will be connected only at certain contact points vertical fracture permeability will be markedly lower than that of a medium with continuous and well-connected fractures.

In summary, within layered sedimentary rocks, fractures that propagate through bedding contacts provide well-connected pathways for vertical fluid flow, therefore increasing permeability. Inversely , fractures which terminate at bedding contacts or that jog or step over a few centimetres at bedding contacts can limit vertical flow and produce highly tortuous flow paths (e.g. Tsang, 1984, Hegelson & Haydin, 1991).

Further in this document the subject will be approached with higher detail but it is clear that the continuity of fractures from one layer to another has a deep impact on fluid migration, whether it is oil, gas (such as CO_2), water or contaminants. Therefore, a better understanding of the connectivity of fracture systems in layered rocks can provide economic and environmental benefits. For this understanding to be achieved it is essential to understand the interaction between interfaces and fractures and that can be done by studying the rock properties which control fracture propagation through layered rocks.

1.5 Project objectives

Taking into account all that was said so far, particularly on the impact of fractures in rock permeability, fluid transport through low permeability rocks and their relation with high fluid pressures, this project aims to investigate the loss of cap-rock integrity through fluid induced failure (hydrofractures) by studying what specific rock properties control fracture propagation through a layered media and what influences fluid flow in these low permeability units. In other words, we intend to attempt to determine the mechanical properties of evaporite rich seals and the mechanisms by which they might fail when subjected to high fluid pressures linked to the injection of CO2. This study will contribute to the understanding of the risks associated with seal failure and therefore provide significant insight on the ability that these rocks have to retain fluids, i.e. it will contribute to determine how much (i.e. what pressure) CO_2 can be contained.

1.6 Rationale and Methodology

This project is part of the Qatar Carbonates and Carbon Storage Research Centre (QCCSRC), a research consortium between Imperial College London, Qatar Petroleum, Shell and the Qatar Science and Technology Park with the objective of improving the knowledge on carbonate reservoirs in order to increase the recovery rates of Qatar's oil reservoirs using carbon dioxide injection (CO_2EOR) while developing the technology for storing this gas in such reservoirs (CCS). QCCSRC is a multidisciplinary research group involving Geosciences Research (which includes fieldwork in Oman, UAE, Spain and the UK with the overall objective of improving the knowledge of the carbonate reservoirs of Qatar. The specific project on which this thesis is reporting is part of the Geosicence Group and, as mentioned, focused on studying the evaporite seals that cap these carbonate reservoirs); Rock-Fluid Research (with the objective of understanding how fluids flow through rocks of varying porosity and heterogeneity) and Thermo-Fluid Research (which aims to understand the thermophysical and transport properties of fluids, i.e., phase behaviour, interfacial properties, viscosity, diffusion coefficient, density).

In Qatar and throughout the Arabian Gulf the main reservoir is the Arab Formation composed mainly of shallow-water carbonates and that can be divided in four members, D to A, where Arab-D member is the most prolific. The Arab Formation is overlain by an evaporite cap rock, mainly formed of anhydrite called the Hith Formation. As mentioned in Section 1.1.3 there are potential risks for the integrity of the cap rock when injecting carbon dioxide into reservoir rocks: seal breaching through mechanical failure as a consequence of excess pressure resulting from buoyancy forces and injection related overpressure or seepage along existing fault systems and fracture networks. It is clear that it is of paramount importance to understand how fractures potentially generated during CO_2 injection operations can propagate through an anhydrite cap-rock such as the Hith Formation and what specific rock properties can inhibit propagation therefore avoiding catastrophic seal failure.

Having that in mind our first priority was to analyse the geological setting of Qatar. Having done that we understood that the main cap-rock overlying the Arab Formation carbonate reservoirs is the Hith Formation of which there are no accessible outcrops. Therefore we have found a location in the UK – the Brightling gypsum mine - which possesses geological characteristics that allowed us to use it as an analogue for the Qatar Hith Fm. To complement the information obtained underground we have also analysed a series of drill-cores obtained from different locations within the same basin where Brightling is located (the Weald Basin) and conducted field studies that provided valuable information on how low permeability evaporite-rich rocks respond to high fluid pressures and on how fractured sedimentary sequences allow or inhibit fracture propagation.

It is important to highlight that the determination of the key mechanical properties of the different rocks making up the seal would traditionally involve the determination of rock strength etc. by mechanical testing of samples (UCS or Brazilian Disc tests). However, the parameters determined from such studies yield values that describe the current properties of the rock. As we wished to know the properties of the rocks 'at the time of fracturing' we elected to exploit the knowledge of brittle failure and fracture arrest in an attempt to determine this.

Both the analysis of the Brightling mine support pillars, the drill-cores and field work have provided information on the sedimentary facies and textures which are typical of evaporite rocks and on the properties that might influence fracture propagation through a layered sedimentary sequence. However in order to deeply understand the particular mechanisms and mechanical parameters that control failure and therefore the propagation of fractures through layered rocks such as these, direct rock analysis is not enough. To try and understand this, we have resorted to numerical modelling using the Finite-Discrete Element Method. This approach is an iterative one where the information obtained from one of the methods feeds the other.

The methods used in this project can be summarized in the following way:

- Field Work (Section 3)

Local Scale: to determine the internal structures within seals that might influence fracture formation. Data was retrieved in gypsum mines, drill cores and outcrop studies.

Regional Scale (Qatar geological context): to determine the stress history of the seal and the likely fractures it could contain as a result of burial, diagenesis and tectonism.

- Theoretical analysis of brittle failure (in particular of fluid induced failure) and the stress state in the crust (Section 4)

- Numerical Modelling using a combined finite-discrete element method technique (Section 5).

Chapter 2
Cap- Rock Seals and Evaporites

2.1 Cap-Rock Seals

2.1.1 General Considerations

In hydrocarbons accumulations, one of the key parameters is the existence of a seal: a rock which prevents natural upward migration of the fluids. The ability of a low-permeability rock – a seal – to retain fluids is related to three major components (Watts, 1987):

- *In-situ* fluid (HC and water) densities
- The capillary entry pressure of the sealing rock
- The hydrocarbon/water interfacial tension at subsurface conditions

When hydrocarbons are trapped beneath a seal, they exert an upward pressure called buoyancy pressure (P_b) which is related to the contrast in density between the water trapped in the pores (connate water – ρ_w) and the hydrocarbons (ρ_p), and the height of the hydrocarbon column (h) above the free water level (FWL – depth at which the water saturation first reaches 100%) at which both are in equilibrium (Gluyas & Swarbrick, 2004). The buoyancy pressure is expressed using the following relation (1) where P_b is expressed in units of pressure (e.g., bars, psi, or Mpa) and the fluid densities are expressed as pressure gradients (e.g., bars m^{-1}, psi ft^{-1}, or Pa m^{-1}):

$$Pb = (\rho w - \rho p)g.h \quad (2.1)$$

where (g) is the gravity force

P_b is the maximum allowed capillary pressure at a reservoir/seal boundary below which a (maximum) hydrocarbon column of thickness *h* is trapped (Smith, 1966).

The capacity of a seal rock to retain fluids is determined by the minimum pressure required to displace connate water from pores in the seal, thereby allowing leakage. This property is called the capillary entry pressure and it can be described as the minimum pressure necessary to squeeze a hydrocarbon droplet through a pore throat. The capillary entry pressure (P_c) of a water-filled rock is a function of the hydrocarbon-water interfacial tension (Υ_h), wettability or the contact angle between the water and the hydrocarbon (Θ_h) and radius of the largest pore throat (r). In order for hydrocarbons to penetrate through the seal rock, their buoyancy pressure has to overcome the capillary entry pressure. When that happens, hydrocarbons pass through (Downey, 1994). Accurate measurements of the capillary entry pressures are made using mercury/air system, where mercury is injected into an (air-filled) sample at gradually increasing pressure. The pore throat size (r) at a given mercury pressure (P_m) is given by equation (2) (Purcell, 1949; Watts, 1987):

$$Pm = \frac{2\Upsilon m.\cos(\Theta m)}{r} \qquad (2.2)$$

Where Υ_m – mercury/air interfacial tension;
Θ_m – mercury/air contact angle

Using this technique, mercury-air capillary entry pressures for some seal rocks have been calculated:

- Siltstones: 20 - 30 MPa (equivalent to a 400-700 m column of 30 ~ API oil sealed at 2.5 km depth),
- Mudstones: 45-55 MPa (900-1200 m oil columns)

From equation (2) it is possible to conclude that the mercury pressure, which is a proxy for the capillary entry pressure of the seal-rock and consequently for its sealing capacity, increases as:

- The throat radius of the largest connected pores decreases
- The wettability decreases
- The hydrocarbon-water interfacial tension increases

In order to calculate maximum hydrocarbon columns a seal can withstand, mercury-air pressure data has to be converted to hydrocarbon-water data, and that can be done using the following formula (3) (Purcell, 1949):

$$Pc = \frac{\Upsilon h.\cos\Theta h}{\Upsilon m.\cos\Theta m} Pm \qquad (2.3)$$

Combining equations (1) and (3) we can calculate the maximum hydrocarbon column held by a seal at membrane seal capacity, i.e. when the buoyancy pressure, P_b, equals the capillary entry pressure, P_c, of the seal.

$$Pb = Pc = (\rho_w - \rho_p)g.h = \frac{\Upsilon h.\cos\Theta h}{\Upsilon m.\cos\Theta m} Pm \quad (2.4)$$

the HC-water contact angle is zero we can write equation (5):

$$h = \frac{Pm.\Upsilon h}{(\rho w - \rho p)g.\Upsilon m.\cos\Theta m} (2.5)$$

In principle any lithology can work as a seal if their capillary entry pressure is greater than the buoyancy pressure of the fluid column in the reservoir. Figure 2.1 shows the seal classification used by Watts (1987) which accounts also for fault related type of seals (a cap-rock seal must be present as well) and other types such as hydrodinamic seals. Cap-rock type of seals, are the ones which we are

interested in this project, and can be divided in two different types based upon the mechanism by which seal failure occurs (Figure 2.2):

Membrane Seals (Capillary Seals): also called capillary seals, membrane seals are single-phase seals that stop hydrocarbons migrating from the reservoir into the seal pore throats by the capillary entry pressure. Trapping of a hydrocarbon column will occur as long as the net buoyancy pressure (related to the difference between the hydrocarbon and water densities) of the hydrocarbons does not exceed the capillary displacement pressure of the seal (Watts, 1987).

Hydraulic Seals (Fracture Seals): when the pore throats are very small and consequently the capillary entry pressure is extremely high (very low permeability) both the water below the FWL and the hydrocarbons at the reservoir seal interface are stopped from migrating to the seal pore-throats. These cap-rocks will fail by fracturing when pore fluid pressure at the caprock reservoir interface is such that the effective minimum stress (assumed horizontal) is reduced to zero, or more correctly below zero to the tensile strength of the rock (Watts, 1987). Tight shales and evaporites such as anhydrite or halite are examples of this type of cap-rock seals.

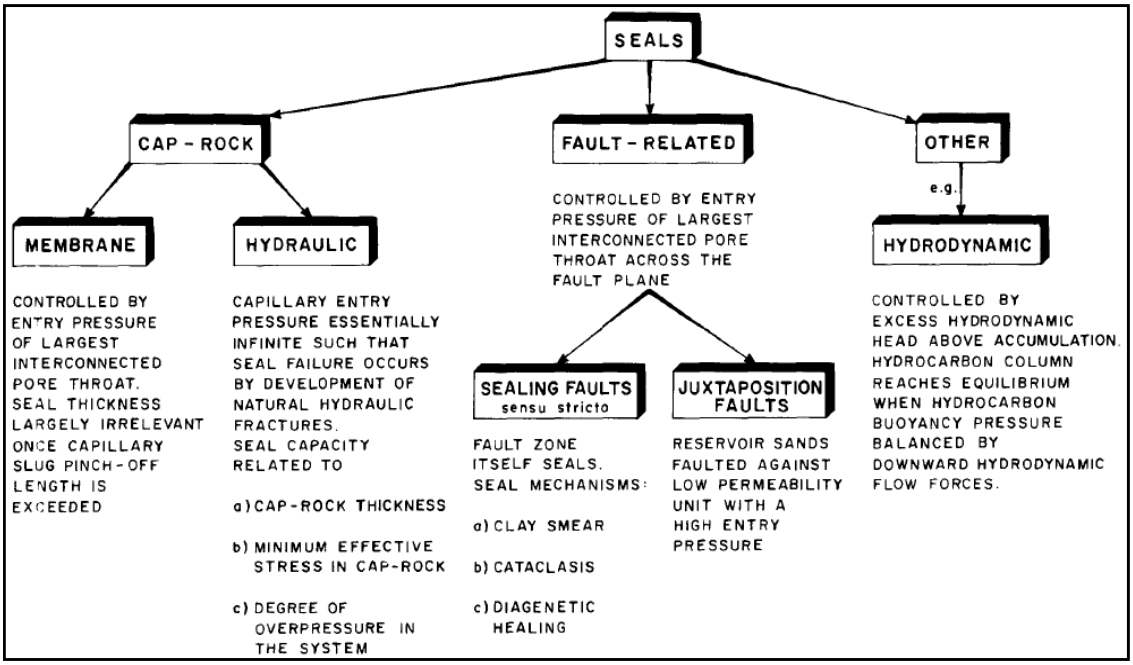


Figure 2.1: classification of hydrocarbon seals based upon the mechanism by which seal failure occurs (Watts, 1987).

Apart from the microscopic properties that allow fluids to be retained and that were outlined above, an efficient seal should also be: laterally continuous, maintain a constancy of properties over a large area, it should be relatively ductile and widespread over the area of a sedimentary basin (Downey, 1994).

2.1.2 Evaporites as cap-rocks

The most effective seals are evaporites (halite, anhydrite etc), fine-grained clastics (claystone, siltstone, mudstone), and organic rich rocks. (>3% of organic matter). These typically have high capillary entry pressures (small pore throats which leads to very low permeability), are relatively laterally continuous and thick (even though thickness is not directly related to sealing capacity as it does not influence the entry pressures of the lithology, it is unlikely that a formation which is a few centimetres thick could be continuous, unbroken and unbreached while maintaining a uniform rheological character over an accumulation (Downey, 1994)), ductile and widespread over the area of the sedimentary basin. Of these, evaporites are probably the most effective as they perfectly fulfil all of the mentioned conditions.

A careful observation of the stratigraphy of the ten largest oil fields in the world reveals the importance of evaporite seals for the effective generation of hydrocarbon accumulations (Figure 2.3). This proves that despite being less than 2% of the sedimentary rocks, evaporites are very efficient seals. Due to this great success as seals, evaporites are generally seen as being able to retain fluids in the reservoir, as a result of their high capillary entry pressure and - unlike lithified shales – because they deform in a ductile manner, not by fracturing. In terms of seal capacity, Figure 2.4 ranks the different types of rocks according to their inherent ductility and sealing capacity (Downey, 1984).

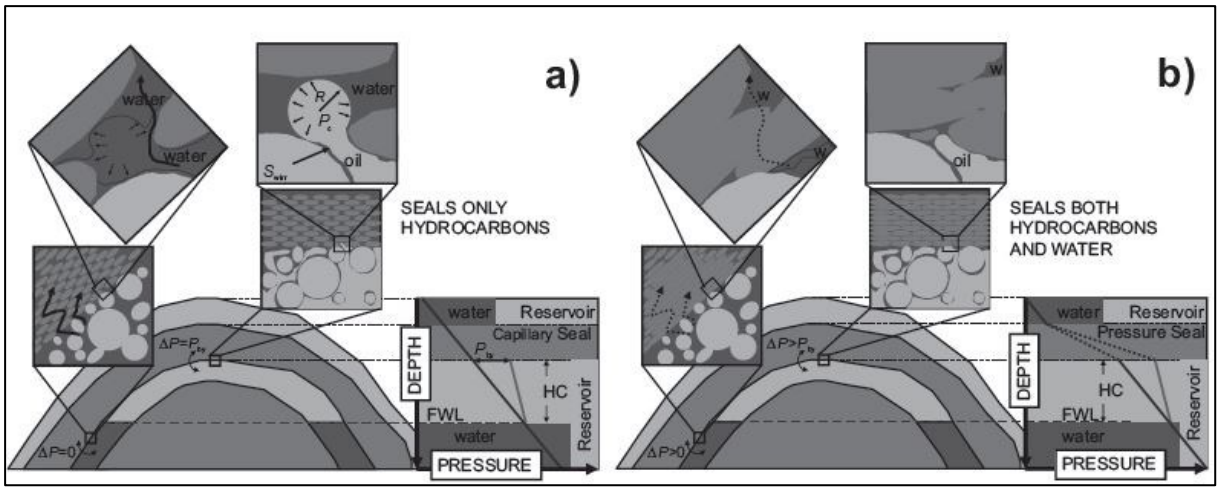


Figure 2.2: graphical representation of the two types of cap-rock seals. a) pressure/depth profile through a membrane sealing cap-rock (of entry pressure Pc) sealing a hydrocarbon column (HC). From equation (1) we know that the buoyancy pressure is related to the density difference between the water and the hydrocarbons. The depth/pressure profile shows that in order for the cap rock to be at seal capacity, the difference between the water and hydrocarbon gradients (the buoyancy pressure - Pb) must equal the maximum allowed capillary pressure at the cap-rock/reservoir interface (Pc), which is depicted in equation (4). b) pressure/depth profile through a hydraulic sealing cap-rock (of entry pressure Pc) sealing a hydrocarbon column (HC). These cap-rocks, due to their extremely low permeability, give rise to higher fluid pressurs. Seal failure will occur by hydraulic fracturing when the total hydrocarbon pressure at the cap-rock/reservoir interface exceeds the horizontal stress (SH) plus the tensile strength of the rock (T) (Casabianca & Cosgrove, 2012).

In terms of permeability, evaporites show very low values which fall beyond the capacity of standard instruments commonly used in the oil industry. Measurements made in salt caverns for waste storage projects, show typical permeability values for halite lower than 10^{-6} md and anhydrite values of 10^{-5} md (Warren, 2007). Figure 2.5 shows a ranking of relative permeabilities for different lithologies.

Largest Oil Fields			
Field Name	**Country**	**Bbl per day**	**Seal**
Bolivar Coastal Field	Venezuela	500,000 - 2.6 million	Intraformation trapping by oil degradation
Ghawar Field	Saudi Arabia	5 million	Anhydrite
Athabasca Oil Sands	Canada	1.98 million	Halite (now removed)
Marun Field	Iran	520,000	Anhydrite
Rumaila Field	Iraq	1.34 million	Anhydrite
Burgan Field	Kuwait	1.3 million	Shales
Upper Zakum Field	UAE	650,000	Intraformation limestones, anhydrite
Samotlor Field	Russia	750,000	clayston, siltstone, shales
Sarir Field	Libya	420,000	shales
Agbami Field	Nigeria	250,000	intra formation shales and mud diapirs

source: http://www.explorationworld.com/

Figure 2.3: the production of ten largest oil fields in the world (2015 data) show that evaporites are extremely important, acting as seals in the five of these fields.

In terms of lithological definition, evaporites are layered crystalline sedimentary rocks that form from brines generated in areas where the amount of water lost by solar evaporation exceeds the total amount of water from rainfall and influx via rivers and streams. These rocks can be formed at either surface or nearsurface. Minerals in evaporite rocks include carbonates (especially calcite, dolomite, magnesite, and aragonite), sulfates (anhydrite and gypsum), and chlorides (particularly halite, sylvite, and carnallite), as well as various borates, silicates, nitrates, and sulfocarbonates. The basic requirements to preserve a layer of salt are (Warren, 2006):

- A high concentration saline solution – brine
- An arid or semi-arid climate where the hydrological conditions are such that are able to maintain substantial volumes of brine at or near the land surface
- Accommodation space – a sedimentary basin – which is not being filled by another sediment
- Burial without flow of undersaturated fluids that dissolve the buried salts.

There are several different types of evaporites which are classified according to their precipitation process and location. These are resumed in Figure 2.6 according to Warren (2007). Primary evaporites are those which correspond to salts precipitated from a brine at earth's surface. These can be carbonates such as aragonite and dolomite; or evaporite salts such as gypsum, anhydrite and halite and form in the intial stages of brine concentration.

Secondary evaporites form in the shallow subsurface in contexts equivalent to the eogenetic and mesogenetic porosity realms defined for carbonates (Warren, 2007 after Choquette & Pray, 1970). Almost every subsurface evaporite corresponds to a secondary texture, presenting fabrics which are indicative of early recrystallization and/or flow of late basinal waters and occurring within the volume of rock which was originally precipitated as a primary evaporite. Figure 2.7 shows an evolution of evaporites in time, positioning each form/texture in the basin architecture context. In the present work we are more concerned with secondary evaporitic textures and these will be looked at with more detail next.

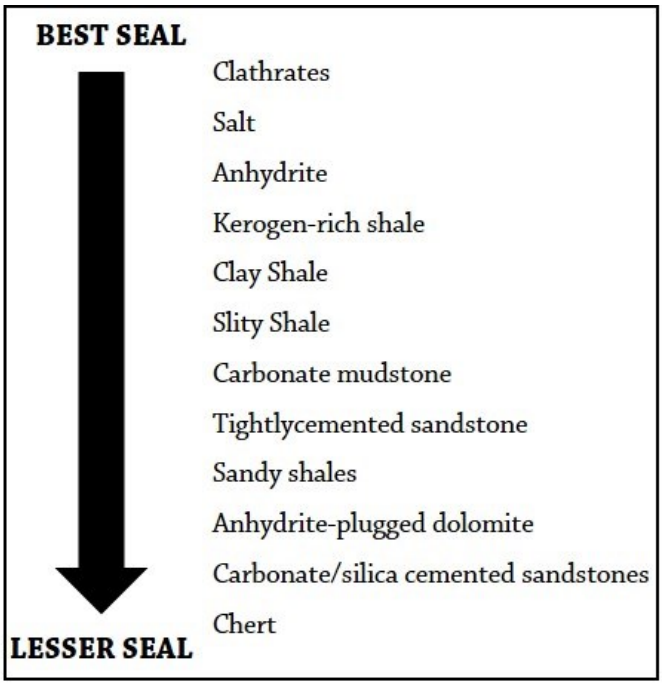


Figure 2.4: ranking of sedimentary rocks according to their ability to form a seal. (Adapted from Downey, 1984).

As previously mentioned, most of the evaporites found in the subsurface are dominated by secondary textures. These correspond to intrasediment crystal growths and replacements or cements deposited both in primary evaporite or other sedimentary hosts. The most common and consequentially more studied secondary evaporites are those formed in evaporitic mudflats environments also known as sabkhas (sabkhat).

Sabkha is an Arabic word used to describe an extensive coastal or inland arid mudflat environment where salt minerals are deposited and that is periodically flooded. The modern geological definition of a sabkha environment implies that evaporitic intra-sediments grow beneath a flat geomorphic surface which is defined by the top of the water table (Warren, 2006 after Warren & Kendall, 1985). The sabkha surface is subaerial and dry for most of the time but a shallow saline water table which lies a few centimeters to a metre below the surface maintains its capillary moisture in place resurfacing periodically. Using Warren, 2006 definition:

Sabkhas are hydrological settings where resurging groundwaters form displacive and replacive evaporite minerals (gypsum, anhydrite, halite, polyhalite, glauberite etc.) in the capillary fringe above a saline water table or in the brine-saturated muds immediately below.

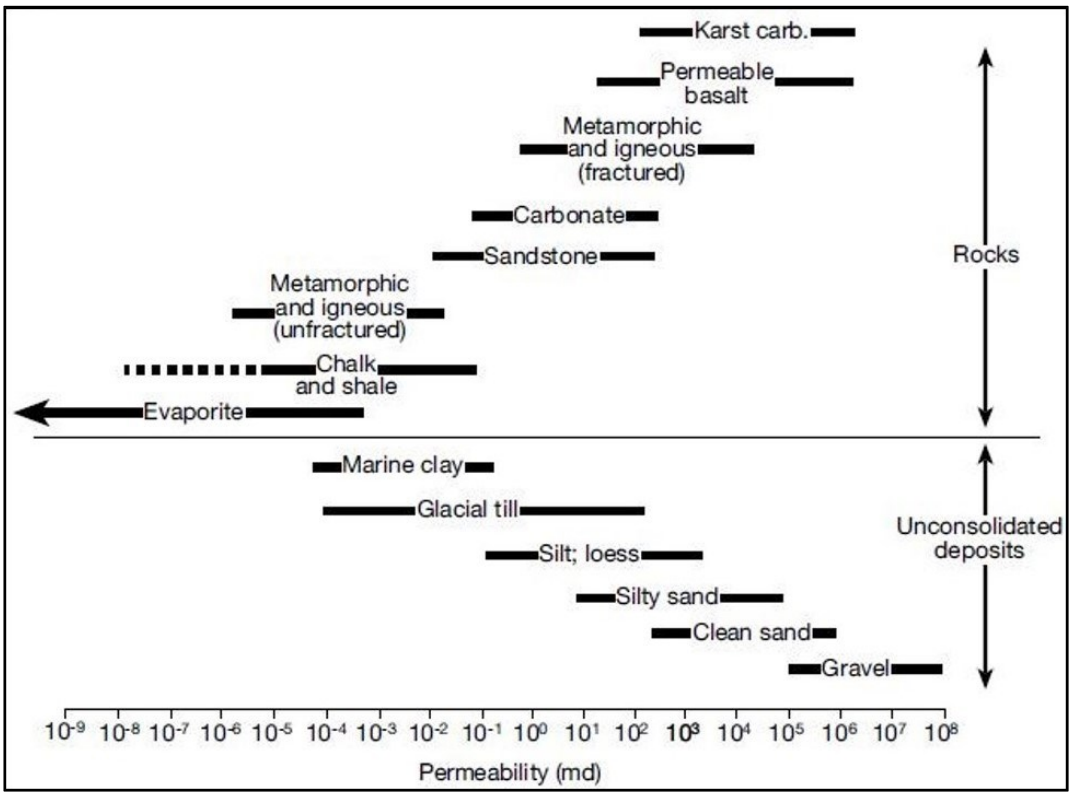


Figure 2.5: relative permeabilities of different lithologies. (Warren, 2007 after Beauheim and Roberts, 2002).

		Type	Precipitation process	Temp (°C)	Hydrological process	
"An evaporite is a rock that was originally precipitated from a saturated surface or near-surface brine by processes driven by solar evaporation"	Remnant primary textures	"Primary" evaporite	An evaporite salt precipitated via solar evaporation from a brine pool at the earth's surface. Crusts, bottom nucleates & pelagic crystals accumulate on brine pool floor.	0-60°C	Gravity and density effects at surface or in zone of active phreatic flow (brine reflux)	Saturation driven by solar evaporation
	Seconday texture dominant	"Secondary" evaporites (include sabkha nodules and the bulk of ancient evaporite beds)	An evaporite salt formed in the shallow subsurface in the zone of active phreatic flow. The concentration process of the brine and the associated gravitational reflux is driven by solar evaporation. May form displacive, replacive or cement textures.			
			A burial diagenetic evaporite phase that replaces earlier evaporite beds. Salt precipitation is driven by fluid mixing or saturation mechanisms driven by burial diagenetic processes. Forms replacive and cement textures.	60 -200°C	Burial effects compactional and thermobaric	Brine saturation not driven directly by solar evaporation
		Burial salts	Subsurface precipitation of evaporite as cements and replacements in non-evaporite matrix from a saturated brine derived from the dissolution of adjacent evaporite beds or zones of brine mixing.			
	No primary texture	"Tertiary" evaporites	An evaporite formed by brine saturation related to partial bed dissolution via re-entry into the zone of active phreatic circulation. Often driven by basin uplift and erosion.	0-60°C	Stagnant to active phreatic flow	
? ?		Hydrothermal salts	Salts (particularly anhydrite) precipitated by the heating of seawater or subsurface water or mixing of hydrothermal waters.	>150°C	Hydrothermal circulation	

Figure 2. 6: Classification of evaporite formation in the depositional-diagenetic setting (Warren, 2006).

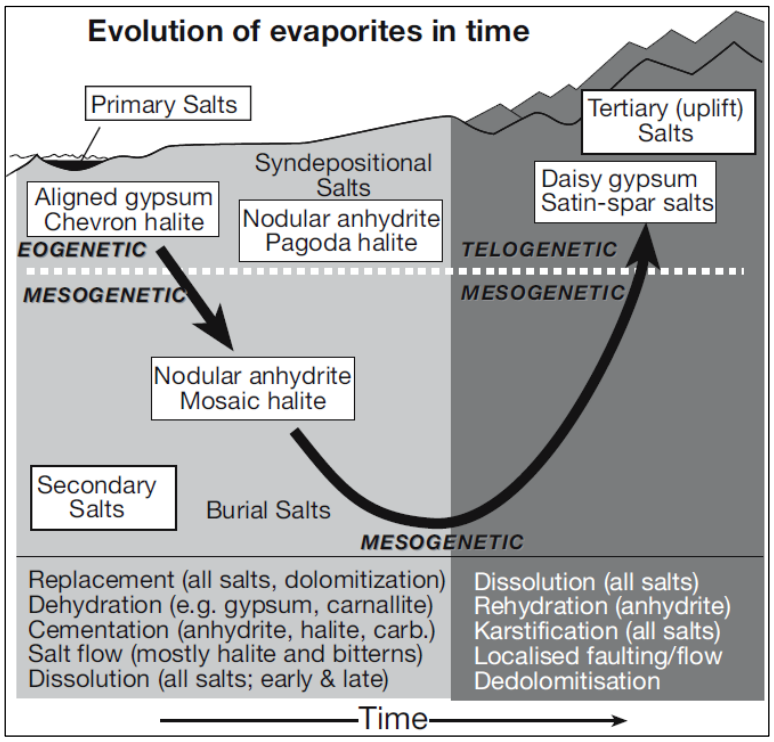


Figure 2.7: postdepositional evolution through time of evaporitic textures and relative position for their formation with regards to the systematic definition proposed by Choquette & Pray (1970) (Warren, 2007).

Several types of sabkhat can be defined according to the depositional setting and the consequent sedimentary response (Figure 2.8) (Handford, 1981): coastal marine, continental (fluvio/lacustrine) and eolian. A more detailed description on these several types of depositional sabkhat will not be made in the present text but can be found in Warren, 2007.

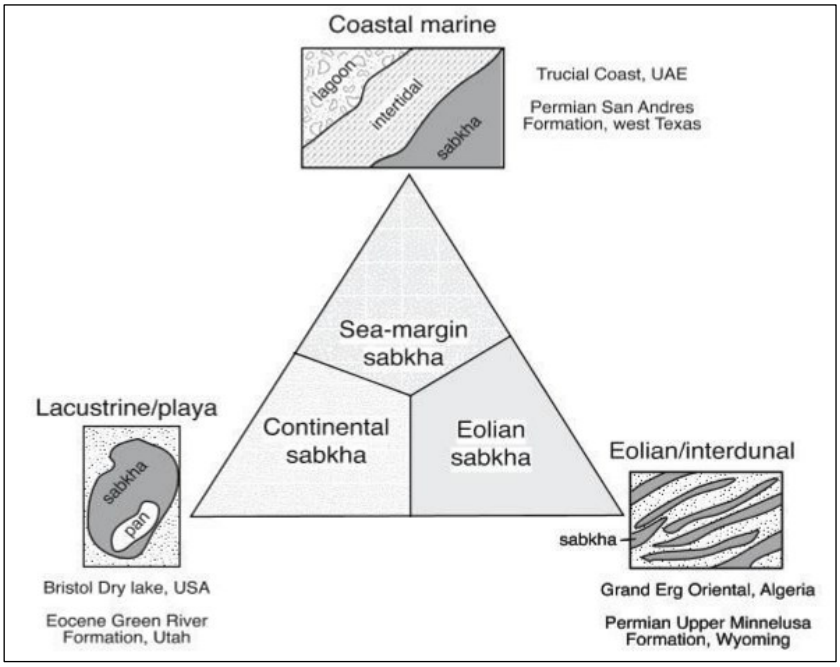


Figure 2.8: sabkha classification (Hanford, 1981)

2.1.3 Evaporite Textures

As mentioned previously there are several types of evaporites which are classified according to their precipitation process and location and that also correspond to different textures with different chemical compositions. Within primary evaporites we can consider both carbonates (aragonite, dolomite, low-Mg calcite) and salts (gypsum, anhydrite, halite etc.). Secondary evaporites are actually diagenetic textural overprints. These are formed through intrasediment crystal growths (displacive growth,recrystallization) and replacement or as cements in pre-existing evaporite and nonevaporite hosts and indicate a superimposed brine chemistry that differs in terms of chemicalcomposition/salinity or temperature from the original (primary) chemistry that formed the primary sediment. (Warren, 2007).

Primary Evaporite Textures

- Carbonates: these are the first evaporite minerals to precipitate from an hypersaline surface water and are composed of aragonite, high- and low Mg-calcite, magnesite and primary dolomite. Their chemistry is conditioned by changes in the water level and salinity changes which influences the Mg/Ca ratio. Normally calcite is an early precipitate and the remaining brine is increasingly richer in Mg. Consequently later carbonates are dominated by aragonite, magnesite or even dolomite (Figure 2.9).
- Salts: after the brine has precipitated the carbonates, salts are deposited. The two main types of salts are those formed mainly by $CaSO_4$ (anhydrite or gypsum) and those formed by NaCl (halite). Figure 2.10 summarizes the main textures.

Secondary Evaporite Textures

Considering that in the geological context most of the evaporites have been subjected to intense secondary alterations, for the present study these are the most important evaporitic features, particularly those which are related to sydepositional intrasediment alterations and burial of sulphate salts (the context in which our field work was conducted).

Nodular anhydrite and gypsum are one of the most common syndepositional (early-diagenetic) intrasediment evaporites. The nodules are formed at the upper phreatic zones beneath the sabkha surface by replacement, displacement and breakage from fluids in the pores of the sediments (Murray, 1964). The formation mechanisms create the characteristic entherolitic and “chicken wire” textures (Imlay, 1940) (Figure 2.11).

More important are the evaporite textures formed during and as a result of burial which are related to the release of entrained structural water (dehydration) from the sulphate rich sediments.

The most common form of $CaSO_4$ at eath's surface is gypsum, being considered by some authors as the original calcium sulfate mineral (Murray, 1964). The existence of anhydrite at the surface is mostly associated with intense solar dehydration, but the thick anhydrite deposits that are common in the geological record are a product of burial dehydration to nodular anhydrite during early burial (Warren, 1991). The process of anhdritisation involves several steps and different textural characteristics which are documented in Figure 2.12.

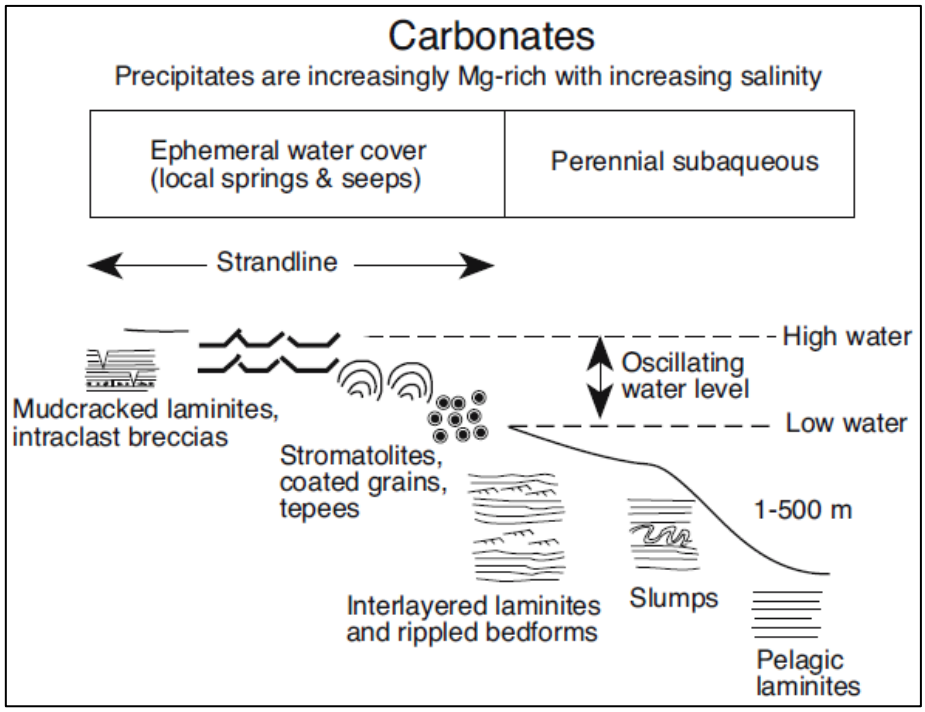


Figure 2. 9: summary of the evaporitic carbonate textures and its depositional significance (Warren, 2006)

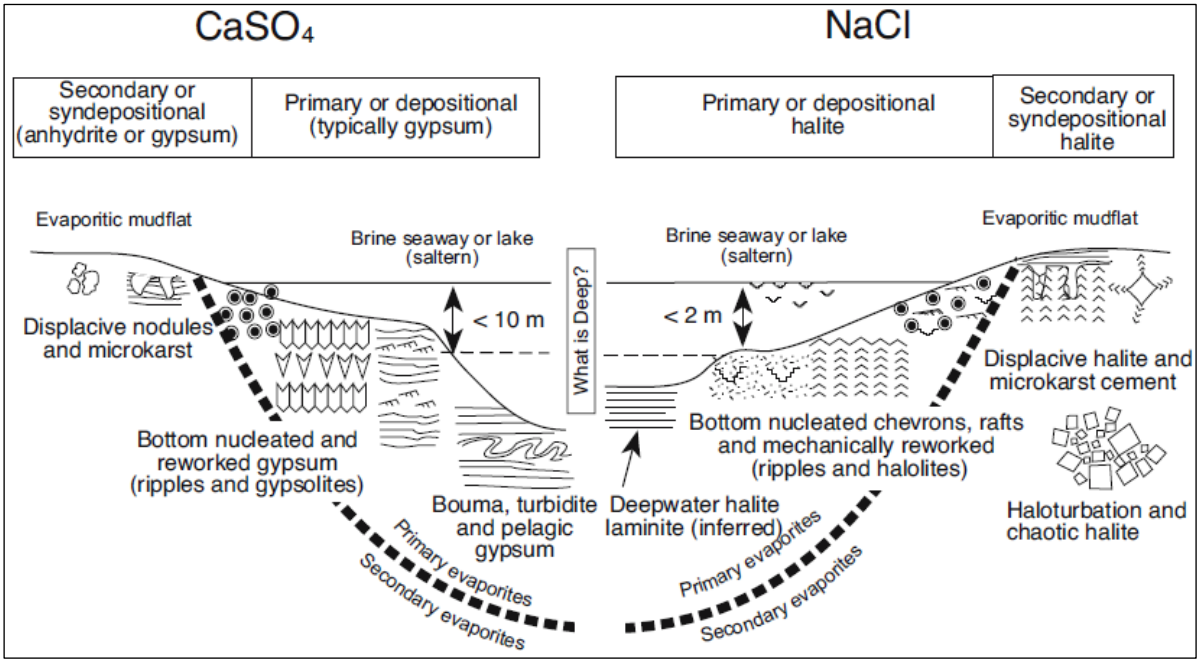


Figure 2.10: summary of the $CaSO_4$ and NaCl syndepositional textures and their typical position in a depositional basin (Warren, 2006)

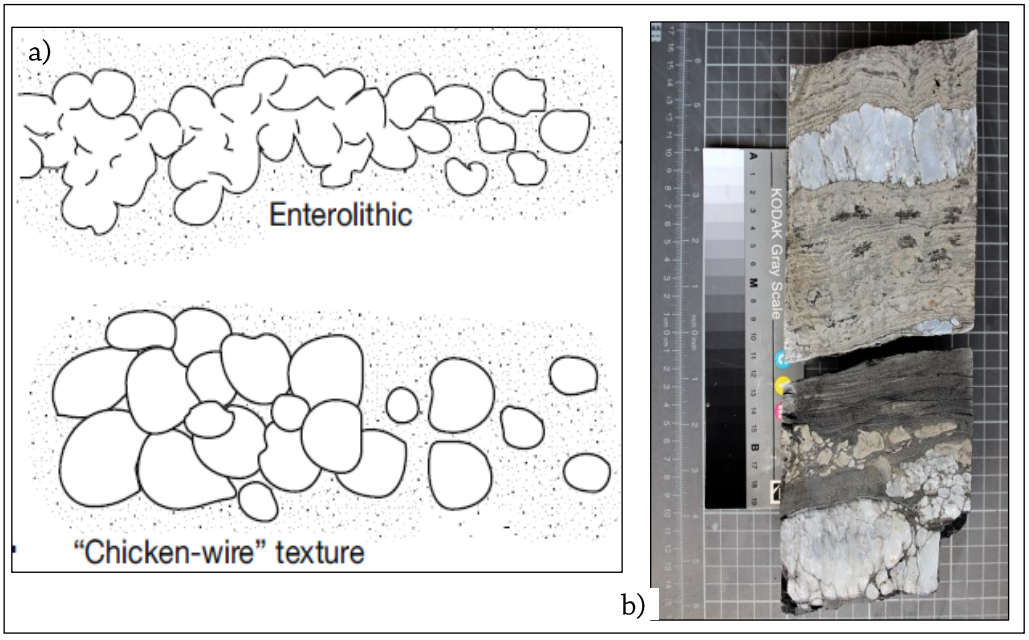


Figure 2.11: a) types of secondary anhydrite textures (Warren, 2006). b) onshore UK core example of these textures.

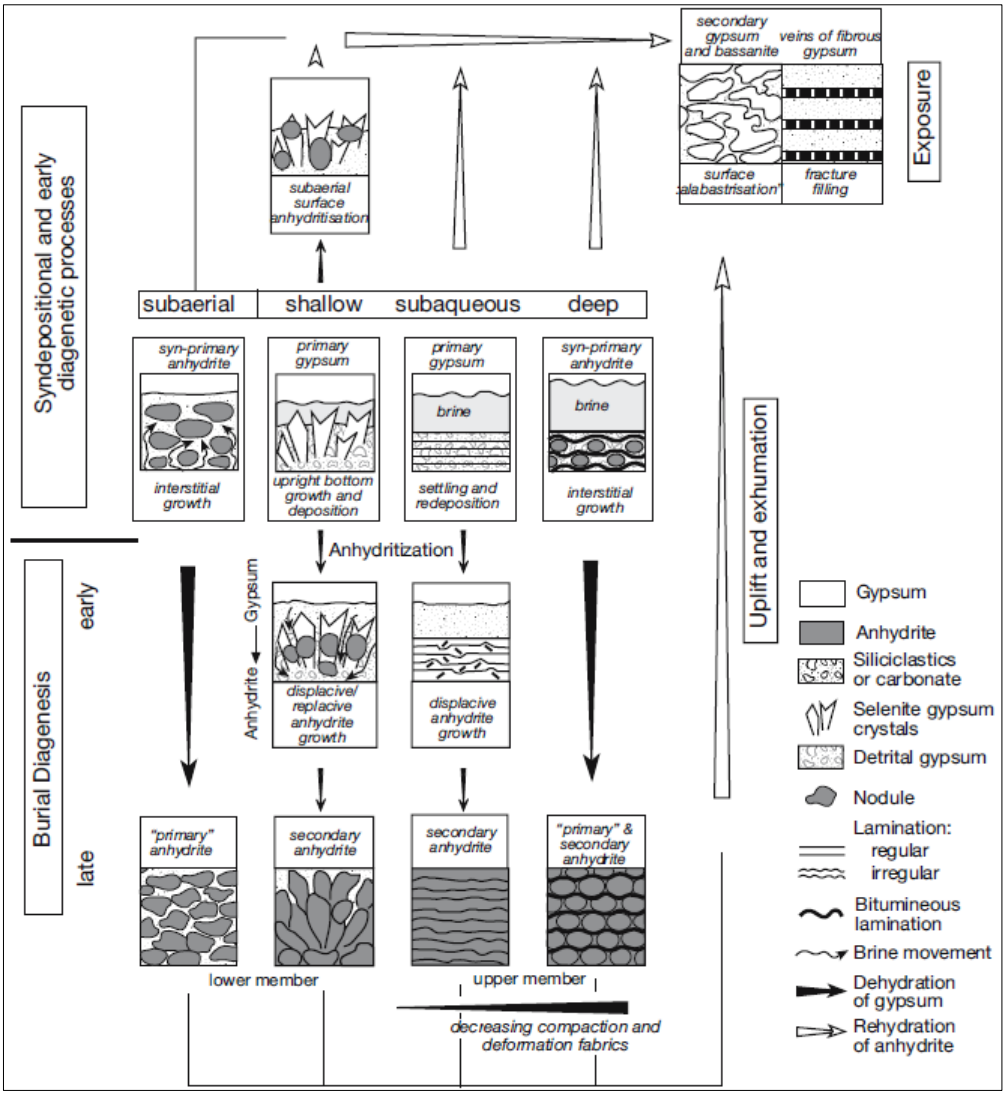


Figure 2.12: evolution of gypsum/anhydrite sediments when subjected to secondary alterations as a result of burial and exhumation (Warren, 2006).

As a summary we can conclude that evaporite sediments can accumulate as carbonates or as more saline salts. Carbonates can be present with different textures such as laminites or intraclast breccias deposited in the strandline zone, stromatolites, or even pelagic laminites at greater water depths. Salts are mainly dominated by gypsum and anhydrite in a large range of crystalline textures.

Most of the evaporites that are found in the geological record show signs of secondary or diagenetic textural overprints which are the result of processes such as displacive growth, recrystallization, back reactions and replacement. The process of anhydritisation is one of the most important occurences and results in textures such as nodular enterolithic and chicken-wire anhydrite.

Rehydration fabrics such as satin spar, porphyroblastic and alabastrine gypsum are important features which are the result of uplift of an evaporite sedimentary sequence and can register the presence of high fluid pressures.

2.2 Evaporites as high fluid pressure indicators

In a sedimentary basin which is not subjected to tectonic forces, pressure at a certain depth is generated by both the lithostatic pressure (also called overburden or vertical stress) i.e. the pressure or stress imposed by the weight of the overlying material; and the hydrostatic pressure – the pressure exerted by a column of fluid. For water and other liquids, calculation of the hydrostatic pressure can be simplified assuming that most liquids can be considered incompressible, hence assuming a constant density provides a reasonable approximation; and since the height of the fluid column to the depth of interest is small compared to the radius of the Earth, variation of gravity can be neglected. Therefore the formula for hydrostatic pressure for a certain depth of interest can be written devised in Equation 6:

$$p = h \rho g \quad (6)$$

where

p = pressure in fluid (N/m^2, Pa, lb_f/ft^2, psf)

h = height of fluid column, or depth in the fluid at which the pressure is measured (m, ft)

ρ = density of liquid (kg/m^3)

g = acceleration of gravity (9.81 m/s^2, 32.17405 ft/s^2)

For a typical porewater column the rate of hydrostatic pressure increase is of around 1.525 psi/m (this rate varies depending on the salinity of the porefluid (freshwater has a lower gradient than a salt-saturated solution). This means that for a depth of 1000m the expected normal pressure would be of 1525 psi (10.5 MPa) and any higher or lower pressure would be considered abnormal. Considering this, abnormal formation pressure is any pressure that exceeds of falls below the normal pressure to be expected at a given depth (Warren, 2006). In order for an abnormal pressure to be formed in a formation, the following conditions have to be met (Warren,2006):

- Porosity must exist as the formation has to have means of storing a fluid.
- A vertical and lateral seal must be present. A formation which is adjacent to a permeable layer will not retain fluids and hence will not form a pressure differential.

According to Hunt (1990), around 80% of the world's abnormally pressured basins are controlled by low permeability seals and in fact most intervals of abnormal pressure are related to faults, thick shales, extensive salt seals or the combination of several of these features.

The most common abnormally pressurized formations are those which are overpressured (in opposition to underpressured) and are generally related to units of rock where the free flow of fluids is prevented by either the formation where the fluids are stored or by a formation acting as an impermeable barrier (this formation can be placed by tectonic activity) that is a cap-rock seal. This

type of overpressuring s called geopressure. Therefore, a pore fluid is overpressured if its pressure exceeds that of the hydrostatic gradient at a specific depth (Osborne & Swarbrick, 1997) (Figure 2.13).

Due to their extremely low permeability, evaporites – which normally form hydraulic seals (Section 2.1) - play an important role in generating abnormal fluid pressures. Some of the highest measured bottom-hole pressures in the world and some of the highest wellhead flow pressures (measured during production) are found in subsalt reservoirs (Warren, 2006). Examples of abnormally high fluid pressures that are sealed by evaporites can be found in: the dolomite reservoirs of the Jurassic Smackover Fm. (Central Mississippi Salt Basin, Gulf of Mexico); the Upper Devonian to Middle Carboniferous carbonates in the Tengiz oilfield (Precaspian basin, Western Kazakhstan); the Rotligende sands in the Southern North Sea. These abnormal fluid pressures, which have clearly been maintained by long term (200-250 Ma) seal integrity can be caused by different mechanisms (Warren, 2006; Osborne & Swarbrick, 1997):

1) Increase in Compressive Stress, which can occur by:
    a. Disequilibrium Compaction
    b. Tectonic Compression:
2. Change in volume, which can be occur by:
    a. Hydrocarbon generation
    b. Transformation from gypsum to anhydrite
    c. Clay conversion
    d. Aquathermal pressuring

3. Fluid flow and buoyancy forces
    a. Potentiometric head
    b. Hydrocarbon buoyancy
    c. Osmosis

From all of these mechanisms the most important are disequilibrium compaction, tectonic compression, aquathermal pressuring (for evaporite seals), gas generation, , transformation from gypsum to anhydrite, hydraulic (potentiometric) head and hydrocarbon buoyancy. These are detailed below.

Disequilibrium Compaction (Figure 2.13): as sediments undergo burial and the vertical loading increases the pore volume is reduced and the formation fluids are forced out. If burial occurs at slow rates (low sedimentation rates or low subsidence), the equilibrium between overburden and reducing

pore-fluid volume is maintained. However if the burial rates are high (high sedimentation rates/ high subsidence) and consequently the overburden stress increase is also high, rapid expulsion of fluids is required. If the fluids cannot be expelled fast enough to maintain a "normal" hydrostatic pressure, the fluid pressure rises above it giving way to what is called disequilibrium compaction. This process is favoured by rapid burial and low permeability. Figure 1 shows a typical depth-pressure curve for a sediment that is undergoing burial and where fluids were expelled at a rate which was lower than the burial rate. Between points A and B, pore pressure increases following the hydrostatic gradient because the fluids are able to escape during the compaction process. However, as subsidence continues and the permeability of the sediment is reduced, fluids start to be retained (Point B – fluid isolation depth) and eventually the pore pressure exceeds the hydrostatic pressure, rising continuously along a path B-C subparallel to the lithostatic gradient.

Although the fluid pressure never exceeds the lithostatic pressure, it can exceed the fracture pressure (the amount of pore pressure a rock can withstand before its tensile strength is overcome and hydraulic fracturing occurs) if its gradient is less than the lithostatic gradient. Apart from the inherent strength of the rock the variable that determines whether a particular rock undergoes hydraulic fracturing is the depth at which fluid isolation occurs: considering the sediment in Figure 1, it is clear that the pressure path that this sediment undergoes never intersects the Leak-Off Pressure (LOP) curve (which represents the magnitude of pressure exerted on a formation that causes fluid to be forced into the formation, i.e. an approximation to the strength of the rock). For hydraulic fracturing to occur, fluid isolation had to happen at a shallower depth.

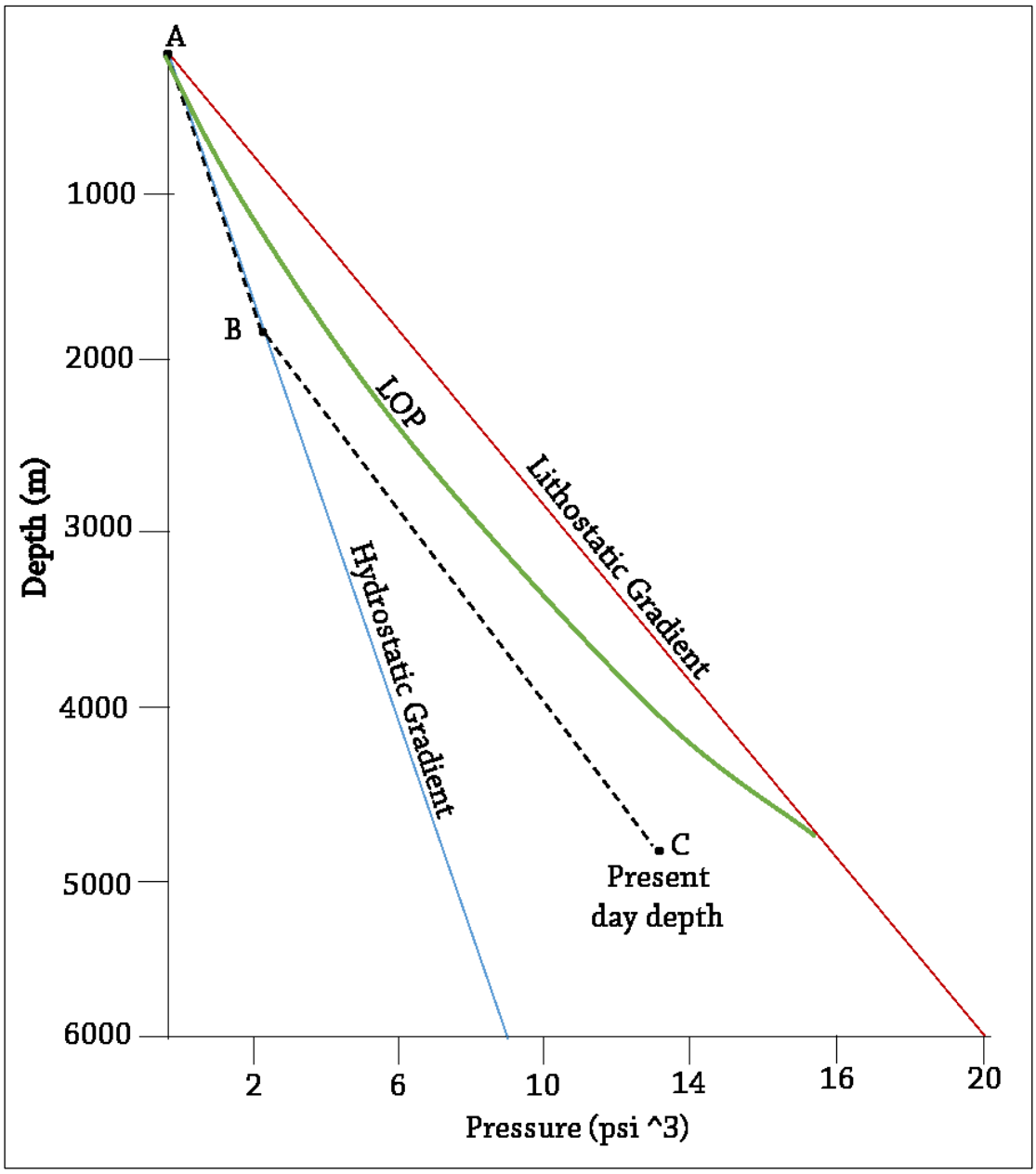


Figure 2.13: During burial of a sediment, the pore pressure increases following the hydrostatic gradient (A to B) because the fluids are able to escape during the compaction process. However, as subsidence continues and the permeability of the sediment is reduced, fluids start to be retained and eventually the pore pressure exceeds the hydrostatic pressure, rising continuously along a path B-C subparallel to the lithostatic gradient (adapted from (Osborne & Swarbrick, 1997). The hydrostatic gradient is assumed to be 1.525 psi/m and the lithostatic gradient to be 3.28 psi/m

Tectonic Compression: In regions where lateral compression of rocks is occurring (subduction and transpression zones) an increase in pore pressures can occur in a similar way that vertical stress can cause overpressuring by disequilibrium compaction. Horizontal compression of sediments is also possible in large basins during shallow burial triggered by the radius of the curvature of the Earth (Price, 1974). However these periods of overpressuring are thought to be transitory as a rapid pressure release through faults and fractures is possible during periods of fault movement and opening.

Aquathermal pressuring: as sediments are heated with burial, so are the fluids contained in them. The expansion of the formation water (which expands more than mineral grains) can generate fluid pressure if the system is close to perfectly sealed and sustains a constant volume as temperature rises. These conditions are very hard to be met and therefore aquathermal pressuring is considered only likely to occur evaporate-rich sequences where the permeability is extremely low.

Gas generation: the generation of methane gas during shallow burial and the release of gas from gas hydrates during subsidence (pressure and temperature increase) can potentially cause overpressuring due to volume increase (Osborne & Swarbrick, 1997 after Barker, 1987 and Hunt, 1979). At higher depths and temperatures oil ultimately converts to methane by thermal cracking which is accompanied by volume expansion leading to extreme overpressures if the system is closed (Osborne & Swarbrick, 1997). Baker (1990), calculated that in an isolated system a 1% cracking of oil to gas is enough to cause pressure to reach lithostatic values and thereafter further cracking should lead to hydraulic fracturing and leakage.

Transformation from gypsum to anhydrite: The conversion from gypsum to anhydrite occurs according to Equation 7 at shallow depths (~400m) when overlain by shale or other gypsum layers in a rift environment, and at greater depths when overlain by salt in a stable cratonic region. This conversion is accompanied by a 39% volume reduction (Jowett & Cathles, 1993 after Zen, 1965 and Hanshaw & Bredehoeft, 1968). If the water released during the conversion cannot escape, the pore fluids become geopressured in a lithostatic pressure regime (eg.sealed in below salt) (Jowett & Cathles, 1993).

Hydraulic (potentiometric) head: the elevation of a water table in mountainous regions creates a pressure in the subsurface of a confined aquifer. In many cases, this hydraulic head (measurement of liquid pressure above a geodetic datum) causes the aquifers to be overpressured.

Hydrocarbon buoyancy: the tendency for a fluid to float or rise when submerged in a fluid of greater density is called buoyancy. Due to the lower density of oil relative to the associated formation water, a reservoir which contains both fluids is subjected to buoyancy pressure. This pressure is a function of the density difference between the two fluids and the height of the hydrocarbon column.

Having established that abnormal fluid pressures – particularly high fluid pressures - can be generated by various different mechanisms and that low permeability units (such as evaporites) play a decisive role in the maintenance of that fluid pressure, it is important to establish the geological features that allow us to conclude that a certain formation as undergone high fluid pressures.

As mentioned in Chapter 1 with the example from the Bristol Channel Mercia Mudstone (Figure 1.11) and its satin spar veins, evaporites register high fluid pressure events, which can be the result of the uplift or inversion of a basin. When this occurs, nodular anhydrite is rehydrated when re-entering the telogenetic zone and comes into contact with low salinity, low temperature waters. Two common types of gypsum textures are porphyroblastic and alabastrine gypsum.

The first texture is the result of the re-entrance of nodular anhydrite from the stagnant phreatic into the deep portion of the zone of active phreatic flow, whereas alabastrine gypsum forms in the zone of more diffuse active phreatic flow (Figure 2.12).

Another common gypsum feature are the veins and fractures filled with satinspar. To illustrate the formation of such features one of the best natural examples is the Bristol Channel Mercia Mudstone, one of our field work areas, where there are red marls contain several evaporite-rich horizons. Cosgrove (2001) demonstrates that the horizontal satin spar veins are the product of high fluid pressures during the inversion of the basin in the middle Cretaceous as a result of a major north-south compression. He points out that the fact that the network of hydraulic fractures is only preserved in the evaporite horizons is related to the volume changes associated with the hydration of anhydrite to gypsum that occurs as the rock mass is exhumed and the relatively low temperature and pressure conditions necessary for the formation of gypsum are encountered (Jowette et al., 1993). This lithogical change should result in an increase in volume of around 63% if all the calcium sulfate is retained within the system (Shearman et al, 1972). Cosgrove goes on to argue that the exhumation phase, during which the hydration occurred, was associated with the tectonic inversion of the basin. Consequently the sediments were experiencing a sub-horizontal tectonic compression during their exhumation causing an increase in fluid pressure and promoting the formation of horizontal hydraulic fractures that were then filled with the excess calcium sulphate in the form of satin spar. No fractures are seen in the evaporite free zones of the mudstone because the absence of evaporites does not allow preservation, meaning that the fractures closed and healed as soon as the fluids past through them and the pressure dropped.

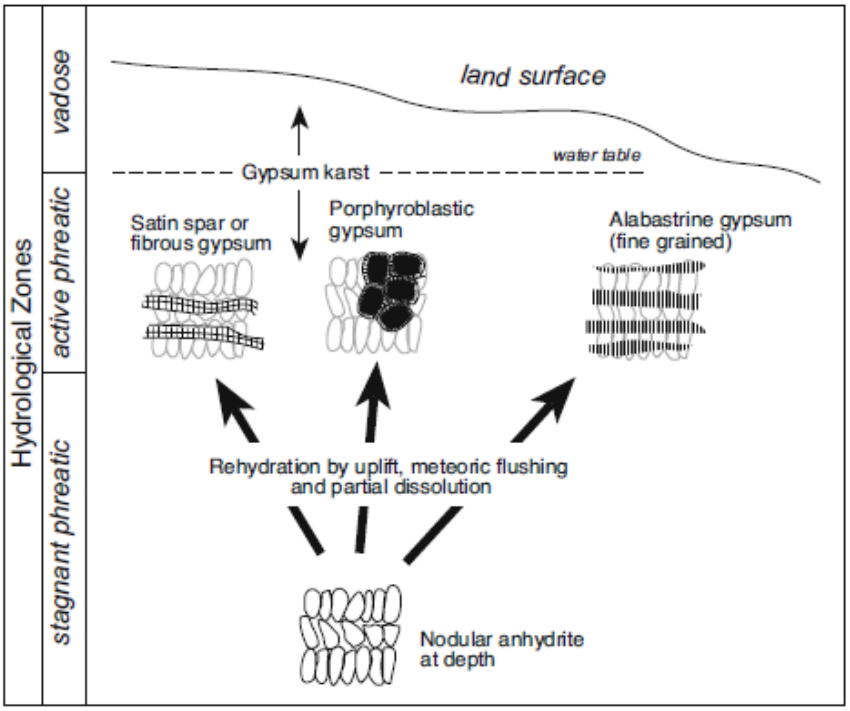






Figure 2.14: a) schematic rehydration of nodular anhydrite to porphyroblastic and alabastrine gypsum (Warren, 2006). b) porphyroblastic gypsum at the Brightling mine, UK; c) alabastrine gypsum Winchester-1, onshore UK.

Chapter 3
Field Work

3.1 Introduction

This chapter describes the field work that was conducted in order to:

- Establish the geological context of Qatar and particularly of the evaporite cap-rock that seals the reservoirs where CO_2 is to be injected.
- Determine the sedimentary and stratigraphic characteristics of evaporite rocks.
- Understand the particularities of hydraulic fracturing in low-permeability rocks.
- Analyse the process of fracture propagation through layered sedimentary sequences.

To achieve these goals, a regional study of the tectonic setting of Qatar was carried, evaporite rich deposits were studied in mines, drill-cores of evaporite rich sediments were studied and field work was conducted at several locations. The results of this work are presented here.

3.2 An analysis of the regional geology of Qatar

The State of Qatar is located in the Southwestern part of the Persian Gulf covering an area of around 11.500 Km^2. It's only terrestrial border is with Saudi Arabia and it forms a North-South trending peninsula projecting into the Persian Gulf (Figure 3.1). In the 1940's Qatar initiated a new chapter in the country's history with the discovery of the onshore Dukhan oil field and in 1960 the first offshore field was discovered. Today, this country is the world's third largest gas producer, and retains about 25 billion barrels of oil.

Qatar is located in the Arabian Plate which originated 25Ma ago when rifting to form the Gulf of Aden and Red Sea split off a fragment of the African continent. It is divided in two major units, the Arabian Shield, dominated by Precambrian rocks with acts as the basement to the overlying sedimentary rocks of the Arabian Platform mainly formed of a Phanerozoic succession that becomes progressively younger and thicker when traced from West to East. The plate measures 2600 km north–south and 3000 km east–west and its boundaries are (Figure 3.2): on the West the Dead Sea transform and Red Sea spreading/rifting axis; on the North a zone of plate convergence made up of the East Anatolian fault, Bitlis suture, and Zagros collision zone; on the East the Owen Fracture Zone; and on the south the Gulf of Aden spreading axis (the Sheba Ridge) (Stern & Johnson, 2010).



Figure 3.1: A satellite image of the Persian Gulf area, with the Qatar Peninsula in the centre.

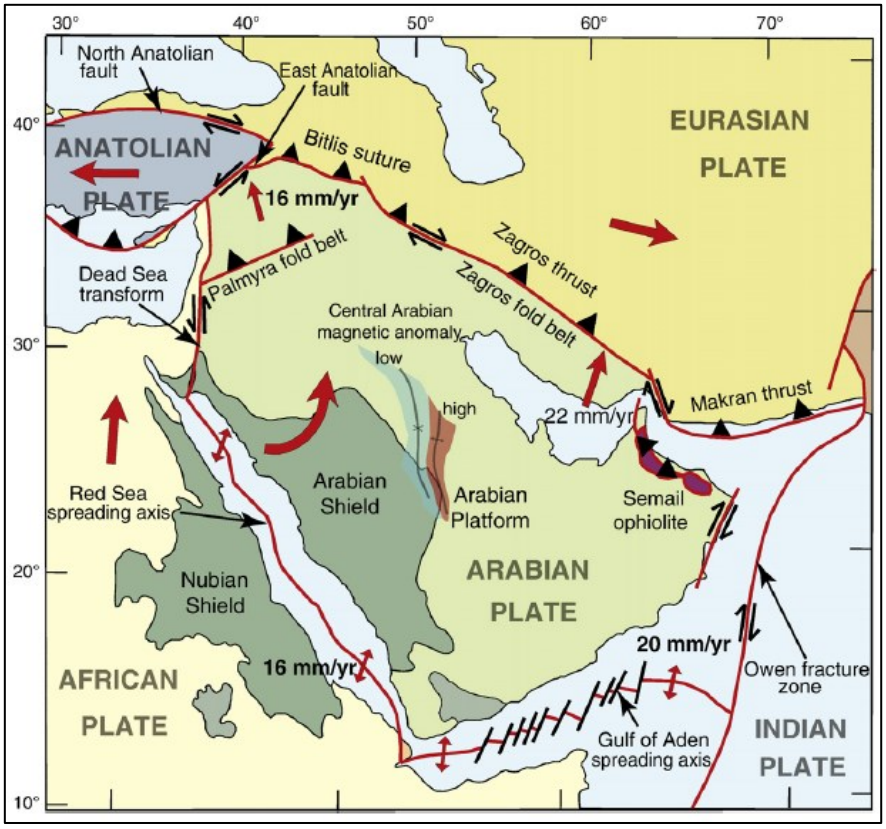


Figure 3.2: A simplified map of the Arabian Plate, with plate boundaries showing the approximate plate convergence vectors, and principal geologic features (Stern & Johnson, 2010). Notice the location of the Qatar peninsula.

In terms of the structural domains, the Arabian Plate can be divided into (Stern & Johnson, 2010; Ziegler, 2001) (Figure 3.3):

1) a western domain comprising the Shield and the south-central part of the Arabian Platform characterized by northerly and north-westerly structural trends. The northerly trends are interpreted as reflecting the Precambrian basement architecture. Some of the well-known northerly structural trends are the Summan Platform, Dibdibah Trough, Khurais-Burgan Anticline, En Nala (Ghawar-Safaniya) Anticline, and the Qatar Arch. The northwesterly grain is visible in the Arabian Shield as the Najd Fault System, and is interpreted as bounding the Arabian Plate along the Zagros Suture.
2) a north-central domain dominated by northerly trends and a broad north-easterly trend
3) an eastern domain marked by north-easterly trends, which trend correspond to the Dibba Fault, Oman salt basins, and the Wadi al Batin lineament, and appears to control the distribution of Infra-Cambrian salt basins of the Arabian Gulf and Oman (Husseini, 1988; Husseini and Husseini, 1990; Loosveld et al., 1996; Al-Husseini, 2000).

Qatar is located in the sediment cover of the Arabian Platform. Because of the specific interest to the present research it is discusses in more detail later in this section. The Pan-African Arabian Shield which is formed of a complex of igneous and metamorphic rocks, will not be described in detail. It is noted however that an N-S trending basement lineament underlies Qatar and that this has a major influence on its structural evolution.

3.2.1 The Arabian Platform

The Arabian Platform is a large wedge-shaped sedimentary basin (Figure 3.4), formed on the north-eastern margin of the Arabian sector of Gondwana, where a very thick, virtually continuous sequence of sediments accumulated from the Late Proterozoic to Holocene (Alsharan & Nairn, 1997; Beydoun, 1991; Edgell, 1996; Konert et al., 2001; Sharland et al,. 2001; Ziegler 2001 as cited in Perotti & al., 2011). The sedimentary sequence thickens from the Southwest (where the Arabian Shield crops out) to Northeast, reaching about 18km (Edgell, 1996) in the Zagros region where it is deformed into a fold-thrust belt as a result of the Arabian-Iranian plate convergence which occurred in the Neogene. The present-day Zagros deformational front runs approximately along the Iranian coastline (Perotti, et al., 2011).

Several authors such as Beydoun (1988), Alsharhan and Nairn (1997), Christian (1997) and Sharland et al. (2011) have have published regional litho- and chronostratigraphic reviews in attempts to comprehend the vast amount of stratigraphic information on the Arabian Platform. Ziegler (2001) has made a paleofacies reconstruction for an interval that covers the Late Permian to the Holocene

where each reconstructed interval is shown with its associated oil and gas fields, illustrating the close relationship between lithofacies, depositional environments, and petroleum reservoirs. The stratigraphic chart created by Ziegler (2001) is shown if Figure 3.5.



Figure 3.3: Selected structural and tectonic features of the Arabian Plate (Ziegler (2001) after Beydoun (1988), Alsharhan and Nairn (1997), Christian (1997) and Sharland et al. (2001)).

The evolution of the Arabian Platform is summarized by Perotti et al. (2011) based on previous work by Alsharan & Nairn (1997); Konert et al. (2001); Sharland et al. (2001) and Ziegler (2001) as follows (Figure 3.6):

Late Proterozoic: After the consolidation of the Arabian Shield by the accretion of oceanic arcs in the Precambrian, an extensional phase (Najd rifting: Husseini, 1988; Al-Husseini, 2000) in the late Precambrian-Cambrian formed several basins, currently located in the Persian Gulf sector and in Oman, in which thick (up to 2.5 km: Edgell, 1996) evaporites, predominantly composed of halite, of the Hormuz Formation (and the equivalent Ara formation in Oman) were deposited.

During the Paleozoic these basins were part of a passive margin/interior margin setting on northeastern Gondwana and were filled with uniform clastic continental and shallow marine sediments.

Carboniferous: during this period the area was affected by the Hercynian orogeny which reactivated the Proterozoic trends (Konert et al., 2001) creating regional uplift with consequent widespread erosion.

Permian – Paleogene: the broad stable passive margin at the northeastern border of the African plate over this long time interval, allowed the deposition of shallow-marine carbonates intercalated with periods of anhydrite and other evaporites and shale deposition.

The northeastern part of the basin has been undergoing shortening as a consequence of collision of the Arabian Plate with the Iranian Plate which is part of Laurasia (Zagros orogeny – 150Ma to 0Ma) which created the Zagros wedge-shaped, low-angle fold-and-thrust belt and a foreland basin that has been the site of mixed evaporitic, carbonate and clastic sedimentation. Several regional unconformities and hiatuses punctuate the sedimentary succession as a consequence of eustatic sea-level changes and epirogenic movements (Sharland et al., 2001).

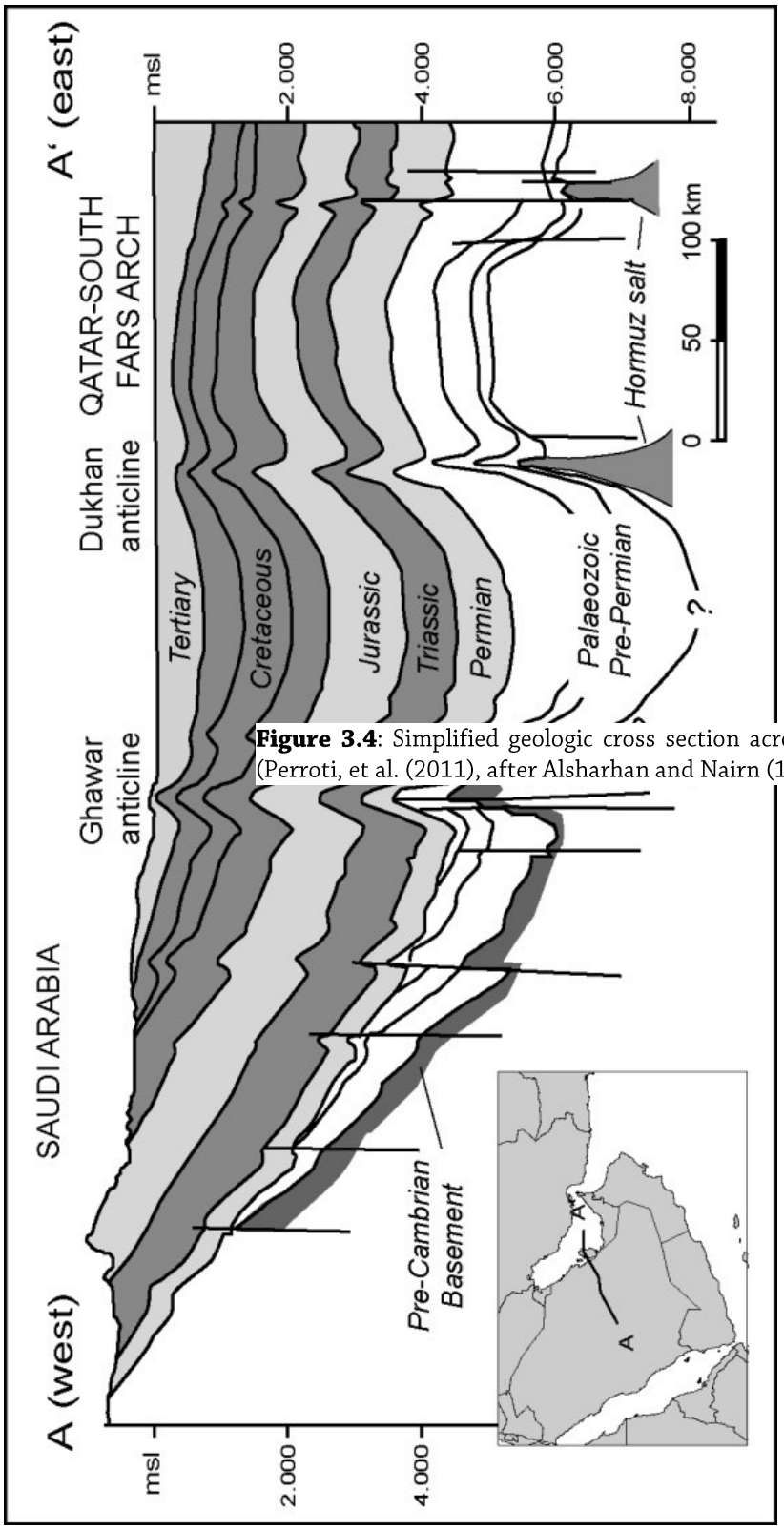


Figure 3.4: Simplified geologic cross section across Saudi Arabia and Qatar from Arabian Shi
(Perroti, et al. (2011), after Alsharhan and Nairn (1997), Konert et al. (2001) and Pollastro (2003)

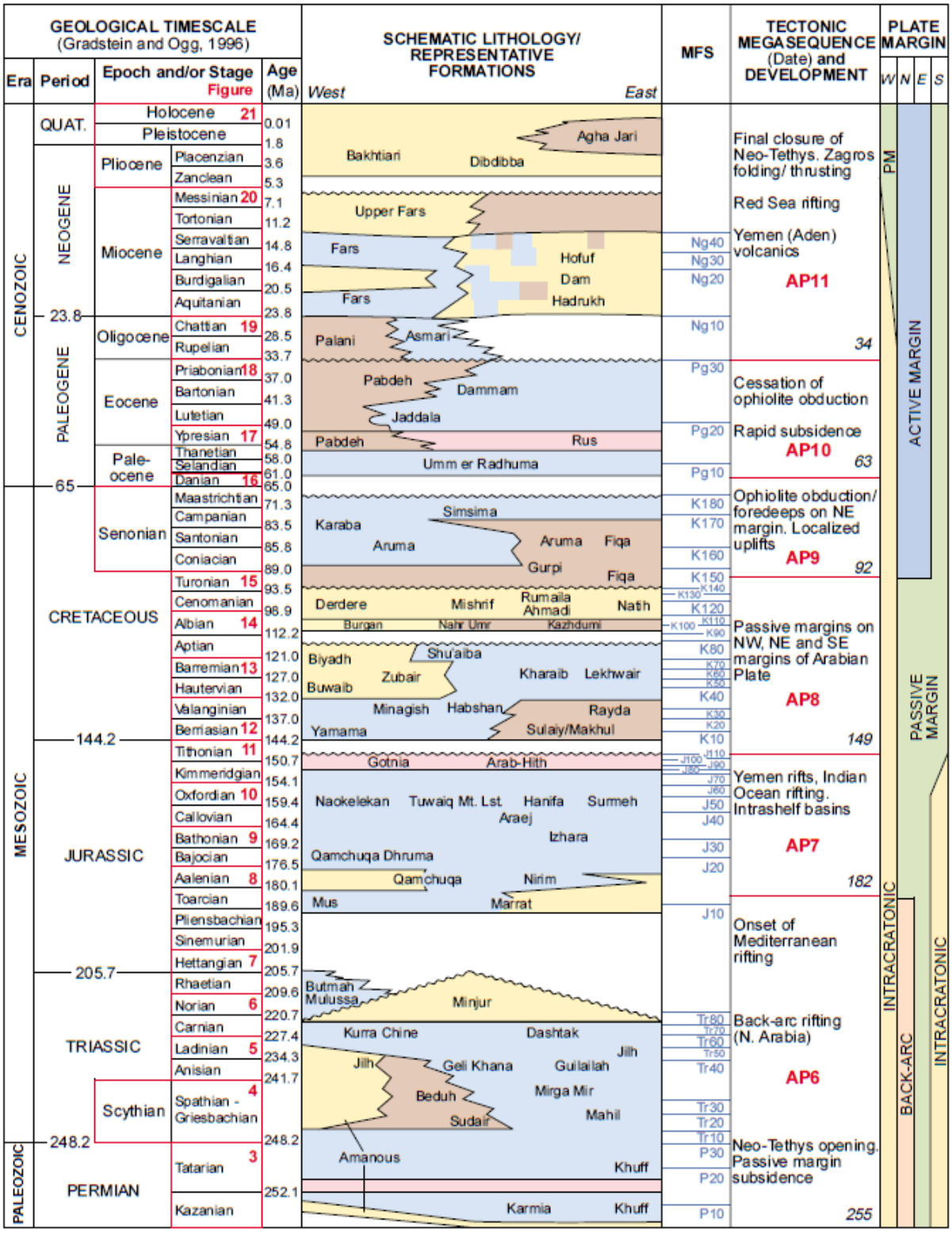


Figure 3.5: Arabian Platform stratigraphic chart (Ziegler (2001) after Sharland et al (2001)

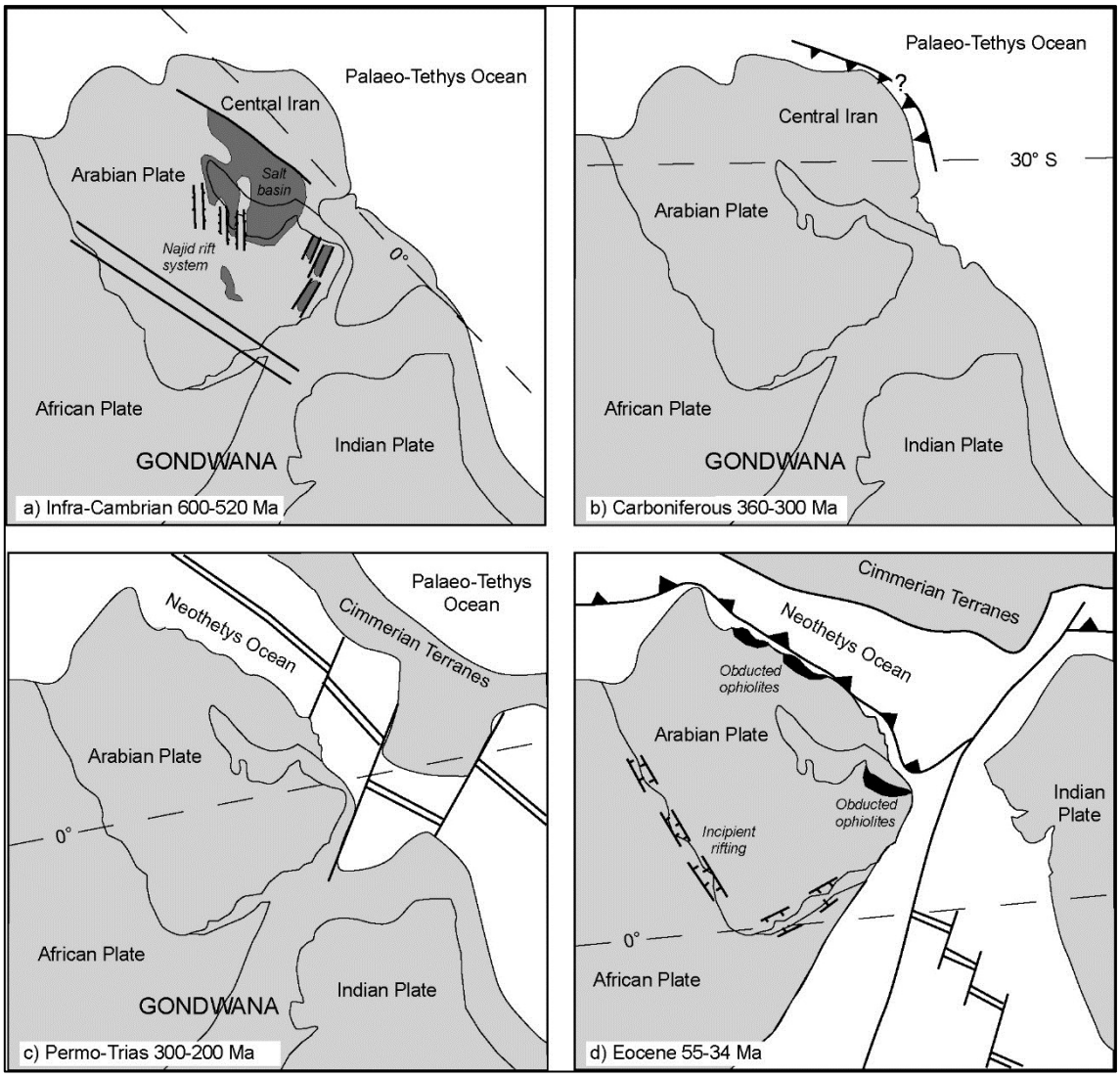


Figure 3.6: Simplified plate tectonic evolution of the Persian Gulf and Arabian Peninsula. (Modified from Loosveld et al. (1996), Sharland et al. (2001), Stampfli and Borel (2004) in Perotti et al. (2011)).

3.2.2 The Qatar–South Fars Arch

The Qatar peninsula consists of outcropping Eocene and Mio-Pliocene units (Alsharhan and Nairn, 1994; Dill et al., 2003; Nasir, et al. 2008), and a structurally consists of a north–south trending, low-amplitude regional anticline. This is the onshore expression of the most prominent structure in the Persian Gulf province: the Qatar-South Fars Arch, a large, very gentle anticline (>100 km wide and 300km long) with a north-northeast to northeast orientation, that developed over a long time-span stretching from the Lower (?) Palaeozoic to the Oligocene (Figure 3.7). Through the use of geophysical data, this structure is known to continue offshore underneath the Quaternary sediments of the Persian Gulf (Perotti, et al., 2011). It separates the Persian Gulf basin into two areas characterized by significant Proterozoic Hormuz salt diapirism namely the Northern and Southern Gulf Salt Basins

both of Infra Cambrian age (Alsharahn & Nairn, 1994) and hosts the biggest gas and condensate field in the world - the South Pars/North Dome Field – which is shared by Iran and Qatar. Each of these basins has its own style of salt tectonics which lead Murris (1981) to conclude that there are differences in the original salt thickness and overburden lithologies.

The origin of the Qatar-South Fars Arch is still controversial. The structure has been described as cored by an Infracambrian basement horst block, initiated during the Infracambrian Najd rifting (Figure 3.3), and repeatedly reactivated during subsequent geological times (Edgell, 1992; Konert et al. 2001; Wender et al., 1998). Different data sources support this hypothesis:

1) Late Proterozoic salt diapirs are present only southeast and northwest of the Arch, which might indicate that there is a north-northeast to northeast basement feature aligned with the other basement structures of the "Arabian trend" that affected the Arabian coastal sector and its interior (Al-Husseini, 2000; Edgell, 1992); which prevented the deposition of salt. This is supported by,
2) the relative thinning of the Mesozoic sedimentary section over the Qatar–South Fars Arch (Alsharan and Nairn, 1997);
3) the growth of the arch by pulses from Early Jurassic to Late Miocene-Pliocene
4) strongly contrasting with the surrounding Quaternary cover, the Qatar peninsula has outcropping Tertiary units indicating uplift and erosion of the sediment cover linked to this basement high.

However, to date there is no published subsurface evidence (well or seismic data) of the basement high below the Qatar–South Fars Arch or adjacent areas in the Persian Gulf. More recently, Perrotti et al. (2011) have outlined other factors that point to a more complex origin:

1) Its continuous growth and extension, which is about one order of magnitude greater than the other north south trending "Arabian structures",
2) the absence of major faults bounding the structure
3) the absence of diapiric phenomena over the top of the arch
4) its northnortheast trend poorly matching with possible compressional and extensional reactivations that acted in a northeast-southwest direction

Using 2D seismic lines crossing the Qatar–South Fars Arch axis in the Iranian sector of the Central Persian Gulf together with analogue modelling using silicone, these authors have interpreted the structure as being linked to lateral withdrawal of the deep Infracambrian Hormuz salt, continuously feeding the several salt plugs and diapirs occurring to the northwest and southeast of the arch, and causing passive folding of the overlying sedimentary succession over a rigid core (a basement high or a non-evaporitic rock unit) into a mega anticline.

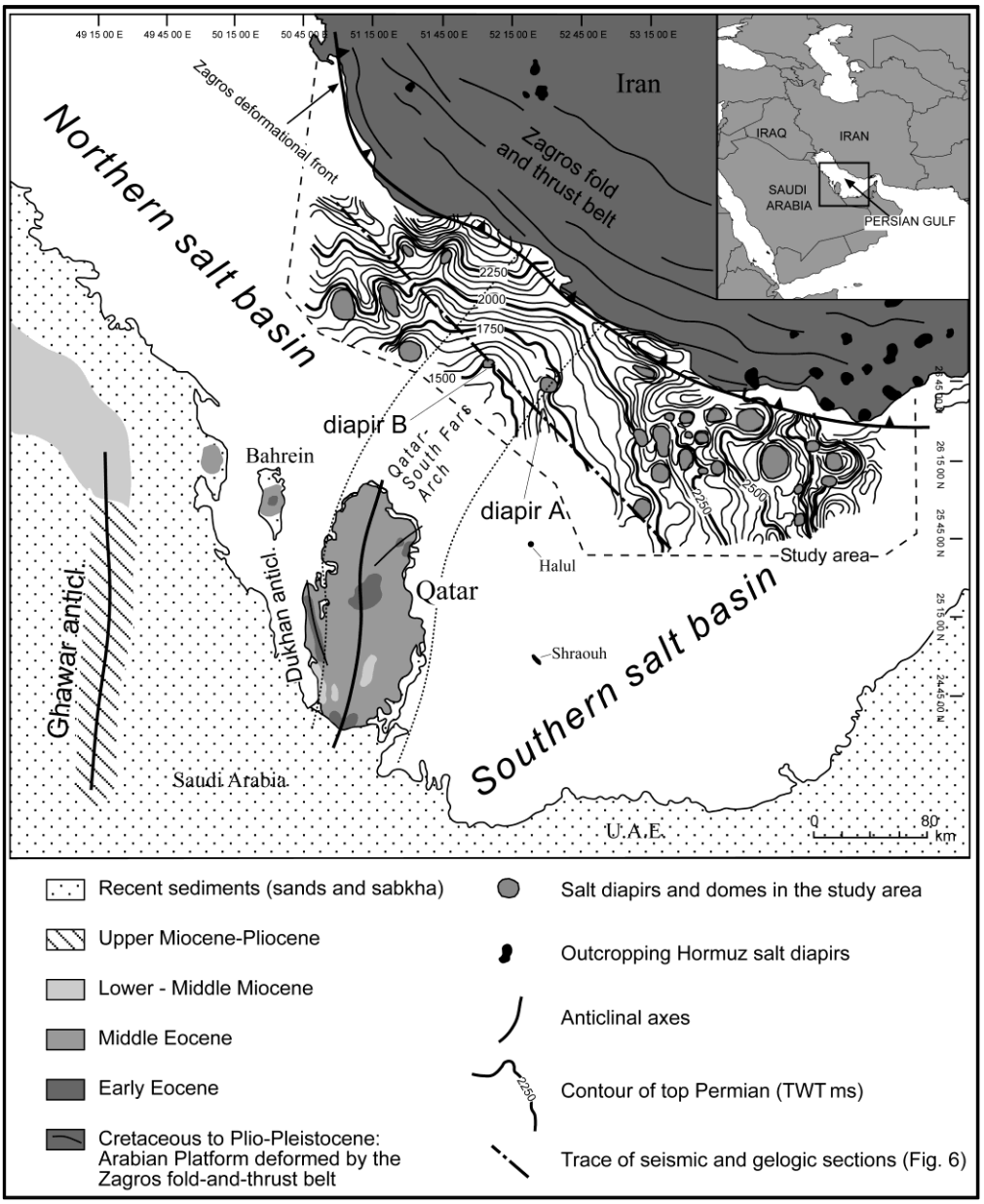


Figure 3.7: Tectonic map of the central Persian Gulf showing the seismic contour map in time (twt ms^{-1}) of near top Permian in the Qatar region (Perotti, et al., 2011).

3.2.3 Stratigraphy of Qatar: The Geological Setting of the Hydrocarbon Play in the Arab Basin.

As mentioned, the sedimentary record on the Arab Platform ranges from the Late Permian to the Holocene (Figure 3.5). As it is outside the scope of this work to give a detailed description of the depositional history of the basin, emphasis will be given only on those units which are relevant to Qatar namely: the Upper Jurassic Hanifa-Jubailah, Arab, and Hith formations which form a source-rock/reservoir/seal triplet and constitute the world's richest single hydrocarbon habitat. The evaporitic Hith Formation, provides the regional seal in the Arab Platform Basin and for that reason

it is the principal focus of our study. For a detailed description of the stratigraphic evolution of the Arabian Plate Alsharhan & Nairn (1994) and Ziegler (2001) are good references.

Late Jurassic: Oxfordian to Tithonian (159.4–144 Ma) (Figure 3.5 and 3.8)

The Late Jurassic started with a relatively rapid eustatic sea-level rise resulting in a generalized flooding of the eastern Arabian Platform. Differential intraplate subsidence led to the development of intra-shelf basins with anoxic euxinic conditions where black organic-rich argillaceous and laminated mudstones and wackstones were deposited forming the Hanifa Formation (Alsharahn & Nairn, 1994; Ziegler, 2001). This rock unit is the main source of the oil in the Upper Jurassic and Lower Cretaceous reservoirs of Qatar, UAE, Saudi Arabia and Bahrain. The overlying Jubailah Formation was deposited in a regressive environment and is made up of mudstones and wackestones which gradually change into higher energy grain-supported carbonates deposited on a shallow shelf bordered by sheltered lagoons and tidal flats (Alsharahan & Nairn, 1994).

In the Kimmeridgian a new passive margin developed along the southeastern coast of Oman following continental rifting and sea-floor spreading between the Afro-Arabian and Indian plates. Widespread deposition of predominantly shallow-marine carbonates occurred as a response to an overall progressive rise in sea level but where numerous transgressive-regressive cycles occurred. This deposition occurred in the form of a complex system of infratidal carbonates to arid, supratidal evaporites in regular shoaling-upward cycles (Figure 3.9). These cycles represent the reservoir Arab Formation, with its four Members (A to D), and the cap-rock sealing Hith Anhydrite (Ziegler, 2001). In sum, the reservoir zones consist of carbonates which are separated by anhydrite layers with the Hith Anhydrite Formation forming the uppermost regional seal Figure 3.8 (Azer & Peebles, 1998).

The Hith Anhydrite marks the final shallowing and infilling of the long established Jurassic sea in which vast thicknesses of carbonate were deposited over much of eastern Arabia. Generally, the Hith exhibits a chicken-wire nodular fabric and is associated with dolomites in its basal part, grading upward into finer crystals, but with a similar texture. Towards the top of the section, thin laminations contain some fine-grained carbonates (Alsharan & Kendall, 1986).

Several authors have made descriptions of this formation in the past: research by Leeder and Zeidan (1977) in a dissolution cavern in Saudi Arabia describes the Hith anhydrite as exhibiting clear evidence of deposition in a sabkha environment. They noted structures including nodular anhydrite, chicken-wire aggregates and enterolithic layers in quartz silt-rich, dolomitzed grainstone hosts.

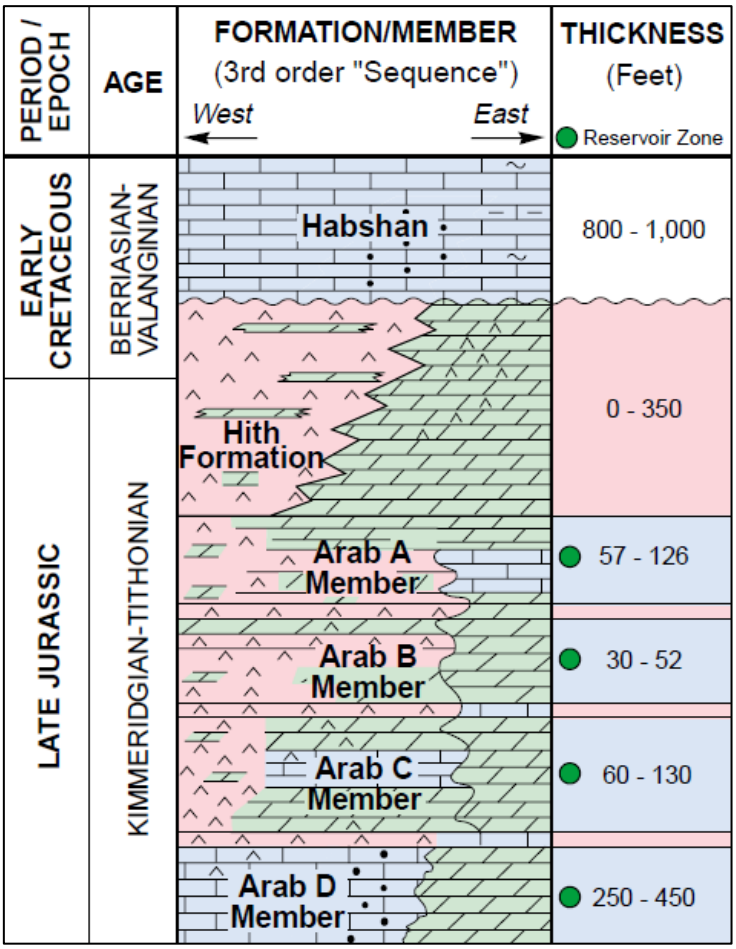
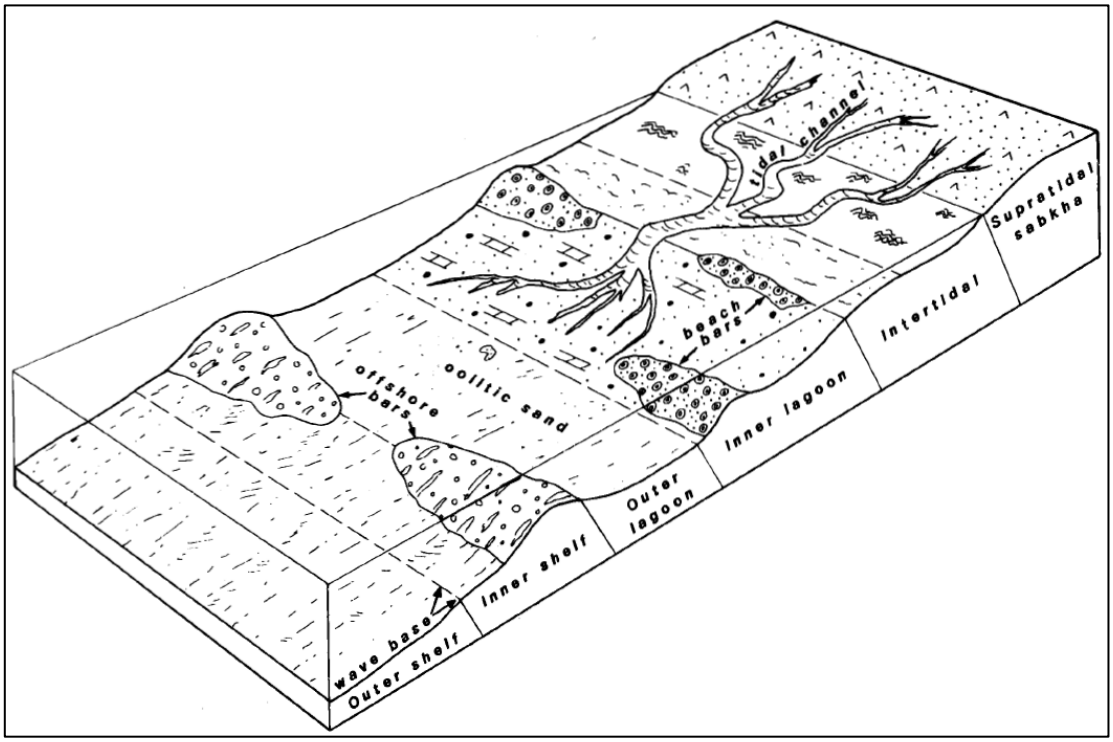


Figure 3.8: Stratigraphic column of the Late Jurassic and Early Cretaceous of the Arab Basin (Azer & Peebles, 1998).

Kendal & Skipwith (1968, in Alsharan & Kendall, 1986) consider that the present United Arab Emirates coastline appears to match some of the evaporite settings of the Hith, but significantly characterized by a series of algal flats that have not been recognized in the Hith.

By analysing cores from the UAE outcrops in Saudi Arabia and Lake MacLeod (Western Australia) which served as an analogue, Alsharhan & Kendall (1994) conclude that the Hith Formation was deposited in a mixture of settings similar to those of coastal playas (or salinas) like that of Lake MacLeod and the carbonate evaporite sabkha sequences presently accumulating along the coast of the UAE but with particularities which are not in full accordance with these two environments. They conclude that in contrast to the relatively limited areal extent of the Lake MacLeod analogue and the Holocene coastal environment of the Arabian Gulf (Southern Persian Gulf), the Hith represents a mega-environment which covered a much greater geographical area and produced a much thicker sequence of sediments dominated by evaporites, with much less carbonate than in the Holocene sabkha environments of Abu Dhabi.

Specifically in Qatar, the Hith has been reported of consisting of about 140m of interbedded nodular anhydrite with numerous stringers of dolomites and massive anhydrite (Figure 3.10). Its upper portion contains dolomitized and oolitic limestones with abundant anhydrite nodules (Sugden & Standring, 1975 in Alsharhan & Kendall, 1994).



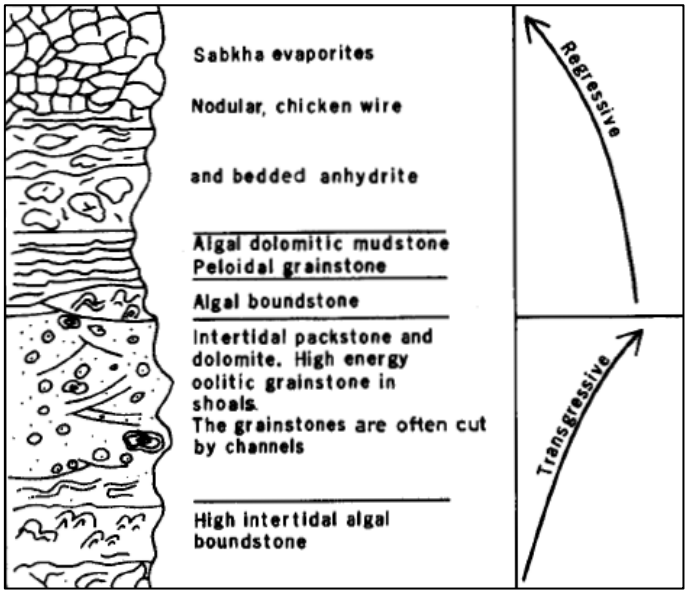


Figure 3.9: Depositional model for the Arab Formation (top) and the corresponding idealized cycles (bottom) proposed by Alsharahan & Nairn (1994).

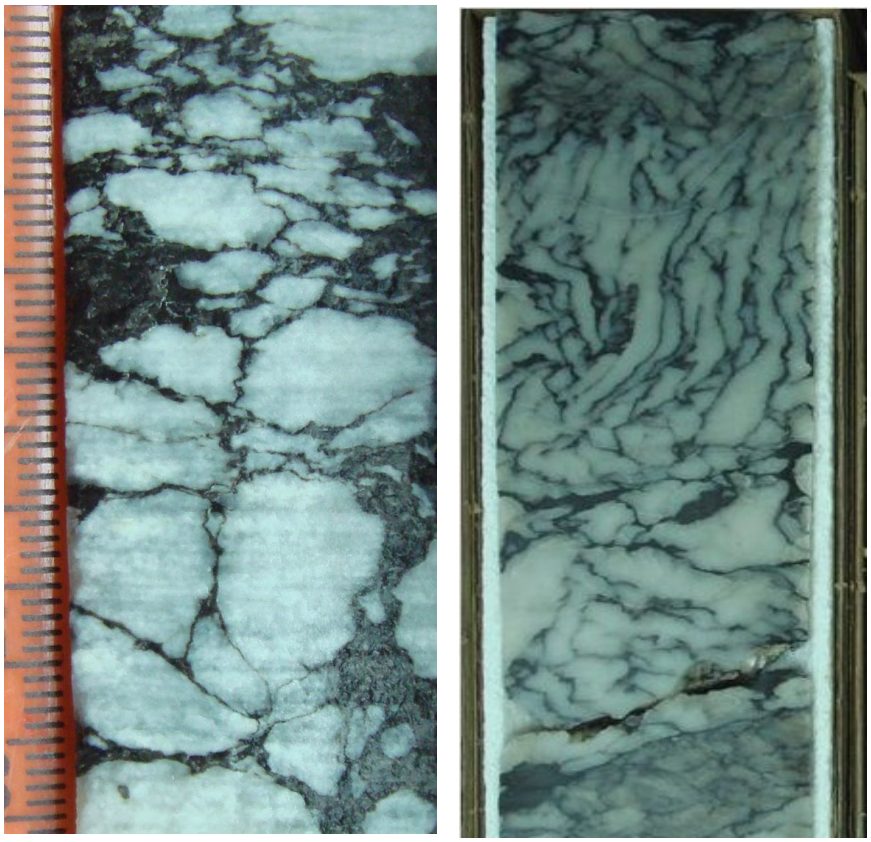


Figure 3.10: drill-cores showing the typical aspect of the Hith Formation. In the left core the nodular texture is very clear and it represents primary anhydrite formed in sub-areal conditions. In the right core the texture is typical of displacive/replacive anhydrite growth that occurs during burial when gypsum is dehydrated. (Confidential source).

3.3 Gypsum Mines Study – Brightling Mine

3.3.1 Introduction

As mentioned in Section 1 the objective of this research is to understand how fractures potentially generated during CO_2 injection operations propagate through an anhydrite cap-rock such as the Hith Formation and what specific rock properties control that propagation, focusing on those that are able to inhibit it.

Having said that the best way to obtain data on how fractures behave when crossing such lithologies would be to directly study anhydrite outcrops, preferentially of the Hith Formation. However the only outcrop known from the Hith Formation is the one studied by Leeder and Zeidan (1977) located in Saudi Arabia which is very difficult to access. Hence, we were forced to find an outcrop analogue for the Hith Formation which would ideally be of similar age and have a similar depositional environment (see Section 2). These requisites were met by the basal anhydrite of the Purbeck Formation (Upper Jurassic – Tithonian (145.0 – 152.1 Ma)) which are perfectly preserved in the subsurface in the Brightling Mine located in East Sussex, Southeasthern England. The Brighling Mine, operated by British Gypsum, is located in the Weald Basin (Figure 3.11).

3.3.2 The Wessex/Weald Basin

The Weald Basin, located in southeastern England (Figure 3.11) is part of a series of basins formed by rapid subsidence associated with thermal relaxation following early Mesozoic extensional block faulting (Butler & Pullan, 1990). Some authors (Butler & Pullan (1990); Chadwick (1993)) consider it to be an easterly extension of the Wessex Basin while others (Lake & Karnerl, 1987) a sub-basin of the wider Wessex Basin and others an independent basin (Underhill & Stoneley, 1998). Although there are differences between these basins, the present author decided to report the common history of both on the basis of their common structural trends, infill and tectonic evolution, considering the Weald Basin part of the larger Wessex Basin and report particularly on its stratigraphic evolution and infill.

The Wessex Basin, covers an onshore area of about 2000 km^2 with at least an equivalent area beneath the English Channel (Chadwick, 1993). The basin is bound to the southwest and west by the Armorican and Cornubian Massifs, to the north by the London Platform and to the south by the Central Channel High, having less precise boundaries to the northeast and northwest (Underhill & Stoneley, 1998).

Reports of the presence of hydrocarbons in southeastern England are as early as 1896 when a well drilled to provide water for the railway station in Heathfield, Sussex, found gas when drilling through the Kimmeridgian strata. This well was England's first natural gas well with a daily production of 1000 scf (standard cubic feet) at the time (Hawkes et al., 1998). Although results were initial disappointing,

during the 20th century the basin was the setting for several discoveries of which the Kimmeridge Oil Field, discovered in 1959 and still in production today, was only the first. Continuing exploration lead to discoveries such as giant Wytch Farm Oilfield – the largest onshore producer - and ten other oil and gas fields subsequently discovered. Cumulative output of oil in the Wessex-Channel Basin province is around 460 MMbo.

The Wessex Basin (and consequently the Weald Basin) is underlain at depth by Paleozoic (Middle Devonian to Lower Carboniferous) rocks which were deformed during the Hercynian orogeny by thrust- and wrench-related structures as a result of a northwards-verging collision zone (Chadwick, et al. (1983); Lake & Karner (1987); Hawkes et al. (1998)). Particularly in the Weald Basin, these structural trends appear to be oriented east-west beneath the western and central Weald and there is some evidence that the Mesozoic development of the basin has also been influenced by northeast-southwest oriented trends of probable Caledonian age as faulting along this orientation occurs in the Upper Cretaceous and Tertiary rocks under South London (Butler & Pullan, 1990).

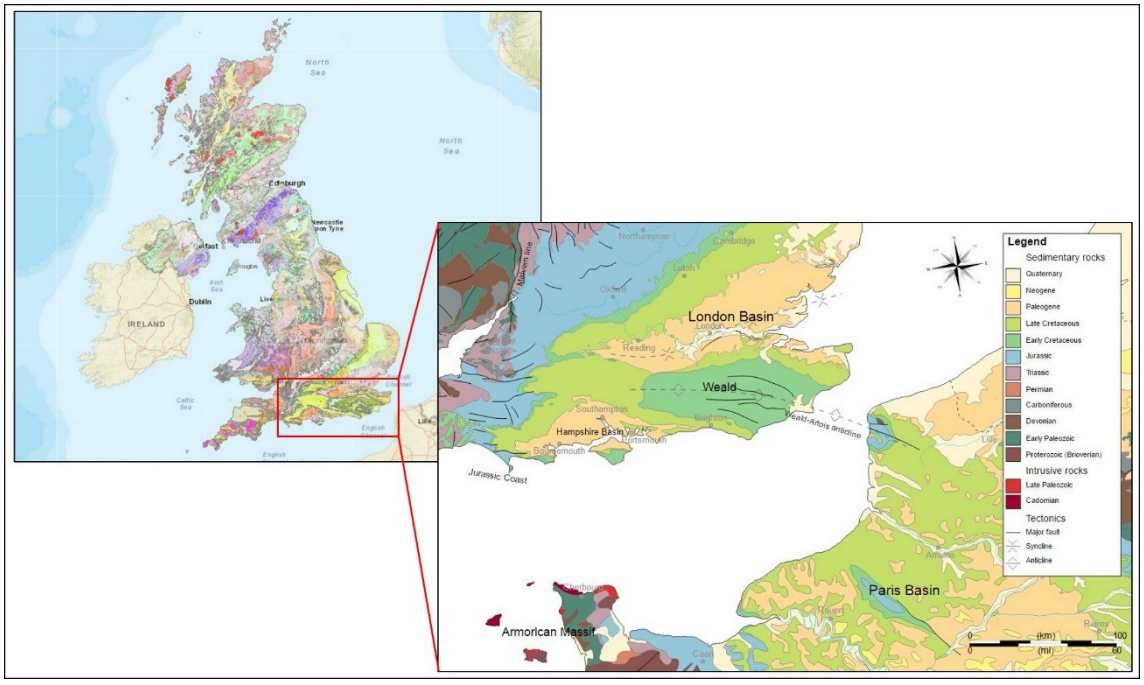


Figure 3.11: Geographical location of the Wessex (here denominated Hampshire Basin) and Weald Basins with the corresponding outcropping geological features. (Source: British Geological Survey).

The present day architecture of the Wessex Basin reflects the tectonic processes dominant in its formation: crustal extension (Permian to Cretaceous) followed by a period of crustal shortening and crustal inversion (Late Cretaceous and Tertiary). The main basin-bounding faults trend is E-W and are

made up of a set of *en-echelon* normal faults which delineate a system of asymmetrical *horts/grabens* that constitute the principal subsurface structural elements of the basin. At the surface the dominant features are those which are the result of the crustal-shortening and inversion period (Figure 3.12) (Chadwick, 1993):

- the surface depressions of the London and Hampshire basins superimposed upon underlying horst blocks of the London Platform and Hampshire-Dieppe Highs;
- the surface positive reliefs of the Weald Anticline and Channel High superimposed upon the earlier Weald and Channel basins.

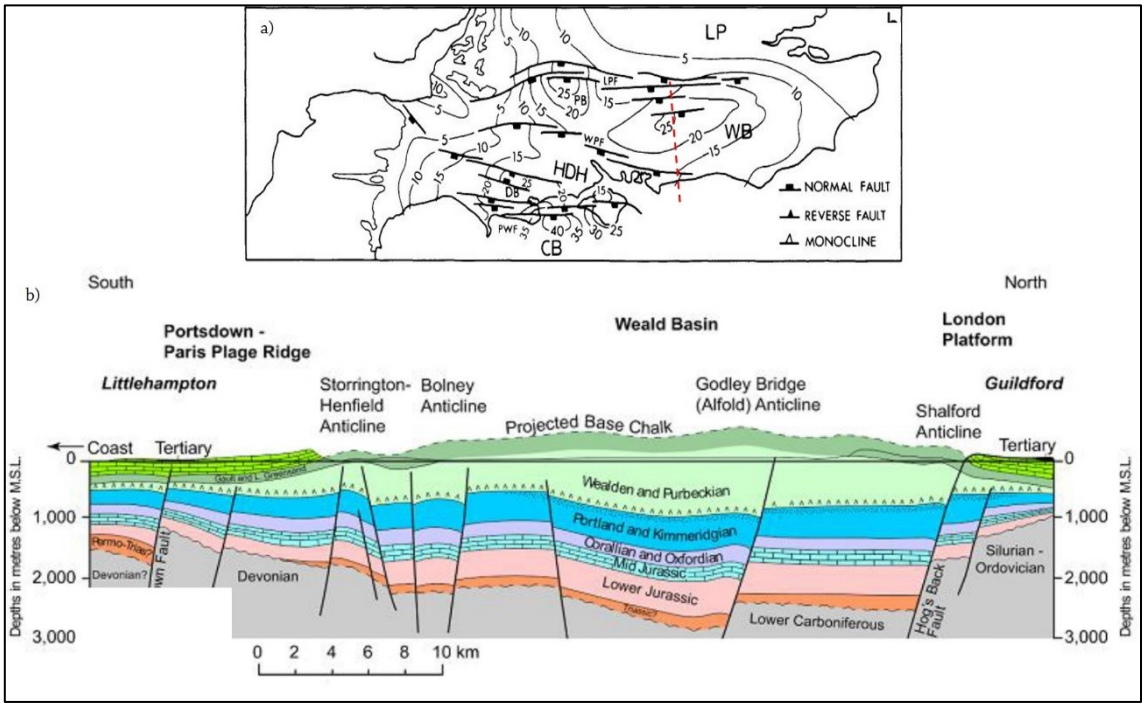


Figure 3.12: (a) Contours (metres x 100) of top Variscan Basement beneath the Wessex Basin. LP, London Platform; WB, Weald Basin; PB, Pewsey Basin; DB, Dorset Basin; HDH, Hampshire-Dieppe High; CB, Channel Basin; LPF, London Platform faults; WPF, Wardour-Portsdown faults; PWF, Portland-Wight faults (adapted from (Chadwick, 1993). (b) simplified north-south geological cross section through the central Weald Basin. Note the anticline of the Cretaceous beds – the result of the Alpine compression (adapted from (Butler & Pullan, 1990).

The tectono-stratigraphic evolution of the basin can be summarized in the following manner (Chadwick, 1993): from the Permian to the Cretaceous pulses of upper crustal extension led to widespread basin subsidence with the development of a system of apparently E-W trending asymmetrical *grabens*. The sedimentary infill comprises a succession of argillaceous continental red-beds (Permo-Triassic), marine shales with minor limestones and sandstones (Jurassic), and an Early

Cretaceous brackish to fresh water clastic sequence. A cessation of active crustal extension and establishment of regional unfaulted subsidence occurred during Mid- to Late Cretaceous leading to the deposition of marine sandstones and shales which gradually change to a thick carbonate succession of chalk. Regional subsidence continued into early Tertiary times, and considerable thicknesses of shallow marine and freshwater clastic sediments accumulated but the growing influence of the tectonic inversion limited to the collision between the African and European plates changed the sedimentary patterns relative to the Mesozoic era. The precise onset of basin inversion is not known but from the present day data the evidences suggest that minor inversion affected the Wessex Basin from the Late Cretaceous through Early Tertiary, probably contemporaneous with the 'Pyrenean' phase of deformation, but the major inversion episode is related to the Alpine deformation, which occurred in the Miocene. Figure 3.13 shows the stratigraphic column of the Wessex Basin which can also be used for the Weald Basin.

Of particular interest to this research and the reason for having chosen Brightling Mine as an analogue, is the deposition of the Late Jurassic Purbeck Beds. These correspond to a marginal marine/brackish depositional system being the top sedimentary unit of an upwards shallowing profile starting with the marine mudstones of the Kimmeridge Clay and progressing to the shallow marine sands of the Portland Sandstones. The Purbeck Anhydrite forms the regional top seal for the Portland sandstones reservoirs (Hawkes et al. , 1998). The isopach map for the Portland Sandstone (Figure 3.14) shows that the Weald Basin, where the Brightling mine is located, was the preferential deposition location, i.e the regional depocentre. The overlying Purbeck Anhydrite is an excellent analogue to the Hith evaporites and can be examined in the mine at Brightling.

3.3.3 Brightling Mine and the Purbeck Formation

Extraction of gypsum at the Brightling Mine (Figure 3.15) has been in continuous operation since 1963 being an important product for the construction industry. It is a room and pillar operation meaning that a series of parallel drifts (horizontal underground openings) are created, with connections made between them at regular intervals creating a close to regular checkerboard pattern of rooms and pillars which support the mine roof. This is a technique that can only be used for flat bedded deposits and is very common in coal, salt and potash operations (Hamrin, 1980). In the case of Brightling mine the pillars are square with side length of approximately 6 m and 4.2 m in height giving a very good lateral and vertical exposure of the evaporite beds.

Evidence from several hundred boreholes drilled in the evaluation of the gypsum resources suggests that the most important structures comprise a series of east-southeast trending normal faults mainly with southward throws which can reach 100 m. These structures are thought to reflect deeper features

in an underlying Palaeozoic basement. Smaller north to northwest-trending normal fault cuts the fault blocks with small throws often larger than 10m. The rocks are gently folded into periclinal structures and it is this folding related to the Alpine inversion that is responsible for bringing the sulphate deposits to their current elevated position (British Gypsum, 2010).

The evaporite resources, gypsum and anhydrite in East Sussex all occur within the basal anhydrite in the Purbeck Formation (or Purbeck Beds) of the Upper Jurassic (Tithonian: 145.0 - 152.1 Ma).

The Purbeck Formation, which conformably overlies the Portland Sandstone Formation consists of carbonate and clay sediments with evidence of formation in shallow waters of various salinities. They represent the products of a major regression at the end of a phase of Upper Jurassic marine sedimentation (West, 1975).

In terms of paleoclimate, the absence of bedded halite, the presence of beds typical of freshwater environments and fossiliferous content point towards a warm-temperate paleoclimate (Arkel, 1947 in West, 1975). West (1975) considers that In Lower Purbeck times southern England must have been situated at the northern limit of the northern hemisphere evaporite-deposition. Although just within the dry (semi-arid or steppe) zone the region was so close to the boundary of the warm-temperate (sub-humid) zone that warm-temperate types of fauna and flora could often exist.

The stratigraphic sequence can be described in the following manner (West, 1975): Purbeck strata commence with the moderately hypersaline, subtidal and intertidal limestone facies overlain by a limestone and gypsum facies of more hypersaline, intertidal origin. The main gypsum facies was probably formed in very hypersaline intertidal to supratidal conditions, being overlain by a facies which originated in moderately hypersaline, subtidal to intertidal, conditions.

This description leads us to believe that the Purbeck Formation was deposited in a generally shallow water environment very sensitive to the variations of the water column, where cycles of tidal-flat deposition alternated with the deposition of more continental beds during regression periods. The climate was probably semi-arid. A modern example of such environments is the Abu Dhabi Trucial coastal flat which as noted earlier is considered to be a good analogue for the Hith Anhydrite It is for this reason that the evaporite succession at the Brightling Mine was selected for this study.

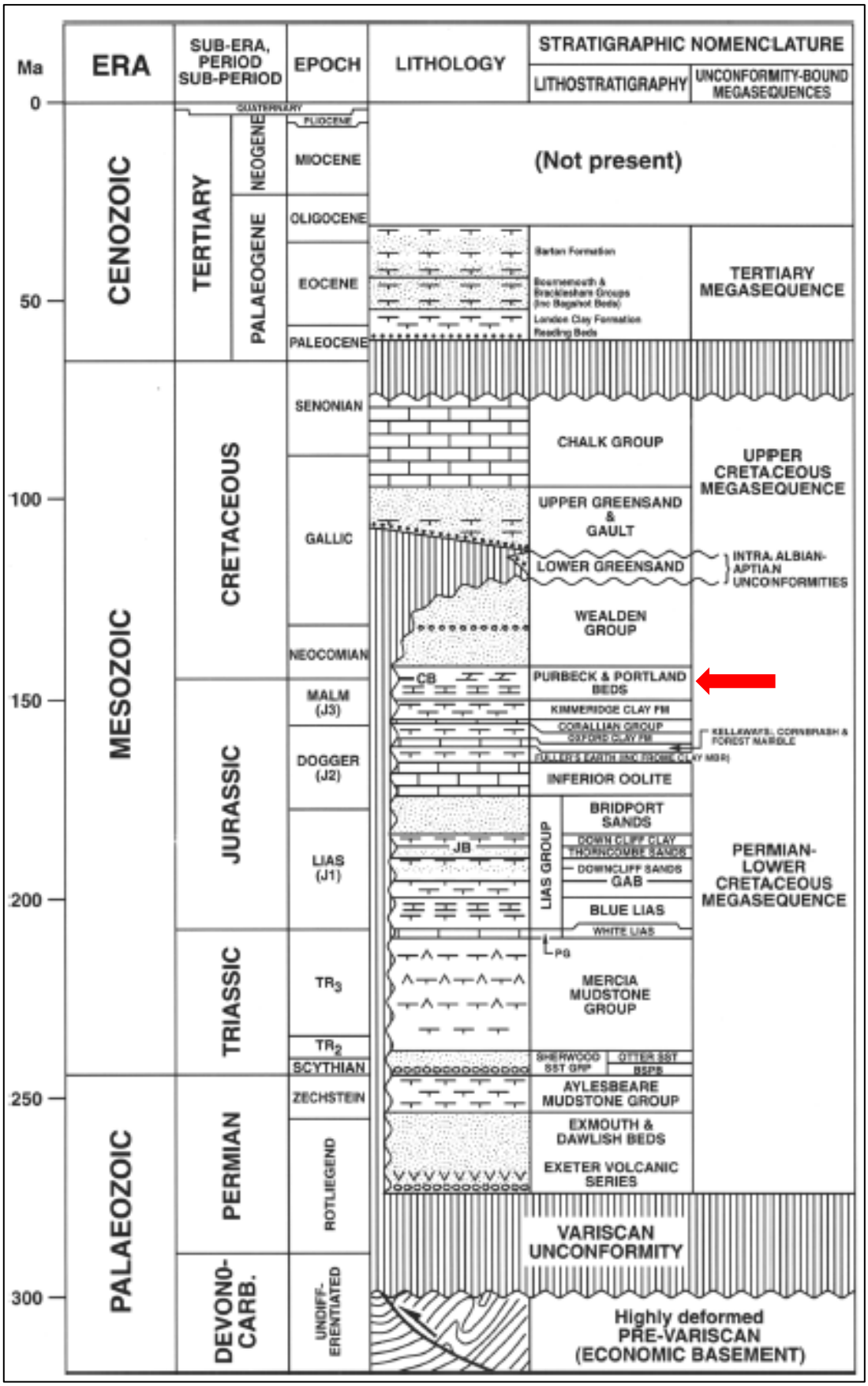


Figure 3.13: Generalized stratigraphical column for the Wessex Basin illustrating the main megasequences and stratigraphic nomenclature currently used in the basin (JB, Junction Bed; CB, Cinder Bed; GAB, Green Ammonite Beds; PG, Penarth Group; BSPB, Budleigh Salterton Pebble Beds).

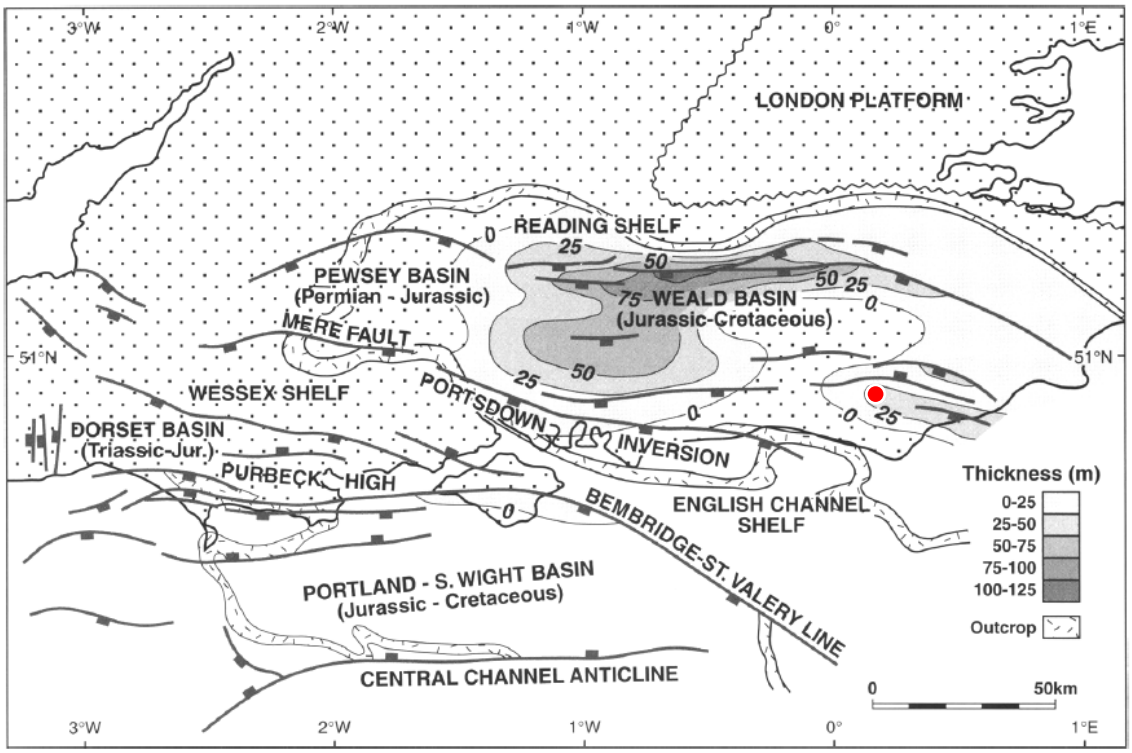


Figure 3.14: Gross isopach map for the Portland Sandstone in the Weald and Wessex basins (Hawkes et al., 1998). The red point marks the approximate location of Brightling Mine.



Figure 3.15: Geographical location and aerial photography of the British Gypsum, Brightling Mine.

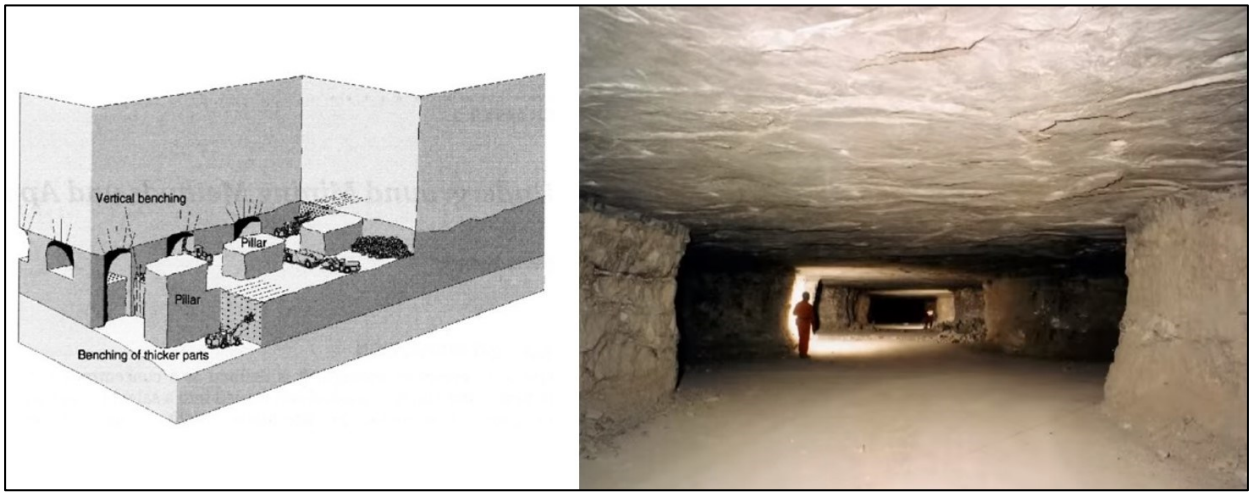


Figure 3.16: traditional room and pillar mining technique (Hamrin, 1980); b) Brighling Mine drift view with the supporting pillars on the left and right hand side.

3.3.4 Pillar Face Analysis

At Brightling Mine the basal (No.4) seam (according to British Gypsum terminology) - in the no.1 Group Gypsiferous Beds of the Lower Purbeck Formation was studied. This seam is located 283m below surface and the analysis was made at several pillars within a chosen area (Figure 3.17). A vertical cross section analysis of the pillar faces was conducted with the following objectives:

- To analyze the stratigraphic sequence in order to understand the sedimentary features of the evaporite succession.
- To evaluate the fracture sets that exist in the stratigraphic sequence (horizontal and vertical).
- To understand the impact of the fractures on the hydration of anhydrite to gypsum.
- To evaluate the potential impact of the bedding-parallel gypsum veins, other strata and bedding interfaces on the propagation of layer-normal fractures

The first characteristic that stands out when looking at the pillars in Brightling mine is the extremely high vertical facies variability (Figure 3.18). Another of the key characteristics of evaporite sequences is that they often show signs of secondary or diagenetic textural overprints which are the result of processes such as displacive growth, recrystallization, back reactions and replacement. Therefore primary depositional textures such as anhydrite nodules and secondary diagenetic features such as anhydrite nodules that evolved from primary gypsum have identical appearances and it is difficult to differentiate between them. In order to obtain a clear picture of the evaporite sequence the lithological and stratigraphic description has been separated from the structural description. The latter focuses on describing the features which can be attributed to the action of tectonic forces and high fluid pressures.

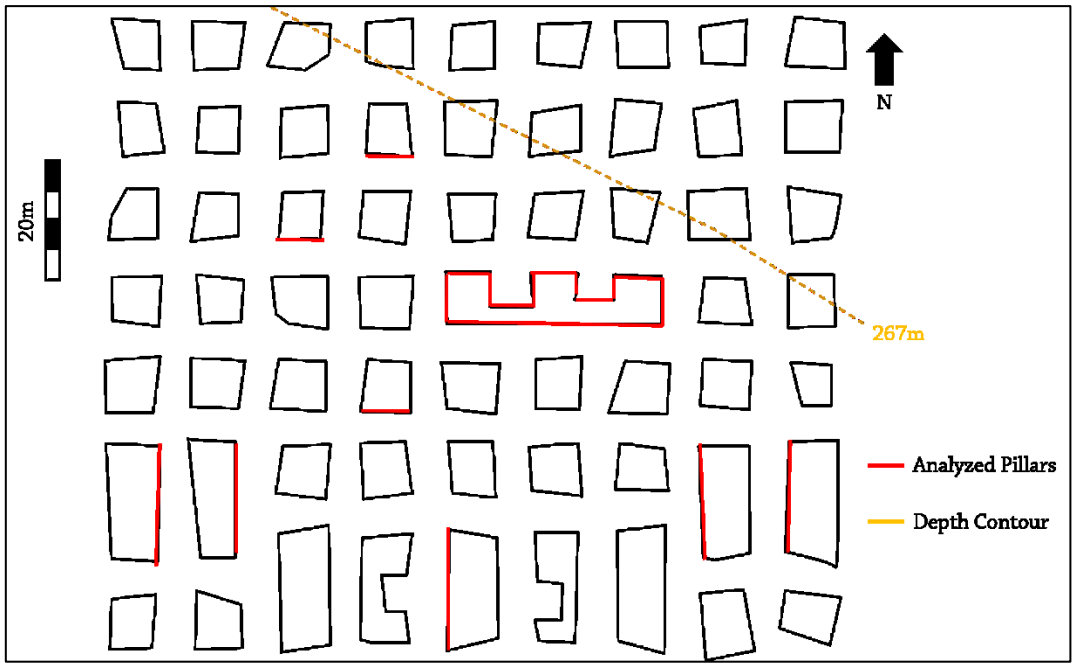


Figure 3.17: Sketch of an aerial view of the study location at Brighling Mine and the analysed pillars.

3.3.4.1 Lithological and stratigraphic description.

As previously mentioned the face of the Brightling Mine pillars are approximately 6 m wide and 4.2 m high (Figure 3.18). Before the start of the analysis these were thoroughly washed in order to reveal the sedimentary features. The following sedimentary facies were identified in several of the analysed pillars (these lithologies were also observed in the drill cores that will be presented in Section 3.4):

F1) Massive to Nodular anhydrite: light-blue to light-grey/white anhydrite in a carbonate matrix. This lithofacies presents several types of textures (Figure 3.18 and 3.19):

Nodular anhydrite: composed of nodules of various dimensions (from 0.2 cm to 15cm) with diverse morphologies but mainly subspherical to ellipsoid-shaped, horizontally enlongated. The larger nodules are occasionally composed of aggregated smaller nodules. Cross sections of the nodular aggregates reveal chicken-wire, palisade and agreggate textures. Abundant gypsum porphyroblasts, euhedral to sub-euhedral, occur in the anhydrite nodules (Brightling Mine).

Banded anhydrite: Bands and also beds of around 5cm thick composed of anhydrite nodules of various dimensions but usually 0.5 to 1cm. Enterolithic texture was observed.

F2) Massive to laminated mudstone: very fine grain, brown to dark grey massive to laminated mudstone with low anhydrite content. Small nodules (<1cm) of anhydrite are often present.

F3) Microbial laminated mudstone: consists of light brown, tan-coloured, fine-grained laminated mudstone with thin dark-brown, organic-rich laminae. Irregular laminations and domal sedimentary structures are present which suggest stromatolitic/microbial origin.

F4) Bioturbated Mudstone: dark grey and very fine-grained mudstone with low to moderate fossil content.

F5) Shale: dark grey to black, fine-grained laminated shale. Forms beds of different thicknesses ranging from a 1-2 cm to 50 cm. Often disrupted by bedding parallel gypsum (satin-spar) veins which seem to have formed in these low strength layers (F7).

F6) Carbonate sandstone (not observed in Brightling Mine)

F7) Secondary gypsum veins: fibrous gypsum veins – satin spar. These form both perpendicular to bedding (interpreted as being related to the opening of the basin) and parallel to bedding (interpreted as being related to the inversion of the Basin). The vertical (bedding perpendicular) veins predate the horizontal (bedding parallel veins) as it will be demonstrated later in this section.

F8) Anhydrite-Mudstone Breccia (not observed in Brightling Mine)

F9) Chert (not observed in cores)

The facies identified in this study point towards a repetitive sequence of depositional environments that are in agreement with those described by West (1975) and with our expectations when choosing this location as an analogue to the Hith evaporites which characterizes the seals in Qatar. It is considered that there are clearly characteristics that indicate a supratidal setting (sabkha environment) a tidal flat setting (intertidal environment where the microbial laminites have developed) and a subtidal environment where mudstones, shales and marls have been deposited. This clearly indicates that the Purbeck Formation of the Weald Basin, UK exposed in Brightling Mine is a , a valid analogue to the Hith Formation of Qatar and that the location is suitable for the study of evaporite textures. Below (Figure 3.18 to Figure 3.22) several examples of the facies described above are presented.

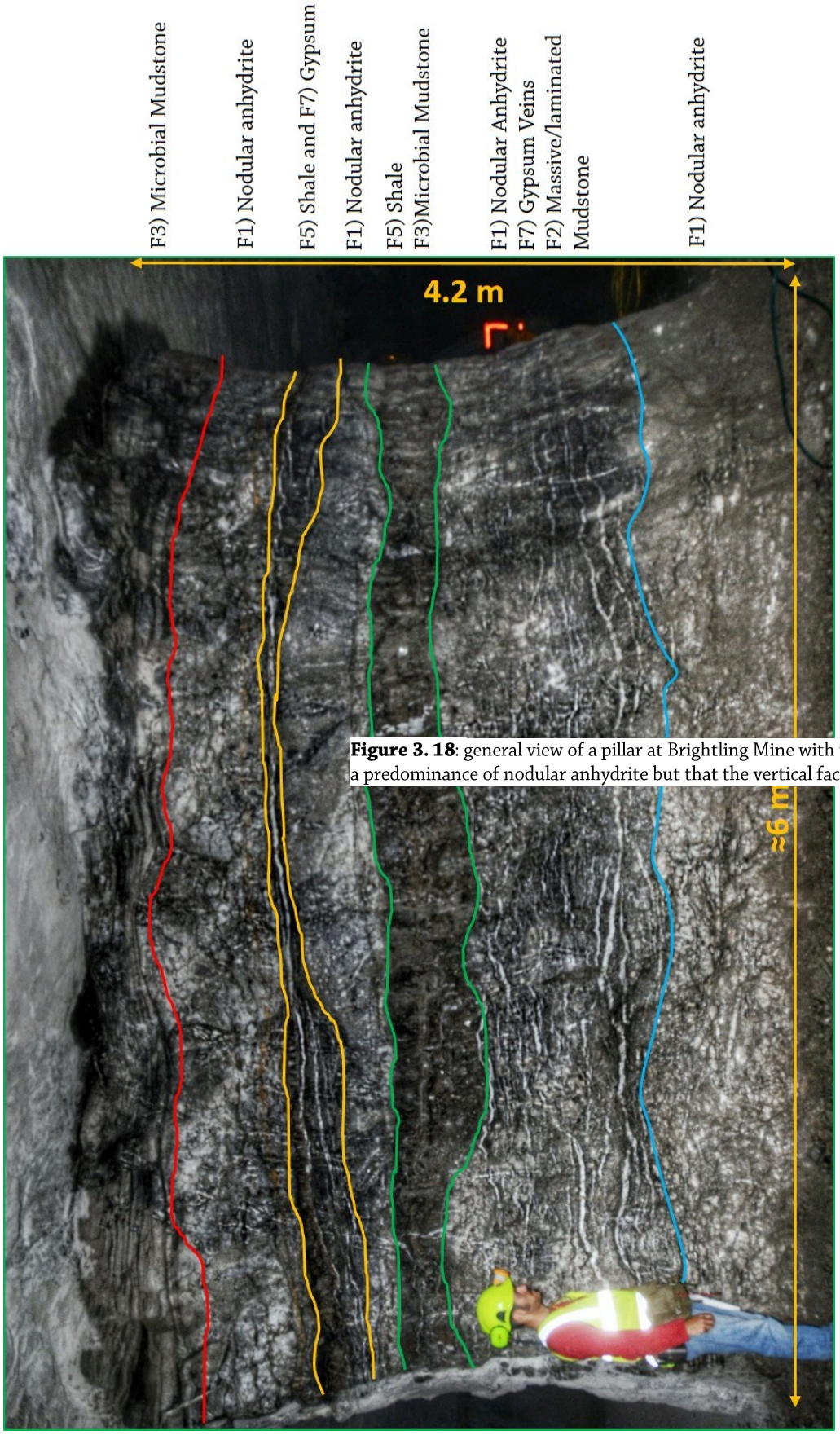


Figure 3. 18: general view of a pillar at Brightling Mine with the observed facies identified on the ri
a predominance of nodular anhydrite but that the vertical facies variability is evident.

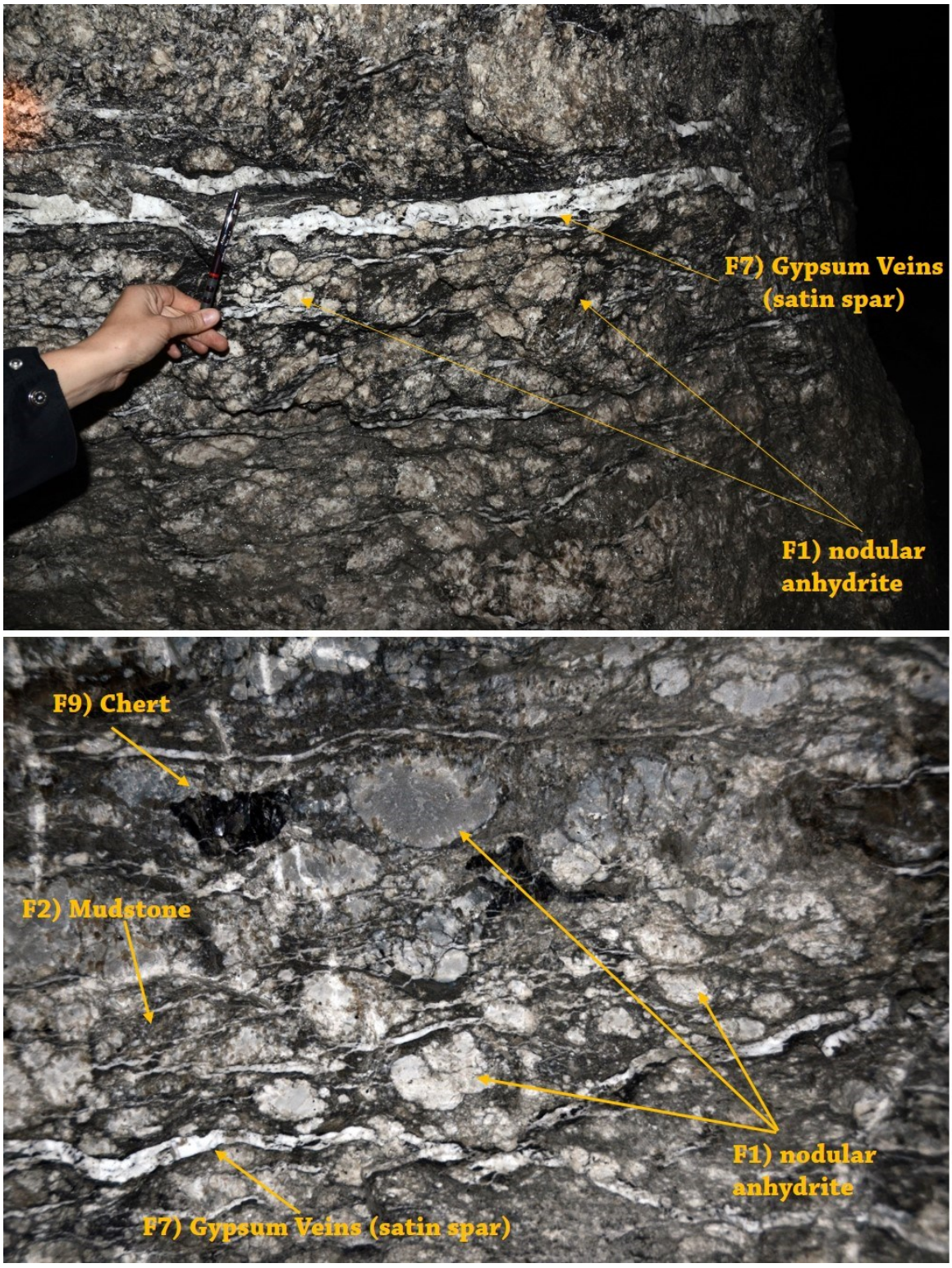
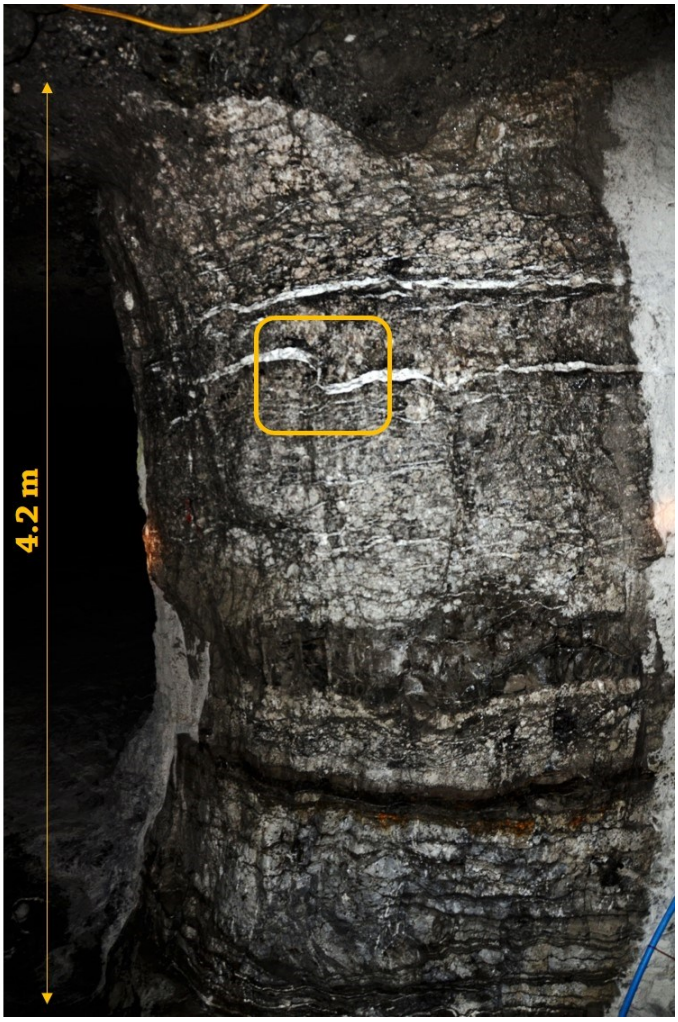


Figure 3. 19: detail of the base of two different pillars at Brightling mine where the different facies can be observed (see Figure 3.18). The following facies can be observed: F1) nodular anhydrite; F2) Mudstone; F7) Gypsum veins; F9) Chert nodules.



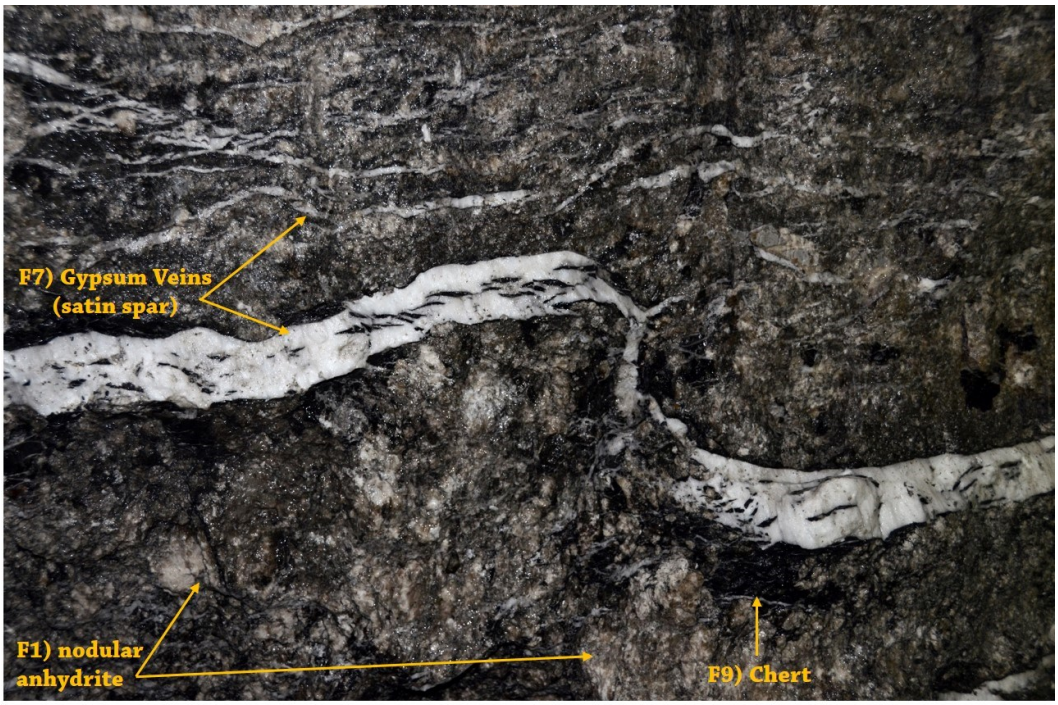


Figure 3.20: Close up view of a pillar of Brightling mine and detail of a secondary satin spar vein that formed in a black shale horizon. Note the clasts of shale *floating* in the gypsum matrix. The following facies can be observed: F1) nodular anhydrite;; F7) Gypsum veins; F9) Chert nodules.

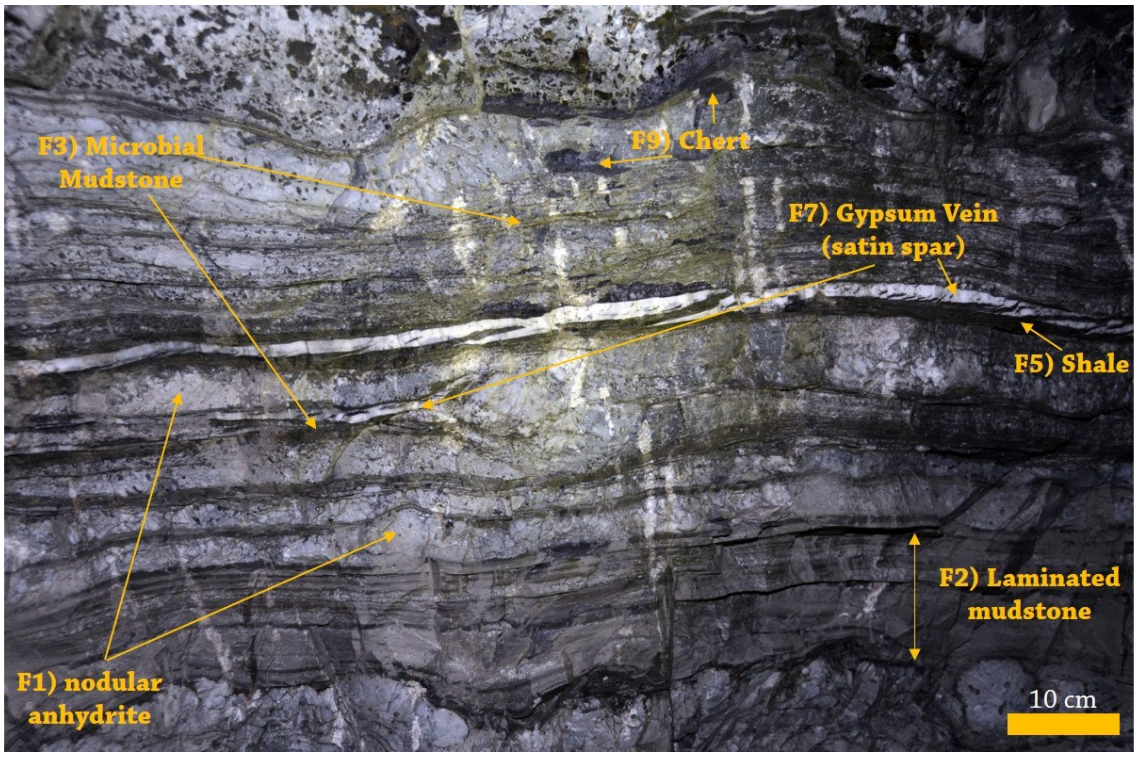


Figure 3. 21: detail of the top section of a pillar at Brightling mine where the different facies can be observed (see Figure 3.18). The following facies can be observed: F1) nodular anhydrite; F2) Laminated mudstone; F3) Microbial mudstone; F5) Shale F7) Gypsum veins; F9) Chert nodules.



Figure 3.22: detailed view of a pillar at Brightling Mine with the various ide

3.3.4.2 Structural description

The observations were made at the rock face, in the pillars that are left to structurally support the mine. The shallow depth at which the mine is currently operating (≈300m) excludes the effects of pillar deformation caused by removal of surrounding rock (the UCS of the rock mass – between 30 and 40 MPa - in the pillars is far from being reached at 300m depth). Figure 3.23 shows a typical wide view of the mine where there is no indication of engineering related fractures. Several fracture sets have been identified during the course of the field work. From their cross-cutting relationships it was possible to determine their relative age, the associated stress fields and relate these to the regional tectonic evolution of the basin. It was also possible to analyse the response of the evaporite succession to high fluid pressures.



Figure 3. 23: General view of the studied pillars in Brightling Mine. There is no indication of engineering related fractures.

Vertical Fractures

VFa: thin barren fractures within a mudstone layer with intercalated anhydrite layers. Orientation: Az. 240-250.

VFb: thin fractures filled with satin spar. They are cut by the horizontal fractures infilled with statin-spar, indicating that they predate these. Orientation: Az. 120-140 (Figure 3.24 and 3.26a)

VFc: Large vertical joints with a regular spacing of about a meter and that affect the whole stratigraphic sequence (Figure 3.25). These through-going fractures are barren. Orientation: 120-140. The orientation leads us to correlate them with VFb and with the opening of the Mesozoinc Basin in which the sediments were deposited.
It is interesting to note that these vertical joints are not filled with satin spar unlike the thin fractures shown in Figure 3.24. It is suggested that these barren vertical joints might have been formed during a later tectonic pulse compared to VFb. At this point the excess gypsum had already been deposited in the thin vertical fractures and therefore does not occur in the larger joints.

It is also important to note that both the thin satin spar filled fractures and the large vertical joints arrest at a thin shale layer situated between the mudstone and the overlying anhydrite layer which has been hydraulically fractured and is the location of a bedding parallel satin spar vein. However at the time the vertical fractures were formed this bedding parallel satin spar vein had not yet formed (this was related to the inversion of the Basin and therefore poste-dates the formation of the vertical fractures). It is therefore argued that not only are the horizontal gypsum veins able to impact on fracture propagation but also thin shale horizons can have the same effect. It will be shown in Section 3.5.4 where the field work carried out in Somerset is presented, that this is the case.



Figure 3. 24: image of a mudstone rich section at the base of one of the pillars in Brightling Mine. Notice the intense vertical fractures filled with satin-spar veins (VFb), and how they are all arrested at the bedding-parallel satin-spar vein that formed at the boundary of the shale layer and the overlying anhydrite.



Figure 3. 25: pillar showing large joints (VFc) highlighted in yellow with no infill. These we related to the opening of the Bristol Channel Basin.

Horizontal Fractures

HFa: these are 0.5 - 2cm wide, filled with satin-spar and present throughout the whole visible stratigraphic sequence but with predominance in the lower part (Figure 3.26).

It was observed that the horizontal veins formed either:

1) within thin shale horizons
2) at shale/anhydrite boundaries

These features are interpreted as hydraulic fractures generated during the inversion of the basin when σ_1 was horizontal and σ_3 was vertical. This occurs, we argue, because the inherently weak shales would be the chosen sedimentary horizon for sub-horizontal fracture opening. It is noted that during the inversion both the tectonic stress regime (with σ_3 vertical) and the intrinsic properties of the shale (namely its marked horizontal planar fabric) favour the formation of horizontal fractures. It will be discussed in Section 4.4.1, that in certain situations the effect of the stress field and the material properties of the sediments do not act constructively. In this section, it is shown that it is possible for fractures to open against σ_1 when the beds are particularly anisotropic. One can therefore argue that the sub-horizontal fractures now filled with satin spar were formed under the same stress regime of basin opening (σ_1 vertical), i.e. at the same time as the vertical veins are thought to have formed. However, this hypothesis was discarded because of the cross-cut relation constantly observed in various locations of the mine: the horizontal satin-spar veins invariably post-date the vertical veins. We argue that these horizontal satin-spar veins are analogue to the bedding parallel veins of the same material found in the rocks of Somerset where it was concluded that they formed during basin inversion (see Section 3.5.5 for discussion).

Of the various textures and features observed within the evaporites of Brightling Mine, we consider that the following are those which most likely would have an impact on fracture propagation vertically through the sedimentary section:

a) Bedding parallel satin spar veins (Figure 3.26)
b) Shale layers
c) Lithological heterogeneity

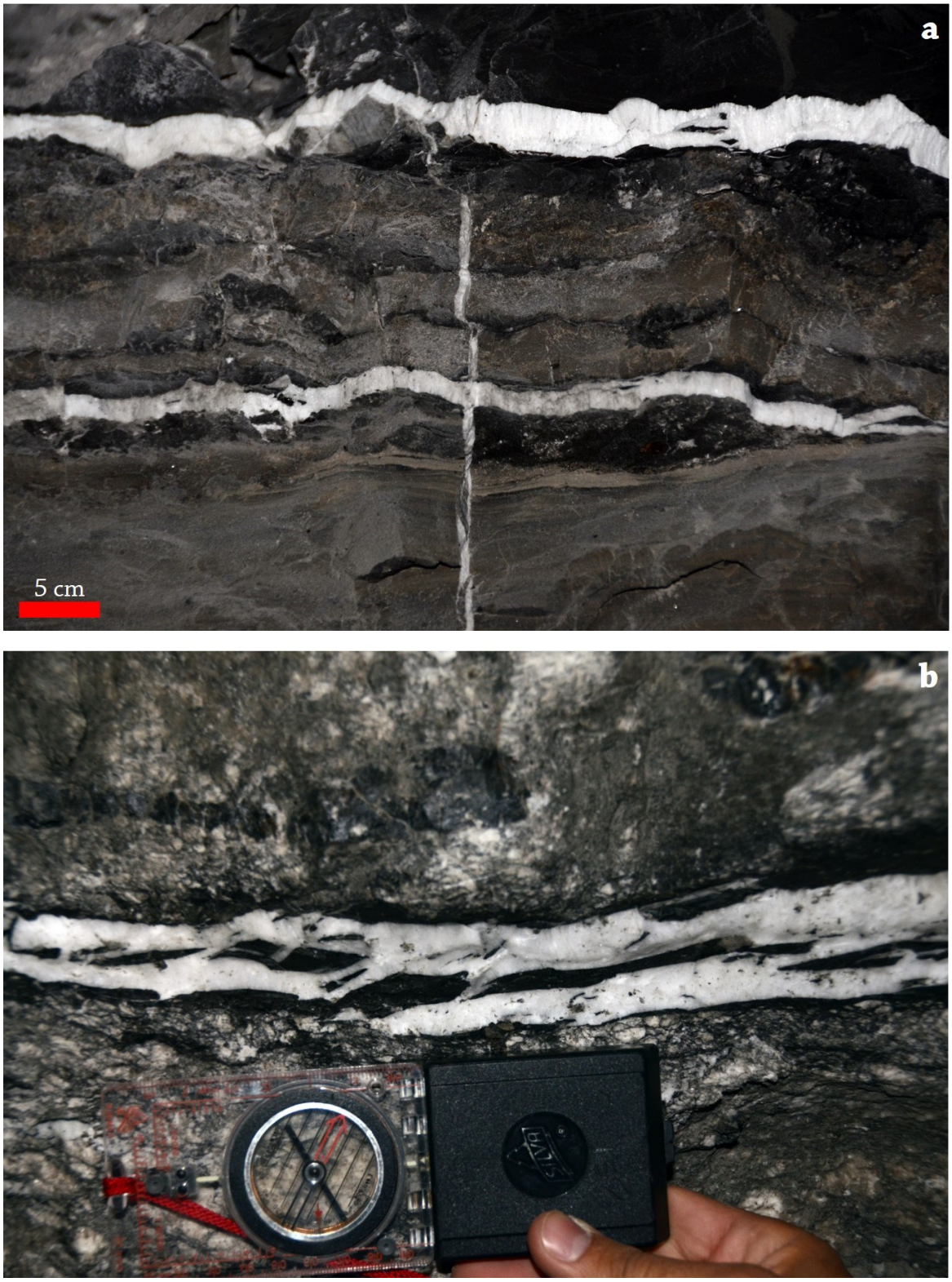


Figure 3. 26: Detail of the rock face showing a) horizontal fractures (HFa) filled with satin spar cutting a vertical fracture also filled with satin spar (the cross cut relation on this image shows that the horizontal fractures postdate the vertical fracture); b) a horizontal fracture (HFa) filled with satin spar that opened in a shale horizon. Notice the clasts of shale floating within the veins.

3.4 Core Analysis

In order to complete our assessment of the Purbeck evaporite succession we were granted access to several drill-cores from the Weald Basin stored at the British Geological Survey. We have analysed and described the evaporitic sections of four wells: Goodley Bridge-1, Winchester-1, Normandy-1 and Warlingham. The locations of these wells can be found in Figure 3.27. Table 4.1 outlines the general data on each of the wells.

Table 3.1: General information on the analysed wells. Warlingham well did not have a well report available.

Well	Operator	Date	Total Depth (m)	Depth of Purbeck (TVDSS m)
Winchester-1	BP	Oct 1959	1781	474
Goodley Bridge	Conoco	Nov 1982	2583	867
Normandy-1	Conoco	Fev 1986	1357	511
Warlingham	-	-	-	-

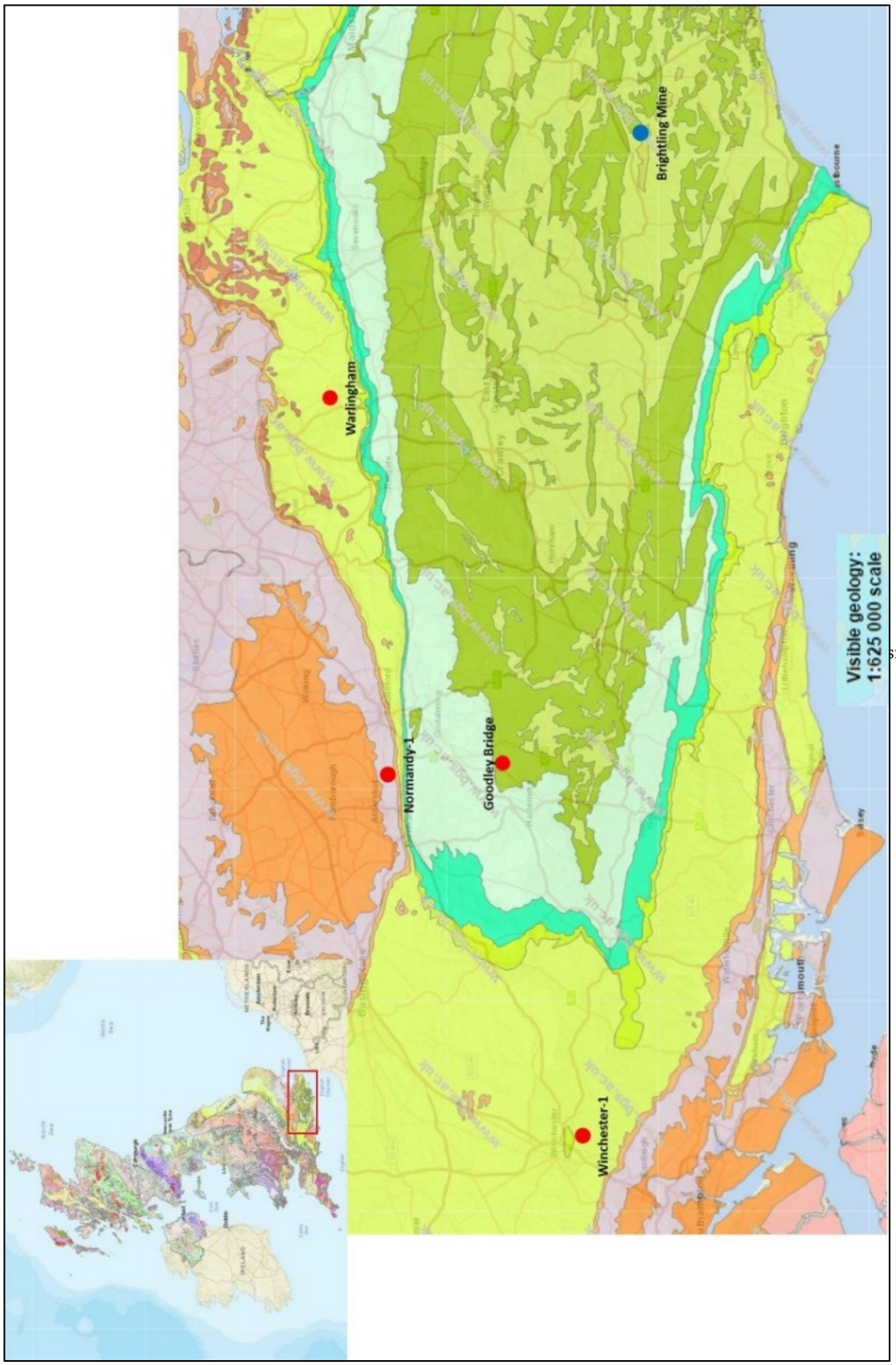
Considering that these wells were drilled within the same sedimentary basin in which Brightling Mine is located – the Weald Basin – it was decided to use the same facies description. Therefore the facies identified in the cores are:

F1) Massive to Nodular anhydrite: light-blue to light-grey/white anhydrite in a carbonate matrix. This lithofacies presents several types of textures:

Nodular anhydrite: composed of nodules of various dimensions (from 0.2 cm to 15cm) with diverse morphologies but mainly subspherical to ellipsoid-shaped, horizontally enlongated. The larger nodules are occasionally composed of aggregated smaller nodules. Cross sections of the nodular aggregates reveal chicken-wire, palisade and agreggate textures.

Banded anhydrite: Bands and also beds of around 5cm thick composed of anhydrite nodules of various dimensons but usually 0.5 to 1cm. Enterolithic texture was observed.

F2) Massive to laminated mudstone: very fine grain, brown to dark grey massive to laminated mudstone with low anhydrite content. Small nodules (<1cm) of anhydrite are often present.



sin showing their location relati

F3) Microbial laminated mudstone: consists of light brown, tan-coloured, fine-grained laminated mudstone with thin dark-brown, organic-rich laminae. Irregular laminations and domal sedimentary structures are present which suggest stromatolitic/microbial origin.

F4) Bioturbated Mudstone: dark grey and very fine-grained mudstone with low to moderate fossil content.

F5) Shale: dark grey to black, fine-grained laminated shale. Forms beds of different thicknesses from 1 to 5cm

F6) Carbonate sandstone (not observed in Brightling Mine)

F7) Secondary gypsum veins: fibrous gypsum veins – satin spar. Contrarily to Brightling mine only bedding-parallel were observed.

F8) Anhydrite-Mudstone Breccia

As can be seen from the diverse list of facies presented above, and in Figures 3.28 to 3.31, the evaporite succession in the Weald Basin (both in the cores and in Brightling Mine) is diverse. In addition the sedimentary textures are extremely varied. As noted the main aim of the study of the Purbeck evaporites of the Weald Basin is to obtain an understanding of the features they contain that are likely to act so as to inhibit the vertical propagation of fractures induced in an underlying reservoir being charged with CO_2. A detailed description of the sedimentary structures and their particularities regarding the environment in which they were formed is outside the scope of this study. However the cores from the Weald Basin (where Brightling Mine is located) provide an outstanding section through the evaporites. Their reproduction in Figures 3.29 to 3.31 enables the reader to see at a glance some of the features identified in the succession at Brightling Mine and which are considered to be important arresting vertical fracture propagation.

The field work carried out at Brightling Mine, on the cores and Bristol Channel area (described in the next section) provide a remarkable insight into the mechanical properties of evaporite successions and enable a focused series of numerical models to be designed which quantify the effect of the various features in inhibiting fracture propagation trough such potential scales.

A brief description of the wells is presented below with more detail relating to Normandy-1 well because of its highly variable stratigraphic sequence. It is considered that this well is very good example

of how complex evaporite sequences can be and how their diverse mechanical heterogeneity can make these lithologies remarkably efficient in inhibiting the propagation of hydraulic fractures.

Winchester-1(Figure 3.27 and 3.28): This well presents the shortest core section examined although the well report states the existence of an approximately 14m thick Purbeck Evaporite section (590.7m– 604.41m). The predominant lithologies are laminated mudstone (F2) at the top and nodular anhydrite (F1) at the base.

Date – Oct 1959
TD - 1781
Completion Status –
Purbeck Anhydrite – 590.7m– 604.41m

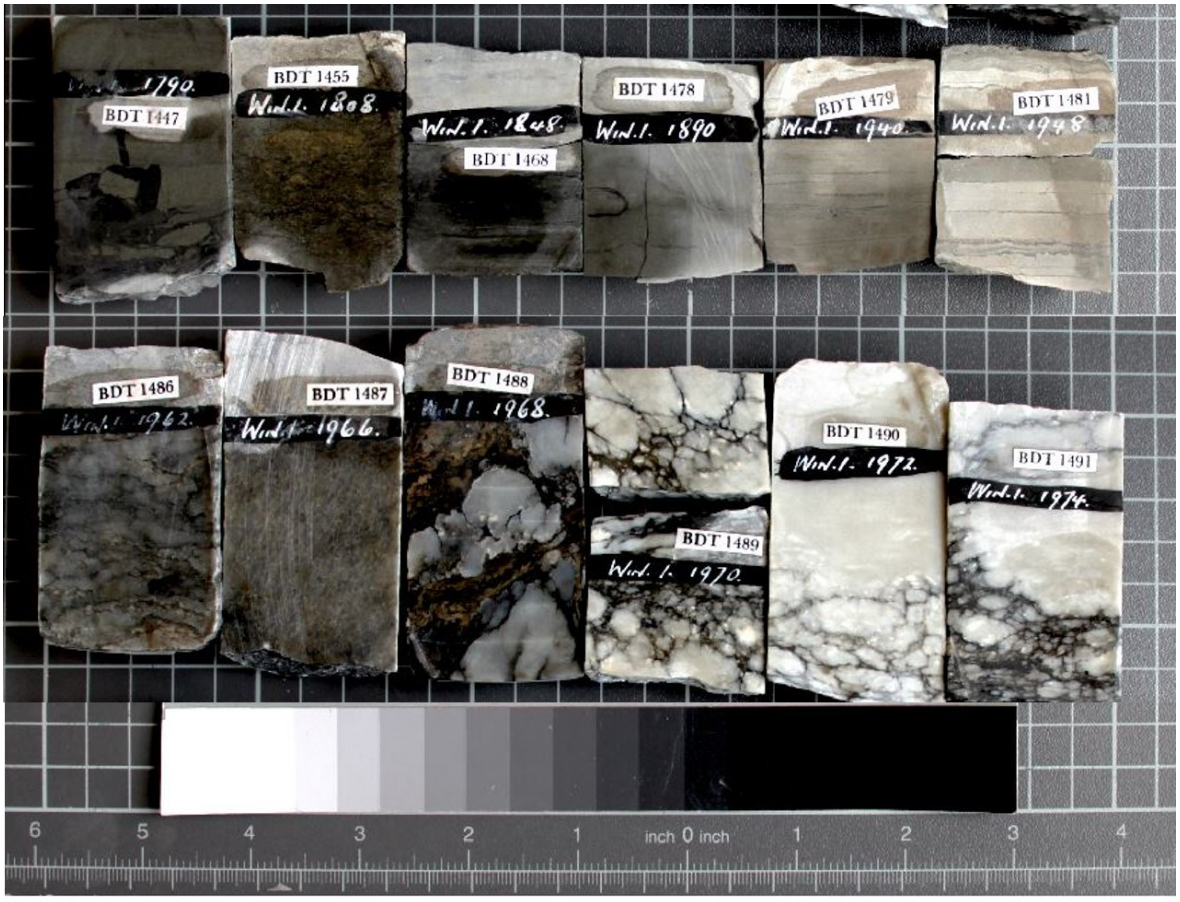


Figure 3.28: Winchester-1 side wall cores showing the sequence of evaporites, where the predominant lithologies are laminated mudstone (F2) at the top and nodular anhydrite (F1) at the base.

Goodley Bridge (Figure 3.27 and 3.29): In the Goodley Bridge well the Purbeck Anhydrite section is approximately 6m thick. The predominant facies is nodular anhydrite (F1) – with nodules of sizes ranging between 1 and 17cm - and laminated mudstone (F2) with sparse shale layers (F5). At the top of the core section where nodules are predominant, evidence of pressure solution at the contact points of adjacent nodules is observed. Towards the base of the core section where the mudstone content is higher and the nodules do not contact each other, they are subspherical to ellipsoid-shaped.

Date – November 1982
TD - 1357.884m
Completion Status – Dry Hole
Purbeck Anhydrite – 940.3m – 946.0m

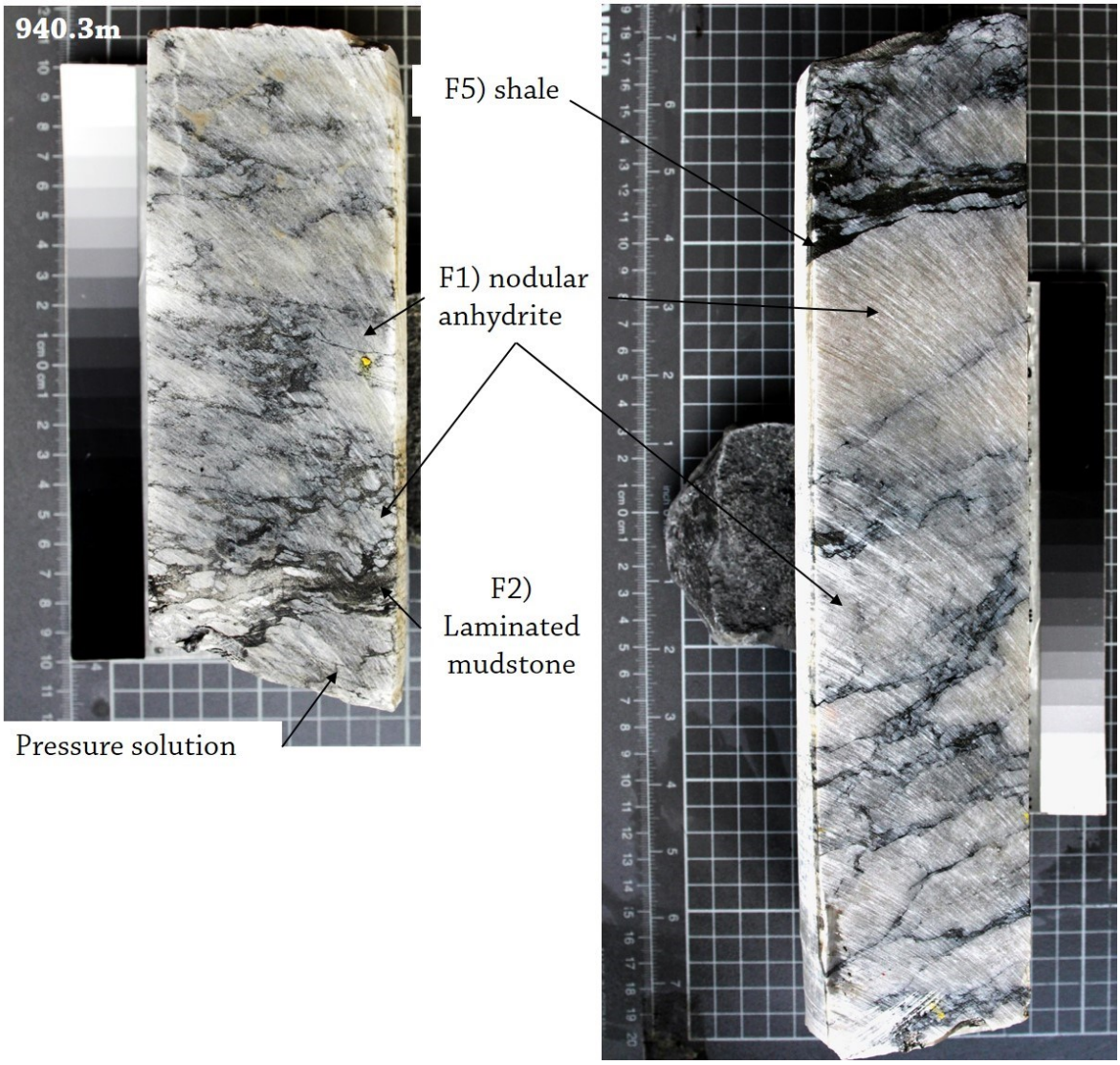


Figure 3.29: section of core from the Goodley Bridge well showing massive to nodular anhydrite (F1) in a dark mudstone matrix (F2) with occasional shale layers (F5). The nodules are irregularly shaped but have a tendency to be ellipsoids of varied dimensions (5mm to 7cm). The contacts between nodules showing evidence of pressure solution.

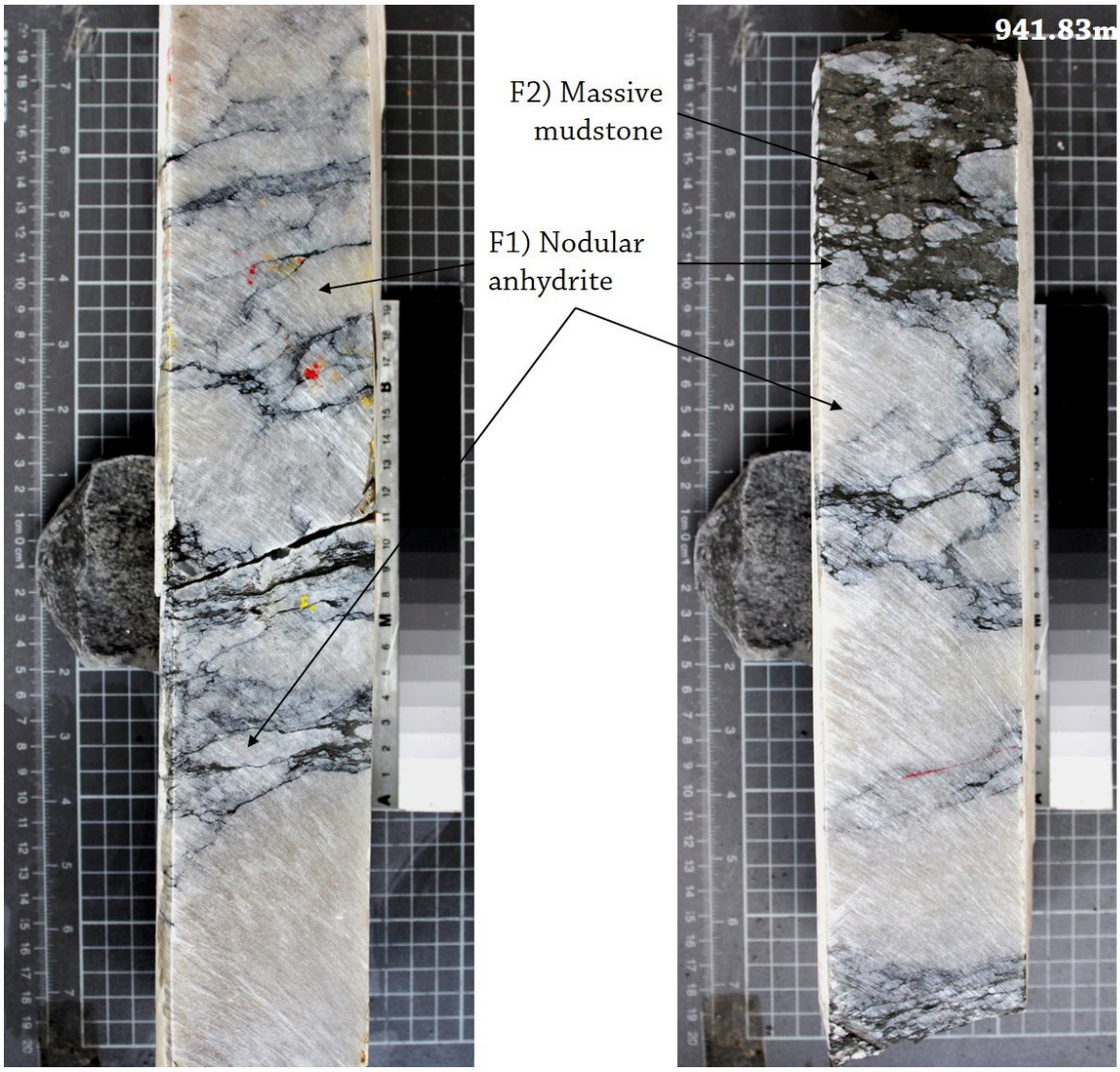


Figure 3.29 (continued): section of core from the Goodley Bridge well showing massive to nodular anhydrite in a dark mudstone matrix with occasional shale layers. Nodules are irregularly shaped but have a tendency to be ellipsoids of varied dimensions (5mm to 7cm). The contacts between nodules showing evidence of pressure solution.

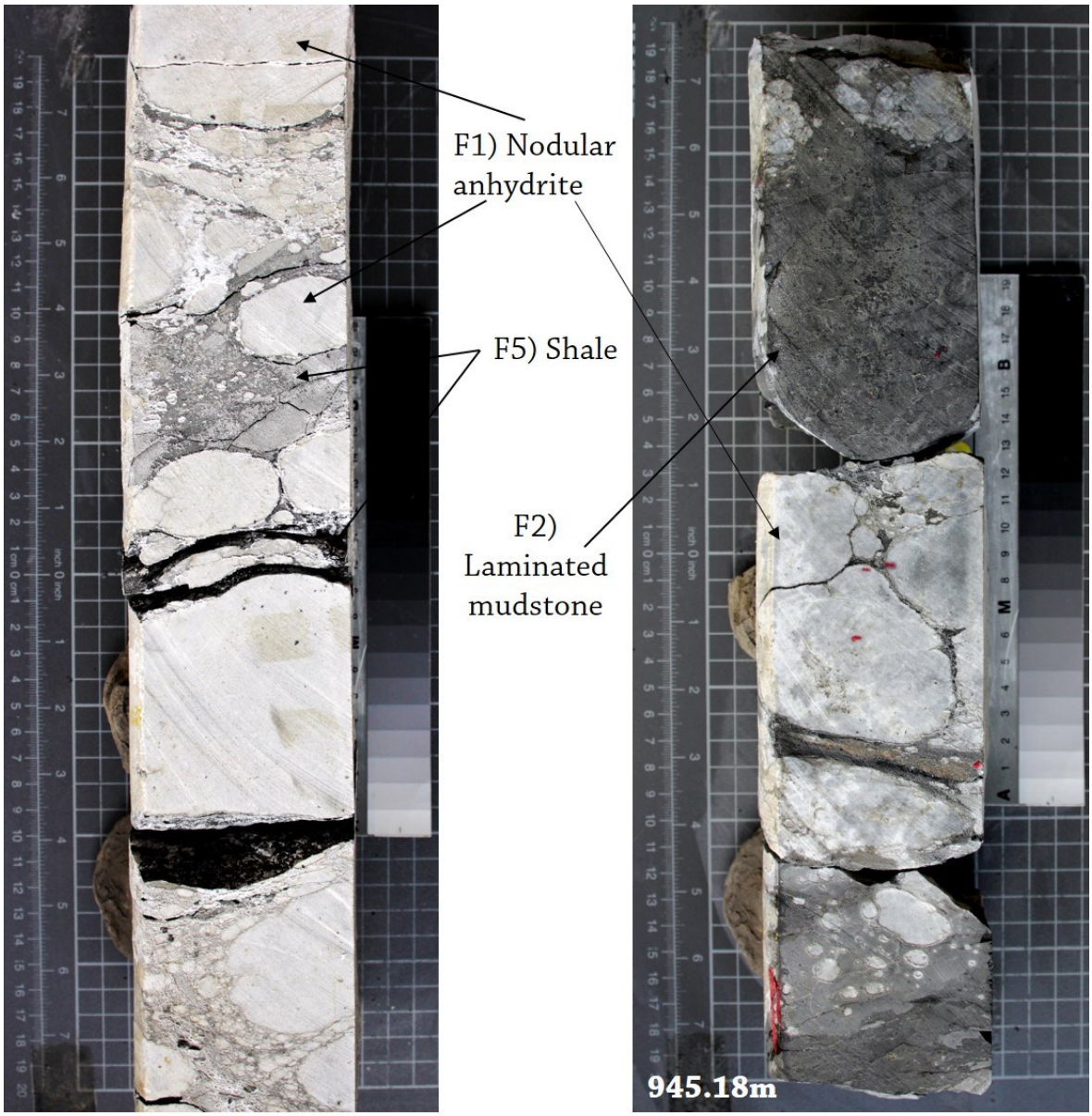


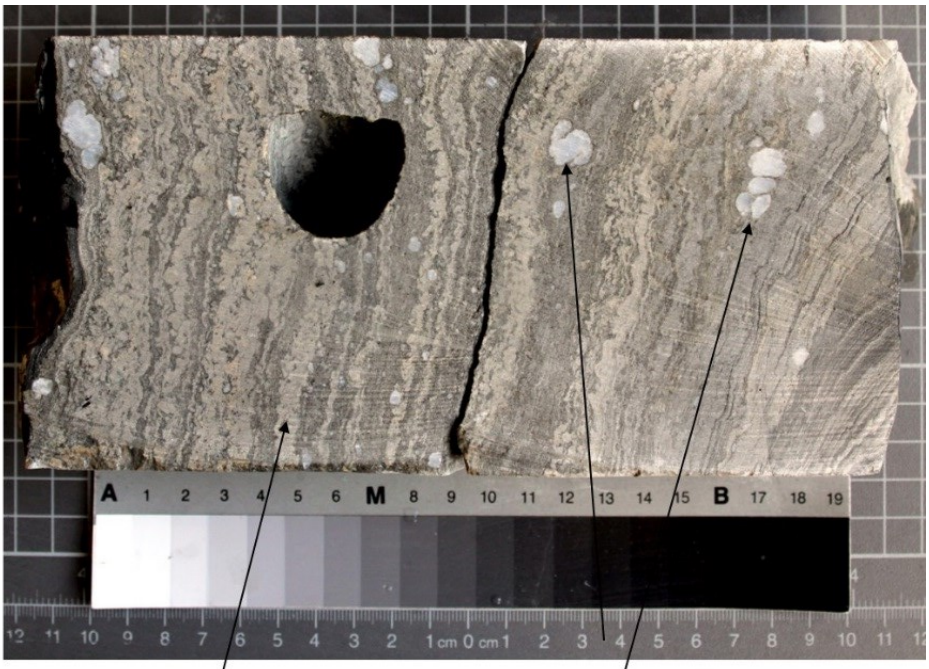
Figure 3.29 (continued): section of core from the Goodley Bridge well showing nodular anhydrite in a dark mudstone matrix with occasional shale layers. Nodules are ellipsoid shaped of varied dimensions (5mm to 7cm).

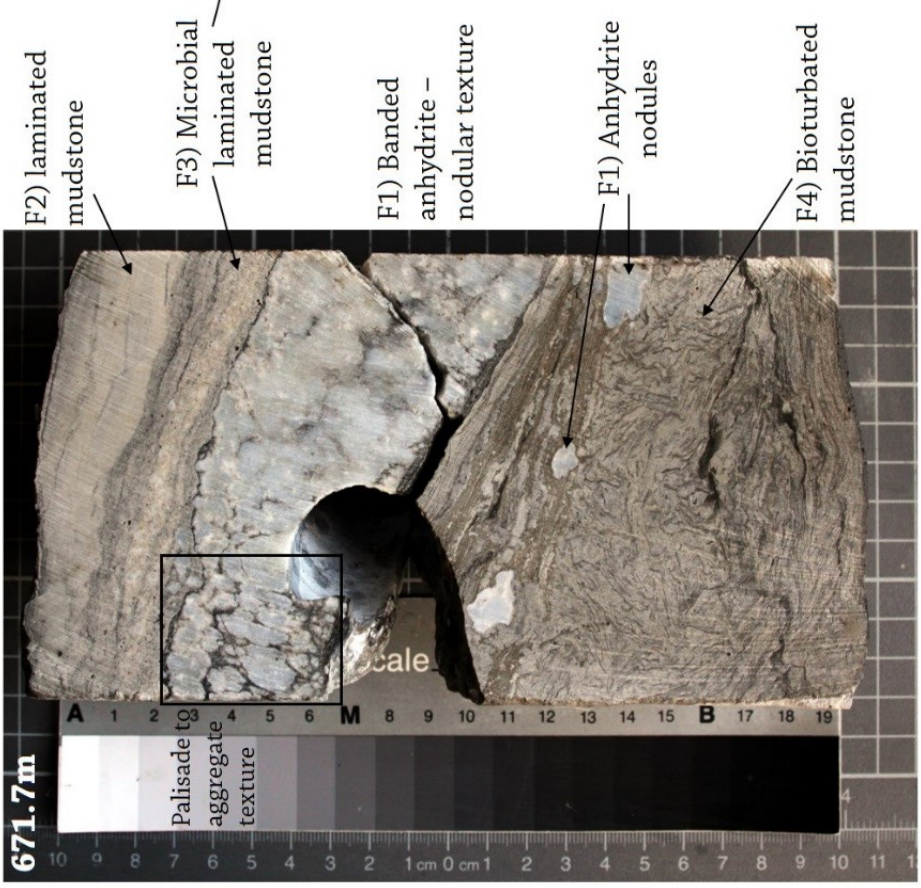
Normandy-1 (Figure 3.27 and 3.30): In the Normandy well the Purbeck Anhydrite section is approximately 11m thick, being the longest drill-core section analyzed. It displays six of the eight facies previously presented and a very diverse nodular evaporite texture (see Section 2.1.3). Other relevant facies include bedding parallel fibrous gypsum veins and an evaporitic breccia composed of a shale/mudstone matrix with clasts of several dimensions of anhydrite.

The evaporite section starts at 671.7m with laminated mudstone (F2) intercalated with a microbial laminated mudstone (F3) with sparse anhydrite nodules and a band of nodular anhydrite (F1). At the base of the core a section of bioturbated mudstone (F4) is present. It follows (673.2m) a sequence of around 80 cm of almost pure anhydrite in the form of nodules and massive anhydrite, which gradually

gives way (673.9m) to a sequence of around 60 cm of anhydrite nodules and a layer of massive mudstone with sparse anhydrite crystals followed by another layer of nodular to massive anhydrite. In the next core section (674m) a band of nodular anhydrite with an enterolithic texture occurs within a microbial laminated mudstone. This is followed by laminated mudstone and nodular anhydrite. This gives way to an alternation of anhydrite layers (F1) massive and nodular (chicken-wire texture) with shale laminae. The core section at 675.7 m shows crystalline anhydrite nodules in a matrix of microbial mudstone and a laminated mudstone at the base. There is also a bedding-parallel secondary fibrous gypsum vein at the base of the core section. The next core section (676.6m) shows a 40cm continuous interval of massive to nodular anhydrite with sparse thin horizons of dark shale. At the base of this section a very clear nodular anhydrite section is seen followed by a microbial mudstone with sparse anhydrite nodules. The following core section at 677m starts with a massive anhydrite interval followed by anhydrite nodules in a microbial mudstone and anhydrite nodules in a carbonate matrix. At 678.4m an irregular distribution of anhydrite nodules and microbial mudstone with anhydrite predominance occurs, which gives way to a microbial mudstone (F3) with disperse anhydrite nodules (F1) and massive to laminated mudstone with sandstone laminae (F6) at 679.39m. The core section that follows (680.31m) shows a bioturbated mudstone with nodular anhydrite and shale clasts (F4), alternated laminating mudstone (F2) and anhydrite (F1) and microbial mudstone (laminated with stromatolite domes). It is followed (681.22m) by an interval of bioturbated mudstone with nodular anhydrite terminating with an interval of a breccia formed of a shale/mudstone matrix with anhydrite and chert clasts of varied dimensions and irregularly shaped. The origin of this breccia is difficult to determine. It is unlikely to have occured as a result of exposure because it is at the base of the succession. It therefore argued that these textures may have been induced by high fluid pressures.

Date – February 1986
TD - 2582.5m
Completion Status – Abbandoned Gas Well
Purbeck Anhydrite - 671.7m - 683.3m





obial laminated mudstone (F3) with sparse anh
ent.

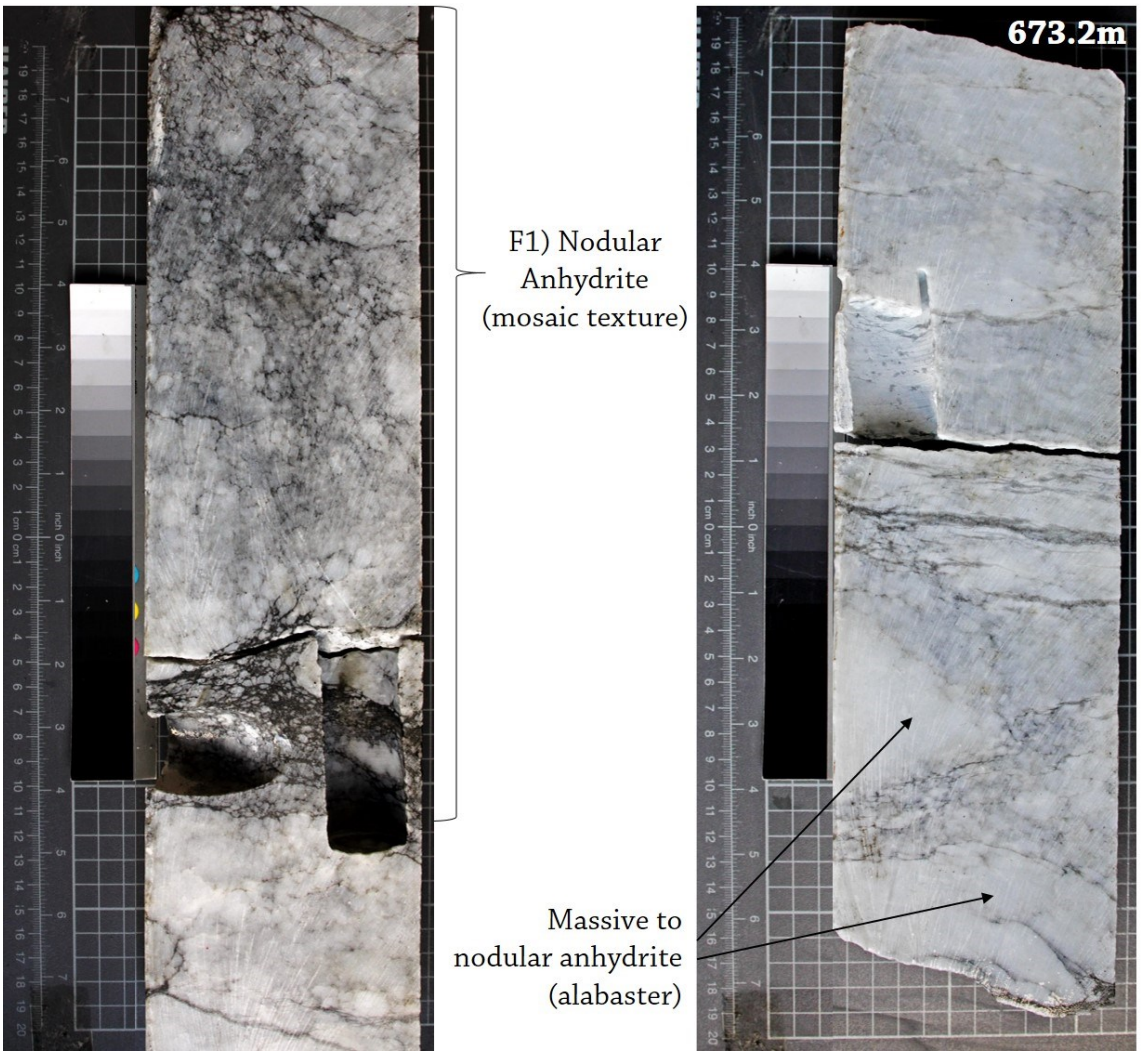


Figure 3.30 (continued): section of core of from Normandy-1 well showing a sequence of around 80 cm of almost pure anhydrite in the form of nodules and alabaster (F1).

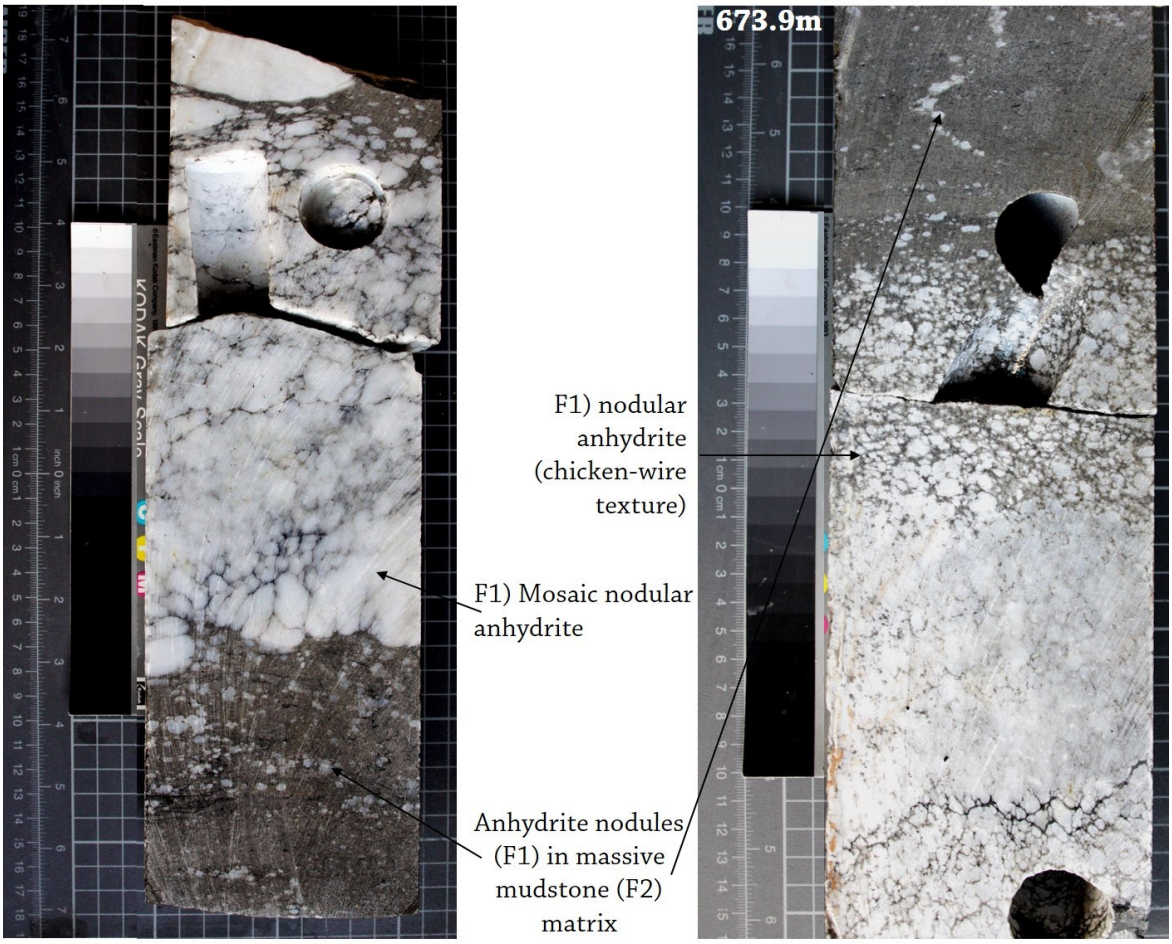


Figure 3.30 (continued): section of core of from Normandy-1 well showing a sequence of around 60 cm of anhydrite nodules and a layer of massive mudstone with sparse anhydrite crystals.

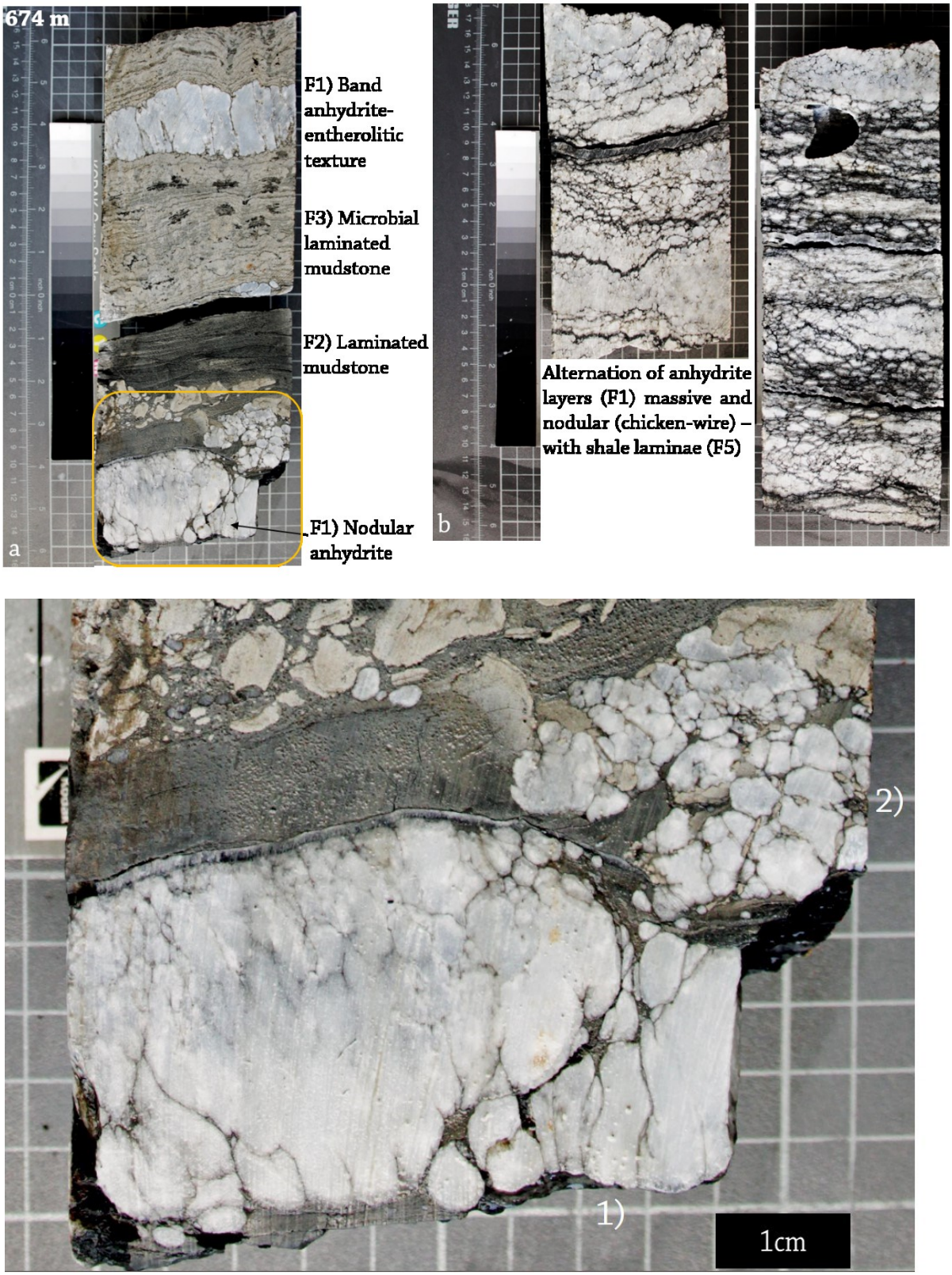


Figure 3.30 (continued): section of core of from Normandy-1 well. A) section showing a band of nodular anhydrite-(enterolitic texture) within a microbial laminated mudstone followed by laminated mudstone and nodular anhydrite (see c); b) Alternation of anhydrite layers (F1) massive and nodular (chicken-wire texture) –with shale laminae (F5); c) detail of the nodular anhydrite in a) disposed in 1) vertically elongate individuals (palisade texture) and 2) nonaligned aggregate texture.

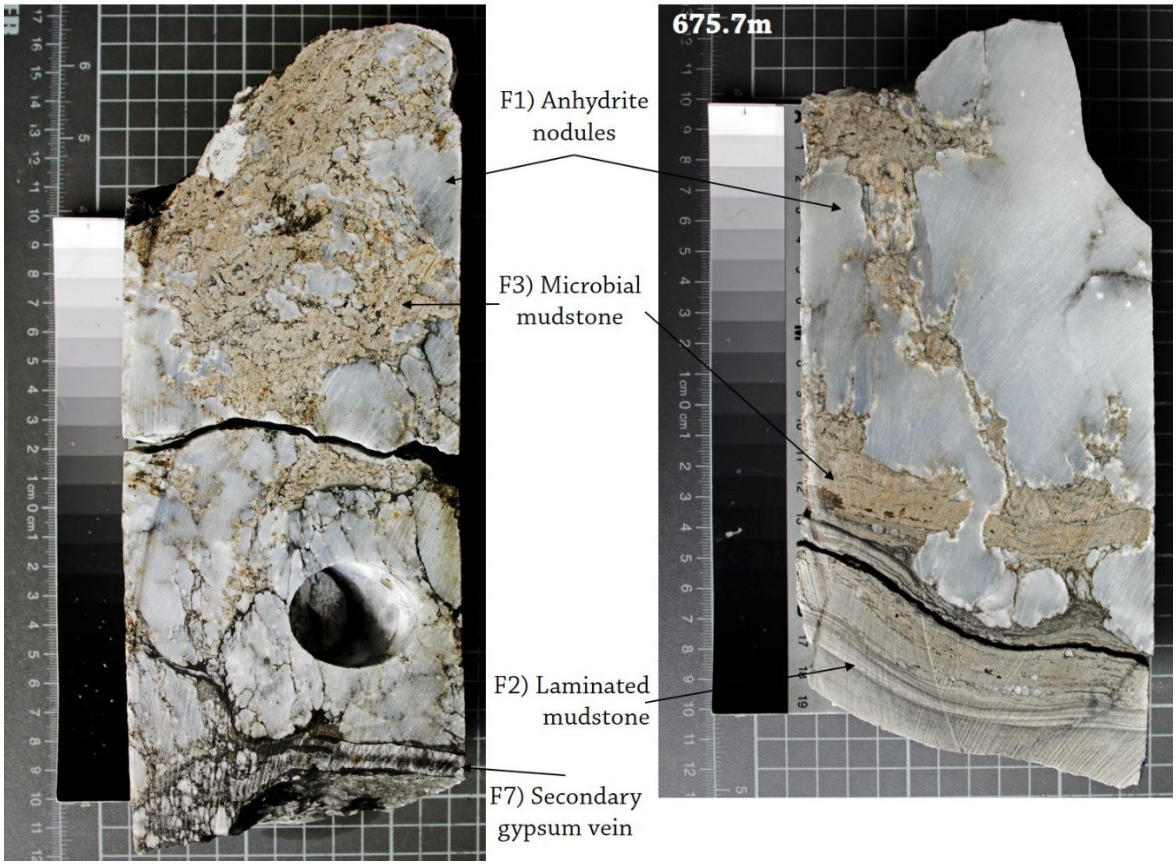


Figure 3.30 (continued): section of core of from Normandy-1 well showing crystalline anhydrite nodules in a matrix of microbial mudstone. Notice the secondary fibrous gypsum vein at the base of the left-hand side core section.

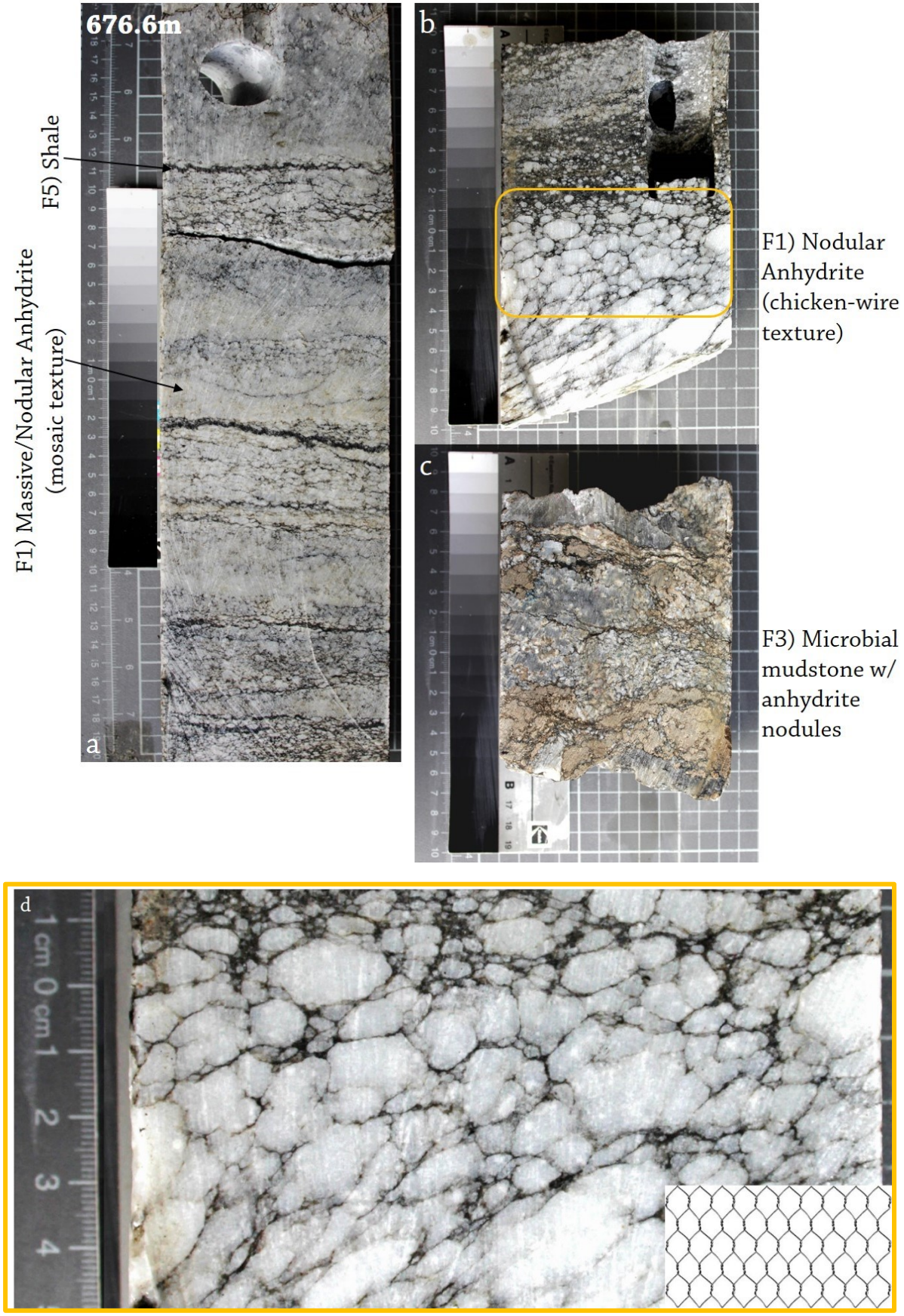


Figure 3.30 (continued): section of core of from Normandy-1 well showing several types of nodular anhydrite textures. (a, b, d) and the aspect of a microbial mudstone with anhydrite nodules; c) an example of chicken wire texture, where the disposition of the grains resembles that of a metallic chicken-wire used in fences (see sketch).

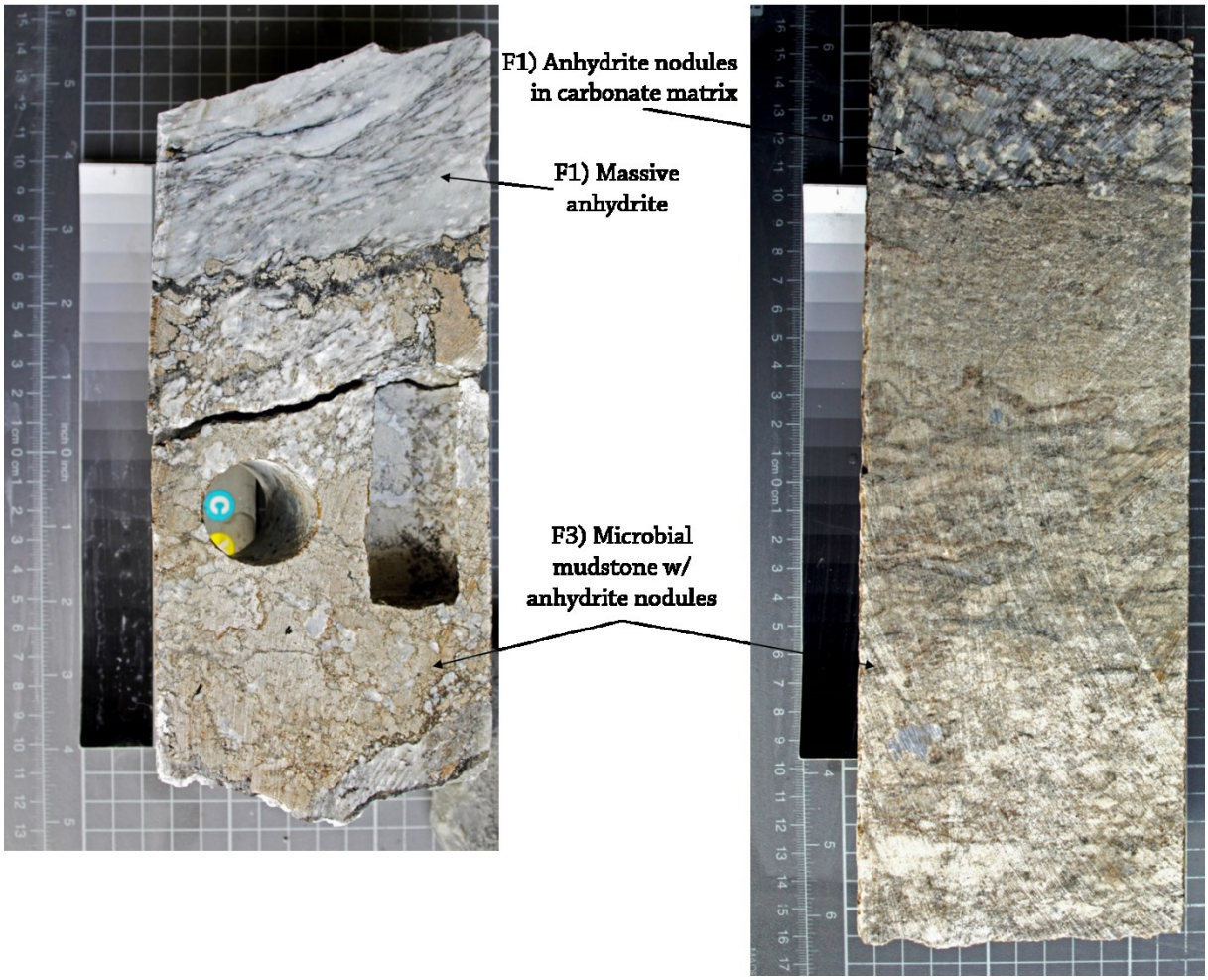


Figure 3.30 (continued): section of core of from Normandy-1 well showing massive anhydrite followed by anhydrite nodules in a microbial mudstone and anhydrite nodules in carbonated matrix.

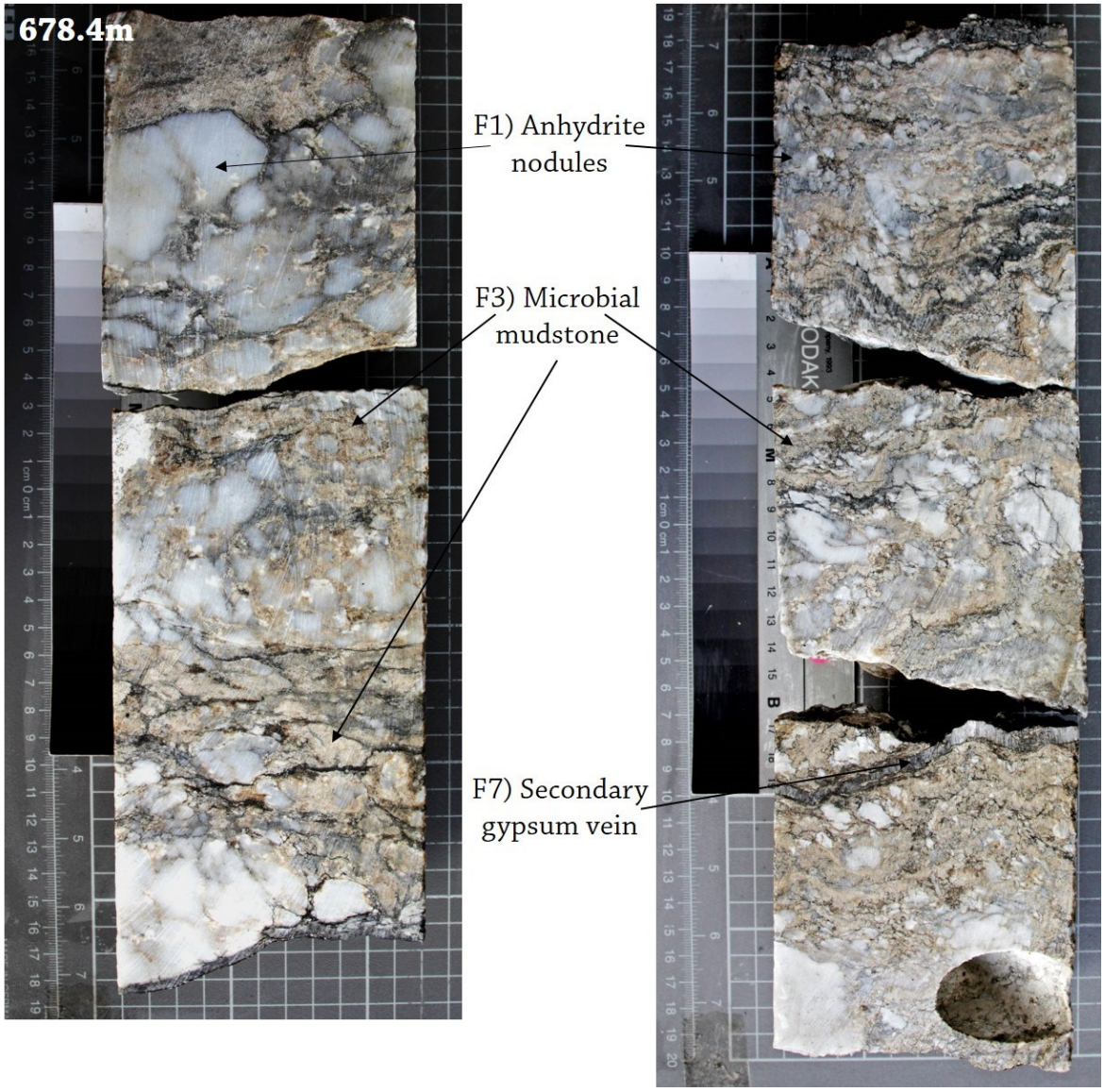


Figure 3.30 (continued): section of core of from Normandy-1 well showing an irregular distribution of anhydrite nodules and microbial mudstone with anhydrite predominance.

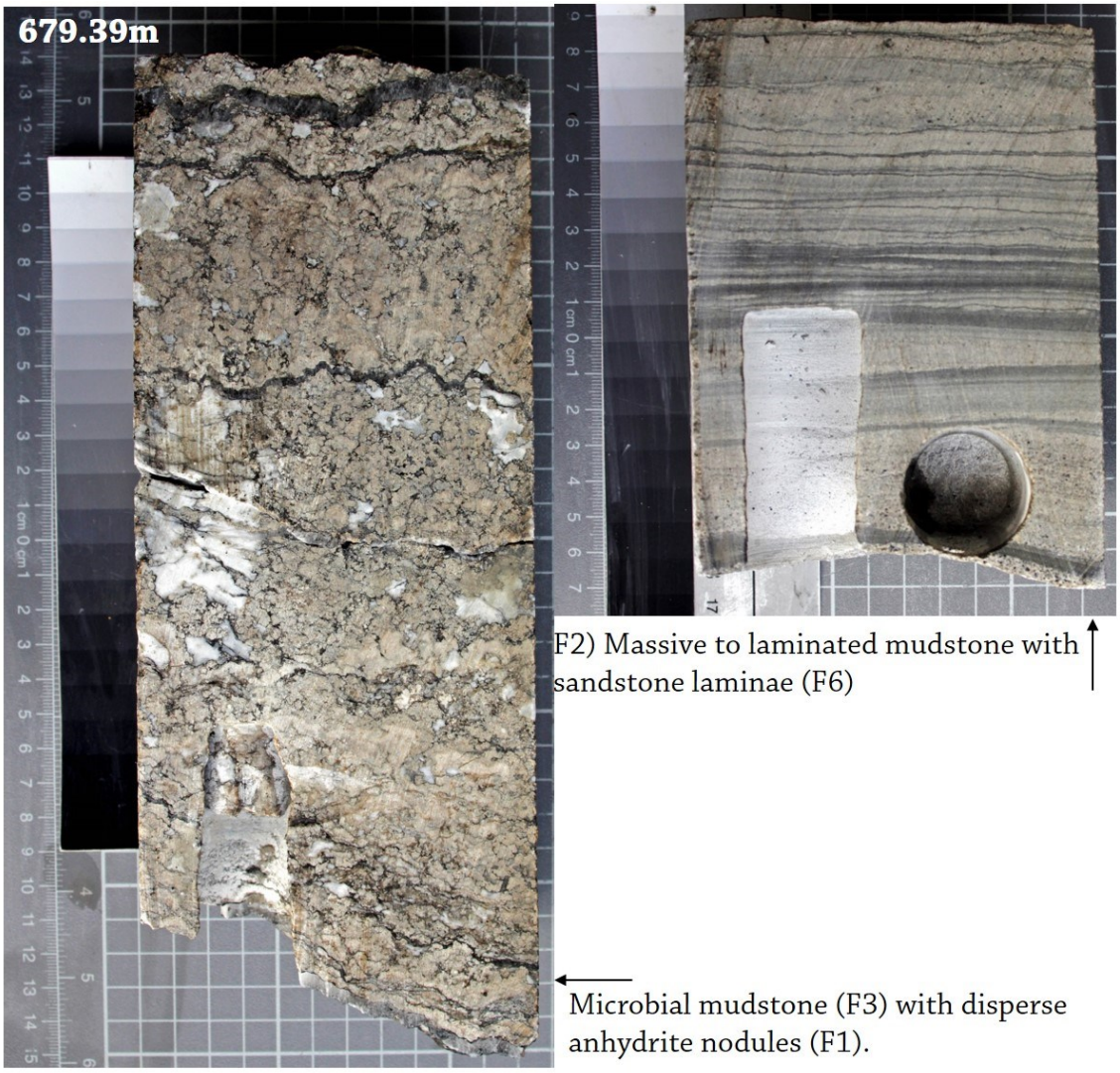


Figure 3.30 (continued): section of core of from Normandy-1 well showing a microbial mudstone (F3) with disperse anhydrite nodules (F1) and massive to laminated mudstone with sandstone laminae (F6).

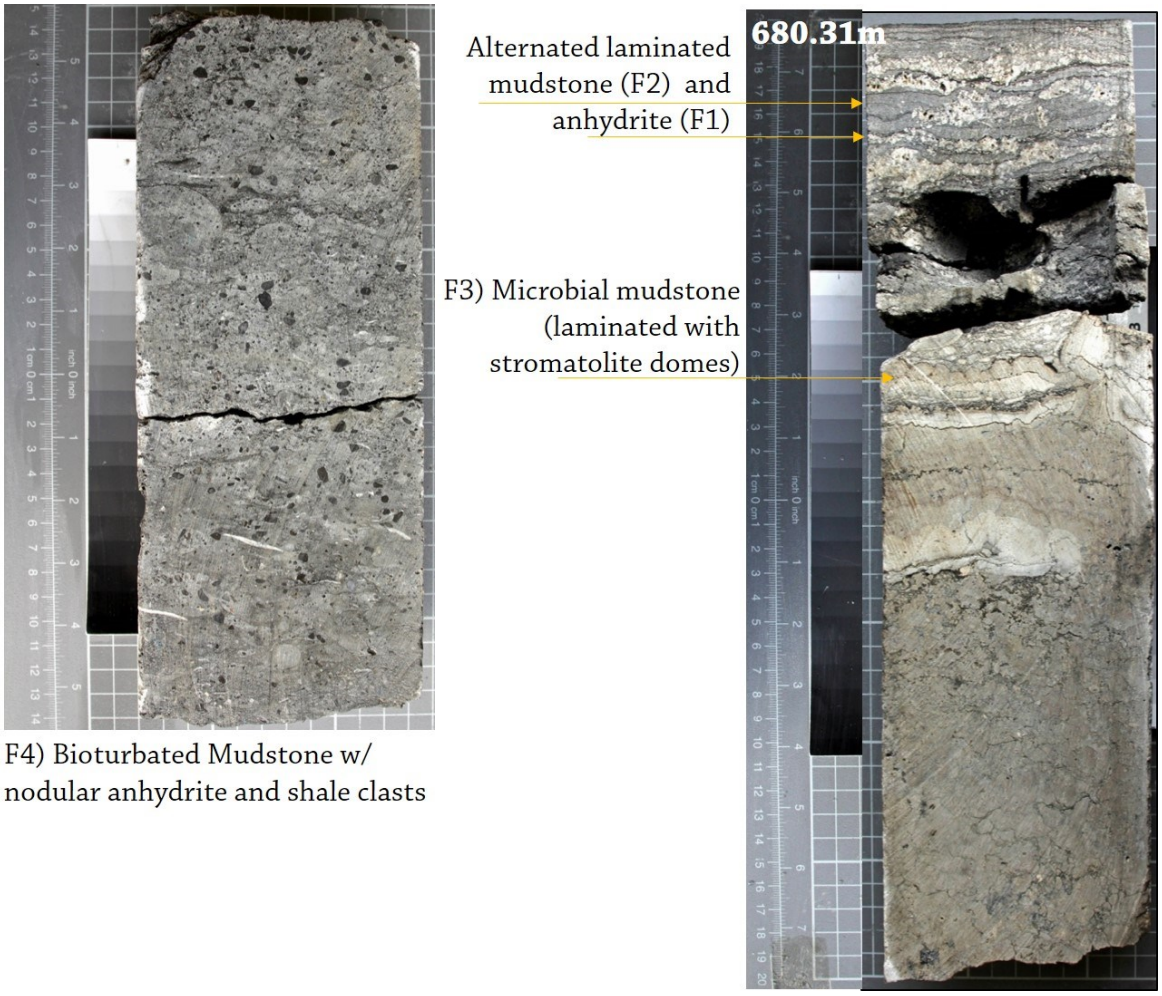


Figure 3.30 (continued): section of core of from Normandy-1 well showing a bioturbated mudstone w/ nodular anhydrite and shale clasts (F4), alternated laminating mudstone (F2) and anhydrite (F1) and microbial mudstone (laminated with stromatolite domes).

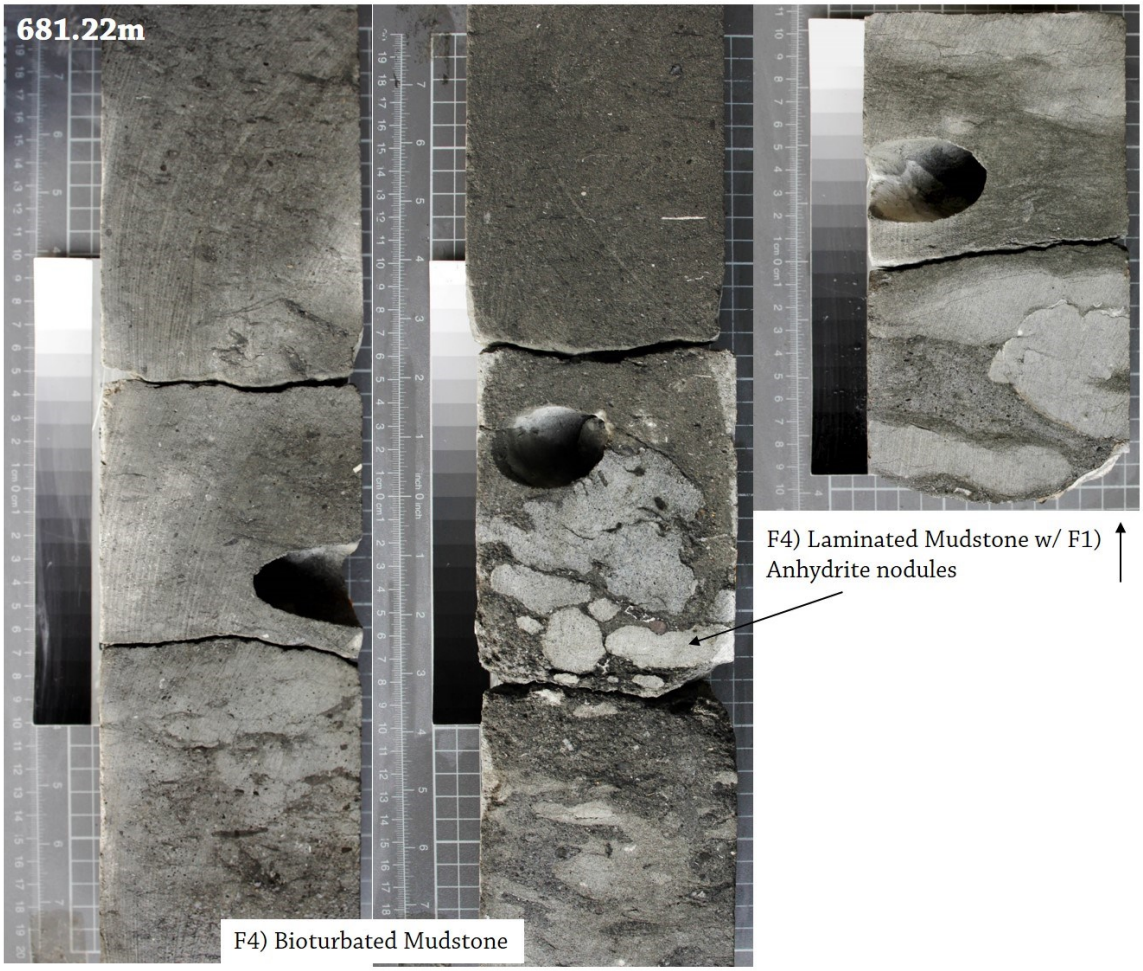


Figure 3.30 (continued): section of core of from Normandy-1 well showing a bioturbated mudstone w/ nodular anhydrite.

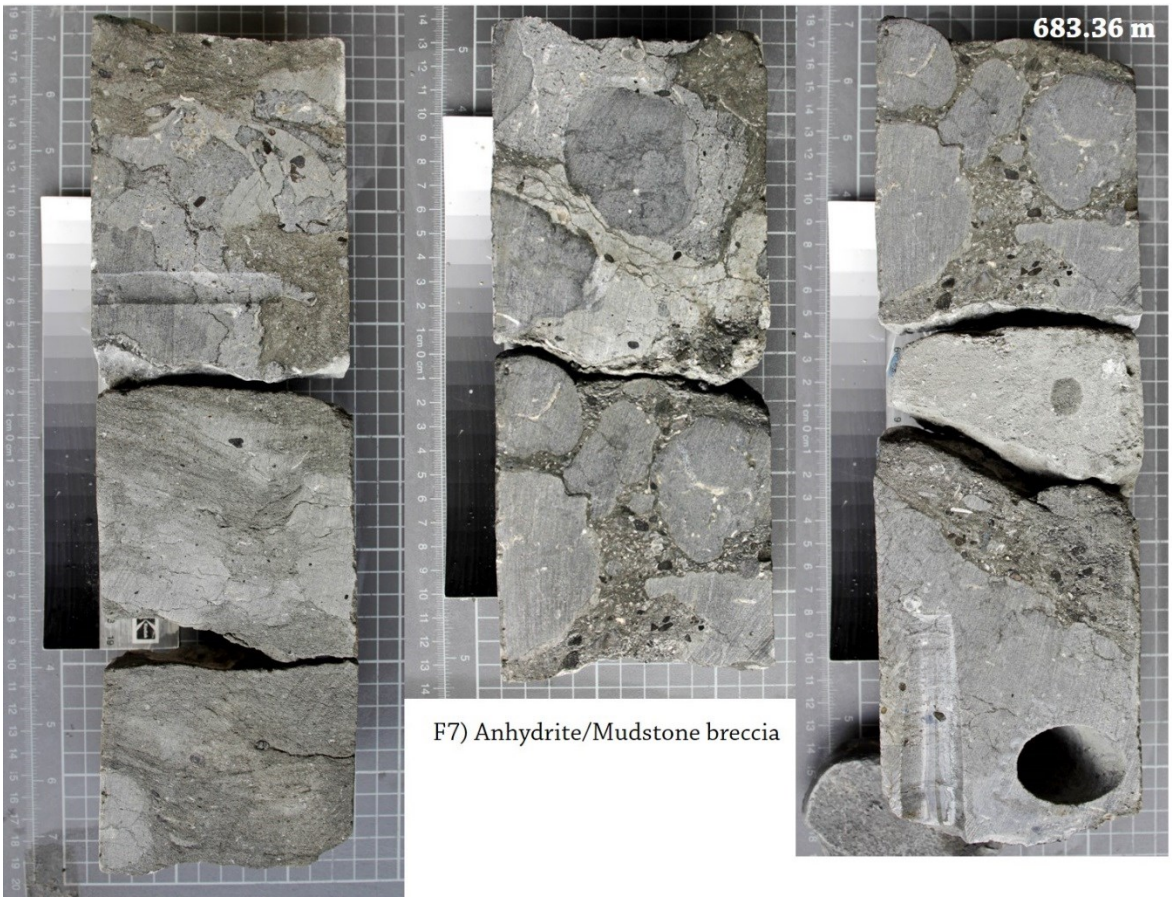


Figure 3.30 (continued): section of core of from Normandy-1 well showing a section of a breccia formed by a shale/mudstone matrix with anhydrite and chert clasts of varied dimensions and irregularly shaped.

Warlingham (Figure 3.27 and 3.31): the Purbeck Anhydrite section in the Warlingham well is approximately 5m thick (648.0m – 653m). It is a section in which laminated and massive mudstone are predominant but where nodular anhydrite is also present in bands of different thicknesses and with different evaporitic textures. At around 650m, within a section approximately 6cm thick a series of shear fractures is visible. These fractures do not propagate below a sedimentary horizon which seems to be mechanically different from the upper section (Figure 3.31c). It is interesting to note that although of similar lithology, no shear fractures were observed in Brightling Mine. It is suggested that this is related to the higher differential stresses acting in the rocks of the Warlingham well. A simple calculation can clarify this hypothesis. Table 3.2 shows the data we can easily obtained from both the well and the mine and that we can be used to calculate the acting differential stresses (See Section 4.22).

Table 3.2: data used to calculate the differential stresses

	Evaporites (Core)	**Anhydrite (Mine)**
Depth (m)	651	283
Density (kgm^{-2})	2200	2200
Poisson's Ratio	0.2	0.2
Poisson's number	5	5
Gravitic Acc.(ms^{-2})	9.8	9.8

Considering a situation where a section of the Earth's crust of uniform properties and completely elastic is subjected to gravitational loading with lateral strain being inhibited in all directions by the surrounding material, then a cube of unit sides will be subjected to a vertical stress resultant of the weight of the overburden:

$$\sigma_z = z\rho g \qquad (18)$$

where

ρ – bulk density of the material;

g – the acceleration due to gravity

z- depth relative to the surface.

The orientation of the shear fractures in Figure 3.31c (they are normal faults) show that during the time when they were formed the vertical stress was σ_1, i.e. we can write $\sigma_1 = \sigma_2$. The resultant stress at the Brightling Mine:

$$\sigma_1 \text{ (core)} = 651 \times 2200 \times 9.8 = 1.40 \times 10^7 \text{ Pa} = 14 \text{ MPa}$$

$$\sigma_1 \text{ (mine)} = 283 \times 2200 \times 9.8 = 6.10 \times 10^6 \text{ Pa} = 6.1 \text{ MPa}$$

We also know that:

$$\sigma_H = \frac{\sigma_v}{m-1} \qquad (19)$$

Where σ_H is the horizontal stress, σ_v the vertical stress (in this case it is equal to σ_1) and m, the Poisson's number (m=1/ υ). By substitution we obtain σ_3:

$$\sigma_3 \text{ (core)} = \frac{1.4e7}{\frac{1}{0.2}-1} = 3.5 \times 10^6 \text{ Pa} = 3.51 \text{ MPa}$$

$$\sigma_3 \text{ (mine)} = = \frac{6.1e6}{\frac{1}{0.2}-1} = 1.53 \times 10^6 \text{ Pa} = 1.53 \text{ MPa}$$

We can now calculate the differential stresses for both locations:

$$\sigma_1\text{-}\sigma_3 \text{ (core)} = 14 - 3.51 = 10.49 \text{ MPa}$$

$$\sigma_1\text{-}\sigma_3 \text{ (mine)} = 6.1 - 1.53 = 4.57 \text{ MPa}$$

As postulated the differential stress acting in the core of Wharlingham well is around two times larger than the differential stress acting at Brightling Mine. This might justify why shear fractures have formed in Walingham but not in Brightling.

Considering the four analysed wells and the multitude of textures and features observed, we consider that the following are those which most likely would have an impact on fracture propagation vertically through the sedimentary section:

1) Shale layers intercalations (Figure 3.31 – 649.2m)
2) Banded anhydrite layers (Figure 3.30 – 671.7m)
3) Laminated mudstone intercalations (Figure 3.30 – 674m and Figure 3.31 - 648m)
4) Satin spar bedding-parallel veins (Figure 3.31 – 649.2m and Figure 3.31 – 650.44 m b))

Warlingham
Date –
TD -
Completion Status – Dry Hole
Purbeck Anhydrite – 648.0m– 553.0m

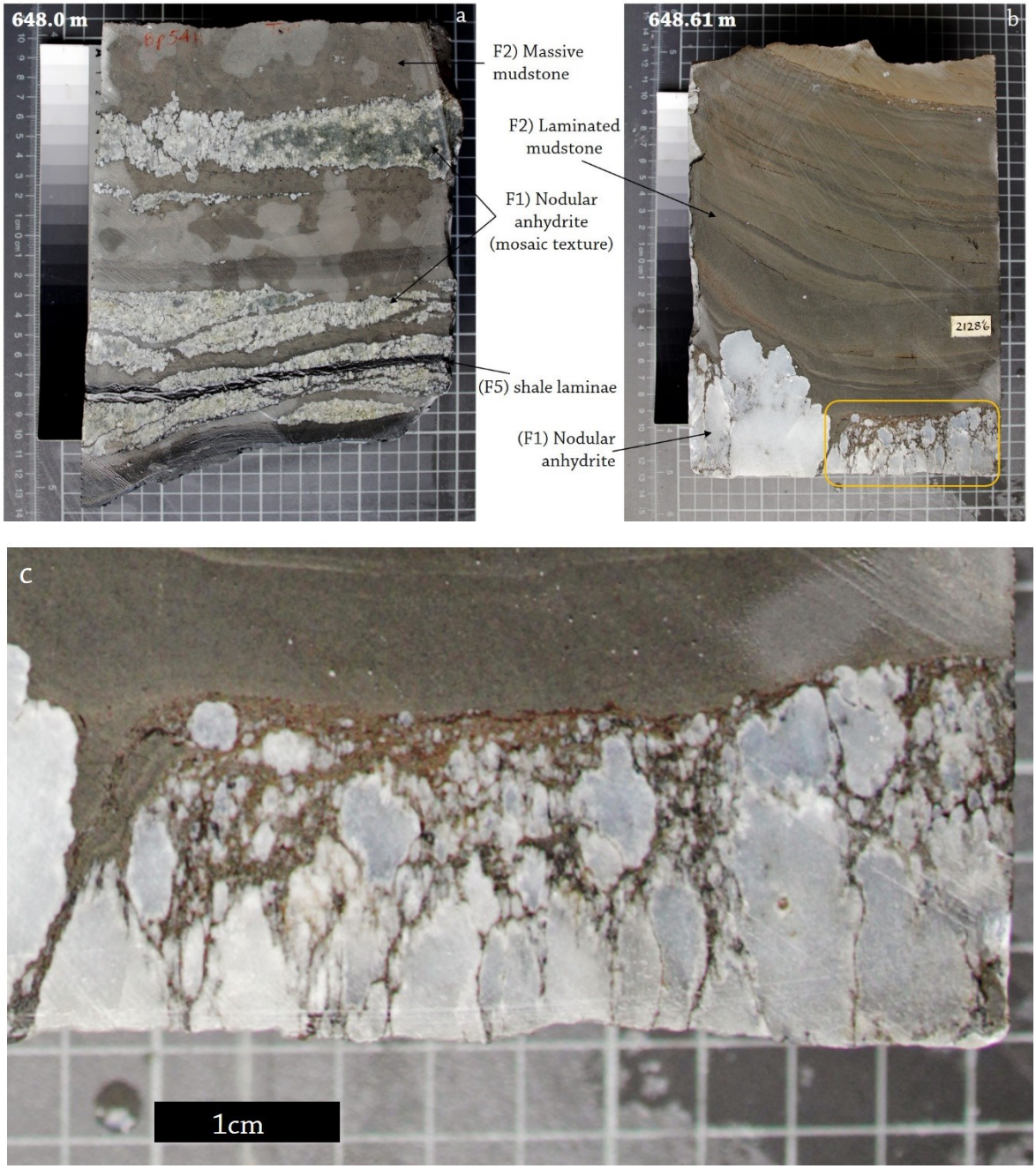


Figure 3.31: section of core of from Warlingham well showing intercalations of nodular anhydrite of different textures and mudstone (a and b); c) nodular anhydrite disposed in vertically elongate individuals (palisade texture).

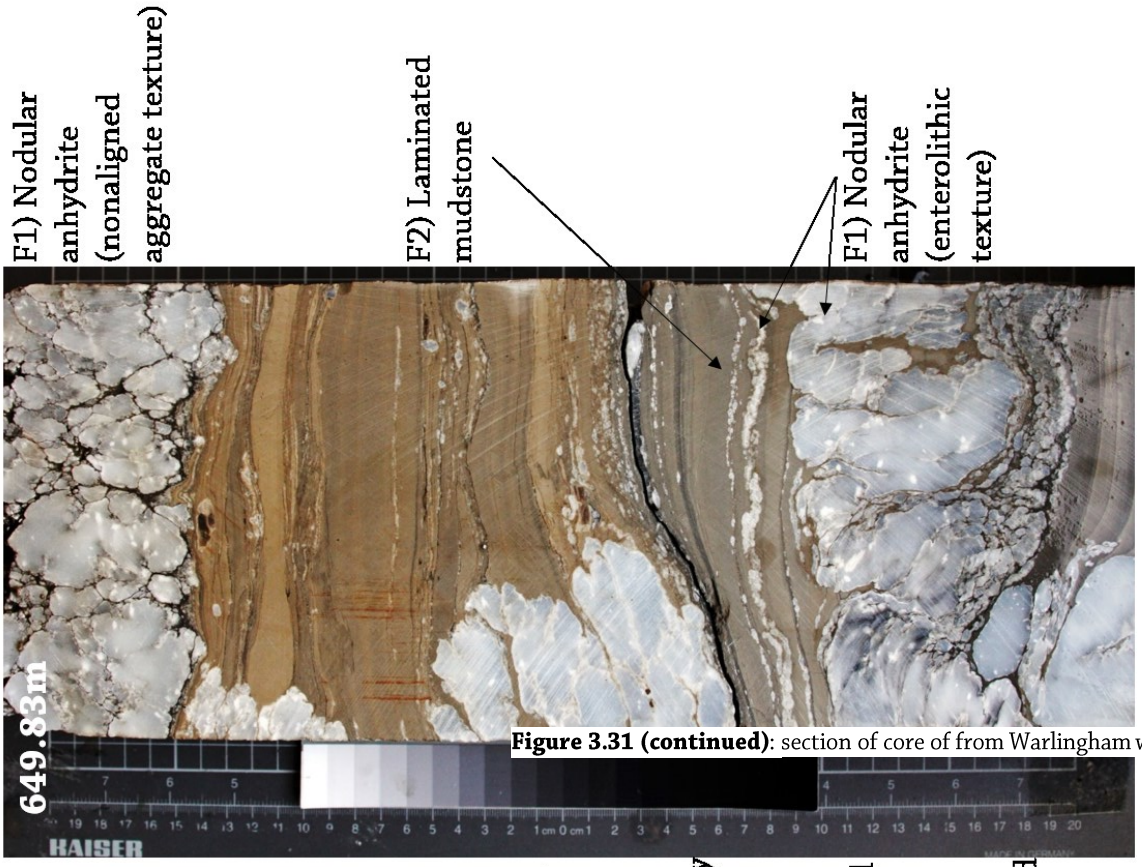
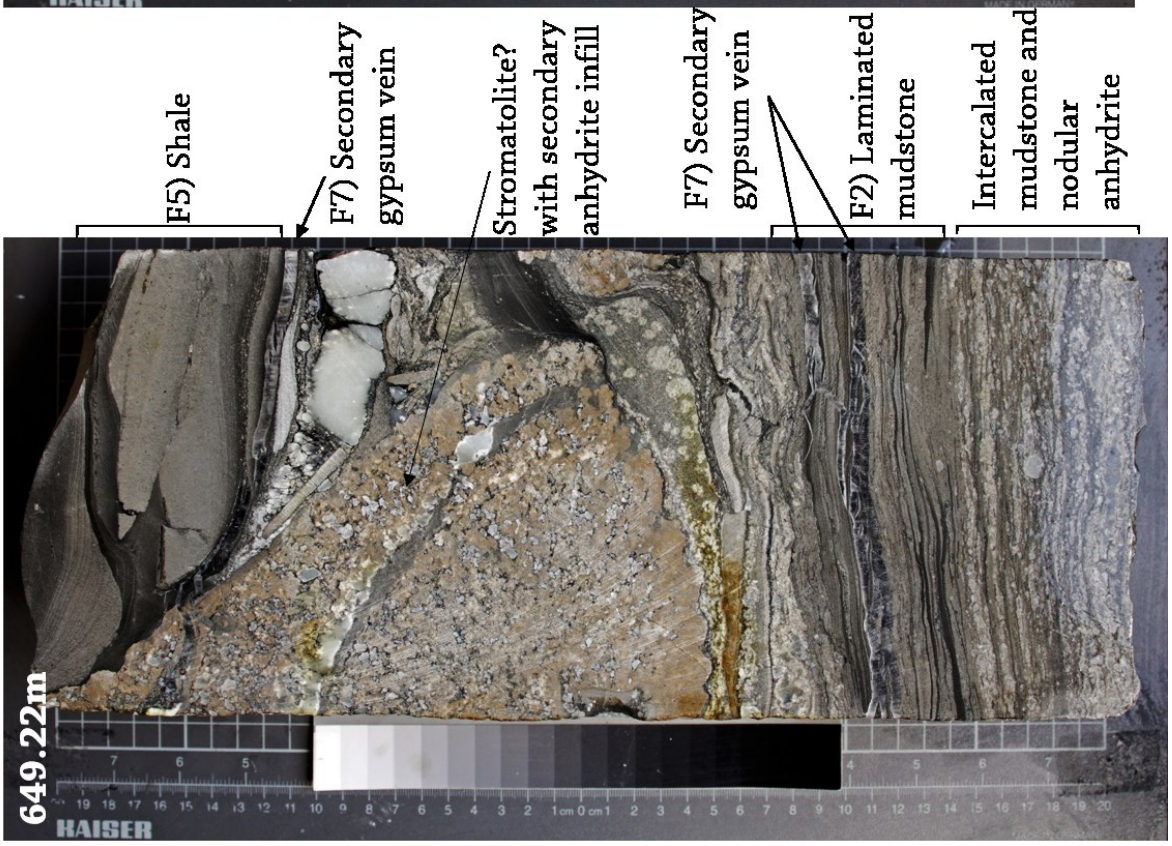


Figure 3.31 (continued): section of core of from Warlingham well showing a multitude o



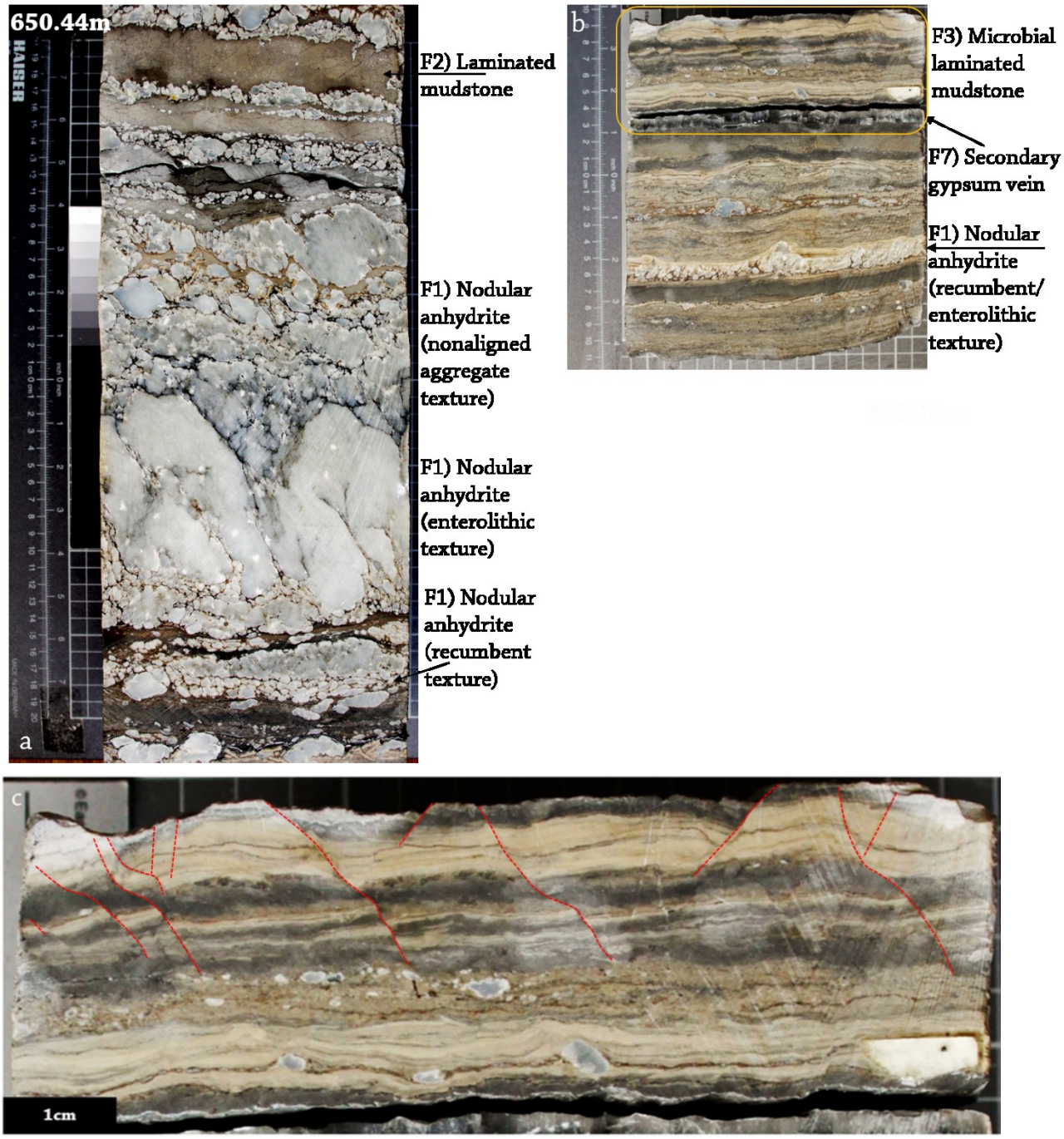


Figure 3.31 (continued): section of core of from Warlingham well showing a sequence of nodular anhydrite with different textures (a) and laminated microbial mudstone (b). c) Shows in detail the shear fractures that affect the microbial laminated mudstone section. Notice that these fractures do not propagate below a certain sedimentary horizon, suggesting that there is a mechanical property of the rock that impedes propagation.

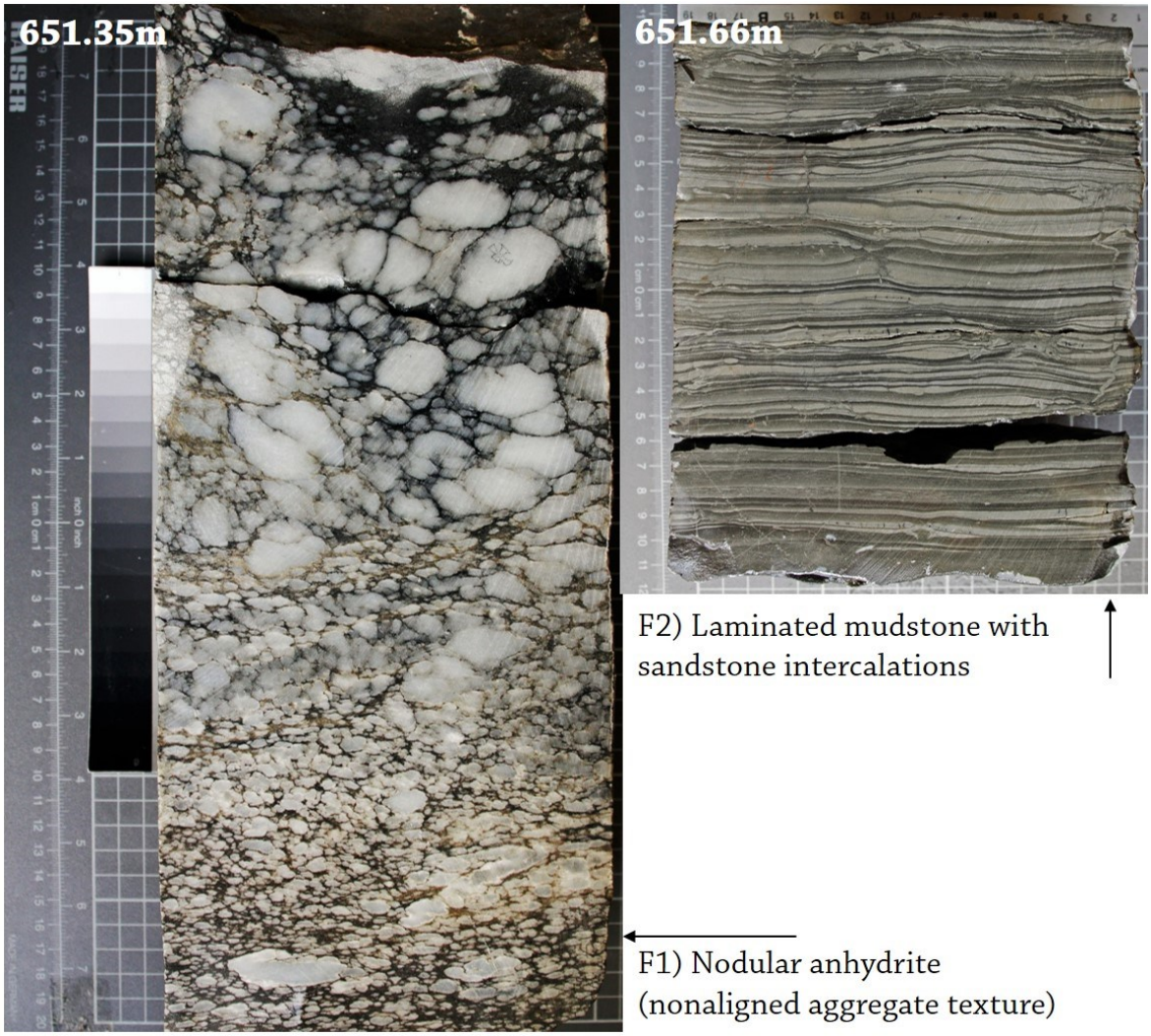


Figure 3.31 (continued): section of core of from Warlingham well showing a sequence of nodular anhydrite (aggregate texture) and a laminated mudstone with sandstone intercalations.

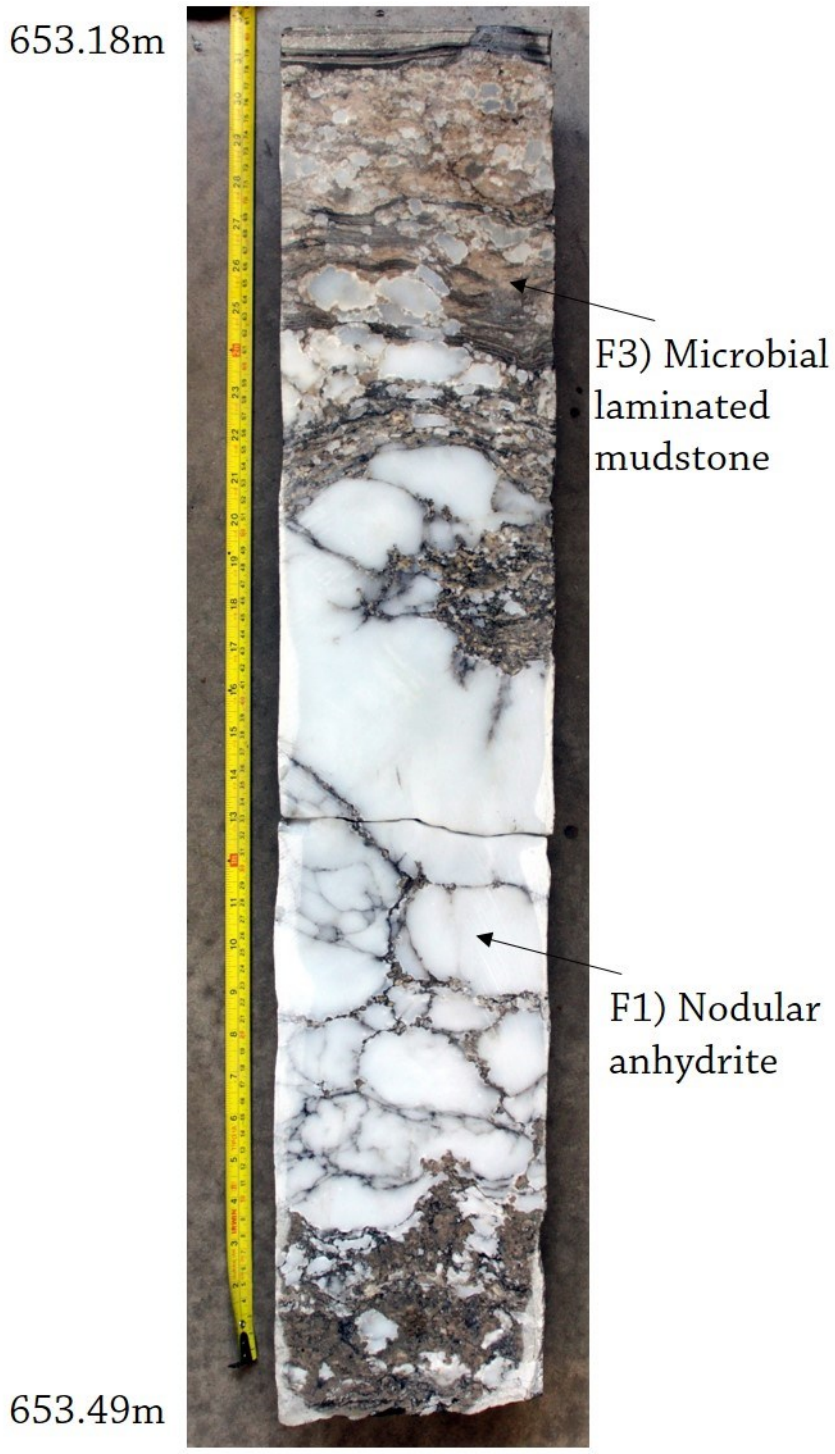


Figure 3.31 (continued): section of core of from Warlingham well showing nodular anhydrite and microbial mudstone.

3.5 Outcrop studies in Gloucestershire & Somerset

3.5.1 Introduction

Two field work areas, both located in the region of the Bristol Channel have been studied. In order to place the areas into a structural and tectonic context, a short description of the geological evolution of this region is presented below.

The region where the field work areas are located (Figure 3.32) has been subjected to three major tectonic events, namely the Hercynian Orogeny which resulted in E-W trending folding and thrusting, the Permo-Triassic rifting that formed the E-W trending Bristol Channel Basin and the Alpine inversion. A N-S cross section through the Bristol Channel (Figure 3.33) shows how the impact of these three tectonic events in the region and the relation between structures and stratigraphic sequences.

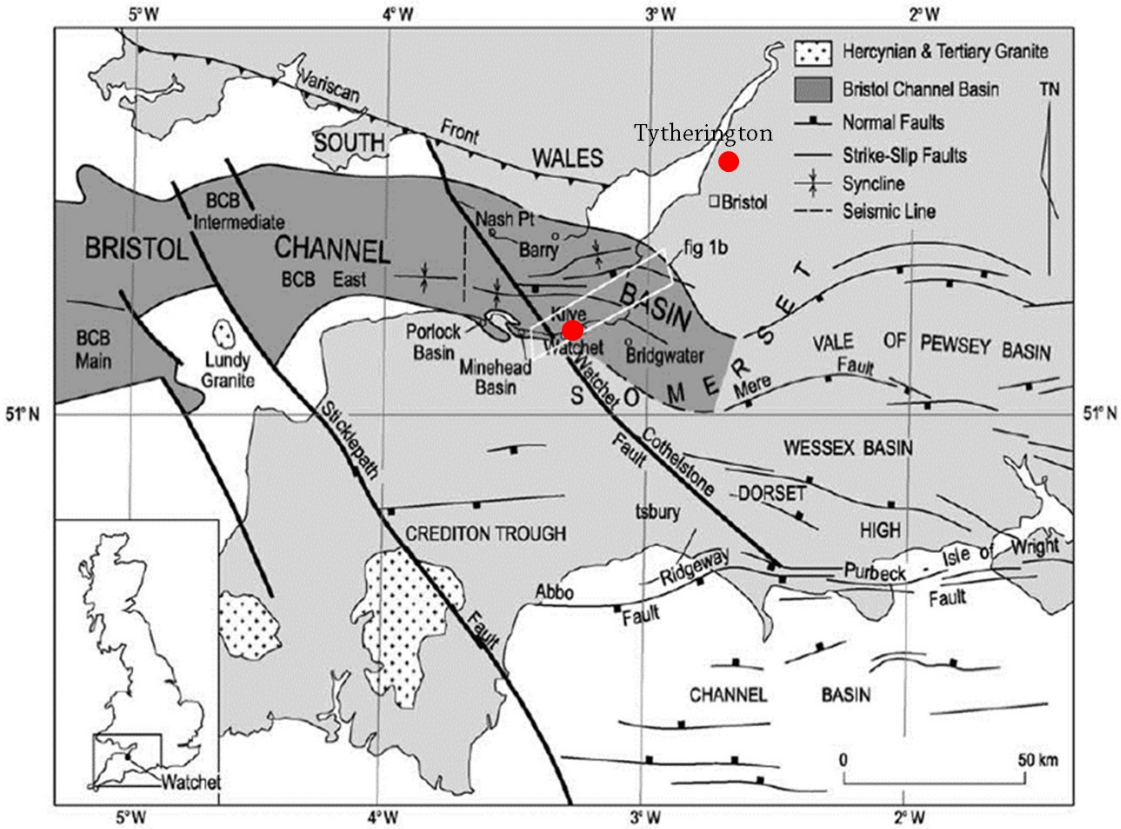


Figure 3. 32: Location and structural map showing the Bristol Channel Basin in relation to surrounding basins in southwest England (source: Glen, Hancock, & Whittaker, 2005). The red spots show the locations where field work was conducted: Wachet, Lilstock and Tytherington Quarry.

The Hercynian Orogeny, responsible for the formation of Pangea, is represented in the region by a fold thrust-belt with approximately E-W trending folds verging towards the north and southward dipping thrusts, both created by a major compression linked to the collision of Gondwanaland in the south with Laurasia in the north. The Carboniferous rocks of Tytherington Quarry present a series of thrusts characteristic of this tectonic phase (See Section 3.5.3 Tytherington Quarry Field Work).

Unconformably overlying the Carboniferous rocks is the Permo-Triassic sequence, which is relatively undeformed. This sequence was deposited in approximately E-W trending rift basin which represents the tectonic break-up of the Pangea Supercontinent. The Bristol Channel and the English Channel Basins were initiated at this time. The rocks studied in Watchet and Lilstock were deposited during the formation of the Bristol Channel Basin. This Basin is a relatively small WNW-ESE trending structure, 155 Km long (E-W) and 30 Km wide (N-S) bordered to the north and south by Variscan structures (Nemcok, Gayer, & Miliorizos, 1995).

The basins continued to open until the Late Cretaceous when the collision of the African and European plates arrested this opening and generated the Alpine Orogeny. A change in the tectonic regime occurred from a N-S extension to a N-S compression, reversing the normal faults sense of motion from down-dip to up-dip. This Alpine deformation was accommodated by reverse-reactivation of normal faults, new thrust faults, new strike-slip faults, and by hanging wall buttress anticline (the buttress effect is defined by Beck et al. (1993) as resistance to displacement arising from a space problem) (Engelder & Peacock, 2001).

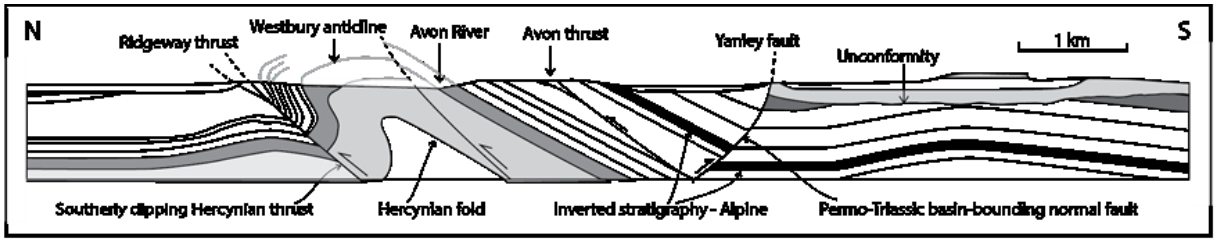


Figure 3. 33: N-S cross section through the Bristol Channel area showing the impact of the three major tectonic events that have affect the region: the Hercynian folding and thrusting; the Permo-Triassic rifting that generated the normal faults and allowed the deposition of the Permo-Triassic sequence; and the Alpine inversion. A major angular unconformity separates the folded and thrust Carboniferous rocks from the overlying relatively flat-lying Permo-Triassic rocks.

3.5.2 Rationale

The mechanical principles involved in the propagation/arresting of fractures through different layers and interfaces is of general nature and not specifically linked to layered evaporite successions, it therefore felt appropriate in view of the lack of outcrops of evaporite successions to study other outcrops. The succession that was selected for the study was:

i) A Carboniferous succession of limestone and shales at Tytherington

ii) the Liassic limestones and shales alternations at Lilstock

iii) the Mercian Mudstone (Triassic) with intercalated evaporite horizons

Data obtained from the study of these outcrops was used to complement the information obtained from the underground studies on the effects of high fluid pressures on low permeability rocks and on the features that tend to inhibit fracture propagation.

Before presenting the results of this work, it is important to make a distinction between vertical and horizontal fracture analysis. When executing fracture analysis, the structural geologist is usually interested in understanding how the fracture network developed in a rock and what it can tell us about the evolution of the regional stress regimes through geological time. i.e. how the rock mass deformed in the past. The analysis attempts to answer questions such as:

1. What is the magnitude of the stress regime that generated the fractures (extensional or shear)?
2. What was the orientation of the stress field at the time the fractures were generated?
3. What is the regularity of the fracture sets formed?
4. What is the 3D geometry and therefore the properties of the fracture network formed in the rock mass as a result of the superimposition of several fracture sets?

The key to fracture analysis is the determination of the relative chronology of the different fracture sets making up the fracture network that currently exists in the rock mass. This is achieved by looking at fracture interaction. The essential feature is that later fractures often curve towards and abut against earlier fractures. In bedded successions fracture analysis is normally carried out by observing the bedding plane. However, one of the key questions being addressed by the current research is what mechanical properties control fracture propagation through layered evaporites. Thus we are more interested in the propagation of fractures vertically through sub-horizontal successions and the fracture analysis carried out is on a vertical plane, i.e. perpendicularly to the bedding plane. This 90º rotation of the plane of analysis represents a different approach to fracture analysis and one better adapted to the objective of the study.

3.5.3 Tytherington Quarry Field Work

Tytherington quarry is a Geological Site of Special Scientific Interest located between the town of Thornbury and the village of Tytherington, South Gloucestershire, approximately 20 km NE of Bristol (Figure 3.34). The activity in the quarry – aggregates exploitation – occurs in the NE flank of a large syncline formed in Carboniferous limestone beds which are dipping 30° towards the SE. These relatively massive limestone beds have thicknesses varying between 0.5 and 3m and in some cases are separated by centimetre thick clay/marl beds (Figure 3.35).



Figure 3. 34: geographical location and aerial photo of the studied section at Tytherington Quarry.



Figure 3. 35: Exposure of the 30° dipping limestone occurring ath Tytherington Quarry. Photograph taken looking towards NE.

As previously noted (see 3.5.1), the structures present in the quarry are small scale examples of the effect of Hercynian deformation which occurred in the Late Carboniferous. During this orogeny the stress field was such that the minimum principal compression (σ_3) was vertical (maximum principal compression – σ_1 - was horizontal) leading to the formation of a series of southerly dipping thrusts and northerly verging folds. The thrusts provide a very good insight into the slippage processes that occurs between rock layers and ultimately into the interaction between fractures and bedding planes as it will be explained in this section.

During the collision of tectonic plates such as occurred during the Hercynian orogeny, fold-thrust belts form adjacent to the main collision zone. As the name implies the zone is characterized by both ductile and brittle deformation. The thrusts which ideally should dip at approximately 30° often exploit the sub-horizontal bedding planes, which they follow, only occasionally cutting across the stratigraphy in a series of ramps. The profile of the thrust therefore has a *staircase* geometry (Figure 3.36) comprising flats (where the thrust is parallel to bedding) and ramps (when it cuts the bedding). The thrusts seek out the bedding-parallel zones of weakness within a sedimentary sequence such as those formed by layers of clay, marls or salt. When, due to the mechanical properties of the layers, the thrust is no longer able to propagate along the bedding, it will cut through it to a higher stratigraphic level – usually

at an angle close to 30° - until it reaches another level where it is able to form another *decollement*, i.e. detachement horizon along the bedding.

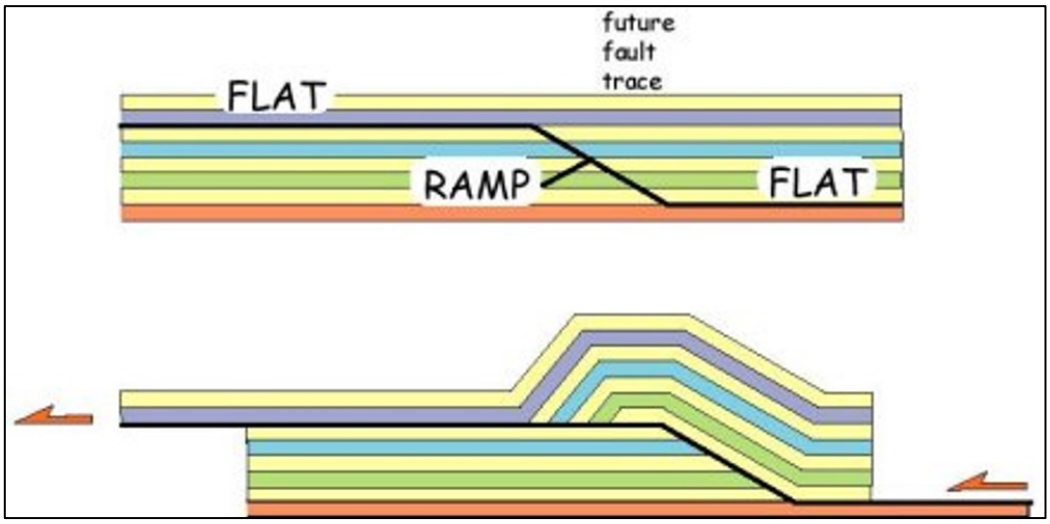


Figure 3. 36: stages of evolution of a thrust. See text for details.

At Tytherrington it is observed that the mechanical properties of the bedding planes that separate the limestone beds are diverse. In general two different types of bedding planes are observed: those where the limestone beds are directly in contact with each other, and those where a thin clay horizon is present (Figure 3.37).

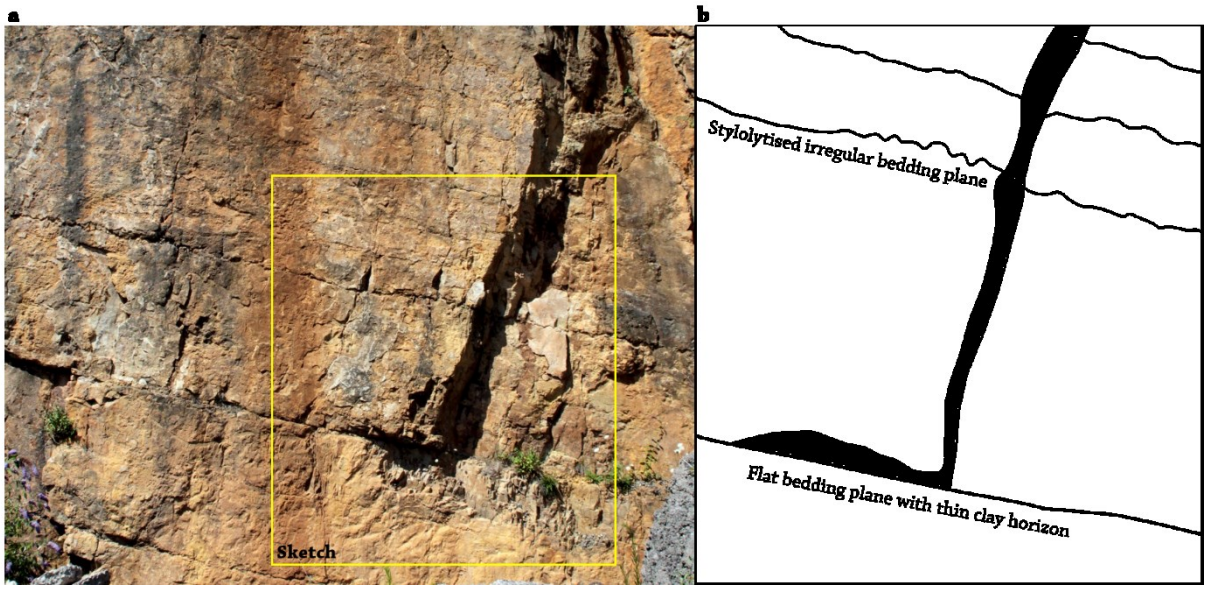


Figure 3. 37: a) A 2m thick limestone bed bounded by two different types of bedding planes, an upper irregular stylolite plane and a lower, smooth plane defined by a thin layer of clay b) detail sketch of a)

In the first case, when two adjacent beds are in direct contact with each other, pressure solution occurs along the bedding plane in response to the vertical loading that occurs during burial and diagenesis, leading to the formation of stylolytes, serrated bedding surfaces within a rock mass (Figure 3.37 and 3.38). This process causes the interlocking of the two adjacent beds, inhibits slippage and contributes to the propagation of the thrusts obliquely across the stratigraphy, i.e. the formation of ramps.
When a thin layer of clay is present (Figure 3.37) between two adjacent limestone beds, stylolytisation is prevented and the bed remains flat. The presence of the clay also facilitates bedding-plane slip therefore contributing to the propagation of the thrusts along the bedding plane resulting in the formation of: *decollements* or flats.



Figure 3. 38: two different views of stylolite surfaces that have formed by pressure solution along a bedding plane in limestones of Thyterrington Quarry as a result of the overburden load. a) cross section through a stylolyte. b) Exposed bedding plane.

As noted earlier, thrusts form when the least principal compression is vertical and the maximum principal compressive stress is horizontal (Figure 3.39c). However, as deformation progresses and the thrusts become stacked on top of each other, the vertical stress increases and may eventually become σ_2 ($\sigma_1 > \sigma_2 > \sigma_3$). At this point the stress regime changes from thrusting to strike-slip (Figure 3.39 c to b). Evidence of this change from a thrust to a strike-slip (wrench) regime having occurred in the late Hercynian is present in Tytherrington Quarry in the form of large, closely spaced vertical fractures that cut through the complete sedimentary sequence including the previously formed thrusts (Figure 3.40 and 3.41).



Figure 3. 39: The three stress configurations linked to the three major types of shear fractures (faults), normal (σ1 vertical), wrench or strike-slip (σ2 vertical) and thrusts (σ3 vertical). The orientations of the extensional fractures that would form under these stress configurations are indicated by dashed lines (Cosgrove & Hudson, 2016)

From the theory of brittle failure, it is known that in a particular stress regime, both extensional and shear fractures can be generated – depending on the magnitude of the differential stresses - and that extensional fractures form normal to the least principle compression (Figure 3.39). At Tytherington both the extensional fractures and the associated strike-slip faults occur (Figure 3.39b and 3.42).

Apart from the features associated with brittle failure, the rocks in and around Tytherington also contains ductile structures such as buckle folds (the Westbury anticline is an example of such folds – See Figure 3.33). When, as in a fold and thrust belt, the folds and thrusts form in response to the same stress field the folds axes are parallel to the strike of the thrusts (Figure 3.43). The local stress variations around a fold can give rise to fracturing as described by Ramsay, (1967) and Stearns (1964). A profile section taken at right angles to the fold hinge shows that there are various fractures found in association with buckle folds (Figure 3.44).



Figure 3. 40: Overall view of the quarry cliff face towards the NE (top) and SE (bottom). The closely spaced vertical fractures linked to the formation of wrench fault are visible. The Note the 'zig-zag' profile of the quarry face is due to the occurrence of the conjugate set of wrench faults, see Figure 3.43.

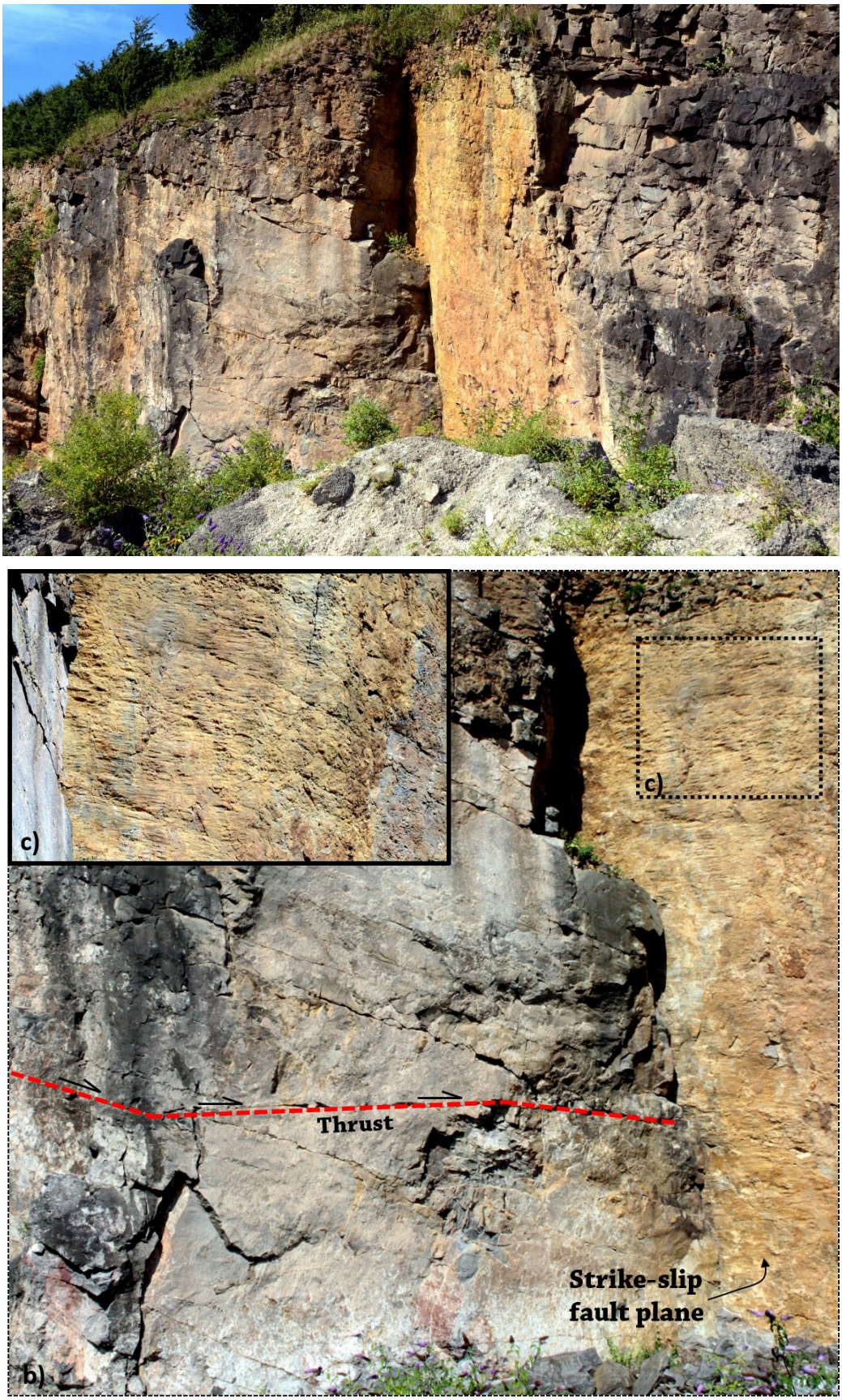


Figure 3. 41: example of a thrust plane being cut by a through-going strike-slip (wrench) fault in the limestones of Thyterrington Quarry. a) general view b) detail view of the the thrust and strike-slip faults. The faults are vertical, through-going fractures and on some (as in this example), slickenslides (c) provide evidence of sub-horizontal movement.



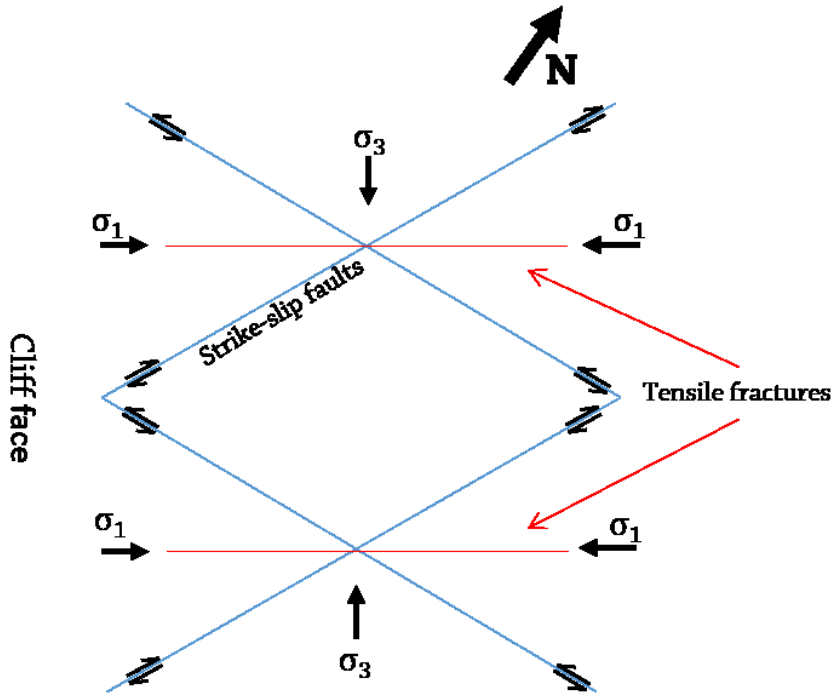


Figure 3.42: photograph of the cliff face where a conjugate pair of strike slip faults planes showing the vertical tensile fractures that intersect them (red arrows) can be seen. Below a sketch shows the position of the most compressive principle stress and how the tensile fractures are positioned relative these and to the strike-slip faults. Note the intense stylolitisation that has occurred along the bedding planes.

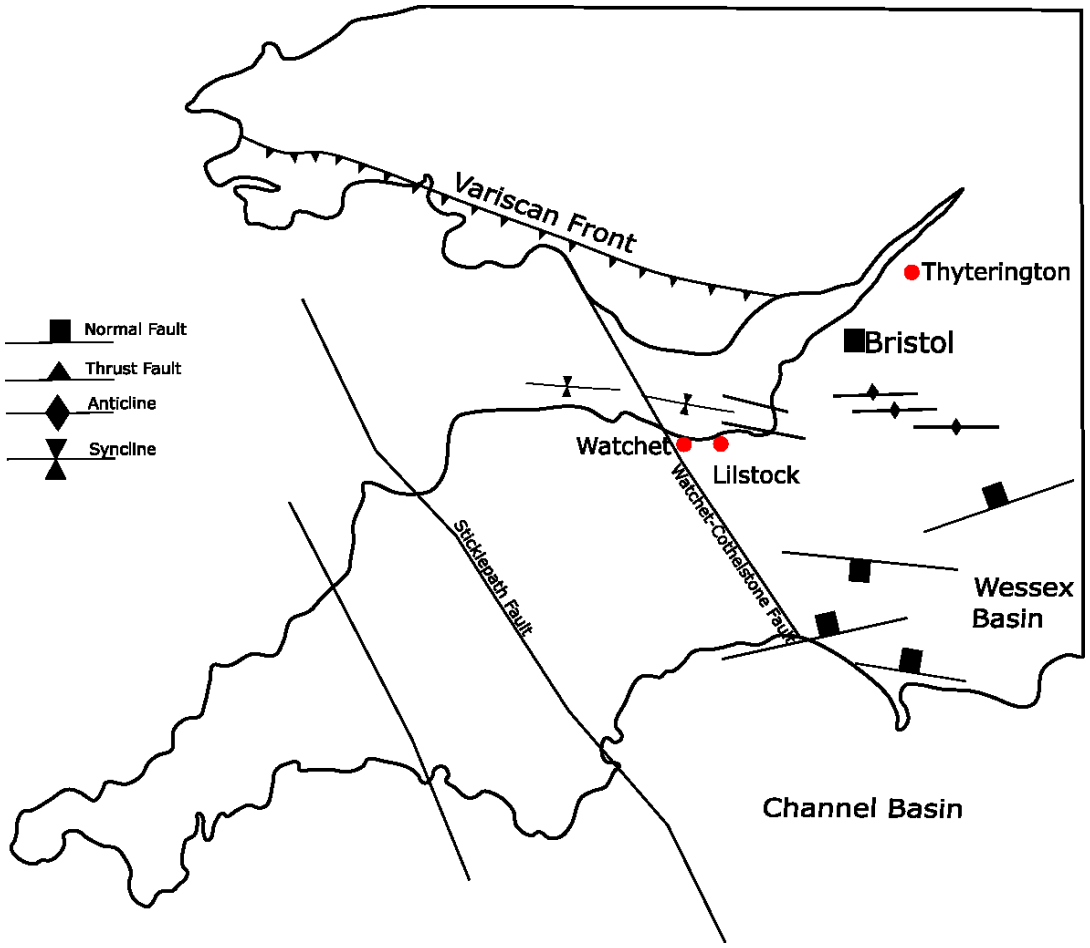


Figure 3. 43: structural map of the Bristol channel area showing the approximately E-W trending folds and thrusts associated with the fold-thrust during the early stages of the Hercynian orogeny, cut by the dextral and sinistral wrench faults associated with the late stages. After Anderson, (1951) and Glen et. al. (2005).

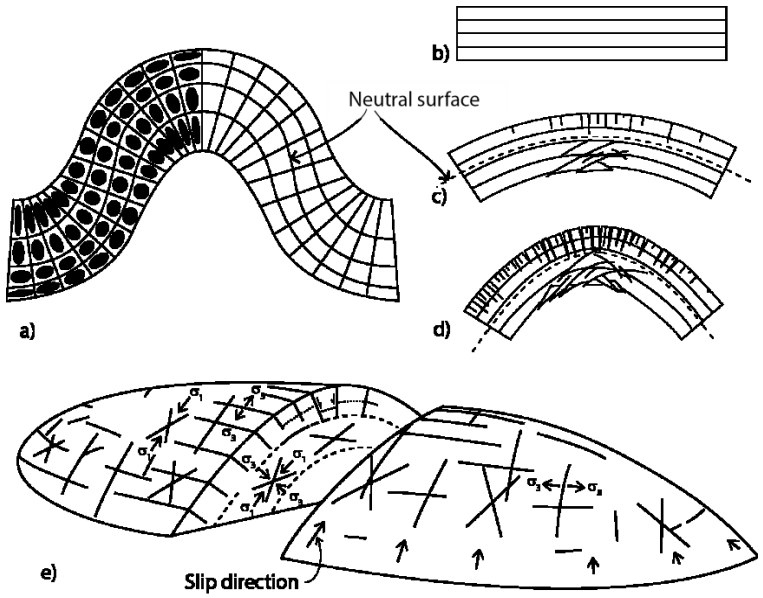


Figure 3. 44: The strain distribution in a buckled homogeneous isotropic layer. Stretching occurs in the hinge region above the neutral surface and compression below. The development of the fractures that might result from this local deformation is shown in b), c) and d). After Ramsay, (1967). e) The different sets of fractures that can be generated in a pericline as it amplifies. After Stearns 1964.

The structures at Thyterington Quarry can be summarized as follows (in chronological order) :

1. Thrusts
2. Buckle folds
3. Fold related extensional fractures
4. Strike-slip faults
5. Strike-slip related extensional fractures

All these structures occur in Carboniferous rocks and are Hercynian age. Structures related to the Alpine are not seen in the quarry. This event occurred with an approximate compression direction of NNW – SSE which is approximately co-axial with the Hercynian compression. Therefore the effect of this later collision is likely to reactivate the Hercynian fractures rather than generate new ones.

After establishing the origin and the chronological order of the fractures which are present at the study site, a study on the way these fractures behave when they meet an interface (a bedding plane or an earlier fracture) was made. Two situations were observed:

a) A fracture meets a stratigraphic interface and is able to propagate across it – through-going fracture.
b) A fracture meets an interface and it does not propagate through that interface, becoming strata-bound.

We observed that whether a fracture propagates across an interface or becomes strata bound is closely related to the type of contact existing between layers. In general if limestone beds are directly in contact with each other (and are consequently stylolitised) the vertical fractures are able to cross the interface. In contrast, if there is a thin clay horizon between the limestone layers the fractures are arrested at the interface. Figures 3.45 to 3.48 illustrate these observations.
It is proposed that the propagation through an interface which is stylolitised is related to the fact that the interface is locked by the serrated stylolite surface. This inhibits slippage between beds preventing the dissipation of the fracture tip stresses, therefore allowing the fracture to cut-cross the interface. When the limestone beds are separated by a thin clay layer, slippage can occur. The tensile stress at the fracture tip is dissipated and the fracture is arrested at the interface. This process will be further discussed in Section 4.6.

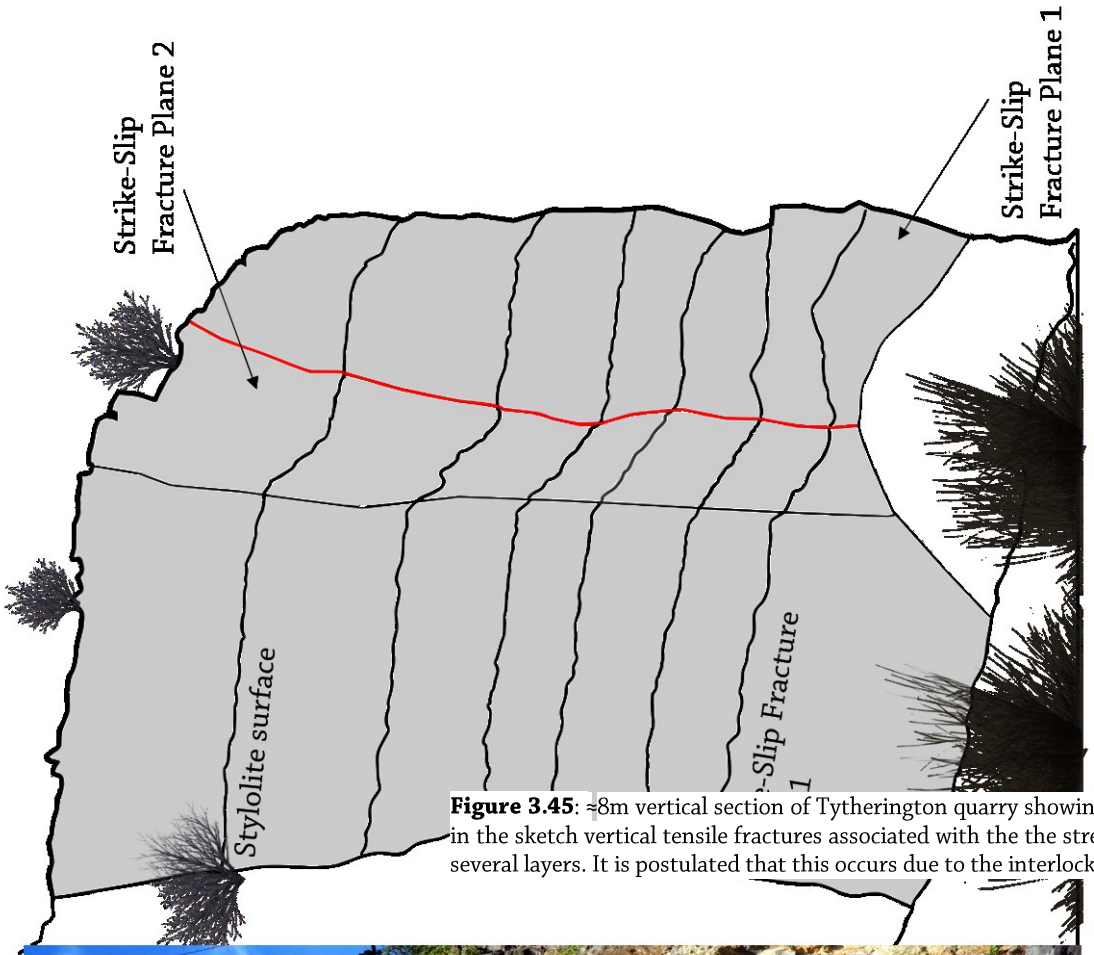


Figure 3.45: ≈8m vertical section of Tytherington quarry showing 7 limestone layers where the
in the sketch vertical tensile fractures associated with the the stress regime that gave rise to str
several layers. It is postulated that this occurs due to the interlocking of the limestone layers cau



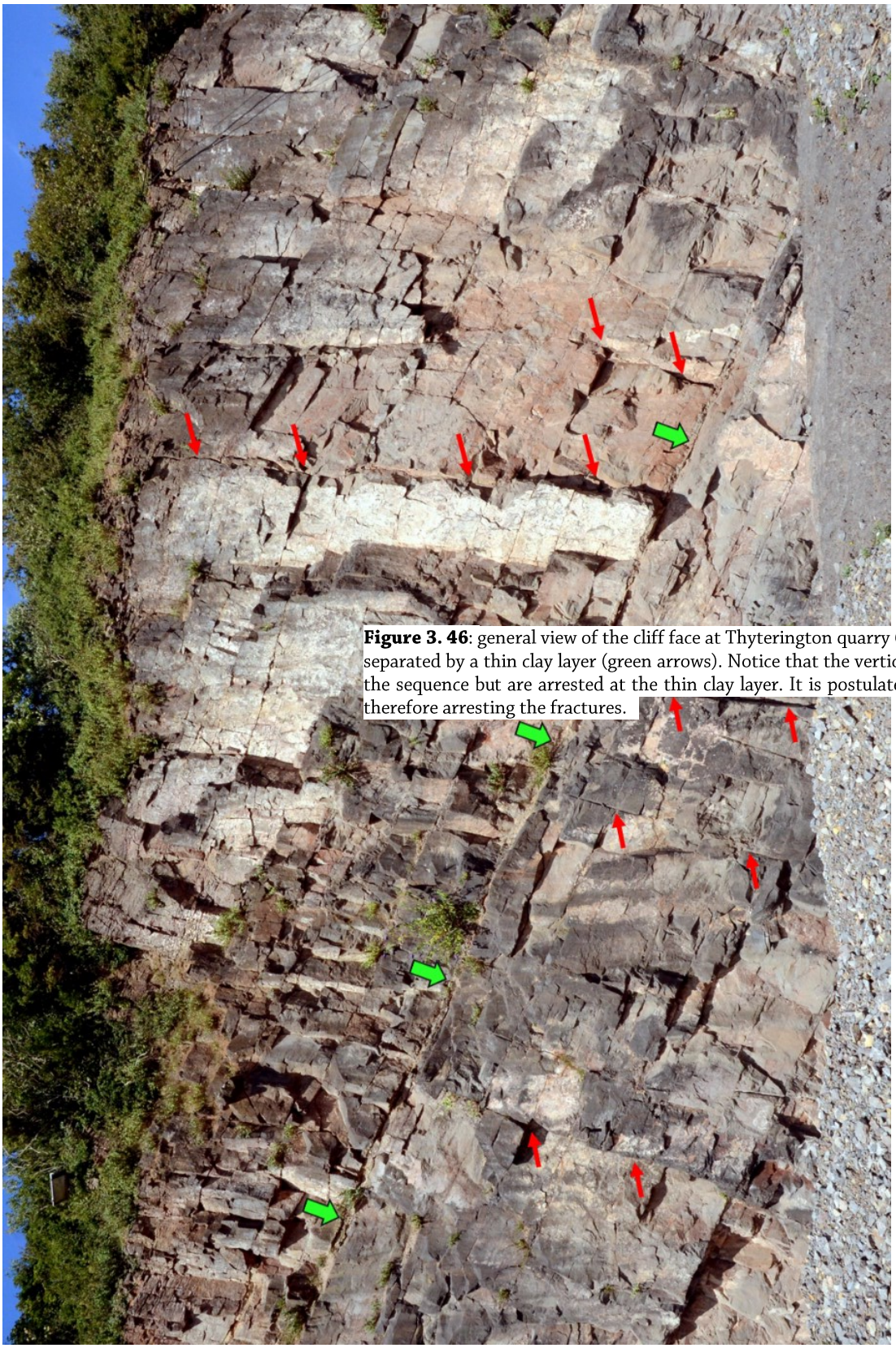


Figure 3. 46: general view of the cliff face at Thyterington quarry (≈16m tall) showing two thick
separated by a thin clay layer (green arrows). Notice that the vertical fractures (red arrows) of b
the sequence but are arrested at the thin clay layer. It is postulated that slippage occurs at thi
therefore arresting the fractures.

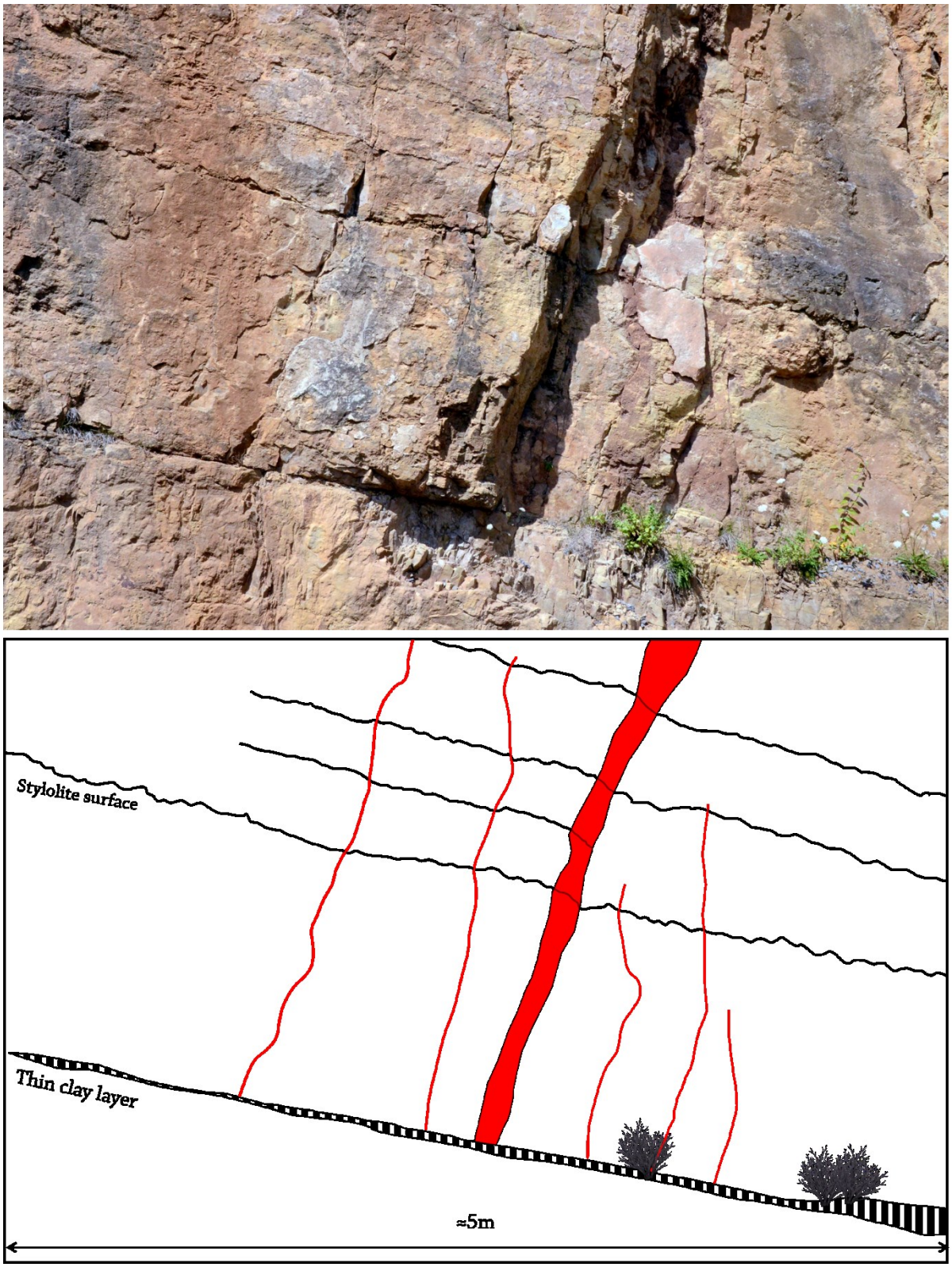


Figure 3. 47: photograph and sketch of a small section of the cliff face at Thyterington quarry showing how bedding-normal (red lines in the sketch) are able to cut through the stylolitized interfaces between limestone layers but are arrested at a very thin clay layer.

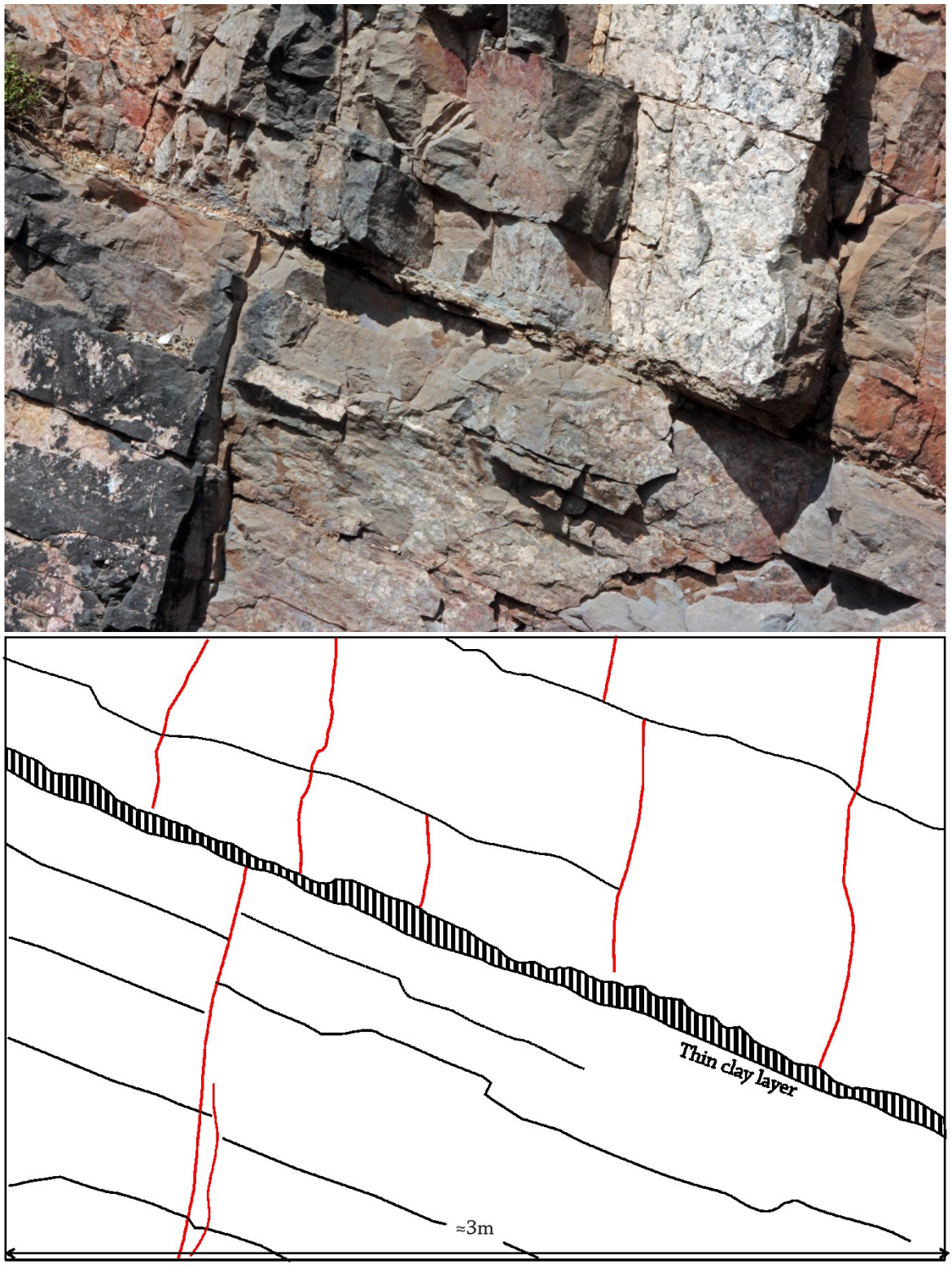


Figure 3. 48: photograph and sketch of a small section of the cliff face at Tytherington quarry showing how vertical fractures (layer-normal) (red lines in the sketch) are able to cut across the bedding planes between limestone layers in contact with each other but are arrested when they are separated by a very thin clay layer.

3.5.4 Field work in Lilstock Beach

Lilstock Beach is located on the Southern margin of the Bristol Channel Basin, approximately 50 Km SW of Bristol. Here, the Blue Lias Formation - Rhaetian (208.5 to 201.3 Ma) to Sinemurian (199.3 - 190.8 Ma) - outcrops with more than 50 limestone beds between 5 and 40 cm thick interlayered with shales of various thicknesses (Engelder & Peacock, 2001 after Whittaker and Green, 1983) (Figure 3.49.



and general view of the outcrops in Lilstock Beach, S

Structurally, Lilstock Beach features a set of four north-dipping, high-angle dip-slip faults (normal faults) that are offset by later NW-SE strike-slip faults. There is also large buttress fold, the Lilstock buttress anticline, with a gently dipping north limb and relatively steep south-dipping beds (Figure 3.50). This anticline originated as a reverse-drag fold during the Mesozoic normal faulting and was amplified during reverse-dip-slip movement on one of the normal faults present in the area (Engelder & Peacock, 2001).

Peacock & Sanderson (1999) have shown that the stress and deformation history of the Somerset coast varies over very short distances along strike because of the influence of regional-scale structures, specifically faults. The authors consider that at Lilstock the structural history is as follows:

1. 150°oriented extension which produced 060° striking joints, veins and possibly faults;
2. approximate north-south extension producing approximate 095° striking normal faults and veins;
3. east-west contraction which produced sinistral shear on some of the 095° striking normal faults;
4. dextral reactivation of some of the 095° striking normal faults;
5. north-south contraction produced reverse-reactivation of normal faults and the development of thrusts;
6. joints postdate the faults generated in 5.

Engelder & Peacock (2001) have identified at Lilstock Beach, a number of joint sets in the limestones of the Jurassic Blue Lias:

- J1(33°±310°),
- J2 (310°±295°),
- J3 (295°±285°),
- J4 (285°±275°),
- J5 (275°±265°),
- J6 (<265°).

During the field work carried out by the author these were observed in the outcrops of Lilstock beach. However the main focus was not on establishing the cross-cut relationship between them or to identify the deformation phases to which they belong, but to use them to help understand the mechanisms of fracture propagation and arrest in layered rocks such as the limestone and shale intercalations found at Lilstock. Figures 3.51 to 3.57 illustrate some of the observations made which are pertinent to this task. The following observations were made:

- Vertical tensile fractures arresting at the interface between the limestone and the adjacent shale (Figure 3.51 and Figure 3.56).
- Vertical tensile fractures propagating through the adjacent shale layer and suffering a trajectory change – they become oblique (Figure 3.52, 3.53 and 3.54).
- Fracture strike mismatch between limestone layers separated by a shale layer (Figure 3.56). Note that there is also different fracture families in each of the limestone layers.

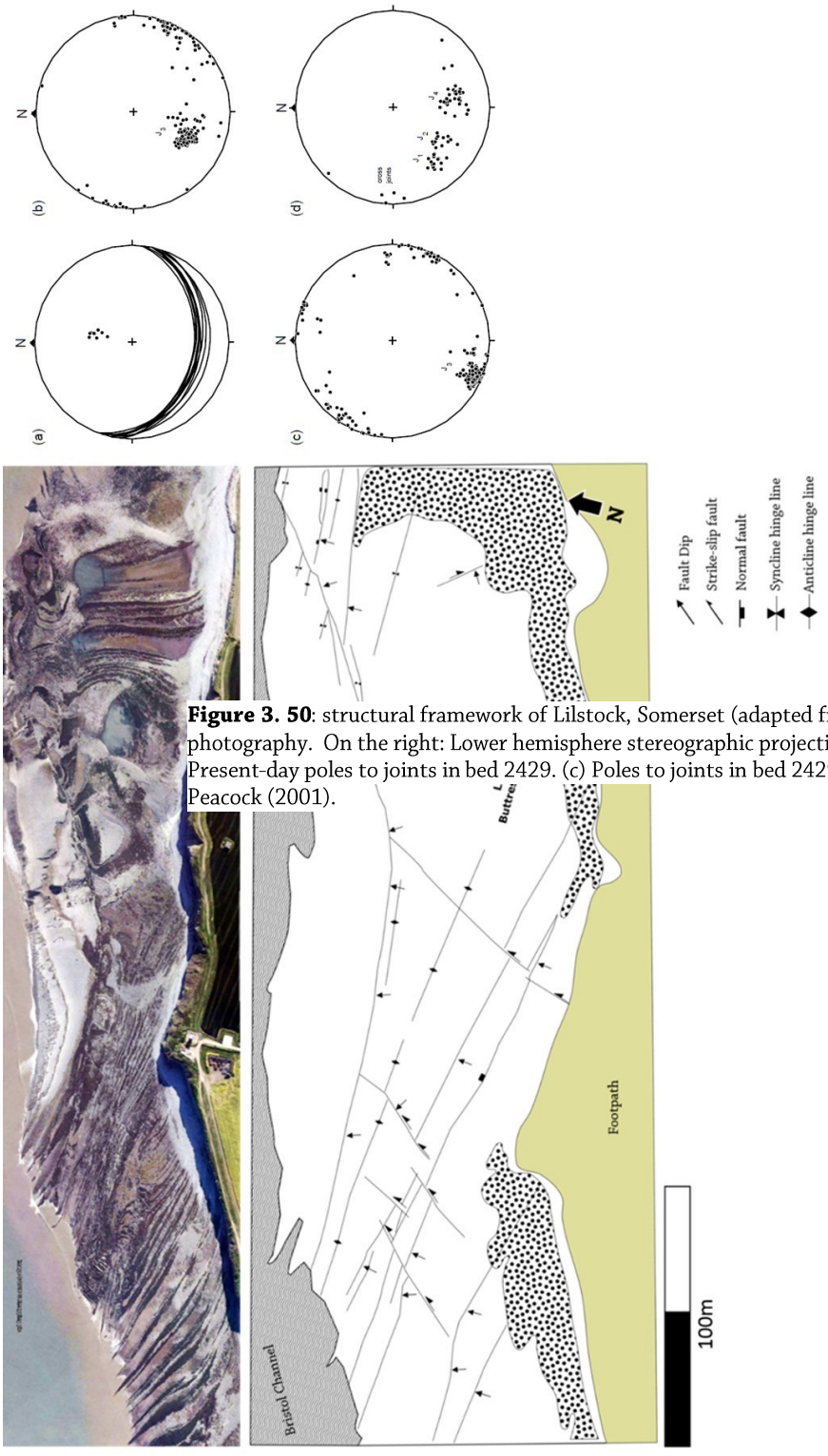
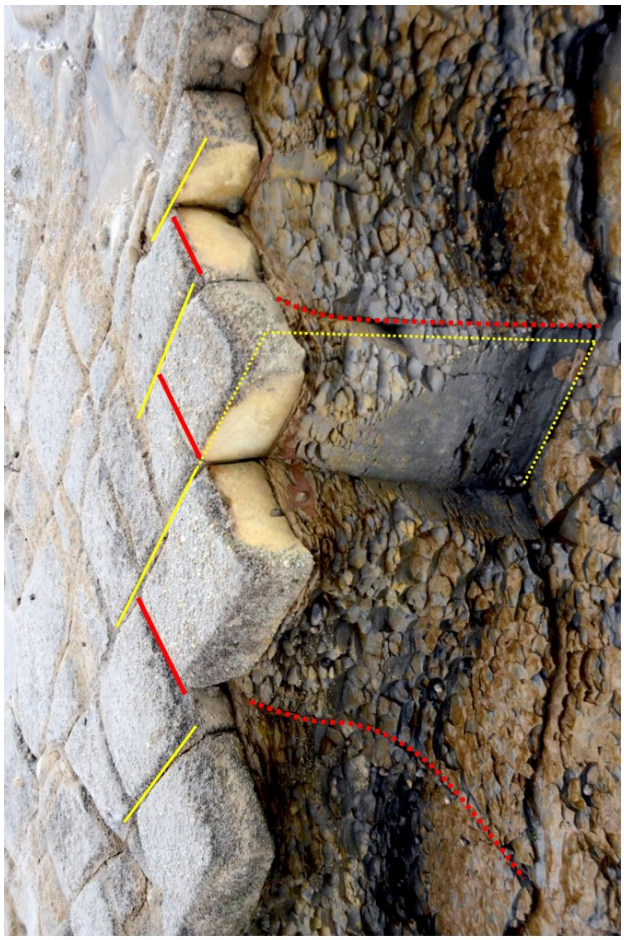


Figure 3. 50: structural framework of Lilstock, Somerset (adapted from Engelder & Peacock (2001) after
photography. On the right: Lower hemisphere stereographic projections for beds and joints in fault block 1
Present-day poles to joints in bed 2429. (c) Poles to joints in bed 2429 with bed dip removed. (d) Present-d
Peacock (2001).



Figure 3. 50: Vertical tensile fractures being arrested at the interface between a limestone (where they have formed) and a shale.



ɔse which are highlighted in yellow an
es" seem to be arrested at the interfac
ıe shale layer.with an orientation cha
cally.





Figure 3. 52: a) view of the cliff face at Lilstock Beach. The yellow box highlights the locations of b) and c) which shows from different angles two independent tensile fractures that have formed in the competent limestone layers being linked by an oblique fracture – shear fracture? - that formed in the shale; d) sketch of b) illustrating how the tensile fractures opened in the limestone layers (off plane perpendicularly to the fracture wall) and the direction of opening of the fracture in the shale.



Figure 3. 53: The vertical fractures aligned with the photo and highlighted in red are able to propagate into the shale horizon immediately overlying the limestone. However the fractures of the topmost limestone layer are all arrested at the interface between the limestone and the shale.

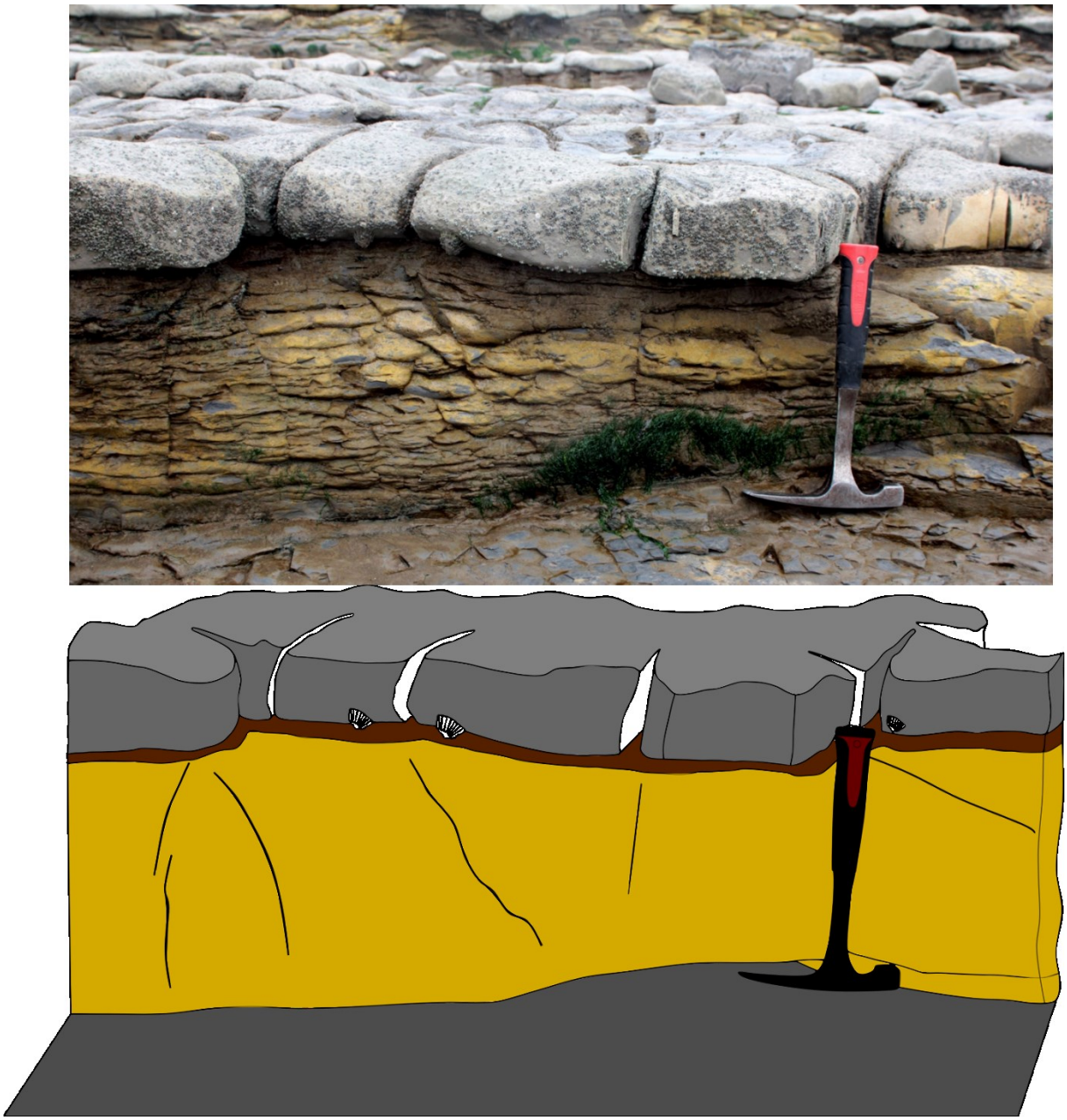


Figure 3. 54: A limestone-shale interface at Lilstock Beach. Notice that between the topmost limestone layer and the lower yellow shale layer, there is a thin mudstone/shale layer which hinders the propagation of the tensile fractures that formed in that limestone layer into the underlying shale layer. However there are several fractures which have formed in the "yellow" layer and that do not seem to be connected to the tensile fracture of the top limestone layer.



Figure 3. 55: in this picture three fracture families are identified. Those highlighted in red are the earliest fractures to have formed. They have propagated across the limestone layers "a" and "b" which are separated by a thin shale layer not visible in the photograph. The fractures highlighted in yellow in "Layer a" have an orientation very similar to the orientation of the "red" fractures. However they do not have correspondence on "Layer b". The fractures highlighted in green are the latest to have been formed as they abut almost perpendicularly against the other two fracture families. They seem to affect both "Layer a" and "Layer b".

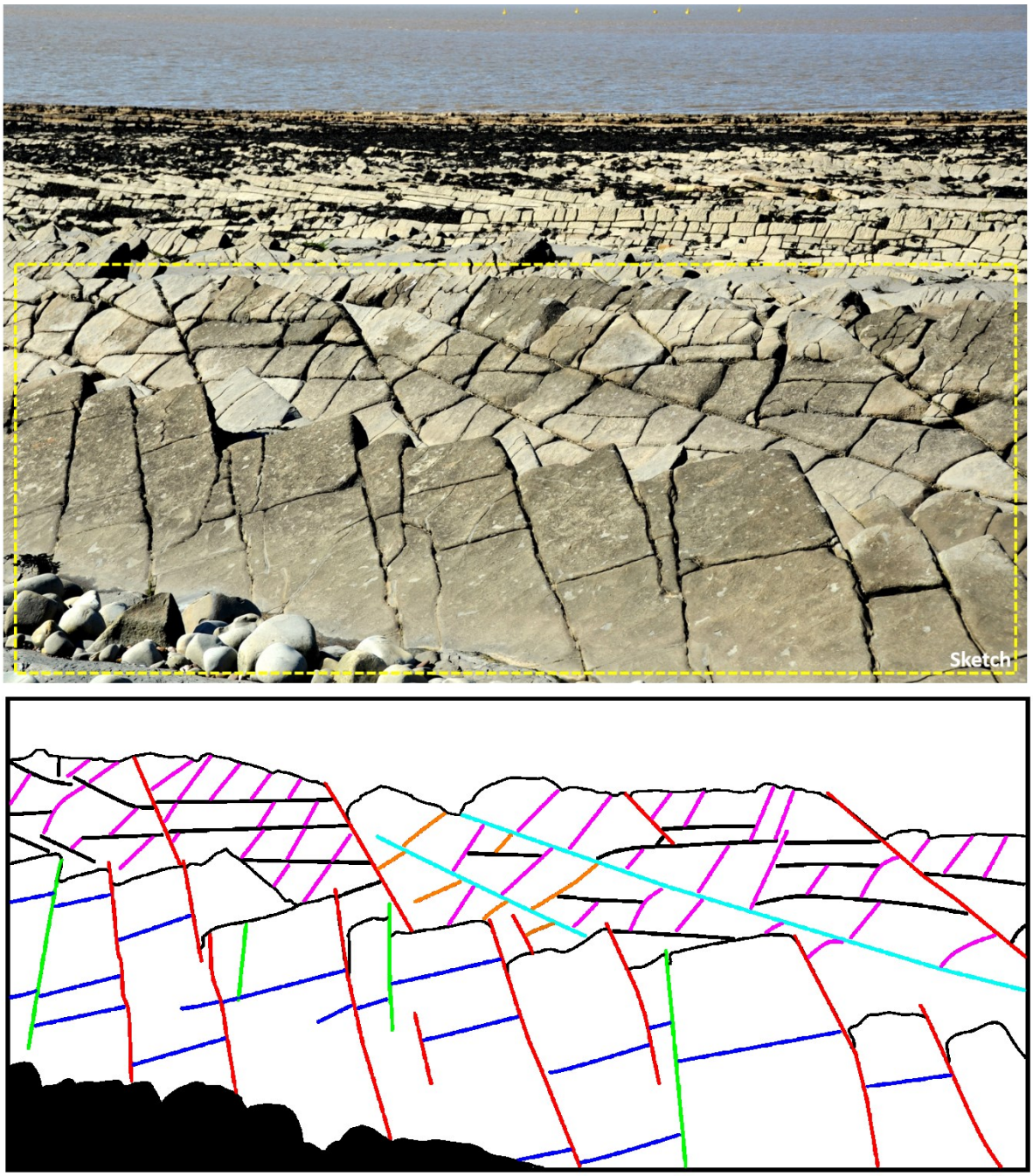


Figure 3. 56: As in Figure 3.56, several fracture families were identified in this section of Lilstock Beach. In the sketch it is possible to visualize through the colour coding that there are 7 fracture families in the two limestone beds. It is clear from the sketch that most of these fracture families are not present in both limestone beds.

3.5.5 Field work in Watchet – Mercia Mudstone

The Mercia Mudstone Group was deposited in a mudflat environment in three main ways during the Mid Triassic (Anisian) to Late Triassic (Rhaetian) (Hobbs, et al., 2002):

- Settling-out of mud and silt in temporary lakes;
- Rapid deposition of sheets of silt and fine sand by flash floods;
- Accumulation of wind-blown dust on the wet mudflat surface.

It is composed mainly of red and, less commonly, green and grey mudstones and siltstones and it overlies in most areas sandstones of the Sherwood Sandstone Group, but locally unconformably overlain Carboniferous or older rocks. The Mercia Mudstone Group is overlain by the grey to black, fossiliferous mudstone of the Westbury Formation of the Penarth Group (Howard, AS et al., 2008). Figure 3.58 shows the distribution of this formation in England and Wales and Figure 3.59 the litho-stratigraphic chart of the Triassic. Figure 3.60 shows the studied area on the North Somerset coast.
Although a minor constituent throughout the group, sulphate deposits (gypsum and anhydrite) and sandstone beds are common at some stratigraphic levels (Figure 3.61). These evaporite rich stratigraphic levels are important from a structural point of view as they provide an insight into how low permeability sequences respond to high fluid pressures. In areas where the Mercia mudsone is characterized by evaporites it shows a pervasive fracture network of satin-spar veins (Figure 3.62). These have been interpreted as a transient permeability path that helped relieve the excess of fluid pressure which was high as a result of the inversion of the basin in response to the Alpine orogeny. It is argued (Cosgrove, 2001) that when fluids penetrated the system as a result of hydraulic fracturing, they hydrated the anhydrite present in the evaporite rich-horizons to gypsum with a volume increase of around 60%. The anhydrite was converted to gypsum and the excess volume of gypsum precipitates in the bedding-parallel fractures to form satin-spar veins. These veins thus present the transient fracture system generated by high fluid pressure that allowed fluids to move through and out of the impermeable host rock. Cosgrove (2001) argues that a similar fracture system also developed in the adjacent evaporite-free mudstones – the top part of the outcrop does not contain satin-spar veins- but the mineralogy was not adequate to preserve it. It is important to note that such satin spar veins are prevalent features of bedded evaporite seals (see for example the succession studied at Brightling Mine). The similarities between the veins in the Mercia Mudstone and at Brightling are very clear. At Brightling there is evidence of extensional fractures in the rocks at two different times. An early time during basin opening in the Mesozoic when the fractures formed are vertical, and a later time during basin inversion in the Tertiary where the fractures are horizontal. At Brightling satin spar veins occurred during both these events and cross cutting relationships show that the vertical fractures predate the horizontal. At Watchet the early vertical fractures are filled by both sandstone dykes and by satin spar (Figure 3.63). These are then cross-cut by the bedding parallel satin-spar veins.

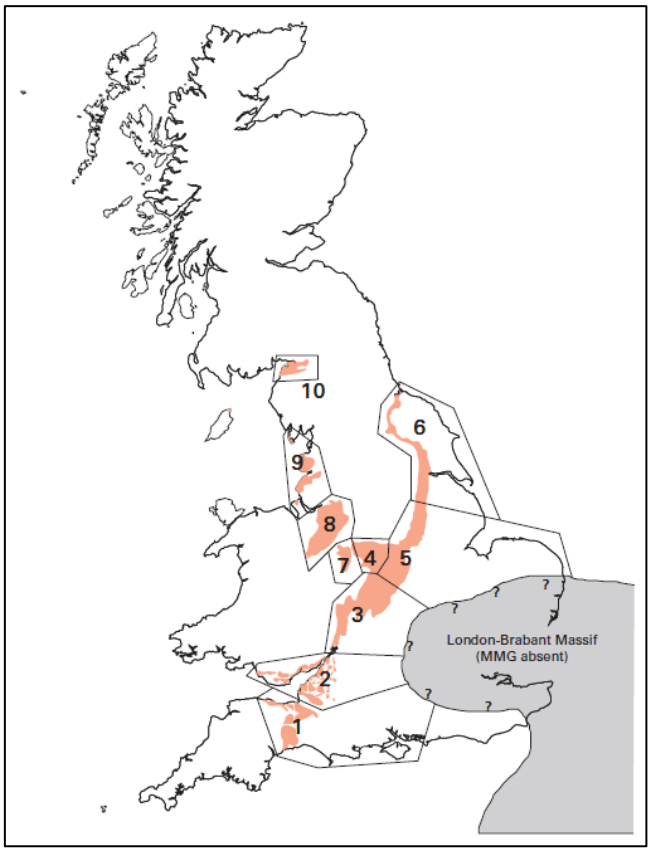


Figure 3. 57: Outcrops of the Mercia Mudstone Group in England and Wales. The numbered regions are as follows: 1 Wessex Basin; 2 Bristol/South Wales; 3 Worcester/Knowle Basins; 4 Needwood Basin; 5 East Midlands Shelf (South); 6 East Midlands Shelf (North); 7 Stafford Basin; 8 C heshire Basin; 9 West Lancashire; 10 Carlisle Basin(Howard et al., 2008).

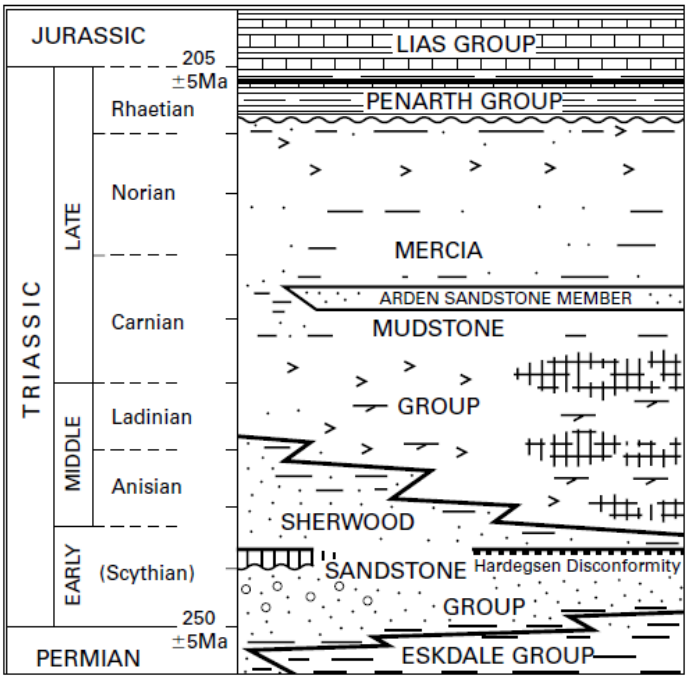


Figure 3. 58: Triassic lithofacies in England and the Southern North Sea. The evaporite members in the Mercia Mudstone are shown by gridded ornamentation (after Warrington and Ivimey-Cook, 1992).

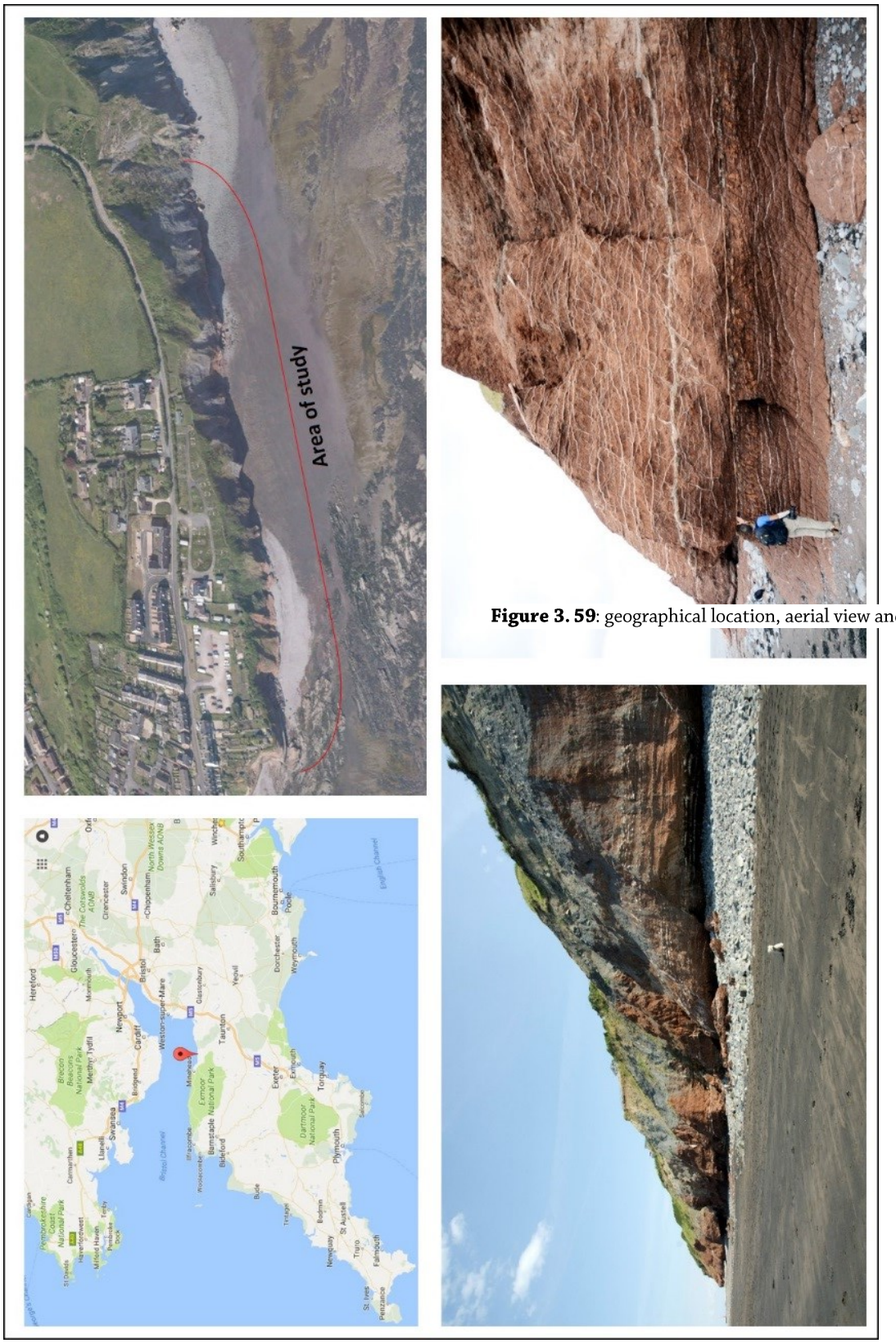


Figure 3. 59: geographical location, aerial view and genral view of the studied sec



Figure 3. 60: base of the Mercia Mudstone outcrop analysed in Watchet showing the layers of primary anhydrite nodules (now hydrated to gypsum). The excess gypsum generated by this hydration is precipitated in the bedding-parallerl hydraulic fractures as satin-spar veins (See Figure 3.62) thus preserving this fluid induced fracture system (see text for details)

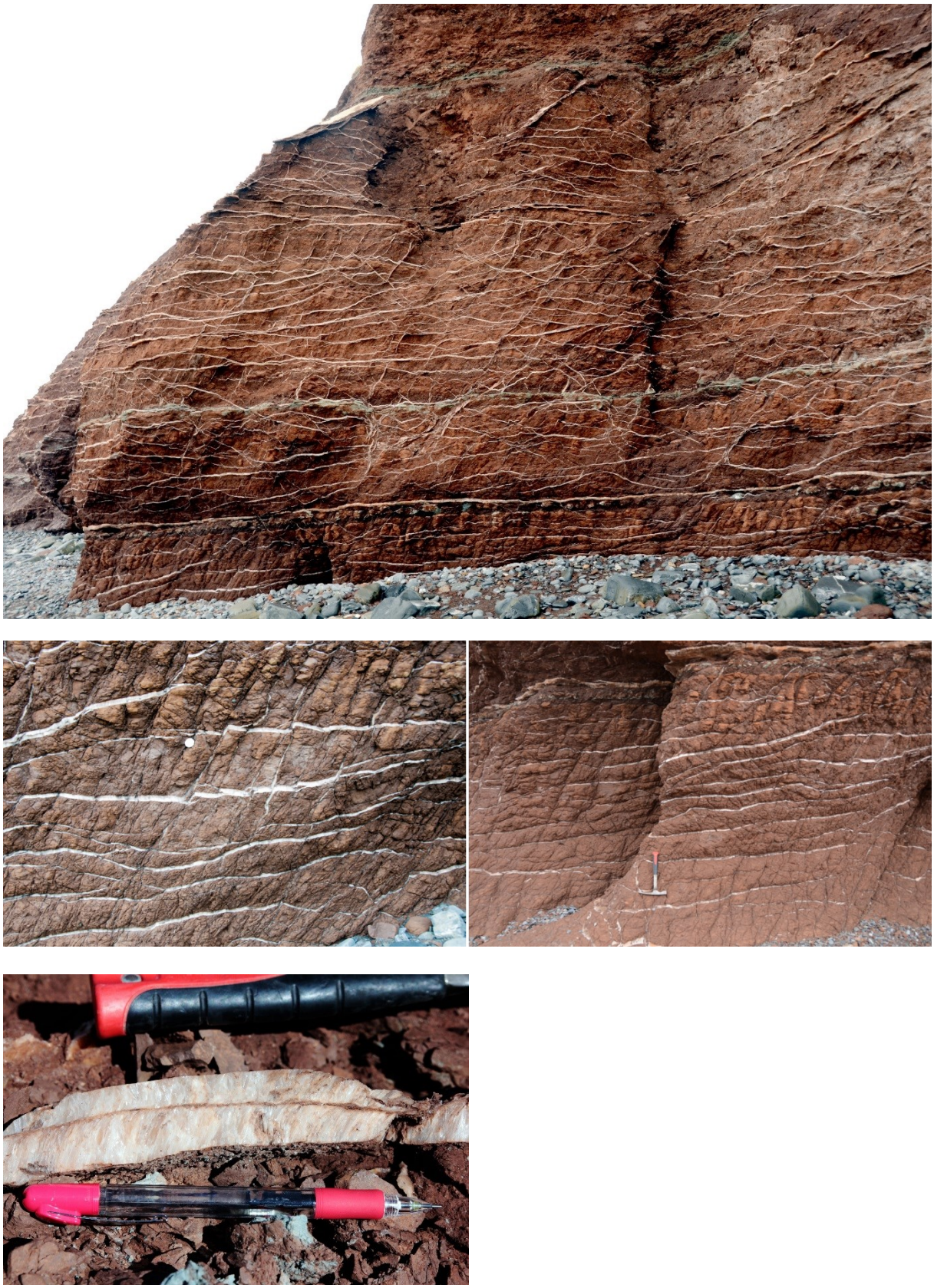
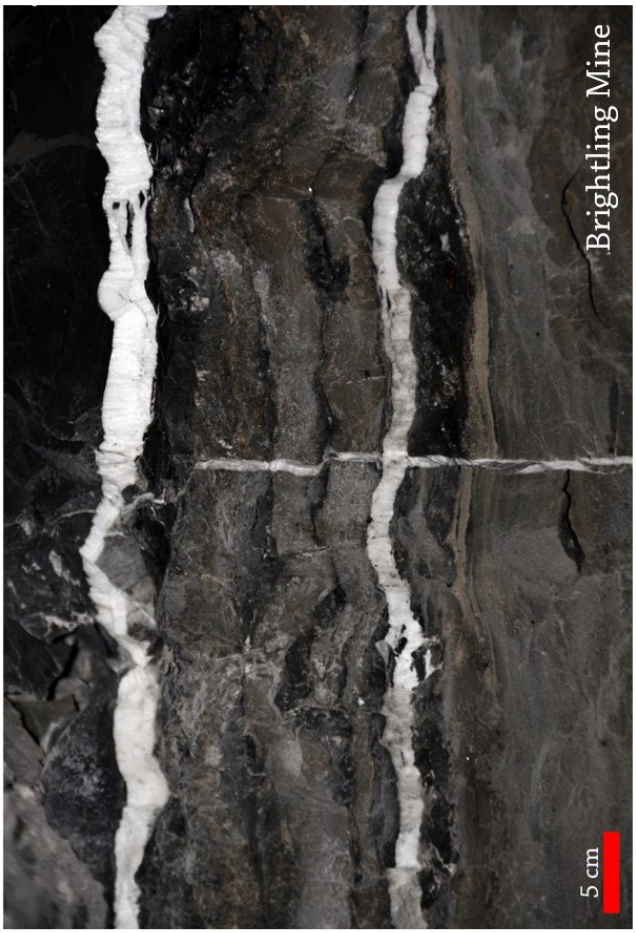


Figure 3. 61: Close up of the cliff face at Watchet showing the pervasive network of satin spar veins of the Mercia Mudstone. When fluids penetrated the system, they hydrated the anhydrite present in the evaporite rich-horizons to gypsum with a volume increase of around 60%, the excess volume of gypsum precipitates in the fractures in the form of satin-spar thus preserving them.





e of the satin-spar veins observed in Mercia
al veins postdate the vertical veins.

3.6 Summary and learnings obtained from the field observations

From the work conducted at Brightling Mine, the observations made on several drill-cores through evaporite-rich successions from the Weald Basin, and from the field work conducted in Thyterington Quarry, Lilstock Beach and Watchet the following conclusions can be made:

1. From Brighlting and the core analysis:

   Evaporite sequences are not homogenous in terms of their lithological and textural properties. A high lithological heterogeneity both vertically and laterally and a multitude of textures exists within sabkha evaporite successions, ranging from massive to nodular anhydrite (which in its turn has different textures such as chicken-wire, palisade or aggregate), intercalated with massive to laminated mudstones, microbial laminated mudstones or shales. There are both primary (related to the depositional environment and diagenesis) and secondary layers and interfaces (linked to natural hydraulic fracturing such as satin-spar veins) which have a major impact on the mechanical properties of the succession. A fracture which propagates through these formations will encounter different lithological units with different mechanical properties separated by interfaces. Due to the lateral variations presented by these evaporite-rich successions, it is considered that rather than actual barriers to fracture propagation (and fluid movement), they are can be seen as *baffle* zones which impede fractures propagation where they exist but allow propagation where they do not.

2. From Thyterington Quarry:

   The contacts between layers – of the same or of different lithology – play a very important role in fracture propagation from one layer to another. Irregular or serrated contacts created by pressure solution such as those that occur when two limestone layers are in direct contact with each other – stylolites - hinder interfacial sliding between layers and therefore promote the formation of through-going fractures, i.e. fractures that are able to cut-cross through an interface and become multilayer fractures (through-going). In contrast, the presence of a thin clay/mudstone layers between two carbonate layers allows interfacial sliding to occur, dissipating the tensile stress at the fracture tip and thereby arresting the fracture at the interface, i.e. the fractures remain strata-bound.

3. From Lilstock Beach:

   Field work in Lilstock was conducted with the objective of understanding how fractures behave when meeting an interface between two layers of different lithology particularly

an interface between a more competent limestone and a less competent shale. It is concluded that vertical tensile fractures in the limestone beds tend to be arrested at the interface between the limestone and the adjacent shale. However several exceptions to this were observed and fractures propagating from the limestone into the shale layer were observed. They either continued to propagate into the shale vertically or took on an oblique trajectory. Some of these oblique fractures in the shale connect offset vertical tensile fractures in the two limestone layers which are separated by that shale layer.

Another important observation is that there is often a strong fracture mismatch between limestone layers which are separated by a shale layer, i.e. fracture families that are present in one limestone layer are not present in the adjacent layer.

4. From Watchet:

   Observations in Watchet are related to the response of low permeability units to high fluid pressures. It is known that sedimentary rocks such as mudstones are very efficient in retaining fluids due to their very low permeability. In situations such as basin subsidence or basin inversion this causes the build-up of fluid pressure which is then relieved by the formation is hydraulic fractures. In the Mercia Mudstone, the presence of sulphate-rich – anhydrite – horizons results in these hydraulic fractures (which are normally transient features which close and heal after the high fluid pressure have been dissipated) to be preserved. It is argued that this process is very similar to what occurs in sabkha evaporite successions such as those observed in Brightling Mine and potentially what may occur in the evaporites of Qatar when the fluid pressure is raised during CO_2 injection operations. These features are thought to be of first order importance in terms of influencing the vertical propagation of a fracture.

Chapter 4
Theoretical Analysis

4.1 Introduction

The field work presented in Section 3 demonstrated that although valid for some evaporites like chlorides (halite, sylvite, etc.) which often display a high ductility, the general concept that cap-rock seals are ductile and able to avoid fracturing, does not hold all rock types such as the sulphates (specifically anhydrite). The field examples shown in section 3.5.5 (Mercia Mudstone, Figures 3.61 and 3.62) demonstrate that low permeability cap-rocks can and do fracture under specific stress conditions and that the general explanation for this failure is directly related to the very low permeability these rocks possess which allows pore pressures to rise to values much higher than hydrostatic pressure. In situations such as these, if the pressure is greater than the sum of the minimum stress and the tensile strength of the rock, the seal can fracture by hydraulic fracturing forming extensional fractures. We consider that the evaporites studied in this project have characteristics (i.e. low permeability) which can lead to failure by hydraulic fracturing.

Work by other authors has also demonstrated that low permeability rocks have properties that allow them to undergo fracturing. Davies et al. (2012) have used three-dimensional seismic data collected offshore of West Africa and mid-Norway to map vertical fractures that cut the stratigraphic sequence including reservoir and seal rocks. They have presented data that show that natural hydraulic fractures cluster, forming pipe-like features that often extend for great vertical distances (offshore Namibia where the cap-rock is an evaporite, fractures extending vertically for as much as 1000m have been identified – Figure 4.1).

Casabianca & Cosgrove (2012) challenge the assumption made by authors like Gaarenstoom et al. (1993) that seal is the base of the cap-rock, i.e. the low matrix permeability formation immediately overlying the reservoir. Using a structural model of an hypothetical fault sealing high pressure prospect, they propose that the seal does not occur at the reservoir–caprock interface, arguing that the caprock is likely to be intersected by a system of fractures orientated along the crest line of the fault block and associated with the bounding fault – the damage or waste zone (Figure 4.2a). The ultimate seal (hydraulic seal) coincides with the upper tip of this fracture system defined at a stratigraphic interface capable of containing further propagation of the waste zone fractures. In this study the authors propose that the average LOP (Leak-Off Pressure) measurements at a given depth for a given rock are the best proxy for fracture propagation pressure for that rock and define the hydraulic seal as the cap-rock formation not cut by large fractures and critically not cut by fractures connected to the reservoir fluid pressure (Figure 4.2b).

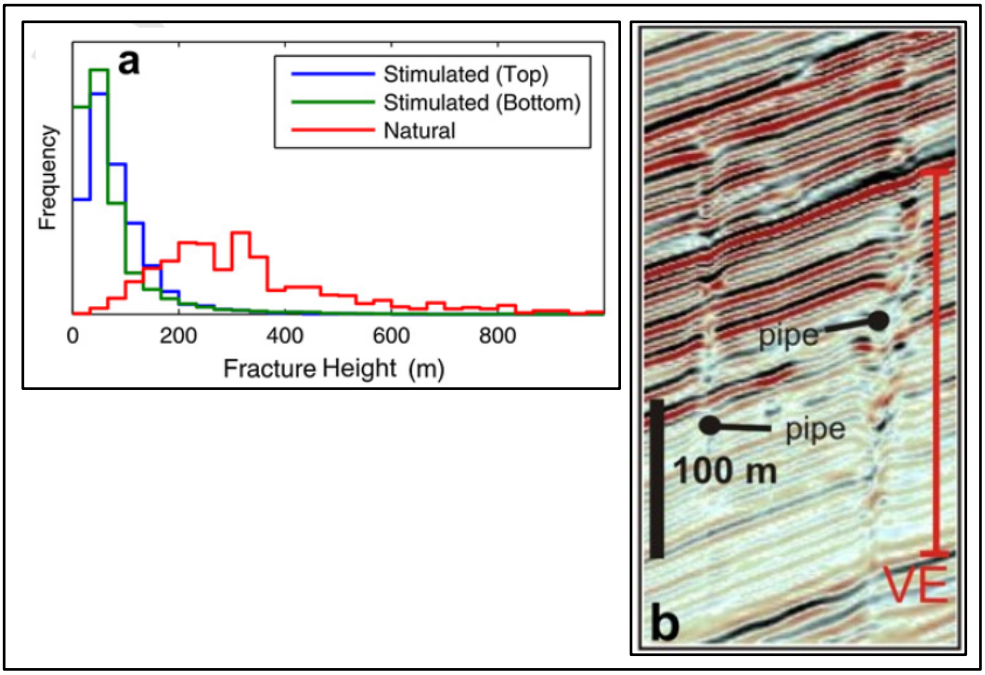


Figure 4. 1: A graph of frequency against vertical extent for natural hydraulic fractures (pipes) identified on 3D seismic data from offshore Mauritania which demonstrates that natural occurring fractures can extend for hundreds of meters, b) Seismic line from offshore Mauritania showing a representative vertical pipe imaged on 3D seismic reflection data and its vertical extent (VE). (Davies & al, 2012)

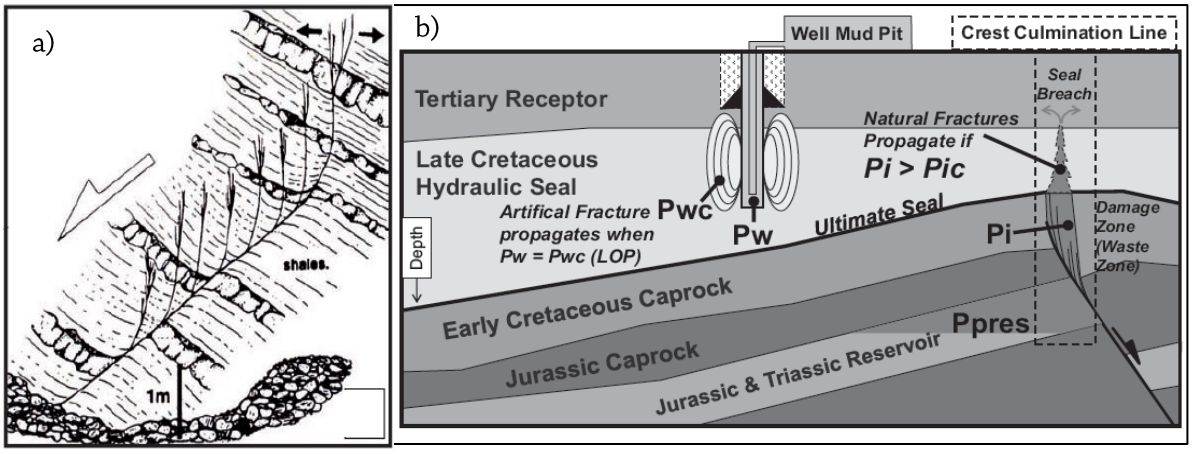


Figure 4.2: a) Sketch of a normal fault and associated damage zones in Jurassic (Liasic) rocks at Kilve, Somerset (McGrath & Davison, 1995); b) Structural model across the crest of a hypothetical high pressure prospect relating the propagation of artificial fractures of LOP experiments within the Cretaceous with the propagation of natural fractures from the Jurassic caprock into and through the Cretaceous hydraulic seal (Casabianca & Cosgrove, 2012). Ppres – reservoir pore fluid pressure; Pi – pressure at the waste zone fractures; Pic - waste zone fractures propagation pressure at the ultimate seal boundary; Pw – well mud pressure ; Pwc - critical wellbore pressure – it is determined by the means of a LOP.

Having said this both our field work and the work done by other authors enable us to conclude that hydraulic seals – such as those formed by evaporites like anhydrite cap-rocks – have characteristics (very small pore throats and in consequence a very low intrinsic permeability) which can give rise to fluid pressures that may be sufficient to overcome the tensile strength of the rock and the horizontal stress, causing fractures to form and propagate through the sedimentary sequence.

In light of the research goals presented in Section 1 (i.e. to "determine the mechanical properties of evaporite rich seals and the mechanisms by which they might fail when subjected to high fluid pressures linked to the injection of CO2"), it is essential to understand the state of stress and the magnitude of fluid pressures that exist in the Earth's crust so that, by applying the mechanical principles that control how rocks fail, we are in a better position to predict the stability of evaporite cap-rocks. The present section outlines the most important set of principles we have used to study the problem. The following topics are considered:

- Stress and strain in the Earth's crust
- The relationship between stress and strain
- Brittle deformation
- Fluid pressure, effective stress and hydraulic fractures
- Fracture propagation within and through layered media
- Fracture spacing and saturation

4.2 Stresses in the Earth's Crust

Stress on a surface is a first order tensor (a vector) and can be regarded as the ratio between a force (F) and the area across which the force acts. Two types of surface stresses exist: normal (σ_n) and shear stress (τ). They can be distinguished by the orientation of the stress vector relative to the surface on which is acting. Normal stress acts perpendicularly to the surface while shear stress acts parallel to the surface. Because most principal stresses act obliquely on a surface, then the stress vector can be decomposed into both normal and shear stress components (Figure 4.3) and then the equations for these two stress components derived from simple trigonometry.

Note that in the Earth's crust, stresses are usually compressive and for that reason, geologists conventionally consider compressive stress as being positive. Any normal stress that acts on a surface along which there is no shear stress is defined as a principal stress. Any stress state can be defined by three principal stresses (σ_1, σ_2, and σ_3). If two of these are zero the stress state is defined as being uniaxial. When one of the principal stresses is zero, the stress sate is biaxial and when none are zero the stress state is defined as triaxial. The latter is the state most common stress state encountered in the Earth's Crust. In such a triaxial stress situation, the maximum principal stress is denoted by σ_1, the intermediate by σ_2 and the minimum by σ_3.

The state of force on any plane in the material, inclined at an angle θ to the applied force, can be determined by resolving the force into components normal and parallel to the plane, i.e., F_N (Equation 4.1) and F_P (Equation 4.2) respectively

$$F_N = F\sin\Theta \qquad (4.1)$$

$$F_P = F\cos\Theta \qquad (4.2)$$

The normal and parallel forces that are acting on a surface can be re-expressed as normal and shear stresses by dividing them by the area over which they act (Figure 4.4):

- Normal Stress: $\sigma_n = \sigma_1.\sin^2\Theta$

$$\sigma_n = F_N/a' = F\sin\Theta / a = F\sin\Theta / (A/\sin\Theta) = (F/A)\sin^2\Theta = \sigma_1\sin^2\Theta \qquad (4.3)$$

- Shear Stress: $\tau = \sigma_1 \cos\Theta.\sin\Theta$

$$\tau = F_P/a' = F\cos\Theta/a = F\cos\Theta/(A/\sin\Theta) = (F/A)\cos\Theta.\sin\Theta = \sigma_1\cos\Theta.\sin\Theta \qquad (4.4)$$

In a situation where two different stresses are operating over a body the same logic can be applied and we obtain the following biaxial stress equations:

- Normal Stress: $\sigma = \sigma_1 \sin^2\Theta + \sigma_3 \cos^2\Theta$ (4.5)
- Shear Stress: $\tau = (\sigma_1 - \sigma_3) \sin\Theta.\cos\Theta$ (4.6)

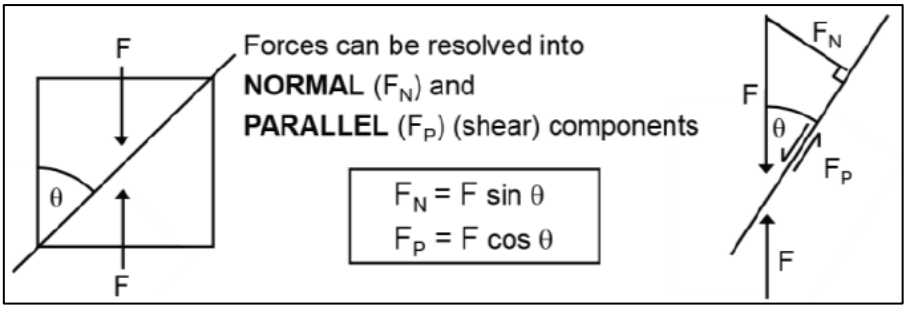


Figure 4.3: The resolution of a force into its normal and shear force components (adapted from Cosgrove & Hudson, 2016) .

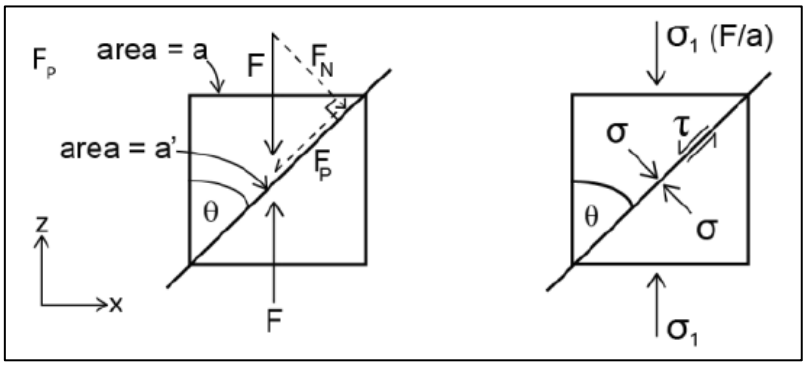


Figure 4.4: The resolution of stress in a uniaxial stress field (adapted from Cosgrove & Hudson, 2016).

The state of stress at a given point can be defined by a stress ellipsoid, a stress tensor, or a Mohr circle:

a) Stress Ellipsoid (Figure 4.5)

The surface of the ellipsoid represents the endpoints of all normal stresses acting on all planes passing through the centre of the ellipsoid. The length of the axes of the ellipsoid are proportional to the magnitude of the three principal stresses. Note that the 3 planes which are normal to the 3 principal stress are planes along which there is no shear stress.

b) Stress Tensor (matrix)

Using a cube (Figure 4.6) to represent the point, the stress acting on it can be defined by nine components: three normal stress components and six shear stress components. Using a matrix to represent the stress tensor:

$$\begin{bmatrix} \sigma_{11} & \sigma_{12} & \sigma_{13} \\ \sigma_{21} & \sigma_{22} & \sigma_{23} \\ \sigma_{31} & \sigma_{32} & \sigma_{33} \end{bmatrix}$$

In this matrix the normal stresses σ_{11}, σ_{22} and σ_{33} occupy the diagonal and the shear stresses are the off diagonal terms. In a stable situation, stresses are in equilibrium so we can write: $\sigma_{12} = \sigma_{21}$, $\sigma_{31} = \sigma_{13}$, $\sigma_{23} = \sigma_{32}$ and represent the stress tensor by:

$\begin{bmatrix} \sigma_{11} & \sigma_{12} & \sigma_{13} \\ \sigma_{12} & \sigma_{22} & \sigma_{23} \\ \sigma_{13} & \sigma_{23} & \sigma_{33} \end{bmatrix}$. If we orient the cube with the principal stresses along the edges of the reference axes the matrix simplifies to:

$\begin{bmatrix} \sigma_{11} & 0 & 0 \\ 0 & \sigma_{22} & 0 \\ 0 & 0 & \sigma_{33} \end{bmatrix} = \begin{bmatrix} \sigma_1 & 0 & 0 \\ 0 & \sigma_2 & 0 \\ 0 & 0 & \sigma_3 \end{bmatrix}$ where the three principal stresses will be $(\sigma_1, 0, 0)$; $(0, \sigma_2, 0)$ and $(0, 0, \sigma_3)$.

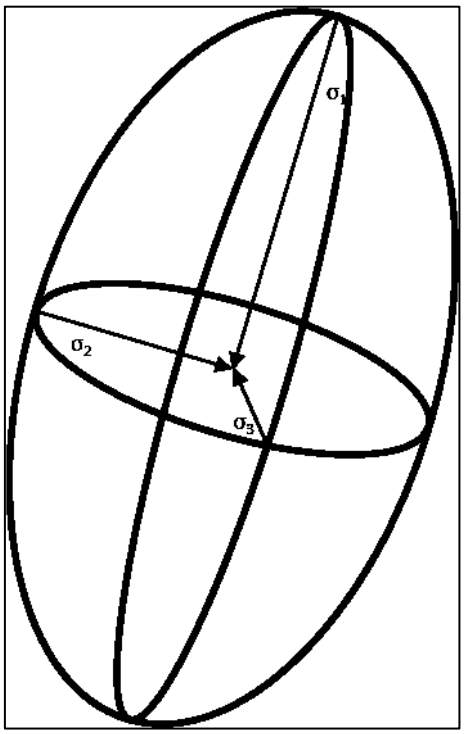


Figure 4.5: stress ellipsoid showing the principal stresses acting on a point in the centre of the ellipsoid.

c) The Mohr Circle

Using the the Mohr diagram created by German engineer Otto Mohr (Figure 4.7) and the two stress equations (equations 4.3 and 4.4), it is possible to plot the normal stress against the shear stress for all planes oriented between Θ=0 and 180° to σ_1. The result is that the maximum and minimum principle stresses are plotted on the horizontal axis and act on planes oriented 90° and 0° to σ_1. As

noted both these planes have zero shear stress acting along them. The distance between them (the differential stress σ_1-σ_3) defines the diameter of a circle – the Mohr circle. Any point of this circle represents a state of stress on some plane inclined at Θ to σ_1 and the value of shear and normal stress can be read directly from the graph τ_0 vs σ_0 (Figure 4.7). It is convenient to express the stress equations (4.3) and (4.4) in terms of 2Θ and by using the identities:

- $\sin\Theta \cos\Theta = (\sin 2\Theta)/2$
- $\cos^2\Theta + \sin^2\Theta = 1$
- $\cos^2\Theta - \sin^2\Theta = \cos 2\Theta$

, and equations (4.3) and (4.4), it can be shown that:

- $\sigma = [(\sigma_1 + \sigma_3)/2] - [(\sigma_1 - \sigma_3)/2] \cos 2\Theta$ (4.7)
- $\tau = [(\sigma_1 - \sigma_3)/2] \sin 2\Theta$ (4.8)

It follows from the geometry of Figure 4.7 that the distance from the origin to C is (σ1 + σ3)/2 and that BC= (σ1 - σ3)/2 which is the radius of the Mohr circle. The angle between the line joining the centre of the Mohr circle to the point on the circle gives the state of stress on the plane inclined at Θ to σ_1 (line CX) and the normal stress axis is 2Θ. As already noted the magnitude of τ (the shear stress on any plane of interest inclined at Θ to σ_1 is represented by the distance XP which from the geometry of the figure can be seen to be defined by resolving

$$sin2\Theta = \frac{XP}{XC}$$

$$XP = \left(\frac{\sigma_1 - \sigma_3}{2}\right).sin2\theta \quad (4.9)$$

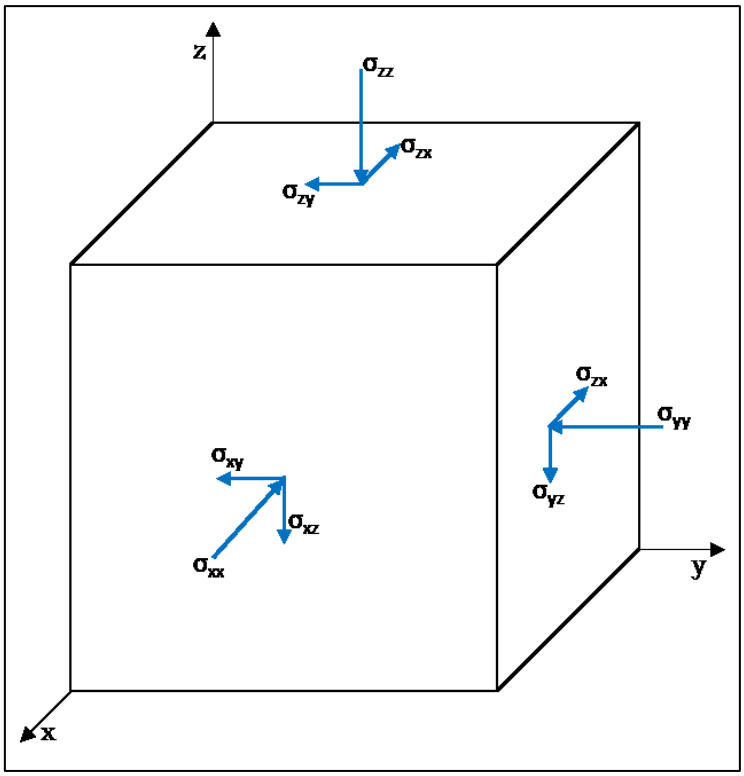


Figure 4.6: stress components acting on the faces of a small cube that represents a point (adapted from Fossen, 2010).

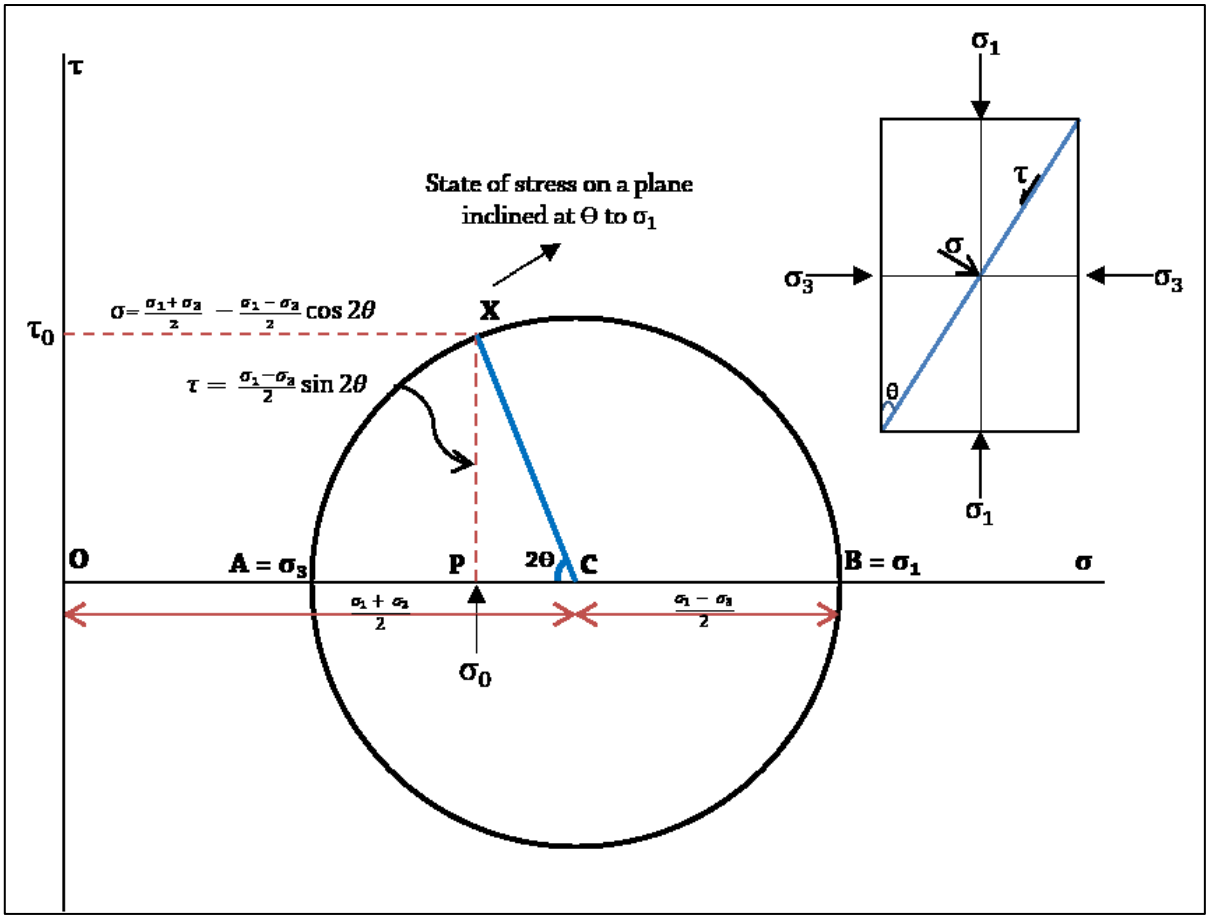


Figure 4.7: The Mohr circle: Graphical representation of Equations (11) and (12). Adapted from Price & Cosgrove, 1990.

4.2.1 Relation between stress and strain

When subjected to stress the particles in a body (a rock for example) are displaced. Strain measures the displacement between particles in the body i.e. the deformation. Strain is homogeneous when is constant trough a body and heterogeneous when the displacement gradient varies through that body. Because heterogeneous strain is difficult to analyse, a heterogeneously strained region can be subdivided into smaller domains that experience homogeneous deformation.

In two dimensional, homogeneous strain, straight lines remain straight and parallel lines remain parallel, while a circle is transformed into an ellipse (the strain ellipse). However the length of a line and the angle between two lines change. The first is a measure of the extension in a certain direction and the second a measurement of the shear deformation in that direction (Figure 4.8).

- Length Variation or extensional strain (e) is defined as change in length divided by the original length, l_0, relative to a reference length (original length):

$$e = \frac{l_1 - l_0}{l_0} = \frac{d_l}{l_0} \qquad (4.10)$$

,where l_1 is the original length of a line.

- Angle Variation or angular shear (φ) is the change in angle between two lines that were originally perpendicular. The shear strain is defined as:

$$\gamma = \tan \varphi \qquad (4.11)$$

Two types of homogenous strain that approximate the deformation frequently encountered in the crust are: pure and simple shear (Figure 4.8). The difference between them resides mainly in the rotation of the strain ellipse axis. During pure shear extension parallel to the x axis occurs with no area change and the circle representing the undeformed state is transformed into an ellipse whose axis have not rotated, remaining with the same orientation as in the initial circle. In simple shear the deformation is rotational and the finite strain ellipse is non-coaxial.

When analysing the relation between strain and stress it is important to consider the properties of the materials. As geological materials are very complex it is convenient to use ideal bodies (i.e. rheology). Three different conceptual models for mechanical behaviour of rocks are considered: elastic, viscous and plastic. These allow us to analyse the way rocks deform and fail (strain) under the application of stress.

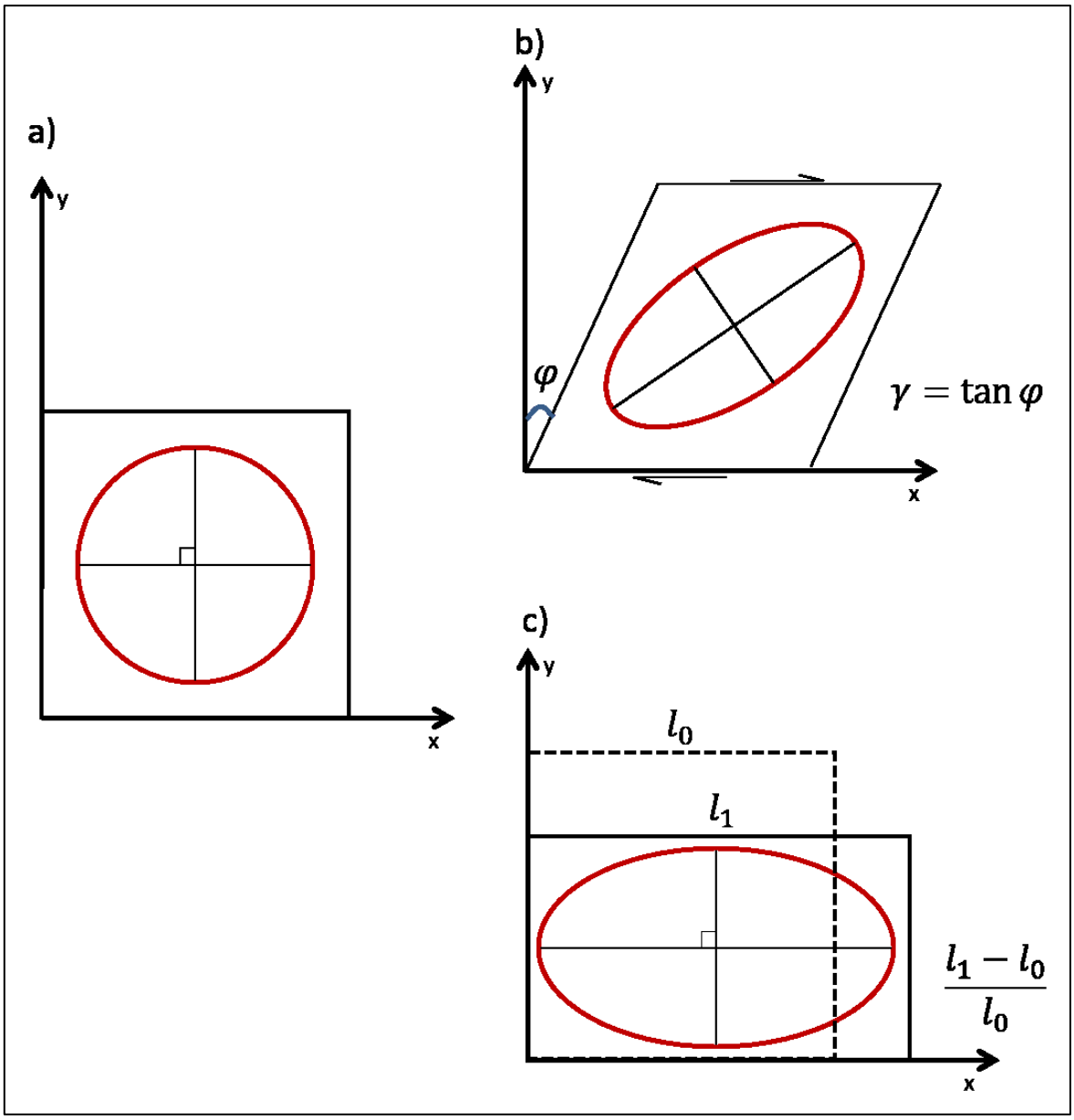


Figure 4.8: Homogeneous strain. a) Undeformed state. b) Simple shear. c) Pure shear.

4.2.2 Elastic vs Plastic Materials

Elasticity is the property of an object or material to recover its normal shape after the stress which deformed it is removed, i.e. the deformation is irreversible. The theory of elasticity is based upon four principles, namely that the elastic material is (Price & Cosgrove, 1990):

1. Homogeneous: globally composed of the same substance
2. Isotropic: hold the same properties regardless of the direction
3. Elastic strains are infinitesimal
4. The material has a linear stress-strain relationship (Hooke's Law)

If the appropriate scale is chosen, points 1. and 2. can be fulfilled as a large volume of material can be considered homogeneous isotropic even when smaller parts of it are not.

The linear elasticity theory was formulated initially by Hooke in the 17th century and developed by Young in the 19th century who suggested the linear relationship between stress and strain observed in several materials could be written as:

$$\sigma = Ee \quad (4.12)$$

where σ is stress; E the Young's modulus and e the strain. It follows that Young's modulus is the stress/strain ration: E= σ/e and it is considered as a measure of the stiffness of a material. Being the ratio of stress (units of pressure) to strain (dimensionless), it has units of pressure and its SI unit is the Pascal.

French mathematician and physician Simeón Poisson, noted that when a vertical stress σ_1 is applied to a body, it causes not only vertical strain (e_z) , but also dilational strains e_x and e_y, such that $e_x = e_y$. This effect is known as the Poisson's effect and it states that for an isotropic material – one where the properties are identical in all directions - the change in dimension will be the same in any direction perpendicular to the direction of stress application. Poisson's expressed this phenomenon as the ratio of the horizontal to vertical strains resulting from the uniaxial stress. This ratio is a material constant, called the Poisson's Ratio:

$$\frac{e_x}{e_z} = \frac{e_y}{e_z} = \upsilon \quad (4.13)$$

The inverse relationship is called the Poisson's number:

$$1/\upsilon = m \quad (4.13a)$$

From this relationship it is possible to obtain the equations that relate the stress and strain in the three dimensional space, and ultimately obtain the relationship between the vertical and horizontal stresses in the crust when only the force of gravity is operating.

From equations (4.13) and (4.13a):

$$e_x = e_y = e_z/m = \sigma_z/(mE) \quad (4.14)$$

Each of the three principal stresses acting on a body will give rise to three strain components in the x, y and z directions. If we consider the strains in the vertical direction, z, resulting from the three principal stresses σ_x. σ_y and σ_z we can write three strain equations:

- $e'_z = \sigma_z/E$ (4.15)

- $e''_x = \sigma_x / mE$ (4.15a)
- $e'''_y = \sigma_y / mE$ (4.15b)

we can now write the total strain in z direction (strains caused by σ_x and σ_y will have a negative sign as they are dillational):

- $e_z = e'_z - e''_x - e'''_y$

by substituting we obtain:

$$e_z = \frac{1}{E}\left[\sigma_z - \frac{1}{m}(\sigma_x + \sigma_y)\right] \quad (4.16)$$

and applying the same logic to the other directions:

$$e_x = \frac{1}{E}\left[\sigma_x - \frac{1}{m}(\sigma_z + \sigma_y)\right] \quad (4.16a)$$

$$e_y = \frac{1}{E}\left[\sigma_y - \frac{1}{m}(\sigma_x + \sigma_z)\right] \quad (4.16b)$$

Considering a situation where a section of the Earth's crust of uniform properties and completely elastic is subjected to gravitational loading with lateral strain being inhibited in all directions by the surrounding material, then a cube of unitary sides will be subjected to a vertical stress resulting from the weight of the overburden:

$$\sigma_z = \rho g z \quad (4.17)$$

,where ρ is the bulk density of the material; g is the acceleration due to gravity and z is the depth from the surface.

Because lateral strain is inhibited there is a lateral stress $\sigma_H = \sigma_x = \sigma_y$ which is able to counterbalance the strain that would have been caused by the vertical load. At the same time $e_x = e_y = 0$. Because E cannot be zero, it can then be written:

$\left[\sigma_x - \frac{1}{m}(\sigma_z + \sigma_y)\right] = 0$; $\sigma_z = \sigma_v$ and $\sigma_x = \sigma_y = \sigma_z = \sigma_H$, therefore the final relationship can be written as:

$$\sigma_H = \frac{\sigma_v}{m-1} \quad (4.18)$$

For the object of this study (loss of seal integrity through brittle failure), elastic theory can be applied to model fracture initiation and growth because at this stage of brittle failure the strain is so small that deviations from elasticity are irrelevant and the elastic theory can be successfully used.

Perfectly viscous materials (fluids) are those which possess no inherent shear strength and for that reason will flow under the action of an infinitesimally small shear stress (Price & Cosgrove, 1990). The ease, with which fluids flow, is described in terms of their viscosity, η. The rate at which fluids

flow is directly related to the magnitude of the shear stress being applied and it is described by the following relationship:

$$\tau = \eta\gamma \quad (4.19)$$

,where η is the viscosity (SI units Pa.s) of the fluid and γ the strain rate. Viscous deformation is irreversible and creates permanent strain.

Rocks can approximate to viscous behaviour especially when deformation of hot rocks is in play (they can display either linear or a non-linear viscous behaviour). For rocks and other solids, elastic deformation is valid for small strain values. Once the elastic limit or yield stress (the stress at which a material starts to behave non-elastically) is achieved permanent strain is added to the elastic strain, it is an elastic-plastic response (Figure 4.9). Plastic strain can be defined as *the permanent change in shape or size of a body without fracture, accumulated over time by a sustained stress beyond the elastic limit (yield point) of the material* (Fossen, 2010). It is commonly found that rocks do not behave as perfect plastic materials (in which stress cannot rise above the yield stress and strain accumulates without change in stress level). Most real materials e.g. metals, show what is called *strain hardening*, where the yield stress increases as deformation increases. Other types of deformation include are: *creep,* when the material deforms without any increase in the applied force or stress; and *strain softening* where the yield stress decreases with increasing deformation. Figure 4.10 sums the three fundamental types of deformation.

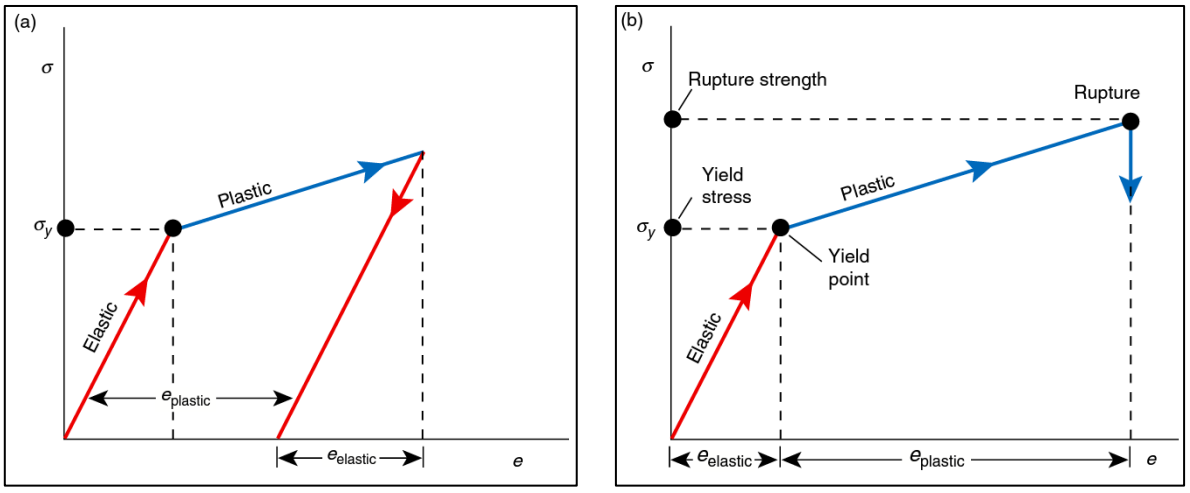


Figure 4.9: stress-strain curve for elastic-plastic deformation. a) Elastic strain is replaced by plastic strain when the yield stress is achieved (σy). When stress is removed the elastic strain is released and the plastic strain remains. b) in this situation stress is increased to the point of brittle rupture. (Fossen, 2010).

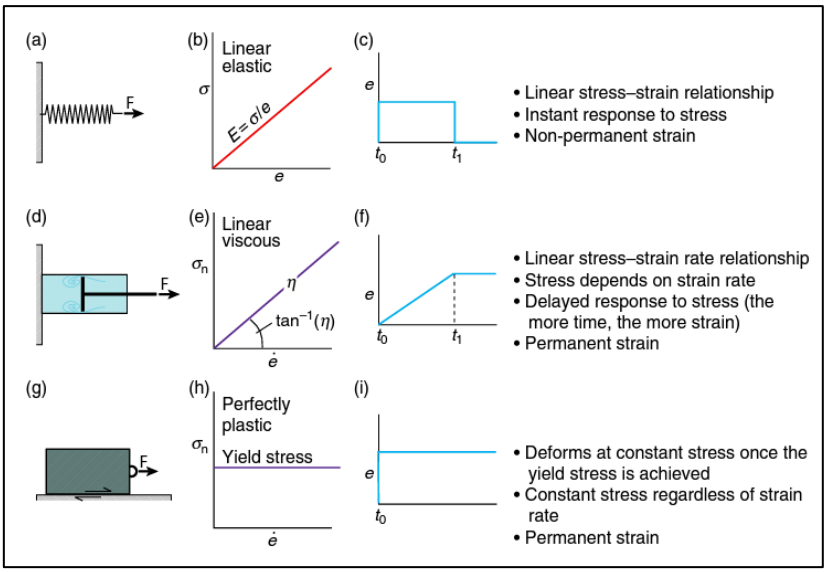


Figure 4. 10: three types of deformation (elastic, viscous and plastic) illustrated by mechanical analogs (a); stress-strain rate curves (b) and strain history curves (c) (Fossen, 2010).

4.3 Brittle Deformation

Two fundamentally different types of deformation occur in the Earth's crust: brittle and ductile. The major difference between them lies on whether or not the deformation involves the loss of continuity of the rock mass. Brittle deformation occurs by mechanisms such as frictional sliding along grain contacts, grain rotation and grain rupture, which lead to fracturing. Deformation where the continuity of the rock mass is maintained is named ductile deformation (e.g. folding).

Fractures are discontinuities caused by the rupturing of the rock material. They may be restricted to individual grains or may cut continuously through rock bodies over distances varying from millimetres to kilometres (Mandl G. , 2005). Macroscopic rock fractures can be divided in two major classes according to the relative movement of the fracture walls and their orientation relative to the principle stresses that generated them (Figure 4.11): joints (tensile fractures) and faults (shear fractures). As it is shown in the following section these two groups of fractures are the result of two different modes of brittle failure: tensile failure and shear failure respectively. Tensile fractures are also called Mode I and shear fractures Mode II.

In geology compressive stresses are considered to be positive, while tension is regarded as negative. This arises from the fact that the crust is dominated by compressive stresses. Fractures are thus the result of the application of stress to the earth's crust.

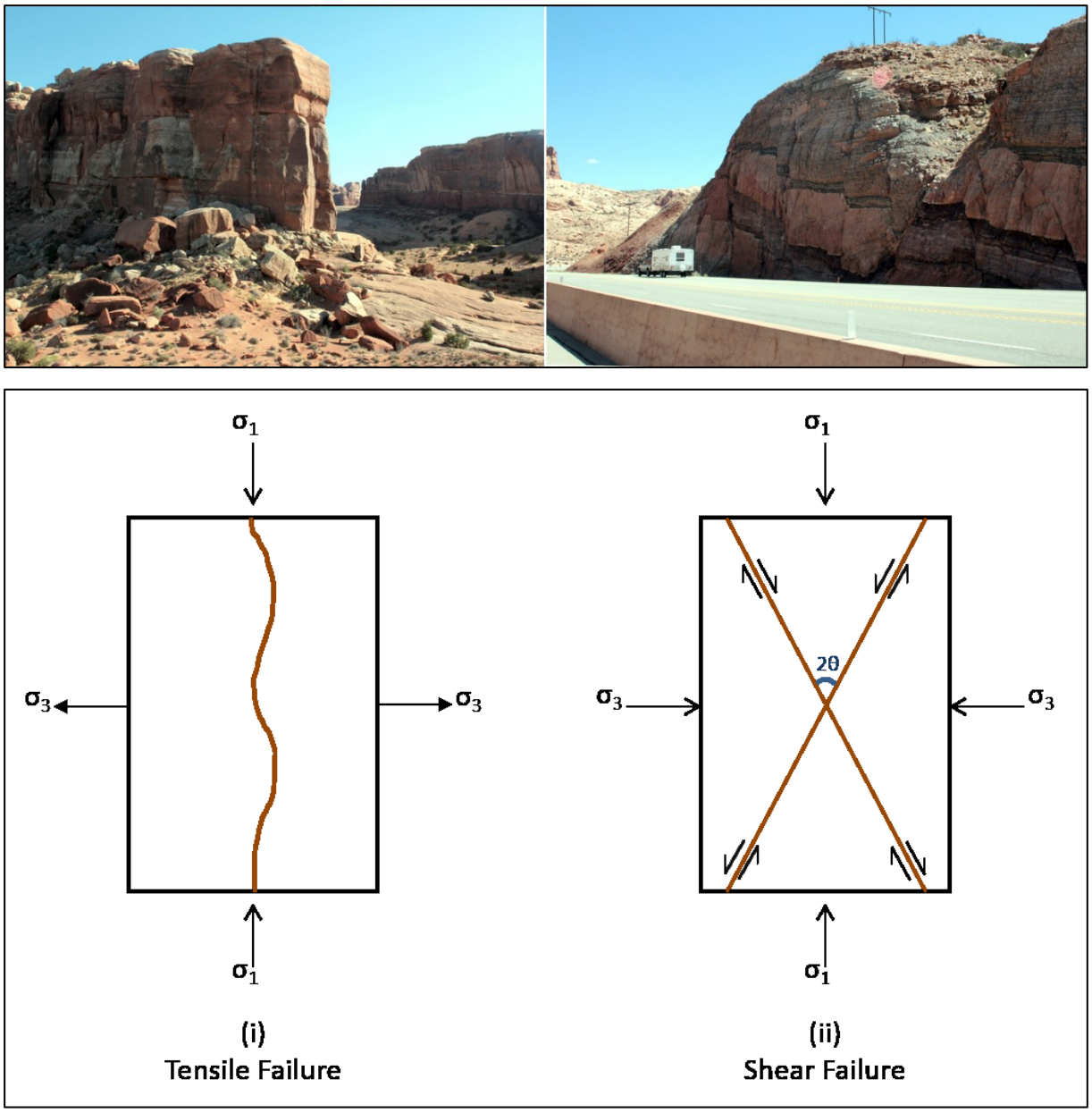


Figure 4.11: a) Natural examples of extensional and shear fractures in Utah, USA b) the two modes of brittle failure: i) Shear failure and ii) Tensile Failure. They can be differentiated by the orientation of the fractures relative to the principal stresses and the relative motion of the fracture walls (adapted from Cosgrove, 2005).

4.3.1 Failure and failure criteria

Two main failure criteria have been proposed to explain brittle failure of rocks:

1. The Navier-Coulomb/Mohr-Coulomb criterion
2. The Grifith criterion

Navier-Mohr-Coulomb Failure Criteria: Shear Failure

In the 18th century, French physicist Charles Coulomb developed a criterion of brittle shear failure which is based on a principle another French scientist, Amonton, developed almost a century before – Amonton's Law of frictional sliding:

$$\tau = \mu\sigma \quad (4.20)$$

This law states that the frictional resistance to the sliding of a block, i.e the shear stress (ʊ) necessary to move the block, is directly proportional to the applied load (σ) and that the force of friction is independent of the area of contact. The coefficient of sliding friction (μ) is defined as the tangent of the angle of sliding friction (ϕ) (for a block at rest on an inclined plane, it is the angle at which the plane must be inclined before the block starts to slide). From these principles Coulomb formulated a theoretical criteria for failure:

$$\tau = C_0 + \sigma_n \tan\Phi \quad (4.21)$$

He argued that in order for shear failure to occur along a potential plane in a material (dotted line in Figure 4.12a) the shear stress acting along that plane must be large enough to rupture the material, i.e. to overcome it's shear strength C (known as the cohesion) and to cause slip along that plane (Equation 4.21).

Through laboratorial experiments using a tri-axial deformation rig (Figure 4.12 b and c), where the confining pressure (σ_3) and axial loading (σ_1) are adjusted to the point of failure of the rock, it is possible to obtain a series of pairs of σ_1 (the maximum compressive stress sustained) and σ_3 (confining pressure) at failure. Plotting these values on a graph of axial load versus confining pressure (Figure 4.13), the uniaxial strength of a rock – the maximum stress a material can sustain before undergoing permanent deformation - can be obtained. It is the load needed to cause shear failure of the rock when the confining stress is zero and is given by the intersection of the line with the axis of maximum principal compression. This representation of the experimental data also shows that increasing confining stress leads to greater axial loading needed to fracture the rock, i.e. rock strength increases with depth.

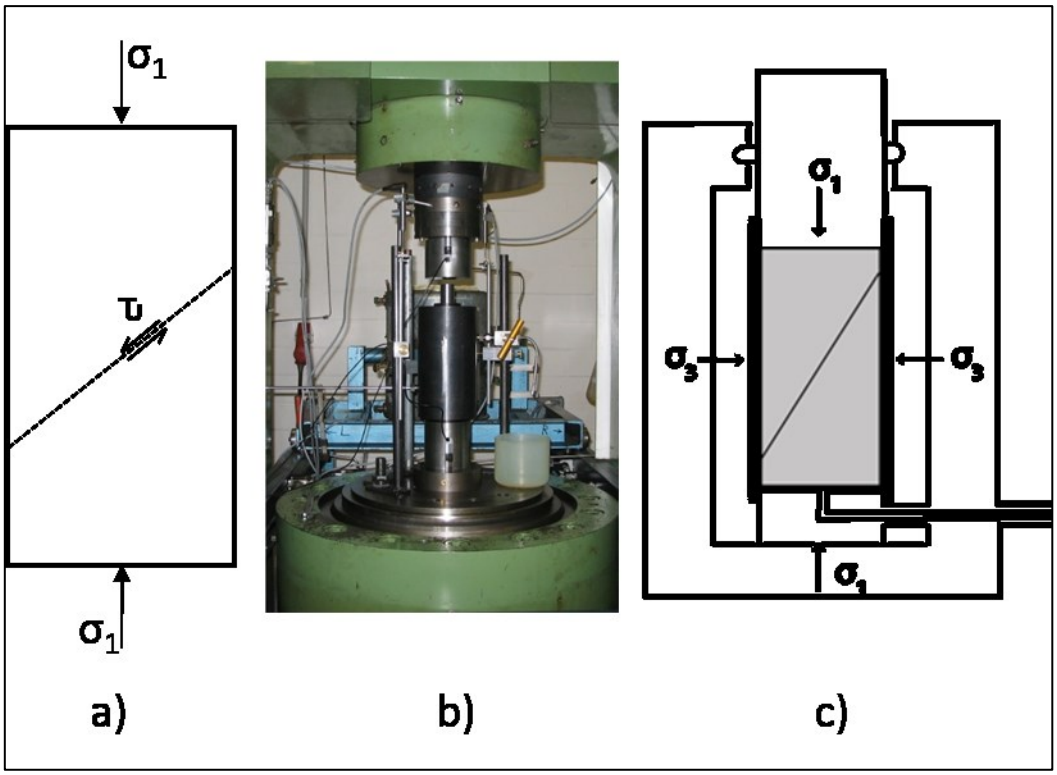


Figure 4. 12: a) potential shear failure plane; b) and c) triaxial deformation rig set up in which a confining pressure (σ_3) is applied via a fluid pressure, Pf. The sample is then loaded axially (σ_1) until failure is achieved.

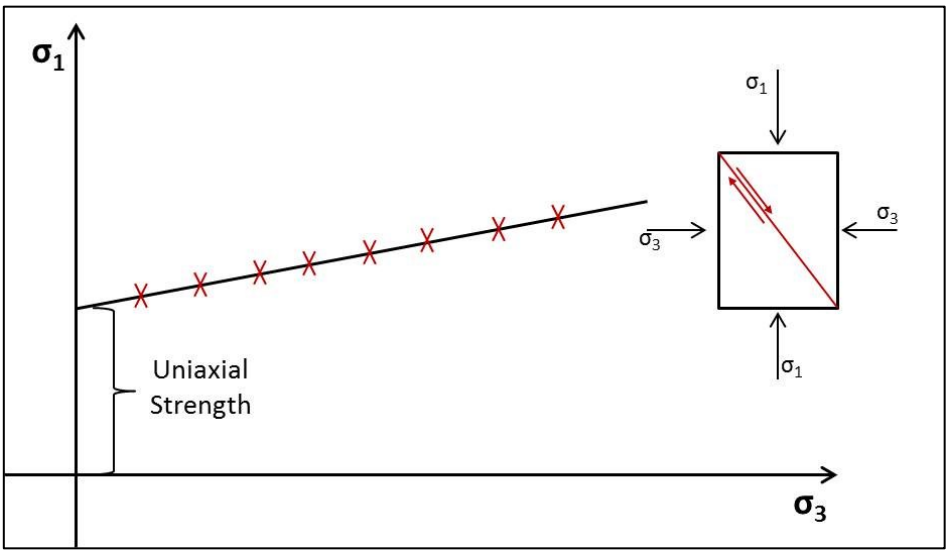


Figure 4.13: graphical expression of the results rock failure experiments (see Figure 4.11). Axial load vs confining stress at failure enables the uniaxial strength of the rock to be determined and shows that rock strength increases with increase in confining pressure (adapted from Cosgrove, 2005).

Another form of representing the data from these laboratorial experiments is to plot the series of pairs of σ_1 and σ_3 as Mohr circles in a graph of τ vs σ (Figure 4.14). The tangent to the sequence of circles represents the failure criterion for shear failure – the Mohr- Coulomb shear failure criterion. Any stress state represented by a Mohr Circle that does not intersect the failure envelope, will contain no plane on which the shear stress is of sufficient magnitude to cause failure and will therefore represent a stable stress state. If the tangent to the Mohr circles is a straight line (Figure 4.14) then the equation of the failure criterion is the line $\tau = C+\mu\sigma$. This experimentally derived shear failure criteria is identical to the theoretically derived criteria by Coulomb (Eq. 4.21). It follows therefore that the intersection with the vertical axis (τ) represents C_0 – the internal cohesion of the material and the slope of the line the angle of sliding friction.

The orientations of the planes where this criterion is first met can be found by substituting the biaxial stress equations (4.5) and (4.6) into the shear failure criterion (4.21) and solving it for the minimum. It is found that the optimum orientations for shear fractures are (4.22):

$$\sigma = \sigma_1 \sin^2\Theta + \sigma_3 \cos^2\Theta \qquad (4.5)$$

$$\tau = (\sigma_1 - \sigma_3)\, \sin\Theta.\cos\Theta \qquad (4.6)$$

$$\tau = C_0 + \sigma_n \tan\Phi \qquad (4.21)$$

$$\theta = \pm(45º - \frac{\Phi}{2}) \quad (4.22)$$

,where Θ is the angle between the maximum compressive stress (σ_1) and the failure plane (Figure 4.11i) and Φ the angle of internal friction of the rock. The optimal angle can also be read by using the point of intersection of the Mohr Circle with the failure envelope (Figure 4.15).

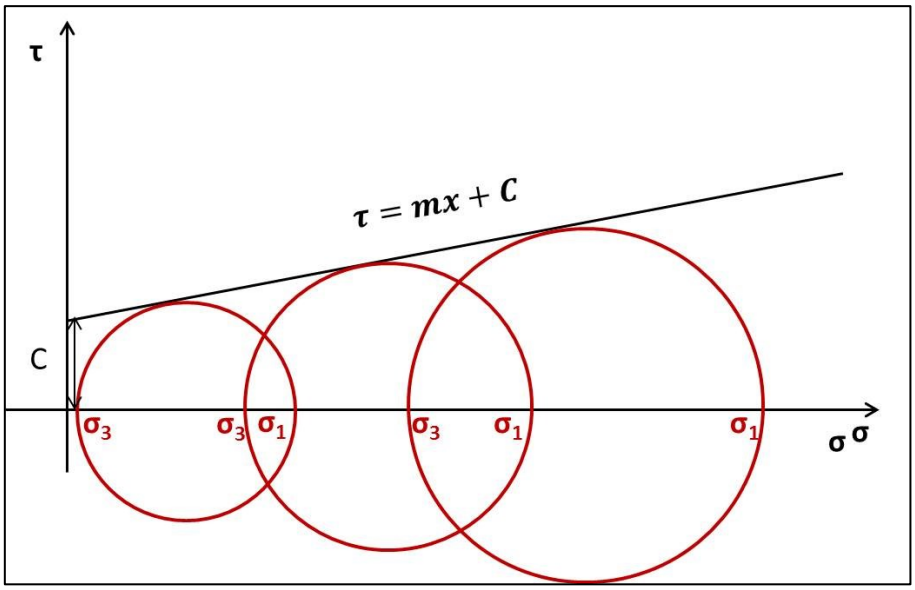


Figure 4.14: same data as Figure 4.12, plotted as a series of Mohr circles. The tangent to these circles defines the shear failure envelope (Cosgrove, 2005)

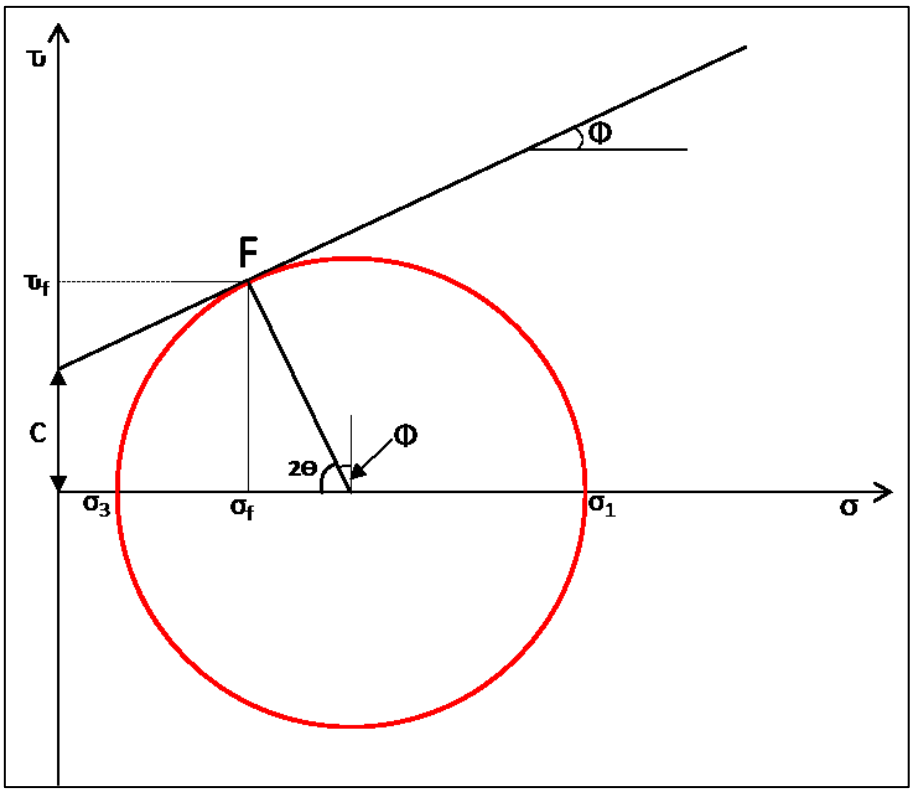


Figure 4.15: Mohr circle representing a stress state that causes rock failure. Values of shear and normal stress that cause failure are given from the axis at point F (τf and σf). Note that 2Θ= 90 – Φ and consequently Θ= 45-Φ/2. Considering that most rocks have an internal friction angle of 30, the most likely angle (Θ) between a shear fracture plane and the maximum principle compressive stress (σ_1) should be ≈30°.

Griffith criterion: Tensile Failure

Griffith studied tensile failure and argued that theoretically there should be a relationship between the interatomic bond strength of a material and its tensile strength. No such correlation was found and the measured tensile stress was several orders of magnitude less than the predicted value. Griffith realised that this difference was due to the flaws existing in the materials and postulated that this was a result of intense local stress concentration developed around the tips of these microscopic flaws (Figure 4.16). For mathematical convenience he assumed elliptical shaped flaws with large eccentricity, and calculated the stress concentration around them using a 2D thin plate model subjected to tensile stress. On the first plate (Figure 4.16 a) the stress is evenly distributed, while on the plate that contains a flaw (Figure 4.16 b and c), stress is magnified around the flaw tips. This magnification depends on the orientation of the flaw relative to the principle stresses and its eccentricity: the larger the eccentricity, the larger is the stress magnification.

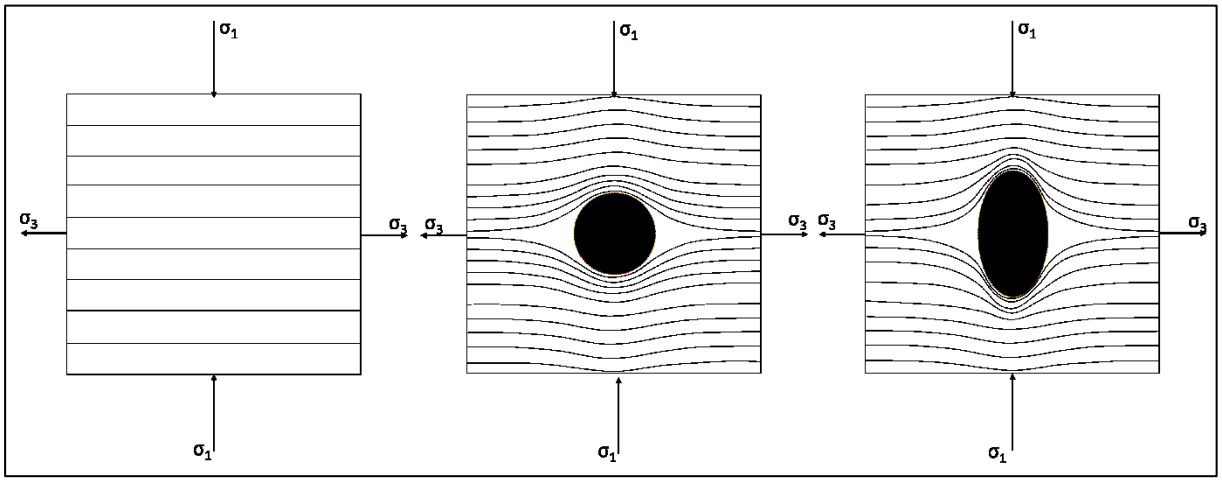


Figure 4. 16: schematic representation of stress concentration around a microscopic flaw inside a body subjected to tensile stress. Notice that an increase of the eccentricity of the flaw causes a magnification of the stresses around it. Adapted from Cosgrove (2005)

This local magnification may lead to failure even when a relatively low bulk stress is applied. Based on these observations, Griffith developed the following failure criteria:

$$\tau^2 + 4T\sigma_n - 4T^2 = 0 \quad (4.23)$$

The graphical expression of Equation (4.23) is a parabola and it is shown in Figure 4.17. It can be seen that by setting σ_n=0 in equation (4.23), τ=2T, which corresponds to the cohesive strength (C) of the Mohr-Coulomb shear criterion. The two criterion, Mohr-Coulomb and the Griffith criteria, are usually

linked where their slopes are identical. With this it is possible to obtain a complete criterion for brittle failure (Figure 4.18).

What determines whether a particular stress field will cause a shear or a tensile fracture is formed is clearly whether the Mohr circle representing that stress field touches the failure envelope on the shear failure criterion or the tensile failure criterion zones. In Figure 4.18, the dashed Mohr circle represents a stable stress field, i.e. one which will not cause the rock to fail while the blue and the red circles will cause shear and extensional failure respectively. As noted above it is known that C=2T and it follows from the geometry of Figure 4.18 that if the diameter of the Mohr circle is greater than 4T, it will be too large to intersect the extensional failure envelope. Clearly in order satisfy the condition for extensional failure the diameter of the circle (σ_1-σ_3), i.e. the differential stress, must be less than 4T. Conversely for shear failure to occur the differential stress must be greater than 4T. Hence what defines the type of failure is the magnitude of the differential stresses:

- ($\sigma_3 - \sigma_1$)<4T : Tensile failure
- ($\sigma_3 - \sigma_1$)>4T : Shear failure

The orientation of the fractures that form is determined by the orientation of the stresses: tensile fractures open perpendicularly to σ_3 and shear fractures at an angle Θ=45-Ø/2 (see Equation 4.22) to the maximum principal compression σ_1.

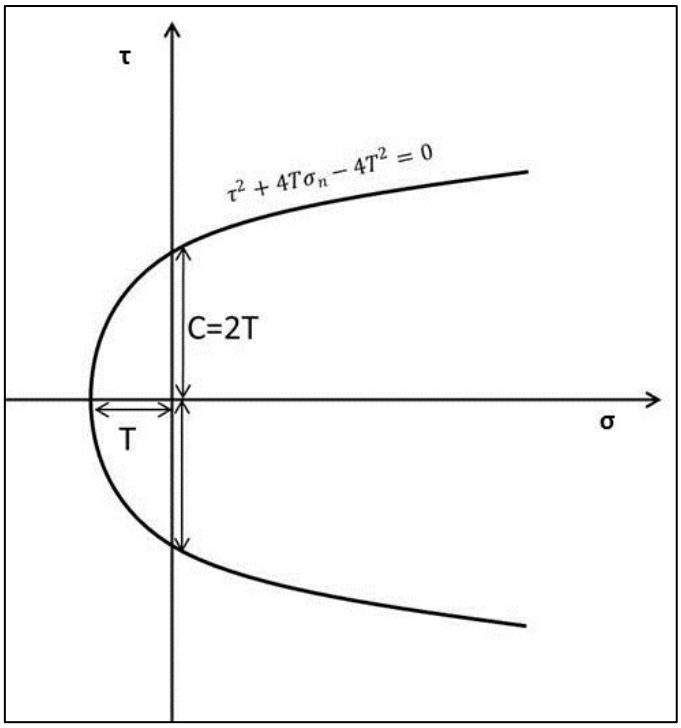


Figure 4.17: graphical expression of the Griffith criterion for tensile failure. The intersection of the parabola with the τ axis gives the cohesive strength of the rock and with the σ axis its tensile strength. Adapted from Cosgrove, 2005.

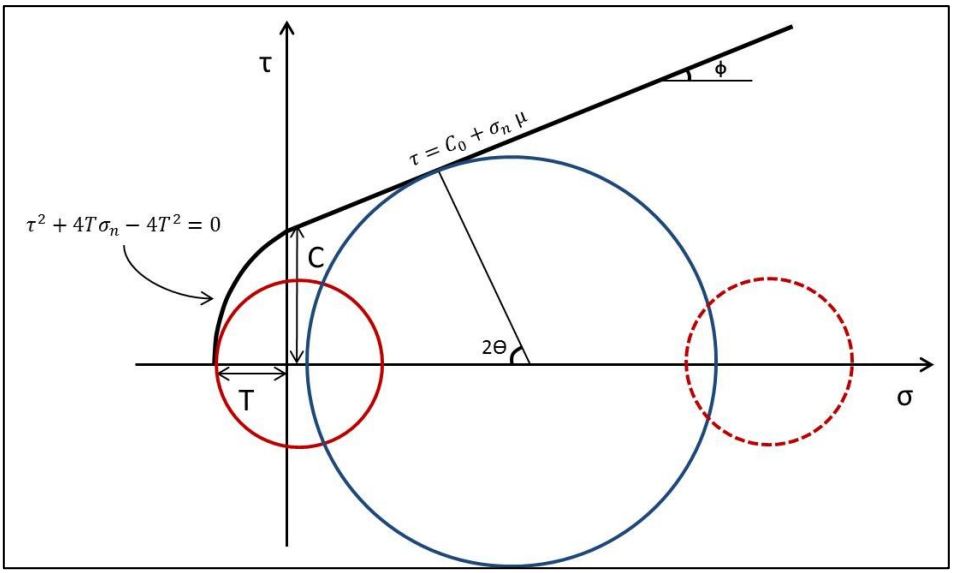


Figure 4.18: the graphical expression of the combined Mohr-Coulomb-Griffith criteria. Adapted from (Cosgrove, 2005).

As demonstrated for the shear failure (Figure 4.15), the magnitude of the stress that causes failure and the orientation of the failure plane can also be determined for extensional fractures (Figure 4.19). In this case, the Mohr circle touches the failure envelope on the horizontal axis at point (– σ, 0) where the state of stress on the failure plane is (τ = 0, σ = – T) and the angle (2θ) between the maximum principal stress (σ_1) and the fracture plane is zero. Therefore, extensional failure fractures form parallel to σ_1, (opening perpendicularly to the least principal stress σ_3) with no shear stress acting along them. Thus, the normal stress must be equal to the tensile strength of the rock (T).

Apart from pure tensile and pure shear fractures, fractures which have characteristics of both extensional and shear fractures exist. These have been termed hybrid fractures and can be represented by the Mohr circle of Figure 4.20. Using the same procedure as above, it can be seen that the angle 2Θ is lower than 60° - the classical angle for shear failure. Hybrid fractures occur in the portion of the failure envelope between (τ = 0, σ = – T) and (τ = τ_o, σ = 0) and therefore Mohr circles will have a diameter larger than 4T but a very restricted set of 2Θ angles. The tensile nature of these fractures is easily explained by analysing the magnitude of both the shear and tensile components: the normal stress on the plane is in the extensional zone (-σ) but the shear stress component is not zero as for pure extensional failure (see Figure 4.20). Therefore the failure plane experiences both extension and shear.

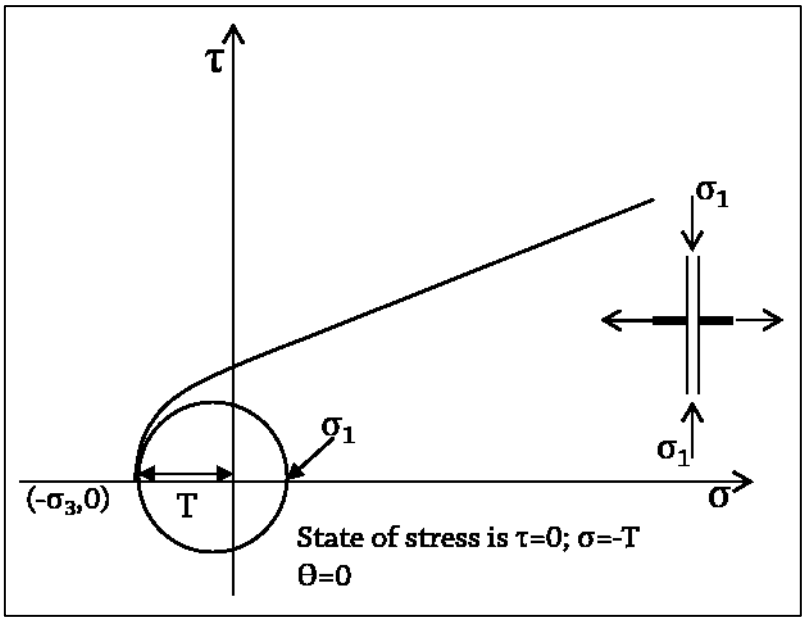


Figure 4.19: Mohr circle representing a tensile fracture. Notice that at failure shear stress on the failure plane is equal to zero and the normal stress is equivalent to the tensile strength of the rock. Fractures will open parallel to σ_1.

Figure 4.21 summarizes the values of differential stress and 2Θ for the three failure modes (extensional, hybrid and shear). In extensional failure, and as seen before, 2Θ= 0 (a situation where the failure plane is parallel to the maximum compression) and the differential stress $(\sigma_1 - \sigma_3) < 4T$. During hybrid failure the differential stress ranges between 4T and 5.66T and the 2Θ angle shows a very rapid rise for this very limited range ($0° < 2\Theta \leq \approx 45°$). In addition it will be recalled that $\Theta = 45 - \frac{\Phi}{2}$ where Φ is the angle of internal friction.

These two factors indicate that the geometry of the hybrid fractures is unlikely and that they will often be difficult to recognize.

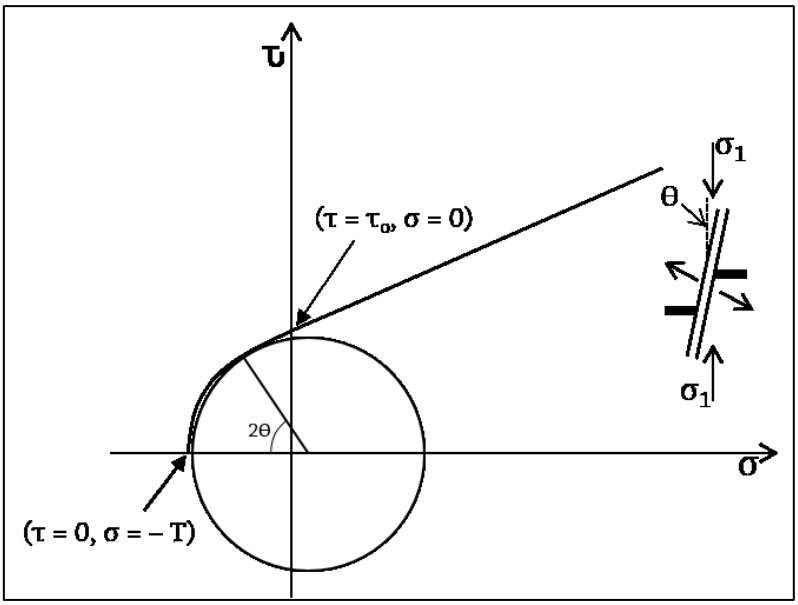


Figure 4.20: Mohr circle representing an hybrid fracture.

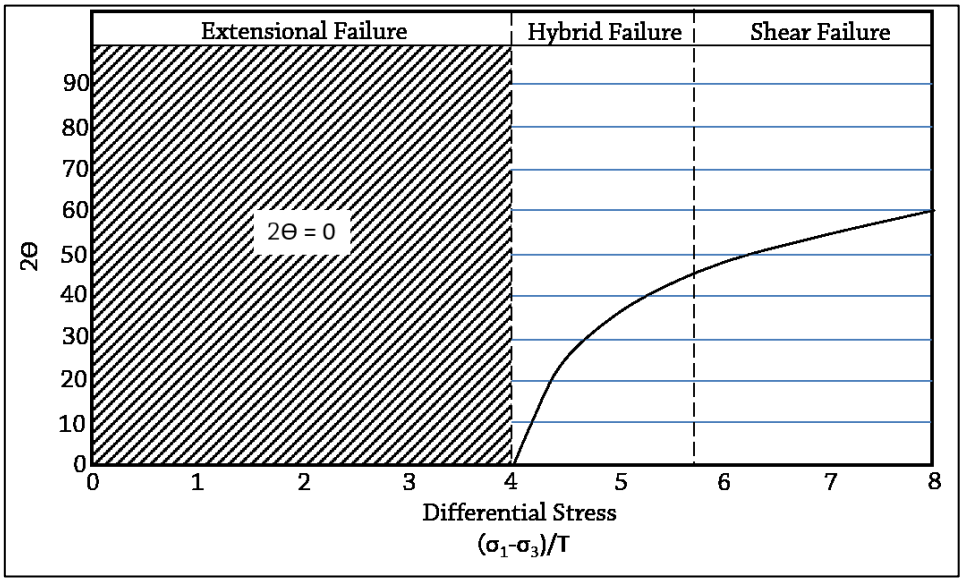


Figure 4.21: Range of magnitudes of differential stress and 2Θ angles for the several types of failure.

4.3.2 The link between extensional and shear failure

Tensile and shear deformation are the two end members and principle modes of brittle failure. These are distinguished because they have different failure criteria, the resulting fractures have different orientation with regards to the applied stress field, they form under different stress conditions and the sense of movement on the fractures is different. However, despite these differences these two

mechanisms appear to be closely related and there are several studies that argue in favour of a fundamental link between shear and extensional failure:

- Kindan & Cosgrove (1996) present field examples that suggest that prior to the formation of either extensional or shear fractures in a rock, small-scale extensional cracks oriented normal to the least principal compression σ_3, develop randomly through the rock. It is the differential stress that determines what occurs next: if the differential stresses favour tensile failure (i.e. when the differential stress is less than 4T, where T is the tensile strength of the rock), some of these fractures extend and link to form macroscopic extension fractures. Conversely, if the differential stress is greater than 4T, the extensional cracks become organised into a systematic en echelon array (Figure 4.22) arranged symmetrically around σ_1 in exactly the same way as classical shear fractures.

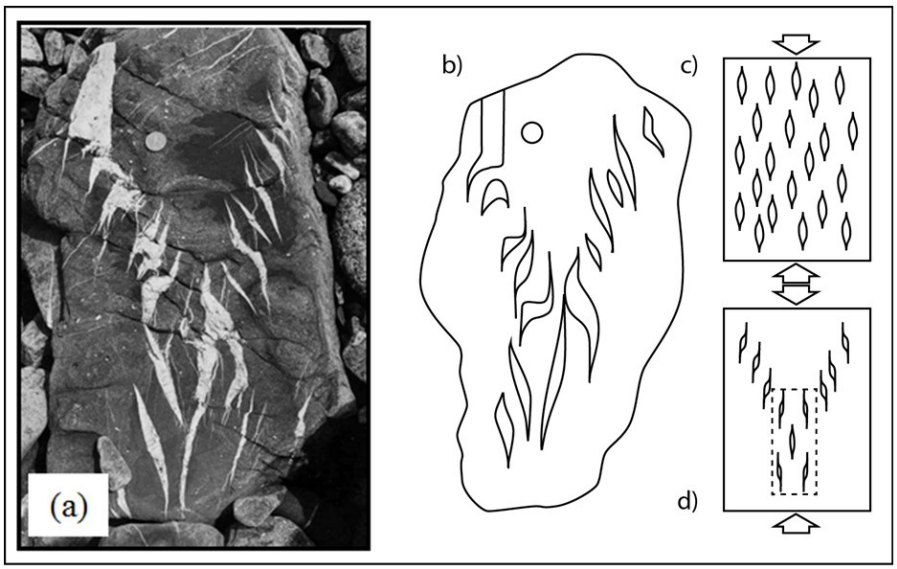


Figure 4.22: Conjugate sets of *en echelon* tension fractures defining zones of shear failure in the rock. b) sketch of a). c) The uniform distribution of tension gashes in a rock representing a 'bulk' extensional failure. d) The organisation of small-scale extensional fractures to produce macroscopic shear failure. From Kidan and Cosgrove, (1996).

- The field work presented in Section 3.5.4 also shows that bedding-normal tensile fractures that form in the competent limestone are linked by inclined cross fractures which cut through the shales (Figure 4.23) to form an embryonic shear fracture inclined at 30° to σ_1. This process is shown in Figure 4.23.



Figure 4. 23: field example of an embryonic shear fracture through a shale layer linking tensile fractures that formed in the limestone layers.

- Hallbauer *et al.* (1973) conducted experimental work by axially loading cylinders of quartzite encased in a strong confining jacket causing the confining stress to rise during loading. He observed that at determined critical load, clouds of micro-cracks begin to form throughout the rock – the onset of microscopic brittle failure. These are mainly inter-granular and tend to be parallel to σ_1. As the differential load increases the density of these fractures also increases and when the point where the shear strength of the material is reached they localise in a shear band (Figure 4.24).

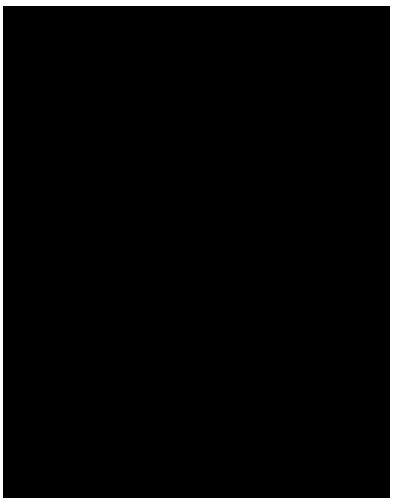


Figure 4.24: Idealised model showing the formation of through-going shear fractures by the linking of individual, isolate extensional fractures. a) From Mandl, (2000) after Hallbauer (1973).

- Numerical modelling was also used to illustrate the link between small-scale extensional and shear fractures. Figure 4.25 shows the results of a numerical experiment for crack propagation where an inclined fracture is incorporated into the numerical sample which is then loaded axially. Initially, extensional wing fractures form at the end of the crack and, as deformation proceeds, more extensional microfractures form which eventually link to form macroscopic shear fractures.

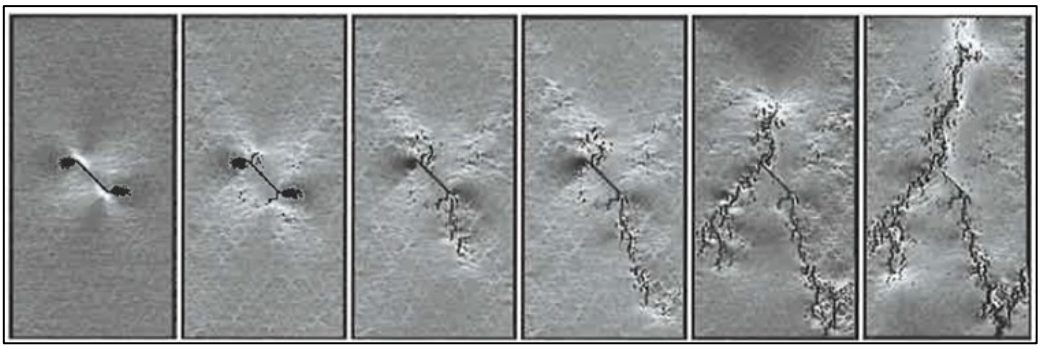


Figure 4. 25: Six stages in the deformation (left to right) of an axially loaded elastic slab in which an inclined crack is initially present. The deformation is dominated by the formation of extensional microfractures which coalesce to form macroscopic shear fractures. From Cosgrove and Hudson (2016) after Tang and Hudson (2010).

4.4 Fluid pressure, effective stresses and hydraulic fractures.

Fluids in rocks can be present as water, brines or hydrocarbons. Their importance in rock strength and in controlling rock failure is well known and has resulted in research into both aspects. Water inside a crystal can reduce its strength to a tenth of what it would be when dry (Rehbinder & Lichtman, 1957); and it can reduce the uniaxial strength of a completely saturated rock to about 45% of its dry strength (Price, 1960). Even though these chemical effects are important, the mechanical effects that fluids have on rocks are of even greater importance. Price & Cosgrove (1990) point out that rocks deform as ductile materials at moderate confining pressures and low fluid pressures, but when the later is close to the magnitude of the confining pressure rock tends to behave as brittle materials – fluid pressure influences the mode of deformation and this is closely related to the concept of effective stress.

In a porous rock subjected to compression (S), stress (σ) is developed in the granular part of the rock, and a fluid pressure (p) in the pores which are filled with fluid (pore pressure can be defined as the sum of all forces that act perpendicularly across the fluid part of a large cross-sectional or surface element (Mandl G. , 2005)). In its simplest form, the relationship found by Terzaghi (1923) and Hubbert & Rubey (1959) between stresses and the fluid pressure can be written as: $S - p = \sigma$, where σ

is the effective stress which causes the deformation of the rock mass. Hence, the effective principal stresses (σ) are not equivalent to the applied stress but are:

$$\sigma_1 = S_1 - p \quad (4.24)$$

$$\sigma_3 = S_3 - p \quad (4.25)$$

The stresses acting on the rock mass are reduced the fluid pressure to an effective stress. It is important to note that the fluid pressure does not have influence on the shear stress since the pore fluid cannot transmit net shear stresses across a macroscopic interface (Mandl G. , 2005). This is apparent when equation 4.24 and 4.25 are substituted into the biaxial stress equations 4.5 and 4.6. σ_1 and σ_3 are reduced but τ is unaffected

$$\sigma = \sigma_1 \sin^2\theta + \sigma_3 \cos^2\theta \quad (4.5)$$

$$\tau = (\sigma_1 - \sigma_3) \sin\theta.\cos\theta \quad (4.6)$$

The importance of fluid pressure is such that it is actually considered the driving mechanism of tensile failure (Secor, 1965). The apparent paradox observed by geologists of the existence of innumerable tensile fractures (joint sets) in the general compressive environment of the crust can be resolved by assuming a hydraulic fracturing mechanism, where the least principal stress becomes tensile under the influence of high fluid pressure:

$$(\sigma_3 - p) > T \quad (4.26)$$

where, T is the tensile strength of the rock. As already mentioned the other requirement for the rock to fail in tension is that the differential stresses are smaller than four times the tensile strength of the rock (Figure 4.26). In other words, extension fractures develop when the differential stress is less than four times the tensile strength of the rock and the fluid pressure equals or exceeds the least principal stress and the tensile strength of the rock:

$$p > \sigma_3 + T \quad (4.27)$$

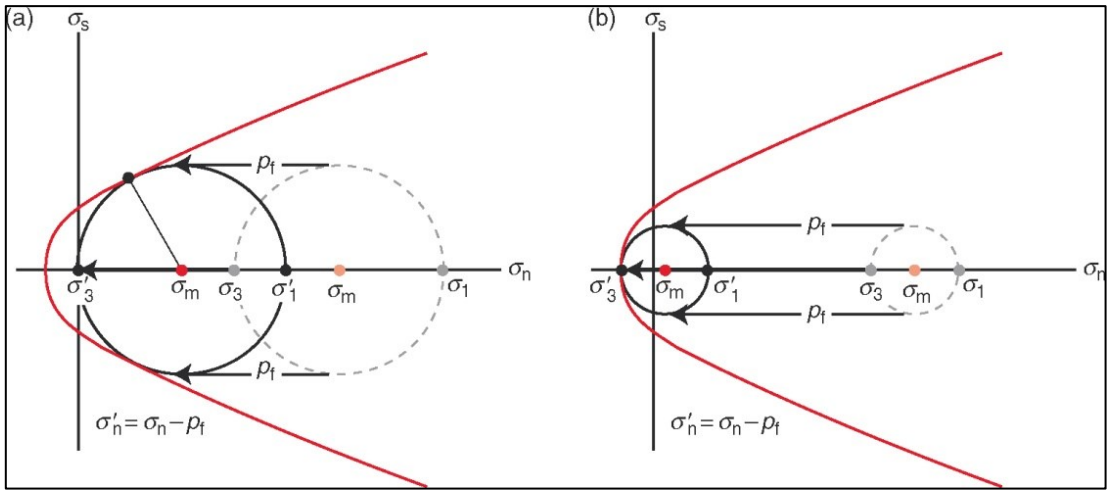


Figure 4.26: effect of increasing fluid pressure p_f in a rock, illustrated by a Mohr Diagram. In rock (a) the differential stresses are larger than 4T which causes the Mohr circle to touch the failure envelope on the shear side and shear fractures (Mode II) to be formed. In rock (b) the differential stresses are small and the rock will undergo tensile failure, with the formation of tensile (Mode I) fractures (Fossen, 2010).

Another important phenomena that is related to the existence of fluids within porous rocks is the poroelastic effect, developed by Biot in 1935 and 1941 and which is consistent with two principles (Detournay & Cheng, 1993):

a) an increase of pore pressure induces a dilation of the rock, and
b) compression of the rock causes a rise in pore pressure, if the fluid is prevented from escaping the pore network.

The best way to illustrate the concept of poroelastic effect and the impact that it might have on fracture formation is by using the explanation provided by Engelder (1993) of a force-balance model, outlined in Figure 4.27. Here a model of a rock constrained by rigid boundaries on all sides is presented. The model consists of grains, elastic grain-grain contacts and interconnected pore space. Assuming that the rock is initially dry, the walls of the container press the grains of the rock together with an average stress normal to walls σ_w. The stress is not evenly distributed along the walls but it is concentrated at the grain-wall contact points. The grain-wall contact stress (σ_{gw}) depends on the area across which it is distributed and it can be expressed in terms of the porosity ($\emptyset$):

$$\sigma_{gw} = \frac{1}{1-\emptyset}\sigma_w \quad (4.28)$$

Filling all the pores with a fluid at a moderate pressure (p_f), causes the pressure against the walls to increase, but not evenly. Pressure will act directly on the zones of the walls which are in direct contact with the fluid and the normal stress (σ_n) at the wall will increase by p_f, whereas at the grain-wall contact points, the normal stress will increase by a fraction of p_f that is αp_f, where $\alpha < 1$. Here the increase in normal stress σ_n will be less than p_f by an amount which is dependent on rock porosity (4.29):

$$\Delta\sigma_n = \emptyset p_f + (1-\emptyset)\alpha p_f \quad (4.29)$$

where, α denotes the Biot's poroelastic parameter. The fractional increase in normal stress is due to the cementation of the grains that act like springs taking up through elastic deformation part of the force exerted by pore fluid pressure. This partial transfer of pore pressure to the boundary is known as the poroelastic effect (Engelder, 1993; after Biot, 1941).

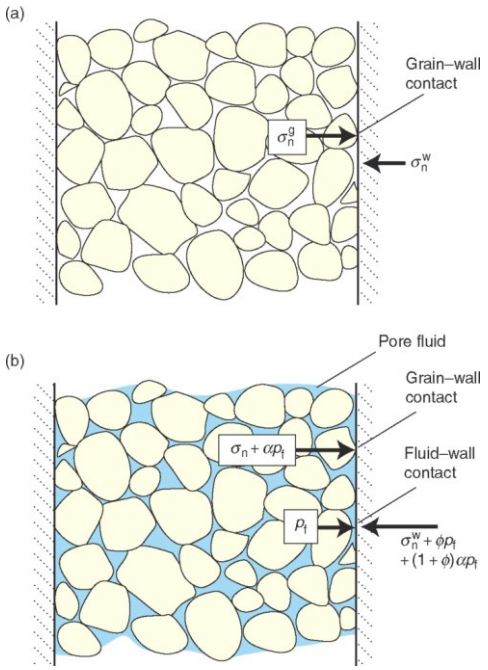


Figure 4. 27: Biot's poroelastic effect as illustrated by a porous rock within a container. a) In a dry rock, stresses are transmitted across the grain-grain or grain-wall contacts; b) when a fluid is added the increase in normal stress at the grain-wall contacts is smaller than the increase in pore pressure due to the absorption of stress by elastic deformation across the grains (Fossen, 2010, after Engelder, 1993).

The poroelastic effect is important in relation to the formation and propagation of tensile fractures. According to the Griffith's theory of brittle failure, stresses are magnified at flaws and these areas are potential locations for fracture nucleation. Increasing the pore pressure by an amount Δp_f gives a pore pressure, p_f, that will be identical within and outside the flaw if the rock is permeable. However at the walls of the flaw in contact with the rock grains, the average normal stress generated by an increase in pore pressure will increase at a lower rate than inside the flaw (where there's only fluid). With the increase in pore pressure, eventually the fluid pressure will exceed the normal stress (which counteract the fluid pressure) exerted by the rock grains creating tensile stresses on the walls of the flaw and allowing it to grow into a larger extension fracture. After the surface area of the fracture increases, the pore pressure drops and propagation stops until the pore pressure builds up again and the process is repeated (Figure 4.28)

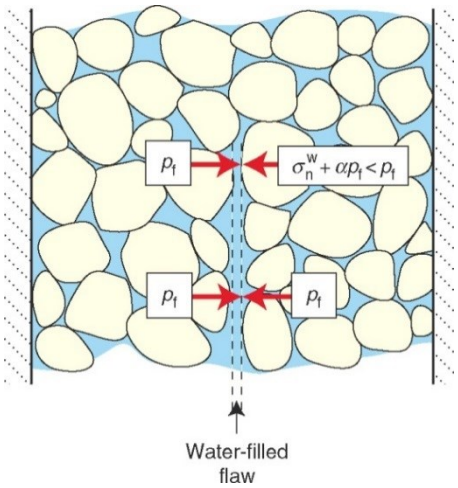


Figure 4. 28: a flaw in a permeable porous rock will "feels" the effect of the poroleastic effect when the stress across the grain-flaw part of the flaw is less than the pore fluid pressure. Tensile stress occurs if the pore pressure is sufficiently high (Fossen, 2010, after Engelder, 1993)

4.4.1 Internal hydraulic fractures, vs hydraulic intrusion fractures

As noted earlier, because the total stress in the Earth's crust is typically compressive, fluid pressures are necessary to change at least one of the principle stresses to an effective tensile stress in order for extensional failure to occur. Fractures that are formed by the action of high fluid pressures are called *hydraulic fractures*. Two types of hydraulic fractures can be considered (Mandl, 2005) (Figure 4.29): internal hydraulic fractures - when the pore pressure inside a rock layer is uniformly raised to a level where it overcomes the least principle compressive stress and the tensile strength of the rock - and hydraulic intrusion fractures that are formed when a rock layer is ruptured by the wedging action of a high-pressurized fluid injected from outside the layer. In the first, the stresses operating in the rock effectively become tensile, whereas in the later the rocks remain under compression.

Internal Hydraulic Fracturing (IHF)

The general process can be summarized as an increase in the internal fluid pressure in order to reduce the smallest effective stress to the value of the tensile strength of the material. The problem arises when considering two different situations: 1) where the layer is completely free to expand in elastic response to a uniform pressure rise and 2) where the layer is confined and not allowed to extend in lateral directions. Despite the fact that the principal stresses remain at the same orientations, the horizontal stress σ_h behaves differently in the two situations. Consider Figure 4.30 a), where a Mohr circle represents a stable stress field, i.e. one not capable of causing failure.

1) Free lateral expansion (Figure 4.30b): If a layer is free to laterally expand, then all stresses are reduced by the effect of the pore pressure and the Mohr circle is shifted towards the tension

domain without a change in diameter, i.e. the differential stress remains constant. Thus if at the onset of the build-up of fluid pressure the differential stress is less than 4T (as in Figure 4.30b) then it will remain so and any resulting hydraulic fractures will be extensional fractures.

2) Confined layer (Figure 4.30c): in a situation where there is a rise in fluid pressure but the layer is confined except in the vertical direction, the total overburden load (σ_v) remains unchanged but there is a raise in the total horizontal normal stress (σ_h). Therefore the decrease in the effective horizontal stress ($\Delta\sigma'_h$) is less than the decrease in the effective vertical stress (σ'_v).This causes the Mohr circle in Figure 4.29c to shrink while it is shifted towards the tension regime by an increase in fluid pressure. As mentioned, in order for failure to occur, the fluid pressure has to overcome the initial horizontal stress (σ_h) and the tensile strength of the rock but conditioned by a factor β related to the poro-elastic response of the rock:

$$\Delta p = (\sigma_h + T).\beta \quad (4.30)$$

Where:

$\beta = 1 - \left(\frac{1-K}{K_s}\right)(1-2\vartheta)(1-\vartheta)^{-1} < 1$ with, K- compression moduli of the bulk material of the rock; Ks – compression moduli of the solid material of the rock and U- Poisson's ratio. Typical values may lie between 0.4 and 0.7 (Mandl, 2005).

Hydraulic Intrusion Fracturing (HIF)

In contrast to internal hydraulic fracturing that forms under effective tensile stresses, intrusion fractures (Figure 3.29b) may be generated in a layer under effective compression, when the pressure of the injected fluid exceeds the sum of the total minimum compressive stress and the tensile strength of the rock. For the formation of such fractures, fluid pressure must satisfy the following conditions (Mandl, 2005):

$$\text{Dykes: } p_f > \sigma_h + T \ (\sigma_h = \sigma_3) \ (4.31)$$

$$\text{Sills: } p_f > \sigma_v + T_v \ (\sigma_v = \sigma_3) \ (4.32)$$

Where,

T–tensile strength when bedding is subjected to layer-parallel extension.

T_v - tensile strength when the bedding is subjected to layer-normal extension.

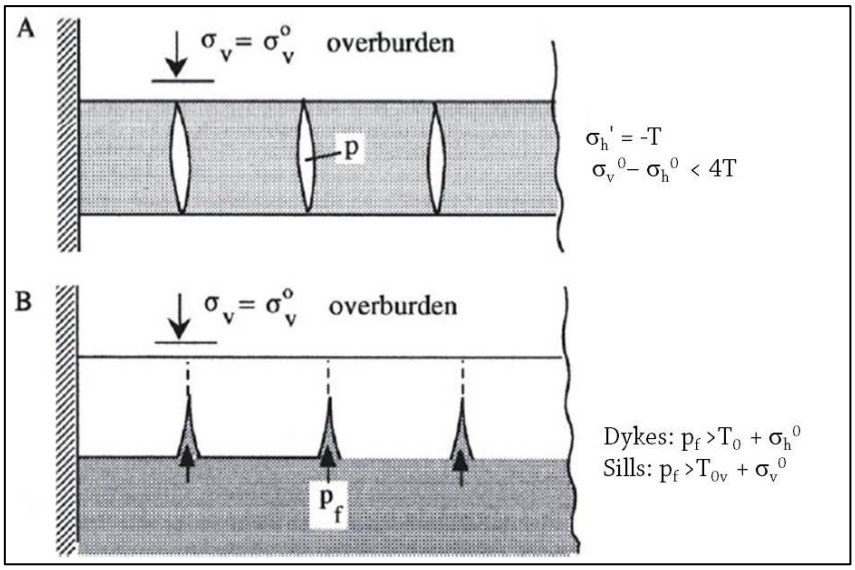


Figure 4. 29: A) internal hydraulic fracturing B) hydraulic intrusion fractures. σ_h'- effective horizontal stress; σ_v^0 – initial vertical stress; σ_h^0-initial horizontal stress; T- tensile strength; pf- pore fluid pressure. (Mandl, 2005).

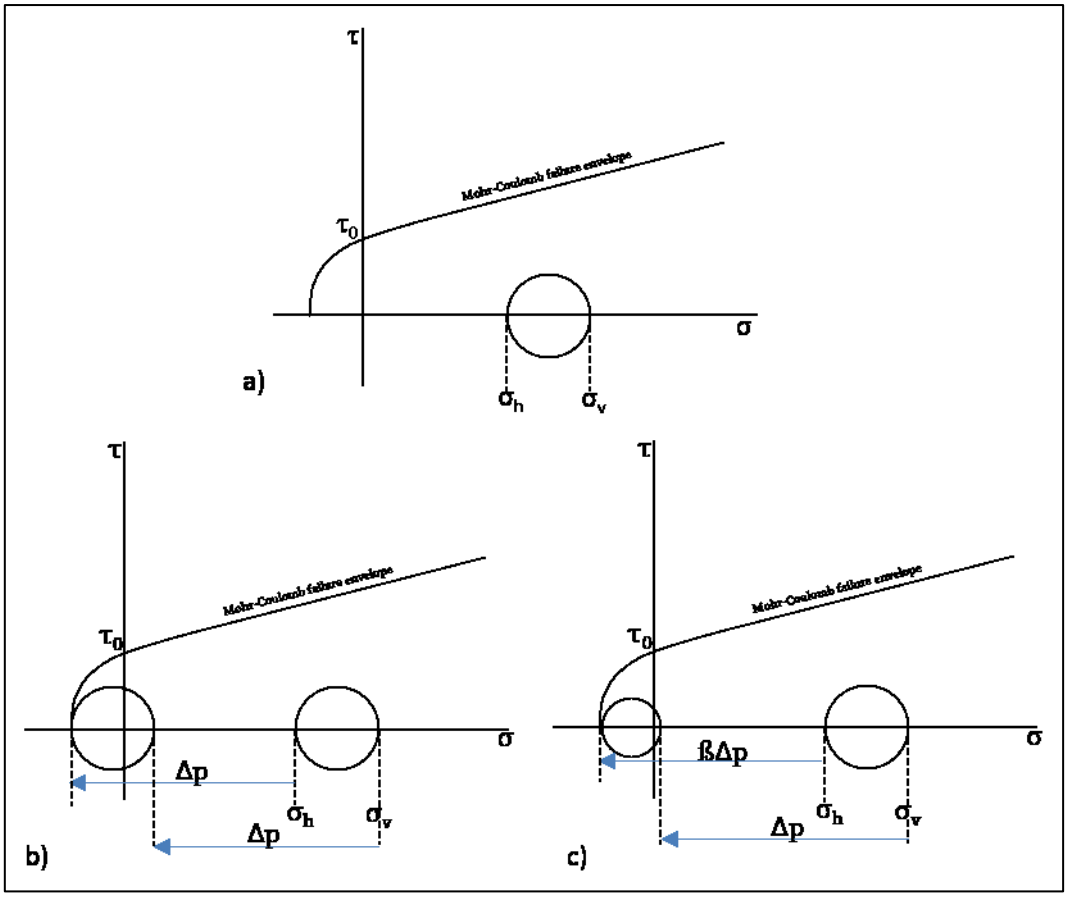


Figure 4. 30: a) Mohr circle representing a stable stress configuration; b) the effect of fluid pressure increase Δp on an horizontally unconfined layer; c) the effect of fluid pressure increase Δp on horizontally confined layer (adapted from Mandl, 2005). Where Δp – variation in fluid pressure; σ- normal stress; τ- shear stress.

An assumption made so far to explain the process of hydraulic fracturing is that the rock is homogeneous and isotropic. In such cases, the tensile strength is constant in all directions and the material properties have no influence on the orientation of the fractures which is completely controlled by the stress. However, most rocks are not isotropic. Instead they possess some form of anisotropy, particularly planar anisotropy such as bedding planes, cleavage or even veins such as those observed in Brightling Mine. In cases such as these, there is an orientation within the rock along which fracturing will occur more easily. Consequently, when the fluid pressure builds up in such a rock the anisotropy of the stress field and of the material compete to control the orientation of the fractures that form. Consider a block of rock as illustrated in Figure 4.31 subjected to an overburden load and an induced horizontal stress. This rock has two distinct tensile strengths, one large parallel to the bedding (Tp) and the other smaller normal to the bedding (Tn). Therefore the applied stress will favour the formation of vertical fractures (normal to bedding) whereas the material properties the formation of horizontal, i.e. bedding-parallel fractures.

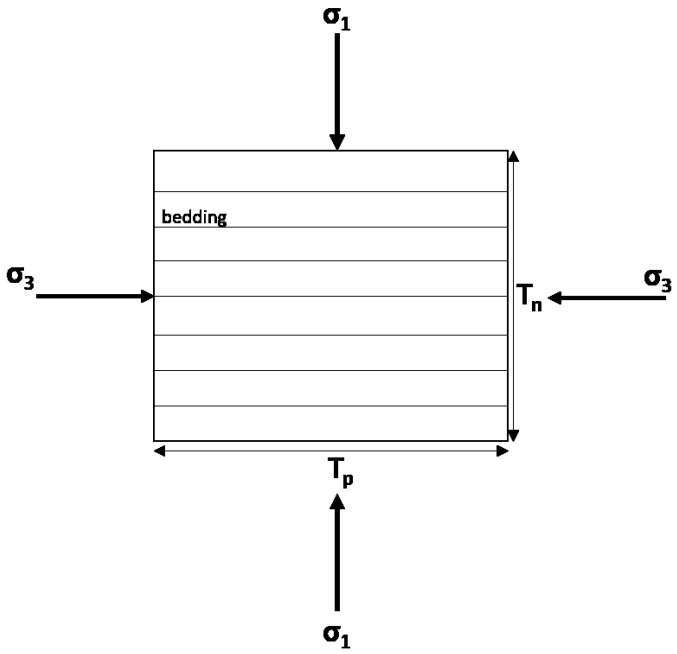


Figure 4. 31: An anisotropic (bedded) rock subjected to a biaxial stress field. Tp the tensile strength parallel to bedding and Tn the tensile strength normal to bedding.

The conditions for the formation of fluid induced fractures in each direction can be found by writing the formulas of the condition for hydraulic fracturing:

i) for vertical fractures the fluid pressure should equal or exceed the normal stress (σ_3) and the tensile stress parallel to bedding (Tp) :

$$Pfluid = \sigma3 + Tp \quad (4.33)$$

ii) for horizontal fractures to form the fluid pressure should equal or exceed the normal stress (σ_1) and the tensile stress parallel to bedding (Tn)

$$Pfluid = \sigma1 + Tn \quad (4.34)$$

However in order for bedding-parallel fractures to form, i.e. for the material properties to dominate and for the fractures to open against σ_1, condition 4.34 should be reached before condition 4.33. That is:

$$\sigma1 + Tn < \sigma3 + Tp \quad (4.35)$$
$$(\sigma1 + \sigma3) < (Tp - Tn)$$

From this, it follows that if the difference between the tensile strengths is greater than the differential stress, the material properties determine the orientation of the fractures and if it is less the stress controls fracture orientation.

4.5 Fracture spacing and saturation

Observation of fractures in layered rocks reveals that they often are organized as sets, i.e. arrays of fractures with the same orientation, and that they tend to present a fairly regular spacing between individual fractures. Several authors have focused their work in trying to understand the mechanical parameters that control this spacing. In this section the theoretical principles that govern fracture spacing and saturation are presented.

The model of Figure 4.32 shows the build-up of tensile stress in a horizontal competent layer by the ductile flow of adjacent, less competent beds. According to Price (1966) such scenario would develop during the subsidence of sediments as a result of the progressive increase in overburden stress. He considers that a fracture formed in a competent layer (A-A in Figure 4.32b) – which occurs when the tensile stress reaches the tensile strength of the rock - would continue to open, relieving the stress

over a wide region, if the layer was completely free to move. However, frictional shearing stresses τ (τ = $\mu\sigma_n$, where μ is the coefficient of sliding friction and σ_n is the normal stress acting normal to the interface between the competent and the incompetent layers) develop along the interface to oppose the opening. Price also notes that the fracture plane forms a free surface where the horizontal stress is reduced to zero but argues that because of the friction along the bedding plane, the stress gradually increases in intensity away from the fracture until it attains its original magnitude at some distance, L. This represents the minimum distance at which a second tensile fracture can develop. By balancing the horizontal forces attempting to extend the layer ($\sigma_T Z$, where z is the layer thickness) against the forces resisting the extension, ($2L\tau_{AV}$ the shear force acting along the top and bottom of the bed along the distance L, where τ_{AV} is the mean shear stress) (Equation 4.36) it can be seen that there is a direct connection between the spacing of joints and the thickness of the bed in which they form and that spacing is also dependent on the tensile strength of the rock in which the fractures are developing (σ_t). This model is in agreement with several field observations.

$$\sigma_T Z = 2L\tau_{AV} \leftrightarrow L = \sigma_T Z/2\tau_{AV} \qquad (4.36)$$

Price's model assumes no cohesion along the bedding plane and that resistance to slip relates only to friction, and an analysis where the layers are assumed to be welded together by strong cohesive bonds which exclude any interfacial slippage has been considered by Hobbs (1967).

Following the analysis made by Cox (1951) regarding the effect of orientation of fibres on the stiffness and strength of paper and other fibrous materials, Hobbs (1967) using a theoretical approach gives an explanation for the formation of tension joints in sedimentary rocks. His model is made up of a relatively strong, elastic layer (Young's modulus, E_1) sandwiched between two weaker layers (Young's modulus E_2, where $E_1 > E_2$) subjected to a uniform layer parallel extension and the theoretical derivation (Equation 4.37) predicts that the distance between two neighbouring joint planes is given by

$$l_2 = d\left(\frac{E}{G_n}\right)^{\frac{1}{2}} cosh^{-1}\left(\frac{e_2}{e_2 - e_2}\right) \quad (4.37)$$

Where:

l_2 : distance between two neighbouring joint planes

d: distance in the vertical direction of the perturbation of the stress system caused by the formation of the joint

E: Young's modulus of the jointed bed

Gn: shear modulus of the neighbouring beds

e_1: strain on the jointed layer

e_2: strain on the neighbouring beds

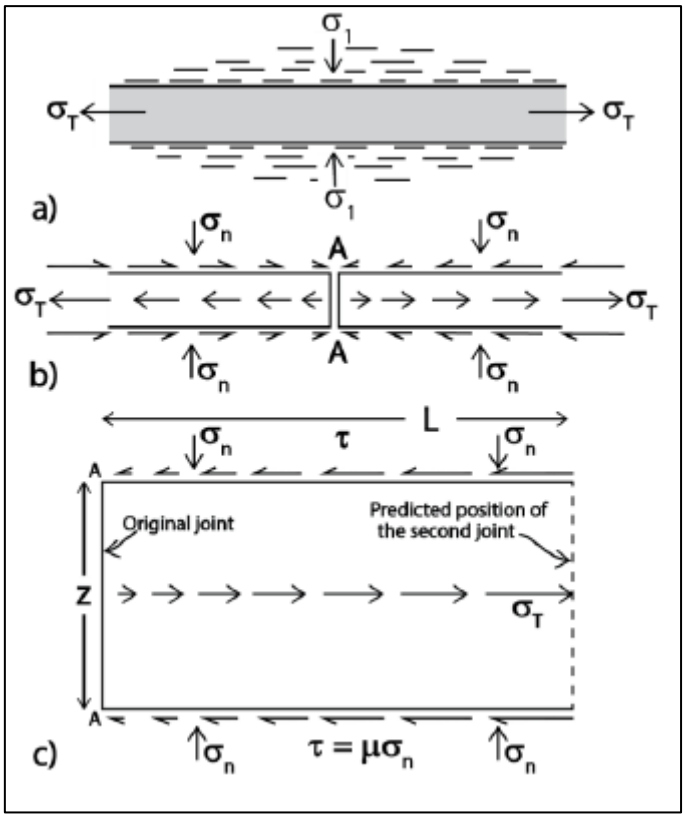


Figure 4. 32: Uniform tensile stress σ_T acting in a single, competent unit caused by the lateral flow of the adjacent, less competent beds in response to a layer-normal load caused by the overburden. b) Indicates the reduction in tensile stress due to the formation of a single joint, coupled with the development of a shear stress along the bedding planes which prevent excessive opening of the joint. c) Details of stress intensity in a section of competent bed length, L, and thickness, z, adjacent to the initial joint (Cosgrove & Hudson (2016), after Price, (1966)).

It follows that as strain increases, the distance between two neighbouring layers (l_2) decreases with increasing tectonic deformation and joint frequency is proportional to:

- the inverse of the bed or band thickness;
- the inverse of the square root of the Young's modulus of the bed
- the square root of the shear modulus of the neighbouring beds.

In summary Hobbs concludes that the frequency of occurrence of joints in a sedimentary bed is dependent upon the physical properties of the rock, the physical properties of the surrounding layers, the thickness of the layers, and the degree of tectonic deformation. A logical conclusion of Hobs work is that as strain increases, spacing decreases *ad infinitum*.

Both the mechanical model presented by Price (1966) which assumes no cohesion along the bedding and the occurrence of slip and the model of Hobbs (1967) which assumes total cohesion and no slip, predict a linear relation between layer thickness and fracture spacing and that the spacing is also influenced by the intrinsic properties of the rock, such as Young's modulus, Poisson's ratio and tensile strength.

However the relation between bed thickness and fracture spacing, does not hold when the layer thickness becomes large. Ladeira & Price (1981) have measured thousands of fractures in the Carboniferous turbidites of the Alentejo area (Portugal), in the Carboniferous flysch of Devon and Cornwall (UK) and in the limestones of Figueira da Foz (Portugal); so that the relationships between fracture spacing and bed thickness could be established for two markedly different lithological rock types (Figure 4.33a). The authors found that the linear relationship between bed thickness and fracture spacing predicted by Hobbs's (1967) and Price's (1996) models do not hold when the layer thickness becomes larger. The plots of Figure 4.33b show the data of Figure 4.33a plotted in a graph with the same scale for ordinate and the abscissa. In this figure it becomes clear that there is an initial linear dependence between the fracture density and bed thickness, but as the layer thickness increases beyond a certain limit (different for different rock types), fracture spacing remains constant regardless of the layer thickness.

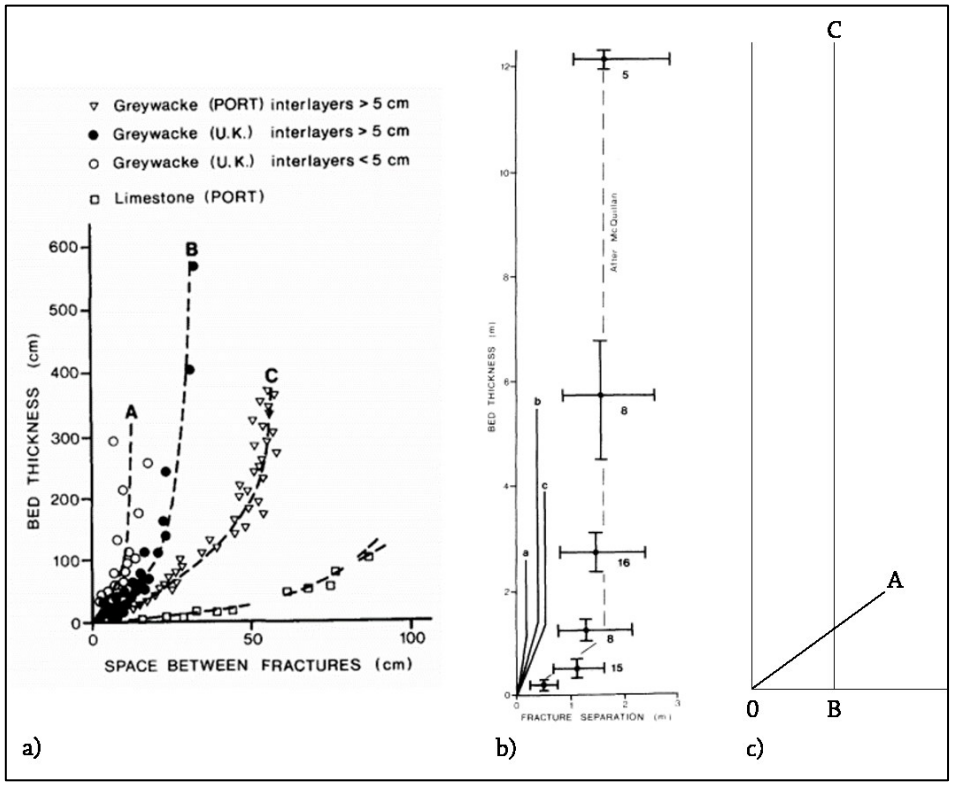


Figure 4. 33: Relationship between fracture separation and bed thickness for different rock types. Each point represents the mean of at least 50 readings (after Ladeira & Price, 1981).

Ladeira & Price, suggest that the data can be represented by two straight line relationships (Figure 4.33d) which are the result of two different mechanisms determining fracture development. The first of these relationships, indicated by line OA in Figure 4.33d) is the linear relationship defined by Price

(1966) and Hobbs (1967) as discussed above and that operates for thin beds. The second part of the relationship shows that the fracture spacing for a particular rock is independent of layer thickness and it comes in play when the thickness of the layer exceeds a determined value. The authors suggest that the fractures that form in thicker beds result from the hydraulic fracture mechanism. As outlined in Section 4.3.1 and 4.4, extension fractures develop when the differential stress is less than four times the tensile strength of the rock and the fluid pressure equals or exceeds the least principal stress and the tensile strength of the rock:

$$p > \sigma_3 + T \quad (4.38)$$

The authors argue that this mechanism also operates in the development of extension fractures in thin beds but because the stresses in such thin beds are mainly controlled by bedding plane slippage the hydraulic fracture mechanism plays a secondary role. It follows that fracture spacing in thick beds is therefore controlled by factors related to the fluid pressure within the rock: when a fracture forms a fluid pressure gradient is created between the low pressure fluid zone inside the fracture and the higher pressure fluid at some distance 'd' into the unfractured rock (Figure 4.34). It is at this distance, related to the gradient of the fluid pressure, the original conditions for fracture formation are met and a second fracture could develop. In turn the fluid pressure gradient is mainly determined by the rate of propagation of the fracture – related to the strain rate – and the permeability of the rock matrix – related to the lithology. In regards to the matrix permeability a logic conclusion is fractures in rocks with higher permeability will have fractures more widely spaced than fractures in rocks with lower permeability.

Ladeira & Price have also found that the development of fractures in the competent beds was also related to the thickness of the adjacent incompetent layers. They observed that when incompetent layers adjacent to fractured competent layers are 'relatively thick' the fractures in the competent layers are more widely spaced, i.e. there is less fractures, than when the adjoining incompetent layers are thin.

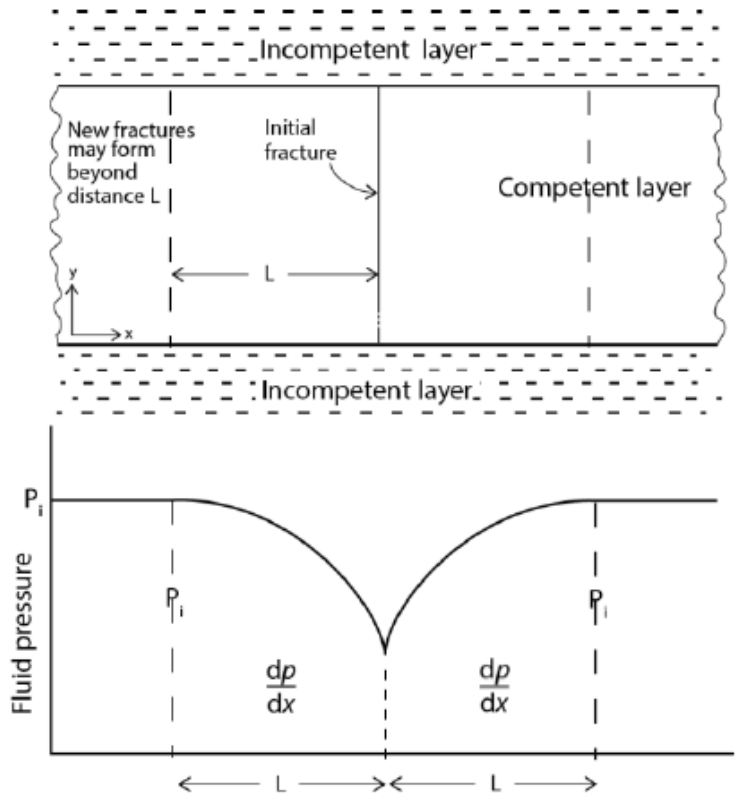


Figure 4. 34: Mechanism for the control of the spacing of hydraulic fractures by the permeability of the rock. Upper sketch: a thick bed under a high fluid pressure P_i which has resulted in the formation of an initial fracture. Lower sketch: the drawdown of fluid pressure around the initial fracture as a result of release of pressure by fluid expulsion along the fracture; the horizontal direction is the x direction (Cosgrove & Hudson (2016) after Ladeira and Price (1980)).

A concept which is closely related to the definition of fracture spacing is that of "fracture saturation". Fracture saturation can be regarded as the moment when a layer that is being subjected to deformation stops forming new fractures and additional strain is accommodated by further opening of existing fractures. Assessing fracture saturation is an important factor when calculating strain for a determined layer based on fracture spacing because this parameter (spacing) varies strongly with applied strain before saturation and at saturation it becomes independent of strain (Wu & Pollard, 1995).

Using analogue and numerical modelling techniques, Rives et al. propose that the spacing of fractures in layers obeys three types of distribution laws: negative exponential, log-normal and normal distribution. The authors suggest that they represent different stages in the evolution of a fracture set. The analogue modelling was accomplished by bending a stack of polystyrene plates in a way that the external part of the fold was subjected to a homogeneous extension (plane strain condition). Results showed that the spacing distribution is negative exponential at a stage with only few fractures, log-normal at intermediate fracture density, and tends towards normal at high fracture density, suggesting that the fracture spacing distribution law evolves with increasing fracture set development

(and with increasing deformation), from a negative exponential distribution to a log-normal distribution to a quasi-normal distribution.

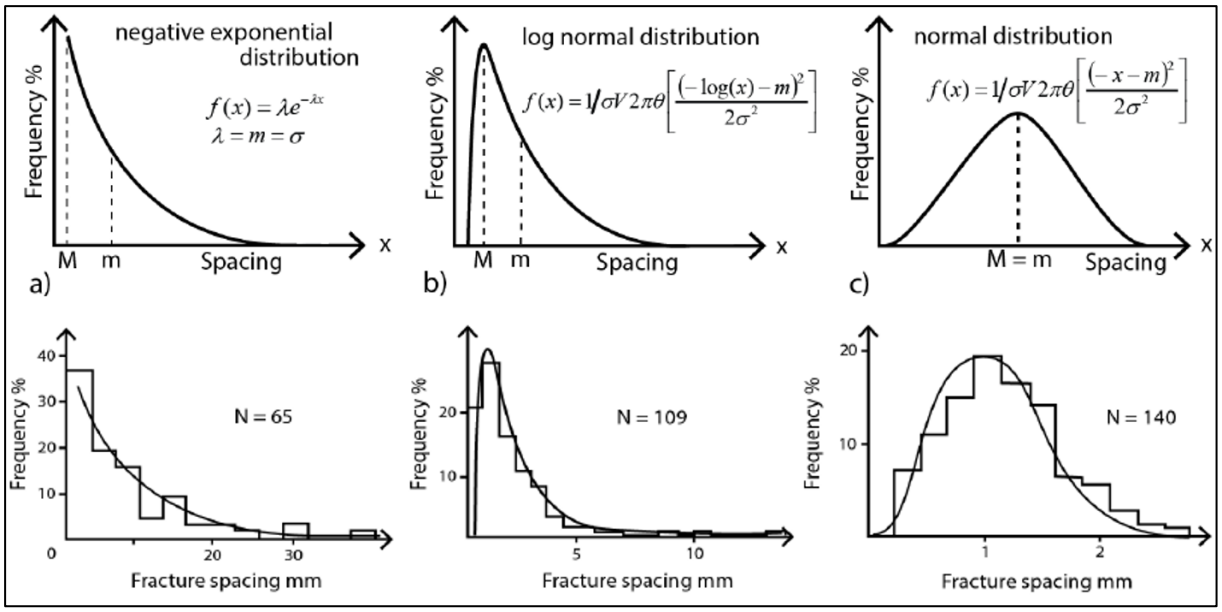


Figure 4. 35: Three types of spacing distribution found in natural fractures (top): a) negative exponential distribution, b) log-normal distribution, and c) normal distribution and (bottom) histograms and fitted distribution curves of the spacing observed at different stages during the generation of fractures in an analogue model. They represent three stages in the evolution of a regularly spaced set of fractures in an originally unfractured bed. M = mode, m = mean and σ = standard deviation. (adapted from Cosgrove & Hudson (2016) after Rives *et al.*, (1992)).

In order to attempt to reproduce and understand the joint development processes observed both in the analogue modelling and in the field, the authors have used numerical modelling. They used different joint spacing development processes and tested them by comparing the spacing in the model to real field data and to the results of the analogue modelling. It was found that a random process of fracture initiation and development, i.e. if at all stages in the evolution of the fracture set the system remains uninfluenced by the generation of fractures, the fracture spacing distribution would always plot as a negative exponential distribution which is in disagreement with the observations. If fact the process which yields results similar to what is observed both in the field and in the analogue modelling is a development process which the authors have named “Interaction Process”. In this process randomly positioned fractures are generated which have shadow zones around them. This was based on previous field and analogue work that demonstrated the existence of overlapping and 'hook' geometries indicating that there is interactions between fractures (Pollard et al. 1982; Segall & Pollard 1983).

Numerical modelling results show an evolution from a negative exponential distribution to a normal distribution which is in agreement with the observations. The authors suggest that, initially, fractures

are generated at randomly distributed irregularities within the material and therefore the histogram of fracture spacing plots on a negative exponential curve. It is argued that the formation of a fracture causes a local reduction in the extensional stress around the fracture and that this inhibits the formation of another fracture in the vicinity. On a later stage, with increasing fracture density, the shadow zones begin to overlap and interact. This interaction influences the fracture spacing and the histogram changes from negative to "Log normal" and finally to a "Normal distribution" when fracture formation ceases: the saturation level. Rives et al. argue that the results also indicate that the spacing distribution might be considered as an indicator of joint set development stage and that the evolution of the mode/mean ratio (from 0 to 1) with increasing number of generated fractures could also indicate the saturation level of a set: a low value (towards 0) signifies that the set is poorly developed; a high value (towards 1) indicates a nearly saturated set.

Bai and Pollard (2000b), argue that for fractures driven by tectonic extension, there is a critical fracture spacing to layer thickness ratio defining the condition of *fracture saturation.* They examined the stress distribution between two adjacent opening mode fractures as a function of the fracture spacing to layer thickness ratio and concluded that when the fracture spacing to layer thickness changes from greater than to less than a 'critical value' (approximately 1.0), the normal stress acting perpendicular to the fractures changes from tensile to compressive precluding further infilling of fractures. However if existing flaws and/or the fractures are driven by an internal fluid pressure or other mechanism fractures may continue to form. The authors found that this critical value of value of fracture spacing to layer thickness:

- Increases with increasing ratio of Young's modulus of the fractured layer compared to the neighbouring layers
- Increases with increasing overburden stress (depth)
- Decreases with increasing Poisson's ratio of the adjacent layers.

They also note that, for geologically realistic values of the elastic constants and depths, the critical fracture spacing to layer thickness ratio varies between 0.8 and 1.2.

4.6 Fracture propagation within and through layered media – the state of the art

Most geological rock formations present a certain level of internal layering, that is, they are not homogenous in terms of their vertical lithological properties. This is even more evident when analysing a sequence formed by several different geological formations, the most common situation in any geological context. A fracture propagating through these formations will therefore encounter different lithological units separated by interfaces. Both the lithologies and the interfaces will have different mechanical properties. This is particularly so for evaporites such as anhydrite rich successions which possess a very high level of vertical sedimentary variability. This interaction between interfaces and fractures strongly impacts the sealing capacity of caprocks formed by such lithologies; hence studying the way fractures propagate, understanding the extent of vertical fracture growth and containment in a layered rock and the parameters that control fracture propagation is of paramount importance when designing CO_2EOR/CCS operations (Teufel & Clark, 1984). What follows is a literature review on the state of the art in fracture propagation in layered sedimentary rocks.

4.6.1 Literature Review

By considering the previous work on the factors that control the propagation of fractures from one layer into another across an interface the key parameters likely to be involved in this process can be identified and used as a guide in planning the numerical modelling aimed at quantifying this process.

Some of the first studies done on how fractures propagate through layered formations were conducted by Daneshy in 1978, working over previous research on the role of the interface in composite materials such as that by Cooper & Kelly (1969). This author has combined a numerical analysis using finite element modelling with mechanical experiments on composite samples made of two different rock types, to determine the variation of the theoretical fracturing pressure when a fracture intersects different types of interfaces. The experiments were made using several cuboid shaped samples where fracture propagation was induced using a closed-loop, servo-controlled hydraulic pressurizer. He concluded that the primary factor in fracturing of layered formations is the strength of the interface: weak interfaces are likely to stop fracture propagation, regardless of the relative properties of the two adjacent layers, while strongly bonded interfaces eventually will allow fracture extension through them. Other authors agree that the strength of the interface is a crucial factor determining whether a fracture propagates across or is arrested at an interface. These include Teufel & Clark (1984) who performed laboratory hydraulic fracture experiments using rectangular composite three-layer specimens and carried out finite element modelling and conclude that fracture arrest can occur whenever the shear strength of the layer interface is sufficiently weak relative to the tensile strength and the minimum horizontal compressive stress of the bounding layers. In such situation the fracture

more easily becomes an interfacial fracture rather than one extending across the interface into the bounding layer. Hegelson & Aydin (1991) who did a field analysis of trace geometry and the associated surface features of joints in layered sedimentary rocks from the Appalachian plateau combined with numerical modelling using Finite Element Modelling; Cooke & Underwood (2001) who have used a Boundary Element Method numerical code to analyse frictional slip and associated opening-mode fracture propagation in two dimensions and Larsen et al., 2010 who measured more than 2000 fractures using LIDAR in order to analyse fracture penetration and fracture arrest in the Lower Cretaceous peritidal deposits exposed in southern Italy also agree that the strength of the interface is a factor to consider.

Another factor that various authors consider to be crucial in determining whether a fracture propagates across or is arrested at an interface is the stiffness contrast between the layer where the fracture is *propagating from* and the layer where the fracture is *propagating to*.

Simonson et al. (1978); discuss the containment or propagation of artificially induced hydraulic fractures using as their basis linear elastic fracture mechanics. The authors analyse three cases: (1) the effect of different material properties between the reservoir and the cap-rock; (2) the characteristics of fracture propagation into regions of varying in-situ stress; (3) the effect of hydrostatic pressure gradients on fracture propagation into overlying or underlying barrier formations. Regarding the first case, they conclude that a fracture will be contained in the reservoir formation, if this formation has lower stiffness (Young's Modulus) when compared to the bounding formations (cap-rock). Hegelson & Aydin, (1991) following previous work by Erdogan & Biricikoglu (1973) and Cook & Erdogan (1972) draw the conclusion that for a situation of a fracture approaching a layer of higher modulus (E2>E1) strain energy decreases and additional energy is then needed to drive the fracture to the interface. When its tip reaches the interface, there should be an increase in the strain energy proportional to the ratio of the moduli, the maximum strain energy corresponding to in-plane extension of the fracture. Larsen et al. (2010) on their field study agree that large elastic mismatch (particularly as regarding Young's moduli) between layers across an interface is crucial for fracture arrest.

However, experimental work by Teufel & Clark (1994), and theoretical modelling applying concepts from the theory of linear elasticity by Van Eelken, (1982) consider that differences in elastic properties of the formations in a layered rock mass do not constitute an effective containment barrier per se. Teufel & Clark (1994) stress that elastic property variations across layer interfaces can affect hydraulic fracture growth indirectly, however, this is related to the fact that elastic property variations affect the minimum horizontal in-situ stress state (layer-parallel compressive stress) of individual layers influencing the potential for fracture propagation.

The third mechanism widely considered are the in-situ stress differences between adjacent layers. Already mentioned authors such as Simonson et al. (1978), Van Eelk en (1982) and Teufel & Clark (1984) plus Warpinski & Teufel (1987) and Baer (1991) all agree that if the bounding layers possess higher in-situ stress (layer-parallel compressive stress) than the rocks where the fracture formed, then those layers serve as a barrier to vertical extension. Simoson et al. (1978) using linear elastic fracture mechanics conclude that an in-situ stress barrier is effective in arresting artificial induced hydraulic fractures at an interface between a lower stressed reservoir and a higher stressed cap-rock. They also conclude that if the fracture does extend into the higher in-situ stress bounding layer (cap-rock), then an increase in pumping pressure should be noticed, the magnitude should be a function of the difference in in-situ stress between the barrier and the reservoir, and the thickness of the reservoir. Teufel & Clark (1984) refer that an increase in the minimum (compressive) horizontal stress in the bounding layer causes the fracture to remain a vertical rectangular fracture bounded by the high-stress layers. For the authors, the effectiveness of the stress barrier depends on the difference in the minimum horizontal stress between the bounding layer and the layer with the propagating fracture. By using field data and triaxial testing, Warpinsky & Teufel (1987) conclude that the in-situ stress distribution is the primary factor controlling containment of a fracture through a layered rock sequence, but when the stress contrasts between layers are small, material property variations may have some effect. Baer (1991), analysed the mechanisms of dike propagation through detailed field examination of small structures associated with the intrusion in outcrops of Israel. He confirms that higher layer-parallel compressive stress in adjacent layers are by far more effective as a containment mechanism than differences in the mechanical properties: fractures could cross an interface into a layer with a shear modulus 5-15 times greater, whereas they would not propagate into a layer with layer-parallel compressive stress only twice as great. He also studied the influence of bedding plane slippage.

Another mechanism which has been widely considered as having potential to influence fracture propagation across an interface is the friction at the layer boundaries (coefficient of sliding friction). In order to evaluate the influence of the coefficient of sliding friction of an interface between materials on the propagation of a hydraulic fracture, Anderson (1981) executed small-scale laboratory experiments and the growth of hydraulically driven fractures in the vicinity of unbonded interfaces was analysed. The author used prismatic samples of sandstone and limestone, and through an apparatus of high pressure steel tubing, injected oil into the rocks to generate fluid induced fractures development. In order to vary the frictional properties of the interfaces between rock elements, lubricants and surface roughening were used. The author found that lowering the interface surface friction coefficient resulted in the need to increase the normal stress in order for a hydraulic fracture to cross the interface. It was also observed that the type of fluid along the interface plays an important

role in the behaviour of the interface: while water saturation lowered the frictional coefficient of the sandstone samples, it had the opposite effect on the limestone samples. This can be explained by the interaction between the limestone and the water that softened the material, causing it to crumble under the sliding action.

Dollar & Steif (1989) achieved the same conclusions as Anderson (1981) through a theoretical and numerical study of a crack impinging perpendicularly on a frictional interface. The authors consider the problem of an infinite sheet subjected to uniaxial tension containing a finite crack which lies normal to the tension axis and has both crack tips impinging normally on frictional interfaces. They show that the frictional interface acts to eliminate the singular stresses at the crack tip and depending on the interface characteristics, the effective blunting of the crack tip may be sufficient to entirely impede propagation of the crack.

In their seminal paper, Renshaw and Pollard (1995), clearly demonstrate the importance of interfacial slippage on fracture propagation. The authors conducted a first order analysis using the linear elastic fracture mechanics solution for the stresses near a mode I fracture tip impinging upon a frictional interface oriented normal to the growing fracture, and created a criterion that predicts whether a growing fracture will terminate at or cross the interface. Using this technique they determined the layer-normal compressive stress required to prevent slippage along the interface at the moment when the stress on the opposite side of the interface is sufficient to initiate a fracture in the adjacent layer. In order to verify the criterion, a series of experiments using three molded planks of brittle material with a hole in the central plank (simulating a fracture) were subjected to compression normal to their longest dimension. The criterion defined by Renshaw and Pollard (1995) can be summarised by the following equation for a frictional interface oriented parallel to the y-axis and implies that slippage along the interface will occur whenever:

$$\tau < -\mu\sigma$$

where, τ is the shear stress along the interface, μ the coefficient of sliding friction along that interface and σ the normal stress acting perpendicular to the interface.

It is important to outline however, that Van Eelken (1982) in his theoretical analysis, Warpinski & Teufel (1987) using field data and triaxial testing, Baer (1991) through field data analysis, all consider that interface slippage will occur only when the stresses normal to these interfaces are low or when the resistance (friction) is extremely low, namely, only at shallow depths or on a very smooth interface.

The thickness of the incompetent layer is the fifth factor to be considered. Again, Hegelson & Aydin (1991) in their field analysis observe that the vertical trace depends on the thickness of an inhibiting shale layer, i.e. the trace is well aligned when the shale layers are absent or thin, and deteriorates (out-of-plane) as the thickness of shale layers increases until finally there is no longer a communication (a

link) between joints in two siltstone layers. The authors consider that the field observations suggest the existence of some degree of communication between a segment (siltstone) on one side of a thin shale layer and another segment on the other side and hypothesize that the basis of this communication is probably some degree of transfer of stresses associated with the joint tip through the impeding shale layer. Despite this, they considered that the arrest or propagation of a fracture across an inhibiting shale layer has more to do with the mechanical properties of that layer rather than the thickness itself.

However, Friedman & French (1994) through field work conducted in the fractured Austin chalk (whose brittle layers are separated by shale-marl layers) paired with a series of laboratory experiments, consider that the most important factors for fracture containment are: the thickness of the shale/marl beds and the existence of low effective confining pressure at the time of fracturing. Their outcrop observations suggest that rarely do fractures transect shale/marl layers in the Austin Chalk that are > IO-cm thick and conclude that the thicker the shale/marl layer the greater the tendency for the containment of fractures in the adjacent brittle layer.

In 2001, Rijken & Cooke, also working in the Austin Chalk, combined field observations with Finite Element Modelling to analyse which material properties control fracture propagation through an alternating chalk and shale sequence and, in agreement with Friedman & French (1994) concluded that the thickness ratio between the stiff chalk layers and the softer shale layers is crucial in determining if a crack propagates through a shale layer.

Rijken & Cooke (2001) also consider another factor to be crucial in determining whether a fracture is arrested or propagates through an interface and that is the type of driving stress. The authors found that incorporating a ductile layer in the numerical models (a very common setup in nature) causes the registered stress intensity factor to be dependent on the nature of the applied load: the models with fluid pressure in a fracture produce greater stress intensity factor at the flaw tips than models with remote tension. The explanation resides on the way the pressure is applied. On an internal fluid pressure driven fracture, the driving stress is applied locally and the shale around the crack-tip experiences large inelastic strains which enhances crack opening, increasing the stress intensity factor and promoting propagation through layers. In contrast, in a remotely loaded crack-tip the extensional strain within the shale is distributed along the layer rather than localized at the crack tip and hence the stress intensity factor is smaller. This means that lower driving stresses are required to propagate fractures through shale layers for fluid pressure driven fractures than dry fractures under remote tension.

4.6.2 Learnings from the literature review – a summary

Considering the previous section in which many of the most important references regarding fracture propagation through layered media are outlined, it is clear that this issue has been concerning researchers for a long time. From this body of work several factors have been identified as being crucial in influencing the way fractures propagate. These are:

1. **Strength of the interface** (Daneshy, 1978; Teufel & Clark, 1984; Hegelson & Aydin, 1991; Cooke & Underwood, 2001; Larsen et al., 2010): for bonded interfaces a strong interface promotes through going fractures and a weak interface is prone to opening and therefore impedes fracture propagation (Figure 4.40).

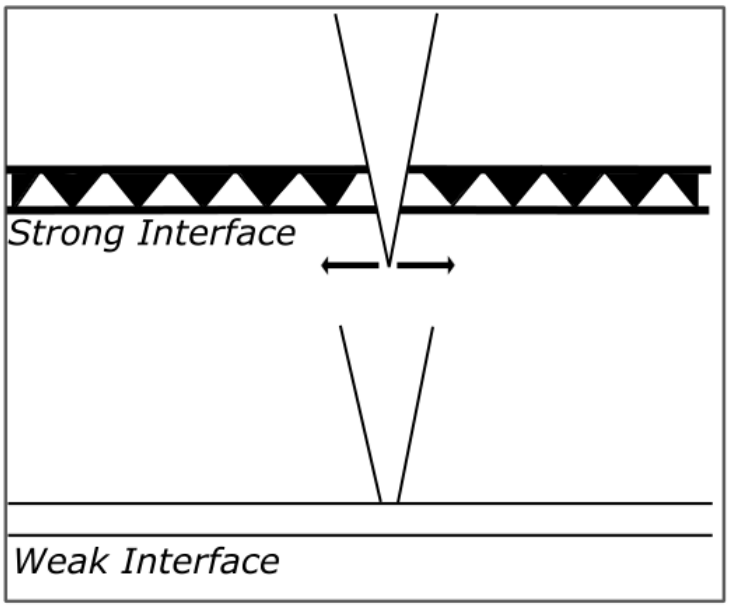


Figure 4.36: fracture propagation at a strong interface vs arrest at a weak interface.

2. **Stiffness** (Young's Modulus) (Simonson et al., 1978; Hegelson & Aydin, 1991; Cooke & Underwood, 2001; Larsen et al., 2010): for a situation of a fracture approaching a layer of higher modulus (E2>E1 i.e. a fracture advancing towards a stiffer layer) strain energy decreases and a fracture will be contained in the formation with lower modulus. However, Teufel & Clark (1994), and Van Eelken, (1982) consider that differences in elastic properties of the formations in a layered rock mass do not constitute an effective containment barrier per se. Elastic property variations across layer interfaces can affect hydraulic fracture growth indirectly, however, in that elastic property variations affect the minimum horizontal in-situ stress state (layer-parallel compressive stress) of individual layers (Figure 4.41).

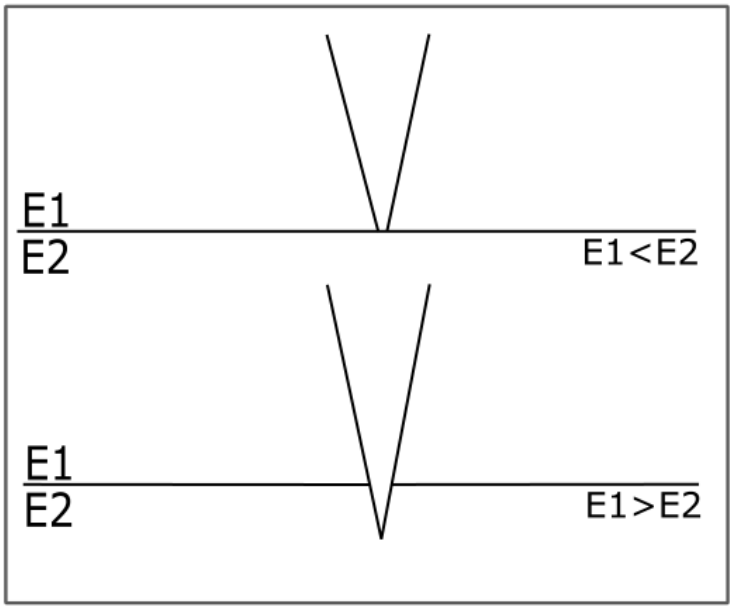


Figure 4.37: influence of the elastic modulus on the propagation of a fracture across an interface.

3. **In-situ stress differences** (Simonson et al. 1978; Van Eelken, 1982; Teufel & Clark, 1984; Warpinski & Teufel, 1987; Baer, 1991): If the bounding layers possess higher in-situ stress (layer-parallel compressive stress) than the rocks where the fracture formed, then those layers serve as a barrier to vertical extension.

4. **Friction at the layer boundaries** (Anderson, 1981; Van Eelken, 1982; Warpinski & Teufel, 1987; Dollar & Steif, 1989; Baer, 1991; Renshaw and Pollard): for unbonded inferfaces with low values of coefficient of sliding friction, the fracture tip stresses are dissipated as they approach the interface due to slip along the interface. They are therefore not transmitted across the interface and the fracture is arrested. Because the resistance to slip is the product of the coefficient of sliding friction and the layer normal stress, low values of interface perpendicular normal stress also promote interface slippage and inhibit fracture propagation (Figure 4.42).

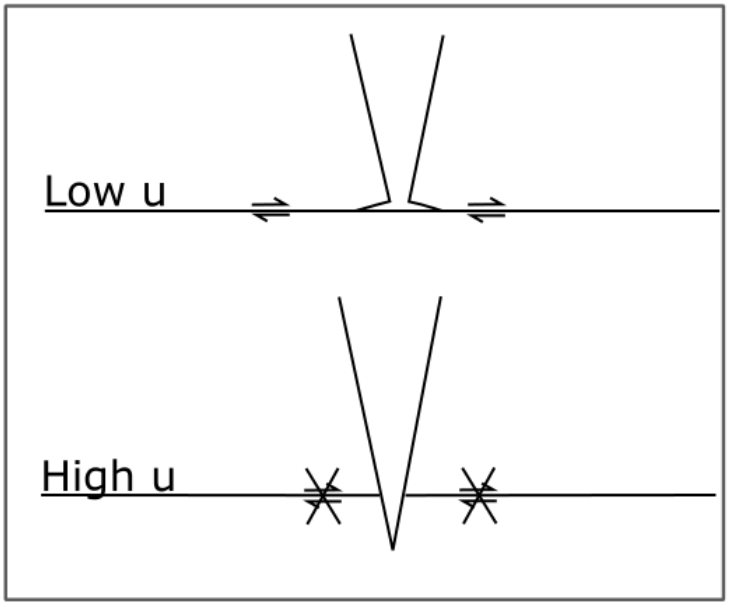


Figure 4.38: influence of the coefficient of sliding friction along a layer interface on fracture propagation across it.

5. **Thickness of the incompetent layer** (Hegelson & Aydin, 1991; Friedman & French, 1994; Rijken & Cooke, 2001): The thickness ratio between the stiff layers and the softer layers is essential in determining whether or not a crack propagates through a soft layer. The thicker the soft layer the greater the tendency for the containment of fractures in the adjacent brittle layer (Figure 4.43).

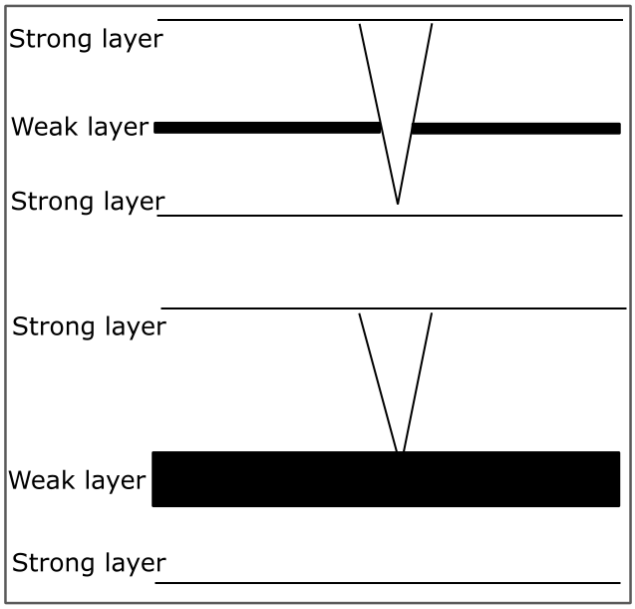


Figure 4.39: influence of the thickness of the incompetent layer on the propagation of a fracture across it.

6. **Type of driving stresses** (Rijken & Cooke, 2001): Lower driving stresses are required to propagate fractures through shale layers for fluid pressure driven fractures than dry fractures under remote tension. This occurs because on an internal fluid pressure driven fracture, the driving stress is applied locally and the shale around the crack-tip experiences large inelastic strains which enhances crack opening, increasing stress intensity factor and promoting propagation through layers.

These factors where used to guide the design of the numerical models described on the following chapter. They were run in part to attempt to quantify these effects of fracture propagation.

Chapter 5
Numerical Modelling

5.1 Introduction - Numerical Methods for the study of fractures

Work conducted in Brightling mine, core analysis and the outcrop studies provided us with valuable information on:

- the general sedimentary and textural properties of evaporite sequences (Brighlting and cores)
- the particularities of fracture propagation and arrest through layered sequences (Thytherington and Lilstock)
- the response of low permeability systems to high fluid pressures (Watchet).

However the information obtained from theses sources does not completely enlightens us on the specific mechanical properties that control whether a fracture becomes through going or remains strata bound. It is therefore essential to conduct a study that allows each mechanical parameter to be tested individually to account which is its influence on the process of fracture propagation/arrest.

Using the Finite-Discrete Element Method as a simulation tool we have modelled the development of two-dimensional fracture patterns in a layered sequence. The main focus of this simulation is to understand what specific mechanical parameters control the propagation or arrest of a fracture under different loading conditions in a layered evaporite sequence. Of particular interest is the effect of slip at layer interfaces (Cooke & Underwood, 2001), the failure of the interface by debonding and subsequently opening and the effect of changes in Young's modulus from one layer to another.

For this simulation, GID (a CAD system which is a user-friendly pre- and post-processor software for numerical simulations; http://www.gidhome.com/) is used to build the geometrical model and define the parameters to be used in the simulations (the boundary conditions). Paraview (an open source, multi-platform data analysis and visualization application) is used to visualize and analyse the results of the simulations.

While an empirical analysis is based upon physical experiment and comparison, analytical analysis uses calculation or modelling to draw conclusions on a specific subject. Numerical methods are part of analytical analysis and can be divided in continuous or discontinuous models. The difference between both models resides in the fact that in continuous models the material is modelled as a continuous medium, whereas in discontinuous models the material is modelled as a system of individual blocks interacting along their boundaries.

In the geological context, the rock mass differs from other engineering materials due to the fact that it has a large range of discontinuities. The question is whether these discontinuities should or not be

considered. Brown (1987) considers that it is the relation between the discontinuity spacing and the size of the problem (the domain) which should be crucial in determining which model to choose. Figure 5.1 shows a general classification of numerical methods for analysis of a rock mass. From these only FEM and DEM are of interest to our analysis and will be further detailed.

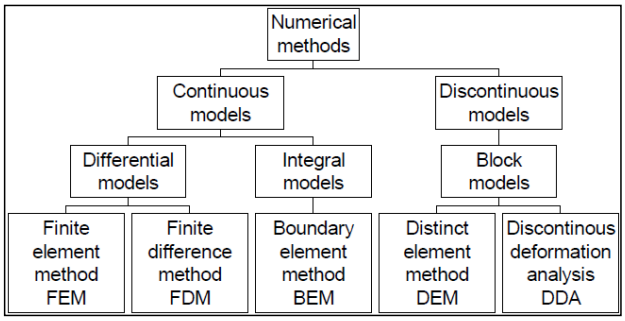


Figure 5.1: numerical methods for rock mass analysis (Scheldt, 2002)

5.1.1 Continuum Problems – Finite Element Modelling

Although the internal structure of most engineering materials, of which rocks are a good example, is discontinuous, it is not always necessary to account this discontinuous nature to solve some of the problems within this field of knowledge. This continuum formulation arises from the fact that the quantities with which engineering problems deals with are large enough so that the microstructure of the material can be represented by average physical properties which are continuous (Munjiza A. , 2004). The physical properties that describe the material are called the physical equations or the constitutive law and they are continuous functions of volume. These are combined with balance principles (a priori physical principles that describe material behavior in sufficient bulk so that the effects of the continuous microstructure can be ignored), to form the governing equations. Conservation of mass, conservation of energy or preservation of momentum balance are examples of balance principles.

Governing equations (that describe the material properties) when coupled with boundary and initial conditions (external actions such as loads or initial velocity) form a boundary value problem, which can be solved using numerical methods like the finite element method (FEM) currently the most advanced method for this type of problems. In FEM the domain is discretized into subdomains, called finite elements, and the solution over these individual elements is an approximation to the exact solution. In general what the FEM does is to divide the interval of integration (the problem) in sub-intervals (finite elements) and choose proper simple functions to approximate the true function. The

numerical result is an approximation to the exact solution and the accuracy of numerical result depends on the number of sub-intervals and approximate function (Figure 5.2). Advantages of the FEM include (Haghighi, 2007):

- Extensive application and use. It can be applied to all physical boundary value problems or structural and solid mechanics.
- The material properties in adjacent elements do not have to be the same allowing application to composite materials.
- The method is not limited to regular shapes and it is able to cope with irregularly shaped boundaries through an approximation using elements with straight sides or elements using elements with curved boundaries.
- The size of the elements can be different allowing the element grid to be changed according to the needs.

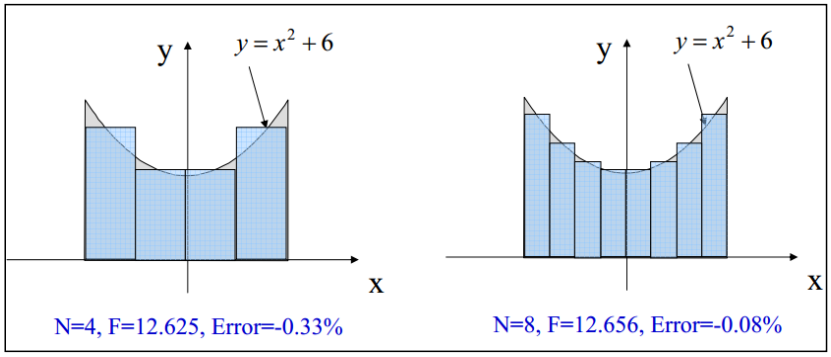


Figure 5.2: numerical integration using the Finite Element Analysis method. The interval of integration is divided into N sections and a function to approximate the variation of f(x) is chosen in each section. The product of this constant function and the length of the section approximate the integration of f(x) over this section. Summing the products of all sections an approximation to the original function is obtained. As the number of sections increases, the error decreases. (source: FEM Introductory Module, University of Colorado, 2006)

5.1.2 Discontinuum Problems – Discrete Element Modelling

Despite the fact that most engineering problems can be solved by continuum models, there are materials which cannot be represented by them. Jointed rock masses or any type of granular materials are an example where continuum mechanics cannot cope with the motion and effect of a large number of small particles. In this situation the use of discontinuum mechanics is more suitable. The fundamental assumption of discontinuum mechanics is that the analysed material consists of independent, discrete particles which may have different shapes and properties. The mathematical formulation of such problems involves the use of an interaction law – that describes how the particles interact with each other - for each couple of contacting particles and the application of the relevant

physical laws. Generally, the rock mass is represented by elements and the rock joints by the space between the elements. There is no restriction on contacts between elements and nodes may interact with nodes or edges (Scheldt, 2002).

The most advanced methods to model discontinuum problems are the Discontinuous Deformation Analysis (DDA) and the Discrete Element Method (DEM). DEM is more suitable for problems involving transient dynamics until the state of rest is achieved and for that reason is more commonly used in geomechanics problems (Munjiza A. , 2004).

5.1.3 Transition from Continuum to Discontinuum –The FEMDEM methodology

Quasi-brittle materials are those that exhibit moderate strain hardening prior to the attainment of ultimate tensile strength and tension softening thereafter. Rocks, concrete and ceramics are examples of quasi-brittle materials and the process occurs by several fracture processes, such as localised micro-cracking, bridging by coarser aggregates, crack branching, etc (Flewitt & al, 2010).There are several engineering problems where this transition from continua to discontinuum can be verified: blasting or crushing of a rock mass in mining operations, demolition of buildings induced by explosive charges, accidental structural collapse of infrastructures like bridges or houses, rock fracturing by fluid induced failure (natural or caused by oil drilling operations). In this transition process there is a change from a static to a dynamic system where contact-impact and energy dissipation mechanisms occur. In situations where there is a transition process of this kind the two types of models (continua and discontinuum modelling) can be used:

- Deformability of individual particles is well represented by a continuum based model
- Interaction amongst individual particles is best represented by a discontinuum based model.

The transition from continuum to discontinuum is modelled through fracturing and fragmentation processes (Guo et al., 2013). There have been several approaches to the process of fracture formation and development which try to account the alteration of the stress and strain fields when a material reaches the point of failure. These include global or local approaches.

The global approach to fracture mechanics is based on the Griffith energy criterion (Griffith, 1926) or the stress intensity factor formulation. The Griffith energy criterion states that a fracture (also called a crack) propagates when the energy available for crack growth overcomes the resistance of the material, which can include the surface energy, plastic work or other type of energy dissipation associated with a propagating crack (Anderson, 1995). Irwin (1957) developed Griffiths approach and defined the energy release rate G as the rate of change in potential energy with crack area for a linear elastic material. In order for fracture growth to occur, $G = G_c$, the critical energy release rate, a measure of fracture toughness. Considering a crack of length 2a (Figure 5.3) subject to a remote tensile stress the energy release rate can be described by:

$$G = \frac{\pi\sigma^2 a}{E} \quad \text{(Equation 5.1)}$$

where,

G - Energy release rate

E - Young's modulus

σ – Remotely applied stress

a – Half crack length

Another way of describing the fracture growth process is to use the stress intensity approach. In this method the stresses at a point near the tip of a crack in an elastic material are written proportionally to a single constant, K_I, called the stress intensity factor (Figure 5.4). This constant completely characterizes the crack tip conditions in a linear elastic material. For a material such as the one illustrated in Figure 5.4, the stress intensity factor is given by (Anderson, 1995):

$$K_I = \sigma\sqrt{\pi a} \quad \text{(Equation 5.2)}$$

where,

K_I – stress intensity factor

σ – Remotely applied stress

a – Half crack length

A relation between the energy release rate and the stress intensity factor can be written:

$$G = \frac{K_I^2}{E} \quad \text{(Equation 5.3)}$$

A fundamental assumption of global fracture mechanics is that both the energy release rate (or the fracture toughness) and the stress intensity factor (or the critical stress intensity) are independent of the size and geometry of the cracked body, which means that a measure of the fracture toughness made in a laboratorial test should be applicable to a structure – a property called similitude. However for linear fracture toughness, tests show that under plain strain small scale yielding there is a size effect associated with the probability of finding a weak point along the crack front through the specimen thickness (Pineau & Joly, 1991). Due to this problem another approach was developed to tackle the problem: the local fracture approach.

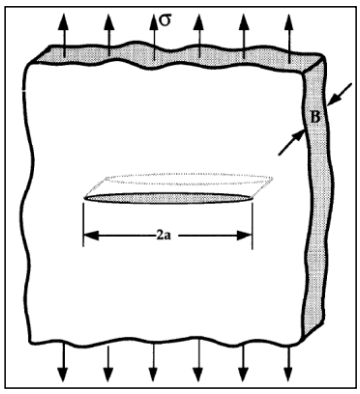


Figure 5.3: Through-thickness crack in an infinite plate subjected to a remote tensile stress. Infinite means that the width of the plate is much higher than the length of the crack in it (Anderson, 1995).

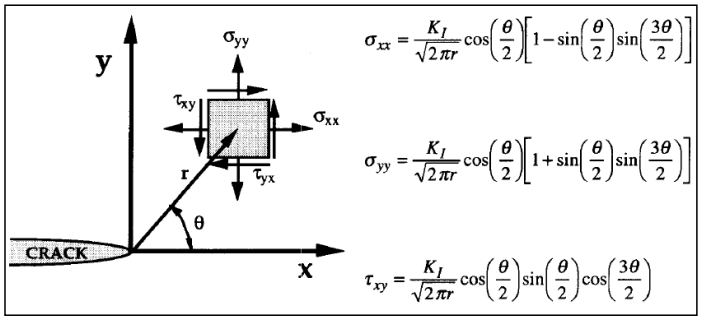


Figure 5.4: stresses near the tip of a crack in an elastic material (Anderson, 1995)

The local fracture approach is based on the fact that it is possible to model macroscopic fracture behaviour in terms of local fracture criteria. It is divided in two different methods that analyse the crack formation process in light of either continuum or discontinuum behaviour assumptions. This local mechanics approach was developed in the 1960's by different researchers while analysing fracture processes in concrete structures. They have introduced the discrete (Ngo & Scordelis, 1967) and smeared (Rashid, 1968) crack models.

The discrete crack concept models a crack as a geometrical discontinuity and it is aimed at simulating the initiation and propagation of dominant cracks. It introduces a crack as a geometric entity and it is implemented by letting a crack propagate when the nodal force at the node ahead of the crack tip exceeds a tensile strength criterion. At that moment the node is divided in two nodes and the tip of

the crack propagates to the next node. When the tensile strength criterion is overcome at this node, it is split and the procedure is repeated (Figure 5.5). The drawbacks of this method are (Rots & Blaauwendraad, 1989):

- The approach implies a continuous change in nodal connectivity, which does not fit the nature of the finite element method.
- The crack is constrained to follow a predefined path along the element edges.

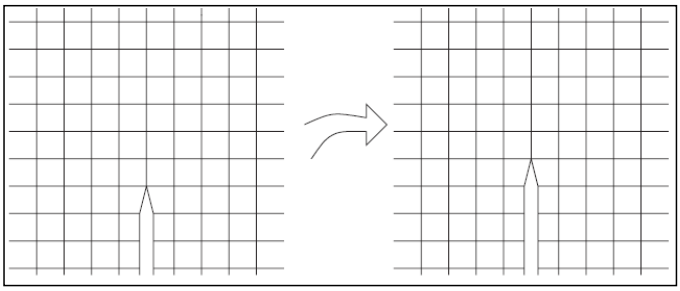


Figure 5.5: Mode I fracture propagation in a discrete crack model (De Borst & al., 2004)

The smeared crack concept (Rashid, 1968) imagines a cracked solid to be a continuum and it is based on the idea that the heterogeneities and reinforcements on concrete (material on which these models were developed) cause various small cracks to nucleate and link up on a later stage to form one or more dominant cracks – blunt crack band - enabling a description of the process in terms of stress-strain relations. The general principle is that when a combination of stresses satisfies a specified criterion, e.g. the major principal stress reaching the tensile strength T; a crack is initiated (De Borst & al., 2004). This procedure preserves the topology of the original finite element mesh and does not impose restrictions with regards to the orientation of the crack planes (the axis of orthotropy) (Rots & Blaauwendraad, 1989). Although the discrete crack model better fits the general concept of a fracture (straight, true geometrical discontinuity), the smeared crack approach is considered to be more realistic as it is able to represent the bands of micro-cracks commonly in materials like and similar to concrete.

The state of the art methodology to deal with problems that involve the transition from a continuous to a discontinuous media was developed in the 1990's by Ante Munjiza and it is called combined finite-discrete element method (FEMDEM). In this method each particle is represented by a single discrete element that interacts with elements that are close to it. Each of these discrete elements is then discretised into finite elements and the corresponding finite element mesh. Each of these finite element meshes is able to capture the deformability of a single discrete element (particle or body).

Continuum behaviour is thus modelled by finite elements while discontinuum behaviour is modelled by discrete elements (Munjiza A. , 2004). For the application to fractured and layered systems, the separate bodies can be the rock materials on opposite sides of a fracture wall or bedding planes.

The two-dimensional combined finite-discrete element code, used in this work is similar to the code originally published with Munjiza's (2004) book *The Combined Finite-Discrete Element Method* having been added a friction parameter by Xiang et al. (2009). This extended version now being used was launched in 2009 by collaboration between Queen Mary University London and Imperial College London.

In the finite-discrete element method, the model is implemented using as a proxy experimental stress/strain curves for concrete in tension. The standard finite element formulation for the hardening part of the constitutive law is combined with the single-crack model for the softening part of the stress/strain curve (Figure 5.6). Finite elements are used to model behaviour of the material up to the ultimate tensile strength while a discrete crack model is implemented through crack opening and separation along edges of finite elements (Figure 5.7). The model is named combined single and smeared crack model (Munjiza A. , 2004). Geomechanical modelling based on the FEMDEM technology can characterise the deformation and interaction of rock matrix bounded by pre-existing fractures (Latham et. al., 2012). The embedded smeared crack model further permits the simulator to capture the emergence of new fracturing which potentially leads to critical changes for the connectivity of fracture systems, without considerable additional CPU requirements (Munjiza et al. 1999).

A fractured rock represents a solid system which combines matrix (the bulk material) and fractures (the discontinuities). These are represented in 2D by a discontinuous discretisation of the model domain using three-noded triangular finite elements and four-noded joint elements embedded between edges of triangular elements (Lei & Latham,2015 after Lisjak and Grasselli 2014) (Figure 5.8). This means that crack initiation and propagation is constrained by the boundaries of finite elements (Munjiza et al., 1999). Mesoscopic fracture opening and sliding are characterised based on the deformed configuration of finite elements located along fracture walls: a fracture is represented as the median polyline determined by the current nodal coordinates of opposite fracture walls (Lei, Q. et. al., 2014) (Figure 5.9).

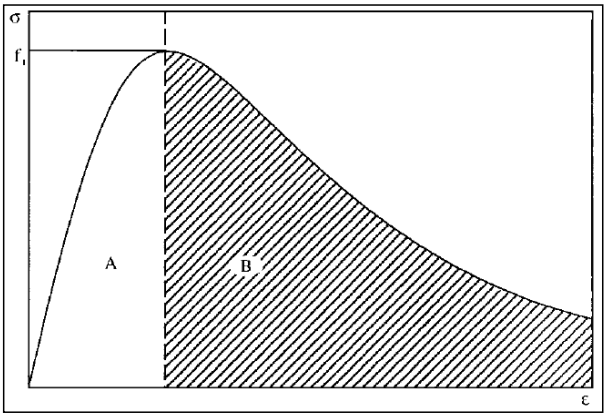


Figure 5.6: strain softening stress-strain curve. Part 'A' is implemented in the finite element method in a standard way through the constitutive law. Part 'B' represents strain softening, where stress decreases with increasing strain. It is modelled through a single-crack model (Figure 5.7) (Munjiza, 1999).

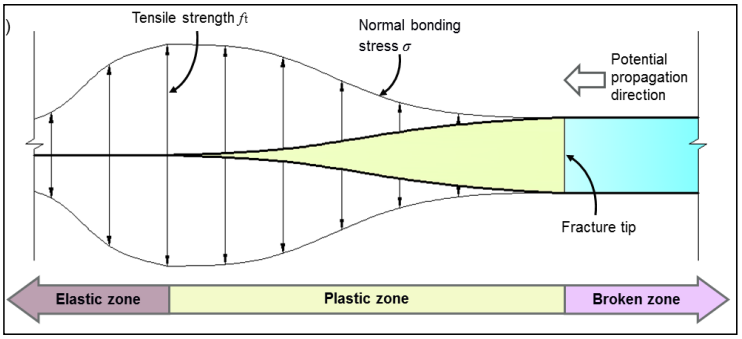


Figure 5.7: Schematic illustration of the transition from the elastic zone to the fracture (broken) zone via the plastic zone around the tip of a mode I fracture: single-crack model. (Lei & Latham, 2015).

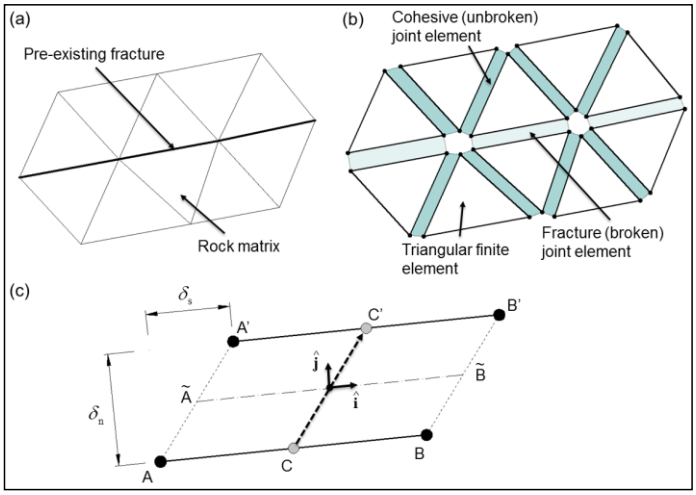


Figure 5.8: Representation of a) a fracture-matrix solid system using a mesh consisting of b) three-noded triangular elements and four-noded cohesive/fracture joint elements embedded between edges of triangular elements. c) Displacements of a joint element (either unbroken or broken) characterised by the geometrical configuration of its nodal system (Lei & Latham, 2015).

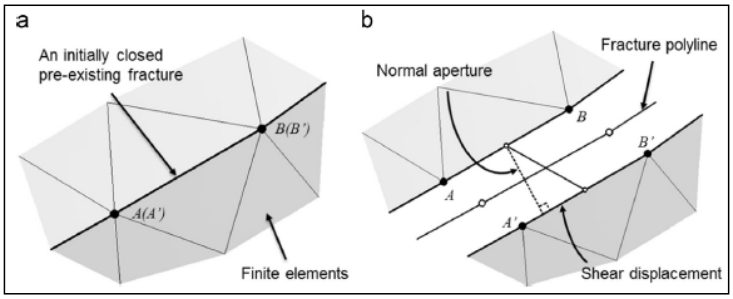


Figure 5.9: representation of a pre-existing fracture in a) the initial closed state, and b) a deformed state after opening and sliding (Lei & al., 2014).

The ability of the FEMDEM approach and of the Y2D numerical code for modelling intact rock fracturing and propagation processes is demonstrated by several authors who have used this methodology. Some examples are outlined below with the objective of demonstrating that the FEMDEM methodology is suitable for using in a study such as the one we are conducting and that it brings considerable advantages when compared to the more traditional DEM or FEM methods.

Latham, J.P. et al. (2012), focused on investigating the influence of in-situ stresses on flow processes in fractured rock. They describe heterogeneous deformation when a rock mass containing pre-existing fractures is subjected to various in-situ stress states and document the resulting changes by applying

FEMDEM geomechanical modelling. The study is based on applying far-field (boundary) stresses to a square region obtained from an outcrop map with a low density fracture pattern. Uniaxial and biaxial stresses were applied to the natural fracture set and phenomena such as fracture-dependent stress heterogeneities, the re-activation of pre-existing fractures (i.e. opening, closing and shearing), the propagation of new fractures and the development of fault zones were modelled, documented in x- and y-directions and then were used for simulating single phase flow.

In regards to the ability of the FEMDEM to deal with geomechanical modelling of fractured rock masses, the authors conclude that this numerical model:

- Is capable of simulating further fracture initiation, propagation, opening and shearing of fracture walls – being the fracture wall interactions handled explicitly by employing the multi body features of DEM.
- It can be used to characterize the fracture geometry and aperture variations of the deformation as required for the fracture and matrix flow model.

FEMDEM modelling of a fractured outcrop also enabled the authors to conclude that this methodology yields better results when compared with previous studies that used only DFN modelling. They have noted that: there is the potential for new fractures to connect with existing fractures, thus increasing the connectivity and flow; blocks can rotate when bounded by fractures; bent fractures lead to locally different aperture development; highly heterogeneous stress distributions emerge naturally, and the rock matrix permeability is not zero, as assumed in many studies.

On a subsquent paper - Latham, J.P. et al. (2012) - the authors apply the FEMDEM numerical method to study the controls on fracture spacing by simulating the growth of two-dimensional fracture networks in a three-layered model - composed by two outer shale layers and a middle limestone layer - using a layer-normal compressive stress regime (Figure 5.10). The verification of the model is made by studying the stress state transition between two neighboring opening-mode fractures maintaining the contacts between layers welded thus forbidding slip from occurring. During the simulation, two loading conditions were considered, direct tension parallel to the layers and indirect tension induced by compression normal to the layers. This approach is similar to the approach by Bai & Pollard (2000) and the results obtained by Latham, J.P. et al (2012) match these authors' observations for the direct tension situation.

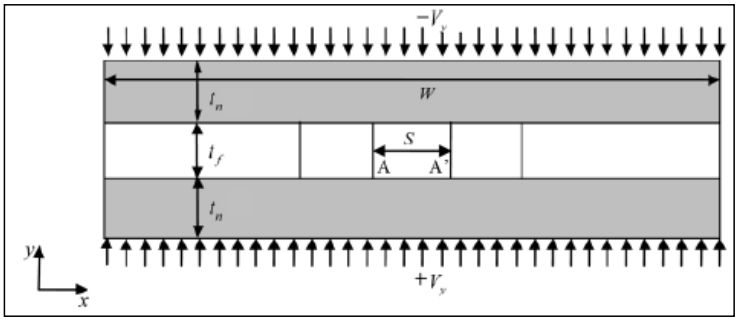


Figure 5.10: Three-layer elastic model and its boundary conditions (Latham, J.P, et al. 2012)

The multi-layered tests conducted are equivalent to a large composite specimen subjected to a rock mechanics test in a plane strain rig (zero strain in *z*-direction). Four models were created corresponding to an increasing confining pressure between 0 and 10Mpa. A Coulomb friction law governs the sliding between opposite sides fractures as well as at the interface between layers (which behave like a pre-existing closed crack with no cohesion), i.e. sliding of the interface occurs when the shear stress exceeds the normal stress and the coefficient of sliding friction: $\tau \geq \mu\sigma_n$. In all models, the friction coefficient (μ) was set at 0.5. Results of this modelling for a confining pressure of 1MPa can be seen if Figure 5.11.

The observations show that critical spacing values at saturation are larger than the bonded models with pre-existing fractures would suggest. The authors conclude that delamination and frictional sliding between layers are crucial in influencing the fracture spacing to layer thickness ratio and that FEMDEM can be used to examine in detail the timing and location of slip and major delamination. The results were compatible with both high and low ratios observed in geological sequences.

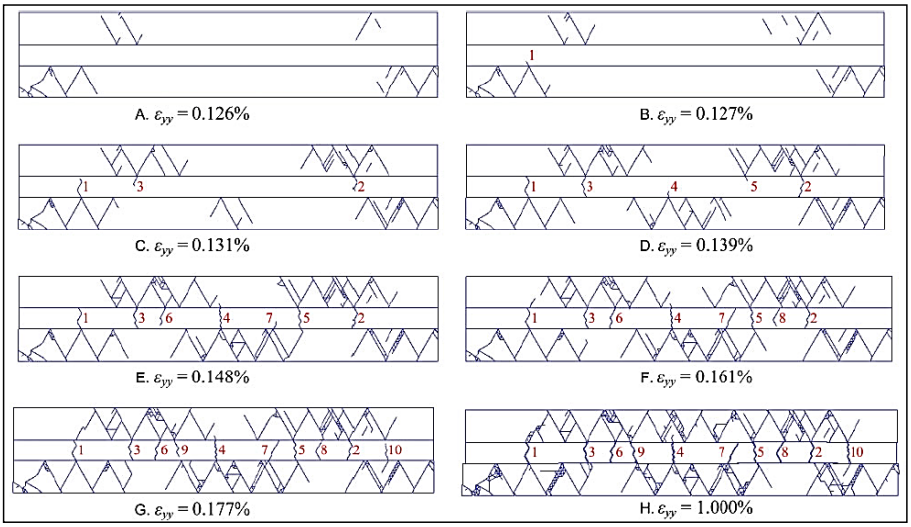


Figure 5.11: model 1, confining pressure 1Mpa. FEMDEM numerical simulation stages of fracture patterns forming in a shale-limestone composite subject to steady shortening normal to the layering at 0.05m· s–1. Shear fractures develop first in the shale and, soon after, the limestone develops extension fractures which infill in a sequence, see numerals (Latham, J.P. et al., 2012).

Following the work of Latham, J.P. et al (2012), Guo, L. et al. (2013) applied the FEMDEM methodology to model the growth of fractures in stratified models. The focus was on the modelling of fractures under different loading conditions, particularly fracture propagation across layer interfaces, the timing of fracture initiation and layer interface delamination. This was achieved by modelling a seven layer all limestone sequence undergoing plane strain (Figure 5.12) and buckling. Such as in Latham, J.P. et al. (2012) a Coulomb friction law governs the sliding between opposite sides of a fracture as well as at the interface. In all models, the friction coefficient μ was set at 0.6.

The authors conclude that vertical normal stresses are decisive in allowing/impeding layer delamination: low vertical stress enables the layer interface between fractured and non-fractured media to delaminate, which can impede tensile fracture propagation across an interface (Figure 5.13 a). The opposite is also true. Regarding the influence of frictional sliding observations were made using the buckling models, and it is suggested that through going fractures are facilitated in the hinges of folds as this region is where slip between units is inhibited.

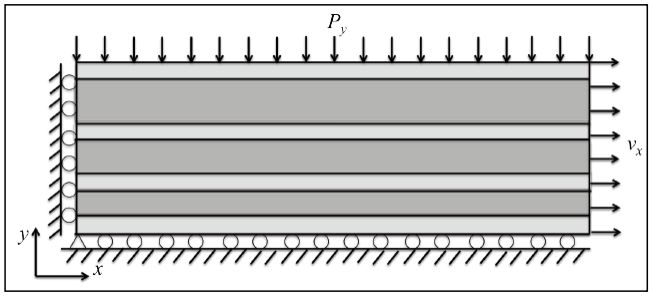


Figure 5.12: seven-layer elastic model and its boundary conditions (Guo, L et al., 2012).

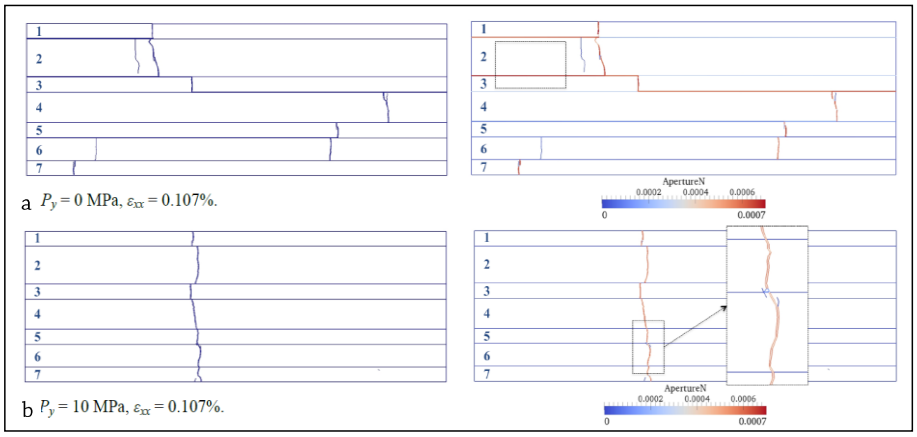


Figure 5.13: effect of an increasing normal stress on fracture propagation through a multi-layered model. A higher normal stress promotes the formation of through going fractures as it impedes delamination (opening of the layer interfaces) (Guo, L. et al., 2012).

5.2 Verification and calibration of the numerical method

One of the key advantages of the FEMDEM approach is that failure laws do not need to be prescribed. This is because the macroscopic behaviour of the material develops as a result of the evolution of micro-scale damage (Munjiza et al., 2011 in Tatone & Grasselli, 2015). However in order to fully capture these complex processes, a high number of input parameters need to be correctly specified and many of them cannot be obtained from laboratory experiments. Hence, in order to determine the correct micro-mechanical parameters, a calibration procedure is necessary so that the simulation results from the computer code are consistent with the observed behaviour (Tatone & Grasselli, 2015). This section presents the verification and calibration procedures made for the FEMDEM/Y2D code relating to:

- The stress distribution in an elastic solid,
- The progressive failure of intact rocks, and
- The frictional sliding between adjacent surfaces.

5.2.1 Stress distribution in an elastic material, and fracturing of multilayered systems.

Latham *et al.* (2012), have validated the use of the FEMDEM (Munjiza, 2004) in combination with the Y2D (Xiang *et al*, 2009) code for the study of fracture mechanics in multilayered systems. They have modeled fractures in a competent layer set in an incompetent matrix in which indirect stretching is taking place. The authors start by validating the FEM part of the code by modelling the stress states between two adjacent pre-existing fractures for an elastic three-layer model (central "limestone" layer surrounded by two "shale" layers) with welded contacts between layers which inhibit slip , an approach similar to that used by Bai & Pollard (2000), and go on to model a similar three-layer model without pre-existing fractures under converging top and bottom boundaries which models layer-normal compression and under different lateral confining pressures (Figure 5.14).

The analysis of the horizontal stress shows that under layer normal compression the shale layers are shortened in the y-direction but extend in the x-direction while retaining a compressive stress in the x-direction. The bonded contacts allow the extension of the shale layers to be transferred to the central limestone layer where it produces higher layer-parallel tensile stresses because of the "limestone's" higher stiffness (Figure 5.15).

Experiments similar to those by Bai and Pollard (2000), where the spacing between two fractures, S, located in the middle limestone layer was varied to analyze the influence of this parameter on fracture formation, were also carried. Results show that the fracture spacing to layer thickness ratio (S/t_f) is an important factor in the development of tensile stresses: when fractures are too close together (in this case $S/t_f < 1$) horizontal tensile stresses cannot develop and no further fractures can occur. If the ratio is higher than "1" then tensile stresses can develop and fractures can continue to form until the gaps between tensile fractures reaches the critical spacing.

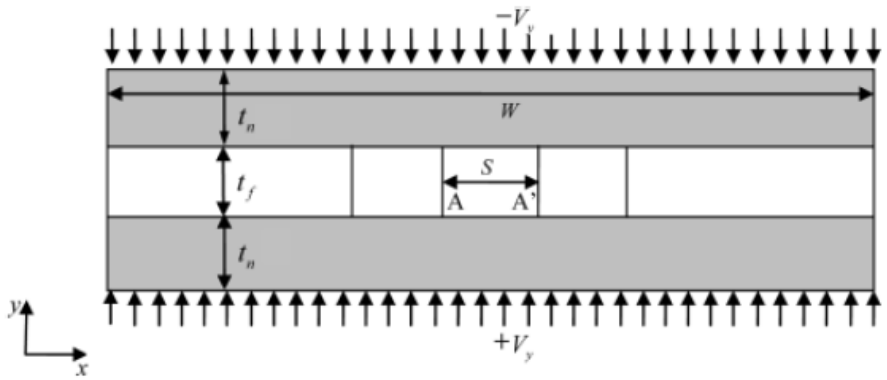


Figure 5.14: Three-layer elastic model and its boundary conditions: the model is stretched horizontally by applying a vertical compression. The left and right boundaries are free from constraints, but a constant mean velocity condition is applied in the y-direction along the top and bottom boundaries of the model to produce compressive stress (Latham et al., 2012).

The multilayer numerical experiments performed in the current study are equivalent to a composite specimen subjected to a rock mechanics test in plane strain. During the experiments a constant velocity (Vy) was applied to the top and bottom boundaries (note that this corresponds to an increase in strain-rate as the experiment proceeds) and constant horizontal (normal) confining pressure (σ_n) to the left and right boundaries which were free from any other constraints (they are free to move horizontally and extend vertically). For these tests a Coulomb friction law governs the sliding between opposite sides of a fracture as well as the potential slip between layers, which were not bonded. The results show that the development of the differential stresses within the layers is sensitive to the material properties (shear fractures develop in the shale and extension fractures develop in the limestone - Figure 5.16) and that confining pressure has a marked influence on the tendency for fractures to propagate across the layer boundaries: more fractures form in the middle layer at higher confining pressures because of the inhibiting effect that these higher pressures have on layer interface sliding. It is also important to note that the contrasting strength and stiffness parameters chosen allow the shale not only but also to extend. These two processes generate shear stresses along the interface between the shale and "limestone" which results in local tensile stresses in the limestone x-direction leading to localized tensile failure. The modelling demonstrated that the method is valid as a tool to model geologically realistic fracture development.

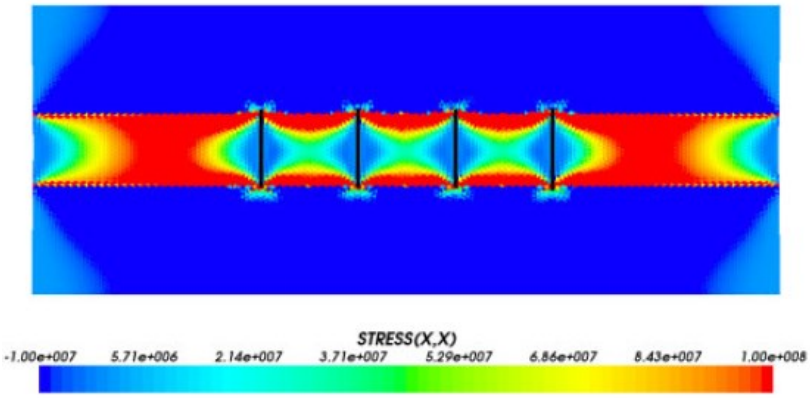


Figure 5.15: horizontal stress distribution within the three-layer model shown in Figure 5.14. Notice that negative values (blue) represent compressive stresses whereas positive values (red) represent tensile stresses (Latham et al. 2012).

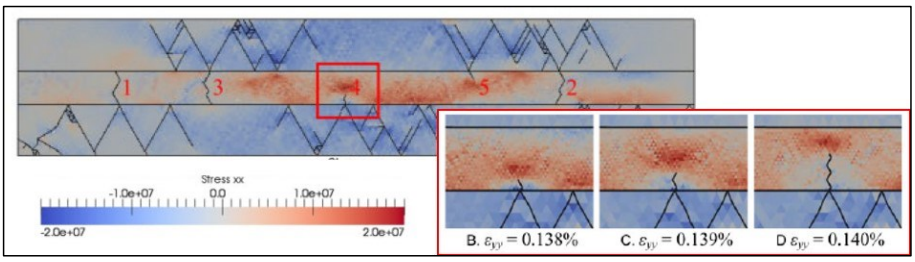
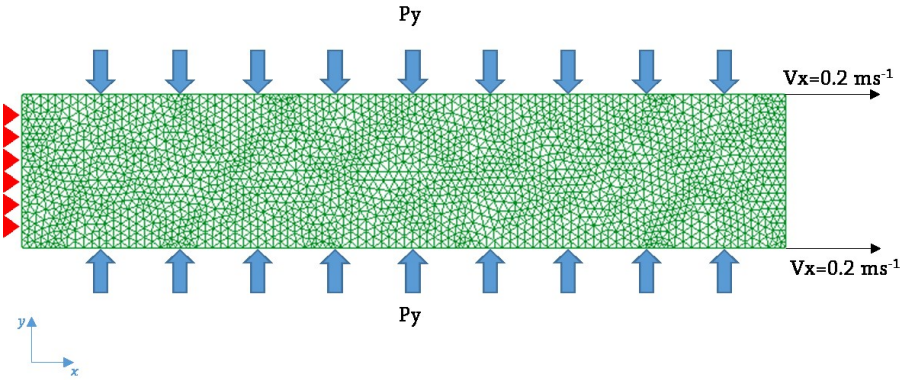


Figure 5.16: 1MPa (confining pressure) model showing shear fractures developing in the bounding shale layers and tensile fractures forming in the limestone middle layer, with detail of the development of the stresses at the fracture tip (adapted from Latham et al., 2012).

In the present study it was decided to introduce a different form of validation, namely an analysis on how the differential stress develops in a single layer model with different boundary conditions. The models were subjected to a horizontal extension velocity (Vx). Four different models were studied each with a successively increased vertical normal load (σ_v). Figure 5.17 shows these boundary conditions and Figure 5.18 shows a comparison of the fracture patterns generated in the four models after 1% of accumulated strain (extension). It is clear that increasing σ_v creates higher differential stresses. This is confirmed by two observations:

- the increasing fracture regularity, i.e. there is a tendency for the fractures to become more regular as the differential stress increases
- the increasing number of shear dominated fractures (green fractures).



Rock Type	Limestone
Density (kg m^{3})	2700
Young's Modulus (GPa)	30
Poisson's Ratio	0.3
Friction Coefficient	0.6
Cohesion (MPa)	25
Tensile Strenght (MPa)	5
Mesh Element Size (cm)	0.002

Length = 0.5 m
Thickness = 0.1m

Figure 5. 17: Boundary conditions used for evaluation of the differential stresses development within a single layer during layer-parallel extension. The left hand side boundary is pinned in the x-direction but all other boundaries are free to move (extend and contract). A linear function is used to apply a uniform horizontal velocity to the top and bottom boundaries and the model remais rectangular. A vertical load normal to the top and bottom boundaries is applied. The material properties are those described in the table and the mesh element size is 0.002 cm.

Extensional fractures form perpendicular to the minimum principal stress, which means that if the differential stresses are large ($\sigma_3 > \sigma_1$ but still <4T, where T is the tensile strength of the rock) a definite direction of relatively easy opening exists and the fractures will be straight and well aligned. As the differential stress decreases the tendency for the fractures to be well aligned also decreases and they become more irregular and less organized. Natural examples of such behaviour can be found in nature (Figure 5.19) and the phenomenon of increasing irregularity with decrease in differential stress can be illustrated schematically using Mohr Circle representation (Figure 5.20).

Quantification of the differential stress during the evolution of the four models is shown in Figure 5.21 confirms that the differential stress does increase with increase in normal load and that after an initial rise to a maximum value it drops to a lower value as a fracture develops and this is generally maintained during further extension of the model. The differential stress values shown in Figure 5.21 relate to the centre of the model (red dot in Figure 5.18).

Further experiments were performed to investigate the variation of stress at different points within

the model specifically the evolution of the horizontal stress (σ_3) (i) at points where fractures were formed and (ii) points which have not been intersected by fractures (Figure 5.22). Significant differences are apparent (Figure 5.23). Whereas the stress profile that represents the stress at a point intersected by a tensile fracture (Figure 5.22 A) is compressive (positive values of horizontal stress, see also the red line on the graph in Figure 5.23) due to the relief of the imposed tensile stress caused by the formation of the fracture at a strain= 0.26%, the point in the model shown in Figure 5.22 B, which is not in the vicinity of a fracture, remains in the tensile region (negative values of horizontal stress) for the whole simulation. Interestingly, the plot of the horizontal stress for this position (Figure 5.23) registers transient drops in the tensile stress caused by the development of nearby fractures – see the stress drops at strains 0.340 and 0.730. However, as can be seen from this Figure, the stress never becomes compressive.

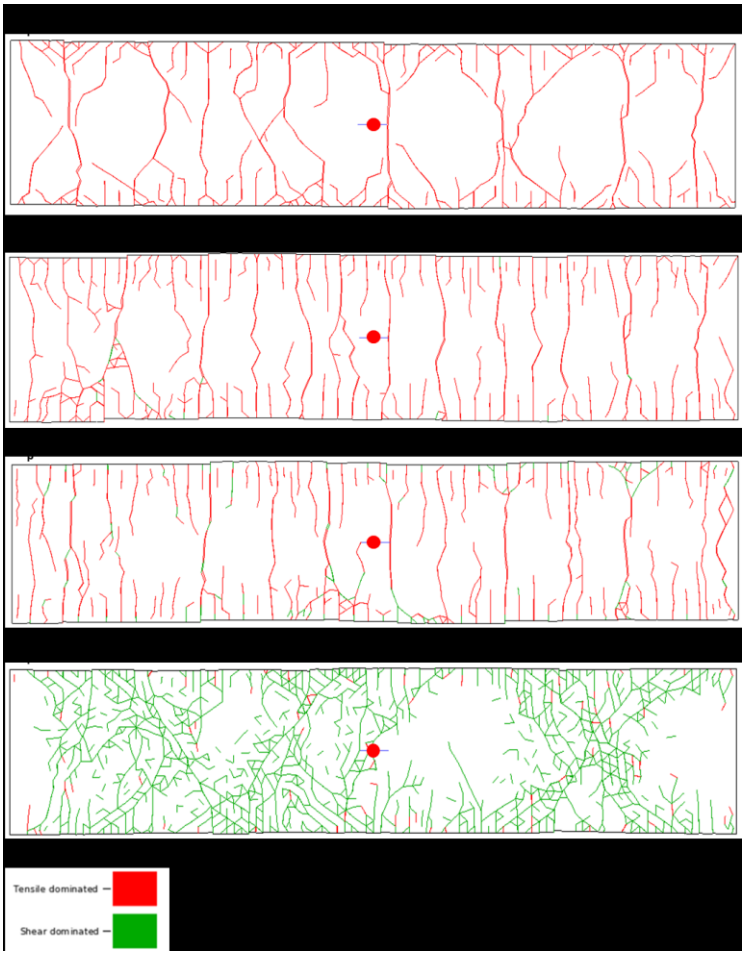


Figure 5. 18: Fracture models showing the change in orientation and fracture type resulting from the increasing differential stresses generated by an increasing vertical load (σ_p). The red represents tensile dominated fractures and green shear dominated fractures. It is evident that at 75MPa of vertical pressure the differential stresses are large enough so that the shear failure envelope is contacted and shear fractures are dominant. The ret dot marks the data retrieving points.

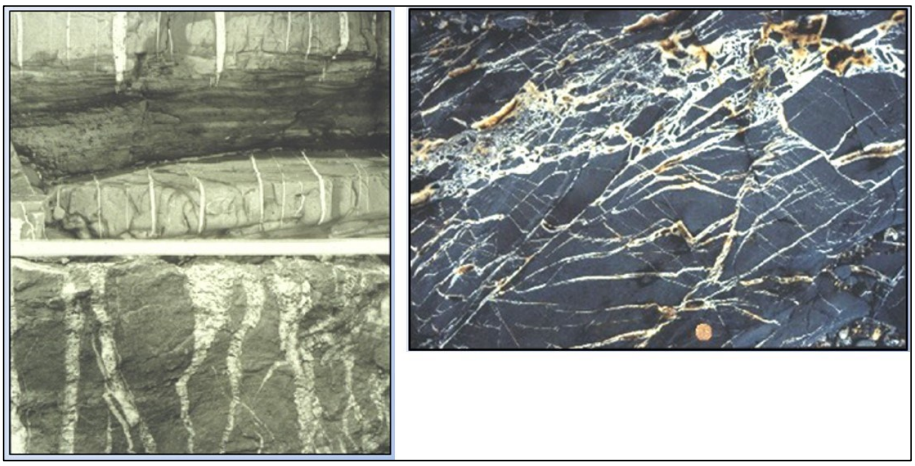


Figure 5. 19: Geological examples showing the effect of the differential stress magnitude on the geometry of extensional fractures. The photo on the upper left, represents a stress sate where the differential stresses are large but sitll less than 4T (Mohr circle i from Figure 5.20) and fractures form perpendicularly to σ_3 (horizontal relative to the fractures orientation on the picture). The image below it shows more irregular extensional fractures which are the result of a lower differential stress. The image on the right represents a situation where the stress state is close to hydrostatic (Mohr circle iv from Figure 5.20) and where there is not a prefferential direction of fracture opening.

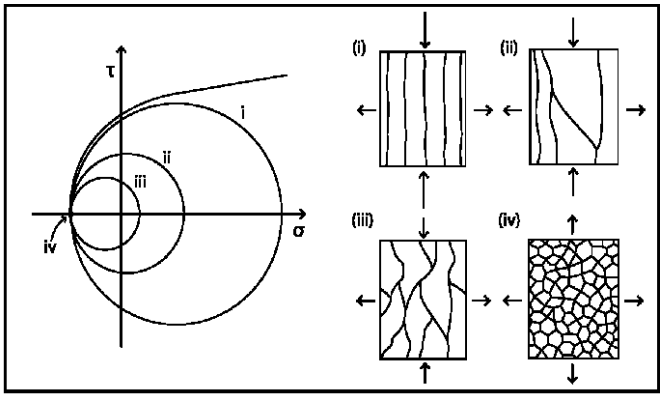


Figure 5.20: In the stress state represented by Mohr circle i (large differential stress), there is a definite direction of easy opening for the tensile fractures, i.e. normal to σ_3. The fractures therefore exhibit a marked alignment normal to this direction. For the stress states represented by the Mohr circles ii-iv, the differential stress becomes progressively smaller eventually reaching the hydrostatic stress state represented by Mohr 'circle' iv where the differential stress is zero (the normal stress across all planes is the same). At this point there is no direction of relatively easy opening for the tensile fractures and fractures will show no preferred orientation. (from Cosgrove, 1997).

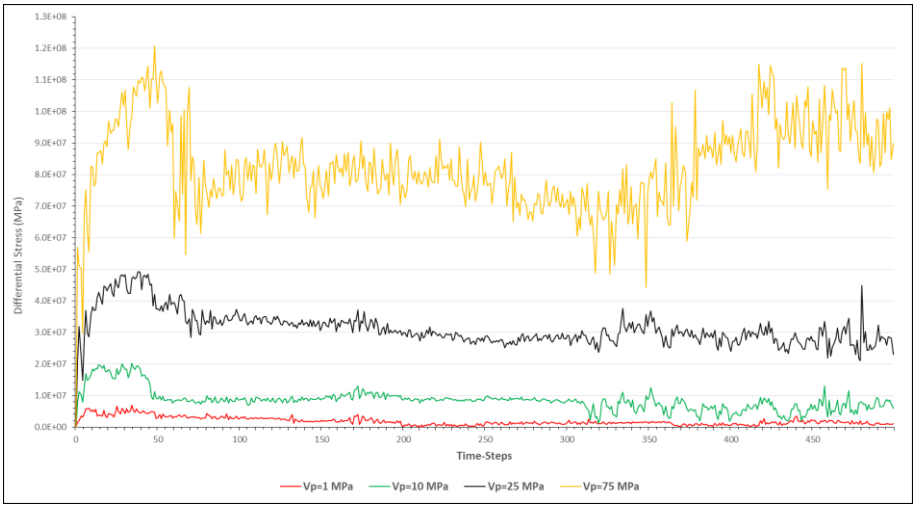


Figure 5. 21: Differential stress build up for different values of vertical pressure (σ_v). The differential stresses are measured at a point in the middle of the models (see the red points on Figure 5.18). It is clear that an increase in the vertical pressure causes an increase in the differential stresses that build-up during the extension of the model.

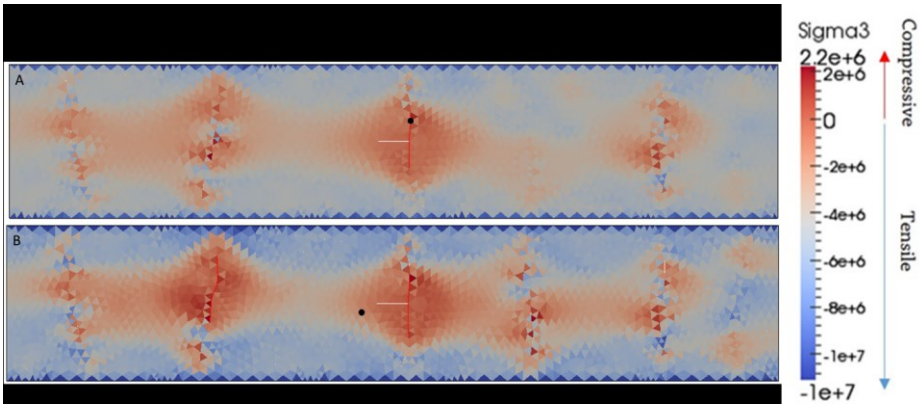


Figure 5. 22: Sampling points (black dots) where horizontal stress data were collected during the course of the experiment. One of the points is in a region intersected by a fracture (A) and the other in a region where no fractures are formed (B). The stress values are presented in Figure 5.23. Note that A and B are the same model at the same accumulated strain.



Figure 5. 23: Horizontal stress plots for a one layer model similar to the one presented on Figure 5.22 (subjected to a 1Mpa vertical load - Vp) versus accumulated strain. The red curve represents the horizontal stress (Sigma 3) development for a sampling point which has been intersected by a tensile fracture (see Figure 5.22 A). The green curve represents the horizontal stress (Sigma 3) development for a sampling point which has been is at some distance from any fracture during the whole simulation (See Figure 4.22 B).

5.2.2 Fracture propagation

A key parameter that controls the formation of fractures within a material is the 'Energy release rate' or 'Strain energy release rate' 'G'. This is the energy dissipated during fracturing per unit of newly created fracture surface area. This quantity is central to fracture mechanics because the energy that must be supplied to a crack tip for it to grow must be balanced by the amount of energy dissipated due to the formation of new surfaces and other dissipative processes such as plasticity. For each of the fracture modes (Mode I – tensile fractures and Mode II – shear fractures) there is a different value of energy release rate which is noted as G_I and G_{II} respectively.

The calibration procedure to obtain these parameters for the numerical modelling is an iterative process that involves running a series of numerical Brazilian Disc (BD) and Uniaxial Compressive Strength (UCS) tests (Figure 5.24, Models I and II) to find a set of input parameters in the numerical modelling that result in emergent values of the Elastic modulus, Poisson's ratio, UCS and BD strength that closely approximate those measured in the laboratory (in our case obtained from literature based on laboratory measurements performed in rocks made by other researchers).

The UCS test is based on a rectangular specimen of 100 mm × 150 mm and the BD test uses a circular disc having a diameter of 120 mm, which are loaded by two rigid platens moving inward at a constant velocity of $v/2$ = 0.05 m/s (Figure 5.24). Tests were conducted using material properties for limestone (Table 5.1), shale (Table 5.2) and gypsum (Table 5.3) based on real rock samples tested by: Lama &

Vutukuri, 1978; Singh & Eksi, 1987; Engelder & Peacock, 2001 and Heidari *et al.*, 2012. The model domains are represented by unstructured meshes with element size $h \approx 1$ mm. The friction coefficient between the platen and specimen is set to be 0.1.

Table 5.1: Assumed material properties used in the numerical modelling of limestone based on rock tests carried by Lama & Vutukuri, 1978 and Engelder & Peacock, 2001.

Parameter	**Value**
Bulk density ρ (kg/m^3)	2700
Young's modulus E (GPa)	30.0
Poisson's ratio υ	0.3
Tensile strength f_t (MPa)	5
Coefficient of friction	0.6
Cohesion c (MPa)	20
Uniaxial compressive strength UCS (MPa)	80

Table 5.2: Assumed material properties used in the numerical modelling of shale based on rock tests carried by Lama & Vutukuri, 1978 and Engelder & Peacock, 2001.

Parameter	**Value**
Bulk density ρ (kg/m^3)	2400
Young's modulus E (GPa)	10.0
Poisson's ratio υ	0.15
Tensile strength f_t (MPa)	1.45
Coefficient of friction	0.5
Cohesion c (MPa)	12
Uniaxial compressive strength UCS (MPa)	42

Table 5.3: Assumed material properties used in the numerical models of gypsum specimens based on rock tests carried by Heidari *et al.*, 2012 and Singh & Eksi, 1987: Gypsum

Parameter	Value
Bulk density ρ (kg/m^3)	2300
Young's modulus E (GPa)	20
Poisson's ratio υ	0.2
Tensile strength f_t (MPa)	1.8
Coefficient of friction	0.6
Cohesion c (MPa)	9
Uniaxial compressive strength UCS (MPa)	32

Following the procedure proposed by Tatone and Grasselli (2015), a series of numerical experiments were designed with the energy release rates (G_I for mode I fractures and G_{II} for mode II fractures) given in Table 5.4, Table 5.5 and Table 5.6 for limestone, shale and gypsum respectively. The results of two numerical models conducted for limestone are shown in Figure 5.25 one for a Brazilian disc test (Fig. 5.25 a) and the other for a uniaxial compressive test (Figure 5.25 b). The values of energy release rates used in these experiments shown are G_I (A) =20 J/m^{2}and G_{II} (B)= 600 J/m^2. The stress-strain plots linked to the two experiments show classical brittle behavior namely a linear increase in strain with increase in stress and sudden failure when the strength of the material is reached.

By repeating these experiments using different values of G_I & G_{II} surfaces defining the simulated UCS and BD strengths as a function of the input fracture energies can be defined, (Figure 5.26 a) & b)). Each point on the surface represents a single combination of G_I & G_{II} (i.e combination AA, AB, BA etc. see Table 5.4). The intersection between this plane and a horizontal plane that represents the *target value* (the real strength of the material determined experimentally) for either tensile strength (BD test) or uniaxial compressive strength (UCS test), defines the line along which the combination of G_I & G_{II} yields that target value, i.e combinations of G_I and G_{II} that result in the model failing at the uniaxial compressive strength and tensile strength measured on the real rock. The intersection point of the UCS and BD intersection lines (Figure 5.26 c)) defines the unique combination of GI & GII that results in the numerical models having the same values of UCS and BD strength as those determined in the laboratory using real rock samples. The procedure was repeated for shale and gypsum and results are presented in Figure 5.27 and Figure 5.28.

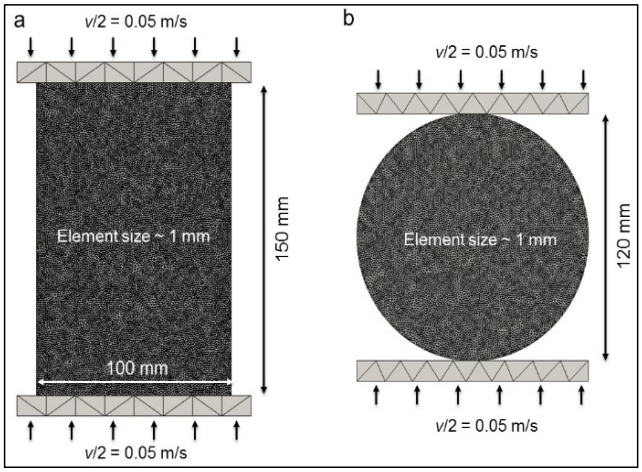


Figure 5. 24: FEMDEM Model setup for a) the uniaxial compressive strength (UCS) test and b) the Brazilian disc (BD) test (Qinghua & Latham, 2015).

Table 5.4: look-up table with the values of BT and UCS obtained for the several experiments with different GI and GII parameters for Limestone. An example of the results is shown in Figure 5.25.

		Limestone									
		A		B		C		D		E	
	G_I	2.00E+01		4.00E+01		6.00E+01		8.00E+01		1.00E+02	
	G_{II}	BT	UCS	BT	UCS	BT	UCS	BT	UCS	BT	UCS
A	2.00E+02	2.62E+06	7.53E+07	3.28E+06	7.58E+07	3.20E+06	7.50E+07	3.29E+06	7.61E+07	3.99E+06	7.52E+07
B	6.00E+02	4.19E+06	7.87E+07	4.30E+06	7.96E+07	4.74E+06	7.85E+07	4.75E+06	7.90E+07	5.61E+06	7.91E+07
C	1.00E+03	4.79E+06	8.09E+07	5.25E+06	8.05E+07	5.65E+06	8.09E+07	5.75E+06	8.10E+07	5.85E+06	8.04E+07
D	1.40E+03	5.04E+06	8.35E+07	5.54E+06	8.38E+07	5.76E+06	8.38E+07	5.88E+06	8.33E+07	5.99E+06	8.25E+07
E	1.80E+03	5.08E+06	8.38E+07	5.00E+00	8.36E+07	5.79E+06	8.37E+07	5.94E+06	8.40E+07	6.06E+06	8.44E+07

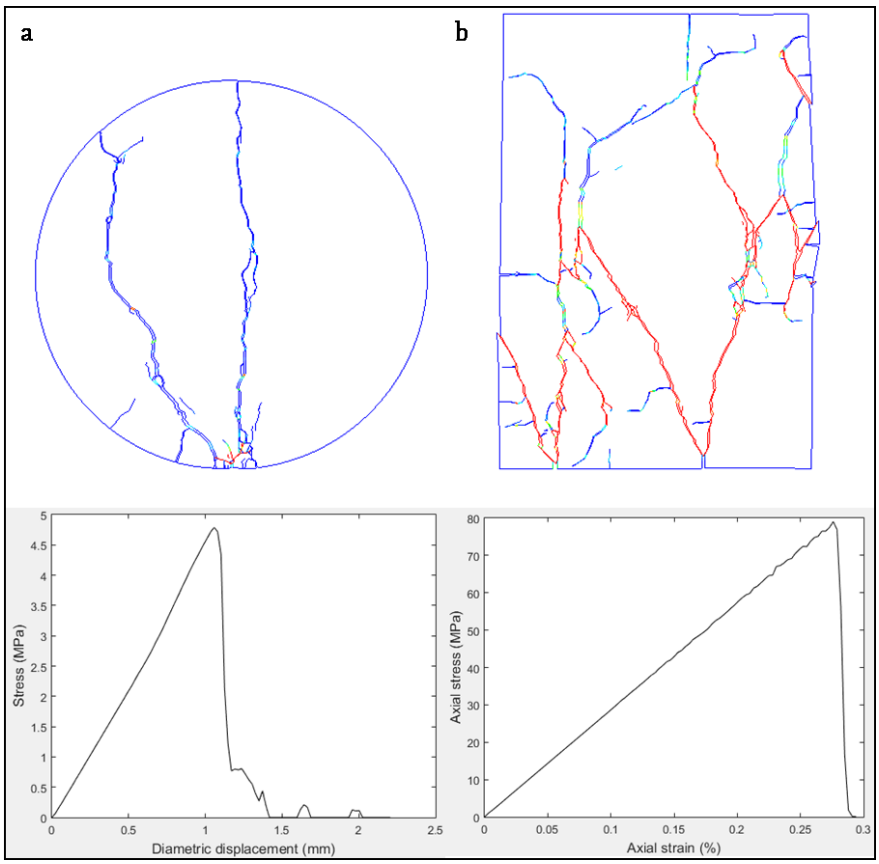


Figure 5.25: results obtained for BD and UCS tests for a value of G_I=20 J/m^{2}and G_{II} = 600 J/m^2 (test AB from Table 5.4)

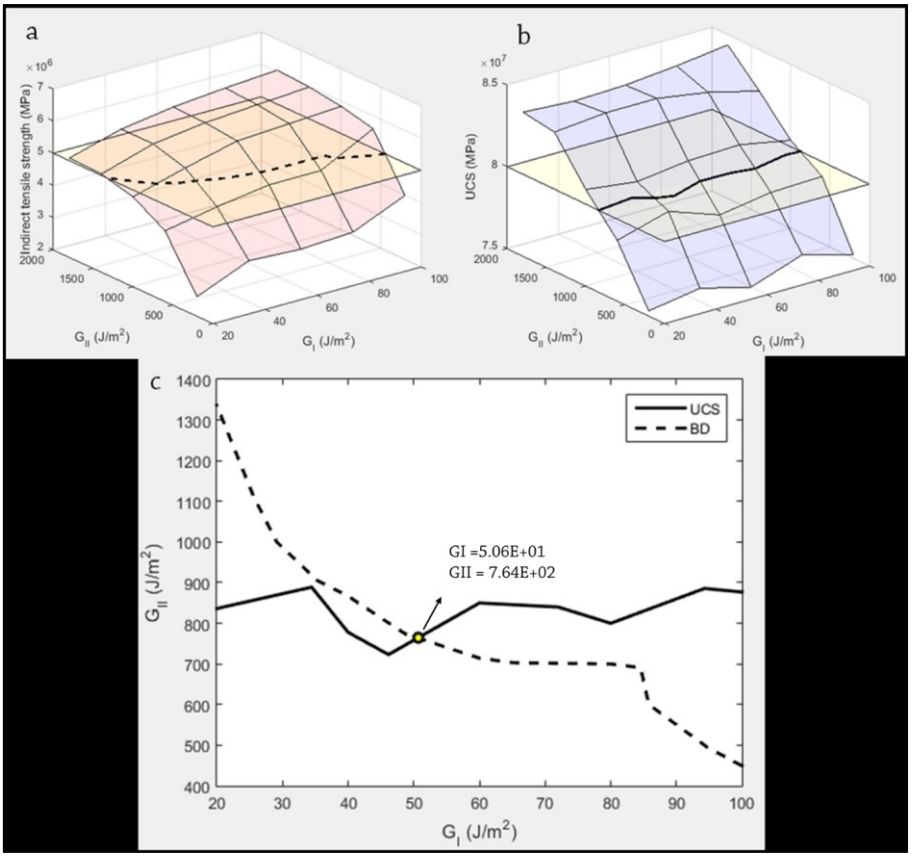


Figure 5.26: Calibration of energy release rates for simulating intact rock failure of a limestone: a) simulated indirect tensile strength as a function of energy release rates GI and GII and the intersection polyline with the plane of target tensile strength (i.e. 5 Mpa) b) Simulated uniaxial compressive strength (UCS) as a function of energy release rates GI and GII and the intersection polyline with the plane of target UCS (i.e. 8 Mpa); c) the intersection point of the projected 2D UCS intersection polyline and BD polyline defines the calibrated combination of GI and GII

Table 5.5: look-up table with the values of BT and UCS obtained for the several experiments with different GI and GII parameters for Shale. Results are shown in Figure 5.27

		Shale									
		A		B		C		D		E	
	G_I	1.00E+00		2.00E+00		3.00E+00		4.00E+00		5.00E+00	
	G_{II}	BT	UCS	BT	UCS	BT	UCS	BT	UCS	BT	UCS
A	1.00E+00	6.55E+05	3.82E+07	1.33E+06	3.66E+07	1.23E+06	3.66E+07	1.25E+06	3.96E+07	1.26E+06	3.73E+07
B	2.00E+00	6.55E+05	3.82E+07	1.33E+06	3.66E+07	1.23E+06	3.66E+07	1.25E+06	3.96E+07	1.26E+06	3.73E+07
C	5.00E+00	6.84E+05	4.03E+07	1.33E+06	4.05E+07	1.23E+06	3.97E+07	1.24E+06	4.12E+07	1.26E+06	4.02E+07
D	1.20E+01	1.02E+06	4.43E+07	1.87E+06	4.42E+07	1.93E+06	4.34E+07	2.07E+06	4.41E+07	2.18E+06	4.42E+07
E	1.50E+01	1.02E+06	4.49E+07	1.81E+06	4.54E+07	2.18E+06	4.66E+07	2.29E+06	4.48E+07	2.18E+06	4.52E+07

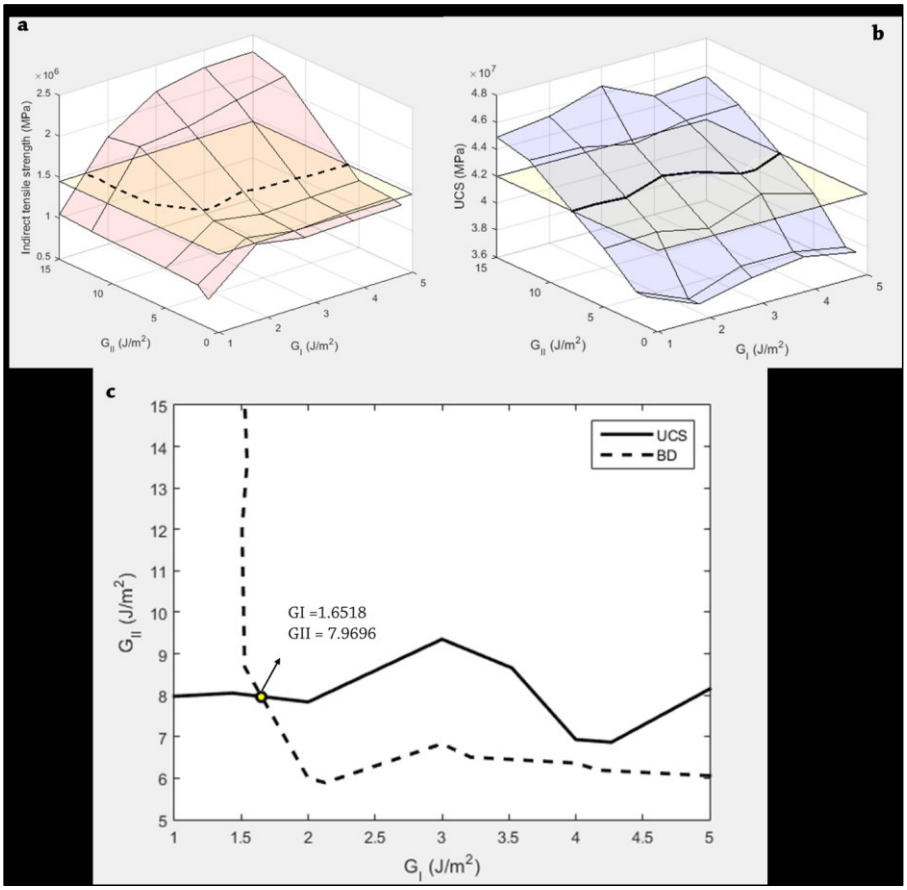


Figure 5.27: Calibration of energy release rates for simulating intact rock failure of a shale: a) simulated indirect tensile strength as a function of energy release rates GI and GII and the intersection polyline with the plane of target tensile strength (i.e. 1.45Mpa) b) Simulated uniaxial compressive strength (UCS) as a function of energy release rates GI and GII and the intersection polyline with the plane of target UCS (i.e. 4.2 Mpa); b; c) the intersection point of the projected 2D UCS intersection polyline and BD polyline defines the calibrated combination of GI and GII.

Table 5.6: look-up table with the values of BT and UCS obtained for the several experiments with different GI and GII parameters for Gypsum. Results are shown in Figure 5.28

		Gypsum									
		A		B		C		D		E	
	G_I	1.00E+00		2.00E+00		3.00E+00		4.00E+00		5.00E+00	
	G_{II}	BD	UCS	BD	UCS	BD	UCS	BD	UCS	BD	UCS
A	5.00E+00	8.14E+05	2.79E+07	8.75E+05	2.59E+07	1.51E+06	1.90E+07	9.68E+05	2.06E+07	1.57E+06	2.59E+07
B	1.00E+01	9.98E+05	2.07E+07	1.36E+06	2.35E+07	1.55E+06	2.82E+07	1.58E+06	2.22E+07	1.14E+06	2.40E+07
C	2.00E+01	1.17E+06	3.79E+07	1.56E+06	2.96E+07	1.82E+06	2.74E+07	1.81E+06	2.93E+07	1.38E+06	2.86E+07
D	3.00E+01	1.56E+06	3.70E+07	1.57E+06	1.92E+07	1.58E+06	3.20E+07	1.60E+06	2.72E+07	1.60E+06	2.89E+07
E	4.00E+01	1.80E+06	4.29E+07	1.95E+06	4.06E+07	2.00E+06	2.56E+07	1.91E+06	4.29E+07	2.02E+06	3.41E+07

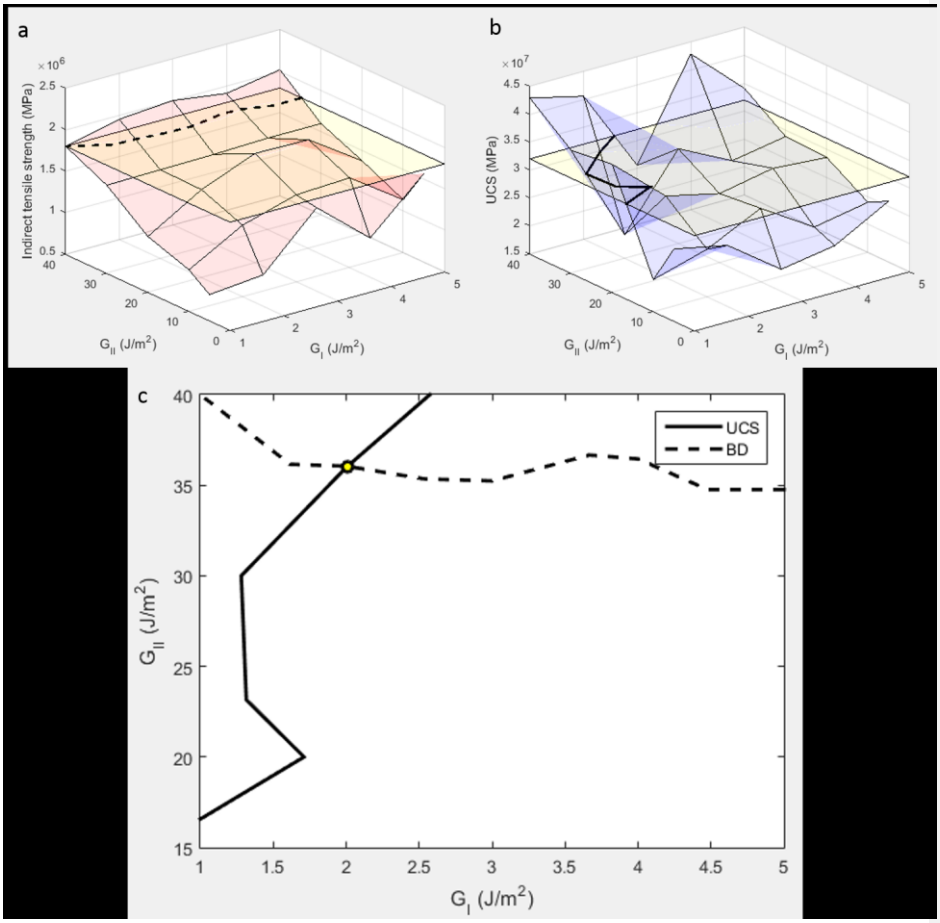


Figure 5. 28: Calibration of energy release rates for simulating intact rock failure of gypsum: a) simulated indirect tensile strength as a function of energy release rates GI and GII and the intersection polyline with the plane of target tensile strength (i.e. 1.8Mpa) b) Simulated uniaxial compressive strength (UCS) as a function of energy release rates GI and GII and the intersection polyline with the plane of target UCS (i.e. 3.2 Mpa); b; c) the intersection point of the projected 2D UCS intersection polyline and BD polyline defines the calibrated combination of GI and GII

5.2.3 Validation of frictional sliding along interfaces

Such as in Latham et. al. (2012), in the FEMDEM code used for the experiments this thesis reports on, a Coulomb friction law governs the sliding between opposite sides fractures as well as at the interface between layers (which behave like a pre-existing closed crack with no cohesion), i.e. sliding of the interface occurs when the shear stress (τ) exceeds the normal stress (σ_n) and the coefficient of sliding friction (μ):

$$\tau \geq \mu\sigma_n \quad \text{(Eq. 5.4)}$$

In order to validate the Coulomb friction law implemented in the FEMDEM/Y2D code, which allows friction at the interface between layers to be assigned independently of the rock friction, a benchmark test was conducted which is similar to that of Guo, 2014. This test consists of a square block resting on a horizontal plane of identical material properties. An initial horizontal velocity (Vxi) is applied to the block. Due to the existence of friction between the block and the base, the block slows and after having travelled a certain distance, the stop distance, will stop. The stop distance L can be theoretically derived and is given by the following equation:

$$L = \frac{v_i^2}{2\mu g} \quad \text{(Eq 5.5, Guo, 2014)}$$

where μ is the coefficient of sliding friction, g is the acceleration due to gravity and Vi is the initial horizontal velocity. Different initial velocities (Vxi = 1, 3, 5 ms^{-1}) were applied for different values of sliding friction (Figure 5.29) of the surface and results are compared with the analytical solution (Figure 5.30). Data shows that the numerical results are in good agreement with the theoretical solution calculated by Equation 5.4 for all the friction coefficients and initial horizontal velocities being tested.

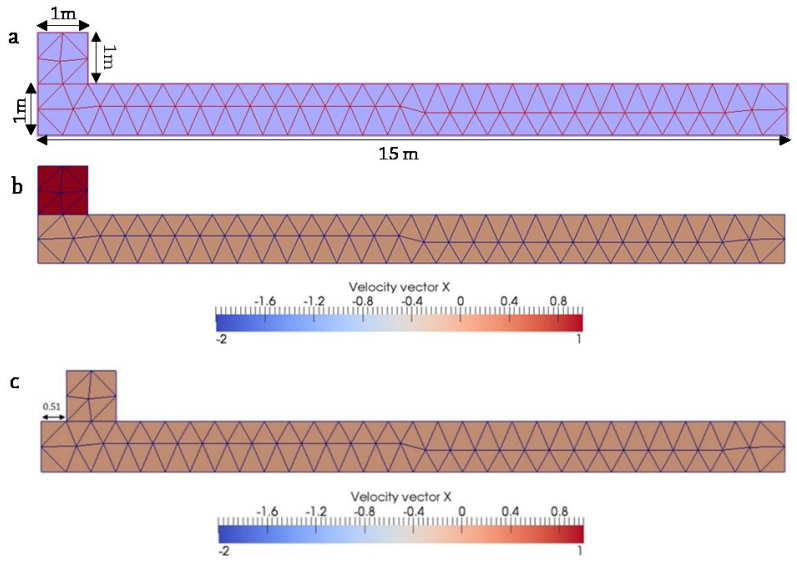


Figure 5.29: a) Model setup and b) & c) Initial and final stages for the model with an initial velocity of 1 ms^{-1} and a coefficient of sliding friction of the interface equal to 0.1. This configuration yielded a stop distance of 0.51m.

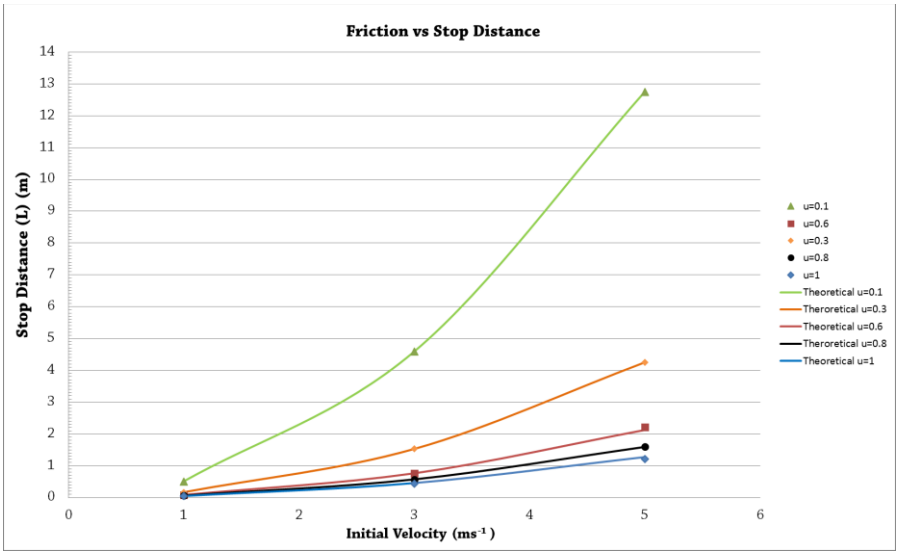


Figure 5.30: Results of the modelling of a sliding block on a horizontal surface. The solid coloured lines show the results predicted from theory (See Eq. 5.4) and the coloured symbols show the results obtained from the modelling. The two are in perfect agreement.

5.3 Numerical Simulations for Fracture propagation through layered rocks

In order to understand the impact of both rock mechanical parameters, textural characteristics of the rocks including bedding planes and stress application on fracture propagation, tests have been conducted to examine the:

- The influence of the coefficient of sliding friction on a layer boundary on fracture propagation
- The influence of the Young's modulus from one layer to another on fracture propagation
- The influence of the thickness of an incompetent layer on fracture propagation to an adjacent competent layer.

The choice of these three numerical tests was based on the learnings obtained from the field work and literature review.

The field work in Section 3 demonstrated the importance of:

- Layer interlocking – which can be understood as a high friction interfaces;
- Incompetent thin layers – both the work in the mines and in Somerset revealed that incompetent thin gypsum and shale layers are common intervals of fracture arrest.
- Vertical facies anisotropy which is associated with elastic modulus exchanges.

The literature review in Section 4 has revealed the most important factors that researchers consider as being able to influence fracture propagation trough an interface. From the six factors identified by these researchers (strength of the interface, stiffness, in-situ stress differences, friction at the layer boundaries, thickness of the incompetent layer and type of driving stresses), we have chosen to analyze those which match what was seen in the field and which are within the abilities of the FEMDEM numerical code. These are outlined above.

Several different set-ups of boundary conditions were tested before finding those which allowed the best insight into the problem at hand: mechanical factors influencing vertical fracture propagation through a layered sequence. As outlined in Section 4, particularly in Section 4.4, hydraulic fracturing is the mechanism behind the formation of fractures in compressive environments – the most common in the earth's crust - and it occurs when the least principal stress becomes tensile under the influence of high fluid pressure.

A rectangular three layered model was used. Although simple this configuration is sufficient to predefine three different materials to the layers while having two boundaries to study how fractures interact with them. Several mesh sizes and shapes were tested and it was found that an unstructured triangular mesh with 5mm sides allowed a compromise between the quality of the data and simulation times.

Although the overall objective of the research was to understand which mechanical parameters influence the vertical propagation of fractures through a layered sequence and that might be created by an increasing fluid pressure inside the reservoir, the FEMDEM+Y2D code used for this research did not include the possibility to simulate fluids. However it was considered that a set-up that generated vertical fractures which intersected the interfaces of the layers would be sufficient to study the problem. This was achieved by modeling the simplest situation: applying a vertical confining pressure to the three layered model – which emulates the overburden – and an horizontal extension up to 1% strain (a 1% strain was chosen so that the formation of fractures that intersected the interfaces was guaranteed) while maintaining its rectangular shape. As it will be seen these boundary conditions allowed the formation of several sets of vertical fractures and the study of the parameters mentioned earlier.

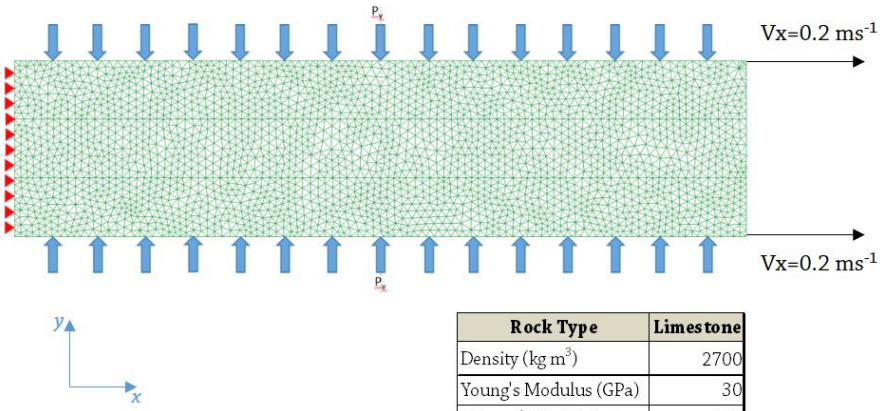
A ramping function was applied. This allowed vertical pressure to build up during the initial steps of the simulation in order to avoid a sudden shock to the model.

5.3.1 Effect of interfacial friction along the interface and of overburden stress.

Numerical models have been run to determine the roles of layer-normal loads and the coefficient of sliding friction along the interfaces between adjacent layers on fracture propagation across an interface. An increase in both these parameters will increase the resistance to slip along the interface ($\tau = \mu\sigma$) and therefore it was postulated that it should increase the likelihood of fracture propagation across it. The investigation involved 3-layer models. The values of the coefficient of frictions used were 0, 0.6, 1 and 2.5 and the layer normal loads were 1Mpa, 10MPa, 25MPa and 75 MPa. Note that although most geological materials have coefficients of sliding friction between 0.3 (fault gauges composed of minerals such as montmorillonite or vermiculite) and 0.6/0.7 (solid rocks), we have chosen to test lower values (μ=0) to simulate a cohesionless boundary – which we argue could be similar to what was observed in Tytherigton quarry (see Section 3.5.3) where limestone layers are separated by thin clay layers causing the interfaces between the layers to remain flat and fractures to be arrested - and very high values (μ=1 and μ=2.5) to simulate a situation where sliding between layers is impossible – similar to what occurs in Tytherington where the stylolites hinder frictional sliding between contiguous limestone layers. A velocity-controlled constraint condition in the x-direction (V_x=0.2 ms^{-1}) was applied to the top and bottom boundaries. This velocity constraint allowed the application of an equal strain value along the model boundaries, through the relation $\varepsilon = 2v/L$ where ε is strain (in decimal scale), v is velocity and L the length of the model. The right hand side boundary moves at the same rate as the top and bottom boundaries extend and the left hand side boundary is pinned in the x-direction. The vertical load (σ_v) is applied at the top and bottom boundaries and the coefficient of sliding friction of the interface between the two layers is varied. The vertical load is then

changed and another suite of experiments performed using various values for the coefficient of friction. The mechanical properties of all three layers are equivalent to those of a limestone (Figure 5.31) and the results of the experimental runs are presented in Figures 5.32 to 5.37.

To study the effect of interfacial friction and overburden stress we have focused on the analysis of the fracture patterns that develop and on the associated change of stress within the layers as the fractures form and grow. Ultimately we aim to understand how these two closely associated parameters ($\tau=\mu\sigma_n$) influence the ability for fractures to propagate across a layer boundary.



Rock Type	Limestone
Density (kg m^3)	2700
Young's Modulus (GPa)	30
Poisson's Coefficient	0.3
Friction Coefficient	0.6
Cohesion (MPa)	25
Tensile Strenght (MPa)	5
Mesh Size	0.005

Figure 5.31: boundary conditions used for modelling the impact of the coefficient of sliding friction and the layer-normal stress on fracture propagation through multilayered sequences. A series of experiments were run involving the systematic variation in the layer normal load and the coefficient of sliding friction along the layer boundaries.

5.3.1.1 The study of the effect of increasing the interfacial coefficient of sliding friction between two layers on fracture propagation across the interface – Fracture Patterns

> Note that in the following figures black lines indicate the boundaries of the model, blue lines are pre-existing fractures (the interfaces are considered to be preexisting fractures so that the Coulomb criteria can be applied to them), red lines fractures that are tensile dominated and green lines fractures that are shear dominated.

Layer Normal Load - 1MPa (Figure 5.32): At a layer normal load (compression) of 1 MPa, all models except "model d", were the coefficient of sliding friction is set at μ=2.5, show strata-bound fractures even when the coefficient of sliding friction is very high (μ=1). In model d) two fractures appear to cross the interface forming a through going fracture. However, this occurs by the joining of two independent fractures that form in the middle and bottom layers (fractures 1 and 2) rather than by the propagation of a single fracture from one layer to the next. All the fractures formed in this first series of experiments are tensile.

Layer Normal Load - 10MPa (Figure 5.33): When the layer normal load is raised ten fold to 10 MPa it was found that a few fractures were able to cross the interfaces when μ=0.6 (Figure 5.33 "model f", fractures 1 and 2). When the coefficient of friction was set at 1 (Figure 5.33 "model g") one fracture developed which interesects the two interfaces connecting the three layers (Figure 5.33 "model g", fracture 1). When the coefficient of friction was set at 2.5 (Figure 5.33 "model h") four through-going fractures (fractures 1, 2, 3 and 4) formed. Fractures 2, 3 & 4 intersect the bottom interface and connecting the bottom and middle layers, fracture 1 intersected all three layers. All the fractures are tensile.

Layer Normal Load - 25MPa (Figure 5.34): When the layer-normal load is 25 MPa, through-going fractures form for all values of friction at the layer interfaces. Some through-going fractures affect only two layers and others three. All fractures are tensile.

Layer Normal Load - 50MPa (Figure 5.35): When the layer-normal load is 50 MPa, all models developed through going fractures. In "model o" 11 through-going fractures are developed and some have sections which are shear dominated. The effect of these can be clearly seen in "model m" fracture 4, and in "model p" fracture 2.

Layer Normal Load - 75MPa (Figure 5.36): When the layer-normal load is 75Mp, most of the fractures occur by shear failure and they are mostly through going for all values of coefficient of sliding

friction at the interfaces. The dip-angle of these fractures (which coincides with the mesh elements boundaries) and the breaking up of the model, leads us to conclude that the geometry of the mesh has a major impact on the orientation and formation of shear fractures.

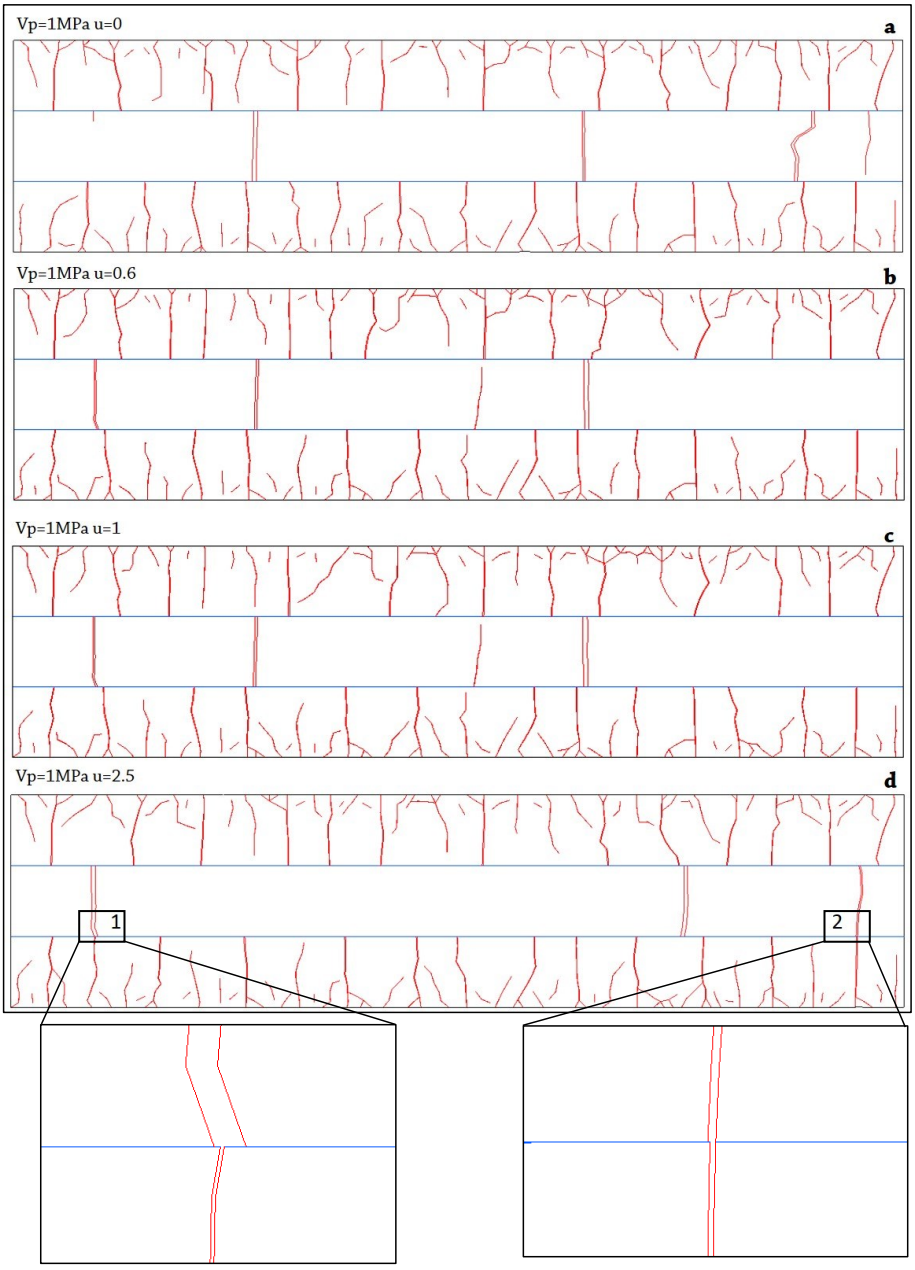


Figure 5.32: Numerical models testing the influence of the coefficient of sliding friction of layer boundaries on the propagation of fractures through a multilayered sequence when the layer normal load is 1MPa. The properties are those of a limestone and are the same for all the layers and models. The coefficient of sliding friction (μ) is increased for each model. The numbers correspond to fractures that have developed and were able to cross an interface. Accumulated strain for all models = 1%.

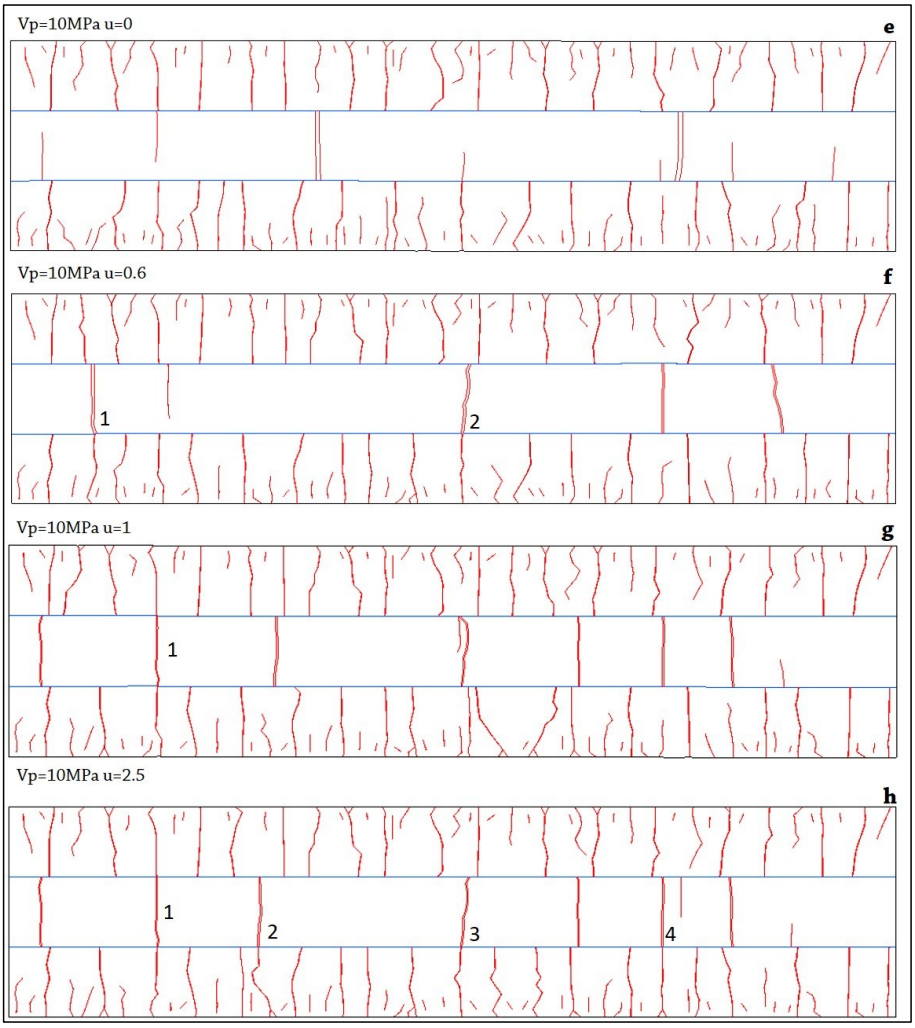


Figure 5.33: Numerical models testing the influence of the coefficient of sliding friction of layer boundaries on the propagation of fractures through a multilayered sequence when the layer normal load is 10MPa. The properties are those of a limestone and are the same for all the layers and models. The coefficient of sliding friction (μ) is increased for each model. The numbers correspond to fractures that have developed and were able to cross an interface. Accumulated strain for all models = 1%.

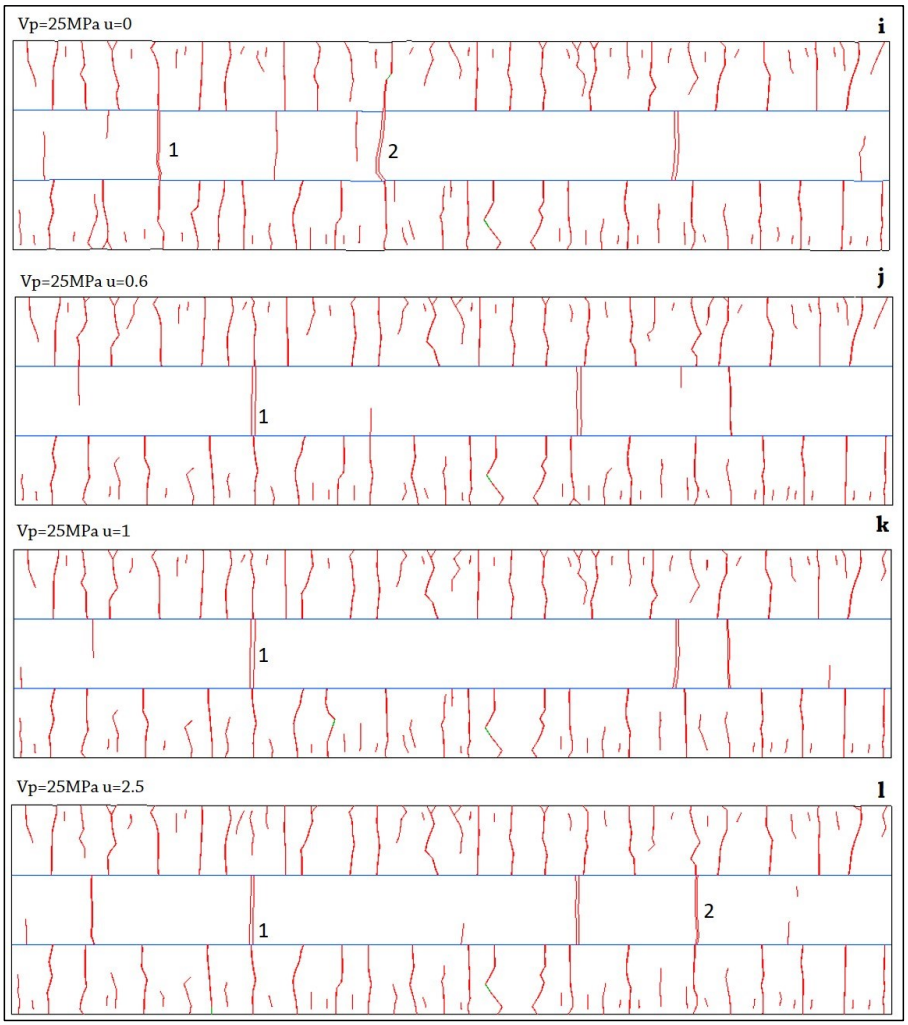


Figure 5.34: Numerical models testing the influence of the coefficient of sliding friction of layer boundaries on the propagation of fractures through a multilayered sequence when the layer normal load is 25MPa. The properties are those of a limestone and are the same for all the layers and models. The coefficient of sliding friction (μ) is increased for each model. The numbers correspond to fractures that have developed and were able to cross an interface. Accumulated strain for all models = 1%.

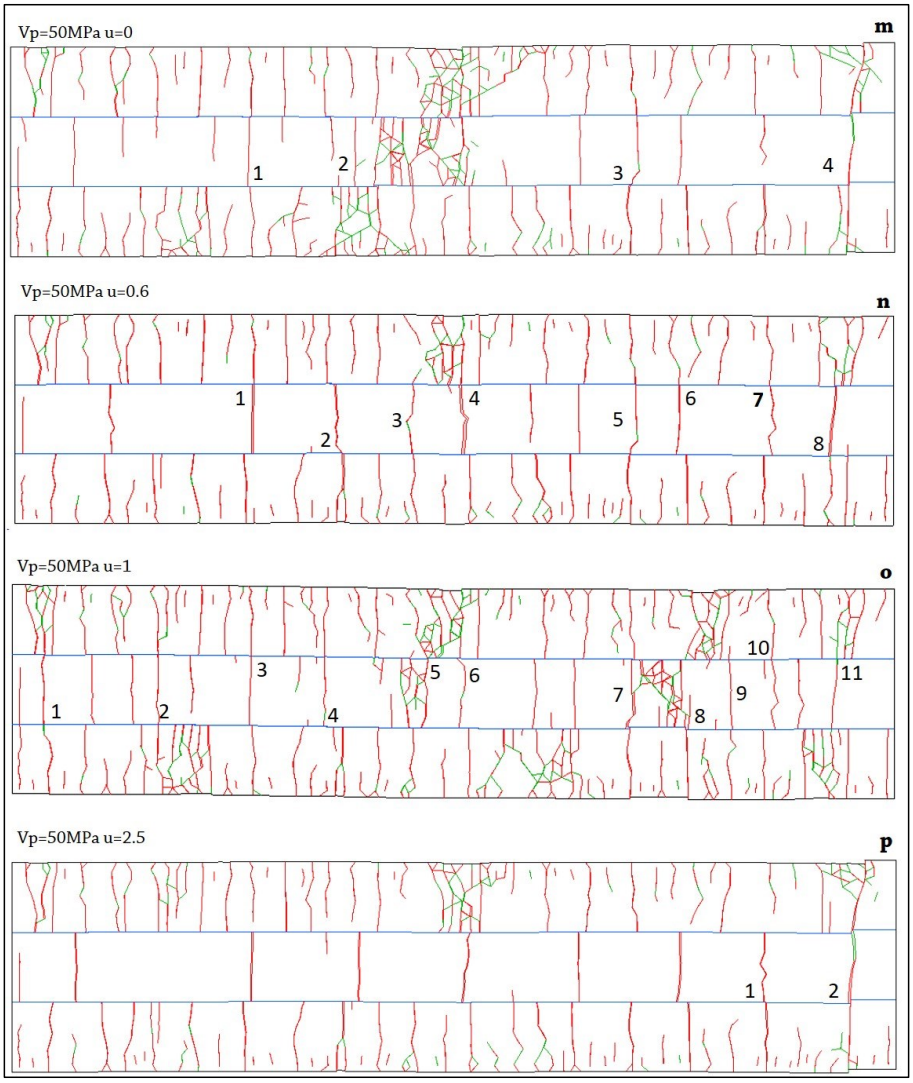


Figure 5.35: Numerical models testing the influence of the coefficient of sliding friction of layer boundaries on the propagation of fractures through a multilayered sequence when the layer normal load is 50 MPa. The properties are those of a limestone and are the same for all the layers and models. The coefficient of sliding friction (μ) is increased for each model. The numbers correspond to fractures that have developed and were able to cross an interface. Accumulated strain for all models = 1%.

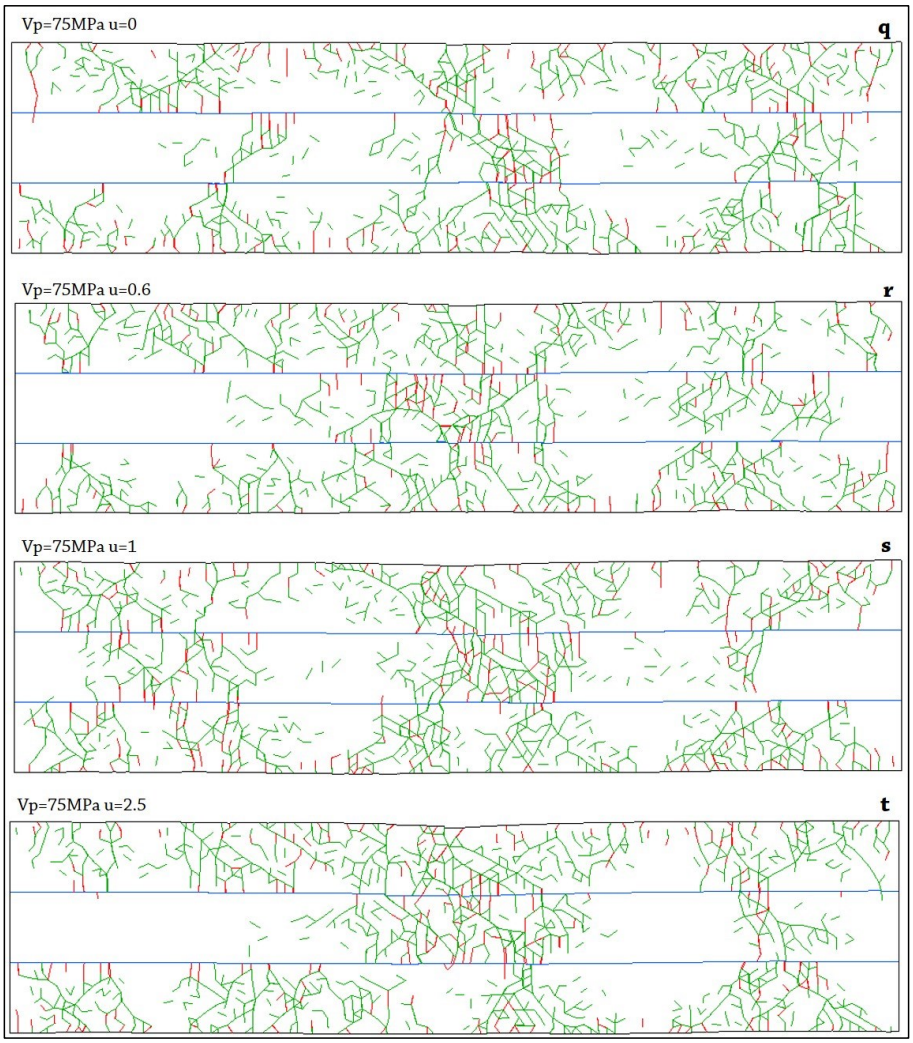


Figure 5.36: Numerical models testing the influence of the coefficient of sliding friction of layer boundaries on the propagation of fractures through a multilayered sequence when the layer normal load is 75 MPa. The properties are those of a limestone and are the same for all the layers and models. The coefficient of sliding friction (μ) is increased for each model. The numbers correspond to fractures that have developed and were able to cross an interface. Accumulated strain for all models = 1%.

5.3.1.2 A Study of the impact of vertical (layer-normal) load on fracture propagation – Fracture patterns

A series of experiments can be extracted from the data that Figures 5.32 to 5.36 provide which can be used to explore the impact of an increase in the applied layer-normal compression on fracture propagation across an interface. These experiments which have the same coefficient of sliding friction (μ=0.6) (Figure 5.37) show that:

1. The first fracture forms at the different strain values for each experiment. With an increase in the layer normal load, there is an increase in the layer-parallel extension required before fracture begins. These results are summarized in Figure 5.38 and Figure 5.39:
   1 MPa: 0.032%
   10 MPa: 0.046%
   25 MPa: 0.072%
   50 MPa: 0.114%
   75 MPa: 0.128%

2. Higher applied layer-normal load leads to an increase in the differential stress (see Figure 5.21 for the one layer model) which in its turn:
   - Leads to the formation of straighter fractures (see explanation in Section 5.2.1, Figures 5.19 and 5.20).
   - Promotes the formation of shear fractures (see Section 4.3.1)

3. There are more through-going fractures in models with higher applied normal stress.

Commented [LJ1]: You must show results plotted on graphs for different confinements and different frictions.

It follows from these observations that;

- An increase in layer-normal stress inhibits fracture formation
- An increase in the differential stress (achieved by an increase in the applied normal stress) leads to the formation of straighter extensional fractures
- An increase in layer-normal stress encourages the formation of through-going fractures
- An increase in layer-normal stress encourages the formation of shear fractures rather than extensional fractures.

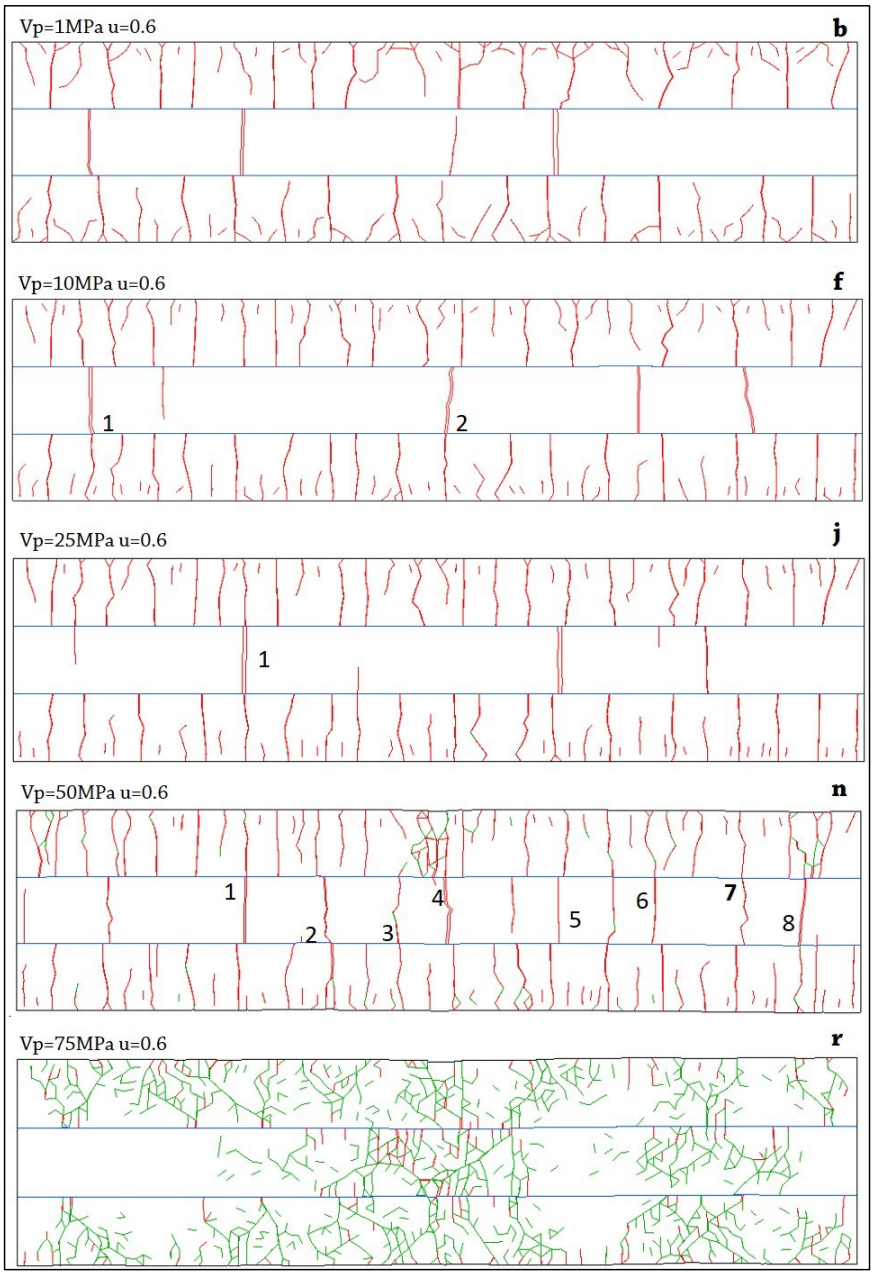


Figure 5. 37: sequence of models that compares the effect of increasing the layer-normal load on fracture development. The boundary conditions are the same for all models and the coefficient of sliding friction (μ) along the layer boundaries is 0.6.. The numbers refer to the order in which the fractures where developed. Accumulated strain is 1% in every model displayed.

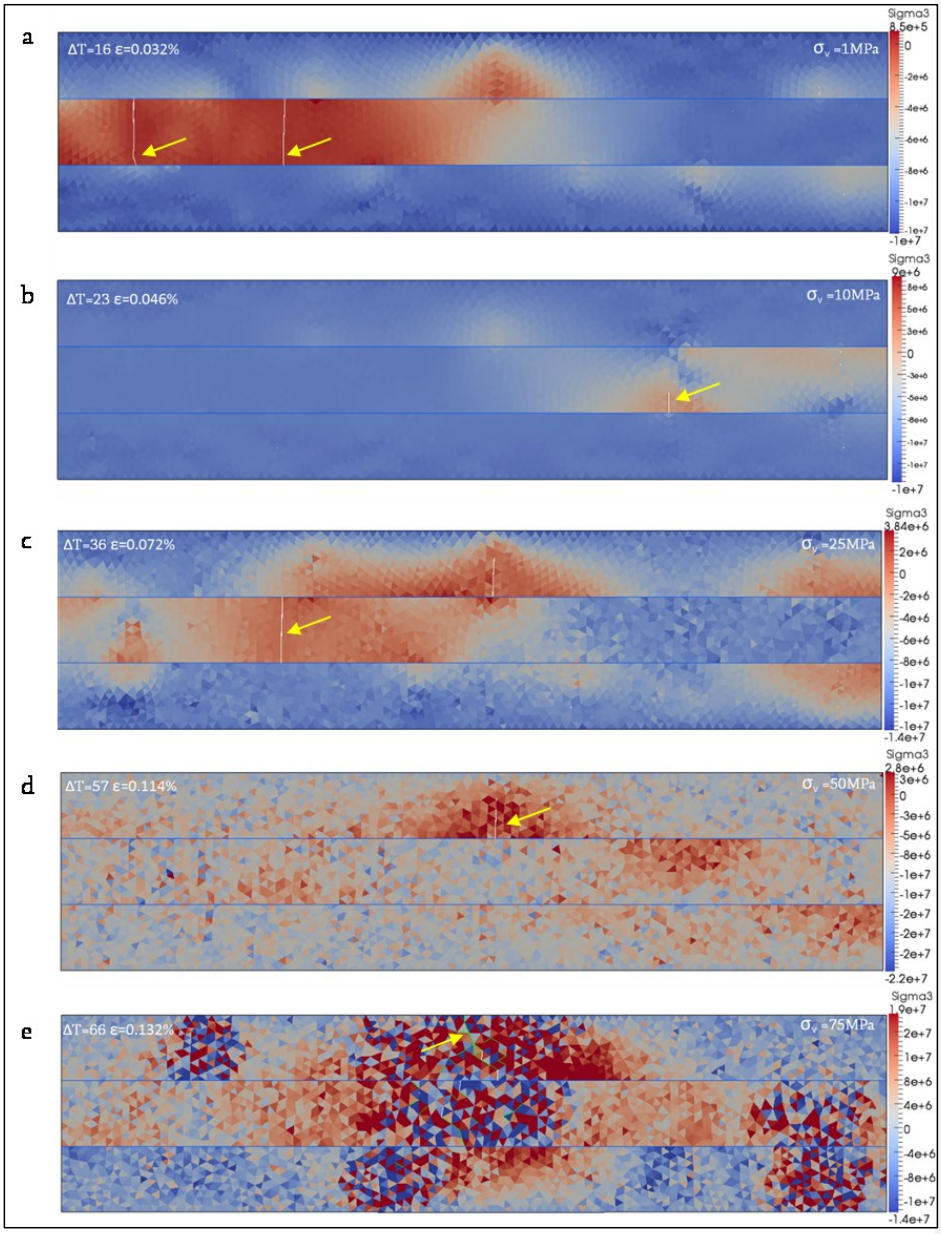


Figure 5. 38: Stress distribution in the 5 experiments represented in Figure 5.37 at the moment where the first fracture appears, showing how an increasing applied vertical stress delays the formation of the first fracture in the models. Each image corresponds to a different model: a) σ_v=1MPa; b) σ_v=10MPa; c) σ_v=25MPa; d) σ_v=50MPa; e) σ_v=75MPa. The yellow arrows indicate the first fractures to have been formed in the model (see also Figure 5.39). For convenience of visualization, tensile fractures are depicted in white and shear fractures in green. Blue colour represents a tensile stress state whereas red a compressive stress state. The coeficient of sliding friction at the layer boundaries is μ=0.6.

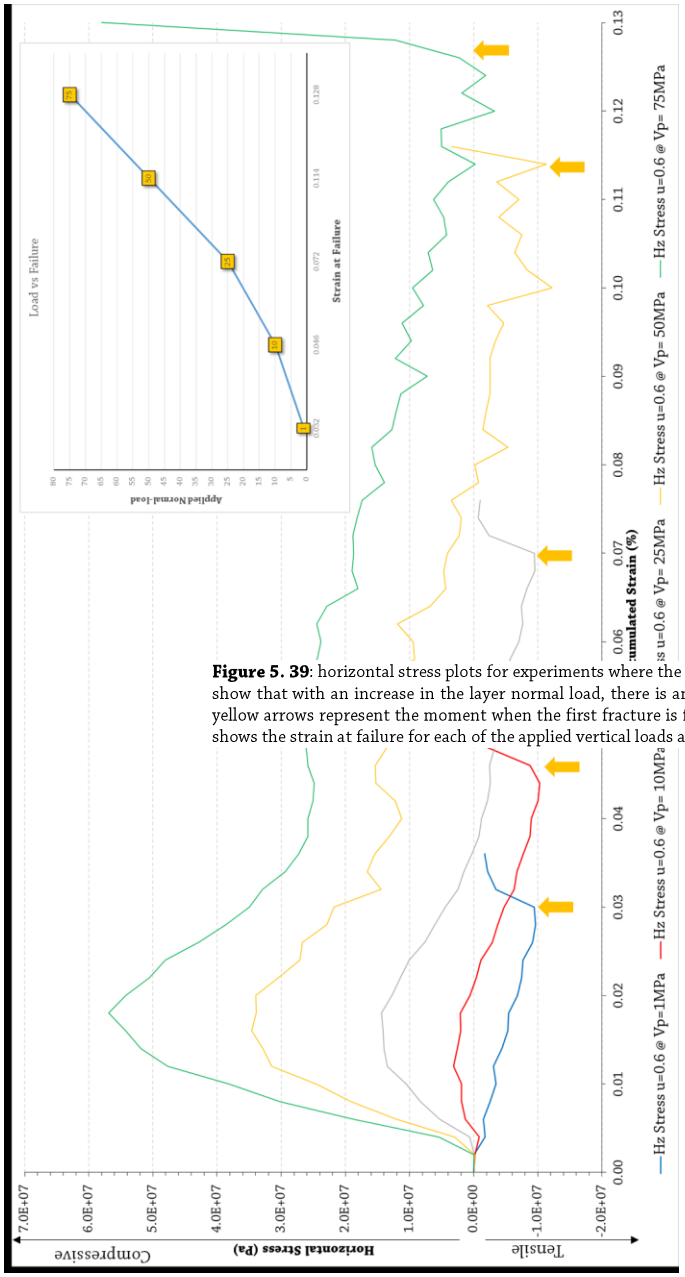


Figure 5. 39: horizontal stress plots for experiments where the coefficient of friction is 0.6 to the point where the first fracture is formed. These show that with an increase in the layer normal load, there is an increase in the layer-parallel extension required before a fracture begins. The yellow arrows represent the moment when the first fracture is formed for each of the layer-normal loads. The graph on the top right hand-side shows the strain at failure for each of the applied vertical loads and shows that this value is higher for higher applied loads.

5.3.1.3 Relation between the coefficient of sliding friction along the layer interfaces, normal load and fracture formation on the development of horizontal stresses.

The aim of this section is to examine the impact of:

i. the coefficient of sliding friction along the layer interfaces;
ii. the layer normal load;
iii. fracturing;

on the build up of horizontal stresses within a multilayered model comprising 3 identical layers being subjected to a horizontal extension. The boundary conditions are the same as for the previous models (Figure 5.31) and a range of coefficients of sliding friction were examined, each subjected to a range of layer-normal loads.

In the models used in these experiments measurements were taken at three different points.: Point A is located in the middle of the model, Point B in the middle layer but on the right and Point C on the top layer on the left (Figure 5.40). The aim of choosing three different locations within the model to monitor the stress state was to eliminate the effect that the mesh has on the horizontal stress build up and to have a better understanding of stress development within the model. This section will demonstrate that of the three parameters considered (i- iii), fractures are the most important factor determining the stress distribution within the model.

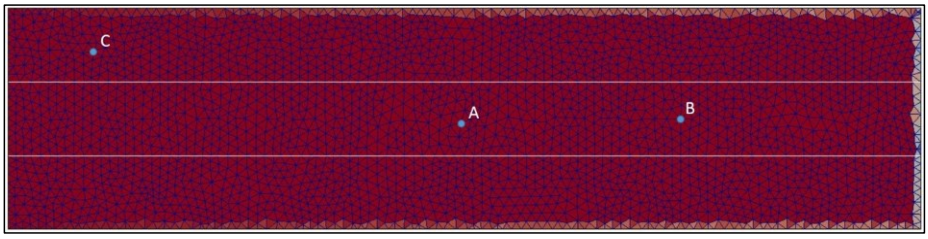


Figure 5. 40: location of the sampling points at which the horizontal stress was monitored in the three-layer models used to investigate the impact of the coefficient of friction along the layer interfaces on fracture propagation.

1) The impact of the coefficient of friction along a layer interface on the stress distribution in the model

The following set of experiments looks at the stress distribution around points A, B and C (Figure 5.40) when μ along the layer interfaces is zero for various layer-normal loads.

Stress variations around Point A, μ=0

For layer-normal loads, σ_v, up to 25 Mpa (Figure 4.3.27), the horizontal stress curves for the region

around point A show a very similar pattern (notice that a downward horizontal stress curve indicates tensile stress build up, whereas an upward trending horizontal stress curve a reduction of the tensile stress and therefore an increase of the compressive stress). The main difference between them is the magnitude of the accumulated strain at which the first fracture is formed (see Figure 5.39). After the formation of the first fracture the σ_h oscilates between -5e6MPa and 5e6 MPa: this represents the accumulation of tension (negative horizontal stress values and a downward trending curve) in the model and its subsequent release when a new fracture is formed (positive [compressive] horizontal stress values and an upward trending curve).

As discussed below, for σ_v of 50MPa (Figure 5.42) and 75MPa (5.40), after the formation of the first fracture, the horizontal stress curve for the region around point A shows a very different pattern to those shown in Figure 4.41. This probably reflects the fact that the first formed fractures develop in differente layers and in different positions in the five experiments. This will clearly influence the stress profile at A and explain why although the curves have a similar pattern they are not approximately the same. It can be argued that if we plot the stress profile for a point adjacent to the first formed fracture in all five experiments a greater similarity will be seen (Figure 5.45).

The yellow line on Figure 5.42 shows the horizontal stress profile measured at point A when the layer-normal stress is 50 MPa. The shape of the curve is similar to those generated when the layer-normal stress was lower until 0.36% of accumulated strain has developed in the layers around ε=0.38%. The analysis of the horizontal stress profile between this point and time step ε=0.574% shows that whereas in the models where the layer-normal loads are 1, 10 and 25 MPa the horizontal stress is mainly in compression, in this model it is in tension. This occurs despite the formation of a mixed-mode fracture (tensile fracture with a shear component) when 0.38% of accumulated strain has developed in the layers and a decrease in the tensile stress (upward trending curve) is registered (see arrow 1 in Figure 5.42 and Figure 5.44 a). Subsequent reductions in the tensile stress correspond to the widening of fractures that have formed in the middle layer. At around 0.45% of accumulated strain a tensile fracture develops and it is registered by a reduction in the tensile stress (see arrow 2 in Figure 5.42 and Figure 5.44b). At around 0.551% of accumulated strain (ε), a cluster of shear and tensile fractures form in the top layer, directly above point A (see arrow 3 in Figure 5.42 and Figure 5.44c) and immediately after (ε=0.556) the horizontal stress profile starts a steep positive trajectory representing an increase in layer-parallel compression (see arrow 4 in Figure 5.42 and Figure 5.44d). It is suggested that this is the result of the formation of a tensile fracture close to point A and the associated shadow which develops around it in which the tensile stress is locally relieved.

The green line on Figure 5.43 shows the horizontal stress profile measured at point A (Figure 5.40) when the layer-normal stress is 75MPa: the first steep increase in tensile horizontal stress occurs at a strain of ε=0.142% and immediately preceeds the initiation of a new fracture (Figure 5.43 arrow 1) -

a shear fracture. This local and dramatic increase in the layer parallel extensional stress results in a local increase of the differential stress – precisely the condition needed for the formation of shear fractures ($(\sigma_1 - \sigma_3) > 4T$, where T is the tensile strength of the rock – see Section 4). From then on, as strain accumulates other sets of shear fractures form in all three layers. At $\varepsilon = 0.641\%$ (Figure 5.43 arrow 2) the model seems to be saturated with fractures (Figure 5.37) and the accumulation of tensile stress stops, no more fractures are formed and horizontal stress oscilates around zero.

The concept of fracture saturation is discussed in Section 4.5 where it is demonstrated that there is a minimum value to fracture spacing below which it is not possible to generate layer-parallel tensile stresses and consequently extensional fractures. On the basis of the above and similar experiments, it can be argued that a layer can become saturated with shear fractures.

It was noted earlier in this section that the dip angle of the shear fractures in these experiments tends to be controlled by the orientation of the mesh element sides. This problem could be resolved by using a much finer mesh in which the orientation of the shear fractures approximately corresponds to the orientation predicted by the Navier-Coulomb theory of shear failure. Although this is technically possible, a mesh in which the elements are half of what was used in these experiments is extremely time consuming and therefore not practical.

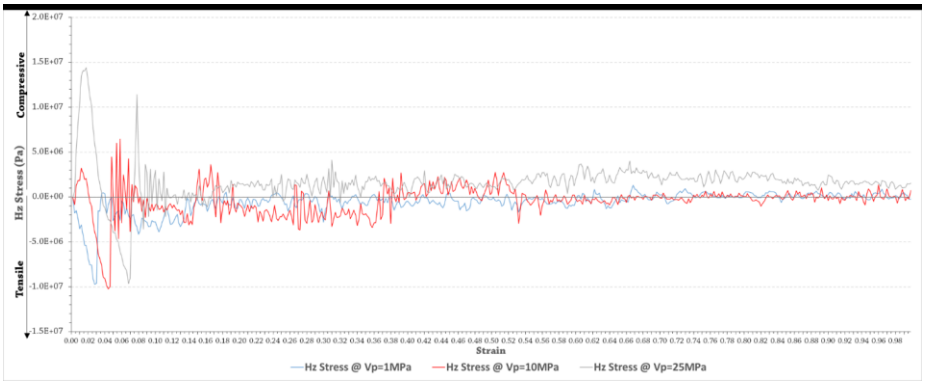


Figure 5. 41: Horizontal stress profiles for 3 models with a coefficient of friction along the layer interfaces of zero (μ=0). The measurements were taken at point A (Figure 5.40). The curves show profiles for experiments where the layer-normal stress, σv, was 1Mpa (blue line), 10MPa (red line) and 25Mpa (grey line).

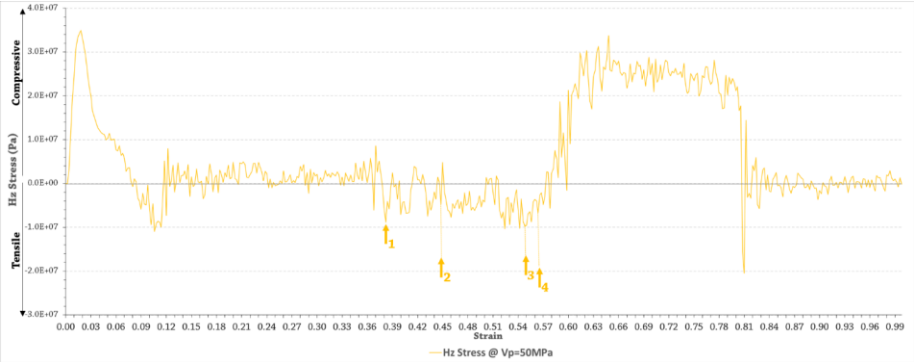


Figure 5. 42: Horizontal stress profiles for a model in which the coefficient of friction (μ) along the layer interfaces is zero . The measurements are taken at point A (Figure 5.40). The yellow line is the profile for a vertical (layer-normal) stress σv of 50Mpa. The numbered arrows indicate points mentioned in the text.

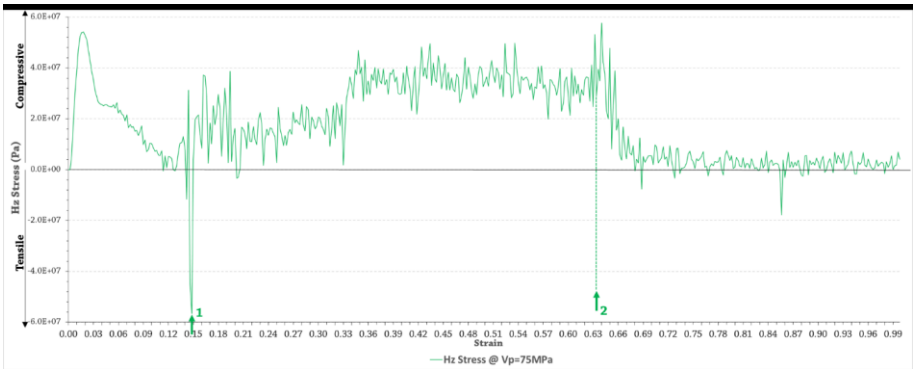


Figure 5. 43: Horizontal stress profiles for a model in which the coefficient of friction (μ) along the layer interfaces is zero . The measurements are taken at point A (Figure 5.40). The green line is the profile for a vertical (layer-normal) stress σv of 75Mpa. The numbered arrows indicate points mentioned in the text.

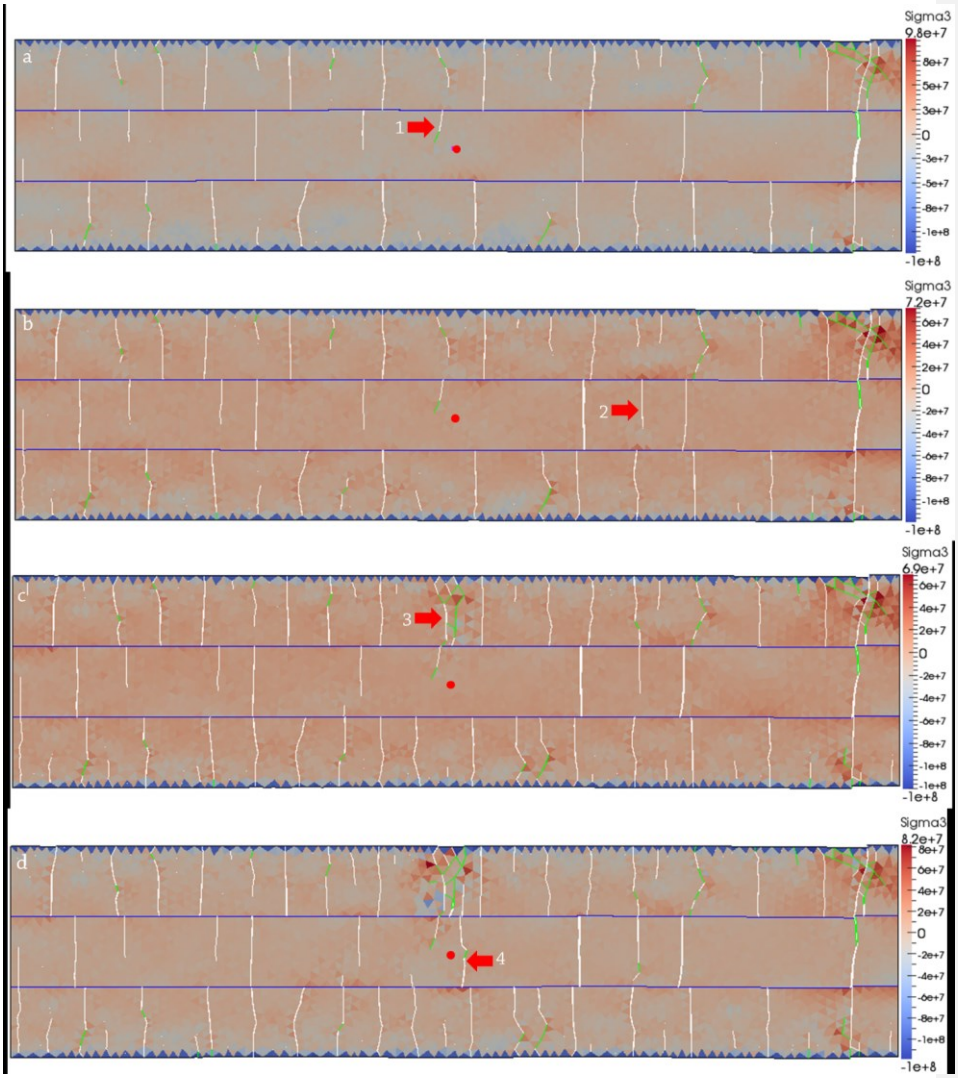


Figure 5. 44: 3-layer fracture model with μ=0 and a σ_v = 50MPa. Each labeled image corresponds to a snapshot taken at a determined time-step and mentioned in the text with the correspondent red arrows pointing to the fractures that are responsible for the stress changes that take place at point A (red dot) and which are registered in the graphic of Figure 5.42.

Stress variations around Point B, μ=0

All the horizontal stress profile curves at point B (Figure 5.40), except the one related to a layer-normal compression (σ_v) of 75MPa, show a similar pattern (Figure 5.45). An abrupt drop of the horizontal tensile stress (transition from a tensile to a compressive environment) illustrated in these curves is associated with the initiation of a new fracture. The point in the deformation history when these fractures first start to appear depends on the layer-normal stress. The larger the layer-normal stress the later in the deformation history do the fractures begin to form (Figure 5.39). Fracture initiation is preceded by an increase of the horizontal tensile stress (downward trending curve) followed by several smaller oscillations which correspond to sequences of stress build-up and release as a new fracture begins to form or when an existing fracture propagates to a new cell, i.e. becomes longer with a larger aperture. In contrast to point A, at point B no shear fractures form in its vicinity unless the layer-normal stress is high (75MPa). Under such a high layer-normal stress (Figure 5.46), shear fractures formed around the measurement point and these events are registered by the horizontal stress curve, which shows a sequence of very steep stress rises (i.e. drops in horizontal tensile stress) between 0.130% and 0.281% of accumulated strain. These rapid fluctuations in layer-parallel stress values correspond to the continuous and intense formation of clusters of shear fracture.



Figure 5.45: Horizontal stress profiles for models in which the coefficient of friction (μ) along the layer interfaces is zero. The easurements are taken at point B (Figure 5.40). The 4 profiles represent the results from 4 experiments with different layer-normal stresses σ_v of 1MPa, blue line, 10MPa, red line, 25Mpa, grey line and 50MPa yellow line.

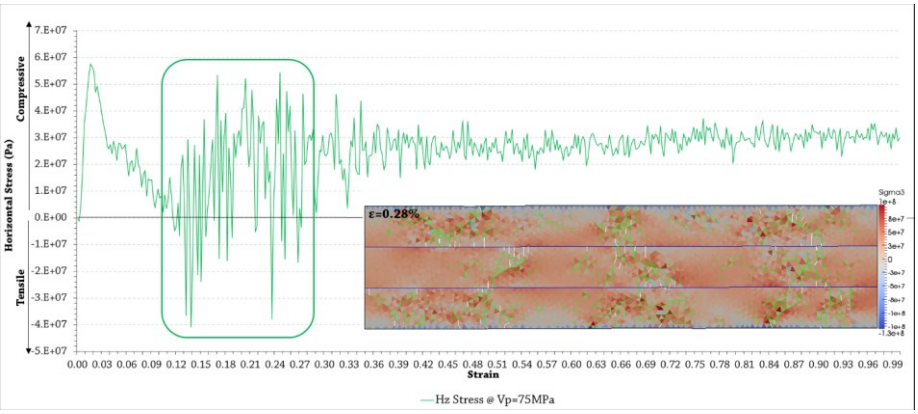


Figure 5. 46: The horizontal stress profile for a model with the coefficient of friction (μ) along the layer interfaces of zero and subjected to a layer-normal stress of 75Mpa. The measurements are taken at point B (Figure 4.3.26). The green box shows the time interval when most of the fractures formed and the distribution of stress within the model shown corresponds to a strain of 0.28%.

Stress variations around Point C, u=0

The horizontal stress profiles for point C (Figure 5.40) which is situated in the top bounding layer, have a different pattern to those generated around points A & B (compare Figure 5.47 with Figure 5.41-5.43 and 5.45 – 5.46),

Although they all show an abrupt tensile stress reduction at the onset of the first fracture formation (Figure 5.47), the general stress state remains tensile during the whole simulation except for the model in which a vertical normal load of 75MPa was applied.

In the experiment in which the layer-normal stress was 1 MPa (Figure 5.48) the first fracture to form occurred in the middle layer at a strain of ε= 0.03% (Figure 5.48 arrow 1 and Figure 5.49a). Other fractures then formed in the model in all three layers in positions remote from point C (the events are recorded in the stress curve as small spikes) until a strain of ε= 0.068% had occurred when a second tensile fracture formed close to point C (Figure 5.48 arrow 2 and Figure 5.49b). As a result of this fracture formation the tensile stress in the vicinity is relieved resulting in an immediate drop in tensile stress as indicated by the rapid rise in the stress profile at ε=0.074. The tensile stress gradually decreases after this time as more tensile stress relaxes from the system as a result of this fracture opening and growing until at ε= ~0.2 when the tensile stress begins to build up again reaching a max value of 8MPa at ε =~0.45. At this moment a tensile fracture that had previously formed in the vicinity of point C extends further resulting in an abrupt reduction of the tensile stress (Figure 5.48 arrow 3 and Figure 5.49 arrow 3). The other abrupt stress variations in the curve represent similar events where fractures form and extend in the vicinity of point C.

When comparing the horizontal stress curves of the experiment in which the layer-normal stress was 1 MPa with the curves that represent experiments with layer-normal stresses of 10 MPa and 25 MPa a very similar profile can be seen, with stress variations (tensile stress build up followed by a rapid relaxation of the tension) being registered at points close to sites where fractures initiate (Figure 5.50).

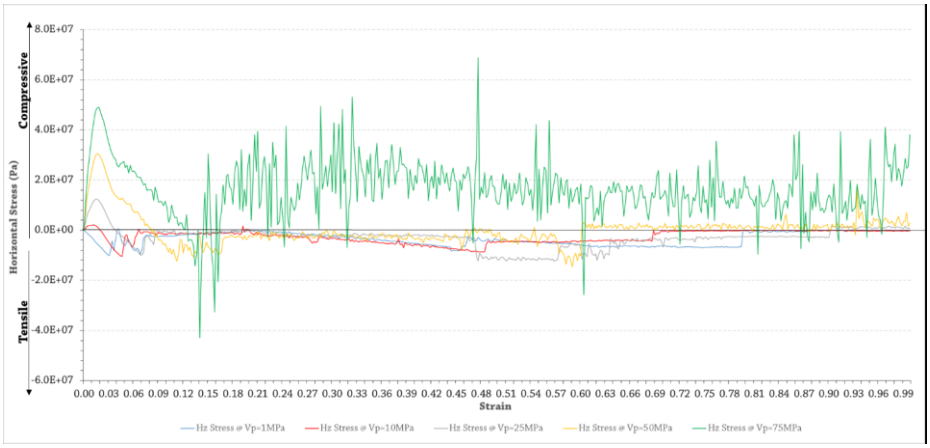


Figure 5.47: Horizontal stress profiles for experiments where the layer-normal stress, σ_v, was 1Mpa (blue line), 10MPa (red line), 25Mpa (grey line), 50MPa (yellow line) and 75MPa (green line) and a coefficient of friction along the layer interfaces of zero (μ=0). The measurements were taken at point C (Figure 5.40).

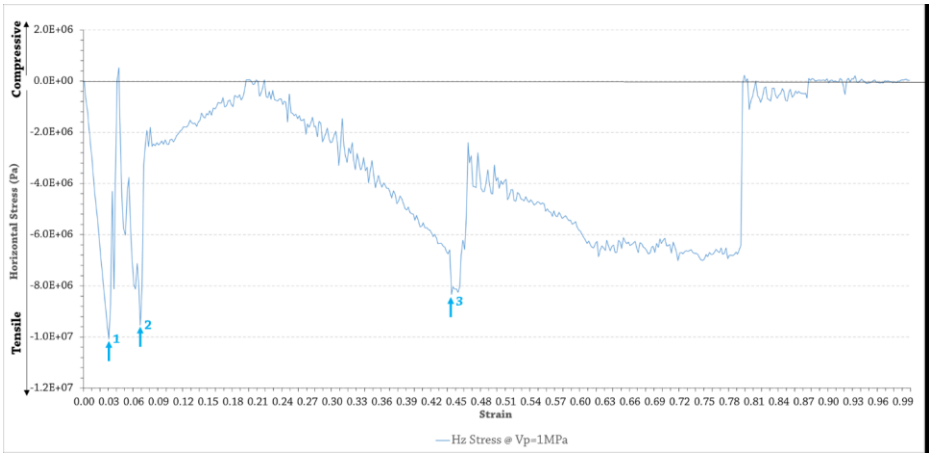


Figure 5. 48: horizontal stress profiles for an experiments where the layer-normal stress, σ_v, was 1Mpa (blue line) and a coefficient of friction along the layer interfaces of zero (μ=0). The stress axis has been expanded relative to Figure 5.47 for clarity. The measurements were taken at point C (Figure 5.40). The numbered arrows indicate points mentioned in the text. They correspond to strain states at which fractures were initiated.

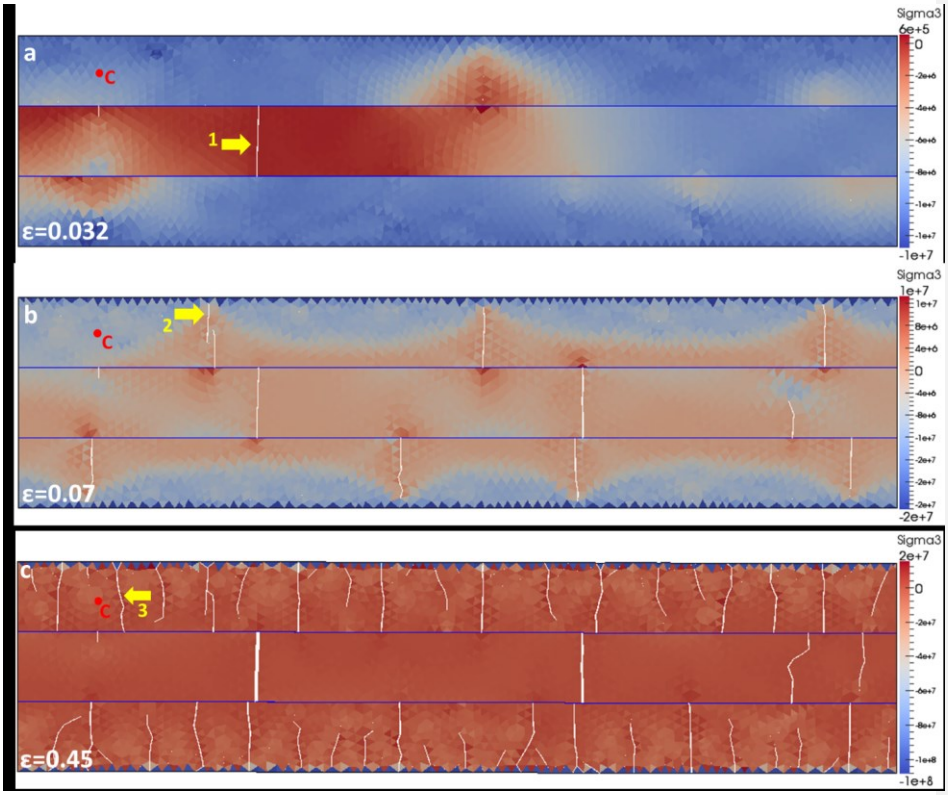


Figure 5.49: 3-layer fracture model with μ=0 and a σ_v=1MPa. Each labeled image corresponds to a snapshot taken at a determined time-step(a ε=0.032; b ε=0.07 and c ε=0.45) and mentioned in the text withe the corresponding red arrows pointing to the fractures that are responsible for the stress changes registered in the graphic of Figure 5.48.

The yellow line on Figure 5.51 shows the horizontal stress profile measured at point C (Figure 5.40) when the layer-normal stress is 50MPa. The first fracture to form, a tensile fracture, occurs at ε=0.112% relatively far from point C (Figures 5.51 and 5.52 arrow 1). The remoteness of the fracture from the measuring point is reflected in the profile by a very subtle reduction in the horizontal tensile stress at ε=0.116. At ε=0.16% a tensile fracture (Figure 5.51 and 5.52 arrow 2) is generated near point C and there is a reduction of the horizontal tensile stress of the same scale of that registered for the first fracture. At ε=0.46 (Figure 5.51 and 5.52 arrow 3) a tensile fracture that had formed at ε=0.342 (notice in Figure 4.3.37 that when this fracture is formed there is not an evident deflection of the profile curve due to its small size) in the vicinity of point C propagates through intact cells reaching the bottom interface of the layer. This is registered as a positive spike in the horizontal stress curve. At ε=0.59% a horizontal tensile stress reduction registers the formation of a cluster of shear fractures generated in

the middle layer near point A (Figure 5.51 and 5.52 arrow 4).

The green line on Figure 5.53 shows the horizontal stress profile measured at point C (Figure 5.40) when the layer-normal stress is 75MPa. The formation of several clusters of shear fractures creates a very unstable profile and it is difficult to identify time-steps of importance. However it is clear that at high layer-normal stresses linked to fracture formation the interval between maximum and minumum horizontal stresses is significantly higher.

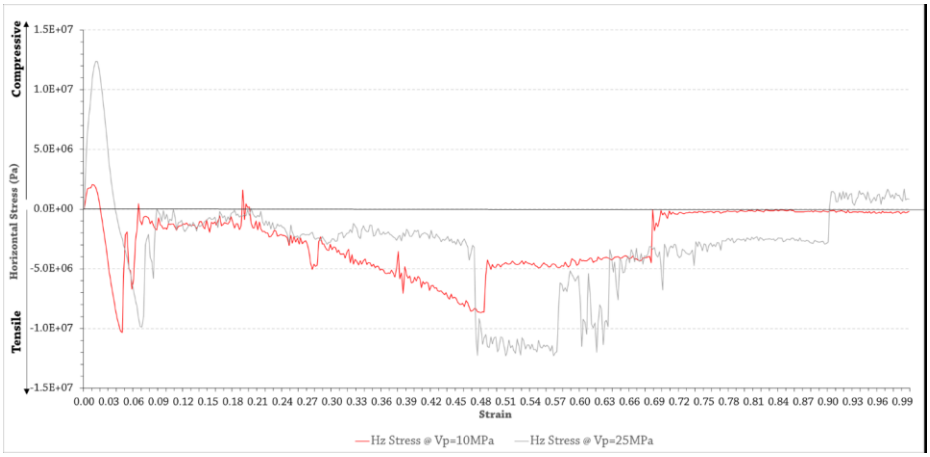


Figure 5. 50: Horizontal stress profiles for models with the coefficient of friction (μ) along the layer interfaces equal to zero subjected to a 10 and 25 MPa of layer-normal stress .The measurements were taken at point C (Figure 5.40).

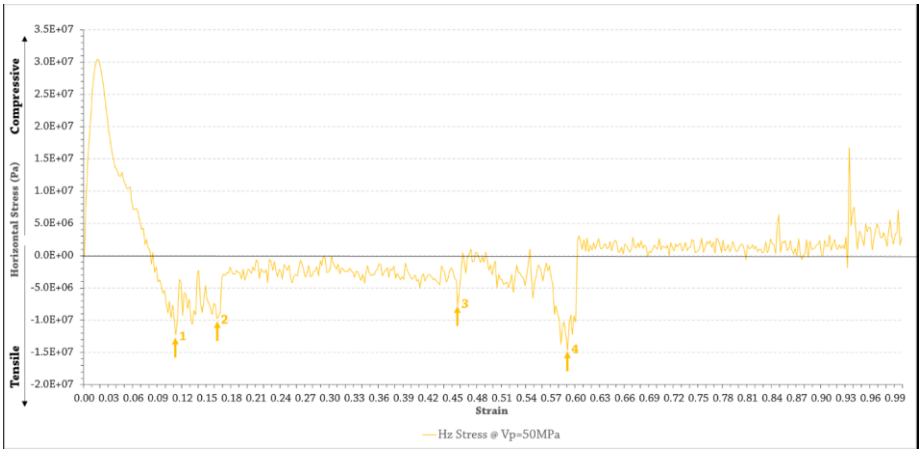


Figure 5. 51: Horizontal stress profiles for models with the coefficient of friction (μ) along the layer interfaces equal to zero subjected to a 50 MPa (yellow lineo) of layer-normal stress .The measurements were taken at point C (Figure 5.40). The numbered arrows indicate points mentioned in the text and that correspond to strain states at which fractures were initiated.

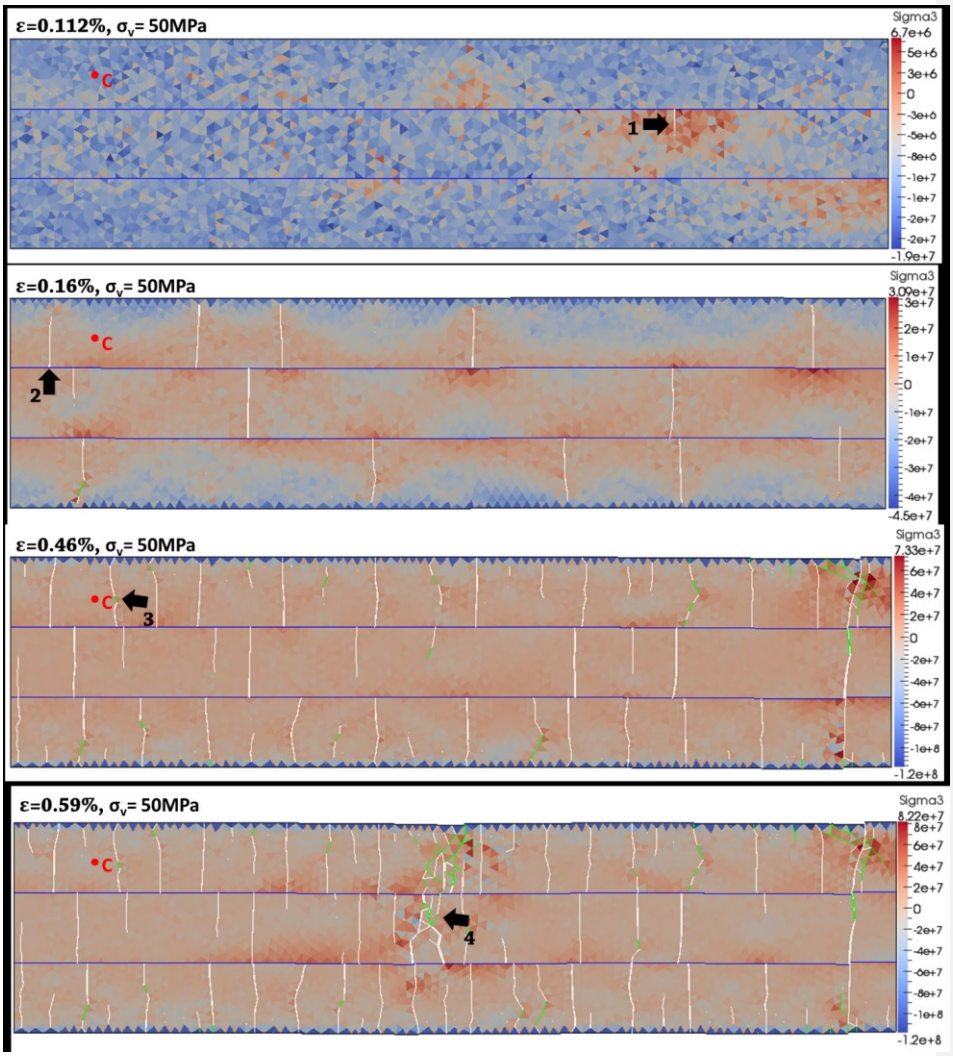


Figure 5. 52: 3-layer fracture model with μ=0 and a σ_v=50MPa. Each labeled image corresponds to a snapshot taken at a determined time-step and mentioned in the text withe the corresponding yellow arrows pointing to the fractures that are responsible for the stress changes registered in the graphic of Figure 5.51.

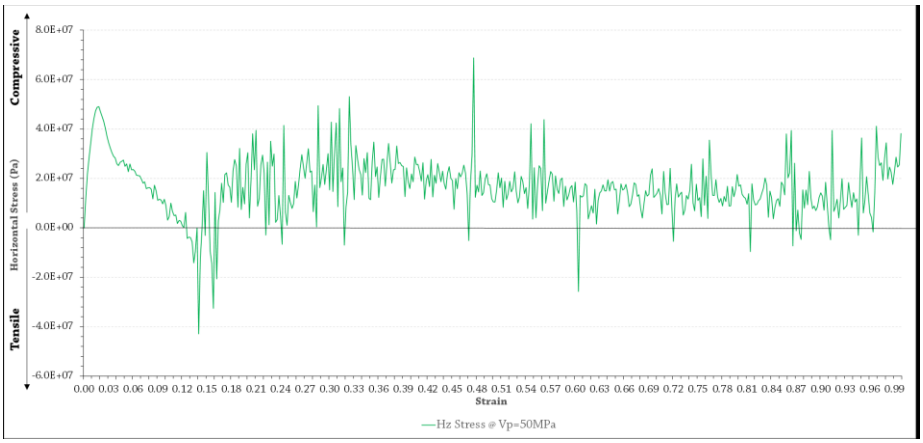


Figure 5. 53: Horizontal stress profile for model with the coefficient of friction (μ) along the layer interfaces equal to zero subjected to a 75 MPa (green line) of layer-normal stress .The measurements were taken at point C (Figure 5.40).

The following section presents a comparison between horizontal stresses measured at the same point (A, B or C) for different values of friction on the layer interface. The objective is to try and understand if by changing only one parameter on the model (the coefficient of friction on the layer interface) while maintaining the other boundary conditions, there is a difference in the way horizontal stresses develop in the layer.

Stress variations around Point A, μ=0.6 vs μ=0

In the experiment in which the layer-normal stress was 1 MPa (Figure 5.54 and 5.55) there are slight differences with regards to the development of the horizontal stress around point A, in a model where the coefficient of friction along the layer interfaces is 0, and point A in a model where this parameter is 0.6. The fact that the two experiments have the exact same boundary conditions, except for the coefficient of friction value attributed to the layer interface leads us to believe that this parameter must be having some influence.

The comparison between the two horizontal stress curves in Figure 5.54 shows that for the interval between around ε=0.03 and ε=0.16 the average horizontal tensile stress is higher for a model where μ=0. This is related to the fact that more fractures have developed in the model where μ=0.6 (Figure 5.55) relieving the tensile stresses.

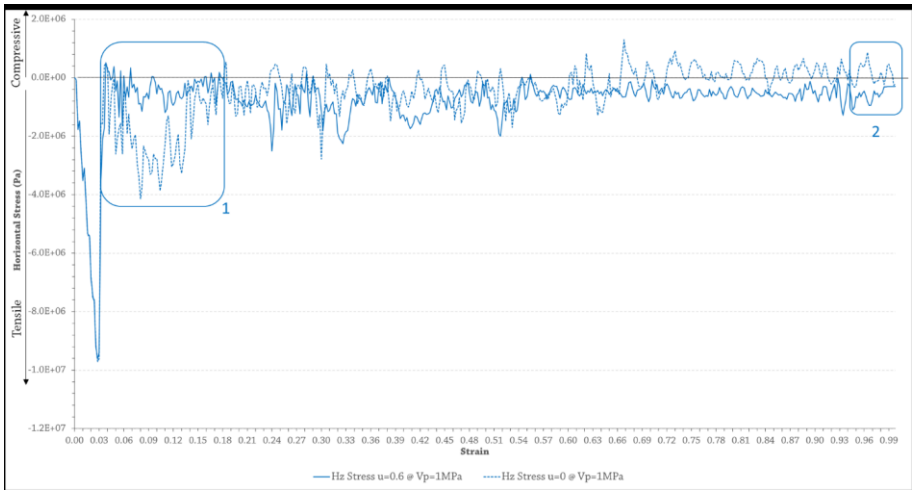


Figure 5. 54: Horizontal stress profiles for models with the coefficient of friction (μ) along the layer interfaces equal to 0.6 (blue line) and 0 (blue doted line), subjected to a 1MPa layer-normal stress . The measurements were taken at point A (Figure 4.3.26). Notice that the horizontal stress curve for a model with μ=0 is very similar to the curve of a model with μ=0.6 but not exctly the same, sugesting that the friction on the layer interface plays a role in stress transmission. Snapshots of the intervals 1 and 2 are shown in Figure 4.3.41.

In the experiment in which the layer-normal stress was 10MPa (Figure 5.56), when considering the two different values of coefficient of sliding friction (μ=0 and μ=0.6), the main difference in the horizontal stress profiles occurs as a result of a tensile fracture forming very close to data point A in the model where μ=0.6 at ε=0.145 (Figure 5.56 arrow 1). This results in a rapid and marked drop in the tensile stress marked by the upward trending profile. After this event, and because of the presence of the fracture, tensile stresses can no longer accumulate in this region of the model and the horizontal stress profile remains practically flat centered around zero stress.

In the experiment in which the layer-normal stress was 25MPa (Figure 5.57) the most significant differences between the models with a coefficient of friction along the layer interfaces of 0 and 0.6 reside in the timing of formation of the first fracture (which occurs earlier in the experiment where μ=0) and in the release of tensile stress which occurs in the μ=0 experiment but which is not registered in the experiment where μ=0.6. Differences are also observed in the way the horizontal stress develops after ε=0.529%: whereas in the μ=0 model the horizontal stress remains virtually at zero, it becomes extensive in the μ=0.6 model. This difference seems to be related to the proximity of point A to the tensile fractures; whereas in the μ=0 model a tensile fracture developed a short distance from point A, in the μ=0.6 model the tensile fractures are further away from the sampling point, allowing tensile

stress to accumulate in the region around point A.

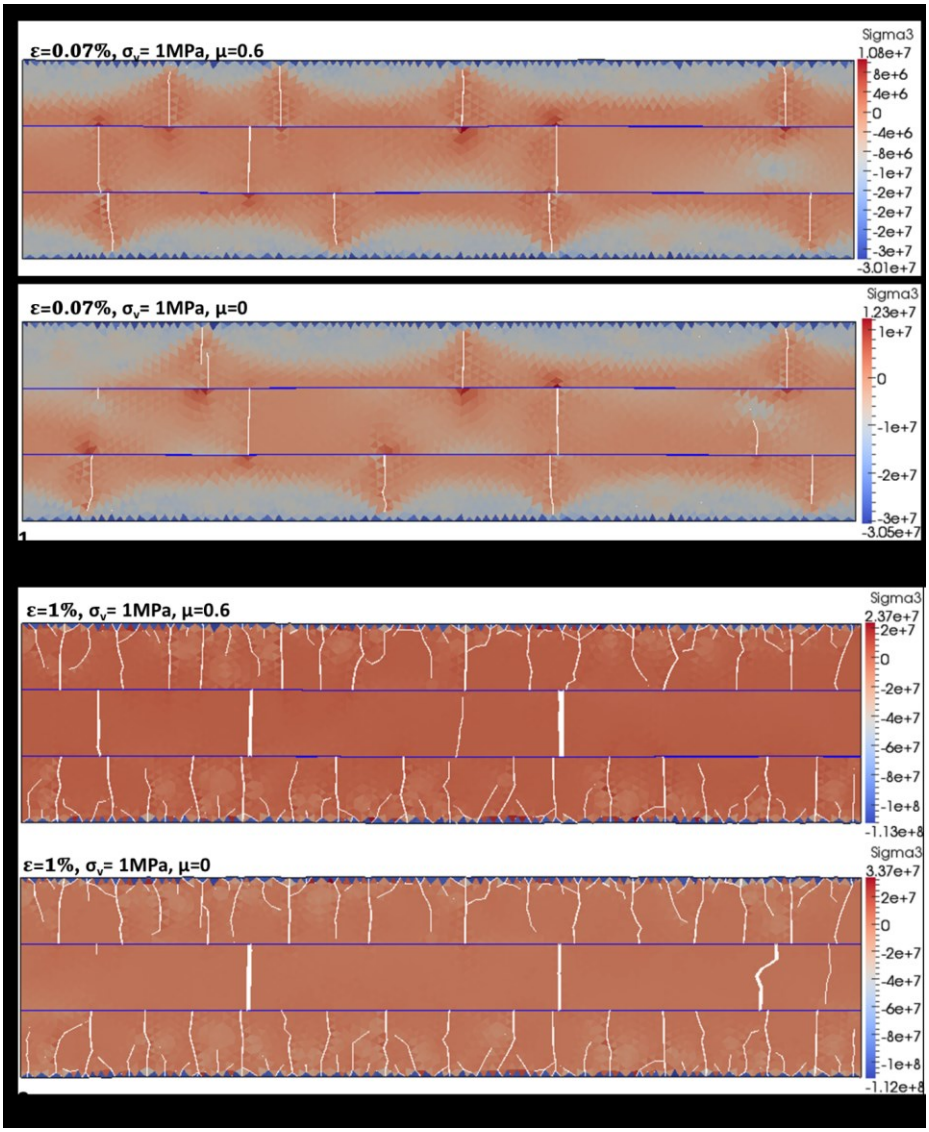


Figure 5.55: comparison between models with a coefficient of sliding friction of 0.6 and 0 at different accumulated strains.

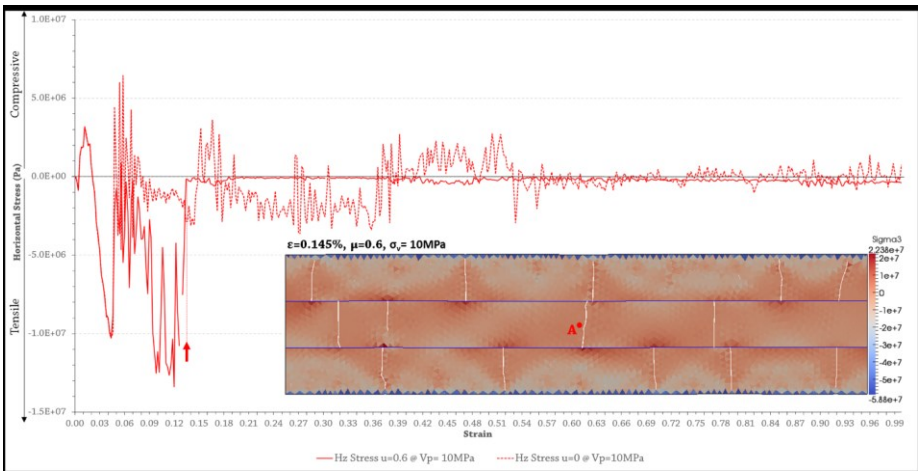


Figure 5. 56: Horizontal stress profiles for models with the coefficient of friction (μ) along the layer interfaces equal to "0.6" (red line) and "0" (red doted line), subjected to a 10MPa layer-normal stress . The measurements were taken at point A (Figure 4.3.26). Notice that the tensile fracture that forms very near data point A impedes the accumulation of tensile stress after its formation.

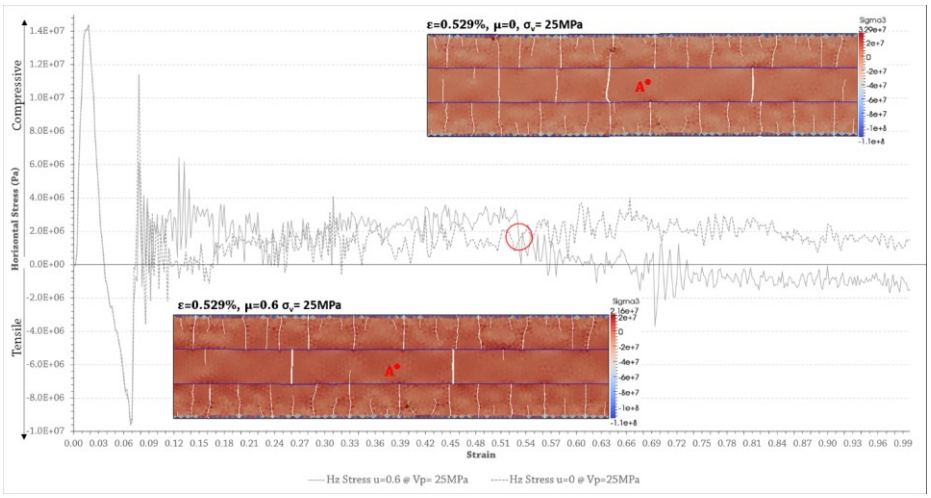


Figure 5. 57: Horizontal stress profiles for models with the coefficient of friction (μ) along the layer interfaces equal to "0.6" (grey line) and "0" (grey doted line), subjected to a 25MPa layer-normal stress . The measurements were taken at point A (Figure 4.3.26).

In the experiment in which the layer-normal stress was 50 MPa (Figure 5.58) differences in the horizontal stress profile for the two models (μ=0 and μ=0.6) are significant from around ε=0.593%. These differences can be explained by the fractures that are formed near the sampling point in the two models. Whereas in the model with a coefficient of sliding friction along the layer interfaces of zero a cluster of fractures (both tensile and shear) intersects the sampling point causing a relief of the tensile stresses and therefore taking the horizontal stress into the compressive region of the scale (positive values), in the model with a coefficient of sliding friction along the layer interfaces of 0.6 only two tensile fractures are formed in the vicinity of the sampling point leading to a stress relief but not in a scale as high as pronounced as in the previous model – see Figure 5.59.

Experiments in which the layer-normal stress was 75MPa, do not present major differences between models with the coefficient of sliding friction at the layer boundary of 0 or 0.6.

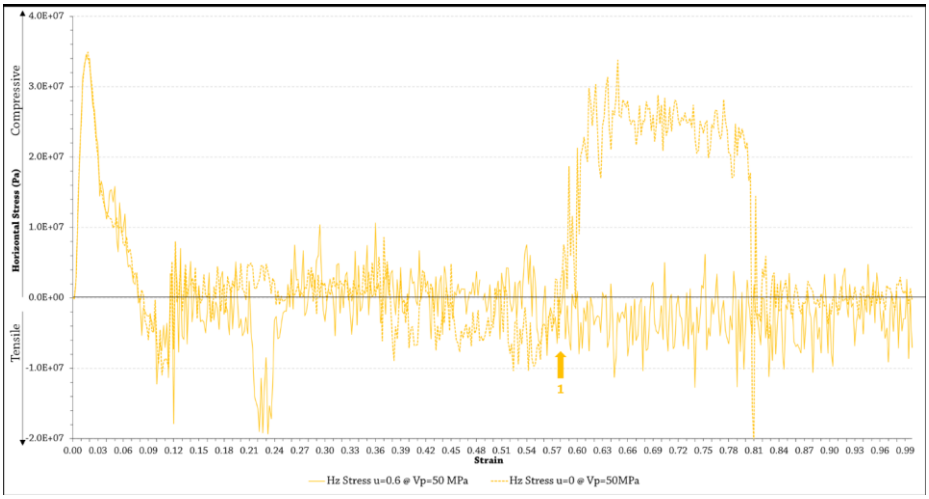


Figure 5. 58: Horizontal stress profile for models with the coefficient of friction (μ) along the layer interfaces equal to "0.6" (yellow line) and "0" (yellow dotted line), subjected to a 50MPa layer-normal stress . The measurements were taken at point A (Figure 5.40).

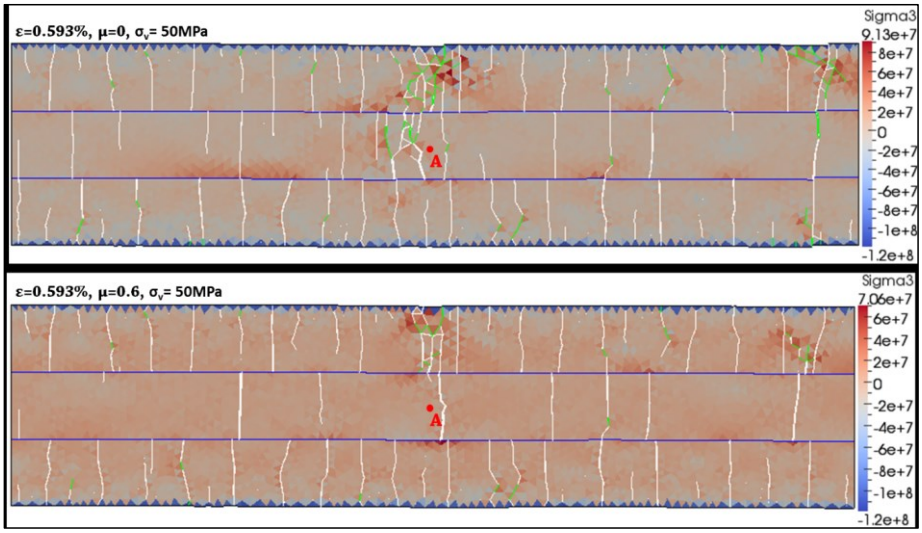


Figure 5. 59: snapshot of two 3-layer models with a layer normal stress of 50MPa and a coefficient of sliding friction along the layer interfaces equal to 0 (top) and 0.6 (bottom) taken at ε=0.593. Notice the cluster of fractures that forms in the model where μ=0 and that is responsible for the intense tensile stress relief indicated with the arrow 1 in the stress profile.

Stress variations around Point B, μ=0.6 vs μ=0

At the data retrieving location B (Figure 5.40), differences in regards to the development of the horizontal stresses between models with a coefficient of friction along layer interfaces of 0 and models where this parameter is set to be 0.6 are significant for models with relatively low normal loads: 1MPa, and 10MPa. As for the experiments carried out to determine the stress variation close to point A, these differences are related to the position of tensile fractures that are created within the model relative to sampling point B where the stress measurements are made (Figure 5.60 a and b; Figure 5.61 a and b and Figure 5.62 a and b). For models where the normal load is 50MPa and 75MPa the horizontal stress profiles practically match (Figure 5.63) due to the similarity in the fracture pattern that develops in the vicinity of point B.

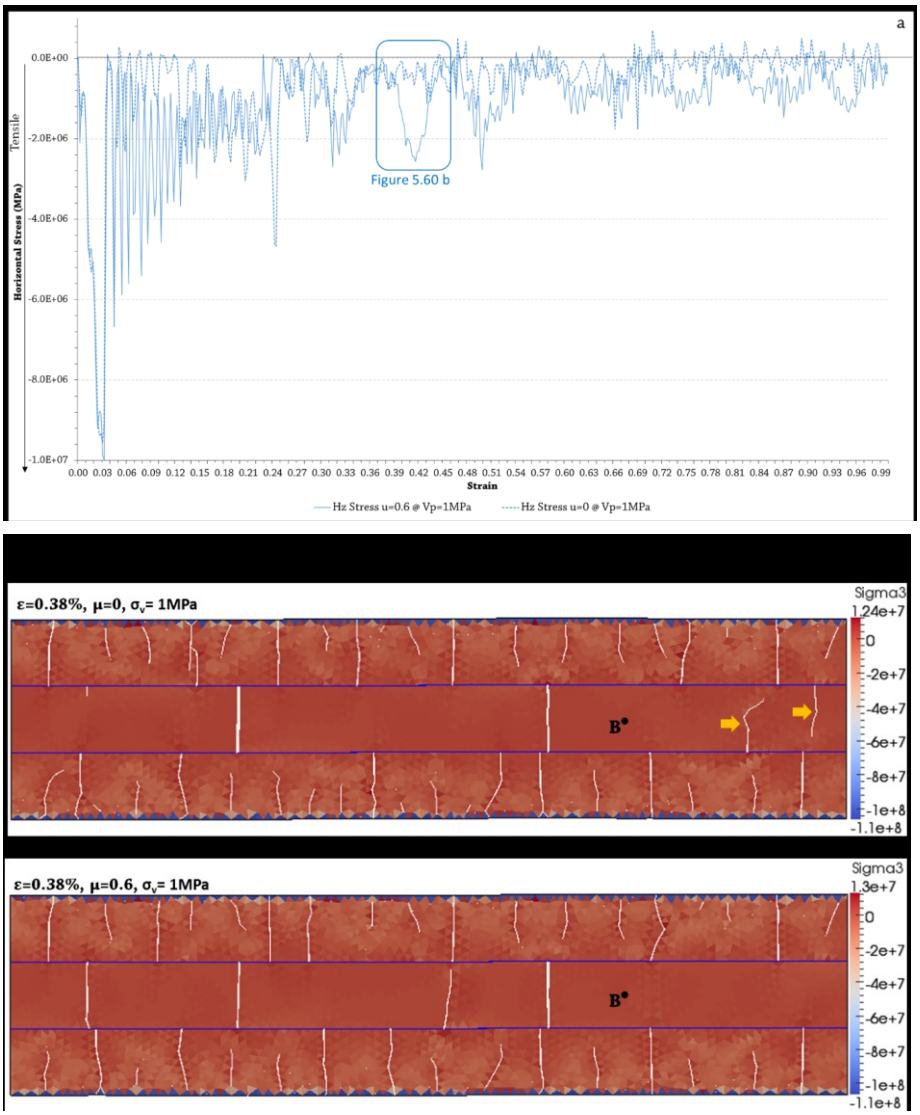


Figure 5. 60: a) Horizontal stress profile for models with the coefficient of friction (μ) along the layer interfaces equal to "0.6" (blue line) and "0" (blue doted line), subjected to a 1MPa layer-normal stress . The measurements were taken at point B (Figure 5.40). b) snapshots of two 3-layer models with a layer normal stress of 1MPa and a coefficient of sliding friction along the layer interfaces equal to 0 (top) and 0.6 (bottom) taken at ε=0.38. Notice the difference in fracture formation near point B. These are responsible for the differences outlined by the box in the stress profile in a).

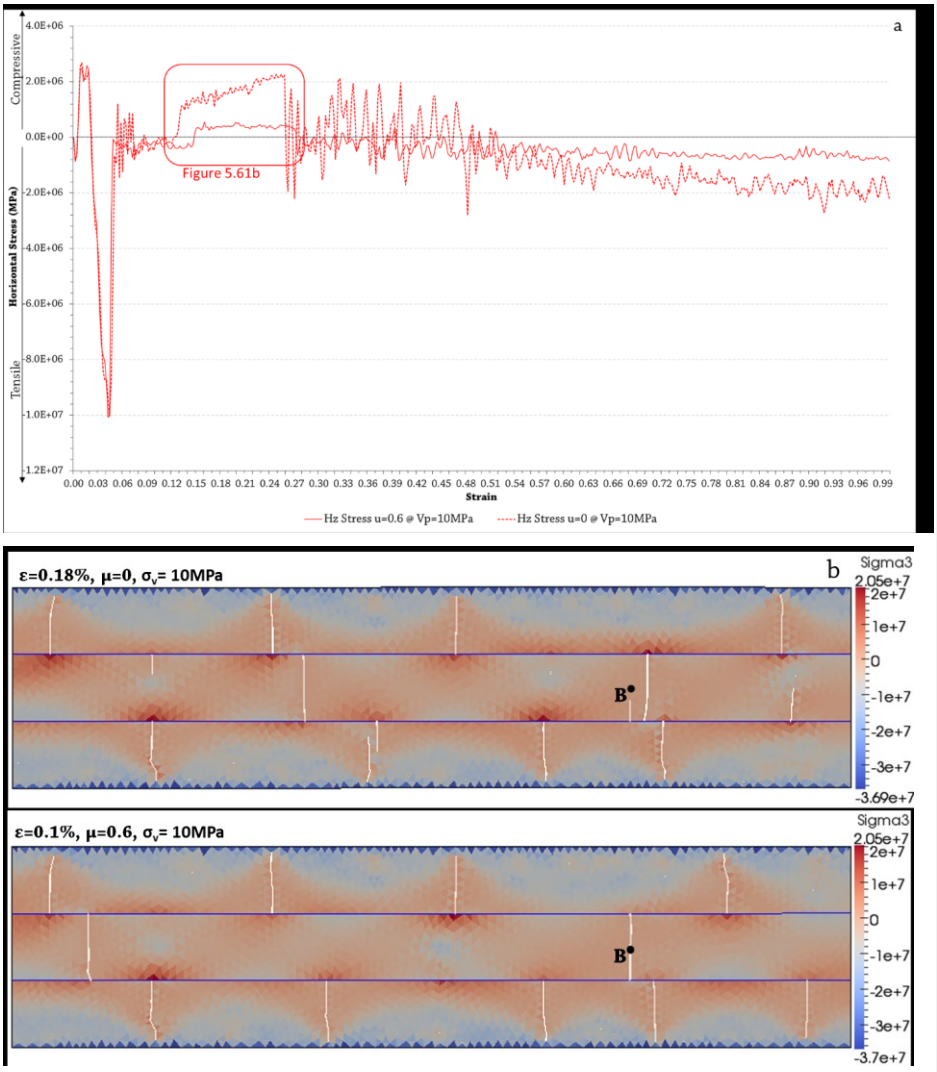
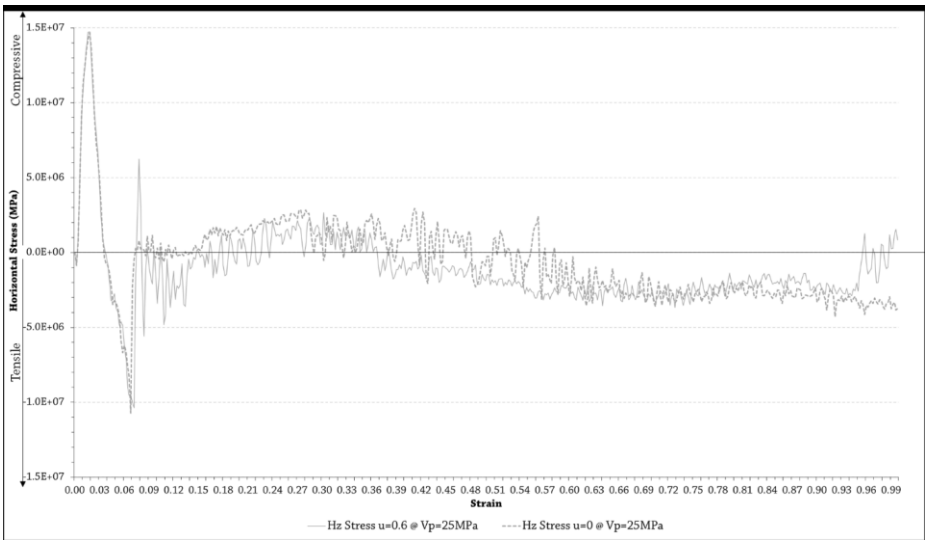


Figure 5.61: a) Horizontal stress profile for models with the coefficient of friction (μ) along the layer interfaces equal to "0.6" (red line) and "0" (red doted line), subjected to a 10MPa layer-normal stress . The measurements were taken at point B (Figure 4.3.26). b) snapshots of two 3-layer models with a layer normal stress of 10MPa and a coefficient of sliding friction along the layer interfaces equal to 0 (top) and 0.6 (bottom) taken at ε=0.1%. Notice the difference in fracture formation near point B. These are responsible for the differences outlined by the box in the stress profile of a).



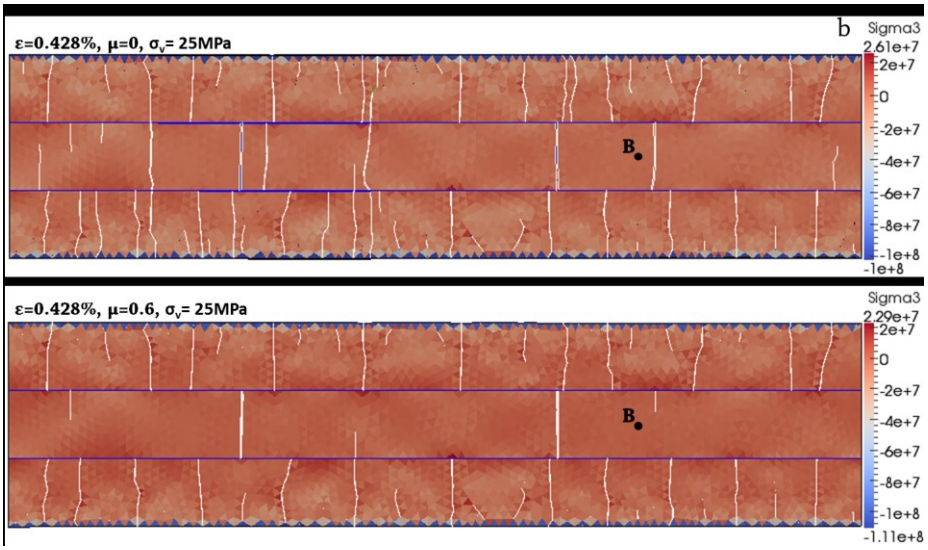


Figure 5. 62: a) Horizontal stress profile for models with the coefficient of friction (μ) along the layer interfaces equal to "0.6" (grey line) and "0" (grey doted line), subjected to a 25MPa layer-normal stress . The measurements were taken at point B (Figure 4.3.26). b) snapshots of two 3-layer models with a layer normal stress of 25MPa and a coefficient of sliding friction along the layer interfaces equal to 0 (top) and 0.6 (bottom) taken at ε=0.428%. Notice the difference in fracture formation near point B. These are responsible for the differences outlined by the box in the stress profile of a).

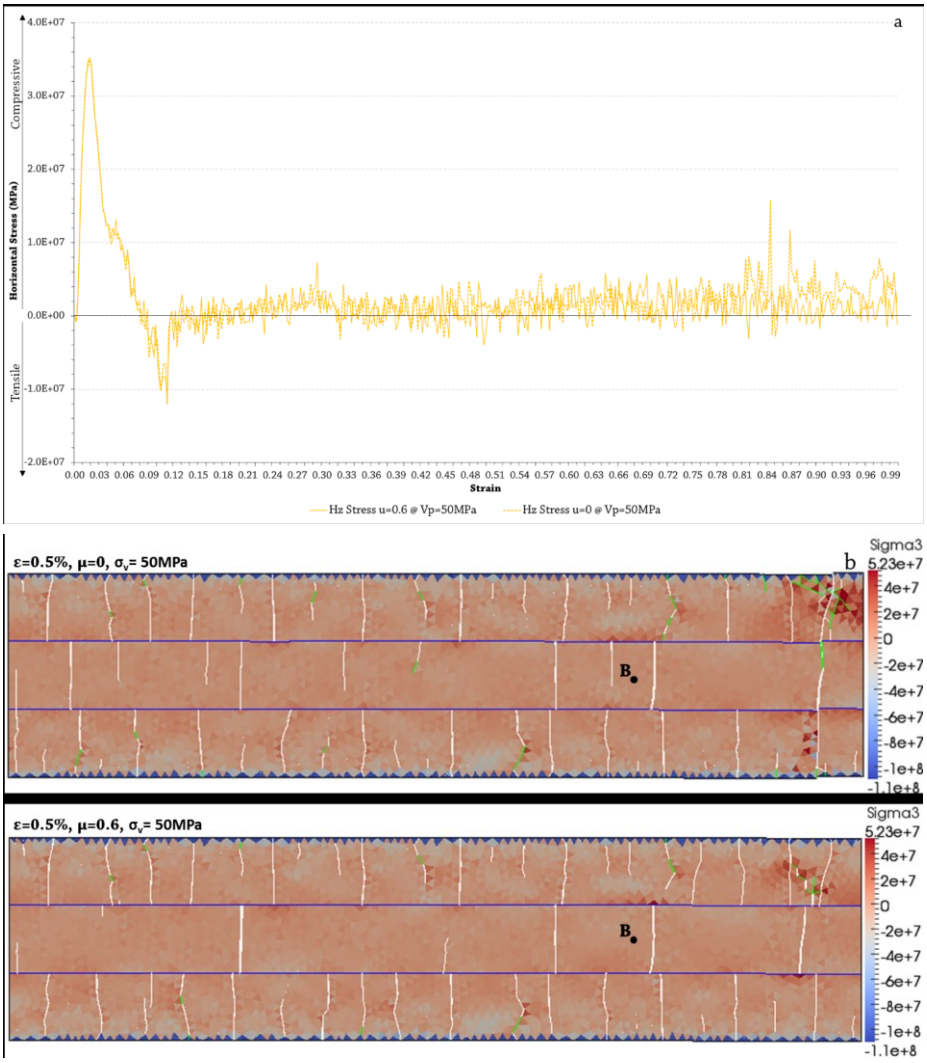


Figure 5. 63: a) Horizontal stress profile for models with the coefficient of friction (μ) along the layer interfaces equal to "0.6" (yellow line) and "0" (yellow doted line), subjected to a 50MPa layer-normal stress . The measurements were taken at point B (Figure 4.3.26). b) snapshots of two 3-layer models with a layer normal stress of 50MPa and a coefficient of sliding friction along the layer interfaces equal to 0 (top) and 0.6 (bottom) taken at ε=0.5%. Notice the difference in fracture formation near point B between the two models is very small creating a very similar profile as shown in a)

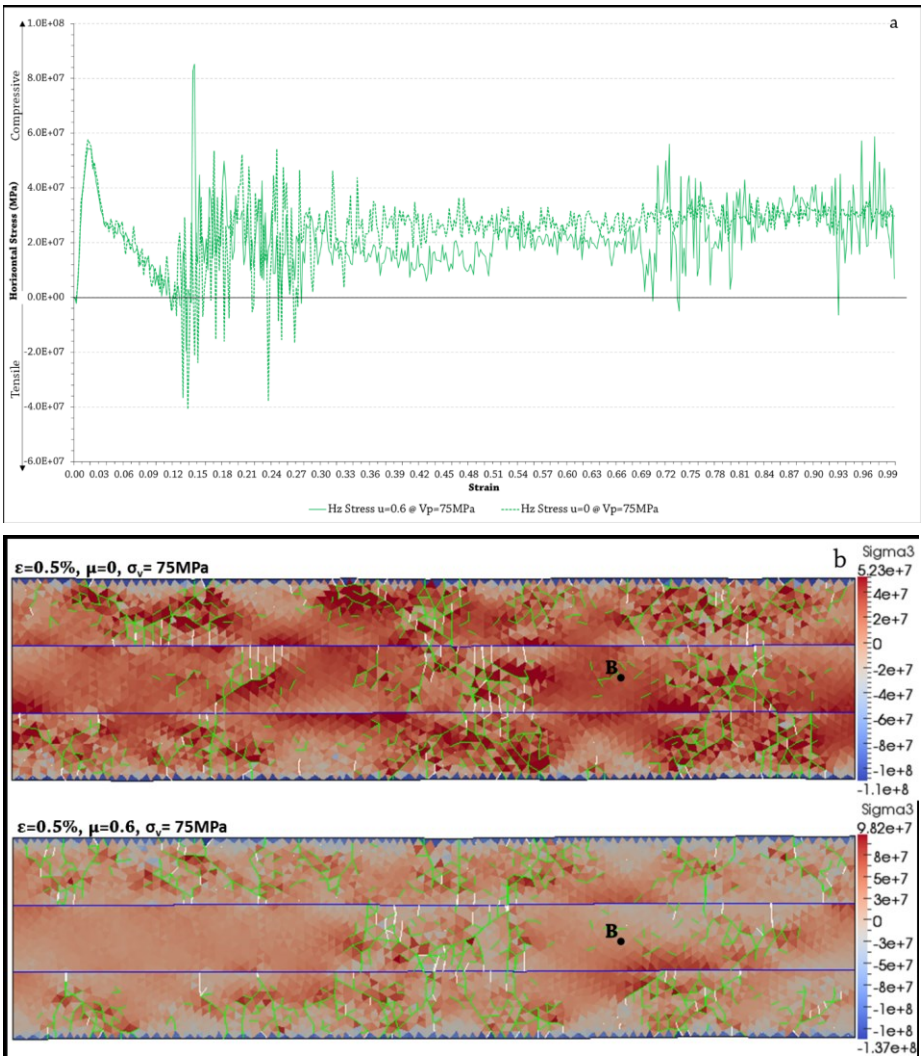
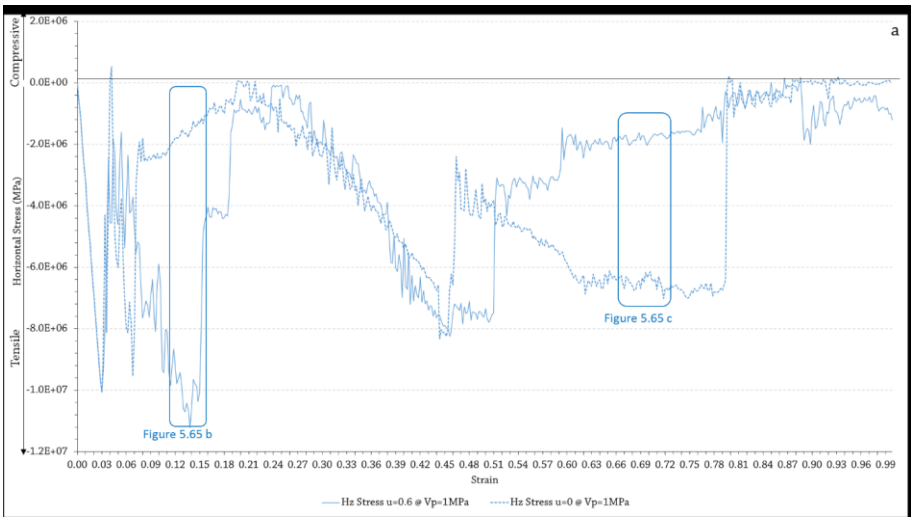
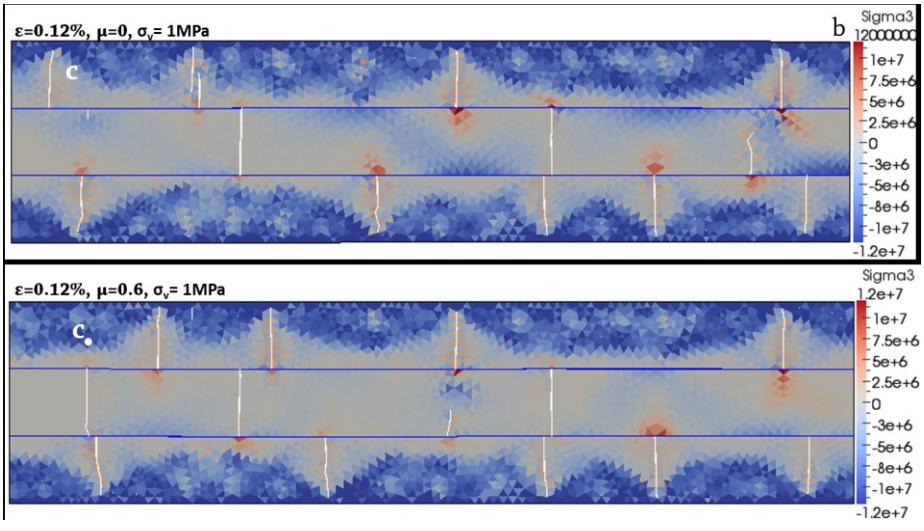


Figure 5. 64: a) Horizontal stress profile for models with the coefficient of friction (μ) along the layer interfaces equal to "0.6" (green line) and "0" (green doted line), subjected to a 75MPa layer-normal stress . The measurements were taken at point B (Figure 4.3.26). b) snapshots of two 3-layer models with a layer normal stress of 75MPa and a coefficient of sliding friction along the layer interfaces equal to 0 (top) and 0.6 (bottom) taken at ε=0.5%. Notice the difference in fracture formation near point B between the two models is very small creating a very similar profile such as shown in a).

Stress variations around Point C, μ=0.6 vs μ=0

At the data retrieving location C (Figure 5.40) differences in the development of the horizontal stresses between models with a coefficient of friction along layer interfaces of 0 and models where this parameter is set to be 0.6 are significant for models for normal loads up to 50MPa. As for the stress profiles observed around point A and B, these differences are related to the relative position of the reference point (C) and the tensile fractures that are created within the model (Figure 5.65 to 5.68). For models where the normal load is 75MPa the horizontal stress profiles practically match (Figure 5.69).





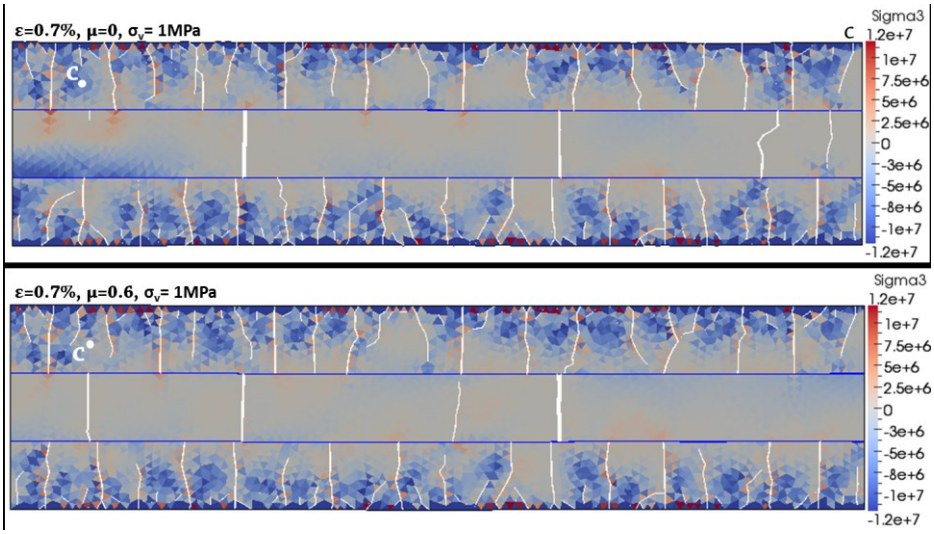


Figure 5.65: a) Horizontal stress profile for models with the coefficient of friction (μ) along the layer interfaces equal to "0.6" (blue line) and "0" (blue doted line), subjected to a 1MPa layer-normal stress . The measurements were taken at point C (Figure 5.40). b) snapshots of two 3-layer models with a layer normal stress of 1MPa and a coefficient of sliding friction along the layer interfaces equal to 0 (top) and 0.6 (bottom) taken at ε=0.12%. Notice the difference in fracture formation in the vicinity of point C between the two models. This is responsible for the differences in the profile shown in a): whereas in the model with μ=0 there is a fracture very close to the sampling point, which reduces the tensile stresses, in the model where μ=0.6 the absence of such fractures allows the accumulation of tensile stress; c) snapshots of two 3-layer models with a layer normal stress of 1MPa and a coefficient of sliding friction along the layer interfaces equal to 0 (top) and 0.6 (bottom) taken at ε=0.7%. The fractures that formed very close to point Cfor the model with μ=0.6 explain the lower tensile stress registered when compared to the model with μ=0.

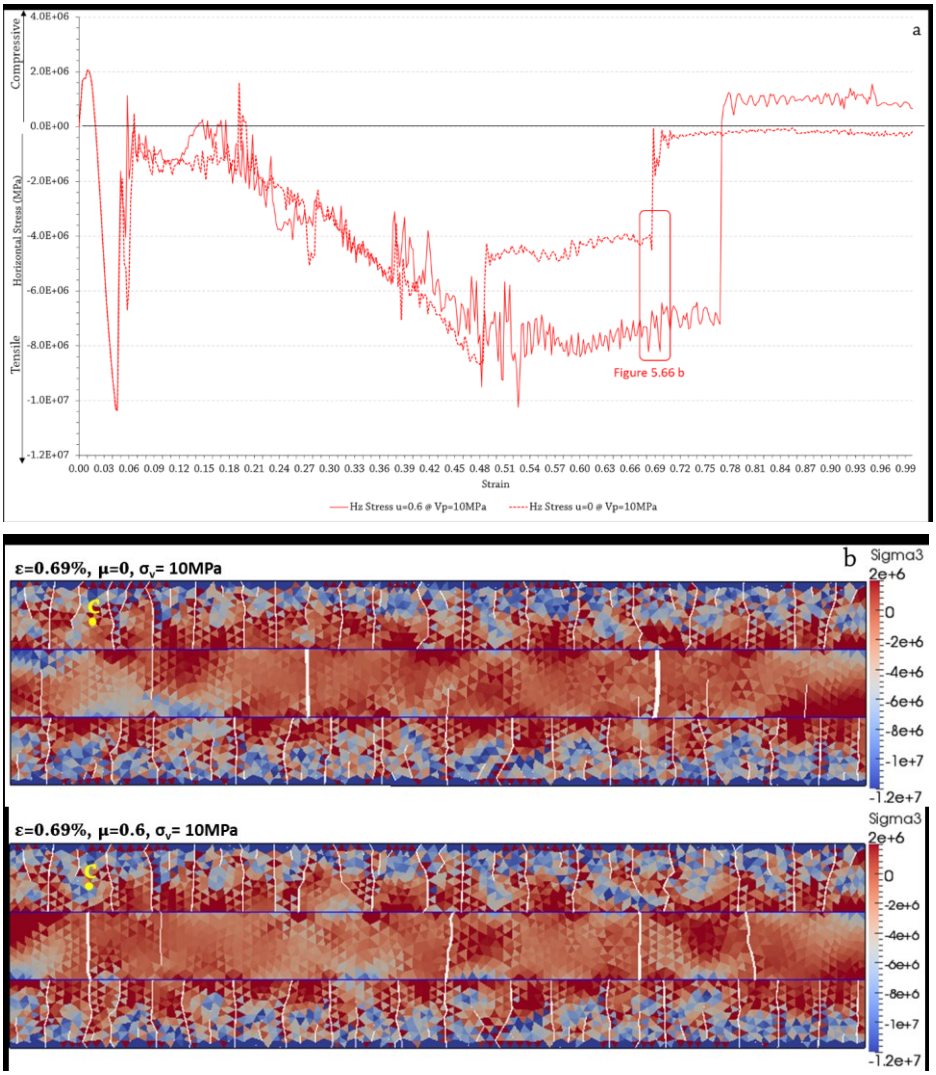


Figure 5.66: a) Horizontal stress profile for models with the coefficient of friction (μ) along the layer interfaces equal to "0.6" (red line) and "0" (red doted line), subjected to a 10MPa layer-normal stress . The measurements were taken at point C (Figure 5.40). b) snapshots of two 3-layer models with a layer normal stress of 10 MPa and a coefficient of sliding friction along the layer interfaces equal to 0 (top) and 0.6 (bottom) taken at ε=0.69%. Notice the difference in fracture formation in the vicinity of point C between the two models. This is responsible for the differences in the profile shown in Figure 4.3.52a): despite the fact that in both models there is a similar number of fractures in the vicinity of point C, in the model where μ=0, one of the fractures is longer in the μ=0 experiment and extends as far as "C" facilitating the reduction of the tensile stresses see a).

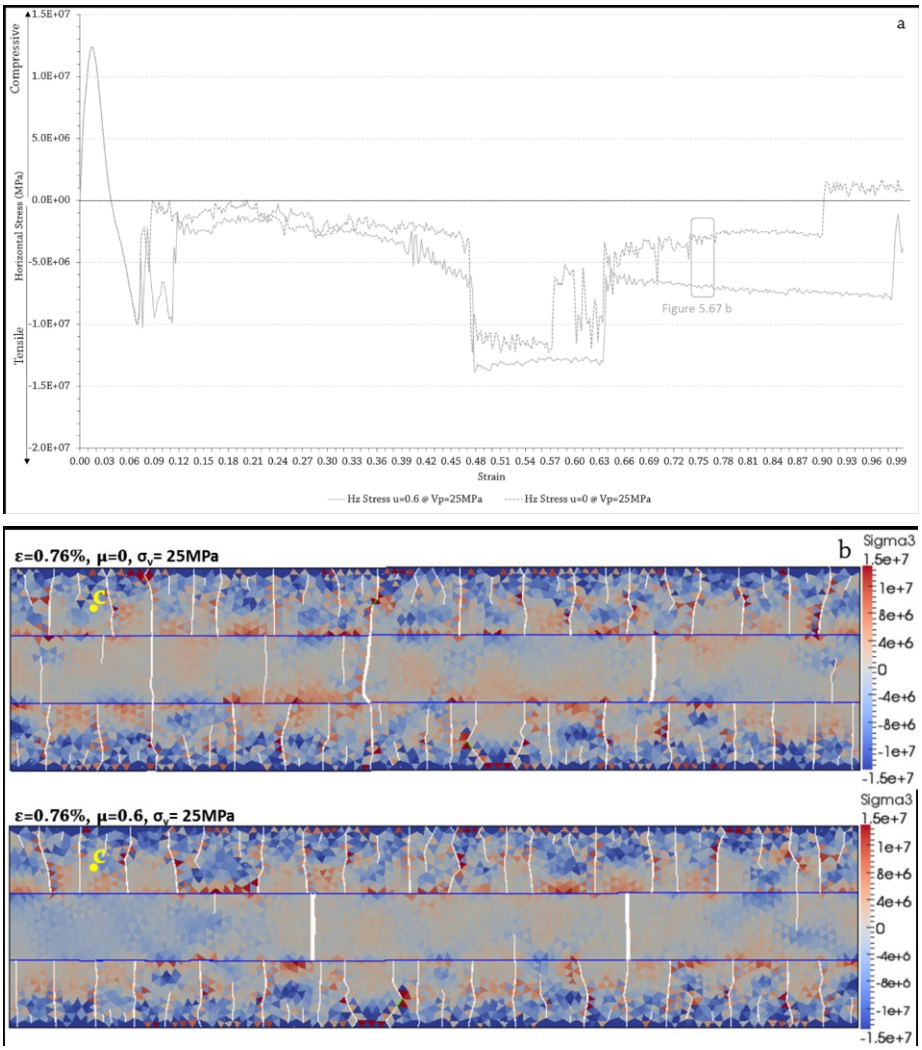


Figure 5. 67: a) Horizontal stress profile for models with the coefficient of friction (μ) along the layer interfaces equal to "0.6" (grey line) and "0" (grey doted line), subjected to a 25MPa layer-normal stress . The measurements were taken at point C (Figure 5.40). b) snapshots of two 3-layer models with a layer normal stress of 25 MPa and a coefficient of sliding friction along the layer interfaces equal to 0 (top) and 0.6 (bottom) taken at ε=0.76%. Notice the difference in fracture formation in the vicinity of point C between the two models. This is responsible for the differences in the profile shown in a): in the model where μ=0 a through going fracture formed in the vicinity of point C causing a reduction in the tensile stresses not observed in the model where μ=0.6.

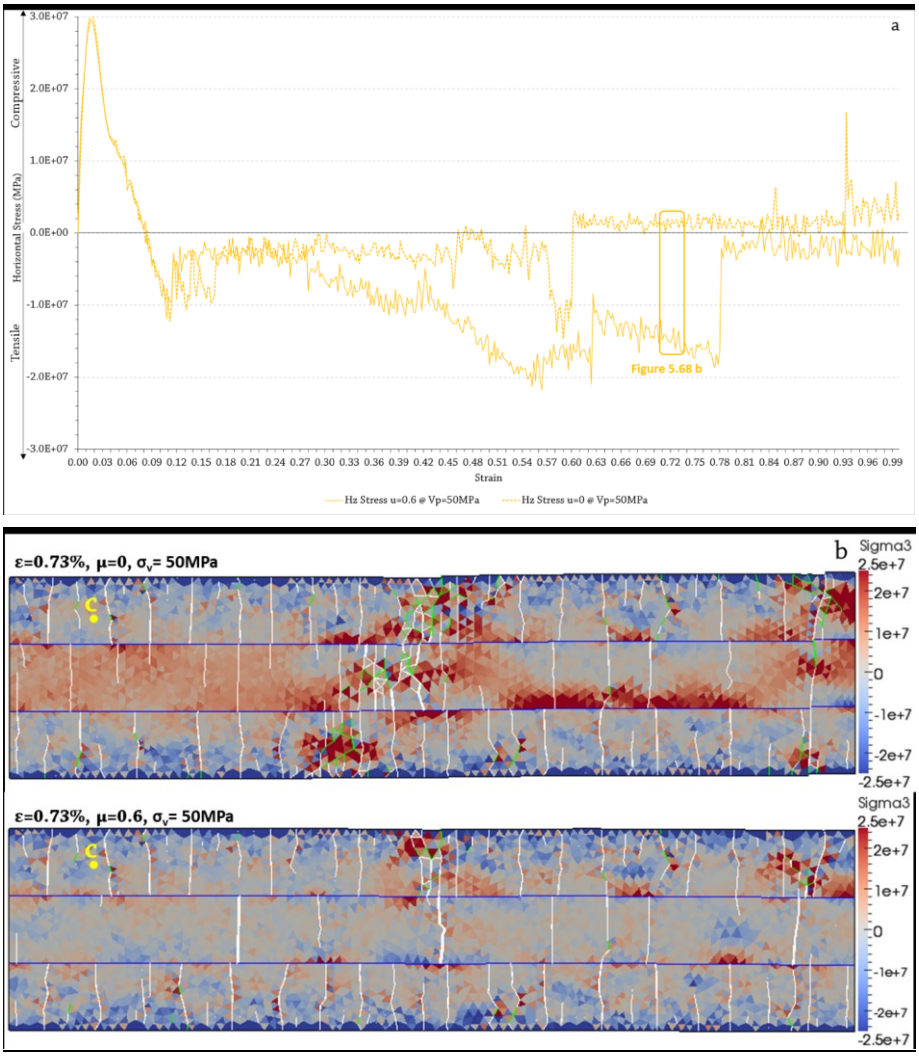


Figure 5.68: a) Horizontal stress profile for models with the coefficient of friction (μ) along the layer interfaces equal to "0.6" (yellow line) and "0" (yellow doted line), subjected to a 50MPa layer-normal stress . The measurements were taken at point C (Figure 5.40). b) snapshots of two 3-layer models with a layer normal stress of 50 MPa and a coefficient of sliding friction along the layer interfaces equal to 0 (top) and 0.6 (bottom) taken at ε=0.73%. Notice the difference in fracture formation in the vicinity of point C between the two models. This is responsible for the differences in the profile shown in a): there are more fractures in the vicinity of this sampling point for the model with μ=0 than for a model where μ=0.6. This causes a greater reduction of tensile stress in the vicinity of point C for the model with μ=0.

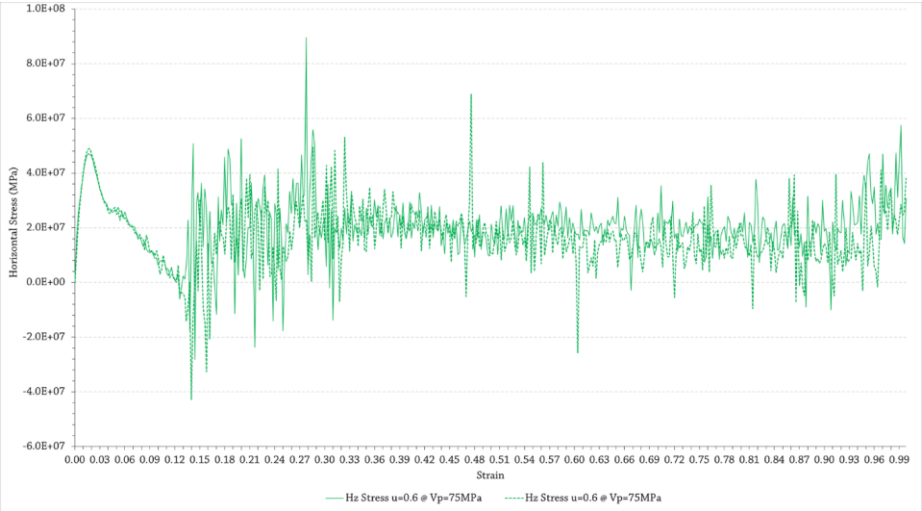


Figure 5. 69: Horizontal stress profile for models with the coefficient of friction (μ) along the layer interfaces equal to "0.6" (green line) and "0" (green doted line), subjected to a 75MPa layer-normal stress . The measurements were taken at point C. Notice that there is no substancial difference between both stress profiles.

Analysis of horizontal stress development adjacent to a frictional interface**.**

To improve the understanding of the impact of the coefficient of sliding friction along an interface between to layers on stress transmission – and on fracture propagation – we compared the development of the horizontal stress between two points on opposite sides of an interface i.e. one point is located in the top layer (whis is actively being extended through its top boundary) and another directly opposite to it in the middle layer.

The rationale behind the experiment:

Experiments where the interfaces between the layers were bonded were carried out. Unsurprisingly it was found that the bonded layers behave like a uniform block and points on each side of the interface experience the same stress state. This is demonstrated by the very similar horizontal stress profiles shown in Figure 5.70. From these results it might be inferred that if the layers are not bonded (slippage along the interface is allowed) the horizontal stress profiles obtained from very close points on opposite sides of the interface are more likely to be different. In order to examine the impact of an unbonded interface on stress distribution either side of the interface, a series of experiments was designed.

Experiments using a 3-layer model where all layers have the same mechanical properties (those of a limestone, see Table 5.1) were conducted. In these experiments the model was subjected to plane strain deformation by applying on the top and bottom boundaries horizontal extension. The extension is applied up to a point when the model has achieved a 1% of accumulated strain. The interfaces between the layers are non cohesive but they possess a coefficient of sliding friction along them which can be changed. Two values of sliding friction on the layer boundaries (μ) were tested: $\mu=0$ and $\mu=0.6$. A very low vertical normal load was applied (1MPa), enough to maintain the layers in contact but without excessively hindering the possibility of slip along the interface. Two sample loctions A and B were chosen near the layer boundary between top and middle layer and the stress values recorded on each side of the boundary (points A/A' and B/B' Figure 4.71). The horizontal stress profiles for each point were obtained.

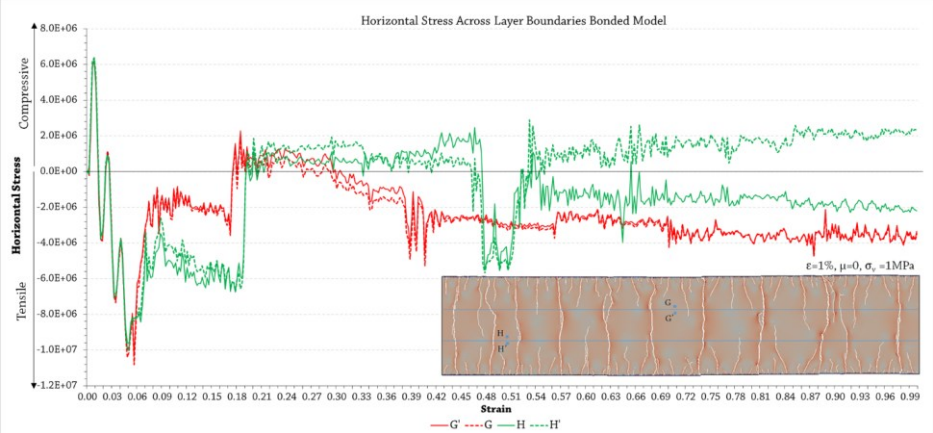


Figure 5. 70: Horizontal stress profile obtained from four points (G - red dotted line/G'- red line and H- green dotted line/H'- green line) on opposite sides of the bonded interface between the top and middle layers and the bottom and middle layers. Notice how they coincide.

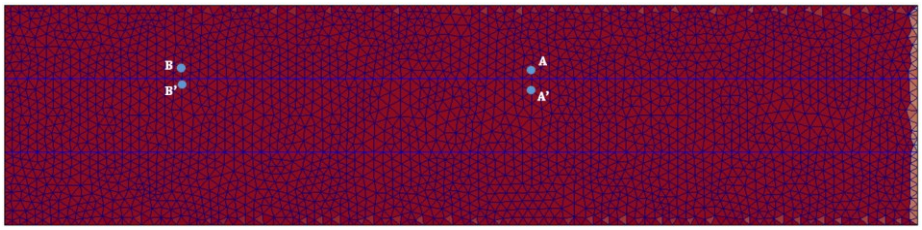


Figure 5. 71: Sampling points to measure stress propagation across layer boundaries.

It is not posible to predict the position where fractures will develop in the models. Therefore, two sets of sampling points were selected at different locations along the same interface to increase the chance of monitoring an area where fractures did not form.

Observations:

As demonstrated in the previous section, dedicated to examining the impact of the coefficient of friction along the layer interfaces (μ) on the build up of horizontal stresses, the stress profiles are complex. They vary both in space i.e. along the layer at any particular time and in time at any particular point. The variation of stress at particular points in the layer (See Figure 5.40) has been considered in detail and shown to be very sensitive to the formation of fractures in the immediate vicinity. During the accumulation of tensile stress (as a result of the application of horizontal extension in the model), the horizontal stress profile shows a downward trajectory before reaching a maximum value of tensile

stress which is then followed by a steep positive trajectory representing the tension release as a fracture forms. Good examples of this are points 1, 2 and 3 in Figure 5.48. The growth of an existing fracture, i.e. its propagation to intact cells also causes a drop in tesile stress, although with a different pattern.
The sensitivity of the stress profile at any given point in a layer to the formation of fractures in its vicinity make the study of the impact of the value of the coefficent of sliding fricion along a layer interface on the stress profile at each side of that interface more difficult to establish. This is because there are two variables potentially influencing the way the stress develops:

a) The distance of the sampling point (A and A' or B and B' – see Figure 4.71) from a fracture;
b) The magnitude of the coefficient of sliding friction along the layer interface.

Horizontal stress data from two different locations within the model were collected to try and establish whether it is possible to attribute the differences seen in the horizontal stress profiles to the coefficient of sliding fricition along the interface or wheter the formation/propagation of fractures dominates the development of stress. The results are presented in Figure 5.72 to Figure 5.75

Observation of the horizontal stress profiles taken from two pairs of points across the layer interface (A-A' and B-B' see Figure 5.71) show that it is difficult to fully relate the differences in the development of the horizontal stress to the value attributed to the coefficient of friction at the layer interface (0; 0.6; 1.0) and this is related to the presence of nearby tensile fractures. This can be seen for both pairs of sampling points.
Consider the sampling pairs A and A' for the three tested values of coefficient of friction of the layer interface. A comparison of the stress profiles (Figure 5.72) shows that there is practically no difference in the way horizontal stress develops when the coefficient of sliding friction on the layer interface is increased. For all the models, after an initial build up and release of tensile stress, the solid line profile which represents point A (above the interface) shows an accumulation of tensile stresses after ε=0.04% (downward trending curve) whereas the dotted profile representing point A' (below the interface) remains practically at zero (no tensile stress builds up). This is because of the formation, in all three models, of a fracture near point A' that releases the stresses (yellow arrow 1, Figure 5.73).
Considering only the solid line stress profile representing point A, at around ε=0.24% (Figure 5.72 red arrow 1) a decrease in the tensile stresses is registered for all models which is related to a nearby fracture propagating towards an intact cell (yellow arrow 2, Figure 5.73). After this moment no more tensile stress is accumulated and the horizontal stress curve remais in the compressive region. At around ε=0.69% (Figure 5.72 red arrow 2) the profile representing point A at the model with μ=1 shows a steep increase in the tensile stress. It is not immediately apparent why this sudden build up of tensile stress occurs at this time but it is suggested that it represents a point in the deformation where the evolution

an opening of the fractures that originally reduced the tensile stress cease and the system is therefore able once more to accumulate a layer-parallel tensile stress.

Consider the two sampling pointsr B and B' (Figure 5.72) for the three tested values of coefficient of friction on the layer interface. Figure 5.74 shows that the stress profiles for models where μ=0.6 and μ=1 are very similar and that the profiles for points on each side of the layer interface are also coincident. However, the profiles for points B and B' in a model where μ=0 show that there is a difference in the development of the horizontal stresses for each sampling point in the early stages of the simulation. This difference resides in the fact that the tensile fracture that develops in the middle layer for models with μ=0.6 and μ=1 (see yellow arrow 1 in Figure 5.75) does not develop in the model where μ=0. The absence of a nearby fracture allows the region around point B' to achieve a tensile state from around ε=0.05% and maintain it throughout the simulation. At the same time point B is registering the formation and propagation of fractures in its vicinity (see yellow arrow 2 in Figure 5.76) and the horizontal stress profile shows that there is practically no tensile stress accumulation until around ε=0.35% when the curve registers a sequence of tensile stress acumulation and release – a profile which represents the various pulses of fracture growth (see green arrow 1 in Figure 5.74).

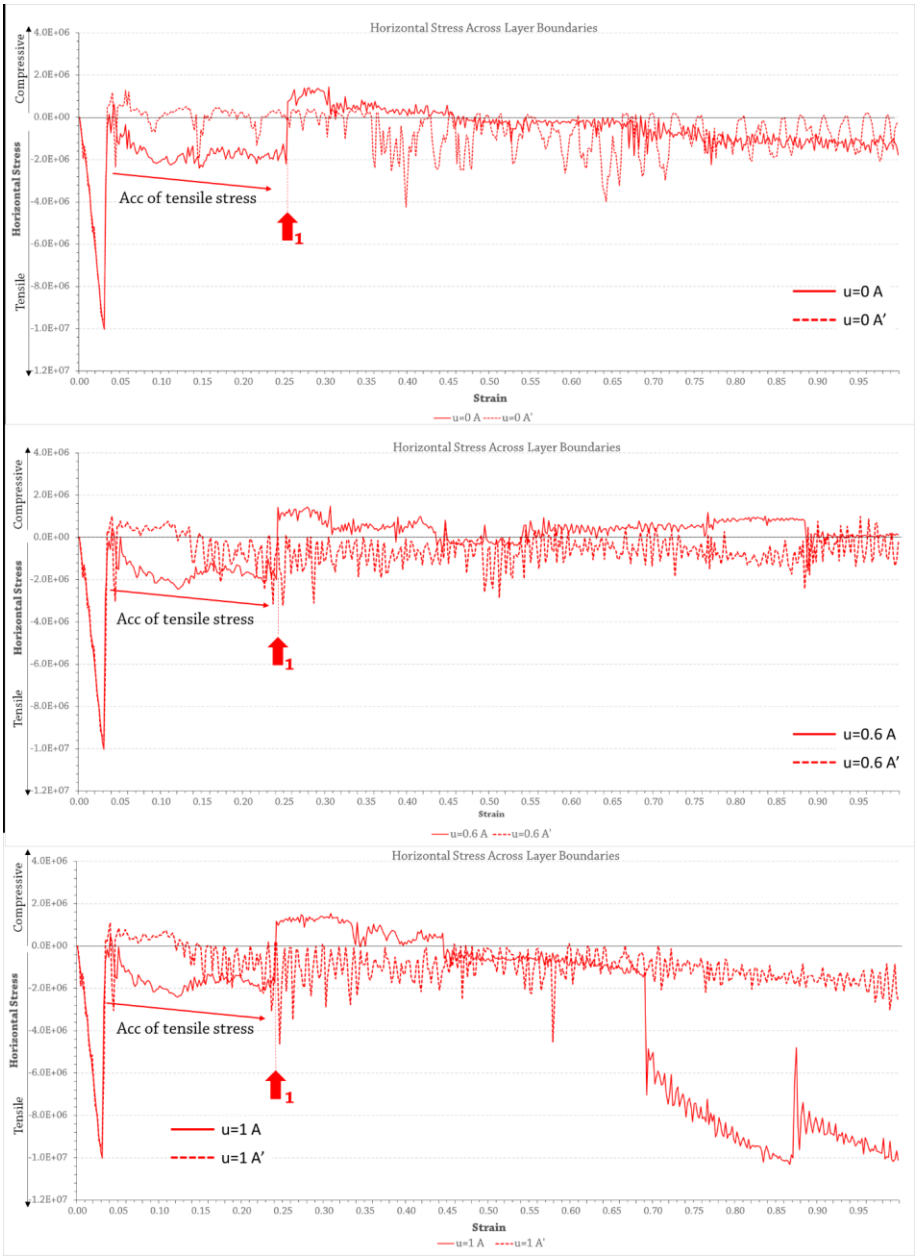


Figure 5. 72: Horizontal stress profiles obtained for points A and A' (see Figure 5.71). a) Horizontal stress profiles of points A and A' with a coefficient of sliding friction on the layer interface of 0. b) Horizontal stress profiles of points A and A'with a coefficient of sliding friction on the layer interface of 0.6; c) Horizontal stress profiles of points A and A' with a coefficient of sliding friction of 1.

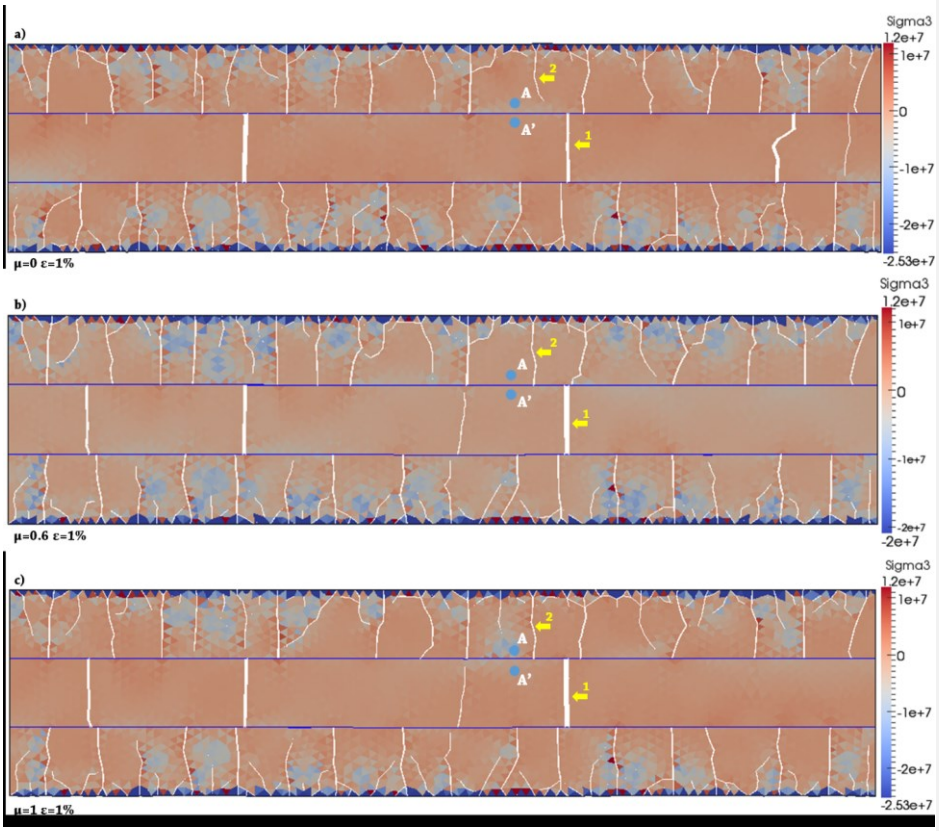


Figure 5. 73: Fracture patterns for a 3-layer model at ε=1% (end of deformation). a) model where the coefficient of friction on the layer interface is μ=0; b) model where the coefficient of friction along the interface is μ=0.6. c) model where the coefficient of friction along the interface is μ=1. Notice the difference in fracture formation near points A and A' (yellow markers) that are responsible for the difference in the horizontal stress profile.



Figure 5. 74: Horizontal stress profiles obtained for points B and B' (see Figure 5.71). a) Horizontal stress profiles of points B and B' with a coefficient of sliding friction on the layer interface of 0. b) Horizontal stress profiles of points B and B' with a coefficient of sliding friction on the layer interface of 0.6; c) Horizontal stress profiles of points B and B' with a coeffcient of sliding friction of 1.

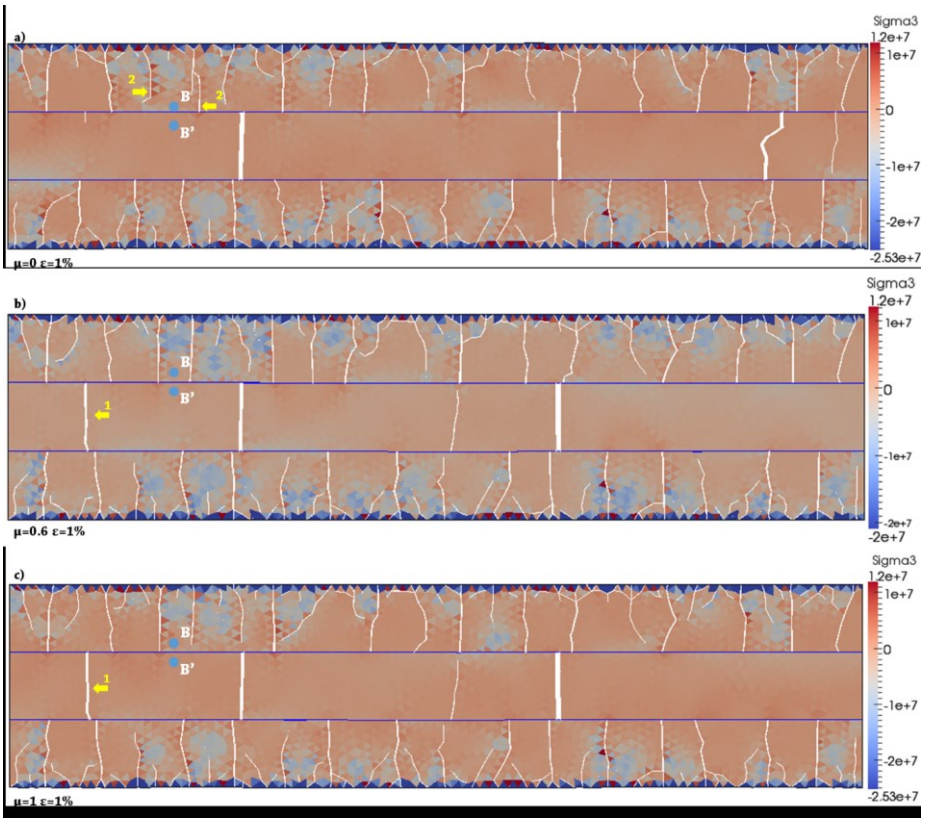


Figure 5. 75: Fracture patterns for a 3-layer model at ε=1% (end of deformation). a) model where the coefficient of friction on the layer interface is μ=0; b) model where the coefficient of friction along the interface is μ=0.6. c) model where the coefficient of friction along the interface is μ=1. Notice the difference in fracture formation near points B and B' (yellow markers) that are responsible for the difference in the horizontal stress prcfile.

Summary and learnings obtained from the numerical modelling on the effect of the coefficient of sliding friction of the layer interface on fracture propagation.

Results can be analysed in light of both the fracture patterns and the stress profiles obtained from several points sampled within the models. Looking at the fracture patterns generated on the several simulations, the data suggests that:

- Low values of the coefficient of sliding friction at the layer boundaries promote the arrest of fractures at these boundaries. However this is only valid for very low values of layer-normal load i.e. shallow depths. It can be seen at Figure 5.34 i), where the layer normal load is 25 MPa (approximately 1000m depth), that through-going fractures have formed at μ=0. This means that the effect of the layer-normal load (or overburden in geological conditions) is able to overcome the effect of a low coefficient of sliding friction and lead to the formation of through going fractures.
- The inverse is also true, i.e. higher values of μ promote the formation of through going fractures as can be seen in Figure 5.32 d) and Figure 5.33 f) where through-going fractures have formed at low values of applied layer-normal load (1 and 10 MPa respectively).

When emphasis is put on the analysis of the stress profiles the following observations can be made:

- When comparing horizontal stress profiles for experiments with the same coefficient of sliding friction along the layer interface but increasing layer-normal stress, it is difficult to establish a trend. Whereas in the data retrived at point A (see Figures 5.40 to 5.43), the horizontal stress profiles are very similar for layer-normal loads up to 50 MPa, the data retrieved from point B (see Figures 5.40, 5.45 and 5.46) shows that the profiles are very similar for layer-normal loads up to 75MPa and the data from Point C (see Figures 5.40 and 5.47 to 5.53) shows stress profiles very different for each of the considered layer-normal loads.
- When comparing horizontal stress profiles (retrieved from points A, B and C – see Figure 5.40) for experiments with the same normal load but with different values of the coefficient of sliding friction along the layer interface (Figure 5.54 to 5.69) , it is not possible to fully establish a relation between the way the horizontal stress develops (the shape of the curve) and the coeffcient of friction assigned to the interface for each of the compared models.
- Of the three parameters considered in the experiments (see Section 5.3.1.3) – the coefficient of sliding friction along the layer interfaces; the layer normal load; and the fracturing – the latter is the most important factor determining the stress distribution within the model. It is clearly the position of the sampling point relative to the fractures that form, that influences the way the horizontal stresses develop along the deformation.

A comparison between models with an increasing layer-normal load but with the same coefficient of sliding friction (Figure 5.36) shows that:

- Fractures form at lower strains for lower vertical stress, i.e. the higher the applied vertical stress more accumulated strain is needed so that the material reaches the tensile strength limit and forms a fracture (see Figure 5.39).
- Higher vertical stress promotes the formation of straighter fractures as explained previously for the validation models and as it can be seen in Figure 5.37.
- Higher vertical stress promotes the formation of through-going fractures as demonstrated by the increasing number of through going fractures in models with higher layer-normal load.
- Higher vertical stress creates higher differential stresses and promotes the formation of shear fractures. (seen where sigma yy ≥ 75MPa).

5.3.2 The effect of the elastic modulus (Young' s Modulus – E) of adjacent layers on the propagation of fractures across the interface between them

Numerical models have been conducted to determine the role of the elastic modulus (Young's Modulus –E) between adjacent layers on fracture propagation from one layer to another. The investigation involved 3-layered models. The values of the Young's Modules used were those shown in Table 5.7 and the normal loads were 25 Mpa to reduce the potential for slippage along the layer interfaces. The shear stress resistance to slip is given by $\tau=\mu.\sigma_v$, and the coefficient of sliding friction along the layer interface (μ) is maintained at 0.6. By selecting a significant layer-normal load (σ_v) the likelihood of slip along the interface is reduced and the impact of the change in Young's Modulus across the interfaces on the propagation of fractures can be determined. A velocity-controlled constraint condition in the horizontal direction (Vx=0.2 ms^{-1}) was applied to the top and bottom boundaries. This velocity constraint allowed the application of an equal strain value along the model boundaries, through the relation $\varepsilon= 2v/L$ where ε is strain (in decimal scale), v is velocity and L the length of the model. The right hand side boundary moves at the same rate as the top and bottom boundaries extend keeping the model rectangular and the left hand side boundary is pinned in the x-direction (horizontal). The vertical load (σ_v) is applied at the top and bottom boundaries and the Young's Modulus of the middle layer is varied. The coefficient of sliding friction on the layer boundaries is fixed at 0.6, the most common value found in real rocks. We have chosen to vary the elastic modulus on the middle layer because as tension is applied to the top and bottom boundaries, this triggers the formation of fractures in the top and bottom layers. By varying the middle layer we can study whether these fractures will propagate into it or not.

The mechanical properties of the outer layers are equivalent to those of a limestone (Table 5.1) and the results of the experimental runs are presented in Figure 5.76 to 5.80 Apart from the Yoyng's Modulus, the mechanical properties of the middle layer are also equivalent to those of a limestone.

The study, focuses on the fracture patterns and on the relation between rock stiffness (Young's Modulus value) and failure.

Table 5.7: Young's modulus values for the bounding (E1) and middle layers (E2) on the 3-layer models used to test the influence of this parameter on fracture propagation across an interface.

Young's Modulus			
Model	E1 (Top and Bottom Layers)	Multiplier	E2 (Middle Layer)
A	3.00E+10	/2	1.50E+10
B	3.00E+10	/10	3.00E+09
C	3.00E+10	/20	1.50E+09
D	3.00E+10	/50	6.00E+08

Model A: Consisting of two bounding layers (E1) with a Young's Modulus of 30 GPa and a middle layer (E2) with a Young's Modulus of 15 GPa had its first fractures forming at an accumulated strain of (ε) 0.072% in the top and bottom layers layer (Figure 5.76a). These fractures formed at the interface between the layers and grew towards the outside of the model. At ε=0.098%, a fracture formed in the middle layer and immediately (ε=0.104%) linked to a fracture that had previously formed in the bottom layer (see yellow box 1 – Figure 5.76c). At ε6=0.504% a fracture that formed in the bottom layer, linked to another fracture that had previously formed in the middle layer (yellow box 2 – Figure 5.76d). At ε=0.622 and ε=0.786% similar events occurred with fractures that had formed in adjacent layers linking to form a through-going fracture (see yellow box 3 and 4 – Figure 5.76e).

Model B: Consisting of two bounding layers (E1) with a Young's Modulus of 30 GPa and a middle layer (E2) with a Young's Modulus of 3 GPa had its first fractures forming at an accumulated strain of (ε) 0.074% in the top and bottom layers layer (Figure 5.77b). At ε=0.506%, two tensile fractures formed in the middle layer, and were the only two fractures to have formed during the whole simulation. These fractures remain strata-bound.

Model C: Consisting of two bounding layers (E1) with a Young's Modulus of 30 GPa and a middle layer (E2) with a Young's Modulus of 1.5 GPa had its first fractures forming at an accumulated strain of (ε) 0.076% in the top and bottom layers layer (Figure 5.78b). These fractures formed at the interface between the layers and grew towards the outside of the model. At ε=0.818% a tensile fracture that had formed in the top layer (top boundary and grew towards the centre of the model) was able to propagate through to the middle layer (see yellow box 1 – Figure 5.78c). A similar event occurred ε=0.946% (see yellow box 2 – Figure 4.63d) and at ε=0.95% (see yellow box 3 – Figure 5.78d).

Model D: Consisting of two bounding layers (E1) with a Young's Modulus of 30 GPa and a middle layer (E2) with a Young's Modulus of 0.6 GPa had its first fractures forming at an accumulated strain of (ε)

0.08% in the top and bottom layers layer (Figure 5.79b). These fractures formed at the interface between the layers and grew towards the outside of the model. Due to the very low stiffness of the middle layer, no fractures are formed in it after 1% of strain had been applied.

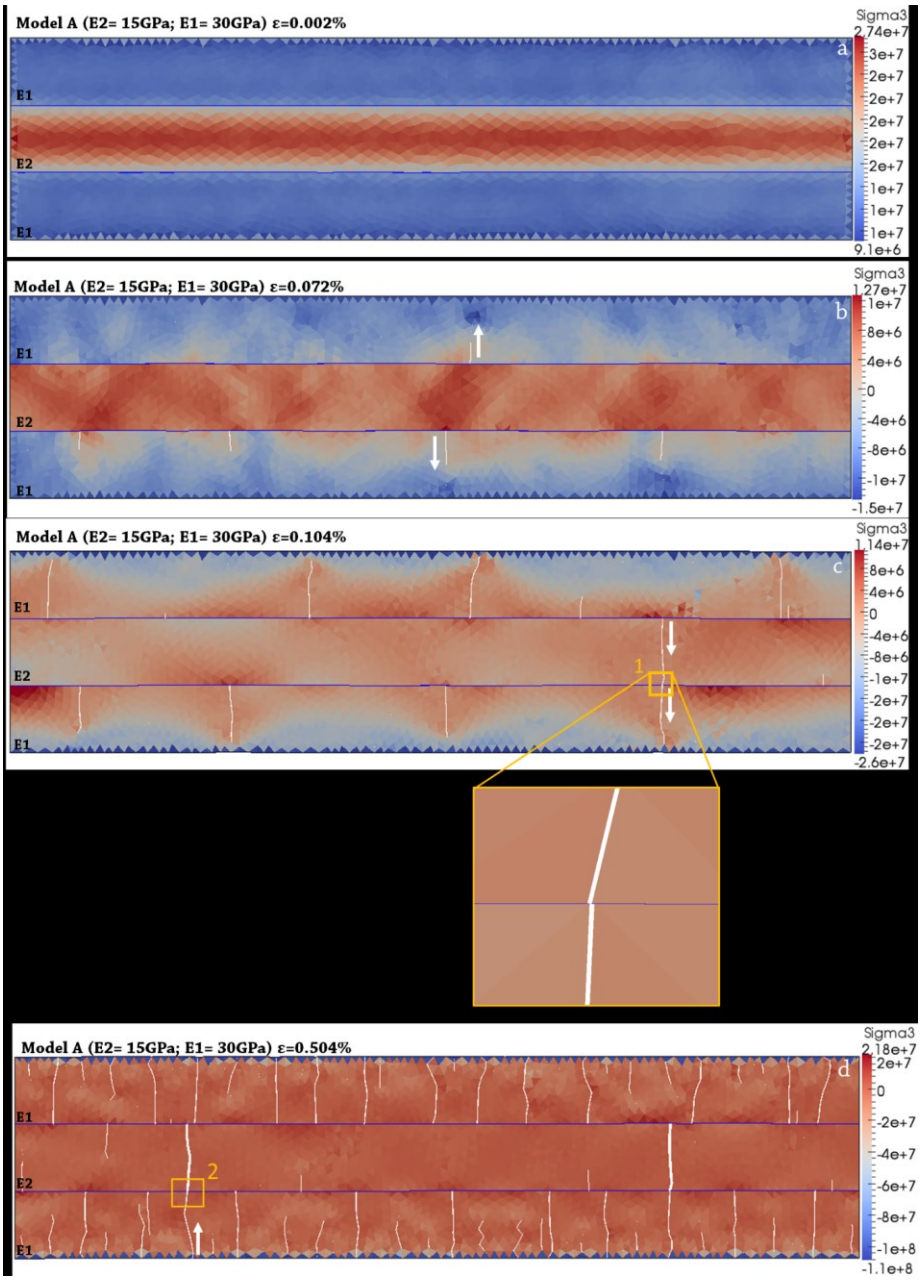


Figure 5. 76: Fracture patterns and stress distribution for a 3-layer model at ε=1% (end of deformation). The coefficient of sliding friction at the layer interface is μ=0.6 and layer-normal load is 25 MPa. The the top and bottom layers Young's Modulus was set at 30 GPa and the middle layer at 15 Gpa.

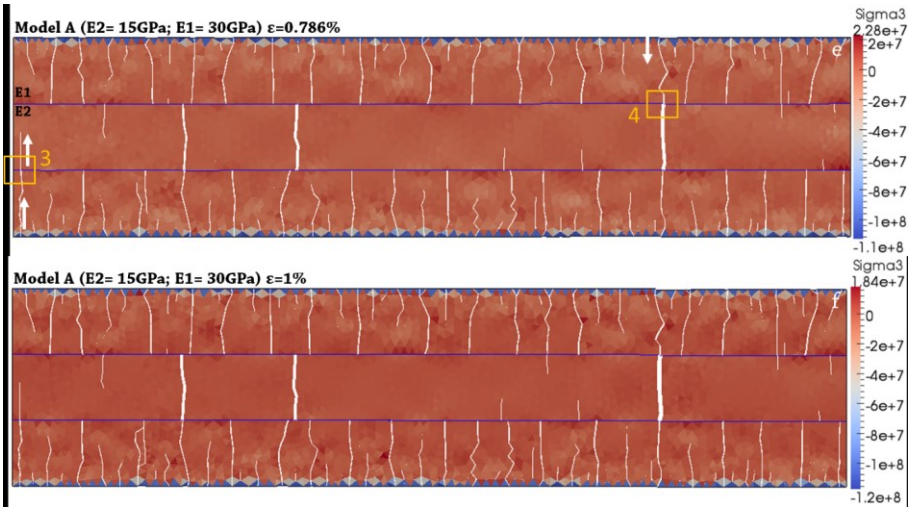


Figure 5. 77 (continued): Fracture patterns and stress distribution for a 3-layer model at ε=1% (end of deformation). The coefficient of sliding friction at the layer interface is μ=0.6 and layer-normal load is 25 MPa. The the top and bottom layers Young's Modulus was set at 30 GPa and the middle layer at 15 Gpa.

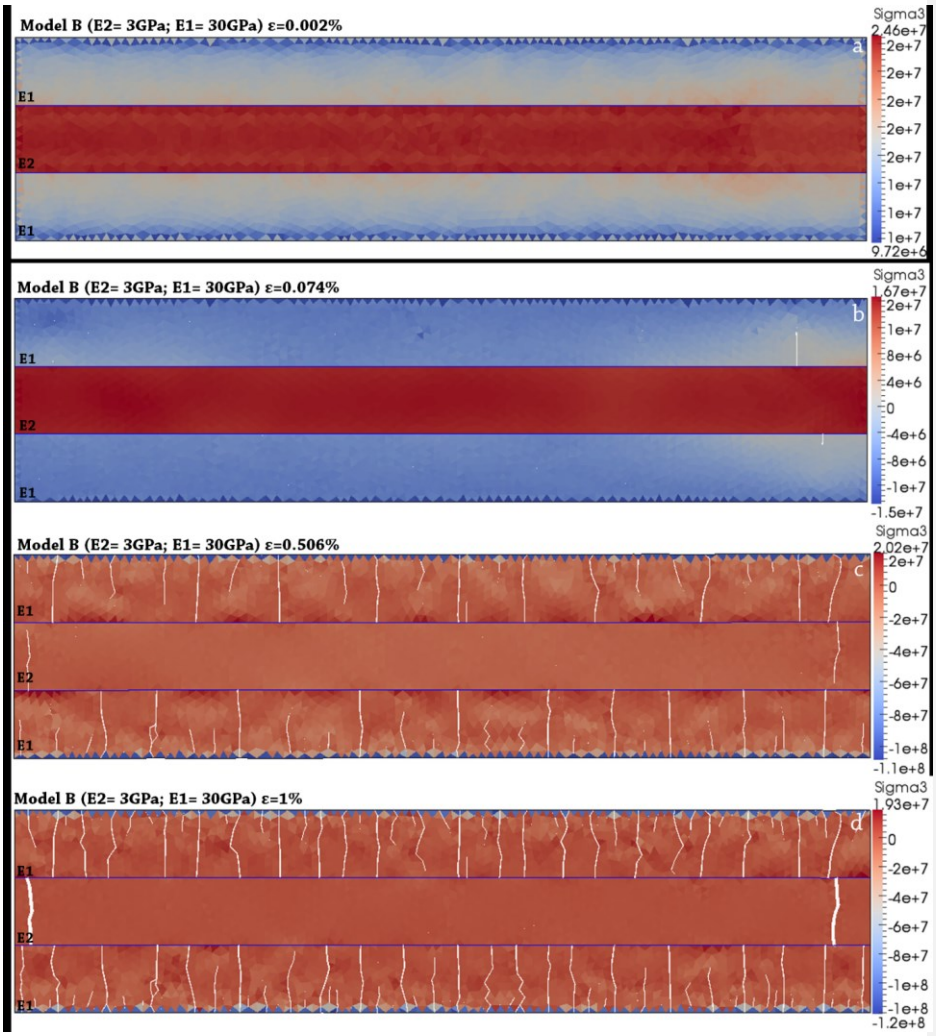


Figure 5. 78: Fracture patterns and stress distribution for a 3-layer model at ε=1% (end of deformation). The coefficient of sliding friction at the layer interface is μ=0.6 and layer-normal load is 25 MPa. The the top and bottom layers Young's Modulus was set at 30 GPa and the middle layer at 3 Gpa.

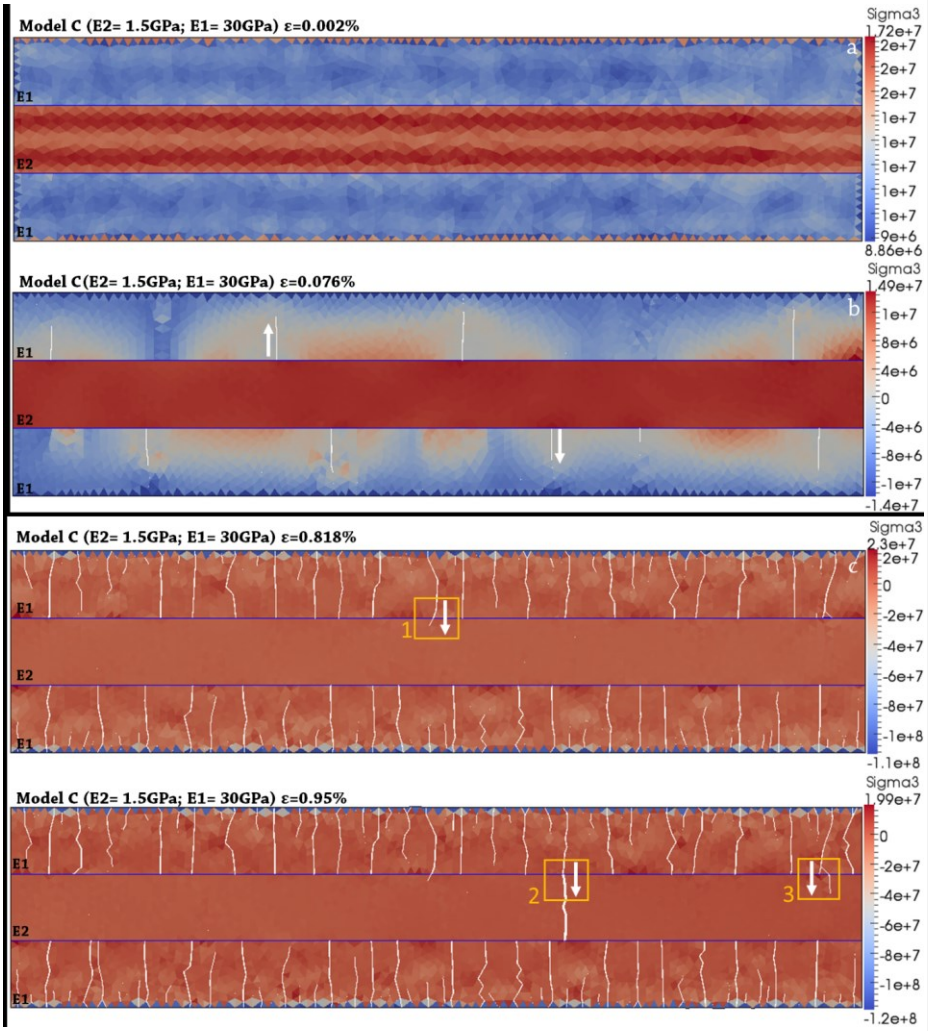


Figure 5. 79: Fracture patterns and stress distribution for a 3-layer model at ε=1% (end of deformation). The coefficient of sliding friction at the layer interface is μ=0.6 and layer-normal load is 25 MPa. The the top and bottom layers Young's Modulus was set at 30 GPa and the middle layer at 1.5 Gpa.

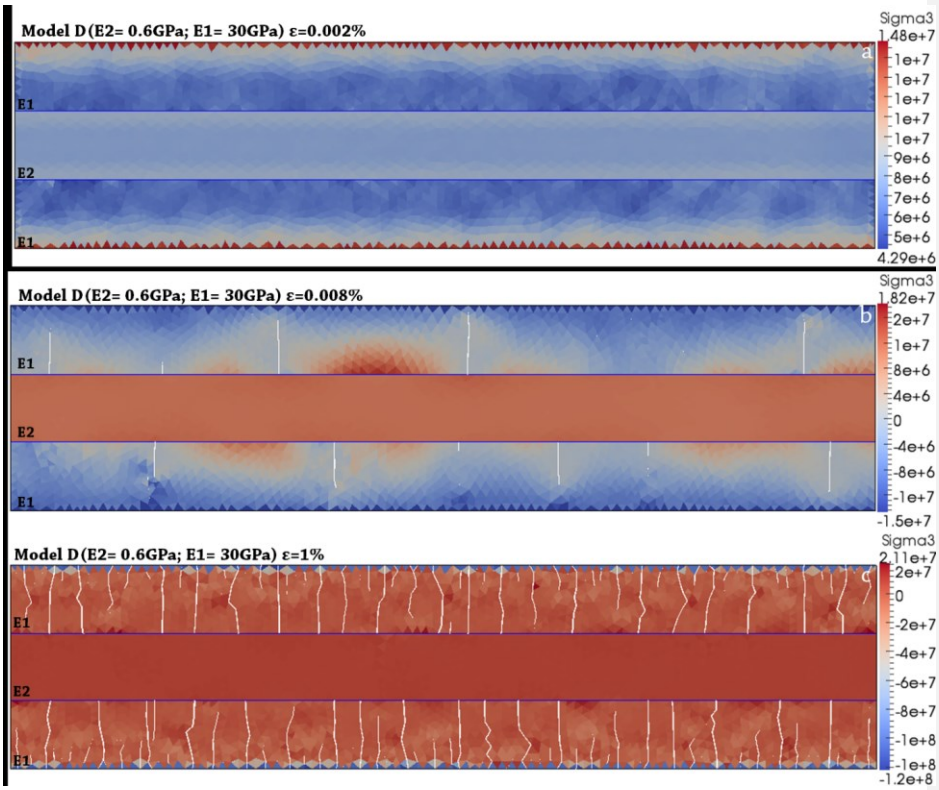


Figure 5. 80: Fracture patterns and stress distribution for a 3-layer model at ε=1% (end of deformation). The coefficient of sliding friction at the layer interface is μ=0.6 and layer-normal load is 25 MPa. The the top and bottom layers Young's Modulus was set at 30 GPa and the middle layer at 0.6 Gpa.

Summary and learnings obtained from the numerical modelling on the effect of the Young's Modulus on fracture propagation across an interface.

- As expected fractures form first - at lower accumulated strain, i.e. earlier in the deformation - in the top and bottom "stiffer" layers.
- In models A and B, although the middle layer is "softer" than the top and bottom layers, no fractures are able to propagate across the interfaces between these and the middle layer. However, through-going fractures are formed by independent fractures that form in top and bottom layers and are linked across by fractures that form in the middle layer.
- In model C, where E1=20E2, three fractures where able to propagate across the interface between the top and the middle layer, suggesting that in order for this to occur there needs to be a minimum ratio between "stiff" and "soft" layers that needs to be observed.
- In Model D, E1=50E2 but no fractures where able to propagate across the interface between the "stiffer" top and bottom layers and the "soft" middle layer. This suggests that whereas the top and bottom layers achieve fracture saturation when ε=1%, the middle layer has not yet achieved a tensile stress state and therefore no fractures are able to propagate across the interface or to form in this layer.

5.3.3 The effect of the thickness of an incompetent layer (low Young's Modulus, low tensile strength) on fracture propagation across it

Numerical models have been conducted to determine the role that the thickness of an incompetent layer (such as a shale layer or a bedding-parallel gypsum vein) plays on fracture propagation into that incompetent layer.

The investigation involved 3-layered models with 50 cm length and variable total vertical thickness. A total of seven models were built where the thickness of the middle layer was progressively increased – from 0.2 cm (Model A) to 20 cm (Model G) while maintaining the thickness of the bounding layers (top and bottom) fixed at 5 cm. A velocity-controlled constraint condition in the horizontal direction ($Vx=0.2\ ms^{-1}$) was applied to the top and bottom boundaries. This velocity constraint allowed the application of an equal strain value along the model boundaries, through the relation $\varepsilon = 2v/L$ where ε is strain (in decimal scale), v is velocity and L the length of the model. The right hand side boundary moves at the same rate as the top and bottom boundaries extend maintaining the rectangular shape of the model and the left hand side boundary is pinned in the x-direction (horizontal). A vertical load (σ_v) of 10 MPa was applied at the top and bottom boundaries and the coefficient of sliding friction of the interface between the two layers was maintained constant at 0.6. The mechanical properties of the top and bottom layers are equivalent to those of a limestone (Table 5.1) and the mechanical properties of the middle incompetent layer are equivalent to a shale (Table 5.2). The results of the experimental runs are presented in Figure 5.80 to 5.96.

To analyze the impact of the thickness of the incompetent layer on the propagation of fractures across it, the fracture patterns that develop and the associated change of stress within the layers as the fractures form and grow were studied.

<u>Numerical Models with incompetent layer thickness of 2mm – Model A (Figure 5.80)</u>

In a model where the incompetent middle layer has a thickness of 2mm we observe the following:

- Tensile stresses developed earlier in and around the thin middle incompetent layer.
- The first tensile fractures formed at an accumulated strain of 0.038% within the competent layer at the interfaces between the layers and propagated towards the outside of the model. In the moments that preceded the formation of these fractures, the middle layer was experiencing a compressive stress state (Figure 4.80 a).
- At a later stage, other tensile fractures developed from the top and bottom boundaries of the model and grew towards the middle layer (Figure 4.80b)
- The first tensile fracture in the middle layer formed at an accumulated strain of 0.042% and independently of other fractures in the model (Yellow arrow 1, Figure 4.80c).
- At an accumulated strain of 0.054% a tensile fracture that had formed at the interface

between the bottom and middle layers, reached the bottom of the model and proceeded to cross the interface between the bottom and middle layers (Yellow square 2, Figure 4.80d).

- At an accumulated strain of 0.526% two independent tensile fractures that had formed in the bottom and middle layers link forming a trough-going fracture affecting the bottom and middle layers (Yellow square 3, Figure 4.80e).
- When the model had registered an accumulated strain of 0.706% a tensile fracture crossed the interface between the bottom and middle layers, forming a trough-going fracture that links obliquely to another tensile fracture in the top layer (Yellow square 4, Figure 4.80f).
- When the strain attained a value of 0.756% a tensile fracture formed in the middle layer and immediately after that the top and bottom interfaces locally decoupled, allowing a linkage of three tensile fractures and the connection of the three layers (Yellow square 5, Figure 4.80g).

Numerical Models with incompetent layer thickness of 6mm – Model B (Figure 5.82)

In a model where the incompetent middle layer has a thickness of 6 mm we observe the following:

- Tensile stresses developed earlier in and around the thin middle incompetent layer. Compared to Model A, in Model B the registered tension is higher for the same accumulated strain (ε=0.002%) (Figure 4.81a)
- The first tensile fractures formed at an accumulated strain of 0.032% within the competent layers and adjacent to the interfaces between layers. They subsequently propagated towards the outside of the model. In the moments that preceded the formation of these fractures, the middle layer was experiencing a compressive stress state. (Figure 5.81b).
- At a later stage, other tensile fractures developed from the top and bottom boundaries and grew towards the middle layer of the model.
- The first tensile fracture to form in the middle incompetent layer occurred at an accumulated strain of 0.04% (Yellow arrow 1, Figure 5.81c)
- At an accumulated strain of 0.308% a tensile fracture that had formed in the top layer (top boundary) and propagated towards the middle layer, crosses the interface between these the layers and links to a fracture that had formed in the bottom layer. This formed a through-going fracture that links the three layers at the left hand side of the model (Figure 5.81d – see enlarged images).
- At ε=0.448% a tensile fracture formed in the middle layer in the vicinity of two tensile fractures that had formed in the top and bottom layers (Figure 4.81e). There is no connection between these. A similar situation occurs at ε=0.618% (Figure 4.81f).
- In the late stages of the deformation, between 0.824% and 1% of accumulated strain, many fractures cross the middle layer interfaces both from top to bottom and bottom to top (Figure

4.81g). Some of these link to preexisting fractures in on or both of the adjacent layers. Others do not.

Numerical Models with incompetent layer thickness of 2.5cm – Model C (Figure 5.82)

- Compared to the previous models, the development of tensile stresses occurs earlier in the top and bottom edges of the model (Figure 4.82a).
- The first tensile fractures formed at an accumulated strain of 0.028% in the competent layer adjacent to the interfaces between layers and propagated towards the outside of the model. In the moments that preceded the formation of these fractures, the middle layer was experiencing a compressive stress state. (Figure 4.82b). On a later stage, other tensile fractures developed from the top and bottom boundaries and grew towards the middle layer.
- The first tensile fracture to form in the middle incompetent layer occurred at an accumulated strain of 0.038% (Yellow arrow 1, Figure 4.82c)
- As deformation progresses other fractures form in the top and bottom layers, saturating the model.
- In the late stages of the deformation, between 0.8% and 1% of accumulated strain, several through going fractures are formed. However all of them are formed by linking of individual tensile fractures that form/grow at different accumulated strains along the simulation in each of the 3 layers. They are not formed by the propagation of fractures from one layer into an adjacent layer.

Numerical Models with incompetent layer thickness of 5cm (three layers of the same thickness) – Model D (Figure 5.83)

- As in previous models A and B, the development of tensile stress occurs earlier in the middle layer than in the top and bottom layers. However the stress distribution shown in Figure 4.83a clearly shows that at an accumulated strain of 0.002 there is no tensile stresses being developed – see the scale bar on the right hand-side of the figure and notice that although in the blue region the values are still positive (compressive). In fact, the layers are only in tension after an accumulated strain of 0.006% (in models A and B the middle layer was in tension immediately the deformation began).
- The first tensile fractures formed at an accumulated strain of 0.036% in the competent layers at the interfaces between the layers and propagated towards the outside of the model. In the moments that preceded the formation of these fractures the middle layer was experiencing a much lower tensile stress than the top and bottom layers (0.12 MPa in the middle layer and 8MPa in the top and bottom layers). Notice that whereas in the previous models this layer

was in compression, here it is in tension (Figure 5.83b).

- The first tensile fracture to form in the middle incompetent layer occurred at an accumulated strain of 0.05%, and at around 0.058% a tensile fracture in the middle layer, that had formed at the interface between the middle and top layers and propagated towards the lower boundary of the middle layer, connected with a tensile fracture in the bottom layer that had formed in the interface between the bottom and middle layers and grown towards the bottom edge of the model (Figure 5.83c).
- As deformation progresses other fractures formed in the top and bottom layers, saturating them with fractures.
- In the late stages of the deformation, between 0.5% and 1% of accumulated strain, several through-going fractures formed. However all were formed by the linking of individual tensile fractures that formed at different times within the model. Non were formed by the propagation of fracture from one layer to another.

Numerical Models with incompetent layer thickness of 7.5 cm – Model E (Figure 5.84)

- As in the previous model D, the development of tensile stresses occurs earlier in the middle layer than in the top and bottom layers, developing at around ε=0.006% (see Figure 5.84b) However it is important to notice that in the beginning of the deformation the top and bottom layers show zones of compressive stress development: there is a zone in the boundary between the top & bottom and the middle layer where the stress is around 8.5 MPa when ε=0.002% (Figure 5.84 a). This "zoning" in the top and bottom layers is again verified when the middle layer achieves tension (ε=0.006%): there is an area close to the middle layer which is in tension and an outer zone that remains in compression (Figure 5.84b)
- The first tensile fractures formed at an accumulated strain of 0.032% in the competent layer at the interfaces between the layers and propagated towards the outside of the model. In the moments that preceded the formation of these fractures the middle layer was experiencing a compressive stress state (Figure 5.84c).
- The first tensile fractures to form in the middle incompetent layer occurred at an accumulated strain of 0.038%, at the interface between the bottom and middle layers and grew towards the top of the model (Yellow arrow Figure 5.84d). At around ε=0.048% other sets of fractures formed in the middle layer at the interface between the top and middle layer and grew downwards
- As deformation progresses other fractures formed in the top and bottom layers, saturating the model.
- During the deformation, several through-going fractures formed. However all of them are

formed by the linking of individual tensile fractures that formed at different times during the extension of the model (Figures 5.84 f and 5.84 g).

Numerical Models with incompetent layer thickness of 10 cm - F (Figure 5.85)

- Although the development of tensile stresses occurred firstly in the middle layer at around 0.006% (Figure 5.85b) of accumulated strain, the first steps of deformation show a very distinct stress distribution with a both a horizontal and vertical stress zoning (Figure 5.85a).
- The first tensile fractures formed at an accumulated strain of 0.03% within the competent layers at the interfaces between layers and propagated towards the outside of the model. In the moments that preceded the formation of these fractures the middle layer was experiencing a compressive stress state that becomes slightly tensile when the fractures form (Figure 5.85c).
- The first tensile fracture to form in the middle, incompetent layer occurred at an accumulated strain of 0.038%, at the interface between the top and middle layers and grew towards the bottom of the model (Yellow arrow 1 Figure 5.85d). This fracture grew until it reached the interface between the middle and bottom layers where it arrested.
- As deformation progressed other fractures formed in the top, bottom and middle layers, saturating the model. None of these fractures crossed the interfaces between the layers.
- At ε= 0.2% the middle layer is practically saturated with fractures and it is not until ε= 0.9% that new fractures were formed. The trough-going fractures were formed by the linking of individual fractures as no fracture was able to cross the interfaces (Figures 5.85e and 5.85f).

Numerical Models with incompetent layer thickness of 20 cm - G (Figure 5.86)

- Unlike Model F, at Model G the development of tensile stress in the middle layer occurred immediately after the beginning of the deformation. These developed firstly in the middle layer.
- The first tensile fractures formed at an accumulated strain of 0.038% in the competent layer at the interfaces between the layers and at the top and bottom boundaries. Propagation occurred towards the outside of the model for the fractures generated at the interfaces and towards the inside of the model for the fractures generated in the top and bottom boundaries. In the moments that preceded the formation of these fractures the middle layer was experiencing a tensile stress state which was lower than the top and bottom layers (Figure 5.85b).
- The first tensile fractures to form in the middle incompetent layer occurred at an accumulated strain of 0.058%, mainly in the middle of the layer but with a few forming at the interfaces

(Figure 5.85c). The fractures that formed in the middle of the layer grew in both directions (i.e towards the top and the bottom of the model). Fractures that have formed in the lower interface grew towards the top and the inverse occurred for fractures formed at the upper interface.

- As deformation progressed other fractures formed in the top, bottom and middle layers, saturating the model. None of these fractures crossed the interfaces between the layers but some linked (Figure 5.85d).
- At ε= 0.066% a tensile fracture that had formed in the top layer and grown towards the bottom was able to cross the interface and propagates to the middle layer (Figure 5.85e see yellow box and the zoomed image below it)
- At ε= 0.12% the middle layer is saturated with fractures and no new fractures form until the end of the simulation. However some fractures form in the top and bottom layers and then link to fractures formed in the middle layer (Figure 5.85f).

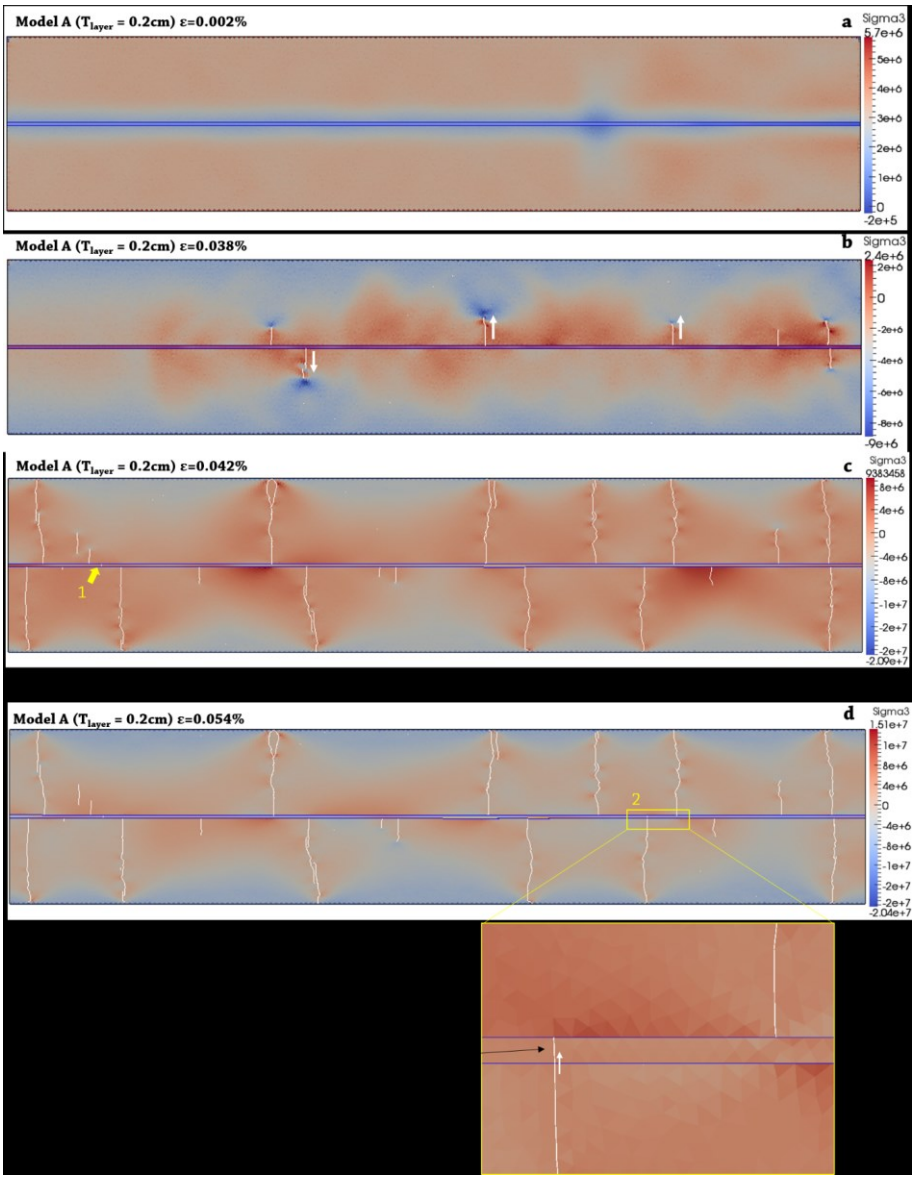


Figure 5. 8081: seven stages in the layer-parallel deformation of a multilayer model containing a thin weak layer (2mm thick) sandwiched between two strong layers showing the evolution of stress and fracturing. See text for discussion.

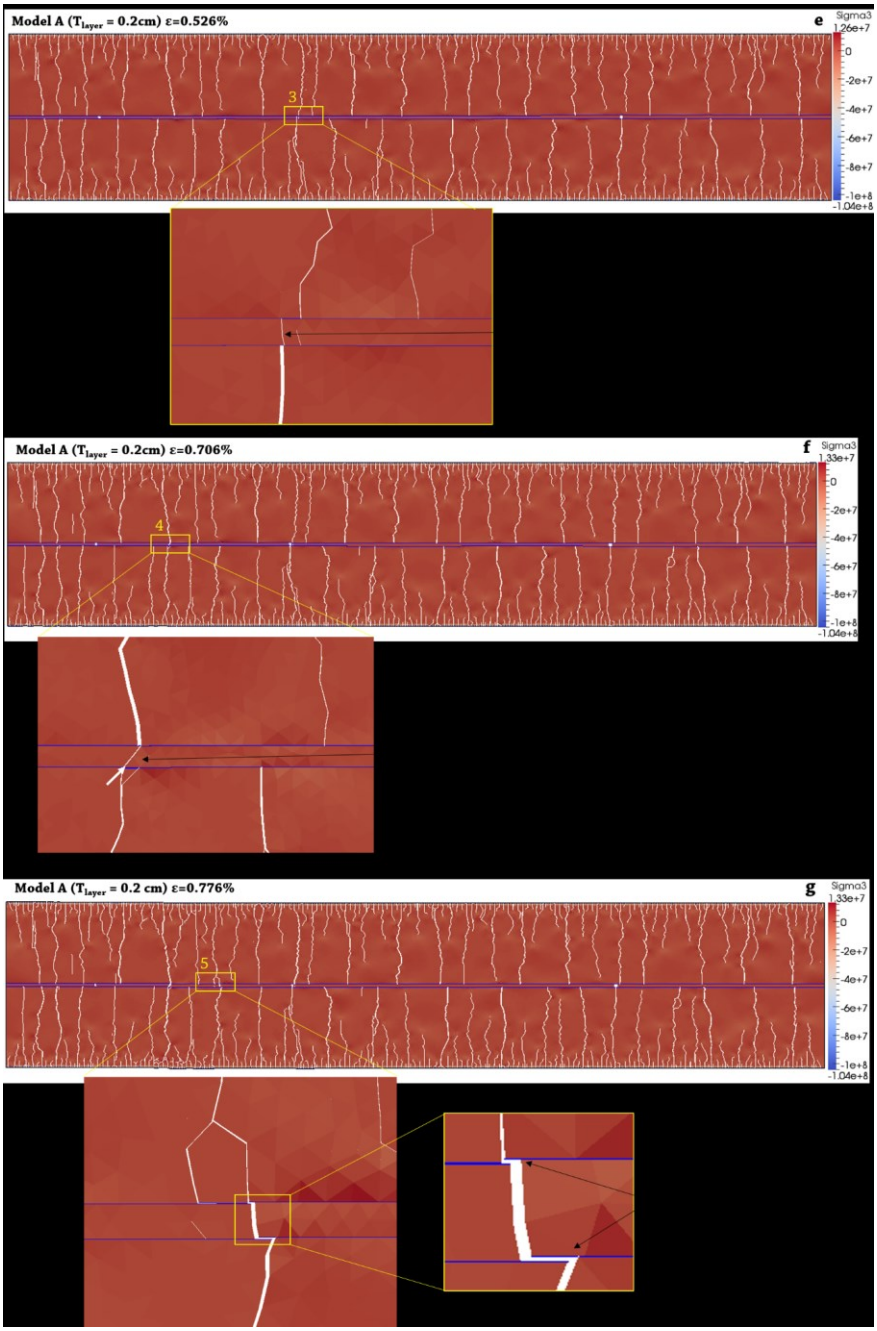


Figure 5. 80 (continued): seven stages in the layer-parallel deformation of a multilayer model containing a thin weak layer (2mm thick) sandwiched between two strong layers showing the evolution of stress and fracturing. See text for discussion.

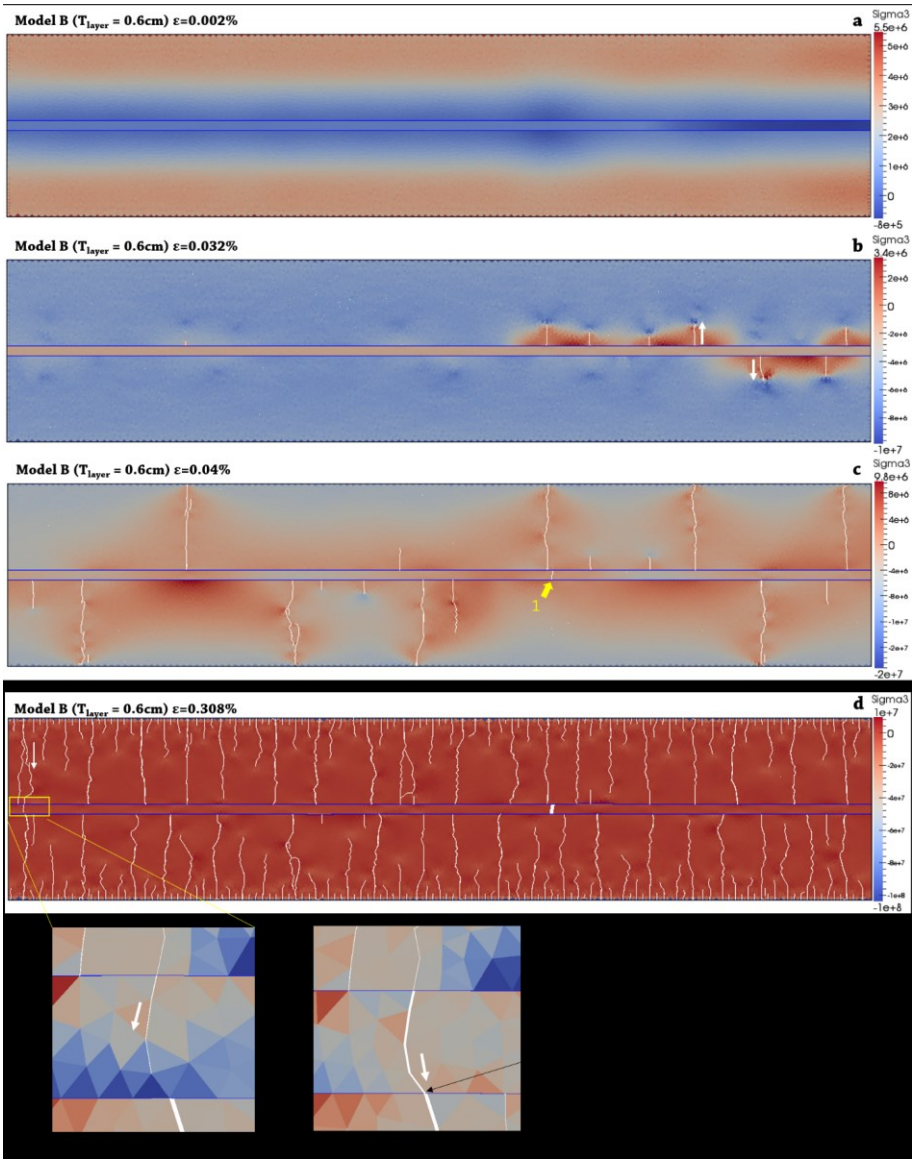


Figure 5. 81: eight stages in the layer-parallel deformation of a multilayer model containing a thin weak layer (6mm thick) sandwiched between two strong layers showing the evolution of stress and fracturing. See text for discussion.

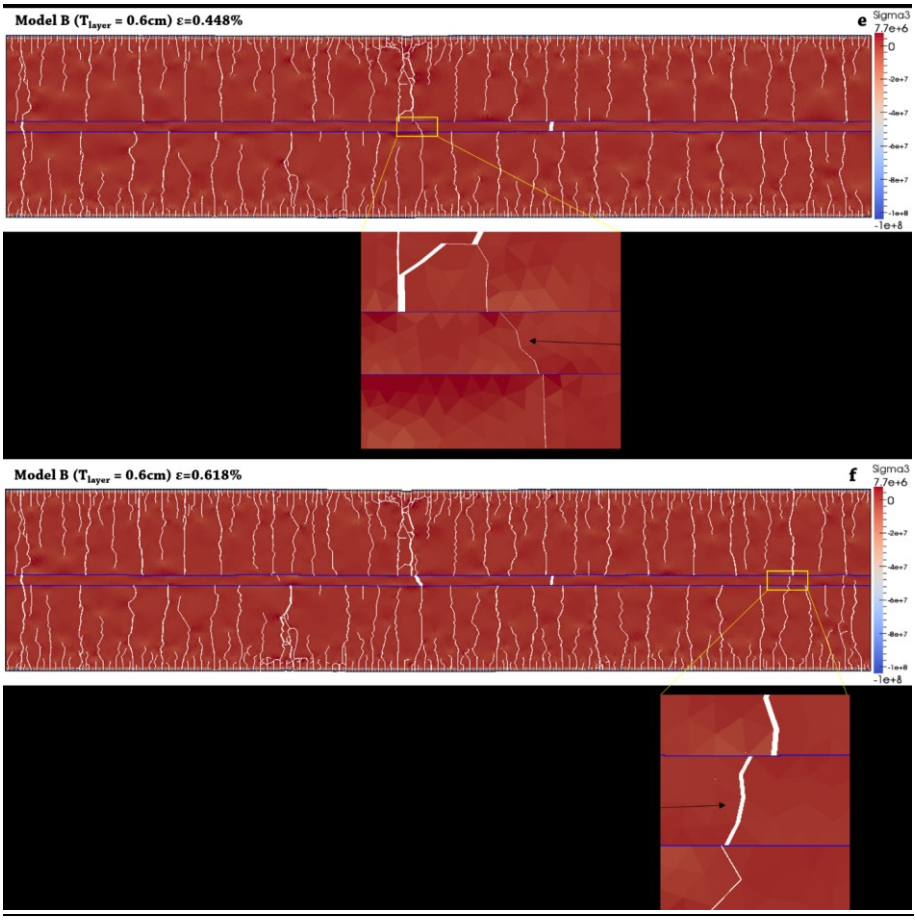


Figure 5. 81(continued): eight stages in the layer-parallel deformation of a multilayer model containing a thin weak layer (6mm thick) sandwiched between two strong layers showing the evolution of stress and fracturing. See text for discussion.

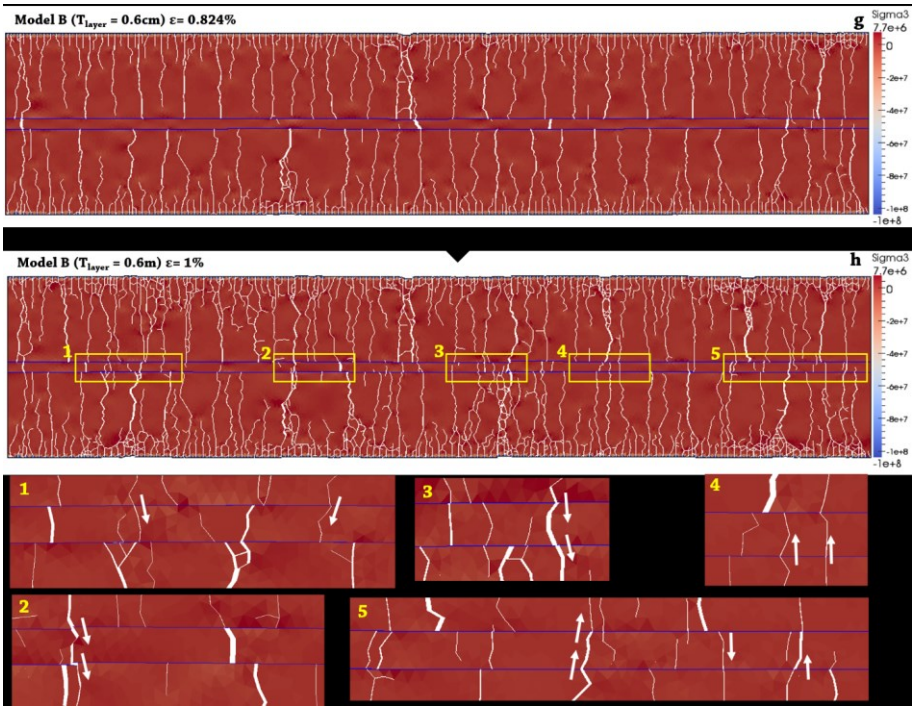


Figure 5. 8182(continued): eight stages in the layer-parallel deformation of a multilayer model containing a thin weak layer (6mm thick) sandwiched between two strong layers showing the evolution of stress and fracturing. See text for discussion.

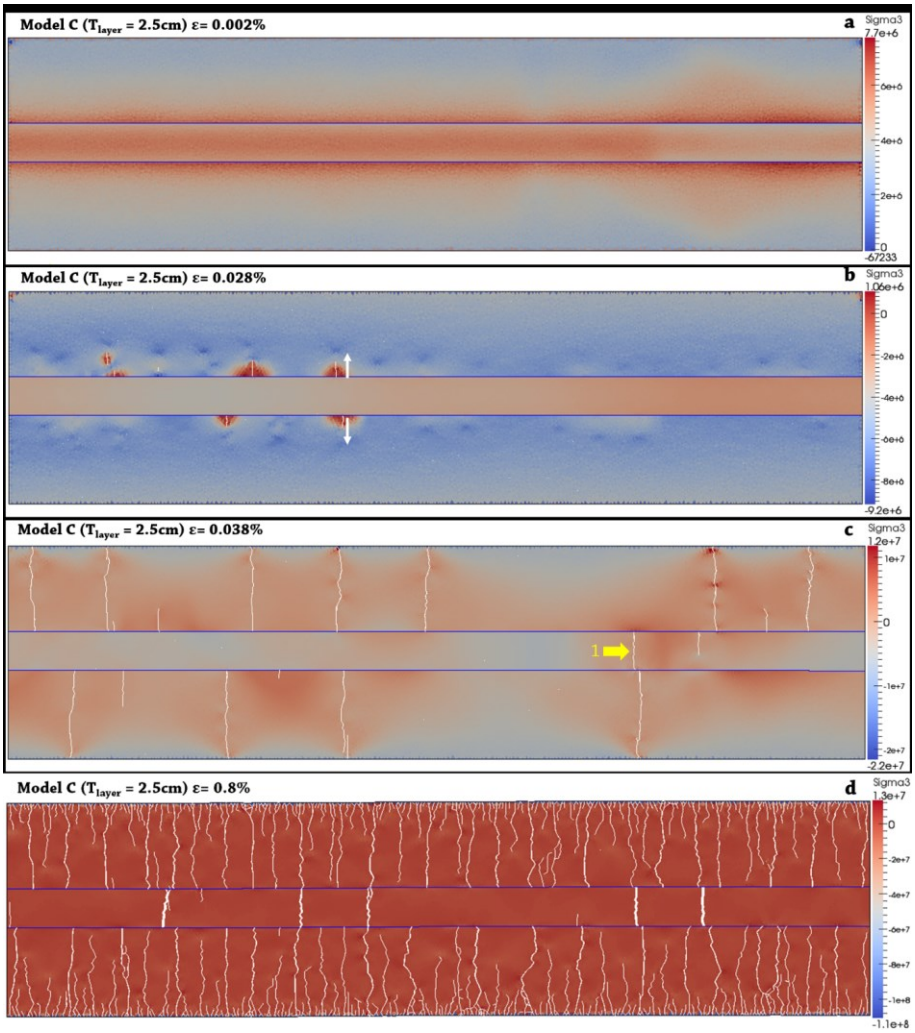


Figure 5. 82: six stages in the layer-parallel deformation of a multilayer model containing a thin weak layer (2.5cm thick) sandwiched between two strong layers showing the evolution of stress and fracturing. See text for discussion.

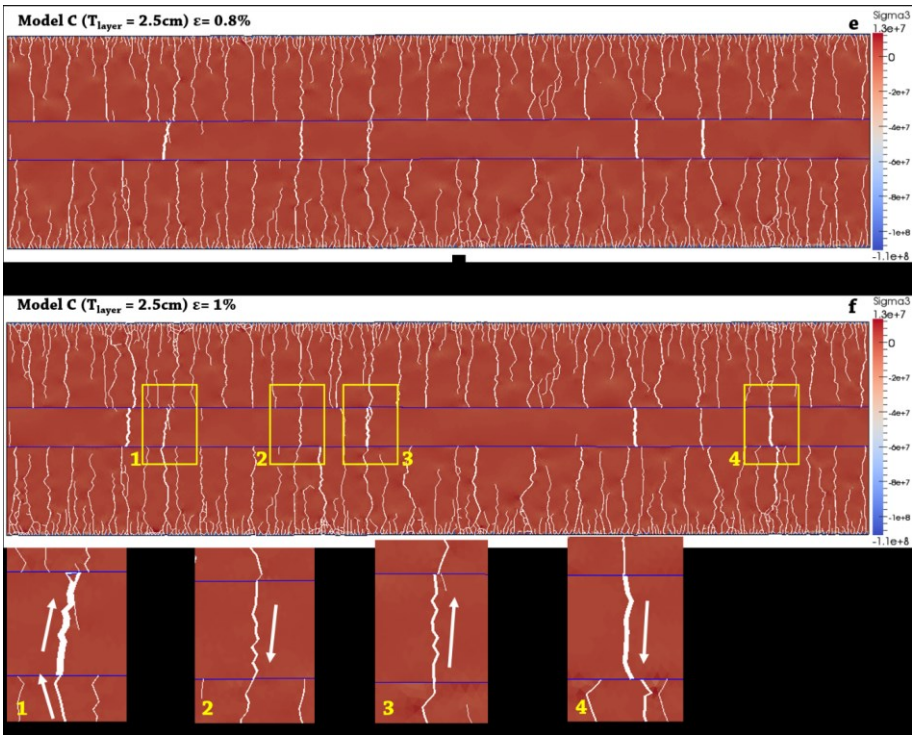


Figure 5. 832 (continued): six stages in the layer-parallel deformation of a multilayer model containing a thin weak layer (2.5cm thick) sandwiched between two strong layers showing the evolution of stress and fracturing. See text for discussion.

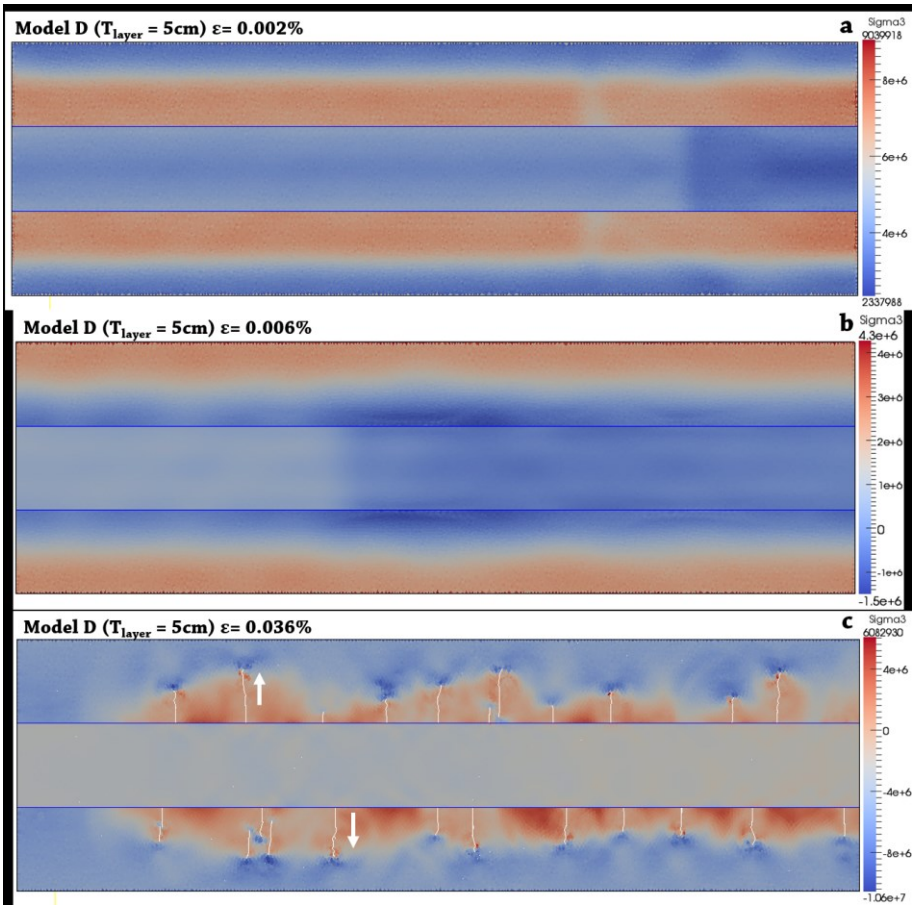


Figure 5.83: six stages in the layer-parallel deformation of a multilayer model containing a thin weak layer (5 cm thick) sandwiched between two strong layers showing the evolution of stress and fracturing. See text for discussion.

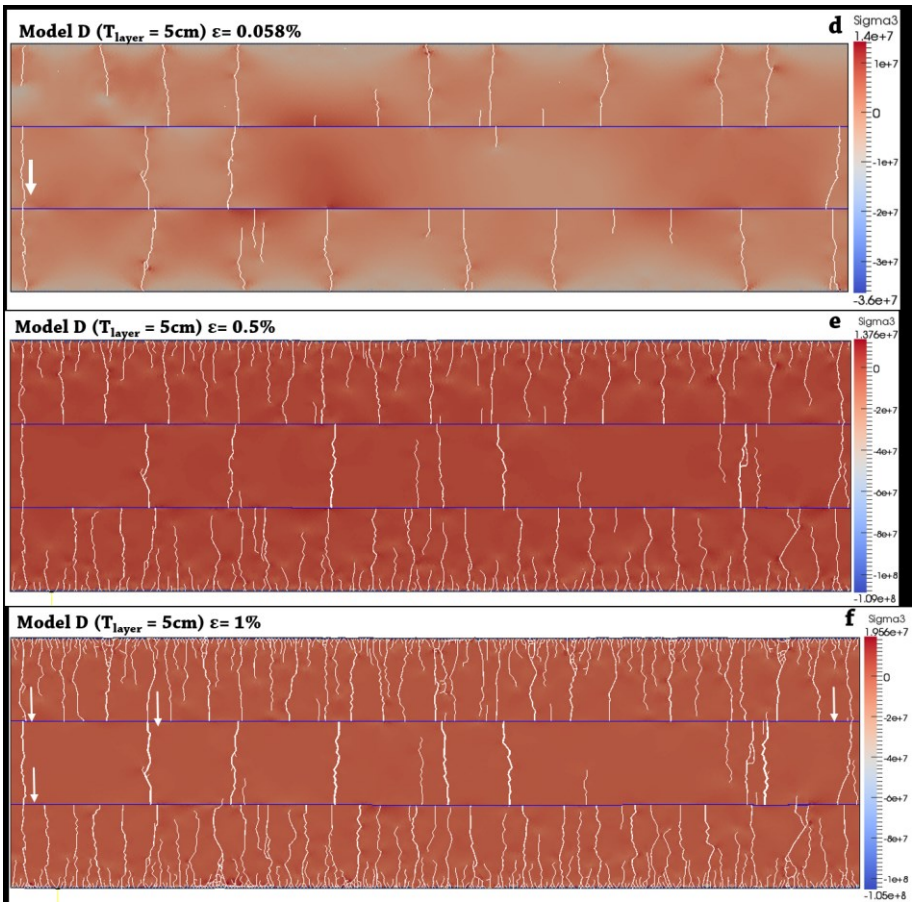


Figure 5. 83 (continued): six stages in the layer-parallel deformation of a multilayer model containing a thin weak layer (5 cm thick) sandwiched between two strong layers showing the evolution of stress and fracturing. See text for discussion.

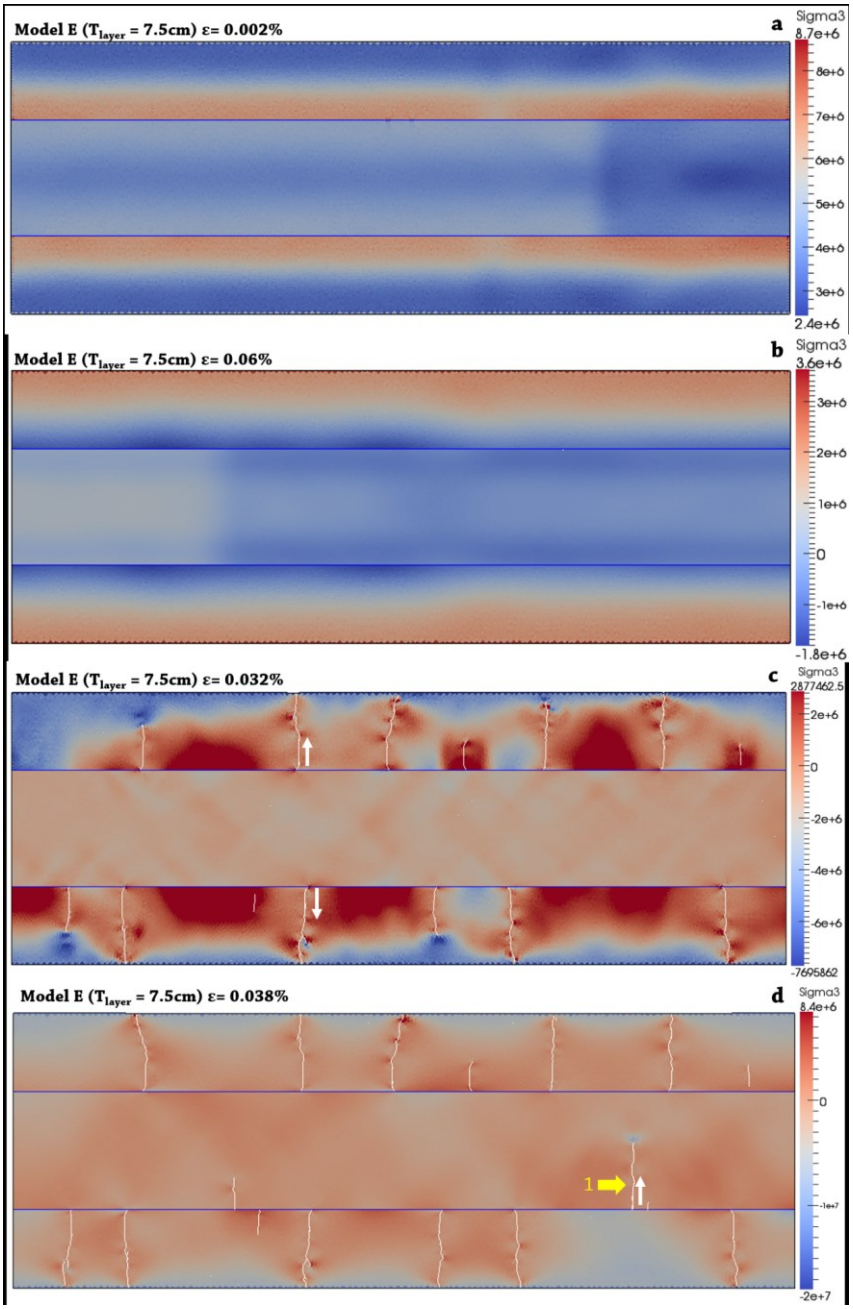


Figure 5.84: eight stages in the layer-parallel deformation of a multilayer model containing a thin weak layer (7.5 cm thick) sandwiched between two strong layers showing the evolution of stress and fracturing. See text for discussion.

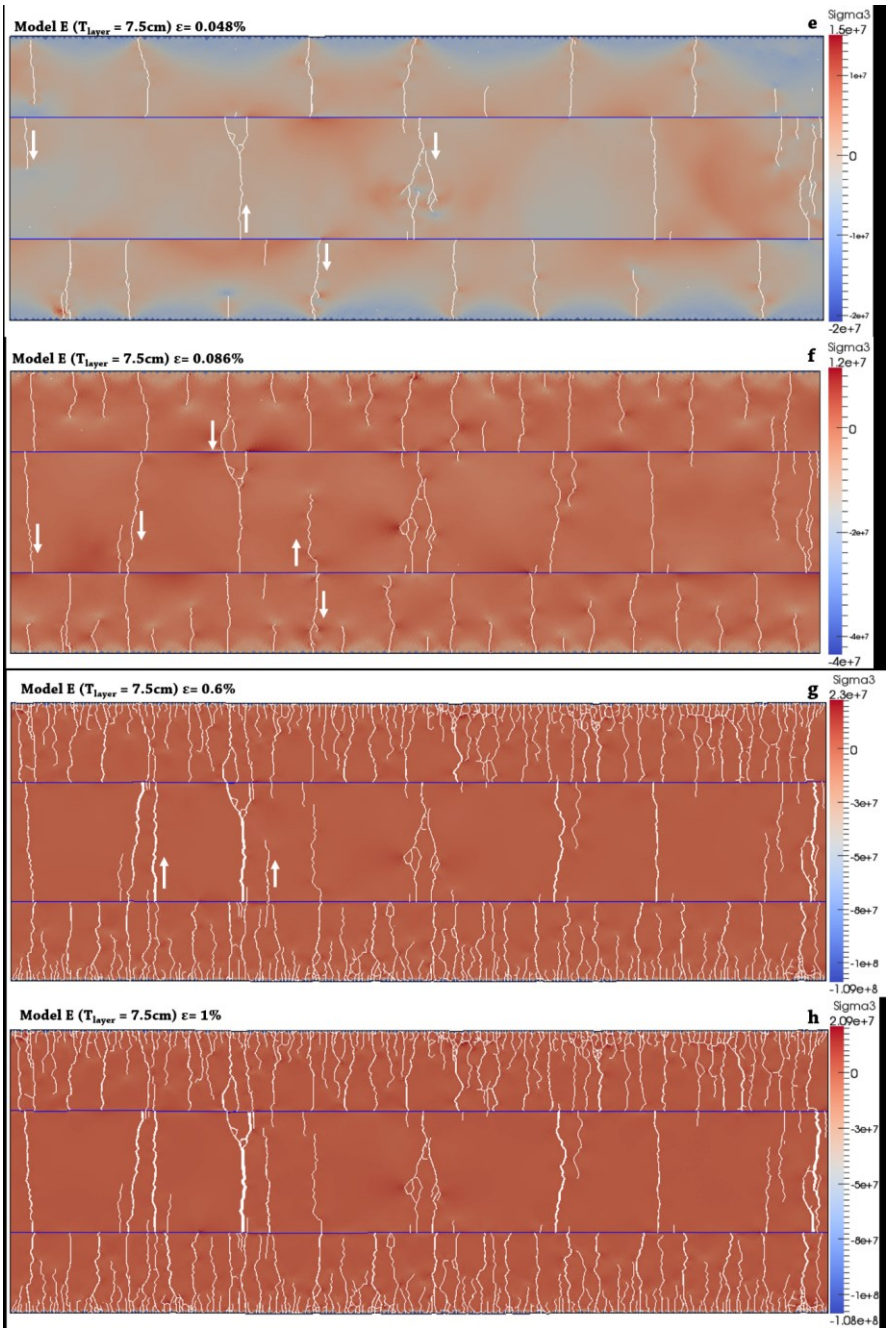


Figure 5. 84(continued): eight stages in the layer-parallel deformation of a multilayer model containing a thin weak layer (7.5 cm thick) sandwiched between two strong layers showing the evolution of stress and fracturing. See text for discussion.

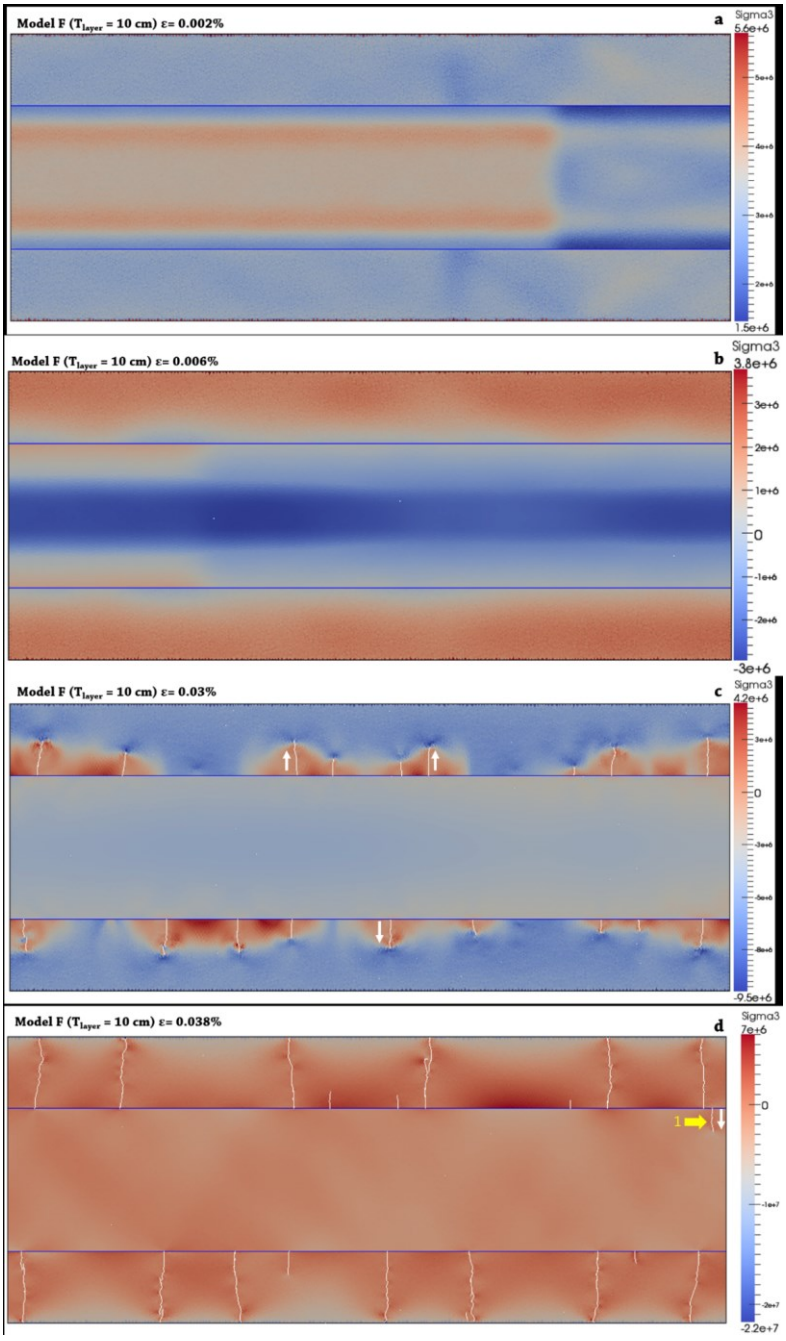


Figure 5. 85: six stages in the layer-parallel deformation of a multilayer model containing a thin weak layer (10 cm thick) sandwiched between two strong layers showing the evolution of stress and fracturing. See text for discussion.

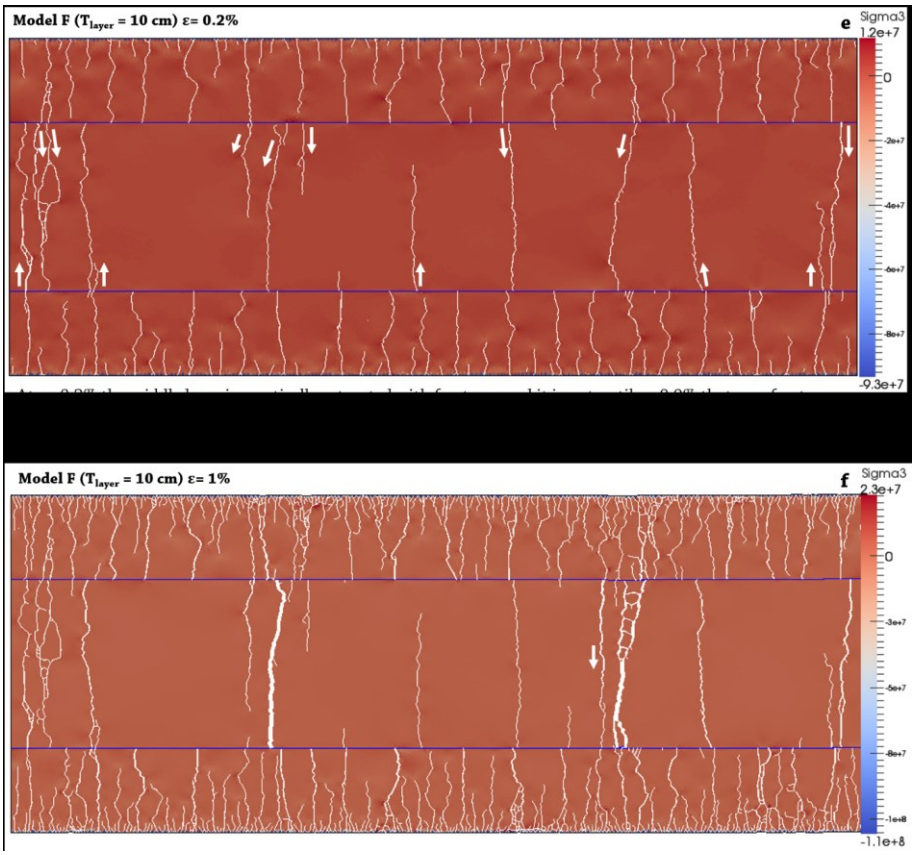


Figure 5. 85(continued): six stages in the layer-parallel deformation of a multilayer model containing a thin weak layer (10 cm thick) sandwiched between two strong layers showing the evolution of stress and fracturing. See text for discussion.

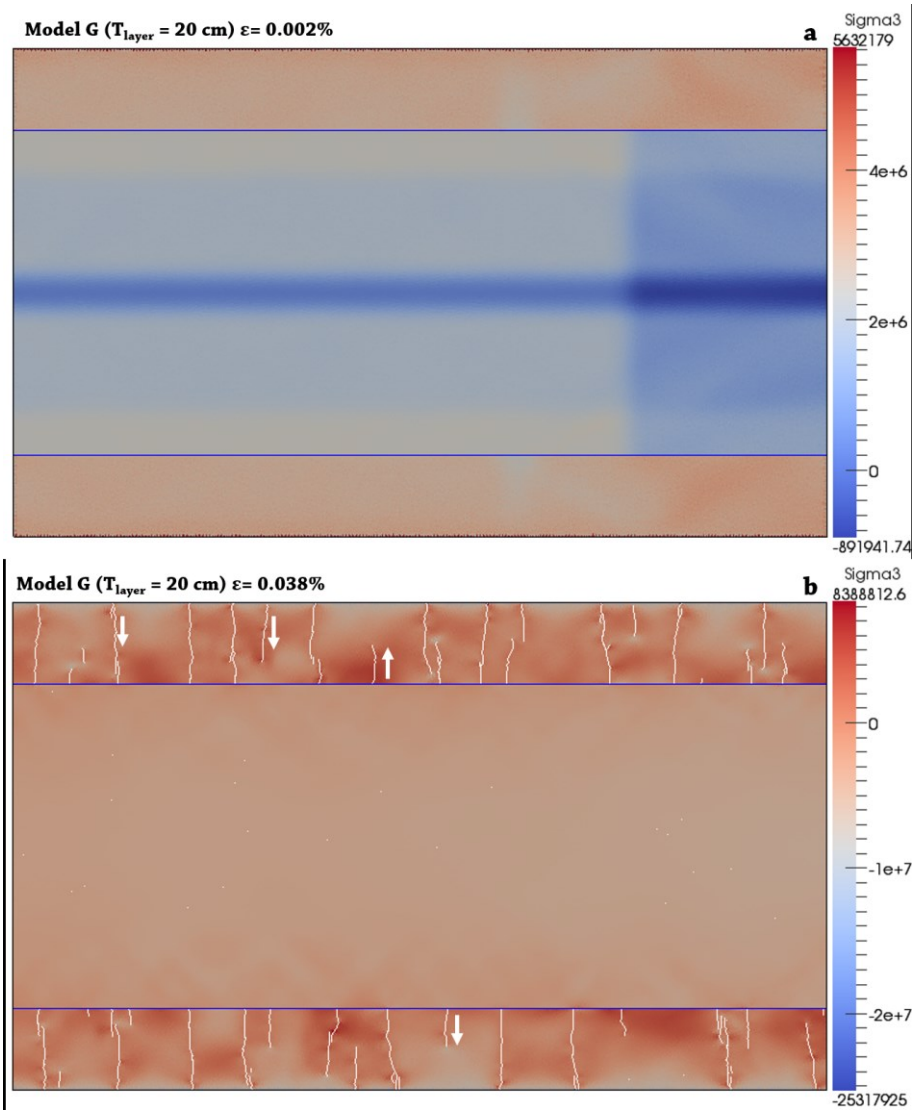


Figure 5. 86: eight stages in the layer-parallel deformation of a multilayer model containing a thin weak layer (10 cm thick) sandwiched between two strong layers showing the evolution of stress and fracturing. See text for discussion.

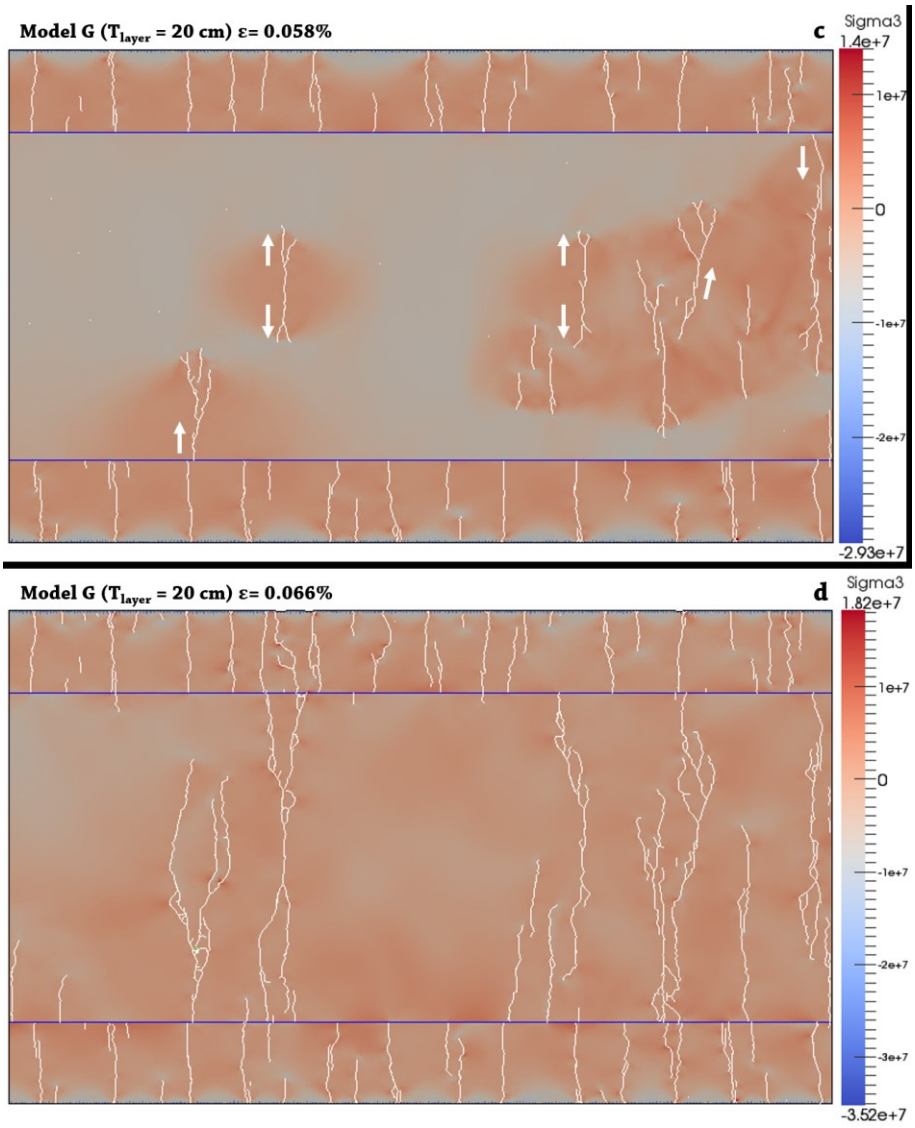
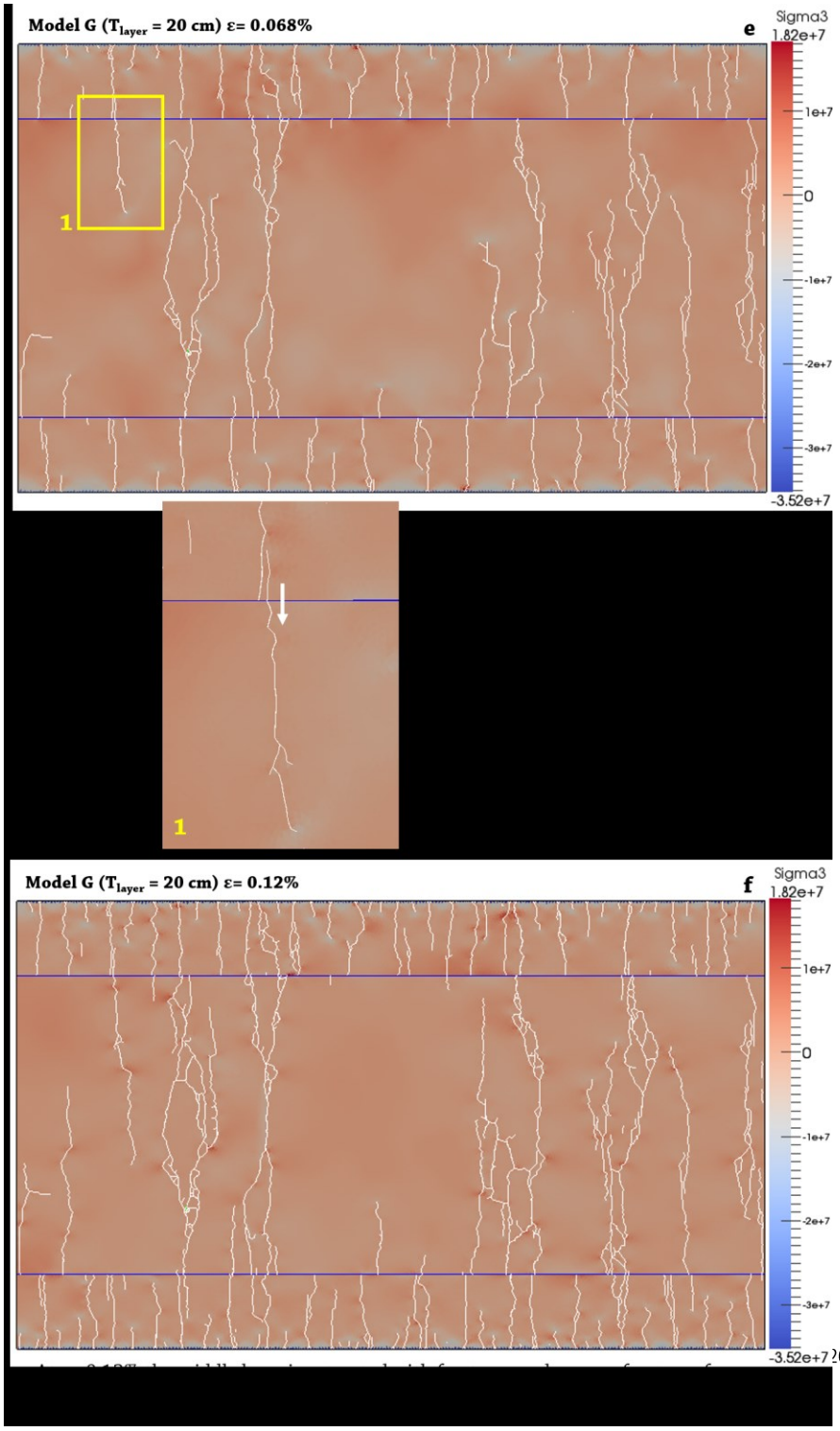


Figure 5. 86 (continued): eight stages in the layer-parallel deformation of a multilayer model containing a thin weak layer (10 cm thick) sandwiched between two strong layers showing the evolution of stress and fracturing. See text for discussion.


Model G (T_{layer} = 20 cm) ε= 0.068%
e
Sigma3
1.82e+7
1e+7
0
-1e+7
-2e+7
-3e+7
-3.52e+7
1
1
Model G (T_{layer} = 20 cm) ε= 0.12%
f
Sigma3
1.82e+7
1e+7
0
-1e+7
-2e+7
-3e+7
-3.52e+7

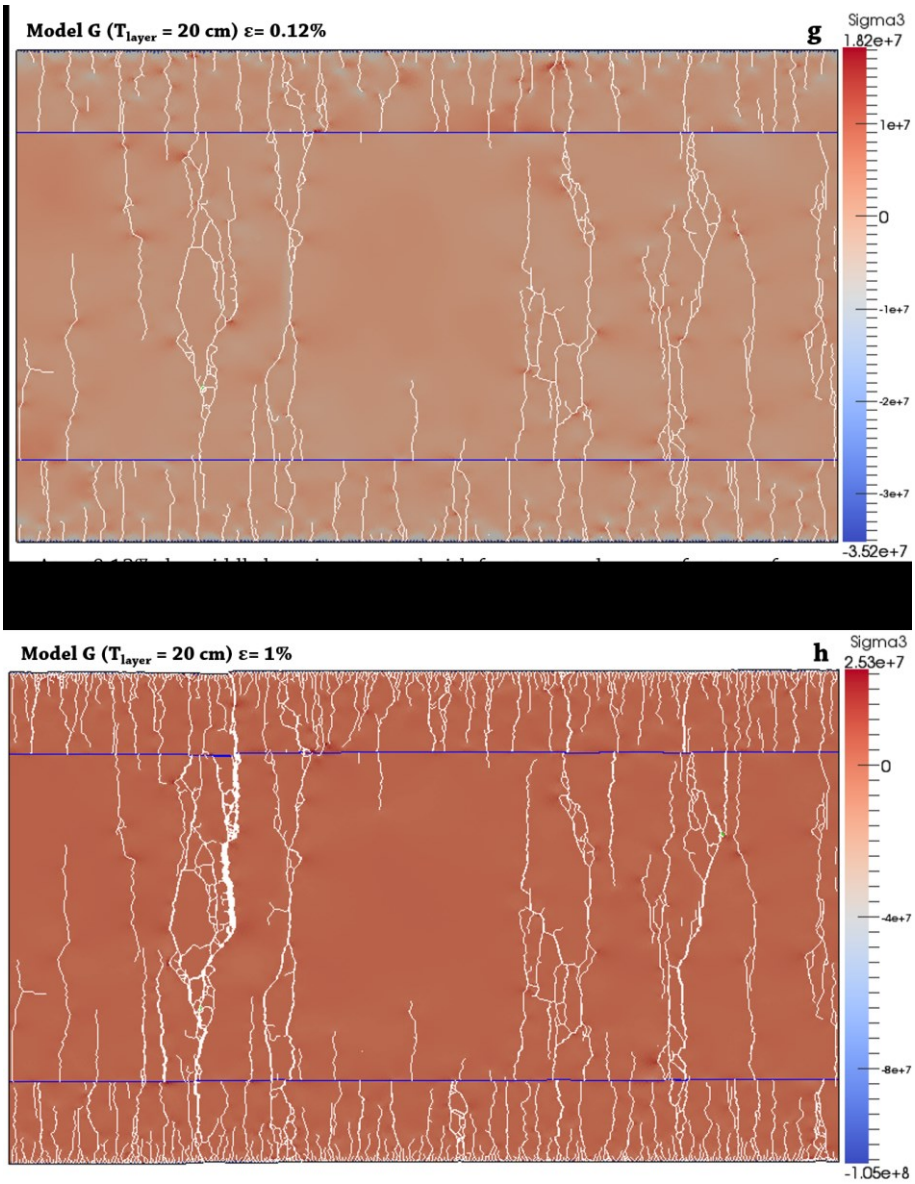


Figure 5.86: eight stages in the layer-parallel deformation of a multilayer model containing a thin weak layer (10 cm thick) sandwiched between two strong layers showing the evolution of stress and fracturing. See text for discussion.

Summary and learnings obtained from the numerical modelling on the effect of the thickness of an incompetent layer on fracture propagation into it.

- As expected fractures form first in the top and bottom competent layers. These fractures propagate towards the outside of the model.
- Through-going fractures can form with different "architectures":
  a) A tensile fracture that forms in the top or bottom competent layer and is able to propagate straight across the interface into the middle layer but that does not extend to the adjacent competent layer (Figure 5.80d).
  b) A tensile fracture that forms in the top or bottom competent layers and propagates straight across the interface into the middle layer linking with another tensile fracture that had formed in the adjacent competent layer (Figure 5.81-d and 5.81-h4).
  c) A tensile fracture that forms in the top or bottom competent layers and propagates across the interface into the middle layer – where it propagates obliquely - linking with another tensile fracture that had formed in the top or bottom layer (Figure 5.80f).
  d) Linking of tensile fractures that forms independently on the three layers (Figure 5.80g and 5.82f)
- Trough-going fractures formed by a fracture that is able to propagate across the interface into another layer occur only in models with very thin incompetent layers, e.g. models A, B and in model G which has the thickest middle incompetent layer of all the seven models. All other models show through-going fractures formed by the linking of individual tensile fractures.
- Thicker middle layers promote the formation of longer, wider and more complex fracture patterns.

5.4 Summary of Numerical Modelling Observations

When analysing the influence of the coefficient of sliding friction of the layer boundaries on the propagation of fractures across an interface it was observed that:

- Low values of the coefficient of sliding friction at the layer boundaries promote the arrest of fractures at these boundaries. However this is only valid for very low values of layer-normal load i.e. shallow depths. The inverse is also true, i.e. higher values of μ promote the formation of through going fractures.
- Another observation that arises from these experiments is that higher vertical stress promotes the formation of through-going fractures as demonstrated by the increasing number of through going fractures in models with higher layer-normal load and creates higher differential stresses promoting the formation of shear fractures.

Regarding the numerical modelling experiments that analysed the influence of the Young's Modulus on fracture propagation across an interface between two layers of different modulus the following was observed:

- As expected fractures form first - at lower accumulated strain, i.e. earlier in the deformation - in "stiffer" layers.
- Although fractures form in the stiffer outer layers and propagate towards the softer middle layers, they do not propagate into this layer in most models. This observation is in clear disagreement with what has been postulated by authors such as Simonson et al., 1978; Hegelson & Aydin, 1991 and Cooke & Underwood, 2001.

Numerical modelling analysing the effect of the thickness of an incompetent layer on fracture propagation into it allowed the following observation to be made:

- Trough-going fractures formed by a fracture that is able to propagate across the interface into another layer occur only in models with very thin incompetent layers, and in a model which has the thickest middle incompetent layer of all the seven models. This suggests that the thickness of the incompetent layer might not be a first order parameter when considering factors that control fracture propagation/arrest through a layer/interface.

Chapter 6
Results Discussion and Conclusions

6.1 Introduction

As demonstrated in Section 1, the sequestration of CO_2 (CCS) and Enahanced Oil Recovery (EOR) using CO_2 are closely related technologies that can contribute to solve two seemingly conflicting problems: lowering CO_2 emissions and provide energy to an increasingly populated world.

Hydrocarbon reservoirs have been considered the best geological formations for storing CO_2 and storage is likely to occur at depths, pressures and temperatures at which carbon dioxide is in its supercritical fluid state. Primary retention of the CO_2 is dependent on the existence of a cap-rock with good sealing properties to ensure this gas remains underground. Therefore, to ensure that CO_2 does not leak, reservoir formations should be overlain by formations that due to their low permeability, thickness and extension, are able to retain the fluids in the reservoir. However potential risks for the integrity of the cap rock when injecting carbon dioxide into reservoir rocks have been previously identified. These include seal breaching through mechanical failure as a consequence of excess pressure resulting from buoyancy forces and injection related overpressure or seepage along existing fault systems and fracture networks.

This project, part of a larger multidisciplinary project with the overall objective of improving the knowledge of carbonate reservoirs in order to increase the recovery rates of Qatar's oil reservoirs using carbon dioxide injection (CO_2EOR) while developing the technology for storing this gas in such reservoirs (CCS), focuses specifically on the potential for evaporite cap-rock (the lithology that seals the carbonate reservoirs of Qatar) integrity loss through fluid induced failure (hydraulic-fracturing). Assuming a worst-case scenario i.e., one where failure occurs and fractures are created, the specific rock properties that control fracture propagation through a layered evaporite and the features that might influence fluid flow in these low permeability units was studied. In other words, this project aims to determine the mechanical properties of evaporite rich seals, the mechanisms by which they might fail when subjected to high fluid pressures linked to the injection of CO_2, and what features may promote/hinder the propagation of fractures through the evaporitic sequence.

In order to achieve this a multidisciplinary approach was used. Field work on various scales was carried out. On a local scale evaporites were studied in a gypsum mine and, drill cores in order to determine the internal structures within seals that might influence fracture formation. On regional scale (i.e the geological setting of Qatar), studies were carried out to determine the stress history of the seal and the likely fractures it could contain as a result of burial, diagenesis and tectonism. A detailed study of the theory of brittle failure (in particular of fluid induced failure) was also conducted in order to lay

down the principles that control stress distribution in the crust. The information obtained from the field work and the theoretical analysis of brittle failure was used to determine the boundary conditions of the numerical models used to look at fracture propagation in layered materials. The FEMDEM (Finite Discrete Element Method) methodology was used. Models were carried out in order to determine the influence on fracture propagation of specific properties and features common in layered evaporite sequences. The flowchart of Figure 6.1 summarizes the flow of information used in this project.

This chapter is divided in three subsections. The first aims to summarize the findings obtained from the field work and the numerical analyses and discusses their validity in the light of the theoretical principles outlined in Section 4. The second part discusses the significance of these results to the problems of injecting carbon dioxide into the carbonate reservoirs of Qatar. Finally the conclusions of the work are summarised and recommendations for future work are presented.

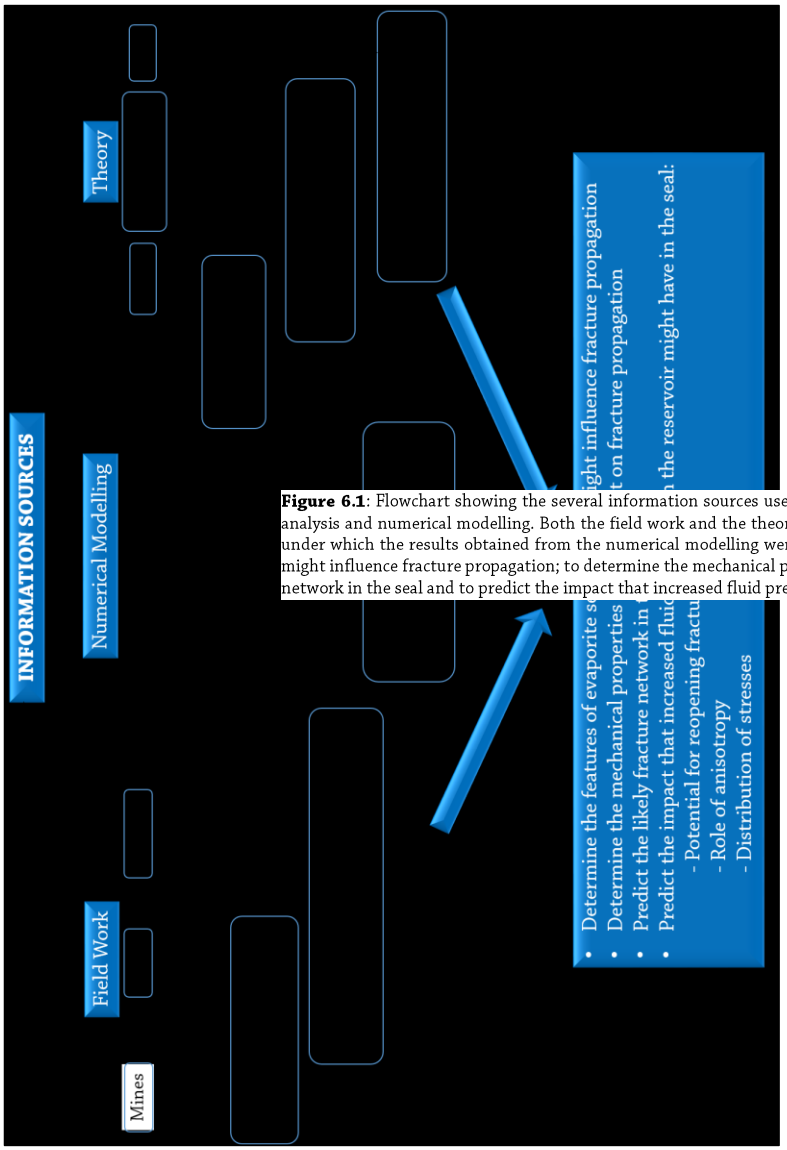


Figure 6.1: Flowchart showing the several information sources used in this project and how they relate to each other. The initial sources were field work, t analysis and numerical modelling. Both the field work and the theoretical analysis have provided information to define the boundary conditions and set the under which the results obtained from the numerical modelling were analysed. This approach allowed conclusions to to determine the features of evaporite might influence fracture propagation; to determine the mechanical properties which impact on fracture propagation through a layered rock; to predict the like network in the seal and to predict the impact that increased fluid pressures in the reservoir might have in the seal.

6.2 Field Work

In this section the results obtained from the field work are summarized and discussed in the context of the theoretical principles outlined in Section 4.

6.2.1 Brightling Mine and Drill Cores

From the field work at Brightling Mine and the analysis of the several drill cores from the Weald Basin (See Section 3.3 and 3.4), two major observations can be summarized:

- Evaporite sequences are not homogenous in terms of their lithological and textural properties. A high lithological heterogeneity both vertically and horizontally exists in these successions and a multitude of textures is found within sabkha evaporite successions, ranging from massive to nodular anhydrite (which in its turn has different textures such as chicken-wire, palisade or aggregate), intercalated with massive to laminated mudstones, microbial laminated mudstones or shales.
- There are both primary (related to the depositional environment and diagenesis) and secondary layers (linked to natural hydraulic fracturing such as the bedding parallel fractures infilled with satin-spar) and interfaces

These layered features and interfaces typical of anhydrite sequences have a major impact on the mechanical properties of the succession and on fracture propagation through them. Observations show that the different lithological units and interfaces can impede fracture propagation.

The effects of both the primary features, which include the gypsum horizons and nodules, anhydrite nodules and the interfaces between the different lithologies (see Section 3.3.4.1), and the secondary features were studied using FEMDEM numerical models in an attempt to understand the factors involved in inhibiting fracture propagation and to quantify these effects. The discussion of the results of these models is presented in Section 6.3.

Although the focus of the research was on the propagation of fluid induced failure planes caused by an increase in fluid pressure in the underlying reservoir i.e. external to the seal, through an evaporite seal, field observations clearly show that fluid induced failure can also occur *inside* the seal i.e. by a build-up of fluid pressure within the seal. There is evidence (for example horizontal and vertical satin-spar veins) that two stages of internal hydraulic fracturing occurred in the evaporite sequence studied at the Brightling, see Chapter 3. In a homogeneous, isotropic system, this would indicate two separate stress regimes: one in which σ_3 was horizontal and in which the vertical veins were generated, and another in which σ_3 was vertical and in which he horizontal veins were formed. However as noted in Section 4.4.1 in anisotropic e.g. layered sedimentary rocks such as evaporite successions studied, this situation is more complex. It was pointed out that both families of veins could have been generated by the same stress regime i.e. that associated with basin opening (when σ_1 was vertical). This stress

regime is clearly appropriate for the formation of the vertical veins but as shown (see equation 4.35, Section 4.4.1) depending on the relative magnitudes of the layer normal and layer parallel tensile strength of a layer it is also possible to generate bedding-parallel, i.e. horizontal veins in this stress field. However, this hypothesis was discarded for Brighling mine because of the cross-cuting relationship between the two sets of veins in the various pillars of the mine. The horizontal satin-spar veins always post-date (i.e. cross cut) the vertical ones. Despite this, it is important to note that the occurrence of these features in non-inverted basins is clearly a possibility and this will be further explored in Section 6.4 (Regional Considerations).

It is also noted in the Brightling Mine that the horizontal veins formed preferentially in shale layers (See Figure 3.19), which were clearly weak intervals prone to opening during the inversion of the basin (i.e when σ_1 was horizontal and σ_3 was vertical). We consider that these horizontal veins have a much more important role (compared to the vertical veins) in controlling the propagation of vertical fractures through a sedimentary sequence. The main focus of this research is to obtain an understanding of the ability of an evaporite seal to prevent the propagation of vertical fractures, induced in an underlying reservoir by an increase in the CO_2 pressure. As indicated by observation in the mine and in the field, these weak bedding parallel fractures act as effective barriers to the propagation of fractures from below.

Another important observation made possible by the remarkable continuity of exposures in the mines, is that there are important lateral variations in the fabric of the anhydrite rich successions. The bedding planes and the secondary satin spar veins die out laterally. Thus in any analysis of the ability of such successions to inhibit the vertical propagation of fluid induced fractures initiated by an increase in pressure in the underlying reservoir, it is important to take these variation into account. It might be argued that because of their tendency to be laterally discontinuous, bedding planes and satin spar veins might be considered analogous to 'Baffles' (rather than Barriers) to fluid flow, i.e. they inhibit the propagation of fractures where they exist but fractures can continue to propagate where they die out.

6.2.2 Tytherington

The observation of the outcrops in the quarry at Tytherington (See Section 3.5.3) provide an excellent insight into the importance of the shape of the interface between two layers on fracture propagation across it. It was found that the contacts between layers – between the same or between different lithologies – play a very important role on fracture propagation from one layer to another. Two situations were noted:

i) Two limestone layers in direct contact with each other (Figure 3.38 and 3.42). In situations such as these, the contacts between the layers are irregular or serrated, showing evidence of pressure solution (stylolites). The vertical (bed-normal) fractures are observed to cut more than one layer, i.e. they are able to cut through the interfaces between layers, to form through-going fractures. This observation is interpreted as being the result of the shape of the interface: serrated interfaces hinder interfacial sliding between layers and therefore allow fractures to propagate across several layers.

ii) Two limestone layers separated by a thin layer of clay/mudstone (Figure 3.47). When there is a thin clay layer between two adjacent limestone layers, the interfaces between the layers remain flat (i.e. no pressure solution occurs) and fractures formed in the limestone are observed to stop when they reach the interface with the clay. This is thought to occur because the flat interface allows interfacial sliding to occur, dissipating the tensile stress of the fracture tip and thus arresting the fracture at the interface, i.e. the fractures become strata-bound.

It is argued that a stylolitised/serrated surface is the equivalent of a very high coefficient of sliding friction between layers and a flat surface of a situation where this parameter is low. These observations prompted the numerical simulations presented in Section 5.3.1 and discussed in Section 6.3. These experiments were carried out to explore the impact of a varying the coefficient of sliding friction along the layer interfaces on fracture propagation. In these simulations a low coefficient of sliding friction (μ=0) represents the flat surfaces along which there is no cohesion whereas a high value (μ=1 or μ=2.5) represents the serrated sytlolitized surfaces along which the two contiguous beds are inter-locked. It is demonstrated that the numerical models confirm the deductions based on observations made at Tytherington.

It is also noted that the observation of a very thin clay layer (which can be considered to be mechanically *weak* layer) arresting a vertical tensile fracture formed in an adjacent thick limestone layer is in contradiction with the findings of Friedman & French (1994) and Rijken & Cooke (2001). These authors conclude that the thickness ratio between the strong and the weak layer plays a key role in determining whether or not a crack propagates through a weak layer, i.e. the larger this ratio (the greater the thickness of the strong layer with respect to the weak layer) the greater the tendency for

the propagation of fractures across the weak layer from one strong layer to another. However, our observations in Tytherington show that very thin incompetent layers are able to prevent fractures propagating from one thick competent limestone layer to another. This indicates that the relative thickness between *stiff* (high elastic modulus - limestones) and *soft* (low elastic modulus – clay) layers might not be a decisive factor in determining whether or not a fracture propagates through the intervening soft layer.

6.2.3 Somerset - Lilstock

Field work at Lilstock was conducted with the objective of understanding how fractures behave when meeting an interface between two layers of different lithology - particularly an interface between a more competent limestone and a less competent shale. We conclude that vertical tensile fractures in a limestone tend to be arrested at the interface between the limestone and the adjacent shale. However, several exceptions to this rule were observed:

- Some *trough-going* oblique fractures were observed extending from the limestone into the shale layer and terminating in this layer.
- Offset extensional fractures in adjacent limestone beds were sometimes linked by oblique fractures in the shale.

Another interesting observation made is that there is sometimes a strong fracture mismatch (in the strike orientation of some of the fracture sets) between limestone layers which are separated by a shale layer, i.e. fracture families that are present in one limestone layer are not present in the adjacent layer.

These observations are discussed individually:

a) Vertical tensile fractures affecting a competent limestone layer being arrested at the interface with an incompetent shale layer (See Figure 3.51):
   We observe in the field work that a weak shale layer often inhibits the propagation of a fracture formed in the adjacent strong layer. This observation is in direct contradiction to most of the theoretical predictions on fracture propagation (Simonson et al., 1978; Hegelson & Aydin, 1991; Larsen et al., 2010). However Van Eeleken (1982) considers that a stiffness contrast, by itself, does not constitute a barrier to propagation of fractures that are driven by viscous fluids at high pressure rates. We offer various possible explanations for this contradictions:
   i) The materials are not behaving elastically and the fracture tip stresses are dissipated on entering the weak layer by the generation of ductile deformation.

ii) Alternatively it could be argued that the strong/weak rock interface is not bonded. In which case the propagation of any fracture will not be controlled by the contrast in material (elastic) properties between the adjacent layer but by the frictional resistance to slip (τ_s)on the interface which is controlled by the product of the layer-normal stress (σ_n) and the coefficient of sliding friction of the layer interface (μ): $\tau_s = \mu\sigma_n$.

iii) Even if the interface is *bonded* the intrinsic mechanical anisotropy of the shale could provide a mechanical equivalent to a frictional boundary.

With the regards to suggestion i), that the incompetent layer is behaving ineleastically, it is interesting to note that one of the theories of tensile failure in a competent layer relies on the occurrence of inelastic incompetent layers on either side (Price, 1966). This has been discussed in Section 4.5 and it is represented in Figure 6.2. The analysis resulting from this work predicts a linear relationship between layer thickness (z) and fracture spacing (L).

$$L=Z\sigma_t/2\tau_{av}$$

Where σ_t is the tensile strength and τ_{av} the mean shear stress acting along the top and bottom of the bed along the distance L.

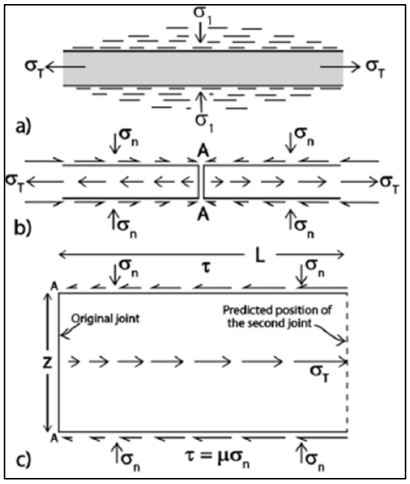
b) Some vertical fractures within the limestone can be traced into the shale layer but show a marked change in dip (Figure 3.52 and 3.54) before stopping within the shale. This observation relates directly to the following observation in which:

c) Offset tensile fractures in two adjacent limestone layers are linked through the shale by an inclined fracture (Figure 3.53). A further observation is that:

d) A marked mismatch in the position of the vertical tensile fractures in two adjacent limestone beds separated by a thin shale layer, i.e. fractures do not form above each other, and the sets which are present in one layer, are not present in the adjacent layer (Figure 3.56 and 3.57).

In regards to observation c), it was noted in Section 4.3.2 that despite the differences between extensional and shear failure, they are fundamentally connected. It was argued that macroscopic shear fractures are generated by the linkage of offset extensional fractures (Figure 4.22 and 4.24). This phenomena can be observed in Liasic sediments of Lilstock where offset extensional fractures within adjacent limestone beds are linked by oblique fractures in the shale as described above. Cosgrove & Hudson (2016) studying the sediments of Somerset, noted that the oblique linkage of offset extensional fractures in a succession of adjacent limestone beds in this way, leads to an embryonic

shear fracture (Figure 6.3). This phenomena, when occurring at a larger scale causes the extensional fractures to open forming rhomb-shaped gaps known as pull-aparts or dilational jogs. The relationship between the extensional and shear failure is also examined numerically in Section 5.3.3 and discussed further in section 6.3.3.



$$\sigma_T Z = 2L\tau_{AV} \leftrightarrow L = \sigma_T Z / 2\tau_{AV} \qquad (4.36)$$

Where,
σ_T :Tensile stress
z: layer thickness
L: distance between contiguous fractures
τ_{AV}: mean shear stress acting along the top and bottom of the bed along the distance L

Figure 6.2: Uniform tensile stress acting in a single, competent unit caused by the lateral flow of the adjacent, less competent beds in response to a layer-normal load caused by the overburden. b) Indicates the reduction in tensile stress due to the formation of a single joint, coupled with the development of a shear stress along the bedding planes which prevent excessive opening of the joint. c) Details of stress intensity in a section of competent bed length, L, and thickness, z, adjacent to the initial joint. A second fracture forms at a distance L from the first when the tensile stress reaches the tensile strength of the layer (after Price, (1966)).

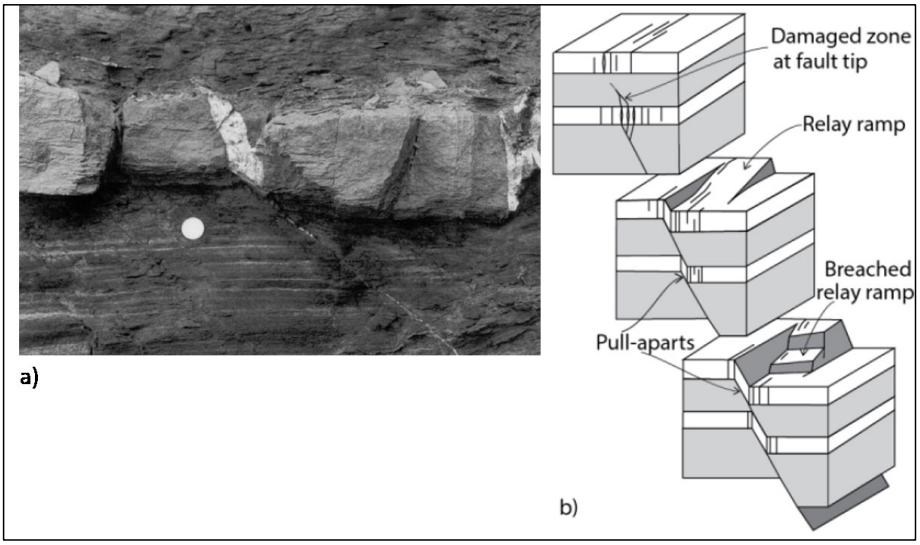


Figure 6. 3: a) Calcite deposited within a dilated extensional fracture in a limestone bed. Note the cross-fractures in the shale. Lilstock, North Somerset, U.K; b) The role of extensional fractures in the formation of a macroscopic shear fracture. The extensional fractures in the limestones link along the dip direction by the formation of cross-fractures in the shales. Movement on the relatively low angle cross-fractures results in a dilation of the extensional fracture (after Cosgrove & Hudson, 2016).

6.2.4 Somerset – Watchet

Observations at Watchet in the Triasic Mercia Mudstones showed the occurrence of bedding parallel hydraulic fracturing (exposed as satin spar veins) both within and outside the evaporite rich successions. In the context of evaporite rich seals these observations indicated the possibility of hydraulic fracture both internal and external to the seal. The theory related to this is discussed in Section 4.4.1.

Spectacular examples of internal hydraulic fractures inflilled with satin spar within evaporite rich horizons have been observed at Brightling Mine and within the cores of the Weald Basin (see Figures 3.19, 3.26 and 3.31). If such fracturing can also occur outside the seal as indicated at Watchet (see Figure 3.62), then such fractures can enhance the ability of the evaporite succession to act as an effective inhibitor to the propagation of vertical fractures.

Note: This may not represent internal and external hydraulic fracturing *sensu stricto* and it maybe that the hydraulic fracturing both within and outside the seal is strictly internal hydraulic fracturing. Nevertheless the suggestion of an extended thickness of succession beyond that of the seal that contain satin-spar veins that could contribute for fracture arrest is of first order importance to the research at hand.

In summary, the bedding-parallel veins at Watchet are related to the response of low permeability units to high fluid pressures. It is argued that the process observed here is very similar to that which occurs in sabkha evaporite successions such as those observed in Brightling Mine and which potentially might exist in the evaporite sediments of Qatar. It is suggested that such fluid induced fractures could be initiated when the fluid pressure is raised during CO_2 injection operations. Interestingly, such fractures whether barren and representing a bedding-parallel non-cohesive interface or infilled with satin spar will act as fracture propagation inhibitors, and therefore will be an advantage when considering the problem of seal failure during CO_2 injection.

6.3 Numerical Modelling

In this section the results of the numerical modelling program are summarized and discussed in terms of the theoretical principles outlined in Section 4.

6.3.1 The effect of interfacial friction along an interface and of an overburden stress

Numerical models have been run to determine the roles of layer-normal loads and the coefficient of sliding friction along the interfaces between adjacent layers on fracture propagation across an interface. The fracture distribution that developed in the experiments and the associated changes of stress within the layers as the fractures formed and grew were described in detail in Chapter 5. The data suggest that:

i) Low values of the coefficient of sliding friction (μ) along the layer boundaries promote the arrest of fractures at these boundaries whereas higher values of μ promote the formation of through going fractures.
   - Regarding the ability of low values of the coefficient of sliding friction to impede fracture propagation across a layer boundary, this observation is only valid for low values of layer-normal load which are conditions equivalent to shallow depths in the crust. It can be seen in Figure 5.34 i), where the layer normal load is 25 MPa (approximately 1000m depth), that through-going fractures formed even when μ=0. This means that the effect of the layer-normal load (or overburden in geological conditions) is able to overcome the effect of a low coefficient of sliding friction and lead to the formation of through going fractures. This has been pointed out by Van Eekelen, 1982 and Warpinsky & Teufel, 1987 who argued that low friction values are only important in preventing fracture propagation across an interface at shallow depths.

   - However, the current author argues that this neglects to take into account the effects of fluid pressure and the associated phenomenon of effective stress (see Section 4.4). This effect reduces the normal stress in all directions, including across the interface, by the magnitude of the fluid pressure. Thus as the fluid pressure increases the ability of any frictional interface to inhibit fracture propagation also increases and it is argued that such interfaces can inhibit fracture propagation at any depths if a fluid pressure of sufficient magnitude exists.

- It can be seen in Figure 5.32 d) and Figure 5.33 f) that when higher values of μ exist along the interface through going fractures formed even when the applied layer-normal load is low (1 and 10 MPa respectively).

- This observation confirms what was postulated during the field work conducted at Tytherington (see Section 6.22). At this field location it was observed that when serrated stylolitsed interfaces developed between two contiguous limestone layers, vertical tensile fractures had no difficulty crossing the interface, affecting several layers. It was argued that serrated interfaces are mechanically the equivalent of a very high coefficient of sliding friction between layers and that this high value would hinder interfacial sliding therby allowing fractures to propagate across several layers. The numerical models clearly confirm this hypothesis.

iii) An increase in layer-normal load also encourages the formation of through-going fractures. This observation is linked to observation i). It will be recalled that the interfaces between layers in the numerical models are non-choesive and that sliding at the interface between layers (which behave like a pre-existing closed crack with no cohesion) occurs when the shear stress (τ) exceeds the product of the normal stress (σ_n)and the coefficient of sliding friction (μ):

$$\tau \geq \mu\sigma_n \quad \text{(Eq. 5.4)}$$

Thus, an increase in the applied normal stress (layer-normal load) will reduce the ability of the interface between layers to slip when a fracture tip reaches the interface. The high tensile tip stress is therefore maintained promoting the propagation of fractures across the interface.

ii) The experiments show that when the layer-normal load is low, fractures form within the layer at a lower strain compared to experiments where the layer-normal load is greater, i.e. the higher the applied vertical stress the greater the accumulated strain required to form tensile fractures (see Figure 5.39). It is considered that the explanation for this is related to the boundary conditions chosen for these experiments (See Figure 5.17). It will be recalled that in this series of experiments the model is placed under a layer-normal compression and then subjected to a horizontal extension, the latter being constant for each model. Both these boundary conditions generate a stress in the model. The horizontal extensional which is the same for all models generates an extensional stress, which will be the same for all models. The vertical load imposes a layer-parallel compression (see Section 4.2) which is directly proportional to the applied load. Thus the net layer-parallel stress is the sum of these two. It follows that as the normal load

increases (in consecutive models) the net layer parallel extension decreases and a greater strain is required before the conditions for extensional failure are satisfied

iii) Examination of the models revealed that an increase in the differential stress (achieved by an increase in the applied normal stress) leads to:
   - The formation of straighter extensional fractures (increasing regularity) as it can be seen in Figure 5.37. This observation was explained in Section 5.2.1 and it is illustrated in Figures 5.19 and 5.20.
   - The formation of shear fractures rather than extensional fractures. The higher differential stress clearly leads to a situation where $(\sigma_1-\sigma_3)>4T$ as explained in Section 4.3.1.

iv) Of the three parameters considered in the experiments (see Section 5.3.1.3) – the coefficient of sliding friction along the layer interfaces; the layer normal load; and the fracturing – the latter is the most important factor in determining the stress distribution within the model. The value of the horizontal (layer-parallel) stress within the models was recorded at a variety of different positions (points) within the model. The evolution of stress at any point durint the experiment was strongly influenced by its proximity to any fracture that might form. It is noted that the stress profiles retrived from various points in the model show that whenever a fracture formed or extended to another cell, there is a reduction in the horizontal tensile stress near the sampling point. The closer the sample point to the fracture the more marked this local reduction is.
   In the broader context of the movement of fluids within a stressed seal it can be seen that this transient stress change around a newly formed fracture will have a tendency to drive fluids out of the intrinsic (matrix) porosity of the rock into the fracture network. The interplay between fractures and fluids during deformation i.e. the manner whereby an increase in stress results in an increase in fluid pressure which can eventually lead to hydraulic fracture and subsequently how these fractures can influence the movement of fluids out of the body of the rock, is poorly understood and it is suggested that models of this type can provide important insight into this process.

6.3.2 The effect of the elastic modulus (Young's Modulus – E) of adjacent layers on the propagation of fractures across the interface between them

In Section 5.3.2, numerical models designed to determine the role of the elastic modulus (Young's Modulus –E) between adjacent layers on fracture propagation from one layer to another were described. The investigation involved 3-layered models. The values of the Young's Moduli used were those shown in Table 5.7, the normal loads were 25MPa and the coefficient of sliding friction on the layer interfaces was set at 0.6 (a realistic value in geological conditions). These parameters (high value of layer-normal load and the coefficient of sliding friction) reduce the potential for slippage along the layer interfaces. Results show that:

i) As predicted fractures form first in the stronger bounding layers. If fractures occur in the central weaker layer they do so after a much greater layer-parallel extensional strain.

ii) In models A and B (see Section 5.3.2), although the middle layer is weaker than the top and bottom layers, no fractures were able to propagate across the interfaces from the stronger to the weaker layers. However, through-going fractures are formed by independent fractures that form in top and bottom layers and are subsequently linked by fractures that form in the middle layer (see Section 5.3.2, Figure 5.76)

iii) In model C, where E1=20E2, three fractures where able to propagate into the middle layer across the interface between the top and the middle layer. However, further propagation of two of these fractures ceased almost immediately.

iv) Model D, E1=50E2. In this model no fractures where able to propagate across the interface from the stronger top and bottom layers into the weaker middle layer.

These observations appear to be in stark contrast to the theoretical predictions relating to fracture propagation from stronger into weaker layers (Simoson et al. (1978); Cook & Erdogan (1972); Erdogan & Biricikoglu (1973); Hegelson & Aydin (1991); Larsen et al. (2010)). The theory predicts that propagation will occur from stronger to weaker but not from weaker to stronger layers. This relates to the magnitude of the fracture tip stress as it crosses the interface. Clearly this tensile stress is larger in the strong layer and as a fracture attempts to propagate into a weaker layer it is more than sufficient to cause fracture formation in the weaker layer and to allow propagation. The reverse is clearly not true.

One mechanism that could prevent fracture propagation from strong to weak layers is slip at the interface between them. This would allow the dissipation of the tip stresses, arresting the fracture at

the interface. However, in the experiments the layer-normal stress (σ_n) is large (25MPa) and the coefficient of sliding friction (μ) is high (0.6). Consequently there is a high resistance to slip on the interface ($\tau=\mu\sigma_n$) and it is argued that slip cannot account for the lack of propagation.

In an attempt to explain the observed arrest of fractures in these experiments it is necessary to consider the boundary conditions and the change in properties of the central layer. The boundary conditions are the same for all four experiments and involve a layer-parallel extension under an applied vertical load. The Young's Modulus of the two bounding layers remain the same for all four experiments and the Young's Modulus for the central layer is progressively decreased. At any stage in the experiment all three layers have extended the same amount (ex.: Figure 6.4). It can be seen from the graph in this figure that for any value of extensional strain the extensional stress in the strong layers is considerably greater than in the weak layers and that as the Young's Modulus of the weak layer (E2) is decreased (A to D) the extensional stress also falls.

In addition to the different stresses generated by the layer-parallel extension shown if Figure 6.4, the layer normal load will induce a layer-parallel *compressive* stress in all three layers (see Section 4.2.2, Equation 4.18). This vertical load is the same for all experiments and because the two competent layers have the same properties for all experiments (A to D) the total state of stress in these layers varies in exactly the same way during the evolution of each experiment. It is for this reason that the onset of extensional failure in these layers occurs at approximately the same strain (ε=0.075%) for all experiments.

As noted, because the Young's Modulus of the central layer is progressively reduced from experiment A to D, the induced compressive layer-parallel stress also varies. The total horizontal stress within the central layer for the four experiments is shown in Figure 6.5. The graphs show that as the central layer becomes weaker (lower Young's Modulus) the layer-parallel compressive stress increases (note that compressive stresses are positive). It is clear from these graphs that the layer-parallel stresses resulting from the layer-parallel extension and layer-normal compression oppose each other. As the strength of the weak layer decreases the impact of the layer-normal compression increases and the resulting layer-parallel compression increases. We argue that the effect of this compression will be to inhibit fracture propagation (Figure 6.6).

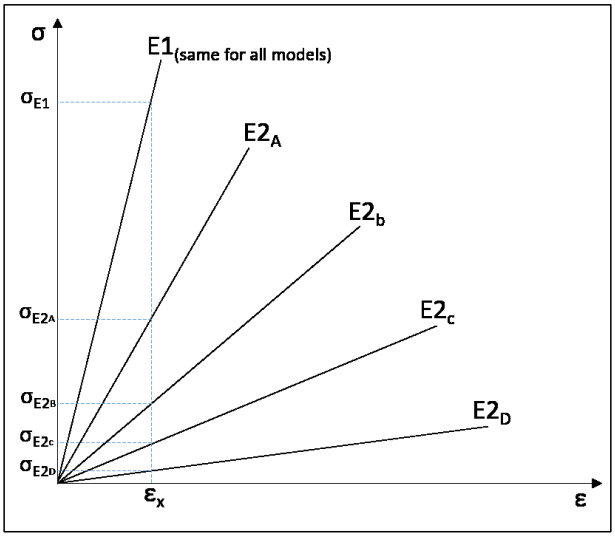


Figure 6.4: graph of strain versus extensional stress for materials with different values of Young's Modulus. For any value of strain the extensional stress in the strong layers is considerably greater than in the weak layers and as the Young's Modulus of the weak layer (E2) is decreased (A to D) the extensional stress also falls.

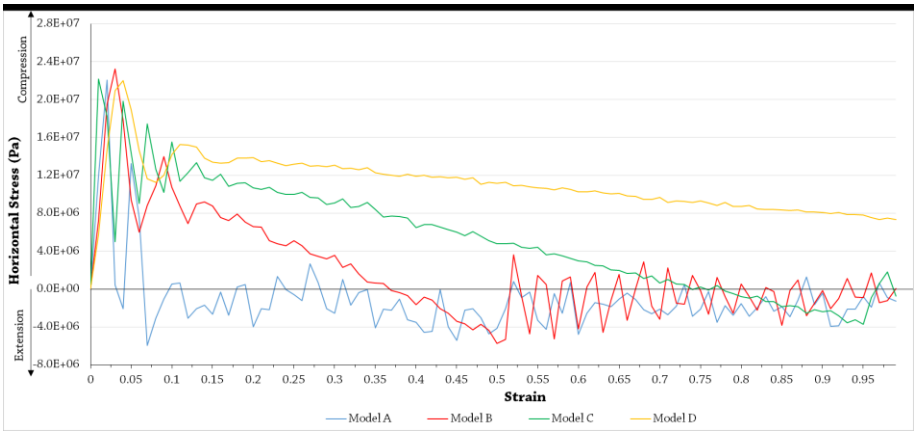


Figure 6. 5: horizontal stress versus accumulated strain within the central layer for the four experiments. Model A (E2= 1.5e10 GPa); Model B (E2= 3e9 GPa); Model C (E2= 1.5e9); Model D (E2=6e8). Note that the total layer parallel (horizontal) stress becomes more compressive as the Young's Modulus of the central layer becomes lower, i.e. as the central layer becomes progressively weaker.



Figure 6. 6: a) fracture propagating from strong to a weak layer across a bonded interface in a model subjected to layer-parallel extension. If both layers are extended the same amount a greater tension occurs in the strong layer than in the weak and the fracture is able to propagate into the weak layer; b) model a) subjected to a layer-normal compression. This induced horizontal compressions in both layers, reducing the tensile stress in the strong layer and creating an effective compressive stress in the weak layer which impedes fracture propagation. E1= Young's modulus of the strong layer; E2= Young's modulus of the weak layer; Ts= Fracture tip tensile stress in the strong layer; Tw= Fracture tip tensile stress in the weak layer; σ_{hz}= layer-parallel extension; σ_n= layer normal compression; σ_{hzc}= layer parallel compression

A series of experiments were run to complement the experiments described above which were identical in every respect except for the applied layer-normal load which was set at a lower value of 10MPa (Figure 6.7). It can be seen that the results are almost identical. Again fractures where inhibited from propagating from the strong to the weak layers and interestingly the anomalous results of Model C were not reproduced.

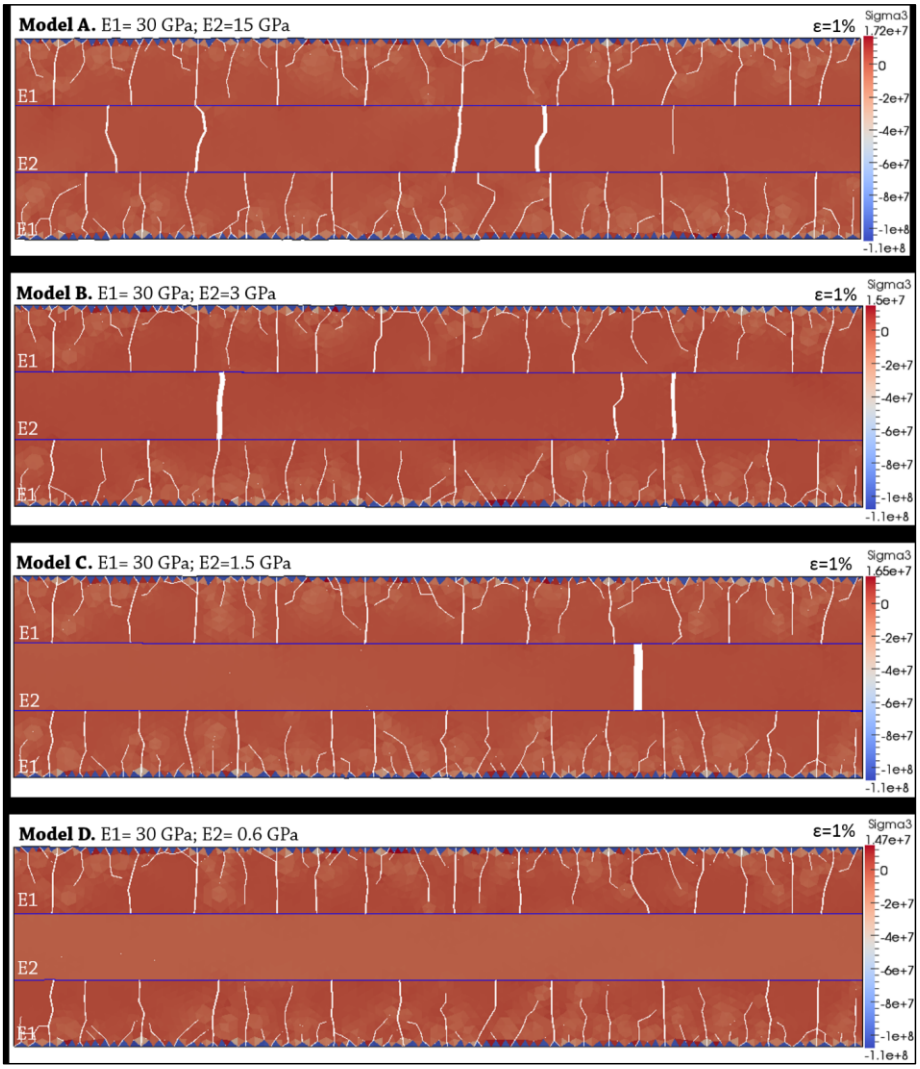


Figure 6.7: Fracture patterns and stress distribution for a 3-layer model after an extension of ε=1% (end of deformation). The coefficient of sliding friction at the layer interface is μ=0.6 and layer-normal load is 10 MPa. The the top and bottom layers Young's Modulus was set at 30 GPa and the middle layer has different values for each model presented.

As a final check on this phenomena, it was decided to repeat the experiments using a model where the layers were bonded, such as assumed by Simoson et al. (1978); Cook & Erdogan (1972) and Erdogan & Biricikoglu (1973); Hegelson & Aydin (1991); Larsen et al. (2010). This being an assumption built-in into the theoretical analysis. The results are shown in Figure 6.8 and show that when the interfaces

are bonded the tensile fractures are able to propagate from the stronger bounding layer into the weak central layer for all the values of Young's Modulus of the central layer. This suggests that boding the layers pre-conditions the results because the model behaves as homogeneous unit where interfaces virtually do not exist.

Many of the observations made in the numerical models are similar to observations made at Lilstock where, vertical tensile fractures that formed in a limestone (strong layer) were arrested at the interface with a shale layer (weak layer). Although it can be suggested that the mechanism proposed above for lack of propagation in numerical models A, B and D which relate to the layer-parallel stress state in the weak layer, could be applied to explain the lack of propagation into the shale layers in Lilstock, the author considers that the more likely explanation is that the shale layers are behaving inelastically and that fracture tip stresses are dissipated by ductile deformation as discussed in Section 6.2.3.

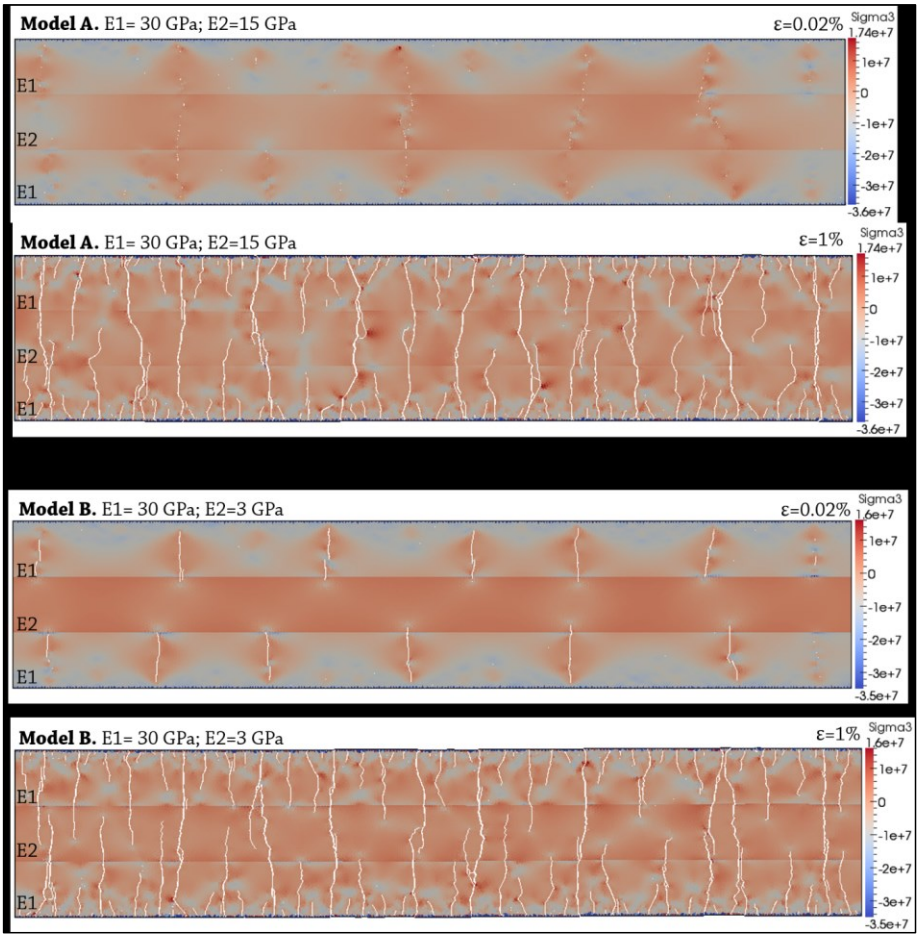


Figure 6. 8: Fracture patterns and stress distribution for a 3-layer model after an extension of ε=1% (end of deformation). The layers are bonded and the layer-normal load is 10 MPa. The Young's Modulus of the top and bottom layers is set at 30 GPa and the middle layer has different values for each model presented.

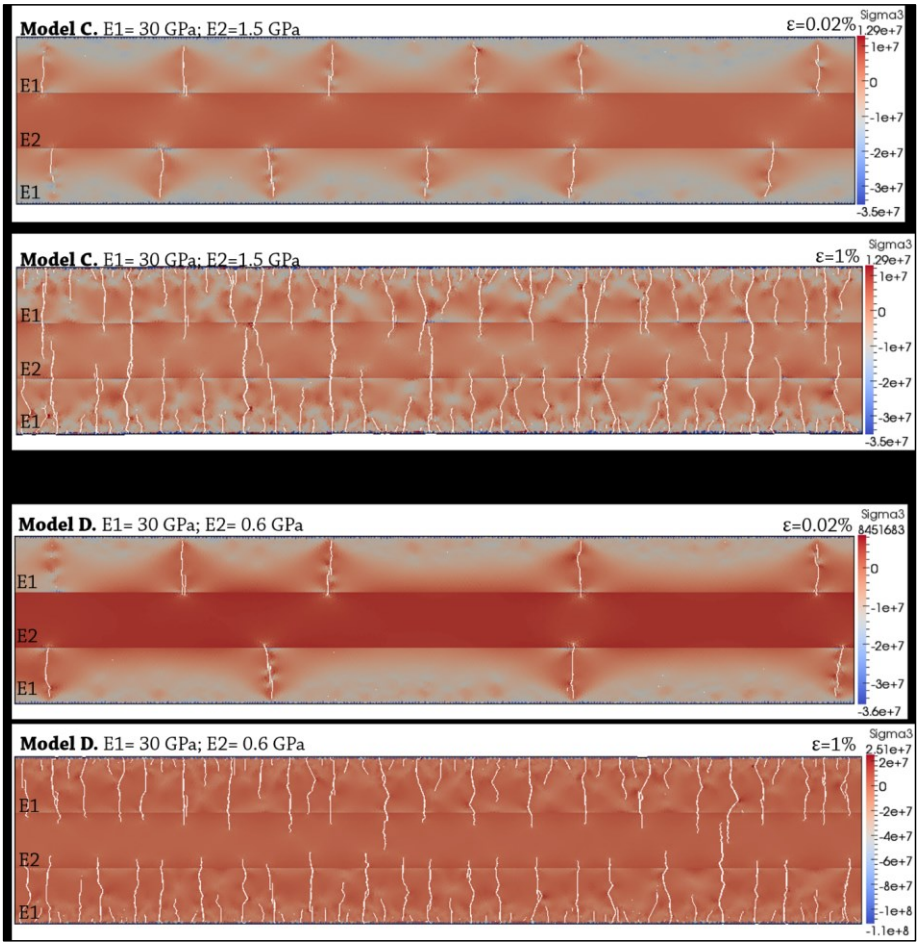


Figure 6. 8 (continued): Fracture patterns and stress distribution for a 3-layer model after an extension of ε=1% (end of deformation). The layers are bonded and the layer-normal load is 10 MPa. The Young's Modulus of the top and bottom layers is set at 30 GPa and the middle layer has different values for each model presented.

6.3.3 The effect of the thickness of an incompetent layer on fracture propagation across it

In Section 5.3.3 numerical are described which were carried out to determine the role that the thickness of an incompetent layer (such as a shale layer or a bedding-parallel gypsum vein) plays on fracture propagation into that incompetent layer. The investigation involved 3-layered models 50 cm in length and with variable total vertical thickness. The mechanical properties of the top and bottom layers were equivalent to those of a limestone and the mechanical properties of the middle incompetent layer were equivalent to a shale. Results show that:

i) As expected fractures form first in the top and bottom competent layers. These form at the interface between the weak and the strong layers and propagate towards the outside of the model

ii) Regarding fracture propagation or arrest at the interface between the strong and the thin weak layer several possibilities were observed:

   a) A tensile fracture forms in either the top or bottom competent layer and is able to propagate across the interface and across the middle layer but that does not extend into the adjacent competent layer (Figure 5.80d).

Tensile fractures in the two strong units appear to develop independently. They can be subsequently linked by fractures that form in the thin weak layer. Two possibilities were observed:

   b) In the first two fractures in the two strong layers are aligned, i.e. one is formed directly above the other. One of these propagates across the interface and the middle layer linking with the other tensile fracture to produce a straight *through-going* fracture (Figure 5.81-d and 5.81-h4).

   c) In the second the two fractures in the two strong layers are not aligned (they are offset) and they become linked as one of the fractures propagates into the weak layer and continues to propagate obliquely across the layer to link with the other fracture (Figure 5.80f).

The linking of extensional fractures in adjacent strong layers by fractures forming in the intervening weak rock is observed both in the models and in the field, to occur in two distinct ways. These are shown in Figure 6.9.

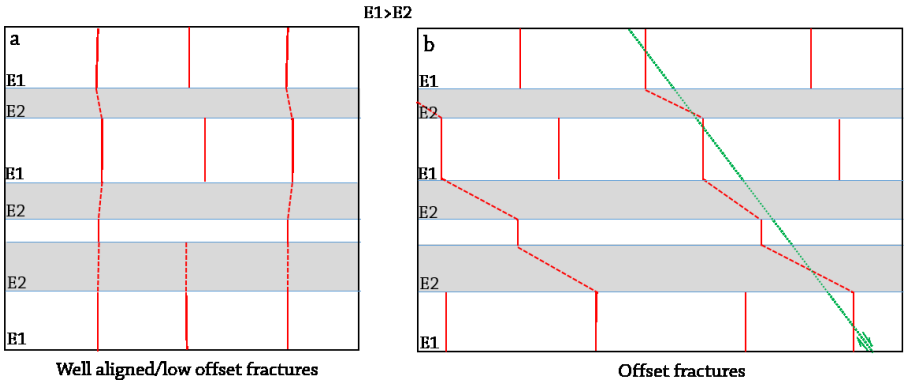


Figure 6. 9: The linking of extensional fractures in adjacent strong layers by fractures forming in the intervening weak rock. Note that if the fractures that form in the strong layers are well aligned the linking occurs by the formation of tensile fractures in the weak layers and a through-going fracture is formed (a). Alternatively, if there is a large offset in the fractures that formed the strong layers the linking occurs the formation of oblique fractures in the weak layers between them. These through-going fractures which are made up of a series of extensional fractures subsequently experience shear movement along them and form a normal fault (green dashed line) (b).

Another mode of fracturing was also observed.

d) This involved the linking of three independent tensile fractures to form a continuous single fracture (Figure 5.80g and 5.82f).

iii) Propagation of fractures across an interface into another layer occured only in models with very thin incompetent layers, e.g. models A, B and in model G which has the thickest middle incompetent layer of all the seven models. In all other models the *through-going* fractures formed by the linking of individual tensile fractures.

iv) Thicker middle layers promote the formation of longer, wider and more complex fracture patterns in the weak middle layer. Often these fractures do not extend to the layer boundaries. Such an organization of fractures of was also observed in the field.

The observations made on point ii) are relevant to the formation of the two types of fractures which categorize layered rocks. They are termed as either through-going or strata-bound, and it is generally implicitly assumed that the trough-going fractures are formed by the propagation of a fracture through successive adjacent layers. However, the models show that this often not the case. A particularly interesting example of the linking of independent extensional fractures to form a *through-going* fracture has been described in the above experiments (see point ii) c) and observed

in the field (see Figure 3.54 and 6.3). These observations show the linking of independent (offset) extensional fractures in adjacent strong beds (limestone in the field) by the formation of oblique fractures in the weak layers between them. These through-going fractures which are made up of a series of extensional fractures subsequently experience shear movement along them and form a normal fault (See Section 4.3.2 and 6.2.3) (see Figure 6.9 b). These field observations and experimental results support the contention that on a deep level shear and extensional fractures are fundamentally related.

It follows from the theory of brittle-failure that the parameter determining which of these two modes of failure occurs is the magnitude of the differential stress (see Section 4.3.1, Figure 4.18). A series of experiments were conducted to explore this (Section 5.3.1.2**,** Figure 5.37). In them it is clear that a higher applied layer-normal load leads to higher differential stresses and the formation of shear fractures. However, it is apparent that the macroscopic shear fractures that develop are formed by the linking of a series of extensional fractures.

6.4 Regional Considerations

Having established in general the likely mechanical properties of evaporite cap-rocks and how these properties might control fracture propagation through these units, it is appropriate in the light of the context of the present study, to consider the specific example of such cap-rock in Qatar. This requires a consideration of its tectonic setting and of the associated regional stress regime. Once this is understood its likely impact on the potential fractures in the evaporite seals when CO_2 is injected into the underlying reservoir can be determined.

As discussed in Section 3.2, Qatar is located on the Arabian Plate which originated 25Ma ago when rifting to form the Gulf of Aden and Red Sea split off a fragment of the African continent. The plate measures 2600 km north–south and 3000 km east–west and its boundaries are (Figure 3.2 – reproduced below): on the West the Dead Sea transform and Red Sea spreading/rifting axis; on the North a zone of plate convergence made up of the East Anatolian fault, Bitlis suture, and Zagros collision zone; on the East the Owen Fracture Zone; and on the south the Gulf of Aden spreading axis (the Sheba Ridge) (Stern & Johnson, 2010).

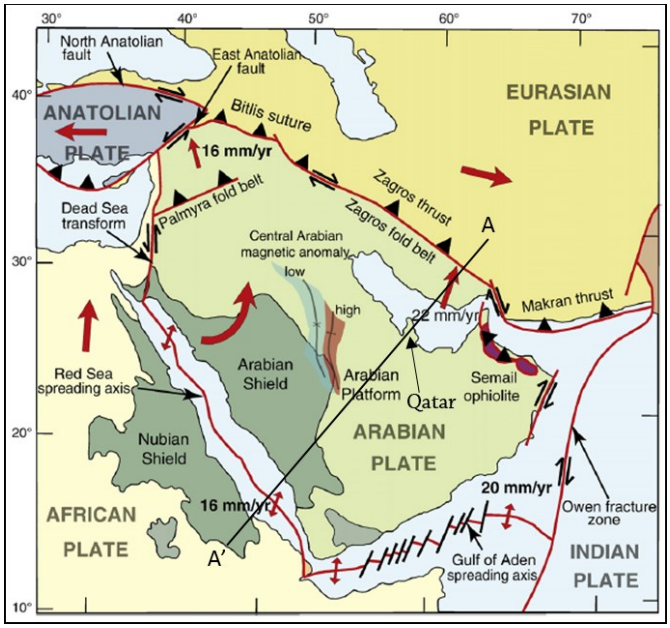


Figure 6. 10: A simplified map of the Arabian Plate, with plate boundaries, showing the approximate plate convergence vectors, and principal geologic features (Stern & Johnson, 2010). Notice the location of the Qatar peninsula. A-A' shows the location of a schematic cross section through the Arabian Plate presented in Figure 6.11

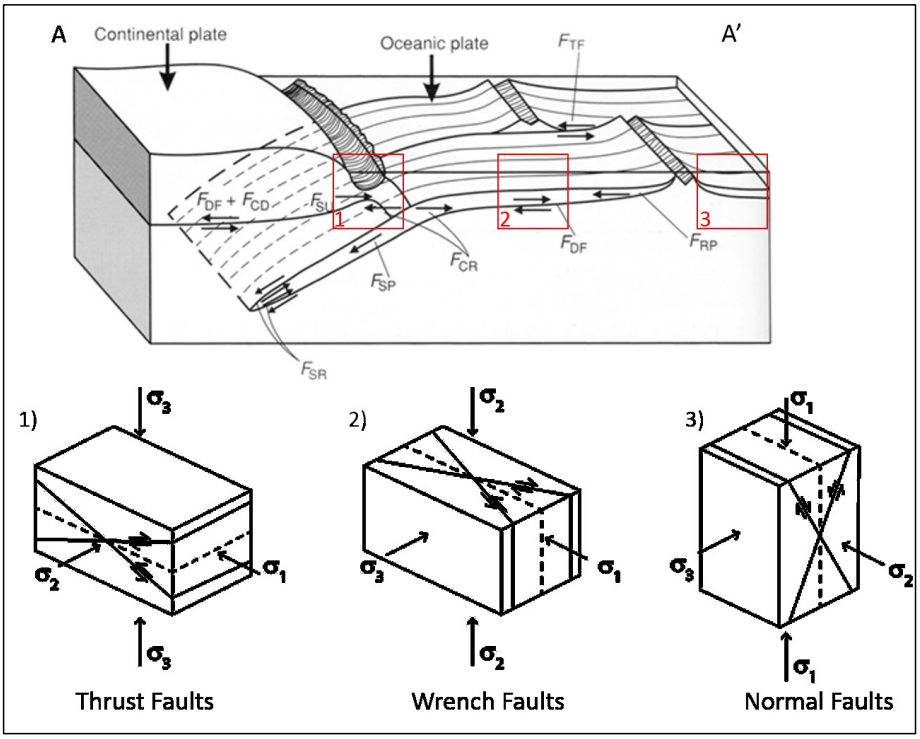


Figure 6. 11. Top: cross-section of a lithospheric plate (which could be equivalent to a cross section along A-A' in Figure 3.2) and the possible forces acting on it. FDF- mantle drag, FCD- mantle drag beneath continents, FRP – ridge-push, FTF- transform fault resistance, FSP – Slap pull, FSR – resistance on descending slab as it penetrates asthenosphere, FCR – colliding resistance, FSU - suction force. The red numbered squares correspond to the stress regimes associated with the formation of a) normal faults b) wrench faults and c) thrust faults presented on the bottom sketches and are located in the region of the plate where these structures form. Each stress regime can also generate extensional fractures (dashed) which bisect the conjugate shear fractures. Adapted from Fowler (2006) and Cosgrove & Hudson (2016).

The change in stress regime within a tectonic plate from the spreading ridge (a normal fault regime) to the subduction zone (a thrust fault regime) is indicated in Figure 6.11. It can be seen from Figure 6.10 that the tectonic setting of Qatar may fall either into the thrust faults (1) or wrench faults regime (2) (Figure 6.11). The fracturing in any reservoir situated in either of these stress regimes would be controlled not only by that regime but also by any existing fractures which may be reactivated. We consider the implications of these two situations in turn.

Wrench Fault Regime.

As discussed in Section 3.2, Qatar is situated above a major Pan-African lineament which is currently thought to be acting as a strike-slip structure. The current plate motion indicates that σ_1 is acting approximately N-S (see Figure 6.10) and if Qatar is situated in a strike-slip stress regime ((2) in Figure

6.11) this would tend to generate conjugate wrench faults trending NNE-SSW and NNW-SSE. Any extensional fractures would be vertical with a ≈N-S strike. In addition any pre-existing vertical fractures within this range of strikes could be reactivated as strike slip fractures (Figure 6.12 a) which would adversely impact on the integrity of any seals in the vicinity.

In addition the large anticline that makes up the Qatar peninsula and which characterizes the geometry of the underlying succession, is situated above a major basement lineament and indeed the anticline itself is thought to be the result of strike-slip motion on this structure. The amplification of the fold would be characterized by the formation of several fracture sets including important sub-vertical (i.e. layer-normal) fractures on the crest of this fold (see Figure 3.44). It follows that both the regional stress-field and the local field would produce fractures that are vertical and therefore could act as potential leakage points if they were to propagate through any cap-rock.

The features of evaporite-rich cap-rocks that might impede fracture propagation of such vertical fractures have been listed and discussed above. An additional effect that might also prevent fracture propagation is the possibility of bedding-parallel fracture formation despite the fact that the stress regime is not one in which σ_2 is vertical and in which new extensional fractures would also have this orientation. This is possible because of the high mechanical planar anisotropy of the cap-rock. It will be recalled from Section 4.4.1 that it is possible to generate extensional fractures that open against σ_1 rather than against σ_3 if when σ_1 is vertical the anisotropy of the horizontal bedding results in a significant difference between the tensile strength parallel to and normal to the layering (Cosgrove & Hudson, 2016). In the context of the present stress regime, where σ_2 is normal to the layering a similar situation can be envisaged, in which bedding parallel extensional fractures rather than bedding normal fractures can form. This would have a major impact on the ability of any seal to maintain its integrity. Such horizontal (bedding-parallel) fractures and any veins that might form in association with them (as for example the satin-spar veins seen in Watchet and at Brightling Mine) would have a major impact on inhibiting the propagation of vertical fractures.

Thrust Fault Regime

A stress regime where thrust faults would form, one where σ_3 is vertical (Figure 6.11 - 1)) may also be a potential scenario for the Qatar peninsula. Thrust relating to this regime currently characterizes the NW-SE trending fold-thrust belt of the Zagros Mountains (Figure 6.10) The thrusts terminate along the eastern margin of the Persian Gulf and do not extend, as far as is known, to Qatar or the Eastern margin of the Gulf. This does not imply however that the stress regime does not extend this far. Indeed numerous *bright* spots observed along bedding on seismic section across the Persian Gulf, indicate clearly an opening of the bedding planes, a phenomenon compatible with this stress regime which is

summarized in Figure 6.12b. The two failure envelopes correspond to the formation of new thrusts or the reactivation of appropriately oriented pre-existing thrusts. As far as is known currently no thrusts exist in this region and the question arises as to whether this stress regime could reactivate the N-S trending strike-slip structure that characterizes the basement beneath Qatar. If it is assumed that the current principal stress (σ_1) is oriented in the same orientation as in the Zagros belt, it trends NE-SW. This is ideally oriented to reactivate the N-S trending basement strike-slip structure in a dextral manner.

The lack of thrusts in the Qatar region indicates that Failure Criteria 3 is not satisfied and because there are no pre-existing thrusts in this region Failure Criteria 4 also remains unsatisfied (see Figure 6.12 b). The possibility exists that Failure Criteria 2, i.e. re-shear on pre-existing, appropriately oriented, strike-slip faults could be satisfied in this region. It is interesting to note that inspection of the seismic map of the Persian Gulf indicates the occurrence of weak seismicity in this region. However this stress regime does not generate vertical fractures either in shear or extensional mode. The associated extensional fractures would be bedding-parallel and as noted above such features are prevalent beneath the Persian Gulf. Such fracturing would inhibit the vertical propagation of other fractures and therefore increase rather than diminish the efficiency of any seal in which they occur.

A final point of interest regarding the specific conditions pertaining to Qatar relates to the possibility of stylolite formation during burial and diagenesis in the sedimentary succession. It can be seen from the stratigraphic succession of the region (see Figure 3.5 part of which is reproduced in Figure 6.12) that numerous limestones occur in the reservoir carbonates that exist beneath the Hith evaporites which form the main seal in the region. It follows that the formation of stylolites along bedding planes is likely to have occurred within the reservoirs during burial and diagenesis. As it was noted in the discussion of these features at Tytherrington (Section 6.2.2), stylolites lock adjacent layers together, inhibiting slippage along the interface and facilitating fracture propagation from one layer to another.

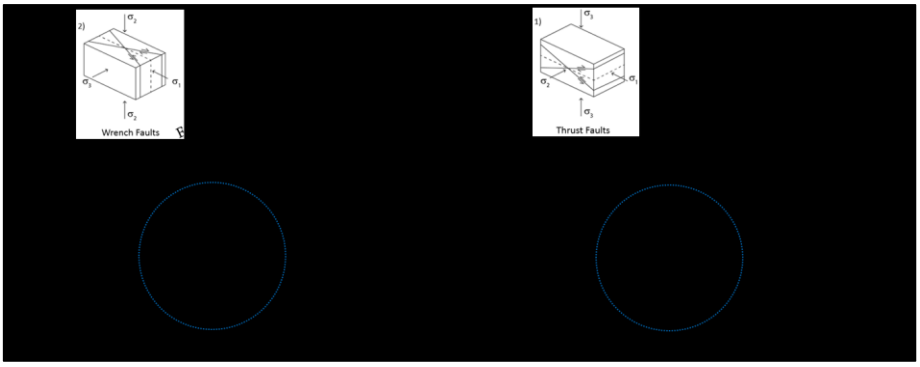


Figure 6.12: a) failure criteria for the formation of new wrench faults (Failure Criteria 1) and the reactivation of an appropriately oriented pre-existing wrench-faults (Failure Criteria 2). b) failure criteria for the formation of new thrust faults (Failure Criteria 3) and for the reactivation of pre-existing appropriately oriented thrusts (Failure Criteria 4).

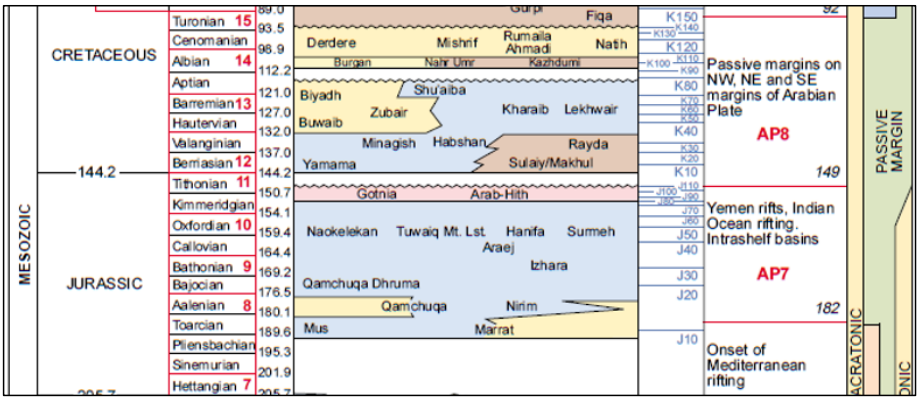


Figure 6. 13: Part of the stratigraphic column for Qatar showing the Hith Formation (the main seal) and the underlying carbonate rich reservoir.

6.5 Conclusions and Recommendations

6.5.1 Conclusions

The observations and conclusions resulting from field work in gypsum mines, observations of drill cores and outcrop studies were used to design a programme of numerical models using the FEMDEM methodology aimed at understanding the ability of evaporite rich seals to resist the propagation of vertical fractures through them. The work was part of a larger project looking into the problem of CO_2 sequestration, specifically in the carbonate reservoirs that underlie Qatar. These reservoirs are sealed by evaporite rich successions.

The research has provided insights on:

1. The likely mechanical properties of evaporite sequences,
2. The propagation of fractures through layered rocks (specifically layered evaporites) ,
3. The potential impact of the mechanical properties of the evaporite seal and the current regional stress field in the Qatar region on the likelihood of propagation of fractures through the cap-rock of Qatar during CO_2 injection operations.

Regrettably, regarding point 3, virtually no information was made available regarding the detailed structure and stress regime of the reservoirs being considered for sequestration in Qatar. We indicate how the current research can be applied to the specific location when this data becomes available

These will be considered in turn.

1) <u>Conclusions regarding the likely mechanical properties of evaporite seals based on field work observations</u>

Work conducted at the Brightling Mine and Watchet and the analysis of drill-cores from the Weald Basin enables the following conclusions to be made on the properties of evaporite rich sequences:

• Evaporite sequences are not homogenous in terms of their lithological and textural properties and are represented by layers of shales, massive and laminated mudstones, microbial laminated mudstones and a variety of anhydrite layers which display several types of textures which include chicken-wire, palisade and aggregate textures.

• These evaporite rich sequences contain both primary and secondary layers. Although the primary layers (related to the depositional environment and diagenesis) dominate, the thin bedding parallel satin spar veins (linked to natural hydraulic fracturing) are thought to play an important role in protecting the sequence from being cut by hydraulic fractures.

• These successions have a very low permeability and therefore act as important seals to carbonate reservoirs. However this very low permeability can cause the build-up of the internal fluid pressure and fluid induced failure can occur inside the seal. This was proven by the presence of horizontal and vertical satin-spar veins in both of the field locations (Brightling Mine and the Mercia Mudstone in Watchet) and in the drill-cores.

• The remarkable 3D exposure of evaporites at Brightling mine demonstrated that these beds are not laterally continuous, and that the bedding planes and the secondary satin spar veins die out laterally. It is argued that the bedding planes and satin spar veins might be considered analogous to 'Baffles' (rather than Barriers) to fluid flow. In addition they can inhibit the propagation of fractures where they exist but fractures can continue to propagate where they die out.

The field work was extremely important in recognizing that anhydrite evaporite seals are in fact layered sequences which contain both primary and secondary layers both with die out laterally. Therefore when modelling these evaporite rich seals, it is important to incorporate these features and not to assume they are massive homogeneous units.

2) Conclusions on fracture propagation through layered sedimentary sequences

Field work conducted in the Bristol Channel area and the numerical models using the FEMDEM methodology enabled several conclusions to be taken regarding fracture propagation through layered sedimentary sequences. These will be considered individually for each of the experiments.

2A) The influence of the coefficient of sliding friction on a layer boundary on fracture propagation

The simple model used to describe friction along the bedding plane is Amonton's Law of frictional sliding ($\tau = \mu\sigma_n$) which states that shear resistance to sliding (τ) is defined by the coefficient of sliding friction (μ) on the layer interface and the applied layer-normal load (σ_n). It follows that by increasing one or both of these parameters the resistance to sliding along an interface also increases. Authors such as Anderson, 1981; Van Eelken, 1982; Warpinski & Teufel, 1987; Dollar & Steif, 1989 have argued that a low shear strength of a bedding plane will favour the dissipation of the fracture tip stresses as the fracture approaches the interface therefore inhibiting propagation. Numerical experiments using un-bonded layers have confirmed this and revealed the impact of different magnitudes of shear resistance to slip on an interface on fracture propagation:

- The coefficient of sliding friction along the layer boundaries has a very important impact on whether a fracture propagates through or is arrested at an interface. This was demonstrated by I)

the observations at Tytherington of both stylolitized limestone bedding planes and perfectly flat bedding planes where two adjacent limestones were separated by a thin clay or shale horizon and II) by the numerical models that analysed the impact of resistance to bedding plane slip on fracture propagation. It was demonstrated that higher values of the coefficient of sliding friction along the layer boundaries (which can be compared to the Tytherington stylolitized surfaces that formed between contiguous limestone layers that lock the layers together) promote the formation of through-going fractures. The inverse is also true, low values of the coefficient of sliding friction along the layer boundaries (in Tytherington low friction surfaces can be compared to the flat surfaces formed in adjacent limestones when there is a thin clay layer separating them) contribute to the arrest of fractures at the interface.

- Numerical models also confirm that for a constant value of the coefficient of sliding friction along the layer boundaries, an increasing layer-normal load (which according to Amonton's Law increases the resistance to slip) promotes the formation of through going fractures. This means that the propagation of a fracture through an interface between two different rock types becomes more likely the deeper in the crust it occurs.

2B) The influence of the Young's modulus from one layer to another on fracture propagation

Theoretical considerations indicate that the fracture tip stress generated by a fracture propagating in a low Young's modulus layer, will not be of sufficient magnitude to drive that fracture into an adjacent layer of higher modulus even if the interface between the layers is bonded. Conversely, a fracture propagating from a stiff (high Young's Modulus) to a soft (low Young's Modulus) layer will be able to cross that interface and propagate into the soft layer.

Interestingly, both field observations at Lilstock where fractures in stiff limestone layers fail to propagate into adjacent shale layers, and numerical models contradict this prediction. Two possible explanations have been given in the discussion above (see Section 6.3.2). The first is that the material (shale) is not behaving elastically and the fracture tip stresses are dissipated on entering the weak layer by the generation of ductile deformation.

The second explanation is related to the boundary conditions used in the modelling. The numerical models were subjected to both a horizontal extension and a vertical layer-normal load. The application of this layer-normal load (which in geological conditions is the equivalent to the overburden) generates layer-parallel compression which is inversely proportional to the elastic modulus of the layer, i.e. as the strength of the weak layer decreases the impact of the layer-normal compression increases and the resulting layer-parallel compression increases. In layers where the Young's modulus is low (weak layers) this layer-parallel compression acts to oppose the action of the applied layer parallel extension and may lead to an effective compressive state inside the layer. This compressive state inhibits fracture

propagation from the strong into the weak layer.

2C) The influence of the thickness of an incompetent layer on fracture propagation to an adjacent competent layer.

The relative thickness between strong (high tensile strength, high elastic modulus - limestones) and weak (low tensile strength, low elastic modulus – clay and shale) layers is not a decisive factor in determining whether or not a fracture propagates from the strong limestone layer into the weak shale layer. This is demonstrated by (i) the field observations which demonstrate the ability of very thin clay layers that occur between adjacent thick limestone layers in Tytherington and by the shale layers of Lilstock, to arrest fractures within the limestone layers; and (ii) by the numerical models described in Section 5.3.3.

As discussed above it may be the case that the thin, weak layer is not acting elastically but in a ductile manner or alternatively the bedding plane which defines the boundary between the two rock types is one of low friction resistance. Both these effects allow the dissipation of the fracture tip stresses and cause fracture arrest.

Clearly bed thickness is not a first order factor controlling fracture propagation.

2D) Another observation that arises from the both the field work and numerical models is that through-going fractures are not always formed by the propagation of a fracture through successive adjacent layers but that instead they occur by the linking of individual extensional fractures to form a through-going fracture. This process of tensile fracture linkage is thought to be the precursor to the formation of shear fractures when offset tensile fractures that have formed in competent limestone layers (for example) are linked across by oblique fractures that form in the weak layers between them. These through-going fractures subsequently experience shear movement along them forming a shear fracture.

3) Application of the findings in Qatar and CO_2 injection.

The observations and conclusions deduced from the field work and numerical modelling outlined above relate to the general problem of the propagation of fractures through a layered evaporite seal. By considering the regional stress field of any particular reservoir together with its detail stratigraphy, specific predictions can be made about the ability of any seal to ~~resist~~ arrest any fractures generated through fluid induced failure resulting from the injection of CO_2 into an underlying reservoir.

With this in mind the regional setting of Qatar was considered and the likely regional and local stress fields have been examined (Section 6.4). Based on this the likely fractures that would form in response

to an increasing fluid pressure were predicted. A detailed understanding of the regional and local stress fields and of the stratigraphy of the reservoirs and seals at Qatar – information which we did not have access to - would enable the general principles outlined above to be applied and specific predictions to be made.

Another important area of research development relates to the chemical properties of CO2. In the process of sequestration the original hydrocarbons in the reservoir becomes replaced with CO2 under high pressure, often in a supercritical condition (see Section 1.XX). A chemically inert fluid is being replaced by an aggressive chemically reactive fluid. In addition the viscosity of this fluid is extremely low and it has the ability of a gas to move through the rock mass and the capacity of a fluid to dissolve the rock. Clearly when considering the impact of such a fluid on the integrity of an overlying seal both the chemical and the mechanical properties of the fluid need to be carefully considered.

6.5.2 Future considerations

Formatted: Heading 2

The results of the field studies, particularly those conducted on evaporite rich sediments (Brightling Mine and Watchet) offer an insight into the process of internal fluid induced failure of low permeability rocks and on the textural and sedimentary characteristics of evaporite seals which might influence fracture propagation across these rock units. The numerical modelling that these observations inspired has provided a more detailed insight into the mechanical parameters that influence fracture propagation through layered rock masses. Having said this some suggestions for future work are presented below:

- Rijken & Cooke (2001) found that when numerical models incorporate a ductile layer (such as was done in the present research and such as occurs in nature) causes the registered stress intensity factor to be dependent on the nature of the applied load: the models with fluid pressure in a fracture produce greater stress intensity factor at the flaw tips than models with remote tension. The explanation resides on the way the pressure is applied. On an internal fluid pressure driven fracture, the driving stress is applied locally and the shale around the crack-tip experiences large inelastic strains which enhances crack opening, increasing the stress intensity factor and promoting propagation through layers. In contrast, in a remotely loaded crack-tip the extensional strain within the shale is distributed along the layer rather than localized at the

crack tip and hence the stress intensity factor is smaller. This observation is of extreme relevance to the present research as the models were all subjected to remote tension. Nevertheless the likelihood of high fluid pressures within the seal (internal hydraulic fracturing) was considered. We suggest that the next versions of the Y2D code include the possibility of modelling fluid driven fractures.

that reason it is considered that being able to include the effect of fluid pressure would be a very important addition to the code as it could significantly alter the results and consequently the predictions for fracture propagation through a layered sequence composed of strong and weak layers.

- Adding to that the possibility of modelling cohesive interfaces would also lend greater strength to the results because layers would be more realistically modelled.

- There is no doubt that the Y2D code is a very powerful tool when it comes to modelling fracturing of intact rock masses. However this author has experienced some difficulties in terms of workflow and leaves the following suggestions:
    1. It is crucial for the research group to improve the integration of the several versions of this code. Very often I was given an "updated" version of the code which had been added a certain parameter/function but removed another and seriously delaying my work. This would be achieved by having a member of the research group that provides data management and keeps the Y2D versions up to date with the several additions and changes that each member of the group makes.
    2. Another important addition would be to edit the source code so that a non-developer user can understand what each line in the code is referring to. A simple comment in front of the code lines would help tremendously. Currently, only a developer can use it efficiently and unless that is the objective, a regular user finds it extremely difficult to grasp the mechanics of the code and what it does.
    3. A user's manual where the specific concepts of the code are explained to "non-modellers" would be a good addition. This would allow a greater range of uses of a very interesting and powerful tool and it would definitely encourage other geologists to use numerical modelling in their research.

- Taking into account that the project was ultimately aimed at understanding the mechanical properties of the carbonate reservoirs and evaporite seals of Qatar, it would be of great help to any future work if stress data from boreholes and rock samples were provided. The stress data from boreholes would allow to accurately predict the local stress state of the reservoirs and

Formatted: Normal, Indent: Left: 0.12 cm, Bulleted + Level: 1 + Aligned at: 1.27 cm + Indent at: 1.9 cm

therefore the fracture sets that could potentially form when increasing the fluid pressure in the reservoir. In its turn the rock samples would allow for a better understanding of the actual mechanical properties that occur in the subsurface and that may impact of fracture propagation/arrest. This would allow the models to be designed with the appropriate rock properties making them more applicable to Qatar's subsurface.

- In terms of workflow when using the Y2D code created in-house, the author considers that:
- It is crucial for the research group to improve the integration of the several versions of this code. This would be achieved by having a member of the research group that provides data management and keeps the Y2D versions up to date with the several additions and changes that each member of the group makes. This would save time as one would always know what each version is capable of doing.
- Another important addition would be to edit the source code so that a non-developer user can understand what each line is referring to. A simple comment in front of the code lines would help tremendously. The way it currently is, only a developer can use it efficiently and unless that is the objective, a regular user finds it extremely difficult to grasp the mechanics of the code and what it does.
- A user's manual where the specific concepts of the code are explained to "non-modellers" would be a good addition. This would allow a greater range of uses of a very interesting and powerful tool and it would definitely encourage ot

Formatted: Normal, Indent: Left: 0.12 cm, Bulleted + Level: 1 + Aligned at: 1.27 cm + Indent at: 1.9 cm

Bibliography

Energy and Minerals Field Institute - Colorado School of Mines. (2005). *Energy and Minerals Field Institute* . Retrieved from http://emfi.mines.edu/emfi2005/ChevronTexaco.pdf

A.S., A., & Kendall, C. (1994). Depositional Setting of the Upper Jurassic Hith Anhydrite of the Arabian Gulf: An analogue to holocene evaporites of the UAE and Lake MacLoeod of Western Australia. *AAPG Bulletin*, 1075-1096.

Aguilera, R. (1983). Exploring for Naturally Fractured Reservoirs. *SPWLA 24th Annual Logging Symposium. SPWLA.*

Al-Husseini, M. (2000). Origin of the Arabian Plate structures: Amar Collision and Najd Rift. *GeoArabia*, 527–542.

Alsharahan, A. S., & Nairn, A. (1994). Geology and Hydrocarbon habitat in the Arab Basin: the Mesozoic of the State of Qatar. *Geologie en Mijnbouw*, 265-294.

Alsharhan, A., & Kendall, C. G. (1994). Depositional Setting of The Upper Jurassic Hith Anhydrite of the Arabian Gulf: An Analog to Holocene Evaporites of the UAE and Lake MacLeod of Western Australia. *AAPG Bulletin*, 1075-1096.

Alsharhan, A., & Nairn, A. (1997). *Sedimentary basins and petroleum geology of the Middle.* Elsevier.

Anderson, G. D. (1981). Effects of Friction on Hydraulic Fracture Growth Near Unbonded Interfaces in Rocks. *SOCIETY OF PETROLEUM ENGINEERS JOURNAL*, 21-29.

Azer, S. R., & Peebles, R. G. (1998). Sequence Stratigraphy of the Arab A to C Members and Hith Formation, Offshore Abu Dhabi. *GeoArabia*, 251-268.

B.S.A.Tatone, & G.Grasselli. (2015). A calibration procedure for two-dimensiona llaboratory-scale hybrid finite–discrete element simulations. *International Journal of RockMechanics & Mining Sciences*, 56-72.

Bachu, S. (2000). Sequestration of carbon dioxide in geological media:Criteria and approach for site selection. *Environmental Geology*, 277-289.

Bachu, S. (2002). Sequestration of CO2 in geological media in response to climate change: road map for site selection using the transform of the geological space into the CO2 phase space. *Enervy & Conversion Management*, 87-102.

Baer, G. (1991). Mechanisms of Dike Propagation in Layered Rocks and in Massive porous sedimentary rocks. *Journal of Geophysical research*, 911-929.

Bai, T., & Pollard, D. D. (2000). Fracture spacing in layered rocks: a new explanation based on stress transition. *Journal of Structural Geology* , 43-57.

Barker, C. (1990). Calculated volume and pressure changes during the thermal cracking of oil to gas in reservoirs. *AAPG Bulletin*, 1254-1261.

Beydoun, Z. (1988). *The Middle East: regional geology and petroleum resources.* Scientific Press, UK.

Beydoun, Z. (1991). *Arabian Plate hydrocarbon geology and potential, a plate tectonic approach.* American Association of Petroleum Geologists, Studies in Geology.

Biot, M., Medlin, W., & Massé, L. (1983). Fracture Penetration Through an Interface. *SPE Journal*.

BP. (2013). *BP Statistical Review.* London: BP.

BP. (n.d.). *BP Global.* Retrieved February 12, 2014, from BP Global : http://www.bp.com/en/global/corporate/about-bp/bp-and-technology/more-recovery.html

British Gypsum. (2010). *Brightling Mine.* British Gypsum.

Brown, E. (1987). *Analytical and Computational Methods in Engineering Rock Mechanics.* London: Allen & Unwin.

Busch, A., Amann, A., Bertier, P., Waschbusch, M., & Kroos, B. (2010). The Significance of Caprock Sealing Integrity for CO2 Storage. *SPE International Conference on CO2 Capture, Storage and Utilization.* New Orleans: SPE.

Butler, M., & Pullan, C. (1990). Tertiary structures and hydrocarbon entrapment in the Weald Basin of Southern England. In Brooks, & Hardman, *Tectonic Events Responsible for Britains Oil & Gas Reserves* (pp. 371-391). London: Geological Society.

Cartwright, J., Huuse, M., & Aplin, A. (2007). Seal bypass systems. *AAPG Bulletin,*, 1141-1166.

Casabianca, D., & Cosgrove, J. (2012). A new method for top seals predictions in high-pressure hydrocarbon plays. *Petroleum Geoscience, Vol. 18,* , 43-57.

Chadwick, R. (1993). Aspects of basin inversion in southern Britain. *Journal of the Geological Society*, 311-322.

Chadwick, R., Kenolty, N., & Whittaker, A. (1983). Crustal Structure beneath southern England from deep seismic reflection profiles. *Journal of the Geological Society*, 893-911.

Christian, L. (1997). Cretaceous subsurface geology of the Middle East region. *GeoArabia*, 239–255.

Cooke, M., & Underwood, C. (2001). Fracture termination and step-over at bedding interfaces due to frictional slip and interface opening. *Journal of Structural Geology*, 223-238.

Cosgrove, J. W. (2001). Hydraulic fracturing during the formation and deformation of a basin: A factor in the dewatering of low-permeability sediments. *AAPG Bulletin V. 85, N°4*, 737-748.

Cosgrove, J. W. (2005). Fractures (Including Joints). *Tectonics*, 352-361.

Cosgrove, J. W., & Hudson, J. A. (2016). *Structural Geology and Rock Engineering* . London: ICP.

Daneshy, A. A. (1978). Hydraulic Fracture Propagation in Layered Formations. *Society of Petroleum Engineers*.

Davies, R., & al. (2012). Hydraulic fractures: How far can they go? *Marine and Petroleum Geology (Elsevier)*.

de Borst, R., & al., e. (2004). Discrete vs smeared crack models for concrete fracture: bridging the gap. *INTERNATIONAL JOURNAL FOR NUMERICAL AND ANALYTICAL METHODS IN GEOMECHANICS*, 583-607.

Detournay, & Cheng. (1993). Fundamentals of Poroelasticity. In C. Fairhurst, *Comprehensive Rock Engineering: Principles, Practice and Projects, Vol. II, Analysis and design method* (pp. 113-171). Pergamon.

Dill, H., & al, e. (2003). Lithological and structural evolution of the norhtern sector of the Dukhan Anticline, Qatar, during early Tertiary: with special reference to bounding surfaces of sequence stratigraphical relevance. *Geoarabia*, 201-226.

Dill, H., Nasir, S., & Al-Saad, H. (2003). Lithological and structural evolution of the northern sector of the Dukhan Anticline, Qatar, during the early Tertiary: with special reference to bounding surfaces of sequence stratigraphical relevance. *GeoArabia*, 201-226.

Dollar, A., & Steif, P. S. (1989). A Tension Crack Impinging Upon Frictionai interfaces. *Journal of Applied Mechanics*, 291-298.

Downey, M. (1994). Hydrocarbon Seal Rocks. In L. Magoon, & W. Dow, *The Petroleum System - from source to trap* (pp. 159-164). AAPG Memoir 60.

Edgell, H. (1996). Salt tectonism in the Persian Gulf. In G. Alsop, D.J.Blundell, & I. Davison, *Salt Tectonics* (pp. 129-151). The Geological Society Publishing House.

Eekelen, H. A. (1982). Hydraulic Fracture Geometry:Fracture Containment in Layered Formations. *SPE Journal* .

Engelder, T. (1993). *Stress Regimes in the Lithosphere.* Princeton University Press.

Engelder, T., & Peacock, D. (2001). Joint Development Normal to regional compression during flexural-flow folding: the lilstock buttress anticline, Somerset, England. *J. Structural Geology* , 259-277.

Flewitt, P., & al, e. (2010). *What is Quasi-Brittle Fracture and How to Model its Fracture Behaviour.* The FESI Bulletin: International Magazine on Engineering Structural Integrity.

Fossen, H. (2010). *Structural Geology.* Cambridge: Cambridge University Press .

Friedman, M., O., K., & French, Y. (1994). Containment of natural fractures in brittle beds of the Austin Chalk. In N. &. Laubach, *Rock Mechanics* (pp. 833-840).

Gibbins, J., & HannahChalmers. (2008, October 31). Carbon Capture and Storage. *Energy Policy*, pp. 4317–4322.

Glen, R., Hancock, P., & Whittaker, A. (2005). Basin inversion by distributed deformation: the southern margin of the Bristol Channel Basin, England. *Journal of Structural Geology*, 2113-2134.

Global CCS Institute; Parsons Brickerhoff. (2011). *Accelerating the uptake of CCS: Industrial use of captured carbon dioxide.* Global CCS Institute.

Gluyas, J., & Swarbrick, R. (2004). *Petroleum Geoscience.* Blackwell Science Ltd.

Gozalpour, F., Ren, S., & Tohidi, B. (2005). CO2 EOR and Storage in Oil Reservoirs. *Oil & Gas Science and Technology – Rev. IFP,*, pp. 537-546.

Griffith, A. A. (1921). The phenomena of rupture and flow in solids. *Philosofical transactions of the royal society of london.*

Griffith, A. A. (1926). The phenomena of rupture on flow in solids. *Phil. Trans. Roy. Soc.*, 163-198.

Gudmundsson, A. (2011). *Rock Fractures in Geological Processes.* Cambridge University Press.

Gudmundsson, A., Simmenes, T. H., Larsen, B., & Philipp, S. L. (2010). Effects of internal structure and local stresses on fracture propagation, deflection and arrest in fault zones. *Journal of Structural Geology*, 1643-1655.

Guo, L., Latham, J.-P., X. J., & Lei, Q. (2013). A Numerical Investigation of Fracture Pattern and Fracture Aperture Development in Multi-layered Rock using a Combined Finite-Discrete Element Method. *ARMA 13.* San Francisco.

Hamrin, H. (1980). *Guide to underground Mining Methods and Applications.* Stockholm : Atlas Copco.

Handin, J., & Hager, R. (1957). Experimental Deformation of Sedimentary Rocks Under Confining Pressure: Tests at Room Temperature on Dry Samples. *AAPG Bulletin*, 1-50.

Hangx, S. J., Spiers, C. J., & Peach, C. J. (2010). Mechanical behavior of anhydrite caprock and implications for CO2 sealing capacity. *JOURNAL OF GEOPHYSICAL RESEARCH.*

Hawkes, P., Fraser, A., & Einchcomb, C. G. (1998). The tectono-stratigraphic development and exploration history of the Weald and Wessex basins, Southern England, UK. In J. Underhill, *Development Evolution and Petroleum Geology of the Wessex Basin* (pp. 39-65). London: Geological Society.

Heidari, M. e. (2012). Predicting the Uniaxial Compressive and Tensile Strengths of gypsum rock by point load testing. *Rock Mech Rock Eng*, 265-273.

HELGESON, D. E., & AYDIN, A. (1991). Characteristics of joint propagation across layer interfaces in sedimentary rocks. *Journal of Structural Geology*, 897-911.

Hobbs, D. W. (1967). The Formation of Tension Joints in Sedimentary Rocks: an Explanation. *Geology Magazine* , 550-556.

Hobbs, P. R., Hallam, J. R., Forster, A., Entwisle, D. C., Jones, L. D., Cripps, A. C., . . . Meakin, J. L. (2002). *Engineering geology of British rocks and soils. Mudstones of the Mercia Mudstone Group.* Keyworth: British Geological Survey.

Howard, A., Warrington, G., Ambrose, K., & Rees, J. G. (2008). *A formational framework for the Mercia Mudstone Group (Triassic) of England and Wales.* Nottingham: BGS.

Husseini, M. (1988). The Arabian Infracambrian extensional system. *Tectonophysics*, 93–103.

Husseini, M., & Husseini, S. (1990). Origin of the Infracambrian salt basins of the Middle East. In J. Brooks, *Classic petroleum provinces* (pp. 279–292). London: Geological Society.

International Energy Agency. (2009). *Assessment of Sub-Sea Ecosystem Impacts.* UK: IEA.

IPCC. (2005). *IPCC Special Report on Carbon Dioxide Capture and Storage.* Canada: Cambridge University Press .

IPCC. (2013). *Climate Change 2013, The Physical Science Basis.* New York: Cambridge University Press.

Irwin, G. (1957). Analysis of stresses and strains near the end of a crack traversing a plate. *J. Appl. Mech*, 361-364.

JAEGER, J. C., & COOK, N. G. (1976). *Fundamentals of Rock Mechanics.* London: Chapman and Hall.

Jafari, A., & Faltinson, J. (2013). Transitioning of Existing CO2-EOR Projects to Pure CO2 Storage Projects. *SPE Unconventional Resources Conference-Canada.* Alberta - Canada: SPE.

Jowett, C., & Cathles, L. (1993). Predicting depths of gypsum dehydration in Evaporitic Sedimentary Basins. *AAPG Bulletin*, 402-413.

Kindan, T., & Cosgrove, J. (1996). The deformation of multilayers by. layer-normal compression; an experimental investigation. *Journal of Structural Geology*, 461-474.

Konert, G., Al-Afifi, A., & Al-Hajri, S. (2001). Paleozoic stratigraphy and hydrocarbon habitat of the Arabian Plate. *GeoArabia*, 407-442.

Ladeira, & Price. (1981). Relationship between fracture spacing and bed thickness. *Journal of Structural Geology,*, 179 to 183.

Lake, S. D., & Karner, G. D. (1987). The strucutre and evolution of the Wessex Basin, southeastern England: an exemple of inversion tectonics. *Tectonophysics*, 347-378.

Lama, R., Vutukuri, V., & Saluja, S. (1978). Handbook of mechanical properties of rocks. *Tech Publications*.

Larsen, B., Gudmundsson, A., Grunnaleite, I., & Sælen, G. (2010). Effects of sedimentary interfaces on fracture pattern, linkage, and cluster formation in peritidal carbonate rocks. *Marine and Petroleum Geology*, 1531-1550.

Larsen, J. W. (2004). The effects of dissolved CO2 on coal structure and properties. *International Journal of Coal Geology*, 63-70.

Latham, J., & al., e. (2012). Modelling stress dependent permeability in fractured rocks including effects of propagating and bending fractures. *International Journal of Rock Mechanics & Mining Sciences*, 100-112.

Latham, J.-P., Guo, L., X.Wang, & Xiang, J. (2012). Modelling the evolution of fractures using a combined FEM-DEM numerical method. In Q. &. Zhou, *Harmonising Rock Engineering and the Environment* (pp. 449 - 454). London.

Leeder, M., & Zeidan, R. (1977). Giant Late Jurassic Sabkhas of Arabian Tethys. *Nature*, 42-44.

Lei, Q., & al., e. (2014). Effects of geomechanical changes on the validity of a discrete fracture network representation of a realistic two dimensional fractured rock. *International Journal of Rock Mechanics & Mining Sciences*, 507-523.

Lei, Q., & Latham, J. (2015). Progressive Rock Mass Failure around a Tunnel Excavation in a Geological Formation with Discontinuities: A Numerical Study.

Lindeberg, E., & Bergmo, P. (2002). The long-term fate of CO2 injected into an aquifer. *Proceedings of the 6th International Conference on Greenhouse Gas Control Technologies* (pp. 489-494). Kyoto, Japan: Pergamon.

Loosveld, R., Bell, A., & Terken, J. (1996). The tectonic evolution of interior Oman. *GeoArabia*, 28–51.

Mandl, G. (2005). *Rock Joints - The Mechanical Genesis.* Springer.

Mandl, G. (2005). *Rock Joints: The Mechanical Genesis.* Springer.

McConaughy, D. T., & Engelder, T. (2001). Joint initiation in bedded clastic rocks. *Journal of Structural Geology*, 203-221.

Melzer, L. S. (2012). *Carbon Dioxide Enhanced Oil Recovery (CO2 EOR): Factors Involved in Adding Carbon Capture, Utilization and Storage (CCUS) to Enhanced Oil Recovery.* Midland, Texas, USA: Melzer Consulting.

Muggeridge, A., Cockin, A., Webb, K., Frampton, H., Collins, I., Moulds, T., & Salino, P. (2013). Recovery rates, enhanced oil and Technological Limits. *Phil. Trans. of the Royal Society A.*

Munjiza, A. (2004). *The Combined Finite-Discrete Element Method.* John Wiley & Sons.

MUNJIZA, A., ANDREWS, K. R., & WHITE, J. K. (1999). COMBINED SINGLE AND SMEARED CRACK MODEL IN COMBINED FINITE-DISCRETE ELEMENT ANALYSIS. *INTERNATIONAL JOURNAL FOR NUMERICAL METHODS IN ENGINEERING*, 41-57.

Murray, R. C. (1964). ORIGIN AND DIAGENESIS OF GYPSUM AND ANHYDRITE . *Journal of Sedimentary Petrology*, 512-523.

Murris, R. (1981). Middle East: Stratigraphic Evolution and oil habitat. *Geology Mijnbouw*, 467-486.

Nasir, S., Al-Saad, H., Alsayigh, A., & Weidlich, O. (2008). Geology and petrology of the Hormuz dolomite, Infra-Cambrian: Implications for the formation of the salt-cored Halul and Shraouh islands, Offshore, State of Qatar. *Journal of Asian Earth Sciences* , 353-365.

Nelson, R. (2001). *Geologic Analysis of Fractured Reservoirs.* Houston, TX: Gulf.

Nemcok, M., Gayer, R., & Miliorizos, M. (1995). Structural analysis of the inverted Bristol Channel Basin: Implications for the geometry and timing of fracture porosity. In J. &. Buchanan, *Basin Inversion* (pp. 355-392). London: Geological Society .

Odum, M. (2009, February 27). Shell Sees Global Oil Demand Doubling By 2050. (NPR, Interviewer)

Orlic, B., Heege, J. t., & Wassing, B. (2011). Assessing the integrity of fault- and top seals at CO2 storage sites. *Energy Procedia*, 4798-4805.

Osborne, J., & Swarbrick, R. E. (1997). Mechanisms for the generation of overpressure in Sedimentary Basins. *AAPG Bulletin*, 1023-1041.

Peacock, D. C., & Sanderson, D. J. (1999). Deformation history and basin-controlling faults in the Mesozoic sedimentary rocks of the Somerset coast. *Proceedings of the Geologists' Association*, 41-52.

Perotti, C., Carruba, S., Rinaldi, M., Bertozzi, G., Feltre, L., & Rahimi, M. (2011). The Qatar–South Fars Arch Developmen t(Arabian Platform, Persian Gulf): Insights from Seismic Interpretation and Analogue Modelling. *New Frontiers in Tectonic Research - At the Midst of Plate Convergence*, 326-352.

Pollastro, R. (2003). *Total petroleum systems of the Paleozoic and Jurassic, Greater Ghawar Uplift and adjoining provinces of Central Saudi Arabia and Northern Arabia-Persian Gulf.* United States Geological Survey Bulletin.

Price, N. (1960). The compressive strength of cal measure rocks. *Colliery Eng.*, pp. 106-118.

Price, N. J. (1066). *Fault and joint development in Brittle and semi-brittle rock.* Oxford: Pergamon Press.

Price, N., & Cosgrove, J. (1990). *Analysis of Geological Structures.* Cambridge: Cambridge University Press.

Purcell, W. (1949). Capillary Pressures - Their measurement using mercury and the calculation of permeability there from. *Petroleum Transactions, American Institute of Mining Engineers, v. 186*, 39-48.

Ramsay, J. G. (1967). *Folding and Fracturing of Rocks.* New York: McGraw-Hill.

Rehbinder, P., & Lichtman, V. (1957). Effects of surface active media in strain and rupture in solids. *Proceedings of the International Congress on Surface Activity*, (p. 563).

Renshaw, C., & Pollard, D. (1995). An Experimentally Verified Criterion for Propagation Across Unbounded Frictional Interfaces in Brittle,Linear Elastic Materials. *Journal of Rock Mechanics* , 237-249.

Rijken, P., & Cooke, M. L. (2001). Role of shale thicknes on vertical connectivity of fractures: application of crack-bridging theory to the Austin Chalk: Texas. *Tectonophysics*, 117-133.

Rives, T., Razack, M., Petit, J., & Rawnsley, K. (1992). Joint spacing: analogue and numerical simulations. *Journal of Structural Geology*, 925-937.

Rots, J., & Blaauwendraad, J. (1989). Crack Models for Concrete: Discrete or smeared? Fixed, multi-directional or rotating? *Heron*, 3-56.

S.C.Blair, R.K.Thorpe, Heuze, F., & Shaffer, R. (1989). Laboratory observations of the effect of geologic discontinuities on hydrofracture propagation. In *Rock Mechanics as a Guide for Efficient Utilization of Natural Resources* (pp. 443-450). Rotterdam: Balkema.

Sachs, J. D. (2008, March). Climate Change after Bali. 33-34.

Sachs, J. D. (2014, January 22). The challenge of deep decarbonisation. *Gulf News.* Retrieved from http://gulfnews.com/opinions/columnists/the-challenge-of-deep-decarbonisation-1.1280798

Sandrea, I., & Sandrea, R. (2007). Recovery factors leave vast target for EOR technologies. *Oil Gas Journal*, 44-47.

Scheldt, T. (2002). *Comparison of Continuous and Discontinuous Modelling for Computational Rock Mechanics.* Department of Geology and Mineral Resources Engineering Norwegian University of Science and Technology.

Scheldt, T. (2002). *Review of Numerical Methods in Rock Mechanics.* Department of Geology and Mineral Resources Engineering.

Secor, D. (1965). Role of Fluid Pressure in Jointing . *American Journal of Science* , 633-646.

SEED - Schlumberger. (2014). *Planet Seed* . Retrieved from http://www.planetseed.com/relatedarticle/weyburn-oil-field-enhanced-oil-recovery

SEED - Schlumberger. (2014). *SEED.* Retrieved from http://www.planetseed.com/relatedarticle/sleipner-carbon-dioxide-capture-and-storage-project

Sharland, P., Archer, R., Casey, D., Davies, R., Hall, S., Heward, A., . . . Simmons, M. (2001). *Arabian Plate sequence stratigraphy.* Bahrain: GeoArabia.

Shearman, D., Mossop, G., Dunsmore, H., & Martin, M. (1972). Origin of Gypsum veins by hydraulic fracturing. *Inst Min Metall Trans*, 149-155.

Shoulders, S. J., Cartwright, J., & Huusec, M. (2007). Large-scale conical sandstone intrusions and polygonal fault systems in Tranche 6, Faroe-Shetland Basin. *Marine and Petroleum Geology*, 173-188.

Simoson, E., Sayed, A. A., & Clifton, R. (1978). Containment of Massive Hydraulic Fractures. *SPE.*

Singh, R., & Eksi, M. (1987). Rock Characterization of Gypsum and Marl. *Minin Science and Technology*, 105-112.

Smith, D. A. (1966). Theoretical Considerations of Sealing and Non-Sealing Faults. *AAPG Bulletin*, 363-374.

Stampfli, G. &. (2004). The TRANSMED Transects in Space and Time: Constraints on the Paleotectonic Evolution of the Mediterranean Domain. In W. Cavazza, F.Roure, W. Spakman, G. Stampfli, & P. Ziegler, *The TRANSMED Atlas: the Mediterranean Region from Crust to Mantle* (pp. 53-80). Springer-Verlag.

Stearns, D., & Friedman, M. (Exploration Methods, and Case Histories). Reservoirs in fractured rock. In R. K. (Ed), *Stratigraphic Oil and Gas Fields-Classification* (pp. 82-106). AAPG .

Stern, R., & Johnson, P. (2010). Continental lithosphere of the Arabian Plate: A geologic, petrologic, and geophysical synthesis. *Earth Science Reviews*, 29–67.

Steve Whittaker, PTRC. (2010). *IEA GHG Weyburn-Midale CO2 Storage & Monitoring Project.* PTRC.

T., B., Pollard, D., & Gao, H. (2000). Explanation for fracture spacing in layered materials . *Nature*, 753-756.

Teufel, L. W., & Clark, J. A. (1984). Hydraulic Fracture Propagation in Layered Rock: Experimental Studies of Fracture Containment. *SPE Journal*, 19-32.

Todd, A. C., & al., e. (2011). CCS – A multidisciplinary global activity for a global challenge. *Journal of the European Federation of Chemical Engineering*, 1443-1445.

Underhill, J. R., & Stoneley, R. (1998). Introduction to the development, evolution and petroleum geology of the Wessex Basin. In J. Underhill, *Development, Evolution and Petroleum Geology of the Wessex Basin* (pp. 1-18). London: Geological Society.

USGS. (2008). *Circum-Artic Resource Appraisal.* USGS .

Vidal-Gilbert, S., Nauroy, J. F., & Brosse, E. (2008). 3D geomechanical modelling for CO2 geologic storage in the Dogger carbonates of the Paris Basin. *International Journal of Greenhouse Gas Control*, 288-299.

Warpinski, N., & Teufel, L. (1987). Influence of Geologic Discontinuities on Hydraulic Fracture Propagation. *Journal of Petroleum Technology*, 209-220.

Warren, J. K. (2007). *Evaporites. Sediments, Resources and Hydrocarbons.* Germany: Springer.

Watts, N. L. (1987). Theoretical aspects of cap-rock and fault seals for single- and two-phase hydrocarbon columns. *Marine and Petroleum Geology, Vol 4, November*, 274-307.

Wender, L., Bryant, J., Dickens, M., Neville, A., & Al-Moqbel, A. (1998). Paleozoic (Pre-Khuff) Hydrocarbon Geology of the Ghawar Area, Eastern Saudi Arabia. *GeoArabia*, 273-302.

West, I. (1975). *Evaporites and associated sediments of the basal Purbeck Formation (Upper Jurassic) of Dorset.*

Whittaker, A., & Green, G. (1983). Geology of the country around Weston-super-Mare. *Memoir of the Geological Survey*.

Wikipedia. (2005). *Wikipedia.* Retrieved from http://en.wikipedia.org/wiki/Supercritical_carbon_dioxide

World Bank - PIK. (2012). *4º, Turn Down the Heat. Why a 4ºC Warmer World Must Be Avoided.* New York: World Bank.

Wu, H., & Pollard, D. D. (1995). An Experimental Study of the Relationship between joint spacing and layer thickness. *Journal of Structural Geology* , 887- 905.

Zhang, X., Jeffrey, R. G., & Thiercelin, M. (2007). Deflection and propagation of fluid-driven fractures at frictional bedding interfaces: A numerical investigation. *Journal of Structural Geology*, 396-410.

Ziegler, M. A. (2001). Late Permian to Holocene Paleofacies Evolution of the Arabian Plate and its Hydrocarbon Occurrences. *GeoArabia, Vol. 6,*.